Crystallography Reports, Vol. 48, No. 4, 2003, pp. 531–535. Translated from Kristallografiya, Vol. 48, No. 4, 2003, pp. 583–587.

CRYSTAL CHEMISTRY

Short Range Order in Powder of Amorphous Anodic Yttrium Oxide

L. A. Aleshina and S. V. Loginova

Petrozavodsk State University, pr. Lenina 33, Petrozavodsk, 185640 Russia

e-mail: svlog@mainpqu.karelia.ru

Received August 23, 2002

Abstract—The characteristics of the short-range order in a powder of amorphous yttrium oxide obtained by anodic oxidation are determined by the Finbak–Warren method. It is established that the first coordination number equals seven. Amorphous oxide is built by irregular coordination polyhedra characteristic of the hexagonal and monoclinic modifications of yttrium oxide. © *2003 MAIK "Nauka/Interperiodica".*

Yttrium oxide is widely used in planar optical devices for electroluminescent screens, in germanium- and silicon-based MIS varicaps and transistors, photoelectric instruments, and nuclear technology. The oxide studied here is one of the most popular materials in micro- and optoelectronics and devices for displaying information. Thin Y_2O_3 films are also used as barriers, efficient luminophor matrices, and dielectric interlayers.

Amorphous Y_2O_3 oxide was studied in a limited number of publications [1]. The present study aimed to determine the short-range order characteristics of amorphous anodic Y_2O_3 oxide. We studied an amorphous yttrium oxide powder obtained by anodic oxidation. X-ray diffraction study of the samples was performed in reflection geometry on a DRON-4.0 diffractometer in automatic mode (Fe- and AgK_α radiations). A graphite monochromator was placed into a reflected beam. The maximum value of the diffraction vector $s = \frac{4\pi\sin\theta}{\lambda}$ was 9.45 Å^{-1}.

All the necessary corrections were introduced into the experimental intensity-distribution curves [2–4]. The recalculation to electron units was made by the Warren method [5]. Figures 1a–1c show the intensity distribution curves $I(s)$ in electron units; s-weighted interference functions $H(s)$ multiplied by the attenuation factor $\exp(-\alpha^2 s^2)$, where $\alpha = 0.1$; and the distribution curves of pair functions $D(r)$, respectively. The details of the $H(s)$ and $D(r)$ calculation can be found elsewhere [2, 4–6].

The Finbak–Warren representation [5, 6] of the $D(r)$ curve as a sum of pair functions,

$$D_{\text{obs}}(r) = \sum_i \sum_j \frac{N_{ij}}{r_{ij}} P_{ij}(r),$$

is the convolution of the pair function $P'_{ij}(r) = \int_0^{s_{\max}} f_i(s) f_j(s) g^{-2}(s) \exp(-(\alpha^2 + \sigma_{ij}^2)s^2)\sin(sr_{ij})\sin(sr)ds$ with the function of spreading of coordination spheres in an amorphous material given in the form of a Gaussian $G_{ij}(r, r_{ij}) = A\exp\left(-\frac{(r - r_{ij})^2}{\sigma_{ij}^2}\right)$. This representation allowed us to calculate the coordination numbers N_{ij} by the least squares method under the condition that the radii of the coordination spheres r_{ij} are known. The method of these calculations was considered elsewhere [2].

In the first approximation, the radii of the coordination spheres were set based on the corresponding data for cubic yttrium oxide, the only phase which is stable under normal conditions. The finite r_{ij} and σ_{ij} values were selected by the method of successive approximations in such a way that the discrepancy between the observed curves and the curves calculated from the obtained set of N_{ij}, r_{ij}, and σ_{ij} curves did not exceed 5% [2–4].

It is well known that the cubic Y_2O_3 phase is related to the Mn_2O_3 structure type (a = 10.6038 Å, sp. gr. $Ia3$) with the structure built by regular and distorted octahedra [7] (Fig. 2a). The Y–O distance in regular octahedra equals 2.284 Å, the average distance in distorted octahedra equals 2.282 Å, with the coordination number being equal to six. Nevertheless, the calculations showed that the Y–O distance in amorphous oxide is much larger, 2.39 Å, whereas the first coordination number equals seven.

Polymorphous transformations in RE metal oxides were studied elsewhere [8]. It was shown [9] that, with an increase in temperature, the structure of yttrium oxide changes from cubic to hexagonal and, with an increase in pressure, from cubic to monoclinic.

1063-7745/03/4804-0531$24.00 © 2003 MAIK "Nauka/Interperiodica"

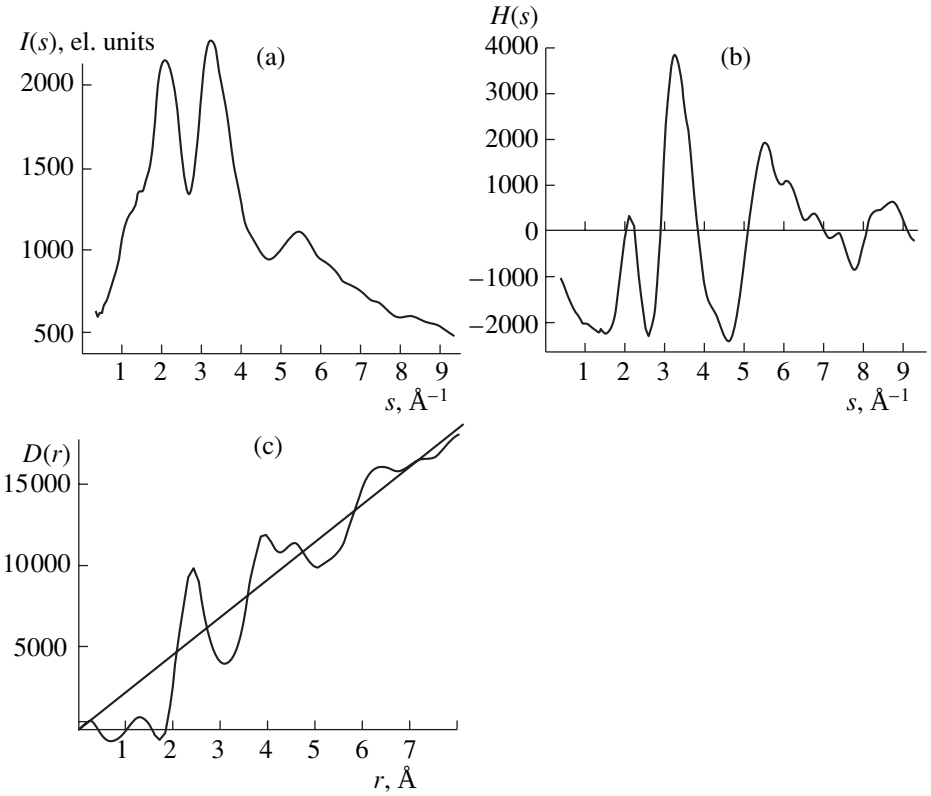

Fig. 1. Distribution of (a) scattered intensities, (b) the *s*-weighted interference function, and (c) pair functions for a powder of the yttrium oxide.

The hexagonal phase is of the La_2O_3 structure type (sp. gr. $P\bar{3}m$, $a = 3.807$ Å and $c = 6.081$ Å [9]). Figure 2b shows the projection of six unit cells of this phase onto the *ac* plane. The Y–O distances in hexagonal yttrium oxide are 2.36 and 2.6 Å for three oxygen atoms, 2.6 Å for three other oxygen atoms, while the seventh atom lies at a distance of 2.43 Å from yttrium, so that the first coordination number equals seven and the average shortest Y–O distance equals 2.47 Å, which exceeds the radius of the first coordination sphere in the amorphous powder studied.

The shortest Y–Y distance in cubic and hexagonal oxides is 3.52 and 3.56 Å, respectively. In the amorphous oxide, this distance is considerably longer, 3.78 Å, despite the fact that the number of Y–Y pairs at this distance corresponds to the respective data for the cubic oxides (see table). The next Y–Y pairs are spaced at distances of 4.02 Å in the cubic oxide, but the contribution to the electron density of this sphere also comes from the Y–O pairs, so that the average weighted radius equals 4.12 Å and the coordination number calculated from the area under the sum of pair functions P_{Y-Y} and P_{Y-O} by the methods suggested in [2] equals 7.5. In the hexagonal oxide, the contribution to the corresponding sphere also comes from the Y–O pairs; therefore the average weighted radius equals 3.85 Å and the coordination number equals 9.34. In the amorphous oxide, this distance is slightly overestimated (4.15 Å); in contrast, the coordination number is underestimated in comparison with both phases and equals 6.5.

The analysis of the next Y–O sphere (table) allows one to see the differences in the radii of coordination spheres and coordination numbers calculated for the cubic and hexagonal phases and the corresponding data for the amorphous oxide. Thus, the cubic oxide has no sphere characteristic of the amorphous oxide (4.88 Å). The coordination number of this sphere in amorphous oxide equals 2.90. At the same time, the cubic oxide has a sphere with $r = 4.73$ Å (c.n. = 7.54), which is absent in both hexagonal and amorphous oxides.

The position of the Y–O sphere with $r = 4.60$ Å in the hexagonal oxide coincides with the position of the corresponding sphere in the amorphous oxide. However, the coordination number of this sphere in the hexagonal modification is twice as high as the coordination number of this sphere in the amorphous oxide.

The next Y–O sphere (5.09 Å) in the hexagonal oxide is displaced toward larger *r* values with respect to the corresponding value for the powder oxide. The coordination number of this sphere (4.84) is overestimated in comparison with the data for the amorphous oxide (6.10).

The Y–Y sphere in the cubic and hexagonal oxides (5.35 and 5.36 Å, respectively) is displaced toward

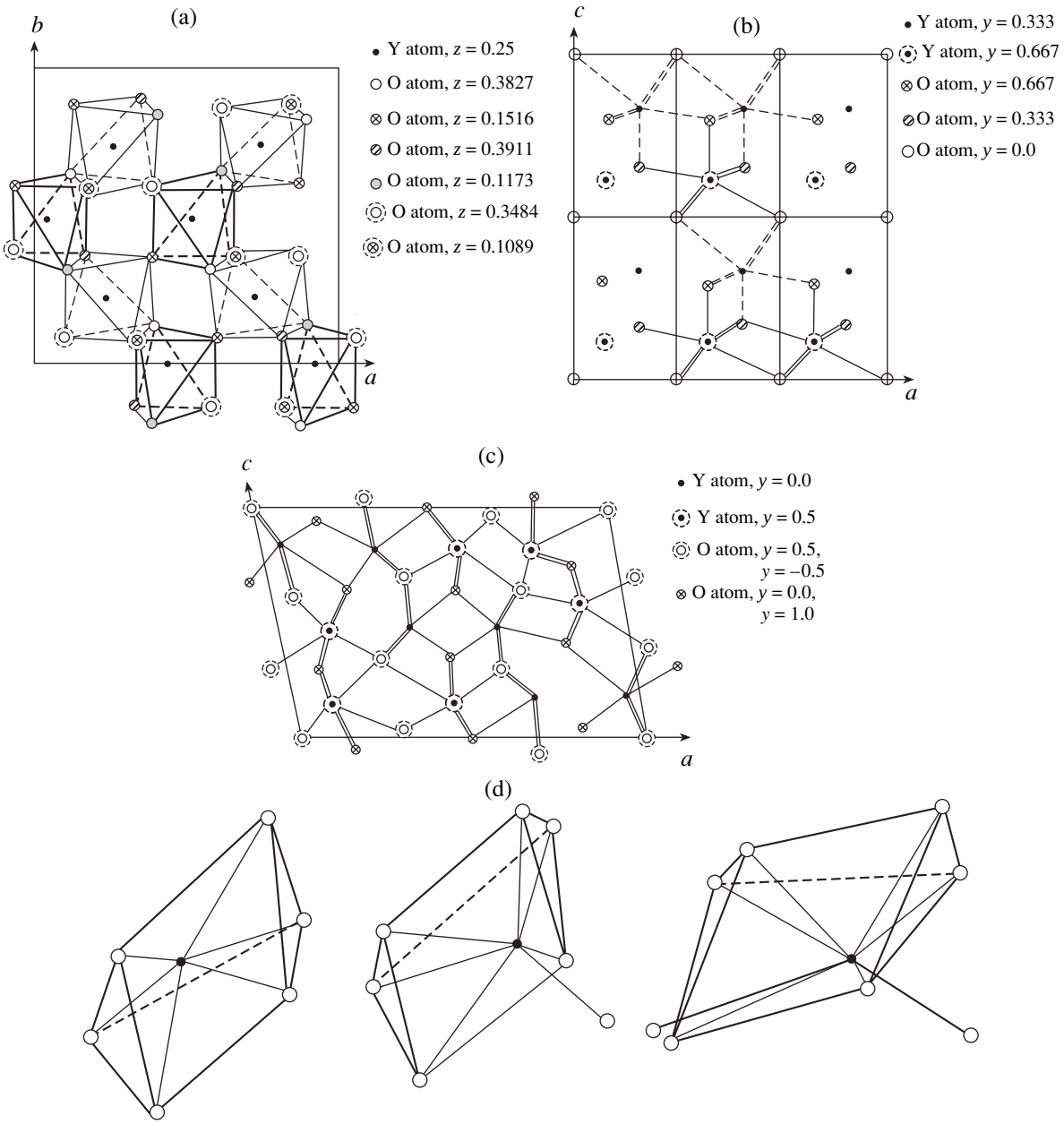

Fig. 2. Atomic arrangements in various modifications of yttrium oxide projected onto the *ac* plane: (a) cubic, (b) hexagonal, (c) monoclinic modification, and (d) coordination polyhedra for three yttrium atoms in the model of the monoclinic Y_2O_3 phase.

smaller *r* values in comparison with the corresponding value for the amorphous oxide. The coordination numbers of this sphere are practically equal for both crystalline and amorphous modifications.

The study of deposited films [1] showed that the specific feature of the formation of the short-range order in their structures is the appearance of the monoclinic phase and an increase in its relative content in comparison with the content of the cubic phase with an increase in the oxygen content in the atmosphere during sputtering. Therefore, at the next stage of the study, it was necessary to calculate the radii of the coordination spheres and coordination numbers for monoclinic yttrium oxide. The monoclinic phase is of the Sm_2O_3 structure type [9–11] (Fig. 2c). The atomic coordinates of the monoclinic Y_2O_3 are unknown, and, therefore, the unit cell of this phase was constructed based on the data for Sm_2O_3 and the transition to the lattice of monoclinic Y_2O_3. The atoms were located in the basic group proceeding from crystallochemical considerations. Figure 2d shows the coordination polyhedra of three yttrium atoms. One of these atoms is surrounded by six oxygens forming a prism. The second yttrium atom is surrounded by seven oxygen atoms, and the coordina-

Radii r_{ij}, spreading of the coordination spheres σ_{ij}, and coordination numbers N_{ij} for a powder of amorphous anodic yttrium oxide and the corresponding data for the cubic, hexagonal, and monoclinic crystalline modifications

Type of sphere	r_{ij} av, Å	N_{ij}	r_{ij} av $\pm \Delta r_{ij}$, Å	N_{ij}	r_{ij} av $\pm \Delta r_{ij}$, Å	N_{ij}	r_{ij} av, Å	N_{ij}	r_{ij}, Å	σ_{ij}, Å	N_{ij}
	cubic phase		hexagonal phase		monoclinic phase		mixture of hexagonal and monoclinic phases (1 : 1)		experimental data for powder oxide		
Y–O	2.28	6	2.47 ± 0.12	7	2.42 ± 0.34	7.0	2.45	7.0	2.39 ± 0.00	0.18 ± 0.00	7.04 ± 0.02
O–O	2.99	5	3.00 ± 0.22	6	2.80 ± 0.15	5.55	2.90	5.8	3.01 ± 0.01	0.35 ± 0.05	8.00 ± 2.00
Y–Y	3.52	6.25	3.56 ± 0.05	3.2	3.62 ± 0.06	10.95	3.59	4.6	3.78 ± 0.01	0.78 ± 0.00	6.00 ± 1.00
Y–Y	4.12	7.48	3.85 ± 0.07	9.34	4.10 ± 0.10	2.05	3.98	7.8	4.15 ± 0.00	0.67 ± 0.02	6.50 ± 0.50
Y–O	4.42	6.92	4.60 ± 0.1	14.22	4.49 ± 0.39	5.24	4.55	13.6	4.60 ± 0.00	0.61 ± 0.05	7.00 ± 2.00
Y–O	4.73	7.54									
Y–O			5.09 ± 0.14	4.84	4.88 ± 0.37	2.90	4.99	3.9	4.92 ± 0.02	0.30 ± 0.00	6.10 ± 0.70
Y–Y	5.35	7.23	5.36 ± 0.11	7.85	5.33 ± 0.42	7.48	5.35	8.8	5.46 ± 0.00	0.50 ± 0.01	7.50 ± 0.50
Y–O	5.75	9.08	5.92 ± 0.18	13.23	5.89 ± 0.14	5.67	5.91	9.4	5.90 ± 0.00	0.37 ± 0.02	9.80 ± 1.00
Y–Y	6.07	5.73			6.20 ± 0.34	16.53	6.20	8.7	6.25 ± 0.00	0.51 ± 0.01	5.90 ± 0.50
			6.35 ± 0.17	9.61							
Y–Y	6.36	8.76			6.60 ± 0.04	4.46	6.55	13.2	6.60 ± 0.06	0.65 ± 0.02	18.00 ± 1.0
Y–Y	6.64	9.48	6.64 ± 0.11	12.4							

Note: Δr_{ij} is the scatter in the interatomic distances in the crystalline phases.

tion polyhedron of this yttrium atom is a prism with one additional oxygen atom lying at a distance of 2.25 Å. The third yttrium atom is surrounded by eight oxygen atoms, of which three form a triangular prism, while two oxygen atoms lie at distances of 2.24 and 3.40 Å from the yttrium atom. According to [1], each samarium atom in monoclinic Sm_2O_3 is surrounded by seven oxygen atoms. The coordination polyhedron around one of the samarium atoms is a distorted octahedron, with the seventh oxygen atom being located on the threefold axis. The coordination polyhedra of two other samarium atoms are distorted triangular prisms, with the seventh oxygen atom being located on the normal to the prism surface. The Sm–O distances vary from 2.25 to 3.12 Å, but the average Sm–O distance is almost the same: 2.45, 2.44, and 2.48 Å for each of the three samarium atoms.

The first coordination sphere Y–O in the monoclinic Y_2O_3 phase has the radius 2.42 Å and c.n. = 7. The radius of the first coordination sphere for the amorphous powder is somewhat different from that of the monoclinic phase, but c.n. = 7.

The shortest O–O distance for the monoclinic modification equals 2.80 Å, i.e., is slightly shorter than the corresponding distance for the oxide studied here (3.01 Å). The number of neighbors on this sphere for the crystalline phase is 5.55, whereas for the amorphous powder, it is 8.0 ± 0.2. For the first Y–Y sphere, a slightly underestimated radius (3.62 Å) and an overestimated coordination number (10.95) are established in comparison with the corresponding data for the powder of the amorphous yttrium oxide.

The second Y–Y coordination sphere has an average radius of 4.10 Å and c.n. = 2.05. The coordination number for this sphere in the monoclinic phase is much lower in comparison with the corresponding value for the powdered amorphous oxide (6.5). However, the total values of the coordination numbers at both Y–Y spheres in the monoclinic phase practically coincide with the corresponding coordination number for the amorphous oxide. The radii and coordination numbers of next two coordination Y–O spheres in monoclinic Y_2O_3 are somewhat less than the corresponding values for the amorphous powder oxide.

The next coordination spheres of the monoclinic phase are also characterized by lower values of radii and coordination numbers than in the amorphous oxide. The only exception is c.n. = 16.53 for the Y–Y sphere with a radius of the coordination sphere of 6.20 Å for the crystalline modification. The corresponding coordination number for the amorphous oxide equals 5.9.

Thus, comparing the radii of the coordination spheres of the amorphous powder and monoclinic yttrium oxide, we could not definitively draw the conclusion that the radii of the coordination spheres of amorphous powder correspond to the radii of the coordination spheres of monoclinic oxide (table). Since the value of the first coordination number in the amorphous oxide coincides with the corresponding data for the monoclinic and hexagonal phases, one can assume that the amorphous oxide has the coordination polyhedra

inherent in both crystalline phases. The table lists the average radii of the coordination spheres and the coordination numbers of the monoclinic and hexagonal phases. It is seen that the correspondence of the coordination numbers and the radii of the coordination spheres to the values calculated based on the experimental data has been improved. The slight discrepancy between these values may indicate that, instead of a simple mixture of two phases, one has to consider a network of polyhedra of both types. This conclusion is also supported by the fact that the spreading of the coordination spheres in the amorphous oxide is more pronounced than the scatter in the interatomic distances in the crystalline phases.

Thus, a film of the amorphous anodic oxide Y_2O_3 is characterized by a first coordination number equal to seven and the existence of irregular coordination polyhedra.

ACKNOWLEDGMENTS

This study was supported by the foundation "Universities of Russia" (UR 01.01.038) and the American Foundation of Civil Research and Development of Post Soviet Union independent States and Ministry of Education of Russian Federation, project no. PZ-013-02.

REFERENCES

1. M. Ya. Gryziv, V. D. Bondar, and S. I. Chykhriĭ, Neorg. Mater. **32** (11), 1372 (1996).
2. L. A. Lugovskaya, L. A. Aleshina, G. M. Kalibaeva, and A. D. Fofanov, Acta Crystallogr. Sect. B: Struct. Sci. **58**, 576 (2002).
3. L. A. Aleshina, V. P. Malinenko, A. D. Phouphanov, and N. M. Yakovleva, J. Non-Cryst. Solids **87**, 350 (1986).
4. B. E. Warren, Kristallografiya **16** (6), 1264 (1971) [Sov. Phys. Crystallogr. **16**, 1106 (1971)].
5. R. L. Mozzi and B. E. Warren, J. Appl. Crystallogr. **3**, 251 (1970).
6. L. A. Aleshina and S. V. Loginova, Kondens. Sredy Mezhfaz. Granitsy **4** (1), 48 (2002).
7. L. Smrcok, Cryst. Res. Technol. **24** (6), 607 (1989).
8. H. R. Hoekstra, Inorg. Chem. **5**, 754 (1966).
9. M. Foex and J.-P. Traverse, Rev. Int. Hautes Temp. Refract. **3**, 429 (1966).
10. T. Atou, J. Solid State Chem. **89**, 378 (1990).
11. D. T. Cromer, J. Phys. Chem. **61**, 753 (1957).

Translated by L. Man

Crystallography Reports, Vol. 48, No. 4, 2003, pp. 536–541. Translated from Kristallografiya, Vol. 48, No. 4, 2003, pp. 588–593.

CRYSTAL CHEMISTRY

Crystallochemical Analysis of Succinic and Maleic Anhydrides

P. M. Zorky, A. E. Obodovskaya, and N. G. Panina

Faculty of Chemistry, Moscow State University, Vorob'evy gory, Moscow, 119992 Russia

e-mail: pmzorky@phys.chem.msu.ru

Received February 27, 2002

Abstract—To reveal characteristic features of the arrangement of molecules in crystals of succinic and maleic anhydrides belonging to the structural class $P2_12_12_1$, $Z = 4(1)$, the energies of molecular interactions were calculated and the shortest intermolecular contacts were examined. The contacts between oxygen atoms and between oxygen and other atoms were analyzed to determine the optimum van der Waals radius of oxygen (R_0). The computations were performed using the CCA program designed for standard crystallochemical analysis. It was found that succinic and maleic anhydrides have analogous structures containing the same type of molecular agglomerates, which allowed us to relate these compounds to the same subclass. The present study confirmed the value $R_0 = 1.29$ Å recommended earlier by Zefirov and Zorky. © *2003 MAIK "Nauka/Interperiodica".*

INTRODUCTION

In recent years, the characteristic features of the molecular arrangement in organic crystals have increasingly attracted the attention of researchers. This interest was stimulated, in particular, by the vigorous progress in supramolecular chemistry, defined by one of its founders, J.-M. Lehn, as "chemistry beyond the molecule" [1]. This does not involve the well-known universal laws and rules, such as the principle of close molecular packing or the principle of the minimum free (or potential) energy of crystals. Here, one is interested in the individual features of the molecular arrangement associated with the nature of a particular chemical compound.

At the same time one can study, first, local characteristics that manifest themselves in certain molecule–molecule contacts and intermolecular atom–atom contacts and, second, the crystal structure as a whole which can be reflected, e.g., in the structural class or subclass [2, 3]. However, usually, the latter aspect (description and analysis of the crystal structure as a whole) escapes the attention of researchers.

Abundant information on both the above aspects of organic crystal chemistry can be obtained from the Cambridge Structural Database (CSD; www.ccdc.cam.ac.uk/prods/csd/csd.html), where the results of numerous X-ray and neutron diffraction studies have been accumulated. Presently, the data on approximately 64 000 organic crystal structures are available from the CSD, and this information continues to increase rapidly.[1] Whereas the description of the conformational characteristics of molecules is based on the concepts, terms, and approaches more or less known and theoretically justified, analysis of the arrangement of molecules in organic crystals does not invoke the commonly accepted standard approaches and is most often limited to the detection of intermolecular hydrogen bonds and the shortest atom–atom distances close to the sums of the corresponding van der Walls radii. Meanwhile, many important fields of modern chemistry (supramolecular chemistry, surface chemistry, etc.) require detailed study of molecule arrangements in crystals and other condensed systems and also of molecular interactions responsible for molecule arrangement.

The concepts and approaches necessary for the development of the crystal-structural aspect of organic crystal chemistry were elaborated in sufficient detail in earlier studies [2, 3]. However, one should make certain efforts to master the application of these concepts and

[1] We call organic compounds those that necessarily include carbon and some of the following nonmetal elements: H, *Hal*, O, S, Se, Te, N, P, As, Si, and B. Today, the CSD contains more than 245 000 entries concerning the results of X-ray and neutron diffraction studies of crystals containing "organic" carbon. However, many of these compounds do not satisfy this definition, because they contain not only the above-mentioned atoms but also some other elements. Also, some entries repeat each other (studies performed by different researchers, in different years, at different temperatures, etc.). Hence, the exact number of different crystal structures can be established only after time-consuming analysis.

1063-7745/03/4804-0536$24.00 © 2003 MAIK "Nauka/Interperiodica"

the corresponding nomenclature. One of the aims of the present study is to clearly demonstrate the application of some of these concepts to the analysis of structures of some organic crystals.

Among the most important crystal-structural notions are *structural class* and *structural subclass*. The structural class units crystal structures described by the same space group and the same distribution of molecules (more precisely, of their centers of mass) over the systems of equivalent positions (orbits). In a homomolecular organic crystal, the molecules usually occupy one system of general (asymmetric) positions. The most widespread structural classes are $P2_1/c$, Z = 4(1) and $P\bar{1}$, Z = 2(1) in racemates and the structural classes $P2_12_12_1$, Z = 4(1) and $P2_1$, Z = 2(1) in chiral crystals [2].

Computation of the energies of interactions between "neighboring" (contacting) molecules in organic crystals showed that these energies (U_{MM}) can substantially differ (by a factor of 1.5–2 or even more).[2] This fact allows one to state that organic crystals usually contain molecular agglomerates, namely, ensembles of molecules most strongly interacting with each other (most strongly bound to each other). Agglomerates can consist of a finite number of molecules (dimers, trimers, etc.) or of all the molecules of the crystal (three-dimensional frameworks), but more often, such agglomerates have the form of chains or layers. Usually, molecules forming an agglomerate are transformed into each other by certain symmetry elements and, consequently, the agglomerate is characterized by a certain symmetry group. Determining the distribution of molecules over the systems of equivalent positions (orbits) of this group, we establish, in fact, the structural class of the agglomerate, for example, P_c2_1, Z = 2(1) or P_l2_1, Z = 2(1) (subscripts c and l correspond to the symmetry groups of a chain or a layer, respectively).

The *structural subclass* is formed by crystal structures that are related to the same structural class and contain molecular agglomerates of the same type, which are identically oriented relative to the coordinate system of the crystal. In principle, the method of potential-function symmetry [2] allows one to enumerate all the structural subclasses possible in a particular structural class. However, subclasses not necessarily have the same number of representatives. The problem of the relative frequency of occurrence of possible subclasses is a subject of special study.

In the structural class $P2_12_12_1$, Z = 4(1) (Fig. 1), whose representatives are considered in the present study, two subclasses are the most probable and, apparently, the most widespread,

$$1-P_{c(z)}2_1,\ Z = 2(1) \uparrow\downarrow P2_12_12_1,\ Z = 4(1),$$

$$1-P_{c(z)}2_1,\ Z = 2(1) \uparrow\uparrow P_{l(xz)}2_1,$$

$$Z = 2(1) \uparrow\downarrow P2_12_12_1,\ Z = 4(1).$$

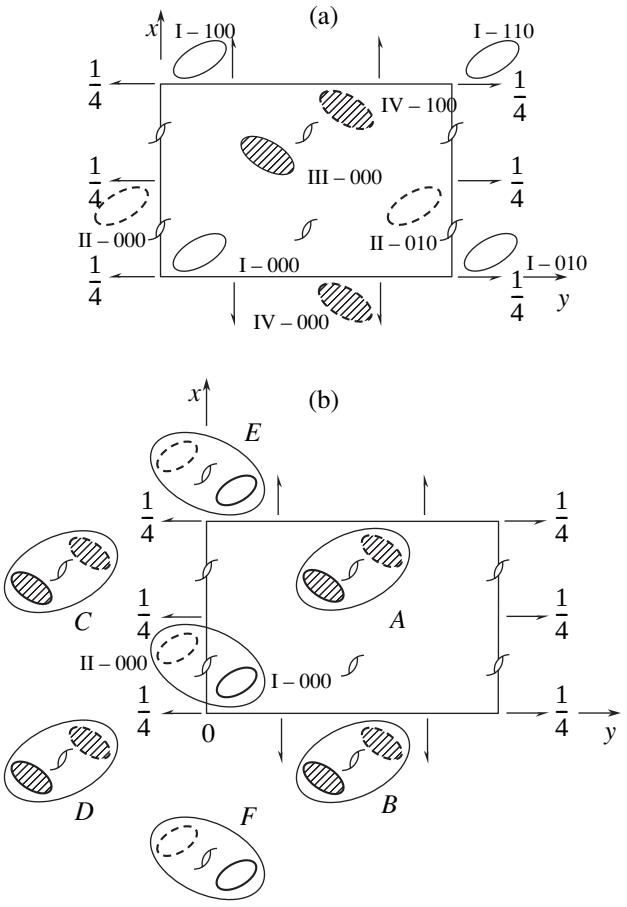

Fig. 1. Schematic representation of the arrangement of molecules in the structural class $P2_12_12_1$, Z = 4(1). The molecules indicated by solid and dashed contours are located at heights $z = z_0$ and $z = z_0 + 1/2$, respectively. The shaded molecules are seen from the opposite side (these molecules are turned over). (a) Projection of the unit cell and (b) projection showing the initial chain surrounded by analogous *A*–*F* chains. The molecules of one chain along the *z* axis are indicated by thin ellipsoids. In the general case, the molecules are indicated as N-HKL, where N is a Roman numeral indicating the molecule orientation, and H, K, and L are integers that denote the translational shifts in each of the four sublattices of the molecules.

The above notation has the following meaning. If $|U_{II–000}|$ has the maximum value of all $|U_{MM}|$ energies (in fact, this is true for any molecule related to the initial molecule I-000 by one of the twofold screw axes 2_1; such a molecule can be transformed into the molecule II-000 by the corresponding transformation of the coordinate system), then the primary molecular agglomerate of the crystal consists of the $P_{c(z)}2_1$ chains, Z = 2(1).

[2] In a homomolecular crystal, 14 or 12 neighboring molecules are generally involved in the environment of each molecule [4].

The antiparallel superposition of these chains gives rise to four equivalent chain–chain contacts generating a crystal of the structural class $P2_12_12_1$, $Z = 4(1)$ related to the first subclass [2]. One such contact is seen in Fig. 1a. The initial chain containing the molecules I-000 and II-000 is in contact with the chain containing the molecules III-000 and IV-000. Figure 1b shows four equivalent chain–chain contacts. If the strongest chain–chain interaction takes place between the parallel $P_{c(z)}2_1$ chains, $Z = 2(1)$ spaced at a distance equal to the lattice period (for definiteness, let it be the *a* period), the superposition of the chains gives rise to the formation of the layer $P_{l(xz)}2_1$, $Z = 2(1)$. Figure 1a shows only the I-000 molecule of the chain spaced at the *a* period from the initial chain. Figure 1b gives a more complete view of the structure as a whole. The antiparallel superposition of these layers leads again to the class $P2_12_12_1$, $Z = 4(1)$ but in the variant corresponding to the second subclass.

In principle, other subclasses of the structural class under consideration are also possible. However, as was indicated, the above two subclasses seem to be most probable. To verify this assumption, it is necessary to perform corresponding computations for a large number of crystal structures of this class. We plan such computations in future.

OBJECTS OF STUDY

To begin with, we considered the simplest objects—the compounds with small molecules composed of the minimum set of chemical elements. These are succinic $C_4H_4O_3$ (**I**) and maleic $C_4H_2O_3$ (**II**) anhydrides:

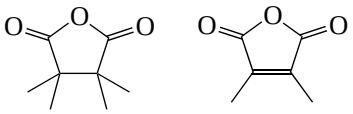

(**I**) (**II**)

The crystallographic data [5, 6] were taken from the Cambridge Structure Database (refcodes SUCANH and MLEICA, respectively). The unit-cell parameters (Å) of these compounds are

	a	*b*	*c*
$C_4H_4O_3$	6.963	11.710	5.402
$C_4H_2O_3$	7.180	11.231	5.390

Projections of the structures are shown in Fig. 2.

COMPUTATIONAL PROCEDURE

The energies of interactions between the initial molecule I-000 and the N-HKL molecules from its nearest environment were computed in the atom–atom approximation using the original program developed in the Laboratory of Crystal Chemistry of the Faculty of Chemistry at Moscow State University:

$$U_{MM} = \sum_{i,j}(\varphi_{ij} + \psi_{ij}),$$

where *i* and *j* are the subscripts indicating atoms from different molecules.

The computations were performed using the 6–exp atom–atom potentials with the Gavezzotti and Filippini parameters [7]. The procedure recommended by these authors differs from the well-known scheme suggested in the classical study by Williams [8] and ignores the effective atomic charges and the corresponding term that takes into account Coulomb interactions. Gavezzotti and Filippini believe that the appropriately chosen parameters of the 6–exp potentials provide the correct computation of energies of molecular interactions even without allowance for atomic charges. In fact, this signifies that the atom–atom potential

$$\varphi_{ij} + \psi_{ij} = -Ar_{ij}^{-6} + B\exp(-\alpha r_{ij}) + q_iq_j/r_{ij}$$

is replaced by the potential containing only the two first terms of three. The parameters *A*, *B*, and α in these two computational schemes have different values, but the shapes of the $\varphi_{ij} + \psi_{ij}$ curves are similar. It should be noted that, at the early stage of the development of the atom–atom potential method, this scheme (which ignores the effective atomic charges) was preferred by Kitaigorodsky and Mirskaya [9].

The highest absolute values of the energies of the intermolecular contacts U_{MM} (exceeding 0.05 kcal/mol) are given in Table 1. This table also lists U_Σ corresponding to the total potential energies of the crystal structures. The energy U_Σ was obtained by summing the energies of the pair interactions U_{MM}, i.e., as the energy necessary for a molecule to escape from the crystal structure (per mole of compound). The multiplicities of the I-000–N-HKL contacts were also taken into account. In the structural class under consideration, the multiplicity is always equal to two. The computations included the molecules spaced from the origin of coordinates by not more than 20 Å (the molecule closest to the origin of coordinates was considered as initial, I-000). This ensured a negligibly small error because of series truncation during summation (not more than 1%).

RESULTS AND DISCUSSION

As can be seen from Table 1, the interactions of the initial molecule I-000 with the II-000 and I-001 molecules are characterized by the highest absolute energies. Both these M–M contacts have a multiplicity of two (in the former case, there are two contacts related by the twofold screw axis 2_1; in the latter case, there are two contacts spaced by the lattice period along the *z* axis). Both these contacts are observed in the $P_{c(z)}2_1$ chain, $Z = 2(1)$. In both compounds, these chains are the

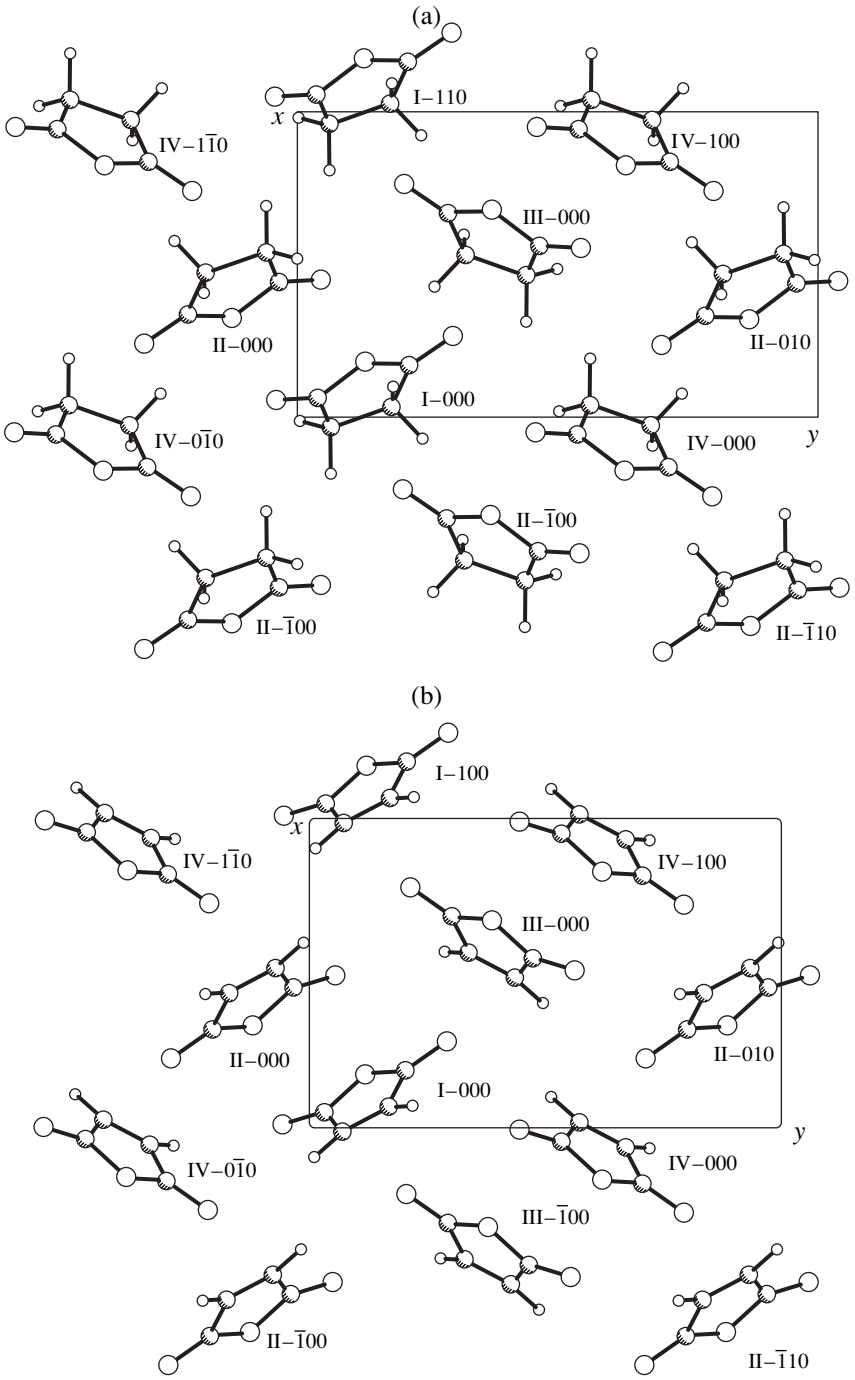

Fig. 2. Projections of the crystal structures of (a) succinic and (b) maleic anhydrides.

most pronounced molecular agglomerates. However, in spite of the fact that the four strongest intermolecular contacts take place within one chain, the chain efficiency is rather low (~35 and ~38% in two structures, respectively; see Table 1). It should be noted that the chain efficiency can be evaluated in another way. In the crystal structures of succinic and maleic anhydrides, the molecular coordination number equals 12. The energies of the interactions of the initial molecule I-000 with its nearest neighbors are 12.24 and 10.92 kcal/mol, respectively. The energies of four strongest M–M contacts in the chain amount to ~42 and ~46% of the energies of interactions between the initial molecule and its nearest neighbors in succinic and maleic anhydrides, respectively. Nevertheless, these chains are not well pronounced molecular agglomerates (at least, in the case of $C_4H_4O_3$).

To relate the crystals to a certain structural subclass, one has to calculate the energies of interaction between

Table 1. Energies of intermolecular interactions in the $C_4H_4O_3$ and $C_4H_2O_3$ crystals

N–HKL	$C_4H_4O_3$		$C_4H_2O_3$	
	$-U$ (kcal/mol)	U/U_Σ (%)	$-U$ (kcal/mol)	U/U_Σ (%)
II–000	1.454	9.811	1.453	10.950
I–001	1.113	7.510	1.047	7.890
IV–000	1.010	6.815	0.916	6.903
III–001	0.965	6.511	0.695	5.237
III–000	0.836	5.641	0.750	5.652
II–$\bar{1}$00	0.742	5.007	0.599	4.514
$-U_\Sigma$	14.82	(34.64)	13.27	(37.68)

Note: The chain efficiencies U_c/U_Σ (where U_Σ is the energy necessary for a molecule to leave the chain) are given in parentheses.

the chains or, more precisely, the energies of interaction of the initial chain (containing the I-000 and II-000 molecules) with the neighboring chains. As can be seen from Fig. 1, there are six such chains. However, the contacts between the *O–A*, *O–B*, *O–C*, and *O–D* chains are equivalent (they are transformed into each other by horizontal twofold screw axes 2_1 parallel to the *x* or *y* axis). The contacts between the *O–E* and *O–F* chains are also equivalent (they are related by a translation). It should be kept in mind that the energy of interaction between two chains, U_{cc}, is the sum of the energies of interactions between molecules comprising the period of the initial chain with all the molecules of another chain (evidently, because of the fast convergence of the series, it is sufficient to take into account only several molecules of the second chain). The computations demonstrated that the energies $U_c(OA)$ are equal to –6.484 and –5.578 kcal/mol for SUCANH and MLEICA, respectively, whereas the absolute values of the energy $U_c(OE)$ are much lower (–1.750 and –1.396 kcal/mol, respectively).

Thus, the formation of the strongest chain–chain contacts (Fig. 1) leads to the formation of a crystal without the stage of layer formation, and the compounds under consideration should be related to the subclass

$$1 - P_{c(z)}2_1,\ Z = 2(1) \uparrow\downarrow P2_12_12_1,\ Z = 4(1).$$

Since succinic and maleic anhydrides contain a substantial percentage of oxygen (27 and 33%, respectively), it was of interest to consider the shortest intermolecular contacts of oxygen atoms both with each other and with other atoms in order to refine the optimum van der Waals radius of an oxygen atom.

Analysis of the published data showed that this characteristic is still open for discussion. Kitaigorodsky [10] included the radius R_0 = 1.36 Å into the table of van der Waals radii. Later, he corrected this value [11] as 1.52 Å. The latter value (1.52 Å) was independently suggested by Bondi [12], and now it is widely accepted by researchers. Zefirov and Zorky [13] proposed a radius of 1.29 Å for oxygen. However, this value has not gained wide acceptance. According to the approach reported in [13], the optimum oxygen radius was estimated based on the main postulate of the theory of close molecular packings. According to this postulate, the molecules in a crystal that are bounded by the external surface of intersecting van der Waals atomic spheres should touch one another, i.e., do not penetrate into one another and do not hang in vacuum. It is necessary to select appropriate van der Waals radii, which are determined based on the reference contacts, i.e., the contacts that provide the formation of a "three-dimensional framework of contacts." The lengths of the reference contacts in succinic and maleic anhydrides, the corresponding shortest intermolecular atom–atom distances, and the types of theses contacts are given in Table 2. The gaps between the atoms (Δr_{min}) were calculated using the radii proposed by Zefirov and Zorky (1.16, 1.71, and 1.29 Å for H, C, and O, respectively). The intermolecular atom–atom distances in SUCANH correlate rather well with the analogous distances in MLEICA, thus demonstrating their practically complete analogy. It should be noted that mainly O···H and O···C contacts are reference ones, with the latter contacts being characterized by lower Δr_{min} values; i.e., it is more reasonable to use these contacts for determining the van der Waals radius of an oxygen atom. The

Table 2. Lengths of the reference contacts and Δr_{min} (Å)

I–000 – *N–HKL*	SUCANH		MLEICA	
	r_{ij}(supp)	Δr_{min}	r_{ij}(supp)	Δr_{min}
I–001	2.587	0.137(O···H)	2.728	0.278(O···H)
II–000	3.097	0.087(O···C)	3.140	0.130(O···C)
III–001	3.018	0.008(O···C)	2.995	–0.015(O···C)
III–000	2.528	0.208(H···H)	2.746	0.296(O···H)
IV–000	2.811	0.361(H···O)	2.666	0.216(H···O)
II–$\bar{1}$00	2.656	0.206(O···H)	3.333	0.453(C···H)

results obtained lead to the conclusion that the selected oxygen radius is suitable for crystallochemical computations. An increase in this radius would lead to an inadmissible overlap of atomic spheres and negative Δr_{min} values.

ACKNOWLEDGMENTS

This study was supported by the Russian Foundation for Basic Research, project no. 00-15-97346.

REFERENCES

1. J.-M. Lehn, *Supramolecular Chemistry: Concepts and Perspectives* (VCH, Weinheim, 1995; Nauka, Novosibirsk, 1998).
2. P. M. Zorky, J. Mol. Struct. **374**, 9 (1996).
3. P. M. Zorky and O. N. Zorkaya, Zh. Strukt. Khim. **39** (1), 126 (1998).
4. P. M. Zorky and Yu. V. Zefirov, Vestn. Mosk. Univ., Ser. 2: Khim. **13** (5), 590 (1972).
5. M. Ehrenberg, Acta Crystallogr. **19** (5), 698 (1965).
6. R. E. Marsh, E. Ubell, and H. E. Wilcox, Acta Crystallogr. **16** (1), 35 (1962).
7. G. Filippini and A. Gavezzotti, Acta Crystallogr., Sect. B: Struct. Sci. **49** (5), 868 (1993).
8. D. E. Williams, Acta Crystallogr., Sect. A: Cryst. Phys., Diffr., Theor. Gen. Crystallogr. **30** (1), 71 (1974).
9. A. I. Kitaigorodsky and K. V. Mirskaya, Kristallografiya **6** (4), 507 (1961) [Sov. Phys. Crystallogr. **6**, 408 (1961)].
10. A. I. Kitaigorodsky, *Chemistry of Organic Crystals* (Akad. Nauk SSSR, Moscow, 1955).
11. A. I. Kitaigorodsky, *Molecular Crystals* (Nauka, Moscow, 1971).
12. A. Bondi, J. Phys. Chem. **68** (3), 441 (1964).
13. Yu. V. Zefirov and P. M. Zorky, Usp. Khim. **58** (5), 713 (1989).

Translated by T. Safonova

Crystallography Reports, Vol. 48, No. 4, 2003, pp. 542–546. Translated from Kristallografiya, Vol. 48, No. 4, 2003, pp. 594–597.

CRYSTAL CHEMISTRY

Investigation of the Localization of H^+ Ions in Stoichiometric $LiNbO_3$

S. V. Yevdokimov and A. V. Yatsenko

Taurida National University, ul. Yaltinskaya 4, Simferopol, 95007 Ukraine

e-mail: lab2@ccssu.crimea.ua

Received October 4, 2002

Abstract—The possible positions of H^+ ions in stoichiometric crystals of lithium niobate are analyzed using computer simulation. It is shown that all hypothetical positions of H^+ ions at the midpoints of the O–O bonds are unstable and must be excluded from further consideration. An analysis of the trajectories of displacement of H^+ ions in the structure of $LiNbO_3$ shows that an H^+ ion is associated with one of the O^{2-} ions of the upper oxygen face of the NbO_6 octahedron and that the direction of the dipole moment of the OH^- group differs only slightly from the direction of the short O–O bond. © *2003 MAIK "Nauka/Interperiodica".*

INTRODUCTION

Already in the early stages of research into the structure of crystalline lithium niobate, it was found that certain amounts of hydrogen ions are incorporated into lithium niobate single crystals in the course of their growth and form OH^- groups [1]. The H^+ ions have a profound effect on the optical and electrical properties of lithium niobate crystals. In particular, it is assumed that H^+ ions are responsible for the so-called thermal fixing of optical holograms during the short-term heating of a crystal with a recorded hologram to T = 413–433 K due to the spatial redistribution of H^+ ions in the illuminated zone of the crystal under the effect of a photoinduced electric macrofield [2].

Herrington *et al.* [3] obtained fundamentally important results regarding the state of OH^- groups in $LiNbO_3$. It was found that the IR absorption spectrum contains two closely spaced maxima at λ = 2.875 and 2.864 μm and that both bands are polarized perpendicularly to the *c* axis of the crystal. These authors concluded that the electric dipole moment of OH^- groups is perpendicular to the *c* axis, to within ±5°, and assumed that the OH^- groups are associated with the shortest O–O bonds (0.272 nm).

Nonetheless, the discussion about the localization of H^+ ions in the structure of lithium niobate has continued for a long time [3–10]. Possible variants of H^+ positions were analyzed. Some of them are shown in Fig. 1: (1) position *a* of direct substitution for an Li^+ ion; (2) position *c* at the center of the lower oxygen face of the $V_{Li}O_6$ octahedron, where V_{Li} is an Li^+ ion vacancy; and (3) positions *b* and *d–g* at the midpoints of the O–O bonds. Based on the experimental studies of the ^1H NMR line shape of polycrystalline lithium niobate samples, the calculations of the second moment of the ^1H NMR line for the above positions, and the available structural data, it was concluded that the H^+ ion should occupy the *b* position [9, 10]. In these studies, it was

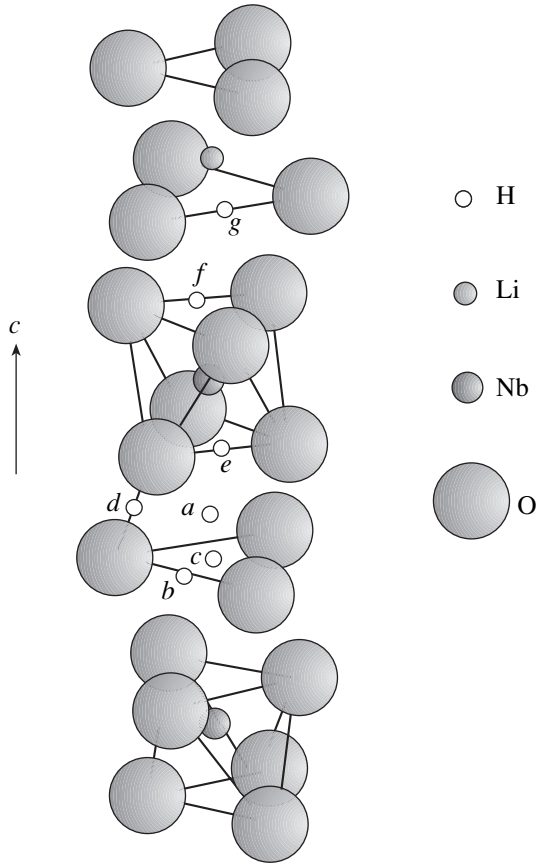

Fig. 1. Hypothetical positions of H^+ ions in the structure of $LiNbO_3$.

1063-7745/03/4804-0542$24.00 © 2003 MAIK "Nauka/Interperiodica"

postulated that the H^+ ion initially substitutes for the Li^+ ion, then is displaced to the lower oxygen face of the $V_{Li}O_6$ octahedron, and finally is located at the midpoint of the O–O bond (0.336 nm) [10].

The second model of localization of H^+ ions in the structure of lithium niobate is based on an analysis of the IR data [11, 12]. It is assumed that the H^+ ion is bound to one of the O^{2-} ions at the upper oxygen face of the NbO_6 octahedron, the dipole moment of the OH^- group is directed along the short O–O bond, and the O–H bond length is 0.0988 nm [11]. This is supported both by the analysis of the excitation conditions for the dipole moments of OH^- groups in lithium niobate [13] and by the fact that, in $HNbO_3$, the length of the short O–H bond is 0.099 nm [14]. The positions of H^+ ions in the structure of lithium niobate according to the data taken from [11] are shown in Fig. 2.

Earlier [3], it was suggested that the positions of H^+ ions in the structure of lithium niobate can be determined by analyzing the potential relief inside the unit cell of the crystal. The results of the analysis carried out in [15] are also presented in Fig. 2; however, these calculations were performed within a very rough approximation. The goal of the present work was to examine the potential relief in the vicinity of the possible positions of H^+ ions in the structure of $LiNbO_3$, which were considered earlier.

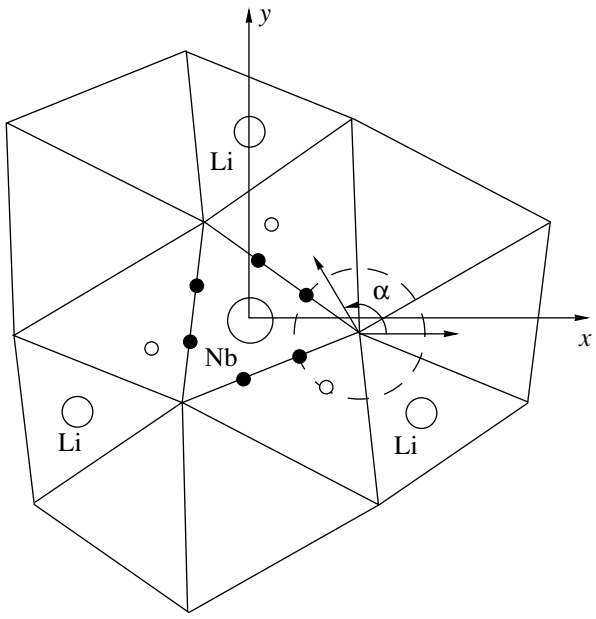

Fig. 2. Projection of the $LiNbO_3$ structure onto the *xy* plane. In the Cartesian coordinate system, the *x* and *z* axes coincide with the *a* and *c* axes of the hexagonal system, respectively. The O–O bonds are shown by solid lines. Small closed and open circles indicate the H^+ positions according to [11] and [15], respectively.

PROCEDURE FOR CALCULATION OF THE POTENTIAL RELIEF

The potential relief was analyzed within the classical electrostatic approach using the modified method of point multipoles. In the calculations of the potential φ and the strength of the local electric field E_{loc}, we considered only the ionic and dipole contributions. The dipole contribution was calculated using a standard iterative procedure with allowance made for the anisotropy of electronic polarizability of O^{2-} ions and the shift of the center of their dipole moment with respect to the nucleus [16]. In order to determine more exactly the effective charges q_{eff} of the ions involved in the crystal and the electronic polarizability of O^{2-} ions, we calculated the spontaneous polarization of lithium niobate with effective charges q_{eff} varying over a wide range. It was found that the most probable values of q_{eff} are as follows: $q_{Li} = 0.98$, $q_{Nb} = 3.376$, and $q_O = -1.452\,|e|$, where $|e|$ is the modulus of the elementary charge. These values were used in further calculations. The ionic contribution was calculated by the transient-region method [17].

The calculation of the potential relief at possible H^+ positions in the vicinity of the V_{Li} vacancy is hampered by the lack of data on the distortion of the lithium niobate structure in the neighborhood of V_{Li}. For this reason, the calculations were performed in the approximation of unchanged coordinates of the O^{2-} ions surrounding the V_{Li} vacancy, and the potential relief was considered as a superposition of the relief in an ideal undistorted structure and an additional contribution made both by the point charge $q_{add} = -0.98|e|$ at the vacant position of the Li^+ ion and by changes in the dipole moments of the O^{2-} nearest neighbor ions under the effect of q_{add}.

The additional polarizing effect of the H^+ ion on the O^{2-} nearest neighbor ions, which results in significant changes in their induced dipole moments, was also included in the calculations. The additional contributions to φ and E_{loc} due the presence of V_{Li} and the polarizing effect of H^+ ions were also calculated with the iterative procedure (seven iterations taking into account the changes in the mutual influence of the dipole moments of O^{2-} ions in spheres 1.5 nm in radius with centers at the H^+ and V_{Li} sites).

Note that the point-multipole method can be used only for crystal zones in which the charge density of the external electron shells of ions is sufficiently low. It is not correct to apply the point-multipole method to calculations of the field at points separated from the center by distances shorter than the ionic radius of O^{2-} (0.13–0.14 nm) [15]. These calculations can be performed only within the *ab initio* approach.

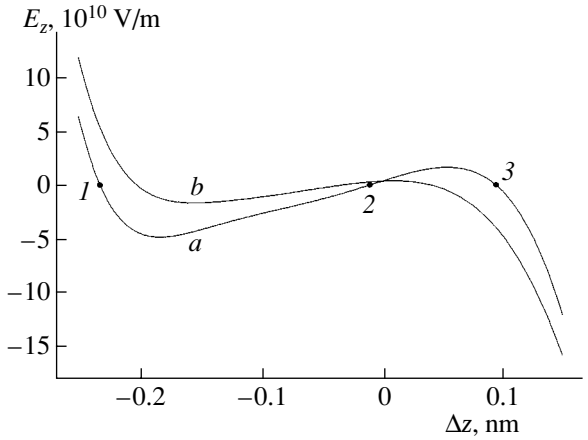

Fig. 3. Dependences of the *z* component (E_z) of the local electric field E_{loc} at the H^+ ion on the displacement Δz of the H^+ ion from the Li^+ position along the *z* axis: (*a*) self-consistent calculation and (*b*) standard steady-state analysis.

ANALYSIS OF THE POSITIONS OF H^+ IONS IN THE $LiNbO_3$ STRUCTURE

At the first stage of the analysis, we examined the possibility of locating the H^+ ions along the threefold axis, which is aligned with the *c* axis of the crystal. It was assumed that the H^+ ion is initially located at the Li^+ position. The calculated dependence of the *z* component (E_z) of local electric field E_{loc} at the H^+ ion on its displacement Δz from the Li^+ position along the *z* axis is shown in Fig. 3. The calculation was performed self-consistently, i.e., with allowance made both for the change in the induced dipole moments of O^{2-} ions within a sphere 1.5 nm in radius upon the displacement of an H^+ ion and for the corresponding changes in the mutual influence of O^{2-} ions. A similar dependence obtained in the calculations without regard for the change in the dipole moments of O^{2-} ions upon the displacement of H^+ is shown in Fig. 3 for comparison. It is clear that the inclusion of the self-consistency significantly affects the results of calculations.

All three H^+ positions lying along the *c* axis, for which $E_z = 0$, are the points of unstable equilibrium. It is possible that, due to thermal vibrations at points *1* and *3*, the H^+ ion is displaced from the threefold axis in the *xy* plane and moves in the direction of the rapidest decrease in the potential. The simulation of the trajectories of further displacement of the H^+ ion from point *1* demonstrated that they enter the region occupied by the outer electron shells of one of the upper O^{2-} ions of the NbO_6 octahedron. Some of the trajectories are shown in Fig. 4a. The incorporation of the H^+ ion into the region of the outer electron shells of an O^{2-} ion leads not only to radical changes in the wave functions of the outer electron shells of this oxygen ion and in the components of its electronic polarizability tensor but also to a severe distortion of the electronic structure of the NbO_6 octahedron as a whole and, possibly, to the formation of the Nb^{4+} polaron. The results of the analysis of further displacement of the H^+ ion from point *3* are illustrated in Fig. 4b.

To a first approximation, the last points of the trajectories obtained lie in the *xy* plane at circumferences 0.123 nm (Fig. 4a) and 0.118 nm (Fig. 4b) in radius, whose centers are shifted from the centers of the O^{2-} ions along the *z* axis by 6.4 and –5.9 pm, respectively. For unambiguity, further analysis was performed for the O^{2-} ion with the coordinates $x = 164.35$ pm, $y = -21.26$ pm, and $z = 87.92$ pm (Fig. 2). The angular dependences of the potential φ for these circumferences are shown in Fig. 5. It is obvious from the figure that both curves have a minimum in the range $\alpha = 200°$–$230°$, which correlates with some positions of the H^+ ions shown in Fig. 2.

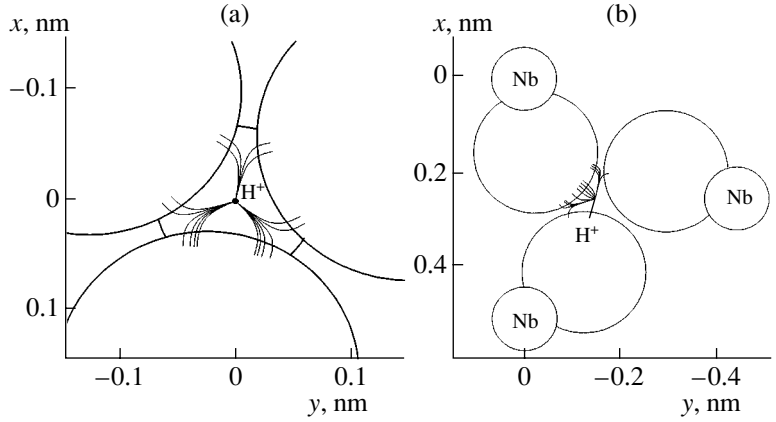

Fig. 4. Projections of the trajectories of the displacement of the H^+ ion from the points of unstable equilibrium (a) *1* and (b) *3* onto the *xy* plane. For the outer neighboring trajectories, the initial directions of the displacement in the *xy* plane differ by 0.1°.

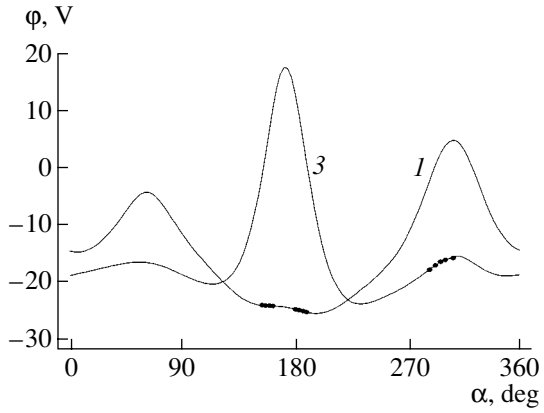

Fig. 5. Angular dependences of φ for conventional circumferences containing the final points (closed circles) of the trajectories of the displacement of the H^+ ion from points *1* and *3*.

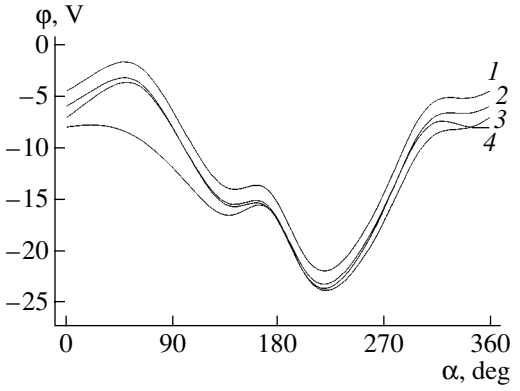

Fig. 6. Angular dependences of φ for the points lying at a circumference 98.8 pm in radius with the center at the position of the chosen O^{2-} ion: (*1*) undistorted structure, (*2*) V_{Li} on the axis above the Nb^{5+} ion, (*3*) V_{Li} immediately above the oxygen layer, and (*4*) V_{Li} under the oxygen layer.

As mentioned above, further calculations for the trajectories of the displacement of the H^+ ion can be performed only within the *ab initio* approach. However, using the point-multipole method, we can analyze the potential relief in the vicinity of the points of the possible location of H^+ ions without regard for the contribution made to the potential by the O^{2-} ion of the OH group but taking into consideration the polarizing effect of the H^+ ion. The results of this calculation are represented (see Fig. 6) in the form of angular dependences of φ for the points that lie in the *xy* plane at a circumference 98.8 pm in radius with the center coinciding with the position of the O^{2-} ion indicated above. As is seen from Fig. 6, for all the configurations of the immediate environment that were considered, the potential φ exhibits a minimum at $\alpha \simeq 220°$. The calculation of the *z* component of E_{loc} for the points corresponding to the minima of φ lends support to the stability of this possible position of the H^+ ion along the *z* axis.

Analogous calculations were performed for all the hypothetical positions of the H^+ ions at the midpoints of the O–O bonds. It was found that all these positions are unstable both in the ideal structure of lithium niobate and in the presence of a V_{Li} defect in the immediate vicinity.

CONCLUSIONS

The above analysis of the potential relief in the vicinity of the points of the possible location of H^+ ions in the $LiNbO_3$ crystal demonstrated that the conclusions drawn in [9, 10] based on the interpretation of the experimental ^1H NMR data are insufficiently substantiated. Note that the ^1H NMR data for $LiNbO_3$ can be interpreted in a different way [15]. We assumed that the most probable positions of H^+ ions in the structure of lithium niobate are close to those determined in [15] and differ from the latter only in α value (220° instead of 235° in [15]).

Final conclusions regarding the location of H^+ ions can be drawn after additional ^1H NMR experiments on a single crystal of $LiNbO_3$ with a volume OH^- concentration of $\sim 10^{19}$ cm^{-3} and by comparing the orientation dependences of the second moment of the NMR line obtained experimentally and calculated from the structural data. Additional information can also be obtained by modeling the experimental angular dependence of the excitation of OH^- groups [11] under the effect of polarized IR radiation on a crystal.

REFERENCES

1. R. G. Smith, D. B. Frazer, R. T. Denton, and T. C. Rich, J. Appl. Phys. **39** (10), 4600 (1968).
2. D. L. Staebler, W. J. Burke, W. Phillips, and J. J. Amodei, Appl. Phys. Lett. **26** (4), 182 (1975).
3. J. R. Herrington, B. Dischler, A. Räuber, and J. Schneider, Solid State Commun. **12**, 351 (1973).
4. W. Bollmann and H. J. Stöhr, Phys. Status Solidi A **39**, 477 (1977).
5. X. Q. Feng and T. B. Tang, J. Phys.: Condens. Matter **5**, 2423 (1995).
6. X. Wu, M. Zhang, F. Yan, and D. Feng, Solid State Commun. **93** (2), 131 (1995).
7. X. Wu, M. Zhang, F. Yan, and D. Feng, J. Appl. Phys. **78** (3), 1953 (1995).
8. Y. Kong, W. Zhang, X. Chen, *et al.*, J. Phys.: Condens. Matter **11**, 2139 (1999).

9. M. Engelsberg, R. E. de Souza, and L. H. Pacobahyba, Appl. Phys. Lett. **67**, 359 (1995).
10. Y. Kong, J. Xu, W. Zhang, and G. Zhang, J. Phys. Chem. Solids **61**, 1331 (2000).
11. Y. Watanabe, T. Sota, K. Suzuki, *et al.*, J. Phys.: Condens. Matter **7**, 3627 (1995).
12. Y. Furukawa, K. Kitamura, S. Tadekawa, *et al.*, J. Cryst. Growth **211**, 230 (2000).
13. A. Gröne and S. Kapphan, J. Phys. Chem. Solids **56**, 687 (1995).
14. J. L. Fourquet, M. F. Renou, R. de Pape, *et al.*, Solid State Ionics **9–10**, 1011 (1983).
15. A. V. Yatsenko, Ukr. Fiz. Zh. **44** (3), 381 (1999).
16. A. V. Yatsenko, Physica B (Amsterdam) **305**, 287 (2001).
17. A. V. Yatsenko, Kristallografiya **46** (3), 411 (2001) [Crystallogr. Rep. **46**, 361 (2001)].

Translated by I. Polyakova

Crystallography Reports, Vol. 48, No. 4, 2003, pp. 547–550. Translated from Kristallografiya, Vol. 48, No. 4, 2003, pp. 598–601.

DIFFRACTION AND SCATTERING OF IONIZING RADIATIONS

Processing of Intensities of Electron Scattering from Amorphous Silicon by Methods of Continuous Wavelet Analysis

A. I. Mashin, O. A. Morozov, E. V. Smelova, and E. A. Soldatov

Nizhni Novgorod State University, pr. Gagarina 23, Nizhni Novgorod, 603950 Russia

e-mail: mashin@phys.unn.rannet.ru

Received March 4, 2002; in final form, February 15, 2003

Abstract—It is shown that intensities of electron scattering from amorphous silicon can be processed by the methods of wavelet analysis. The coordination radii for amorphous silicon at various annealing temperatures are calculated using the intensity distribution of coefficients of the wavelet transform. © *2003 MAIK "Nauka/Interperiodica".*

INTRODUCTION

It is well known that amorphous materials have no long-range order. Atoms and molecules are orderly arranged only within distances to the nearest neighbors. This order is characterized by the radial distribution function $W(r)$, which has a statistical nature. This function indicates the probability of encountering an atom of a certain kind at a distance r from the given atom. The first, second, etc., maxima of $W(r)$ (in the sequence of increasing r) yield the characteristics of the location of the first, second, etc., neighbors or, as is usually said, the characteristics of the coordination spheres, because $W(r)$ depends only on interparticle distances and does not depend on their directions [1].

One of the methods of studying the structure of amorphous materials is electron diffraction analysis [2]. Electron diffraction patterns allow one to calculate the experimental curve of the angular distribution of intensities (Fig. 1). Then, using integral analysis, one can calculate the radial distribution function (RDF) in the form

$$W(r) = 4\pi r^2 u_0 + \frac{2r}{\pi}\int_0^\infty si(s)\sin(sr)ds, \qquad (1)$$

where u_0 is the average atomic density,

$$u_0 = \frac{d}{Mm_H}, \qquad (2)$$

d is the density of the material studied, M is its molecular weight, m_H is the mass of a hydrogen atom,

$$i(s) = \frac{I}{Nf^2} - 1, \qquad (3)$$

I is the scattered intensity, N is the number of atoms, f is the atomic scattering factor determined by scattering

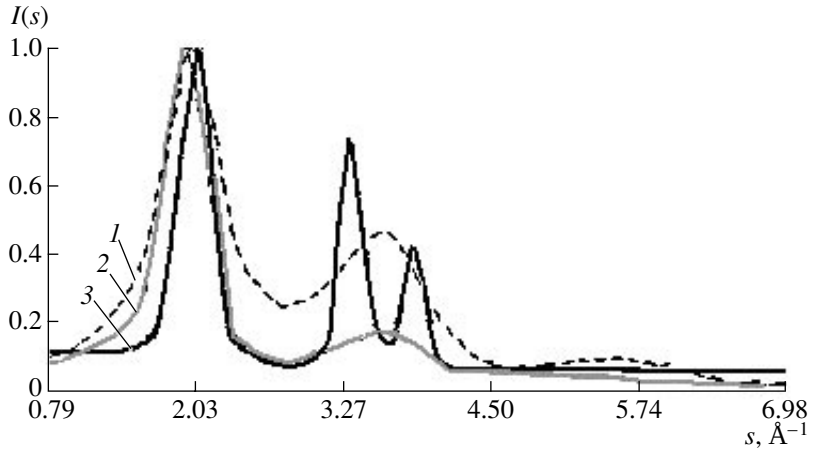

Fig. 1. Experimental intensity curves for electron scattering from amorphous silicon (*1*) prior to annealing, (*2*) upon annealing at 500°C, and (*3*) upon annealing at 700°C.

1063-7745/03/4804-0547$24.00 © 2003 MAIK "Nauka/Interperiodica"

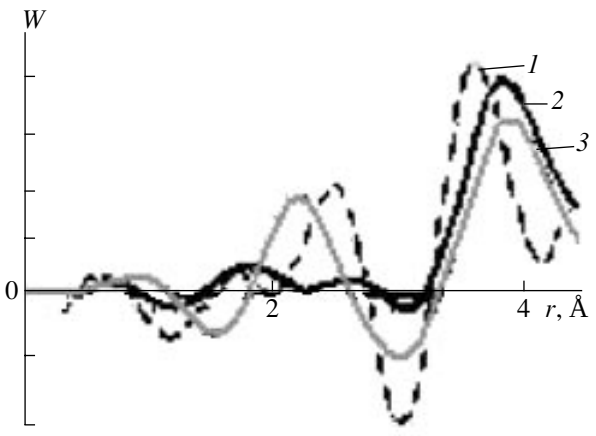

Fig. 2. Radial distribution function for amorphous silicon (*1*) prior to annealing, (*2*) upon annealing at 500°C, and (*3*) upon annealing at 700°C.

of electrons from one atom, and $s = \frac{4\pi\sin\theta}{\lambda}$ is the scattering angle measured in Å^{-1}.

An RDF, being a function of *r*, has a number of maxima (Fig. 2) that allow one to extract two types of information—interatomic distances and the number of the nearest neighbors determined by the area under the maximum. However, in practice, one can obtain data only on the first two or three coordination radii. The difficulty encountered in analysis of a radial distribution function consists in the fact that experimental data are obtained for a rather limited range of scattering angles *s*. This is explained by two facts. First, transmission electron diffraction patterns are obtained at small scattering angles so that the scattered beams overlap with the primary beam. Reflection electron diffraction patterns are obtained at angles such that the scattered beams overlap with the specimen edges. This makes it impossible to determine the run of the intensity curve $I(s)$ from zero to a certain value s_1, so one has to interpolate $I(s)$ values at this interval in an arbitrary way. Second, there also exist some theoretical and experimental limitations and, therefore, it is impossible to determine the intensity curve up to values $s \longrightarrow \infty$ required for calculating the radial distribution function $W(r)$ by Eq. (1). In practice, the intensity curve $I(s)$ is determined up to a certain value $s_2 < s_{\max} = \frac{4\pi\sin\theta_{\max}}{\lambda}$, and the s_2 value is selected experimentally proceeding from the dimensions of the aperture of the recording device and the level of the measurement noise. As a result, the intensity curve is terminated, which gives rise to the formation of spurious maxima that cannot be treated as coordination radii. Moreover, the termination of the curve can change the positions, shapes, and widths of the maxima. Various experimental difficulties and errors in the determination of the absorption coefficient and the incoherent background also produce some negative effect.

PROCESSING OF EXPERIMENTAL DATA BY METHODS OF WAVELET ANALYSIS

We suggest using wavelet analysis in structural studies of a material because it is rather convenient for considering inhomogeneous processes [3, 4]. A wavelet $\psi(t)$ is a function that has such properties as localization, a zero mean, and boundedness (a wavelet should rapidly decrease at $t \longrightarrow \pm\infty$). Unlike the Fourier transform whose analyzing function covers the whole numerical axis, the two-parameter analyzing function is well localized both in time and frequency and, therefore, can be considered as "localized spectral analysis."

The basis of the functional space $L^2(R)$ is constructed using continuous scale transformations and translations of the wavelet $\psi(t)$ with arbitrary basis parameters, the scale coefficient *a*, and the displacement parameter *b*:

$$\psi_{a,b}(t) = |a|^{-\frac{1}{2}}\psi\left(\frac{t-b}{a}\right), \quad a, b \in R, \quad \psi \in L^2(R). \quad (4)$$

Any wavelet of the family $\psi_{ab}(t)$ is obtained from the basis wavelet $\psi(t)$ by the scale and displacement transformations. Then, using this basis, one can write the integral wavelet transform

$$[W_\psi f](a,b) = |a|^{-\frac{1}{2}}\int_{-\infty}^{+\infty} f(t)\psi^*\left(\frac{t-b}{a}\right)dt = \int_{-\infty}^{+\infty} f(t)\psi^*_{ab}(t)dt. \quad (5)$$

In other words, a wavelet transform is a convolution of the initial function with the wavelet extended by a factor of *a* at a fixed value of *b*.

An important role in the application of a wavelet transform to data processing is played by the selection of the analyzing wavelet. We selected the analyzing wavelet in the form of a Morlet complex wavelet and its real part (as an individual wavelet):

$$\psi_{a,b}(t) = \exp\left(ik_0\frac{t-b}{a}\right)\exp\left(-\frac{1}{2}\left[\frac{t-b_0}{a}\right]^2\right). \quad (6)$$

This choice is far from accidental. First, the existence of the sinusoidal part leads to a certain analogue of the sine transformation used in the classical methods of intensity analysis. Second, the form of the modulating exponent is close to an atomic scattering factor (scattering from one atom of the material), which allows one to perform local analysis of intensities at the appropriate scale levels. The use of other wavelets yields no interesting wavelet transforms, so that one can clearly see only the intensity maxima.

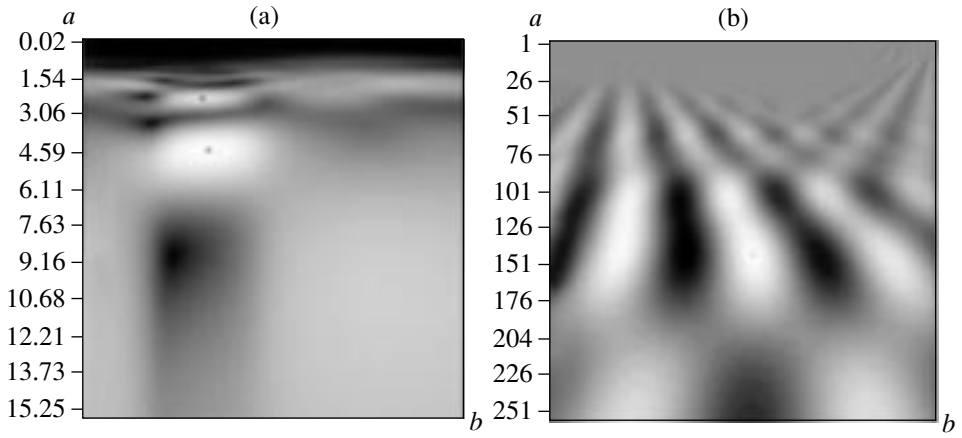

Fig. 3. Wavelet transform of the intensity curve with the use of various wavelets: (a) complex Morlet wavelet and (b) the real part of a Morlet wavelet.

ANALYSIS OF DISTRIBUTION OF COEFFICIENTS OF WAVELET TRANSFORM

The intensity curves of electron scattering from hydrogenated amorphous silicon at a hydrogen concentration of ~40 at. % obtained using several annealing modes are processed by the method of continuous wavelet analysis. The accuracy of the experimental data used ranged from 6 to 8%; the data were analogous to the data used in [5]. The results of the application of the wavelet transform to intensities are shown in Fig. 3 and reflect the dependence of the coefficients of the wavelet transform on the scale coefficient *a* (vertical axis) and displacement *b* (horizontal axis). Figure 3b shows the results of the application of the wavelet transform with the use of the real part of a Morlet wavelet. The treelike structure of the pattern reflects the structure of the material. Analyzing the rather interesting distribution of the coefficients of the wavelet transform is quite difficult, so for the time being we cannot interpret it adequately. Figure 3a shows the wavelet transform with the use of a complex Morlet wavelet. Bright bands on the pattern reflect certain scale levels.

Since the sine transformation allows one to determine the radii of coordination spheres, one can readily estimate these, and possibly also some other, parameters from the wavelet transform. Since the scale coefficient is an analogue of frequency, its value at well-pronounced scale levels can be recalculated and allow one to determine the coordination radii. Figure 3a shows the local maxima of the wavelet transform (for selected areas). Using the value of the scale coefficient *a* at these points, we calculated the parameters as

$$R = \frac{2\pi a}{k_0},$$

where k_0 is the wavelet parameter.

We proceeded from the assumption that the maximum correlation takes place at the frequency of the sinusoidal part of the wavelet and, therefore, the parameters of this part should necessarily influence the value to be determined.

We calculated the coordination radii for amorphous silicon at several annealing temperatures based on wavelet analysis and also from the RDF constructed using the Fourier transform and the methods suggested in [2] (no iteration refinement was made). The results obtained are tabulated. The table also lists the coordination radii for tetrahedral hydrogen-free silicon obtained in [6]. Comparing the results, one should bear in mind that the properties of hydrogenated silicon strongly depend on the conditions of its synthesis and that annealing changes the hybridization of silicon atoms [5], which, in turn, changes the short-range order parameters.

Thus, wavelet analysis allows one to perform qualitative analysis of the intensity curves. Wavelet analysis is convenient because it allows one to process the data without their preliminary recalculation and without

Coordination radii obtained by various methods

	Prior to annealing		At 500°C		At 700°C		Tabulated values without annealing
	wavelet	radial distribution function	wavelet	radial distribution function	wavelet	radial distribution function	
*R*1, Å	2.39	2.45	2.37	1.9	2.39	2.2	2.35
*R*2, Å	4.52	3.62	4.31	3.85	4.49	3.9	3.86

allowing for various approximations, as is necessary in the construction of the radial distribution function. Moreover, it does not require knowledge of such material characteristics as density and the atomic scattering factor, which is of great importance because these characteristics can considerably change during annealing.

ACKNOWLEDGMENTS

This study was supported by the Ministry of Education of the Russian Federation, project no. E02-3, 4-385.

REFERENCES

1. A. F. Skryshevskiĭ, *Structure Analysis of Liquids and Amorphous Materials* (Vysshaya Shkola, Moscow, 1980).
2. L. I. Tatarinova, *Electron Diffraction from Amorphous Materials* (Nauka, Moscow, 1972).
3. N. M. Astaf'eva, Usp. Fiz. Nauk **166** (11), 1145 (1996) [Phys. Usp. **39**, 1085 (1996)].
4. V. I. Vorob'ev and V. G. Gribulin, *Theory and Practice of the Wavelet Transformation* (VUS, St. Petersburg, 1999).
5. A. F. Khokhlov and A. I. Mashin, *Allotropy of Silicon* (Nizhegor. Gos. Univ., Nizhni Novgorod, 2002).
6. E. V. Chuprunov, A. F. Khokhlov, and M. A. Faddeev, *Crystallography* (Fizmatlit, Moscow, 2000).

Translated by L. Man

Crystallography Reports, Vol. 48, No. 4, 2003, pp. 551–556. Translated from Kristallografiya, Vol. 48, No. 4, 2003, pp. 602–607.

STRUCTURE OF INORGANIC COMPOUNDS

Crystal Structure of Tisinalite $Na_2(Mn,Ca)_{1-x}(Ti,Zr,Nb,Fe^{3+})[Si_6O_8(O,OH)_{10}]$

N. A. Yamnova, Yu. K. Egorov-Tismenko, I. V. Pekov, and L. V. Shchegol'kova

Moscow State University, Vorob'evy gory, Moscow, 119992 Russia

e-mail: natalia_yamnova@mail.ru

Received April 1, 2002; in final form, July 12, 2002

Abstract—Crystal structure of tisinalite from the Lovozero alkaline massif (the Kola Peninsula) was established by single-crystal X-ray diffraction analysis (SYNTEX $P\bar{1}$ diffractometer, λMoK_α radiation, $2\theta/\theta$ scanning mode). The structure solution (SHELX97 program package, $R_{hkl} = 0.0565$, 951 independent reflections, anisotropic refinement of thermal atomic displacements) confirmed that tisinalite belongs to the lovozerite structure type (sp. gr. $P\bar{3}$, $a = 10.036(5)$ Å, $c = 12.876(9)$ Å, $Z = 3$). The difference between the structure of tisinalite and the structures of the minerals of the lovozerite group established earlier consists in the nature of the occupancy of both cation and anion positions. © *2003 MAIK "Nauka/Interperiodica".*

INTRODUCTION

Tisinalite, a new mineral of the lovozerite group, was described by Yu.L. Kapustin *et al.* [1] in 1980. This mineral was discovered in the hyperagpaitic pegmatites from the Khibiny alkaline massif (the Kola Peninsula). The formula $Na_3H_3(Mn,Ca,Fe)TiSi_6(O,OH)_{18} \cdot H_2O$ attributed to this mineral is still indicated in the mineralogical nomenclature [2]. It has been established that this mineral belongs to the trigonal system, but its crystal structure and space group remain unknown. Tisinalite was also found in the Lovozero alkaline massif adjacent to the Khibiny massif. Initially, the latter specimen was characterized under the conditional name hydrokazakovite [3]. In the Khibiny massif, tisinalite occurs very rarely, whereas in the Lovozero massif, it is often observed as an accessory mineral of weakly altered hyperagpaitic rocks and pegmatites. According to A.P. Khomyakov [3], tisinalite cannot crystallize alone; it is generated as a product of the transformation of kazakovite $Na_6(Mn,Ca)TiSi_6O_{18}$ when the alkalinity of the medium decreases. No facts that contradict this hypothesis are presently known. This transformation can proceed with the retention of the main structural motif (framework) of the lovozerite-like minerals and is a graphic example of the natural ion exchange according to the general scheme $xNa^+ + xO^{2-} \longrightarrow yNa^+ + (x-y)(\square,H_2O)^0 + (x-y)(OH)^-$ [4]. This transformation may lead to a substantial change in the symmetry because of the different arrangement of large cations, water molecules, and vacancies in the structures of the parent phases and newly formed minerals [5].

The tisinalite sample used for X-ray diffraction study was found in hyperagpaitic pegmatoid naujaites (poikilitic nepheline–sodalite syenites) from the Alluaiv mountain in the Lovozero massif. The tisinalite that replaces kazakovite forms mustard-yellow grains up to 1 cm in diameter. In cavities, tisinalite was found as cuboidal crystals up to 2 mm in diameter. This mineral occurs in association with aegirine, eudyalite, lamprophyllite, serandite, parakeldyshite, lomonsovite, etc. Tisinalite is substantially enriched with Zr and Nb. Its cation composition determined by electron probe microanalysis is as follows: Na_2O, 10.07; CaO, 1.07; MnO, 5.86; Fe_2O_3, 1.99; Ce_2O_3, 0.17; SiO_2, 59.37; TiO_2, 6.38; ZrO_2, 3.06; Nb_2O_5, 3.48; and the sum is 91.45 wt %. The empirical formula calculated for $Si_6(O,OH)_{18}$ is $(Na_{1.97}Ce_{0.01})_{\Sigma 1.98}(Mn^{2+}_{0.50}Ca_{0.12})_{\Sigma 0.62}(Ti_{0.49}Nb_{0.16}Zr_{0.15}$.

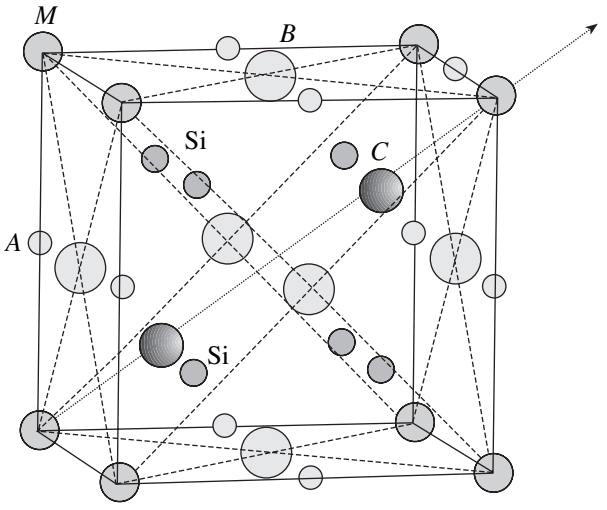

Fig. 1. Schematic representation of the arrangement of cations in the parent cubic unit cell of the lovozerite structure type.

Table 1. Characteristics of X-ray diffraction study of tisinalite

Characteristic	Parameter
Symmetry	Trigonal
Sp. gr.	$P\bar{3}$
Unit-cell parameters, Å	a = 10.036(5)
	c = 12.876(9)
	V = 1123(1) (Å^3)
Number of formula units (Z)	3
ρ_{calcd}, g/cm^3	2.62
Linear crystal dimensions	0.300 × 0.250 × 0.200 mm
Automated single-crystal diffractometer	SYNTEX $P\bar{1}$
Radiation	MoK_α
Monochromator	Graphite
Scanning technique	2θ : θ
Minimum and maximum sinθ/λ	0.039, 1.064
Scan rate	4–24 deg/min
Scan ranges	$0 \le h \le 17$
	$-19 \le k \le 16$
	$0 \le l \le 24$
Total number of measured reflections	1616
Number of independent reflections with $I > 2\delta(I)$	951
R_{int}	0.0983
Program used in computations	SHELX97
Reliability factor:	
R_{hkl} (anisotropic refinement)	0.0565
$wR(F^2)$	0.1525
Weighting scheme in least-squares refinement	$w = 1/[\delta^2(F^2) + (0.0645P)^2 + 3.22P]$, where
	$P = (\max F_o^2 + 2F_c^2)/3$
$\Delta\rho_{max}$, e/Å^{-3}	0.64
$\Delta\rho_{min}$, e/Å^{-3}	−0.47

$Fe^{3+}_{0.15})_{\Sigma 0.95}Si_6[O_{13.05}(OH)_{4.95}]_{18}$. According to IR spectroscopy data, this mineral contains a considerable amount of OH groups in the absence of water molecules and free H^+ ions [6].

A great diversity of mineral species in the lovozerite group is associated with the fact that all the cation positions (except for the positions of the Si^{4+} cations tetrahedrally coordinated with O atoms) can be occupied differently or remain vacant. This fact accounts for both variations in the symmetry of the crystal structures of lovozerite-like compounds and the difference in their unit-cell parameters. The lovozerite structure type is based on pseudocubic blocks (with each one containing one lovozerite-type $[Si_6O_{18}]$ ring) with the parameter $a \approx 7.5$ Å and the general formula $A_3B_3C_2M[Si_6O_{18}]$. In this structure type, cations occupy the following strictly particular positions. The M positions in the vertices of the pseudocubic parent unit cell are occupied by Zr, Ti, and Fe^{3+}; the A and B positions in the midpoints of the edges and centers of the faces of the parent unit cell are occupied by Na and H_2O, respectively; and Mn, Ca, and Na are located in the C positions corresponding to the centers of two octants devoid of the Si^{4+} cations and located on a single threefold axis of the parent unit cell (Fig. 1).

EXPERIMENTAL. SOLUTION AND REFINEMENT OF STRUCTURE

The parameters and symmetry of the trigonal unit cell (a = 10.036 Å, c = 12.876 Å) were refined on an automated single-crystal SYNTEX $P\bar{1}$ diffractometer. The X-ray diffraction data were collected on the same diffractometer. The principal details of X-ray data collection are given in Table 1. The nonequivalent intensities of pairs of the *hkl* and *khl* reflections and the presence of a small number of weak (but more intense than $3\delta(I)$) reflections not satisfying the rule of systematic extinction $-h + k + l = 3n$ indicate two possible space groups, $P3$ and $P\bar{3}$. All the computations were made with the use of the SHELX97 program package [7].

At the first stage, we used the atomic coordinates of lovozerite proceeding from the similarity in composition, symmetry, and unit-cell parameters and considering the presence of the R pseudotranslation. These coordinates were refined within the acentric sp. gr. $R3$ to the final reliability factor R_{hkl} = 0.1147 (anisotropic refinement) [5] and then were used as the starting model for the structure determination. Taking into account the high R_{hkl} factor and a substantial scatter in the Si–O distances in the tetrahedra, we rejected the above space group and performed further computations within the primitive trigonal unit cell (sp. gr. $P3$). The atomic coordinates modified to sp. gr. $P3$ were refined anisotropically by the least-squares method to R_{hkl} = 0.0523.

Analysis of the resulting model of the tisinalite structure revealed the presence of a center of inversion, which was obeyed by all the atoms including those in the C position. By contrast, the latter position is the only position that violates the centrosymmetricity of the lovozerite structure. The anisotropic refinement of the tisinalite structure within the centrosymmetric sp. gr. $P\bar{3}$ converged to the reliability factor R_{hkl} = 0.0565 and gave reliable structural parameters. The final coordinates of the basis atoms are given in Table 2. The extended and simplified crystallochemical formulas of tisinalite are as follows (Z = 3, ρ_{calcd} = 2.62 g/cm^3):

$$(Na_{2.1}\square_{0.9})(Mn^{2+}_{0.2}\,Ca_{0.1}\square_{0.7})_2(Ti_{0.5}Zr_{0.15}Nb_{0.15}Fe^{3+}_{0.1}\square_{0.1}) \cdot$$

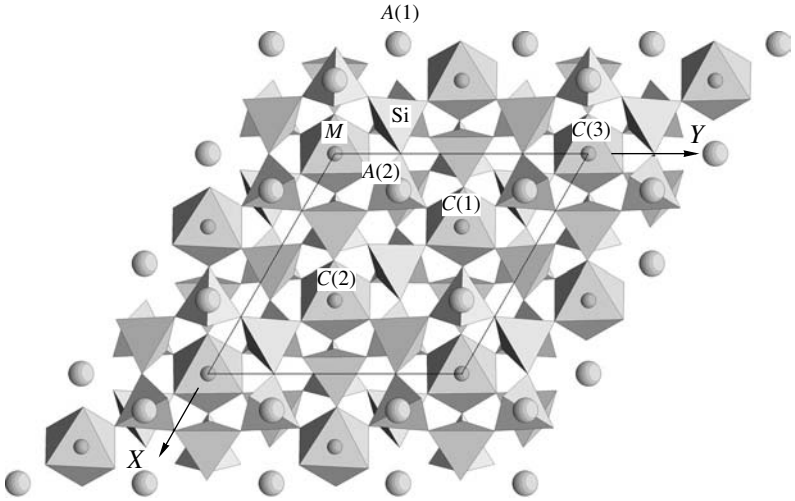

Fig. 2. Structure of tisinalite projected onto the (001) plane.

$[Si_6O_8(O_{0.7}OH_{0.3})_4(OH_{0.7}O_{0.3})_6]$ and $Na_2(Mn,Ca)_{1-x} \cdot (Ti,Zr,Nb,Fe^{3+})[Si_6O_8(O,OH)_{10}]$, respectively, where $x < 0.5$. The idealized formula can be written as $Na_2MnTi[Si_6O_{14}(OH)_4]$.

The anionic part of the structure was divided into the O^{2-} ions and OH^- groups based on calculations of the local valence balance with due regard for the cation–oxygen distances and statistical occupancies of the cation positions according to Pyatenko [8].

RESULTS AND DISCUSSION

The structure model of tisinalite retains the rhombohedral pseudosymmetry. The lowering of the real symmetry to $P\bar{3}$ is caused by a substantial difference in the occupancies of the *M* positions (related by the *R* pseudotranslations) with highly charged cations (Ti, Zr, Nb, Fe^{3+}) (Table 2) and is also associated with the geometric characteristics of the atomic arrangement. The

Table 2. Coordinates of the basis atoms, equivalent thermal parameters, and occupancies of positions in the tisinalite structure

Atom	Position multiplicity	Occupancy of tHe position	*x*/*a*	*y*/*b*	*z*/*c*	$U_{eq} \times 100$, Å^2
A(1)	3	0.68Na	0.5	0	0.5	2.05(9)
A(2)	6	0.70Na	0.3352(5)	0.1681(4)	0.1647(3)	4.73(9)
C(1)	2	0.23Mn + 0.08Ca	0.3333	0.6667	0.9174(9)	7.3(3)
C(2)	2	0.17Mn + 0.09Ca	0.3333	0.6667	0.4228(4)	2.9(1)
C(3)	2	0.23Mn + 0.02Ca	0	0	0.7570(6)	4.7(2)
M(1)	1	$0.64Ti + 0.36Fe^{3+}$	0	0	0	3.50(6)
M(2)	2	0.38Ti + 0.21Zr + 0.20Nb	0.3333	0.6667	0.6667(2)	1.89(2)
Si(1)	6	Si	0.6385(2)	0.81932(2)	0.1032(1)	3.14(4)
Si(2)	6	Si	0.8487(2)	0.6975(2)	0.4349(1)	2.96(4)
Si(3)	6	Si	0.9701(2)	0.4849(2)	0.7679(1)	2.81(4)
O(1)	6	O	0.9118(5)	0.8194(5)	0.9092(4)	6.6(2)
O(2)	6	(O,OH)	0.5138(4)	0.7612(5)	0.5758(4)	5.4(1)
O(3)	6	(O,OH)	0.5681(5)	0.1517(5)	0.2440(4)	6.5(2)
O(4)	6	(OH,O)	0.8967(6)	0.7853(7)	0.3252(4)	7.7(2)
O(5)	6	(OH,O)	0.8858(6)	0.4408(6)	0.6573(3)	7.3(2)
O(6)	6	(OH,O)	0.5509(5)	0.7757(6)	−0.0069(4)	6.4(2)
O(7)	6	O	0.7391(5)	0.7398(5)	0.5004(5)	7.6(2)
O(8)	6	O	−0.0746(7)	0.3356(5)	0.8344(4)	8.2(2)
O(9)	6	O	0.5874(7)	0.6641(5)	0.1672(4)	8.2(2)

Table 3. Extended structural formulas of minerals

Mineral, sp. gr., unit-cell parameters (Å), number of formula units (*Z*)	*A* positions	*C* position	*M* position	Si radical	*B* positions
Tisinalite[1, 2] $P\bar{3}$, *a* = 10.036, *c* = 12.88, *Z* = 3	$(Na_{0.7}\square_{0.3})_3$	$(Mn^{2+}_{0.2}Ca_{0.1}\square_{0.7})_2$	$(Ti_{0.5}Zr_{0.1}Nb_{0.1}Fe^{3+}_{0.1}\square_{0.2})$	$[Si_6O_8(O_{0.7}OH_{0.3})_4(OH_{0.7}O_{0.3})_6]$	$\square_3$
Lovozerite *R*3, *a* = 10.18, *c* = 13.13, *Z* =3	$(Na_{0.8}\square_{0.2})_3$	$(Ca_{0.4}Na_{0.2}Mn^{2+}_{0.1}\square_{0.3})\square_{1.0}$	$(Zr_{0.8}Fe^{3+}_{0.1}\square_{0.1})$	$[Si_6O_{12}(OH)_3(OH_{0.6}O_{0.4})_3]$	$[(H_2O)_{0.3}\square_{0.7}]_3$
Litvinskite[3] *Cm*, *a* = 10.589, *b* = 10.217, *c* = 7.355, β = 92.91°, *Z* = 2	$(Na_{0.8}\square_{0.2})(Na_{0.8}(H_2O)_{0.2})_2$	$(Na_{0.2}Mn^{2+}_{0.1}\square_{0.7})\square_{1.0}$	Zr	$[Si_6O_{12}(OH)_3]\ (OH_{0.75}O_{0.25})_3$	$\square_3$
Kazakovite[2] $R\bar{3}m$, *a* = 10.174, *c* = 13.053, *Z* = 3	Na_3	$(Mn^{2+}_{0.5}\square_{0.5})_2$	Ti	$[Si_6O_{18}]$	Na_3

[1] For easier comparison of crystallochemical formulas, each cation position (*A*, *C*, *M*) in the tisinalite structure is represented as a single position with average occupancy.

[2] *C* positions in the tisinalite and kazakovite structures are related by the center of inversion.

[3] The unit-cell parameters of litvinskite in the *R* setting: *a* = 10.214 Å, *c* = 13.196 Å; the matrix of the transformation from setting *C* of litvinskite into setting *R* is (1/2 –1/2 1, 0 1 0, –1 0 1).

deviations of the atomic coordinates from the positions related by the *R* translations are much larger than the errors of their determination. High thermal parameters of the atoms typical of the representatives of the lovozerite group [5, 9] are explained by the imperfection of the crystals studied and the presence of vacancies in the structure.

The solution of the tisinalite structure (Fig. 2) confirmed that this mineral belongs to the lovozerite structure type, based on the mixed framework of the six-membered silicon–oxygen tetrahedral rings $[Si_6O_8(O,OH)_4(OH,O)_6]$ (average Si–O distance is 1.594 Å) sharing oxygen vertices with isolated *M* octahedra (*M* = Ti, Zr, Nb, Fe^{3+}; average *M*–O distance is 1.957 Å). The latter, in turn, share the oxygen faces with the *C* octahedra (*C* = Mn^{2+}, Ca; average *C*–O distance is 2.347 Å), which are also linked to the Si,O rings. The cavities of the framework are occupied by Na cations, filling statistically two independent eight-vertex *A* polyhedra (the average *A*–O distance is 2.523 Å).

The structure of tisinalite differs from the structures of lovozerite [5], litvinskite [9], and kazakovite [10] in the occupancy of their cation positions (Table 3). The *M* positions in the structures of lovozerite $Na_2(Ca,Na)Zr[Si_6O_{12}(OH,O)_6] \cdot H_2O$ and litvinskite $(Na,H_2O,\square)_3(\square,Na,Mn^{2+})Zr[Si_6O_{12} \cdot (OH,O)_6]$ are virtually completely occupied by Zr cations with an insignificant amount of Fe, Ti, and Hf impurities; this position in the structure of kazakovite $Na_6MnTi[Si_6O_{18}]$ is completely occupied only by Ti cations, whereas the *M* position in the structure of tisinalite $Na_2(Mn,Ca)_{1-x}(Ti,Zr,Nb,Fe^{3+})[Si_6(O,OH)_{18}]$ is split into two independent positions differently occupied by cations. Thus, the *M*(1) position is occupied by Ti and Fe^{3+} cations, whereas the *M*(2) position is filled with Ti, Zr, and Nb. This leads to a lowering of the unit-cell symmetry from rhombohedral (sp. gr. *R*3) observed for lovozerite to primitive (sp. gr. $P\bar{3}$).

The structures under consideration also differ in their occupancies of two *C* positions (per parent cubic unit cell). In the structure of kazakovite, these positions are statistically occupied (50%) by Mn cations. In the structure of lovozerite, only one *C* position is occupied predominantly by Ca and Na cations (together with a small amount of Mn) and is vacant by ~30%, whereas the second *C* position is completely vacant, which disturbs the centrosymmetricity of the mineral structure. In the structure of litvinskite, only one *C* position is partially occupied by Mn^{2+} cations as well (with a low content of impurities Ca and Fe^{2+}) and is 65% vacant, whereas another *C* position is also completely vacant. The structure of tisinalite contains three pairs of *C* positions related by the center of symmetry and occupied predominantly by Mn^{2+} cations and (to a lesser extent) Ca cations and are approximately 3/4 vacant.

The differences in the occupancy are also observed in the *A* positions. In the lovozerite structure, all three *A* positions related by *R* translation per parent unit cell are partially (~3/4) occupied by Na cations with a small amount of K impurity and are ~1/4 vacant. In the litvinskite structure, one position, *A*(1), is also partially (~3/4) occupied by Na and is ~1/4 vacant, whereas the *A*(2) position is ~3/4 and ~1/4 occupied by Na and H_2O, respectively. In the tisinalite structure, as in the litvinskite structure, the *A* position is split into two independent positions denoted by *A*(1) and *A*(2), which are approximately equally occupied (~70%) by Na atoms and are ~30% vacant. In the more symmetrical kazakovite structure, the *A* position is completely occupied by Na atoms.

The *B* positions in the centers of the faces of the cubic parent unit cell are completely occupied by Na atoms in the kazakovite structure, partially occupied (~30%) by H_2O molecules in the lovozerite structure, and are vacant in the litvinskite and tisinalite structures.

The different occupancies of the anion positions are associated with the degrees of occupancy of the *A*, *C*, and *M* cation positions in the structures under consideration (Table 3). All "bridging" (between the Si atoms) positions in all lovozerite-like structures are occupied by O^{2-} ions. In the structures of lovozerite and litvinskite, the vertices shared by the Si tetrahedra and Ti,Zr,Nb octahedra are also occupied by O^{2-} ions, whereas these positions in the structure of tisinalite are occupied by OH^- groups. The remaining anion positions (not linked to the *M* octahedra) are occupied by OH^- groups partially replaced by the O^{2-} ions. In the kazakovite structure, all the anion positions are occupied by O^{2-} ions.

Therefore, the holohedral symmetry (sp. gr. $R\bar{3}m$) of the kazakovite structure, where each cation position is occupied by only one element, is lowered in the structures of tisinalite, lovozerite, and litvinskite because of the mixed filling of the cation positions, the deficit of Na, and, as a consequence, the formation of vacancies (Table 3). After the transformation of kazakovite into tisinalite under hydrothermal or hypergenic conditions, the Si, *M*, and *C* positions remain unchanged. Thus, these positions completely retain their initial cation contents. Decationization of kazakovite occurs because of the changed contents of the *A* and *B* positions. As in zirconium-containing members of the lovozerite group [5, 9], the *B* cavities lose Na completely, whereas the *A* cavities lose Na only partially.

ACKNOWLEDGMENTS

We are grateful to E.L. Belokoneva for her help in collecting X-ray data.

REFERENCES

1. Yu. L. Kapustin, Z. V. Pudovkina, and A. V. Bykova, Zap. Vses. Mineral. O–va **109** (2), 223 (1980).

2. J. A. Mandarino, *Fleischer's Glossary of Mineral Species* (Mineralogical Record, Tucson, AZ, 1999).
3. A. P. Khomyakov, Dokl. Akad. Nauk SSSR **237** (1), 199 (1977).
4. I. V. Pekov, in *Proceedings of 4th International Conference on Mineralogy and Museums, Melbourne* (2000), p. 77.
5. N. A. Yamnova, Yu. K. Egorov-Tismenko, and I. V. Pekov, Kristallografiya **46** (6), 1019 (2001) [Crystallogr. Rep. **46**, 937 (2001)].
6. I. V. Pekov, I. A. Ekimenkova, N. V. Chukanov, *et al.*, Zap. Vseros. Mineral. O–va **129** (1), 45 (2000).
7. G. M. Sheldrick, *SHELX97. Program for the Solution and Refinement of Crystal Structures* (Siemens Energy and Automation, Madison, Wisconsin, 1997).
8. Yu. A. Pyatenko, Kristallografiya **17** (4), 773 (1972) [Sov. Phys. Crystallogr. **17**, 677 (1972)].
9. N. A. Yamnova, Yu. K. Egorov-Tismenko, I. V. Pekov, and I. A. Ekimenkova, Kristallografiya **46** (2), 230 (2001) [Crystallogr. Rep. **46**, 190 (2001)].
10. A. A. Voronkov, Z. V. Pudovkina, V. A. Blinov, *et al.*, Dokl. Akad. Nauk SSSR **245** (1), 106 (1979) [Sov. Phys. Dokl. **24**, 132 (1979)].

Translated by T. Safonova

Crystallography Reports, Vol. 48, No. 4, 2003, pp. 557–562. Translated from Kristallografiya, Vol. 48, No. 4, 2003, pp. 608–613.

STRUCTURE OF INORGANIC COMPOUNDS

Crystal Structure of New Synthetic Calcium Pentaborate $Ca[B_5O_8(OH)] \cdot H_2O$ and Its Relation to Pentaborates with Similar Boron–Oxygen Radicals

N. A. Yamnova*, Yu. K. Egorov-Tismenko*, N. V. Zubkova*, O. V. Dimitrova*, A. P. Kantor*, Ye Danian, and Xiong Ming*****

** Moscow State University, Vorob'evy gory, Moscow, 119992 Russia*

e-mail: elbel@geol.msu.ru

*** Institute of Geology and Geophysics, Deshengmenwai, Beijing, 100029 China*

**** China University of Geosciences, Xue Yuan Road 29, Beijing, 100083 China*

Received August 26, 2002

Abstract—A new representative of pentaborates with the composition $Ca[B_5O_8(OH)] \cdot H_2O$ was synthesized under hydrothermal conditions within the framework of the study of phase formation in the $CaCl_2$–Na_2CO_3–B_2O_3 system. The crystal structure of the new pentaborate was established (a = 6.5303(9) Å, b = 19.613(3) Å, c = 6.5303(9) Å, β = 119.207(2)°, V = 2513(2) Å^3, sp. gr. $P2_1/c$, Z = 4, d_{calcd} = 2.74 g/cm^3, automated Brucker SMART CCD diffractometer, 6871 reflections, λMo radiation, anisotropic refinement by least-squares, R_{hkl} = 0.076). The structure of calcium pentaborate is built by isolated B–Ca–B stacks parallel to the (010) plane. The central fragments of these stacks consists of nine-vertex Ca polyhedra. The Ca layers are located between loose B–O networks composed of $[B_2^t B_3^\Delta O_8(OH)]^{2-}$ pentaborate groups. The arrangement of the polyhedra around large cations in pentaborates with groups of two B tetrahedra and three B triangles was analyzed in terms of crystal chemistry. It is established that the structures of these compounds consist of large isolated polyhedra, columns, layers, and three-dimensional frameworks. © *2003 MAIK "Nauka/Interperiodica".*

INTRODUCTION

The possible practical applications of borate crystals possessing useful nonlinear optical, semiconducting, ferroelectric, and other physical properties and diverse structural motifs associated with the dual coordination of boron atoms stimulate interest in the synthesis of borate compounds and their structural studies. Single crystals of new calcium pentaborate were synthesized under hydrothermal conditions (P = 20 atm, t = 270°C) in the studies of phase formation in the $CaCl_2$–Na_2CO_3–B_2O_3 system with the weight ratio of 1 : 1 : 2. Colorless transparent crystals synthesized have a mica-like platelet habitus. Qualitative X-ray spectral analysis of the crystals grown, which was performed in a Cam-Scan 4DV scanning electron microscope equipped with a Link energy-dispersive attachment (analyst E.V. Guseva), showed that the specimen contained only Ca atoms. Comparison of the powder X-ray diffraction pattern of the crystals synthesized by us with the ICSD database for synthetic and natural borates showed that the new compound has no analogues. The IR spectrum (Fig. 1) was recorded by V.S. Kurazhkovkaya from a fine dispersed thin film on a KBr substrate on a Specod 75 IR spectrophotometer. Analysis of the absorption bands showed the presence in the specimen of borate radicals consisting of B tetrahedra (1100–930 cm^{-1}) and B triangles (1410–1250 cm^{-1}). The distinct absorption band at 1655 cm^{-1} and absorption bands at 3200 and 3300 cm^{-1} are indicative of the presence of water molecules. The absorption band at 3625 cm^{-1} is attributed to OH^- groups.

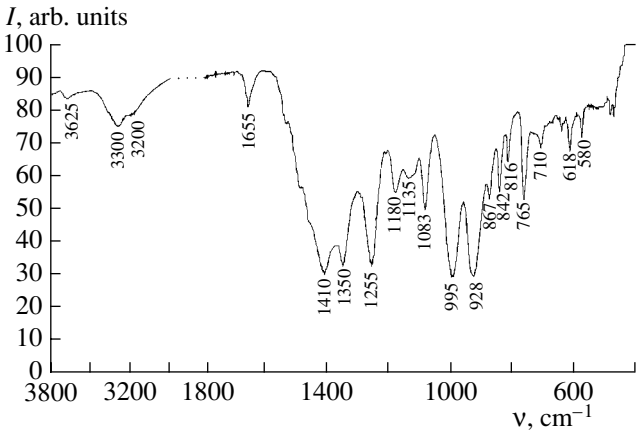

Fig. 1. IR spectrum of synthetic calcium pentaborate $Ca[B_5O_8(OH)] \cdot H_2O$.

1063-7745/03/4804-0557$24.00 © 2003 MAIK "Nauka/Interperiodica"

Table 1. Main experimental data for $Ca[B_5O_8(OH)] \cdot H_2O$

Characteristic	Parameter
Crystal system	monoclinic
Sp. gr.	$P2_1/c$
Unit-cell parameters, Å, deg	$a = 6.5303(9)$ $b = 19.613(3)$ $c = 6.5303(9)$ $\beta = 119.207(2)$
Number of formula units (Z)	4
ρ_{calcd}, g/cm^3	2.34
Linear crystal dimensions, mm	$0.40 \times 0.05 \times 0.20$
Diffractometer	Brucker SMART CCD
Radiation	MoK_α
Minimum and maximum $\sin\theta/\lambda$	0.051, 0.775
Scan ranges	$-10 \le h \le 6$ $-29 \le k \le 28$ $-9 \le l \le 9$
Total number of measured reflections	6871
Number of independent reflections with $I \le 3\sigma(I)$	1336
R_{int}	0.133
Computational program	SHELX97
Reliability factor:	
R_{hkl} (anisotropic refinement)	0.076
$wR(F^2)$	0.221
Weighting scheme in the least-squares refinement	$w = 1/[\delta^2(F^2) + (0.1423P)^2 + 0.00P]$, where $P = (\max F_o^2 + 2F_c^2)/3$
$\Delta\rho_{max}$, e/Å^{-3}	1.36
$\Delta\rho_{min}$, e/Å^{-3}	–0.79

EXPERIMENTAL. SOLUTION AND REFINEMENT OF STRUCTURE

X-ray diffraction data were collected on an automated single-crystal Brucker SMART CCD diffractometer (Laboratory of Crystal Chemistry and X-ray Diffraction Analysis of the China University of Geosciences, Beijing). The main experimental crystallographic data and the results of structure refinement are given in Table 1.

The systematic absence of the $h0l$ reflections with $l \ne 2n$ and $0k0$ reflections with $k \ne 2n$ unambiguously indicated the sp. gr. $P2_1/c$. The structure was solved by direct methods using the SHELX97 program package [1] and then was refined in the anisotropic full-matrix approximation by the least-squares method. Considering the results of calculations of the local valence balance at anions with due regard for cation–oxygen distances according to Yu.A. Pyatenko [2] (Table 2), we manged to single out in the anionic fragment of the structure the oxygen ions, the OH^- group, and the H_2O molecule. The hydrogen atoms of the hydroxy group and the water molecule were established based on difference electron-density syntheses. The established formula $Ca[B_5O_8(OH)] \cdot H_2O$ ($Z = 4$, $d_{calcd} = 2.34$ g/cm^3) corresponds to the final reliability factor R_{hkl} (Table 1) obtained after the refinement of the positional parameters of the hydrogen atoms. The coordinates of the basis atoms and the geometric characteristics of the hydrogen bonds are listed in Tables 3 and 4, respectively.

DESCRIPTION OF STRUCTURE

The structure of calcium borate is built from isolated three-layer B–Ca–B stacks parallel to the (010) plane (Fig. 2). The central fragments of these stacks contain the nine-vertex Ca polyhedra (average Ca–O distance equals 2.56 Å). The polyhedra share the O(1)–O(4) edge to form columns parallel to the c axis and located at heights of 1/4 and 3/4 along the b axis. The Ca layers are confined between loose B–O networks (Fig. 3). Earlier, such networks were observed in many borate structures. The networks consist of building blocks consisting of $[B_2^t B_3^\Delta O_8(OH)]^{2-}$ pentaborate groups built from the B(1) and B(3) tetrahedra (average B(1)–O and B(3)–O distances are equal to 1.468 and 1.474 Å, respectively) and three B triangles (average B–O distances in the B(2), B(4), and B(5) triangles are equal to 1.363, 1.365, and 1.366 Å, respectively). The pentaborate groups related by the a and c translations of the unit cell form both three-membered rings consisting of one tetrahedron and two triangles of the pentaborate group and also nine-membered rings with a triangular configuration. Each side of such a "triangle" corresponds to three edges of the B polyhedra ($3 \times 3 = 9$). Another three-membered boron–oxygen ring involves a B(5) triangle sharing two apical vertices with adjacent BO_4 tetrahedra; it is located normally to the B–O layers and "looks at" an adjacent B–Ca–B stack (Fig. 2). As a result, the B–O layers become polar. The remaining vertex of each triangle is occupied by an OH group.

The centers of the large nine-membered rings in the plane of the B–O layer are occupied by the Ca^{2+} ions centering the hexagonal "bipyramids" (average Ca–O distance equals 2.56 Å). Three horizontal edges of these bipyramids are shared with the B polyhedra of the layer, one vertex is occupied by an H_2O molecule, and the opposite vertex is "replaced" by two O^{2-} ions denoted as O(1) and O(4) forming an edge of the B(1) tetrahedron of the adjacent B–O network of the stack (Fig. 2). There are two B–Ca–B stacks per b period of the borate structure. The stacks are shifted with respect to each other and related by twofold screw axes 2_1 and centers of inversion located between the stacks. The stacks are bound only by hydrogen bonds (Table 4) between the O^{2-} ions, on the one hand, and by H_2O mol-

Table 2. Local valence balance at anions in the $Ca[B_5O_8(OH)] \cdot H_2O$ structure

Anion	Cation									
	Ca	B(1)	B(2)	B(3)	B(4)	B(5)	H(1)	H(2)	H(3)	ΣV_{ij}
O(1)	0.45	0.84		0.73						2.02
O(2)	0.19			0.74	1.11					2.04
O(3)	0.24		0.80		0.92					1.96
O(4)	0.42	0.62			0.97					2.01
O(5)	0.18		1.17	0.72						2.07
O(6)	0.24	0.73	1.03							2.00
O(7)		0.81				0.92	0.15	0.06		1.94
O(8)				0.81		1.10				1.91
$H_2O(9)$	0.28							0.95	0.84	2.07
OH(10)						0.98	0.85		0.16	1.99
Sum	2.00	3.00	3.00	3.00	3.00	3.00	1.00	1.00	1.00	20.01

ecules of one B–Ca–O stack and OH groups of another stack, on the other.

The above-described B–Ca–B stack (the idealized fragment of this stack is shown in Fig. 4b) is topologically identical to one of the two stacks in the structure of volkovskite $KCa_4B_{22}O_{32}(OH)_{10}Cl \cdot 4H_2O$ [3], which also contains two B–Ca–B stacks per *b* period of the unit cell. However, the second stack in the volkovskite structure differs from the first stack—it contains the eight-vertex K polyhedra between the B–Ca–O layers. These polyhedra share vertices occupied by the Cl^- ions to form columns along the *a* axis, similar to those in the first stack (Fig. 4c). In addition, the K polyhedra are also linked to the nine-vertex Ca polyhedra by a common triangular face, on the one hand, and by a common vertex, on the other. The latter is occupied by the water molecule involved in the nine-vertex Ca polyhedron located in the plane of the adjacent B–Ca–O network of the same stack. This arrangement gives rise to the Ba–Ca–K–Ca–B sequence.

Crystallochemical analysis of borates with the pentaborate group consisting of two B tetrahedra and three B triangles (Table 5) demonstrated that the diversity of mineral species in this group of compounds is associated primarily with the fact that the central regions of the three-layer stacks are occupied by Ca, Na, Sr, and K cations. Moreover, the above-mentioned diversity is also explained by the symmetry of the B–O layers and the mutual arrangement of the adjacent B–O networks in a single stack, on the one hand, and of individual isolated stacks, on the other. Since the symmetry relation of the B–O layers was considered earlier [4] in the context of the *OD* theory, it seemed reasonable to analyze in detail the geometry of the arrangement of the large cations in the cavities between the B–O layers in the stacks that form the structural basis of various representatives of this group of pentaborates.

The pentaborate groups are the building blocks of all the structures considered below, but their linkage in the formation of B–O layers is different. Thus, the B–O layers in the structure of gowerite $Ca[B_5O_8(OH)] \cdot [B(OH)_3] \cdot 3H_2O$ [5] (Fig. 4a) are nonpolar because of different orientations of the B tetrahedra and apical B

Table 3. Coordinates of basis atoms and equivalent thermal parameters for the $Ca[B_5O_8(OH)] \cdot H_2O$ structure

Atom	*x*/*a*	*y*/*b*	*z*/*c*	$U_{equiv} \times 100$, Å^2
Ca	0.1815(2)	0.80677(6)	0.5507(2)	1.32(3)
B(1)	0.088(1)	0.8449(3)	0.060(1)	1.1(1)
B(2)	0.688(1)	0.8282(3)	0.973(1)	1.1(1)
B(3)	0.513(1)	0.8398(3)	0.2424(9)	0.9(1)
B(4)	0.776(1)	0.8164(3)	0.6633(9)	0.9(1)
B(5)	0.324(1)	0.9491(3)	0.155(1)	1.5(1)
O(1)	0.2980(6)	0.8117(2)	0.2336(6)	1.07(7)
O(2)	0.7261(6)	0.8097(2)	0.4382(6)	1.12(7)
O(3)	0.6104(6)	0.8279(2)	0.7318(6)	1.16(7)
O(4)	0.0078(6)	0.8087(2)	0.8285(6)	1.24(7)
O(5)	0.5016(6)	0.8211(2)	0.0170(6)	1.12(7)
O(6)	0.9086(6)	0.8343(2)	0.1317(6)	1.31(8)
O(7)	0.1092(7)	0.9172(2)	0.0309(7)	1.38(8)
O(8)	0.5248(7)	0.9133(2)	0.2729(7)	1.55(8)
$H_2O(9)$	0.796(1)	0.0732(3)	0.412(1)	3.3(1)
(OH)(10)	0.3349(9)	0.0188(2)	0.1608(9)	2.9(1)
H(1)	0.19(1)	0.033(4)	0.08(1)	
H(2)	0.89(2)	0.052(4)	0.43(3)	
H(3)	0.67(2)	0.047(7)	0.39(3)	

Note: For hydrogen atoms, only the positional parameters were refined at the fixed thermal parameters (5 Å^2).

Table 4. Geometric characteristics of hydrogen bonds in the $Ca[B_5O_8(OH)] \cdot H_2O$ structure

D–H···*A*	*D*–H, Å	H···*A*, Å	*D*···*A*, Å	*DHA* angle, deg
O(10)–H(1)···O(7)	0.87(3)	1.98(3)	2.830(7)	164.4(3)
O(9)–H(2)···O(7)	0.70(3)	3.07(2)	3.245(7)	98.0(4)
O(9)–H(3)···O(10)	0.92(2)	2.03(3)	2.842(7)	145.7(4)
H(2)–O(9)–H(3) = 109.2(5)°				
H(2)···H(3) = 1.32(3) Å				

triangles normal to the B–O layer. This is associated with the fact that pentaborate groups are related by a gliding plane along the *a* axis, whereas the equally oriented pentaborate groups are related only by translation along the *c* axis. The centers of the large triangular cavities located in the plane of the B–O layers are occupied by the nine-vertex Ca polyhedra (hexagonal "bipyramids") related by the *a* plane. Six vertices of the latter polyhedra are located in the same layer, one vertex is occupied by an H_2O molecule, and two opposite vertices form an edge of an isolated $B(OH)_3$ triangle. As a result, the Ca polyhedra in the gowerite structure are isolated from each other. The B–Ca–O layers related by the twofold screw axes 2_1 are separated by half-translation along the *b* axis (16.36 Å) and are linked only by hydrogen bonds.

In the structures of volkovskite described above (Fig. 4c) and synthetic calcium borate $Ca[B_5O_8(OH)] \cdot H_2O$ (Fig. 4b), Ca polyhedra in the central layer located between the polar B–O networks are incorporated into the columns along the short *a* axis (~6.5 Å).

In the crystal structures of veatchite $Sr_2[B_5O_8(OH)]_2 \cdot [B(OH)_3] \cdot H_2O$ [6] and *p*-veatchite that has an analogous composition [7], two types of Sr polyhedra (ten- and eleven-vertex polyhedra whose central Sr atoms belong to the adjacent polar B–O networks) share edges to form layers. Each cationic layer consists of six alternating Sr(1) and Sr(2) polyhedra, which form corrugated six-membered (in the *bc* plane of veatchite and *ac* plane of *p*-veatchite) rings (Fig. 4d). In the structures of these minerals, the B–Sr–B stacks are also linked only by hydrogen bonds. Analogous layers (with the only difference that they are composed of only ten-vertex Ba polyhedra) were found in the $Ba[B_5O_8(OH)] \cdot H_2O$ structure [8], where the configuration of the layers formed by large Ba cations is virtually identical to that of the layers in the structures of veatchites (Fig. 4d).

We do not consider here the structure of biringuccite $Na_4[B_5O_8(OH)]_2 \cdot 2H_2O$ [9], because in this pentabo-

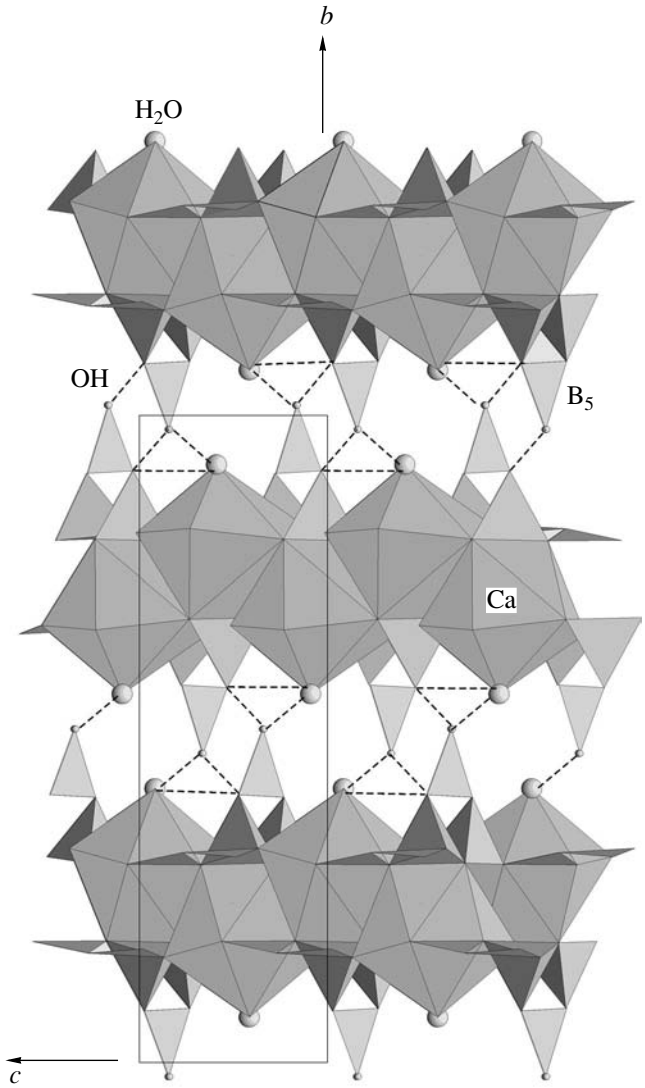

Fig. 2. $Ca[B_5O_8(OH)] \cdot H_2O$ structure projected onto the *yz* plane. Hydrogen bonds are indicated by dashed lines.

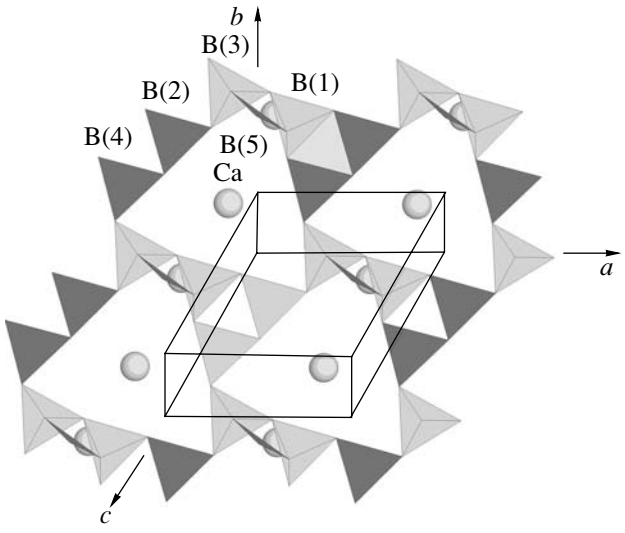

Fig. 3. Boron–oxygen layer of the $[B_2^tB_3^\Delta O_8(OH)]^{2-}$ pentaborate group in the $Ca[B_5O_8(OH)] \cdot H_2O$ structure.

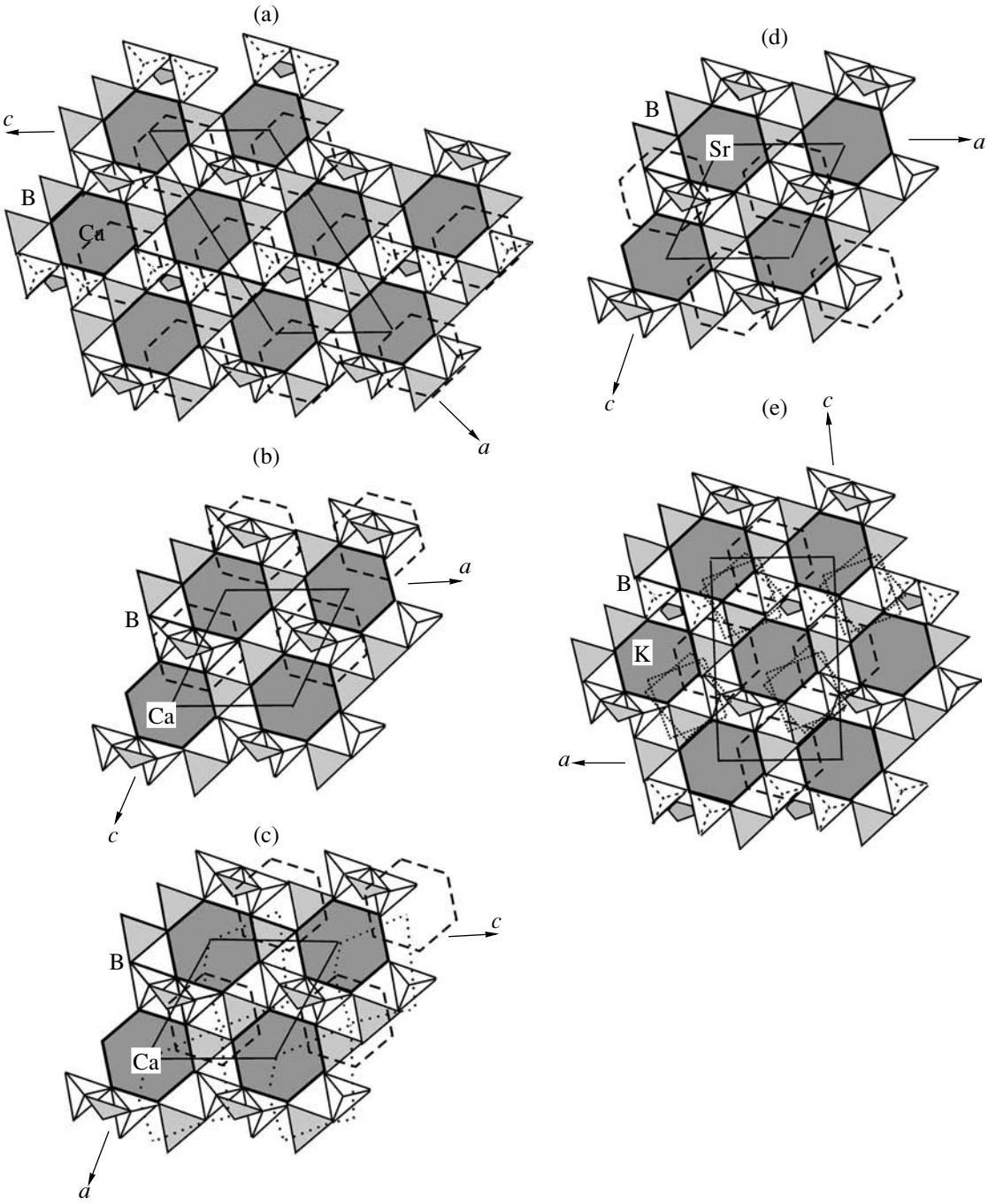

Fig. 4. Fragments of the idealized structures of (a) gowerite, (b) $Ca[B_5O_8(OH)] \cdot H_2O$, (c) volkovskite, (d) veatchite, and (e) K analog of nasinite. Sections of the polyhedra of large cations are indicated by thick solid and dashed lines. Sections of K polyhedra in the structures of volkovskite and K analog of nasinite are shown by dotted lines.

rate, the configuration of the B–O layers (built by analogous pentaborate groups) differs from that in $Ba[B_5O_8(OH)] \cdot H_2O$ because of different orientations of pentaborate groups in the B–O layers. This fact accounts for both the different symmetry ($P2_1/c$ in biringuccite and $P\bar{1}$ in synthetic barium borate) and different unit-cell parameters.

Like the gowerite structure, the structures of nasinite $Na_2[B_5O_8(OH)] \cdot 2H_2O$ [10] and its K analog $K_2[B_5O_8(OH)] \cdot 2H_2O$ [11] consist of nonpolar layers. However, the additional Na^+ (K^+) cation ($Ca^{2+} \longrightarrow 2Na^+(2K^+)$) in the structures of nasinite and its K analogue give rise to the formation of the framework composed of the eight-vertex Na polyhedra linked by common edges (Fig. 4e).

Table 5. Crystallographic characteristics of compounds of the pentaborate group

Borate and its crystallochemical formula	Sp. gr.	*Z*	Unit-cell parameters (Å, deg)			Reference
			a α	*b* β	*c* γ	
Synthetic $Ca[B_5O_8(OH)] \cdot H_2O$	$P2_1/c$	4	6.530	19.613 119.21	6.530	Present study
Volkovskite $\{Ca[B_5O_8(OH)] \cdot H_2O\}_2 \cdot \{Ca[B_5O_8(OH)] \cdot H_2O\}_2 \cdot [B(OH)_3]_2 \cdot KCl$	$P1$	1	6.50 95.68	23.96 119.6	6.62 90.59	[3]
Gowerite $Ca[B_5O_8(OH)] \cdot 3H_2O \cdot [B(OH)_3]$	$P2_1/a$	4	12.882	16.360 121.62	6.558	[5]
Veatchite $Sr_2[B_5O_8(OH)]_2 \cdot H_2O \cdot [B(OH)_3]$	Aa	4	20.860	11.738 92.10	6.652	[6]
p-Veatchite $Sr_2[B_5O_8(OH)]_2 \cdot H_2O \cdot [B(OH)_3]$	$P2_1$	2	6.70	20.80 119.15	6.60	[7]
Synthetic $Ba[B_5O_8(OH)] \cdot H_2O$	$P\bar{1}$	2	6.785 100.07	6.683 91.98	10.629 119.46	[8]
Biringuccite $Na_4[B_5O_8(OH)]_2 \cdot 2H_2O$	$P2_1/c$	4	11.195	6.561 93.89	20.757	[9]
Nasinite $Na_2[B_5O_8(OH)] \cdot 2H_2O$	$Pna2_1$	4	12.015	6.518	11.173	[10]
Synthetic $K_2[B_5O_8(OH)] \cdot 2H_2O$	$Pna2_1$	4	12.566	6.671	11.587	[11]

Analysis of the crystal structures of pentaborates showed that the cationic fragments have different architecture despite the fact that all the structures have topologically identical B–O layers. Among the pentaborates considered above, we found structures with isolated polyhedra formed around large cations (gowerite), columns (synthetic calcium borate described in this paper and volkovskite), layers (veatchite, *p*-veatchite, and synthetic $Ba[B_5O_8(OH)] \cdot H_2O$), and three-dimensional frameworks (nasinite and its synthetic K analog).

ACKNOWLEDGMENTS

We are grateful to Ma Zhesheng and Shi Nicheng of the Laboratory of Crystal Chemistry and X-ray Diffraction Analysis of the China University of Geosciences (Beijing) for their help in collecting X-ray data.

REFERENCES

1. G. M. Sheldrick, *SHELX97. Program for the Solution and Refinement of Crystal Structures* (Siemens Energy and Automation, Madison, Wisconsin, 1997).
2. Yu. A. Pyatenko, Kristallografiya **17** (4), 773 (1972) [Sov. Phys. Crystallogr. **17**, 677 (1972)].
3. R. K. Rastsvetaeva, V. I. Andrianov, E. A. Genkina, *et al.*, Kristallografiya **37** (2), 326 (1992) [Sov. Phys. Crystallogr. **37**, 163 (1992)].
4. E. L. Belokoneva, T. A. Korchemkina, and O. V. Dimitrova, Zh. Neorg. Khim. **45** (11), 1838 (2000).
5. J. A. Konnert, J. R. Clark, and C. L. Christ, Am. Mineral. **57**, 381 (1972).
6. J. R. Clark and U. S. Christ, Am. Mineral. **56**, 1934 (1971).
7. I. M. Rumanova and O. Gandybov, Kristallografiya **16** (1), 99 (1971) [Sov. Phys. Crystallogr. **16**, 75 (1971)].
8. D. Yu. Pushcharovsky, S. Merlino, O. Ferro, *et al.*, J. Alloys Compd. **306**, 163 (2000).
9. E. Corazza, S. Menchetti, and C. Sabelli, Am. Mineral. **59**, 1005 (1974).
10. E. Corazza, S. Menchetti, and C. Sabelli, Acta Crystallogr., Sect. B: Struct. Crystallogr. Cryst. Chem. **31**, 2405 (1975).
11. M. Marezio, Acta Crystallogr., Sect. B: Struct. Crystallogr. Cryst. Chem. **25**, 1787 (1969).

Translated by T. Safonova

Crystallography Reports, Vol. 48, No. 4, 2003, pp. 563–567. Translated from Kristallografiya, Vol. 48, No. 4, 2003, pp. 614–618.

STRUCTURE OF INORGANIC COMPOUNDS

Fracture Toughness and Crystallographic Characteristics of $Li_6GdB_3O_9$ Single Crystals

E. F. Dolzhenkova, V. N. Baumer, and S. I. Gordeev

Institute of Single Crystals, National Academy of Sciences of Ukraine, pr. Lenina 60, Kharkov, 310141 Ukraine

e-mail: baumer@xray.isc.kharkov.com

Received June 21, 2002

Abstract—Characteristics of the structure of single crystals of binary lithium–gadolinium borate $Li_6GdB_3O_9$ with mixed-type bonding (ionic and covalent) are studied. The system of cleavage planes in $Li_6GdB_3O_9$ single crystals is associated with the break of the Gd–O bridging bonds and the longest Li–O bonds in the Li five-vertex polyhedra. The fracture toughness in the cleavage planes is determined by microindentation. It is shown that the character of resistance to deformation and fracture toughness are determined by the orientation of the cleavage planes with respect to the faces where boron–oxygen triangles with directional covalent bonds are located. © *2003 MAIK "Nauka/Interperiodica".*

INTRODUCTION

Binary alkali metal and rare earth alkaline borates are of interest, first of all, because of their spectroscopic properties and low concentration quenching of the Ln^{3+} ions, since rare earth ions occupy rather remote mutual positions in the lattice of these borates [1]. The structure of complex borates is determined by oxygen polyhedra of rare-earth and alkali ions connected by isolated boron–oxygen triangles into a three-dimensional mixed framework. $Li_6GdB_3O_9$ (LGBO) single crystals were considered as a new efficient scintillation material for detecting thermal neutrons [2–4]. The perspective of the practical use of LGBO crystals require the study of their mechanical properties and, in particular, a possible character fracture of LGBO single crystals under deformation. There are some studies on the mechanical characteristics of alkali metal and alkaline-earth borates with predominant covalent bonding widely used in nonlinear optics and piezoelectric technology. Among these borates are lithium triborate LiB_3O_5 and lithium tetraborate $Li_2B_4O_7$ with framework structures determined mainly by the three-dimensional boron–oxygen polyanion [5–7] and beta-barium borate β-BaB_2O_4 with a layered structure in which boron–oxygen complexes form two-dimensional layers [8]. There are practically no data on the physicomechanical properties of complex borates possessing the properties close to the properties of ionic crystals.

In this work, we studied the crack resistance and considered the crystallographic characteristics of Czochralski-grown LGBO single crystals.

EXPERIMENTAL

Lithium–gadolinium borate $Li_6GdB_3O_9$ crystals are isostructural to lithium–holmium $Li_6HoB_3O_9$ and lithium–ytterbium $Li_6YbB_3O_9$ borates [9]. X-ray diffraction analysis of LGBO crystals was performed on a Siemens P3/PC automated four-circle diffractometer (MoK_α radiation, graphite monochromator, λ = 0.71073 Å, $2\theta/\theta$ scan in the angular range $5° < 2\theta < 70°$; 7094 measured reflections of which 3400 crystallographically independent reflections (R_{int} = 3.08%) and 2907 observed reflections with $I > 2\sigma(I)$. The main crystallographic data for $Li_6GdB_3O_9$: M_r = 375.32, T = 290(2) K, monoclinic, sp. gr. $P2_1/c$, a = 7.2201(11) Å, b = 16.495(4) Å, c = 6.6871(11) Å, β = 105.359(12)°, V = 768.0(2) Å^3, Z = 4, $F(000)$ = 676, d_{calcd} = 3.246 g/cm^3, μ(CuK_α) = 8.66 mm^{-1}. The structure was refined using $F^2(hkl)$ and the SHELX-97 program [10] to R = 0.020, $wR2$ = 0.051 for observed reflections and R = 0.028, $wR2$ = 0.052 for the all independent reflections, and S = 1.002.

The variety of crystallographic motifs in the LGBO lattice is determined by many structural and chemical bonds between the atoms (unit cell contains 24 Li ions, 4 Gd ions, and 12 borate ions) and the lowest symmetry (Fig. 1). Each of the Gd cations is surrounded by eight O atoms. Four of the six Li atoms, which occupy independent positions, are coordinated by five O atoms, and the two remaining Li atoms are located in tetrahedra. The Gd and Li polyhedra are cross-linked by the B triangles occupying three independent positions to form a three-dimensional framework. Two thirds of B triangles are located in the $(10\bar{2})$ plane, and one third, in the $(\bar{3}01)$ plane. The average interatomic distance in the

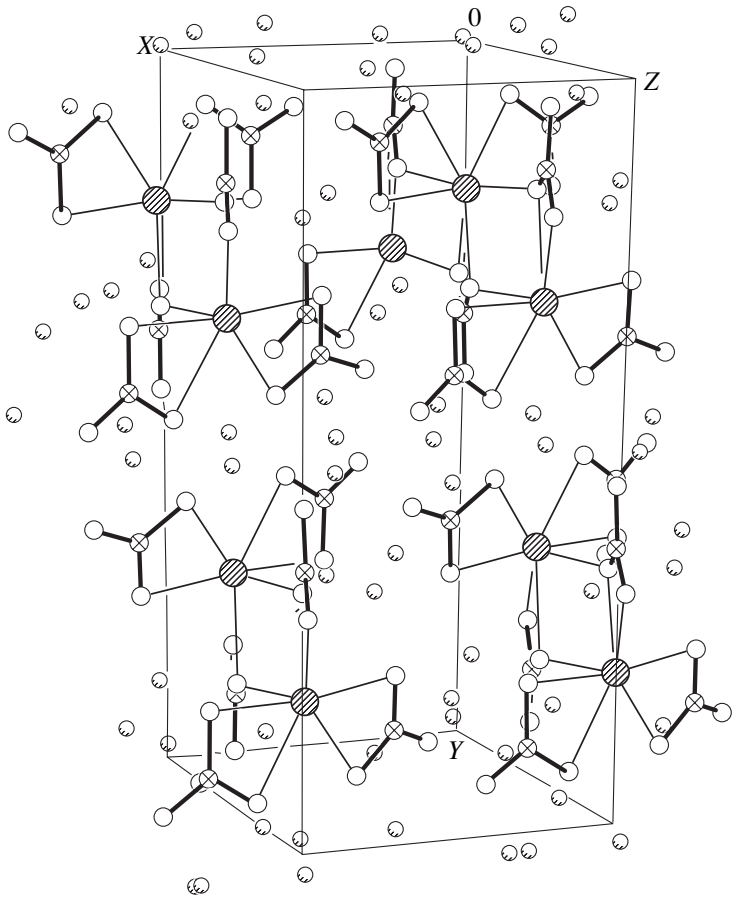

Fig. 1. Structure of an $Li_6GdB_3O_9$ single crystal. The unit cell is shown. Covalent bonds are indicated by bold and ionic bonds by thin lines. Bonds formed by Li atoms are not shown. Notation: ⊘, Gd; ○, O; ⊗, B; and ◌, Li.

Gd–O eight-vertex polyhedra equals 2.4093(7) Å, the distances in the Li tetrahedra range within 1.848(5)–2.087(6) Å, and those in the Li five-vertex polyhedra range from 1.887(5) to 2.419(6) Å. A boron atom in the triangular coordination has an average B–O distance of 1.378(2) Å.

Under mechanical action, LGBO crystals are readily cleared along the $(10\bar{2})$, (010), and (121) planes. In all cases, the study in an optical microscope showed almost perfect cleavages. The main plastic and strength parameters of the cleavages of LGBO single crystals were studied using the microindentation method on a PMT-3 device with a standard quadrilateral indentor under a load of 0.5 N. Microhardness is a complex integral characteristic of a material dependent on many factors, and, first of all, on the type of crystal structure, electronic structure, and type bonding. The microhardness values obtained for different planes were different (Fig. 2). Indentation of the $(10\bar{2})$ face resulted in the formation of an impression surrounded by cleavages. Along with radial cracks, a developed system of lateral cracks parallel to the surface was observed. The hardness number was $H_\mu^{(10\bar{2})} = 480$ MPa. The indentation pattern on the (010) plane is also characterized by radial cracks and a system of almost spherical lateral cracks. The hardness number was lower: $H_\mu^{(010)} = 410$ MPa. The indentation of the (121) plane under the same load was accompanied by the appearance of cracks but with no cleavages around the indentation and no lateral cracks. The hardness number in this plane was much lower: $H_\mu^{(121)} = 360$ MPa.

The quantitative characteristic of crack resistance, i.e., fracture toughness in cleavage planes, was determined by the microindentation method. According to [11], $K_c = 0.68k(c/a)^{-3/2}H\sqrt{a}$, MPa m$^{1/2}$, where a is the length of the half-diagonal of the indentor, c is the length of radial cracks caused by indentation, H is the microhardness, and k is the coefficient equal to 0.035, 0.09, and 0.22 for the $(10\bar{2})$, (010), and (121) planes, respectively. The fracture toughness in the planes under study was $K_c^{(10\bar{2})} = 0.41$, $K_c^{(010)} = 1.53$, and $K_c^{(121)} = 2.7$ MPa m$^{1/2}$.

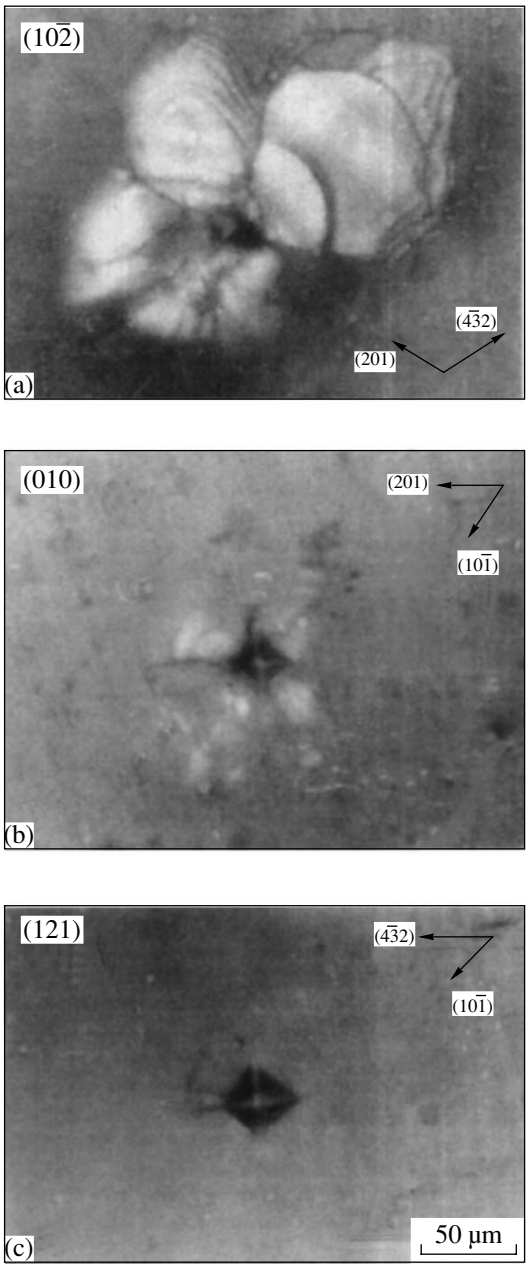

Fig. 2. Microphotograph of cracks around the indentation (P = 0.5 N) on the faces of an $Li_6GdB_3O_9$ single crystal: (a) ($10\bar{2}$), (b) (010), and (c) (121).

RESULTS AND DISCUSSION

LGBO single crystals are characterized by almost perfect cleavage along the ($10\bar{2}$), (010), and (121) planes. As is known, cleavage planes are parallel to atomic layers most weakly bound to each other. A fragment of the LGBO structure with a Gd polyhedron and B triangles linked by oxygen atoms is shown in Fig. 3. The B(1) and B(3) triangles are parallel to the ($10\bar{2}$) plane, whereas the B(2) triangle is parallel to the ($\bar{3}01$)

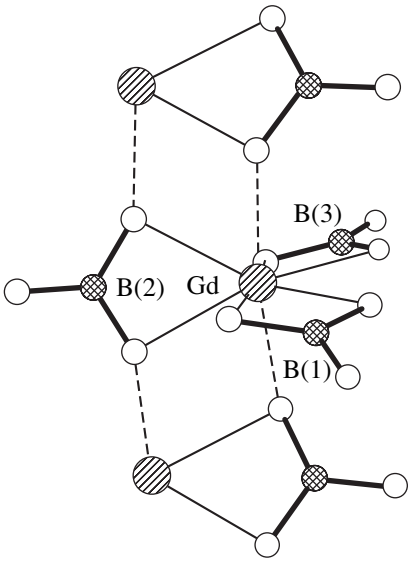

Fig. 3. Fragment of the $Li_6GdB_3O_9$ structure with bridging Gd–O bonds shown by dotted lines.

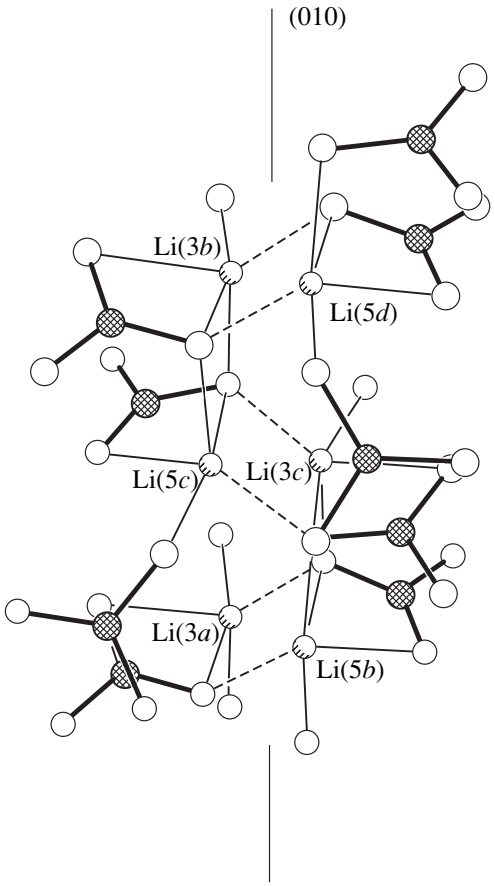

Fig. 4. $Li_6GdB_3O_9$ structure projected along the (010) plane. Gd atoms are not shown. The longest bonds in the Li(3) and Li(5) five-vertex polyhedra are shown by dotted lines.

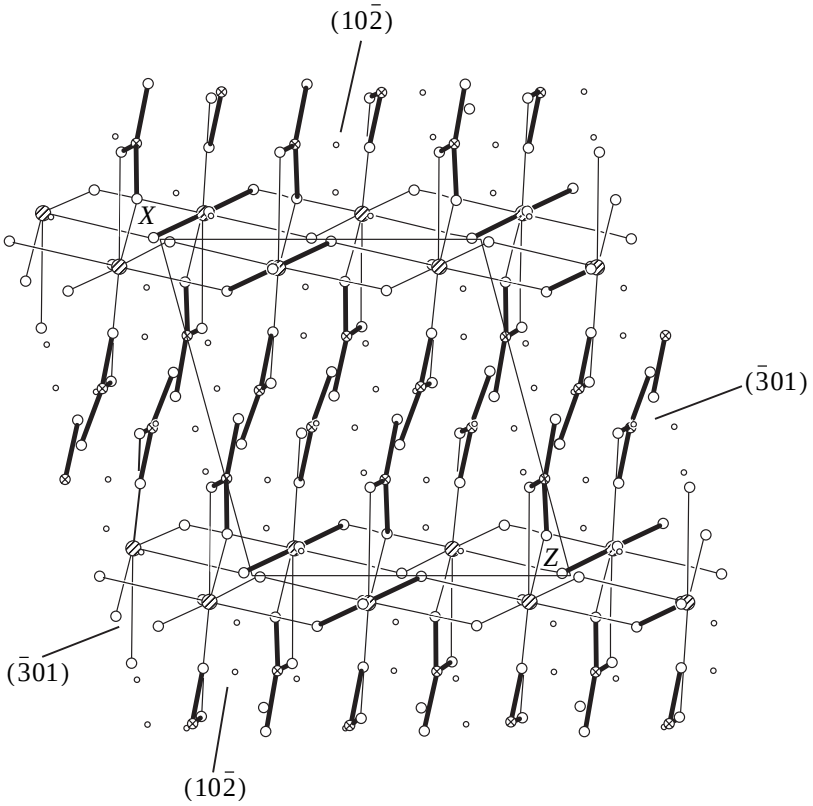

Fig. 5. Part of the $Li_6GdB_3O_9$ structure projected onto the (010) plane. Bonds formed by Li atoms are not shown. The two-dimensional unit cell projected onto the *X*, *Z* plane is shown.

plane. Each of the three groups of B triangles have six Gd–O bonds. In each of these groups, two oxygen atoms are bound to the Gd^{3+} ion. The two remaining positions are occupied by the groups of B triangles (B(2) triangles) in which an oxygen atom is a bridge between the two nearest Gd^{3+} ions. The cleavage parallel to the $(10\bar{2})$ plane is explained by the break of these bridging Gd–O bonds.

The atomic layers of LGBO crystals located parallel to the (010) plane are shown in Fig. 4. It is seen that the crystallobreaks between the atomic layers, i.e., the longest bonds, break in the Li five-vertex polyhedra: Li(3)–O = 2.234 and Li(5)–O 2.419 Å at the lowest resistance to the fracture forces. The projection of the structure fragment with Gd atoms and their bonds in this plane is similar to the projection along the $(10\bar{2})$ plane: in both cases, the Gd–O bridging bonds break. In the cleavage along the $(10\bar{2})$ plane, the longest bonds break, as in the case of the (010) plane, or, in other words, the bonds in the Li(3) and Li(5) five-vertex polyhedra break. The same pattern was also observed for the atomic layers parallel to the (121) plane. Thus, the system of the $(10\bar{2})$, (010), and (121) cleavage planes in LGBO crystals is formed because of the break of ionic bonds along the most weakly bound layers spaced for longest distances.

The character of the crystal resistance to deformation is determined by the characteristics of the internal structure: the type of structure and the character of interatomic distances. The indentation patterns on the cleavage planes substantially differ and are formed as a result of both brittle fracture and plastic deformation. Brittle cleavage is observed around the indentation on the $(10\bar{2})$ plane. The (010) plane is characterized by plastic deformation followed by the formation of radial and lateral cracks. In the (121) plane, plastic deformation predominates. Different patterns are explained by bonding in the crystal, namely, by the presence of directional covalent bonds in the B triangles and nondirectional ionic bonds in the Ln and Li polyhedra.

Brittle fracture upon the indentation of the $(10\bar{2})$ plane is provided by the orientation of this face containing boron–oxygen triangles: two thirds of the B triangles are parallel to $(10\bar{2})$. Deformation in this plane propagates along the boron–oxygen layers with the directional rigid bonds, which causes the high brittleness of the crystal. The Gd–O and Li–O ionic bonds predominate in the atomic layers that emerge onto the (010) plane (Fig. 5). Distortions introduced into the lat-

tice by indentation are of a plastic nature, because they propagate predominantly along the nondirectional ionic bonds. The radial cracks formed upon indentation propagate along the $[\bar{2}01]$ and [103] directions corresponding to the emergence of the $(10\bar{2})$ and $(\bar{3}01)$ planes onto this surface. These planes are perpendicular to the indented face. The cracks are formed only in the planes passing along boron–oxygen triangles with the directional covalent bonds, which are the planes of easy crack propagation. Indentation of the $(\bar{1}21)$ plane did not result in fracture. In this case, the indented surface is inclined toward the boron–oxygen layers. In the cleavage plane under consideration, the resistance to plastic deformation is minimal.

Substantially different values of microhardness and fracture toughness in the cleavage planes are determined by different energies of interatomic bonds in each plane under study. The highest microhardness values and, correspondingly, the lowest fracture toughness values were observed in the $(10\bar{2})$ plane parallel to the boron–oxygen layers. High propensity to brittle failure is also characteristic of the faces cleaved along the boron–oxygen layers of the crystals of beta-barium borate β-BaB_2O_4 ((0001) face) and lanthanum metaborate LaB_3O_6 ($(10\bar{1})$ plane): K_c = 0.38 MPa $m^{1/2}$ [8, 12]. The hardness number is lower and the fracture toughness is higher on the (010) face perpendicular to the planes containing directional covalent bonds in LGBO crystals. The fracture toughness in the (010) plane is rather high: for example, for the known LiB_3O_5 lithium triborate crystals, K_c = 2.0 MPa $m^{1/2}$ [5]; for lithium tetraborate $Li_2B_4O_7$, K_c = 1.5–2.0 MPa $m^{1/2}$ [6, 7]; and for beta-barium borate β-BaB_2O_4, K_c = 1.5 MPa $m^{1/2}$ [8]. The lowest microhardness and the highest fracture toughness are observed in the (121) plane inclined to the B triangles. The fracture toughness in this plane is of the same level as in the sapphire (K_c = 2.1 MPa $m^{1/2}$) and Al_2O_3 (K_c = 2.9–3.1 MPa $m^{1/2}$) single crystals [13, 14].

CONCLUSIONS

The character of resistance to deformation in LGBO single crystals is shown to be determined by their crystallographic characteristics: covalent bonding in B triangles and predominantly ionic bonding in lithium–oxygen and gadolinium–oxygen polyhedra. Being subjected to mechanical action, LGBO single crystals are cleaved along the $(10\bar{2})$, (010), and (121) planes. Cleavage occurs because of the break of Gd–O bridging bonds and the longest bonds in the Li–O five-vertex polyhedra. The $(10\bar{2})$ plane parallel to the boron–oxygen layers shows the propensity to brittle fracture after deformation and the lowest fracture toughness. In the (010) and (121) planes parallel and inclined to boron–oxygen layers (to which mainly the atomic layers with nondirectional ionic bonds emerge), plastic deformation prevails and the values of the fracture toughness are rather high.

ACKNOWLEDGMENTS

The authors are grateful to B.V. Grinev for his interest in our work.

REFERENCES

1. G. Blasse and A. Bril, J. Inorg. Nucl. Chem. **29**, 226 (1967).
2. C. W. E. Van Eijk, in *Proceedings of the Fourth International Conference on Inorganic Scintillators and Their Applications*, Ed. by Yin Zhiwen (Shanghai, China, 1997), p. 3.
3. J. P. Chaminade, O. Viraphong, F. Guillen, *et al.*, IEEE Trans. Nucl. Sci. **48** (4), 1158 (2001).
4. V. N. Baumer, B. V. Grinev, M. F. Dubovik, *et al.*, Poverkhnost, No. 5, 72 (2002).
5. I. P. Babijchuk, E. F. Dolzhenkova, B. P. Nazarenko, *et al.*, Funct. Mater. **6** (4), 721 (1999).
6. N. L. Sizova, V. A. Lomonov, and Yu. V. Pisarevskiĭ, Kristallografiya **42** (2), 331 (1997) [Crystallogr. Rep. **42**, 291 (1997)].
7. I. P. Babiĭchuk, E. F. Dolzhenkova, M. B. Kosmyna, and B. P. Nazarenko, Ukr. Fiz. Zh. **42** (4), 485 (1997).
8. D. Eimerl, L. Davis, S. Velsko, *et al.*, J. Appl. Phys. **62** (5), 1968 (1987).
9. N. I. Leonyuk and L. I. Leonyuk, *Crystal Chemistry of Anhydrous Borates* (Mosk. Gos. Univ., Moscow, 1983).
10. G. M. Sheldrick, *SHELX97. Program Package for Solving and Refinement of Crystal Structures (Pre-Release Version)* (Univ. of Göttingen, Germany, 1997).
11. A. G. Evans and E. A. Charles, J. Am. Ceram. Soc. **59** (5–6), 371 (1976).
12. E. F. Dolzhenkova, A. N. Shekhovtsov, A. V. Tolmachev, *et al.*, J. Cryst. Growth **233** (3), 473 (2001).
13. M. T. Laugier, J. Mater. Sci. Lett. **6**, 355 (1987).
14. R. F. Cook, T. R. Dinger, and D. R. Clarke, Appl. Phys. Lett. **51** (6), 454 (1987).

Translated by E. Yablonskaya

Crystallography Reports, Vol. 48, No. 4, 2003, pp. 568–572. Translated from Kristallografiya, Vol. 48, No. 4, 2003, pp. 619–623.

STRUCTURE OF INORGANIC COMPOUNDS

Crystal Structure of Pr_2B_5 Boride

Yu. B. Kuz'ma*, V. S. Babizhetskiĭ*, R. Guérin, and S. I. Mikhalenko***

** Lviv State University, ul. Kirila i Mefodiya 6, Lviv, 290005 Ukraine*
e-mail: ukuzma@franko.lviv.ua
*** Laboratory of Solid State and Inorganic Molecular Chemistry, UMR CNRS 6511, University of Rennes 1, avenue du General Leclerc, 35042 Rennes, Cedex France*

Received May 23, 2002

Abstract—The crystal structure of Pr_2B_5 boride of a new type was established by single-crystal X-ray diffraction analysis; sp. gr. $C2/c$, a = 15.1603(4) Å, b = 7.2771(2) Å, c = 7.3137(2) Å, β = 109.607(2)°, 2068 reflections, R_F = 0.041, R_w = 0.055. The Pr_2B_5 structure is similar to the Gd_2B_5 structure. © *2003 MAIK "Nauka/Interperiodica".*

INTRODUCTION

According to the phase diagram of the Pr–B system, this system contains three binary compounds. The ~Pr_2B_5 and PrB_4 borides are formed by peritectic reactions at ~2100 and 2350°C, respectively, and the PrB_6 boride is formed congruently at 2610°C and has a narrow range of homogeneity [1]. It was assumed that the ~Pr_2B_5 boride has a tetragonal structure (a = 3.81 Å, c = 3.81 Å), and its formation was explained by presence of carbon impurities [2]. Later, the compound Pr_2B_5 with a low-symmetric structure was reported [3]. Compounds with the composition Ln_2B_5 were also observed in other systems [1]. Isostructural Gd_2B_5 [4] and Sm_2B_5 [5] borides were found to be monoclinic, whereas the crystal structures of the ~Pr_2B_5 and ~Nd_2B_5 borides remained unknown. Studying the interactions in the Pr–M–B systems (M are transition metals), we repeatedly observed the boride of the composition ~Pr_2B_5, whose X-ray diffraction pattern was very complicated and did not correspond to the tetragonal structure with the parameters indicated in [2]. This discrepancy made us undertake a new investigation of the crystal structure of ~Pr_2B_5.

EXPERIMENTAL

Samples containing 50–30 at. % of Pr and 50–70 at. % of B were melted in an arc furnace (Ar atmosphere) equipped with a tungsten electrode. Powder X-ray diffraction analysis of the ingots obtained demonstrated that they consisted of two phases, ~Pr_2B_5 + Pr. The ingots were very dense, which did not allow us to separate small shiny crystallites observed on the ingot fracture. The ingots were stored in glass beakers in air. After two years of storage, metal praseodymium was oxidized into a white powder. A sample for further investigation was selected from the remaining shiny ~Pr_2B_5 crystallites.

The results of the investigation of the crystal structure of the Pr_2B_5 boride are given in Table 1. The atomic coordinates and thermal parameters are listed in Table 2. The interatomic distances are presented in Table 3. Computations were made using the SHELX and CSD program packages.

Table 1. Unit-cell parameters and details of X-ray diffraction study of the Pr_2B_5 structure

Sp. gr.	$C2/c$
a, Å	15.1603(4)
b, Å	7.2771(2)
c, Å	7.3137(2)
β, deg	109.607(2)
V, Å^3	760.08(7)
Number of atoms per unit cell	56
Calculated density, g/cm^3	5.8696(5)
Absorption coefficient, cm^{-3}	250.0
Radiation and its wavelength	MoK_α 0.71073
Refinement mode	F^2_{hkl}
Diffractometer	Kappa CCD-Nonius
Set of reflections	$\lvert F_{hkl}\rvert > 4.00\sigma(F)$
Number of regular point systems	9
Number of independent parameters	31
$2\theta_{max}$, deg	74.05
Number of reflections used	2068
R_F; R_w	0.041 0.055

1063-7745/03/4804-0568$24.00 © 2003 MAIK "Nauka/Interperiodica"

RESULTS AND DISCUSSION

The Pr_2B_5 structure projected onto the *xz* plane and the coordination polyhedra of atoms are shown in Fig. 1. The coordination polyhedra of boron atoms can be described as distorted trigonal prisms completed with three additional boron atoms (B(1), B(2), and B(3) atoms) located above the tetragonal faces or one additional boron atom (B(4)). The coordination polyhedron around the B(5) atom is a distorted [Pr_4] tetrahedron with two additional boron atoms (Fig. 1). Taking into account the metric characteristics, the Pr_2B_5 structure of the new type is closely related to the Gd_2B_5 structure (sp. gr. $P2_1/c$, a = 7.136 Å, b = 7.159 Å, c = 7.183 Å, β = 102.68°) [4] and differs from it in that it has a higher symmetry and one of the unit-cell parameters is doubled. The Pr_2B_5 structure can be described as a packing of distorted Pr_8 hexahedra and face-sharing pairs of deformed B_6 trigonal prisms (Fig. 2). The distorted hexahedra are centered with the virtually regular B_6 octahedra. The trigonal prisms are centered with isolated boron atoms. Analogous packings of centered polyhedra of rare-earth metals (REM) were observed in the Gd_2B_5 [4] and Sm_2B_5 [5] structures.

In the Pr_2B_5 structure, boron atoms from a framework (Fig. 3) of B_6 octahedra linked by pairs of the B(4) and B(5) atoms, with the shortest distances being observed between the B(5) atoms (1.54 Å). In the Gd_2B_5 structure, no such obvious shortening of the distances between boron atoms was observed (shortest B–B distance equals 1.647(4) Å [4]).

All the boride structures in the Pr–B system are characterized by the formation of B_6 octahedra. However, these polyhedra are linked in different ways. The PrB_6 structure (CaB_6 structure type) [6] can be considered as a packing of B_6 octahedra linked in such a way that eight-membered rings of boron atoms are formed between these octahedra. Six mutually perpendicular eight-membered rings form a cuboctahedron centered with a metal atom (Ca or REM) (Fig. 4a). The CaB_6 structure type can be derived from the CsCl structure type by replacing Cs and Cl ions by Ca atoms and B_6 octahedra, respectively. In the PrB_4 compound (ThB_4 structure type [6]), the B_6 octahedra are linked to each other by isolated boron atoms to form seven-membered rings (Fig. 4b). The ThB_4 structure can also be derived from the simpler U_3Si_2 structure type by replacing Si atoms with B atoms and U(1) atoms in the centers of the cubes with the B_6 octahedra. The framework of boron atoms (octahedra and seven-membered rings of boron atoms) are also observed in the Pr_2B_5 structure (projected onto the *yz* plane in Fig. 4c).

Comparison of octahedra in the CaB_6, ThB_4, and Pr_2B_5 structure types shows that the dramatic lowering of the structure symmetry is slightly reflected in the geometric parameters of octahedra, and the distances between boron atoms in the octahedra also vary only

Table 2. Atomic coordinates and equivalent thermal parameters for the Pr_2B_5 structure

Atom	Coordinates*			B_{eq}^{**}, Å^2
	x/*a*	*y*/*b*	*z*/*c*	
Pr(1)	0.11723(3)	0.57111(8)	0.59402(7)	0.41(1)
Pr(2)	0.11720(3)	0.06437(8)	0.72161(7)	0.38(1)
B(1)	0.2527(9)	0.7888(14)	0.831(2)	0.5(2)
B(2)	0.2502(7)	0.921(2)	0.0383(15)	0.5(2)
B(3)	0.1605(7)	0.7518(14)	0.9392(14)	0.3(2)
B(4)	0.7502(8)	0.160(2)	0.411(2)	0.6(2)
B(5)	0.4590(9)	0.255(2)	0.653(2)	0.7(2)

* All the atoms occupy the regular point systems 8(*f*) in the sp. gr. *C*2/*c*.
** $B_{eq} = 1/3[B_{11}a^{*2} + \ldots + 2B_{23}b^*c^*bc\cos\alpha]$.

Table 3. Interatomic distances *d* (Å) in the Pr_2B_5 structure

Atom	*d*	Atom	*d*
Pr(1)–B(1)	2.71(1)	Pr(2)–B(1)	2.69(1)
B(3)	2.72(1)	B(2)	2.72(1)
B(2)	2.74(1)	B(3)	2.72(1)
B(2)	2.77(1)	B(3)	2.73(1)
B(1)	2.77(1)	B(2)	2.77(1)
B(3)	2.78(1)	B(1)	2.79(1)
B(4)	2.81(1)	B(5)	2.82(1)
B(5)	2.82(1)	2B(4)	2.85(1)
B(4)	2.84(1)	B(5)	2.91(1)
B(5)	2.90(1)	B(4)	3.00(1)
B(5)	2.97(1)	B(5)	3.21(1)
B(4)	3.02(1)	Pr(2)	3.713(1)
Pr(1)	3.509(1)	2Pr(2)	3.775(1)
Pr(2)	3.709(1)	B(2)–B(4)	1.78(2)
Pr(2)	3.793(1)	B(3)	1.80(2)
2Pr(1)	3.801(1)	B(3)	1.81(2)
Pr(2)	3.802(1)	B(3)–B(5)	1.71(2)
Pr(2)	3.804(1)	B(4)–B(4)	1.84(2)
B(1)–B(3)	1.78(2)	B(5)–B(5)	1.54(2)
B(4)	1.80(2)		
2B(2)	1.81(2)		
B(3)	1.84(2)		

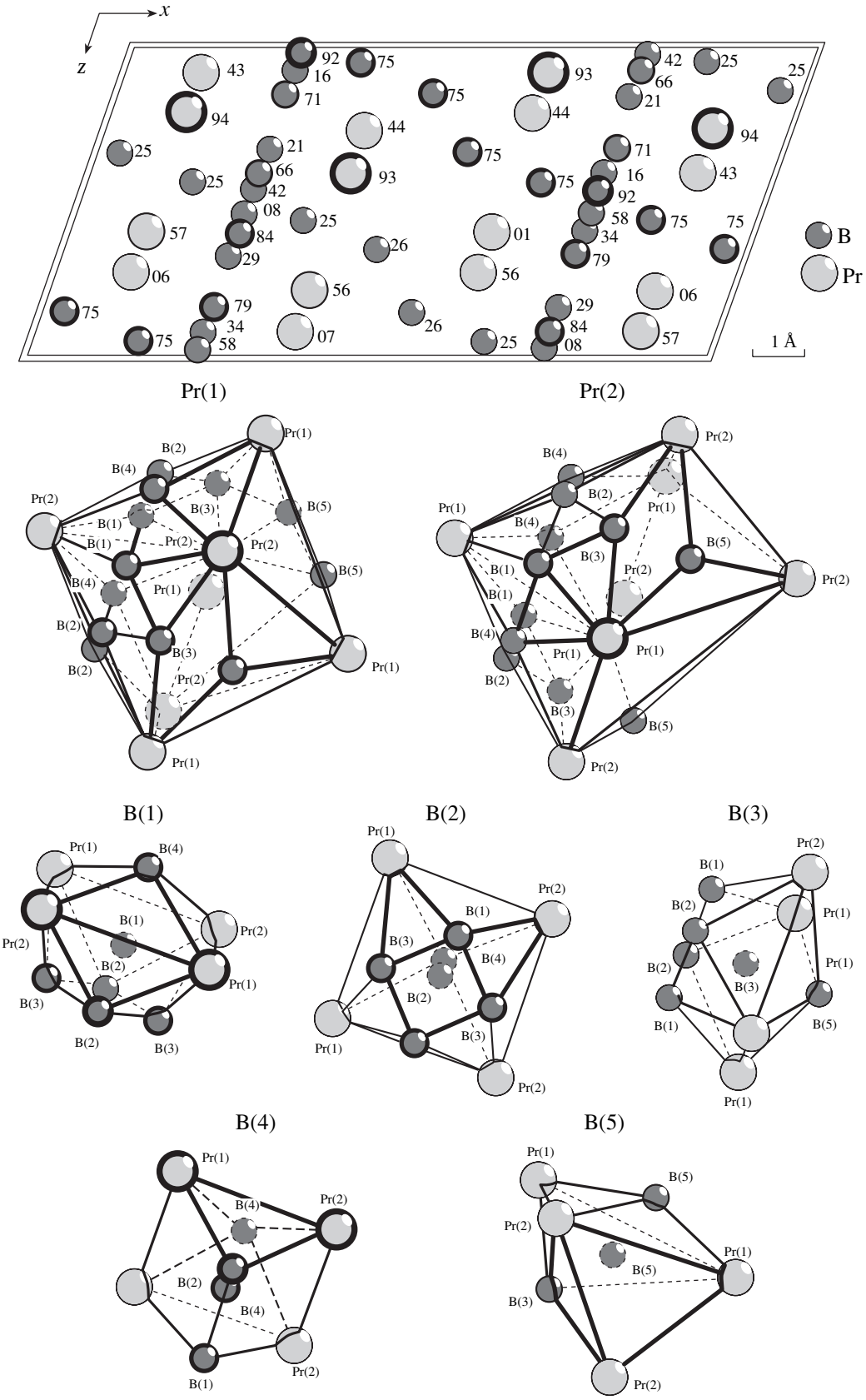

Fig. 1. (a) Pr_2B_5 structure projected onto the *xz* plane (*y* coordinates are indicated in the figure) and coordination polyhedra Pr(1), $[B_{12}Pr_7]$; Pr(2), $[B_{11}Pr_7]$; B(1), $[B_5Pr_4]$; B(2), $[B_5Pr_4]$; B(3), $[B_5Pr_4]$; B(4), $[B_3Pr_4]$; B(5), $[B_2Pr_4]$.

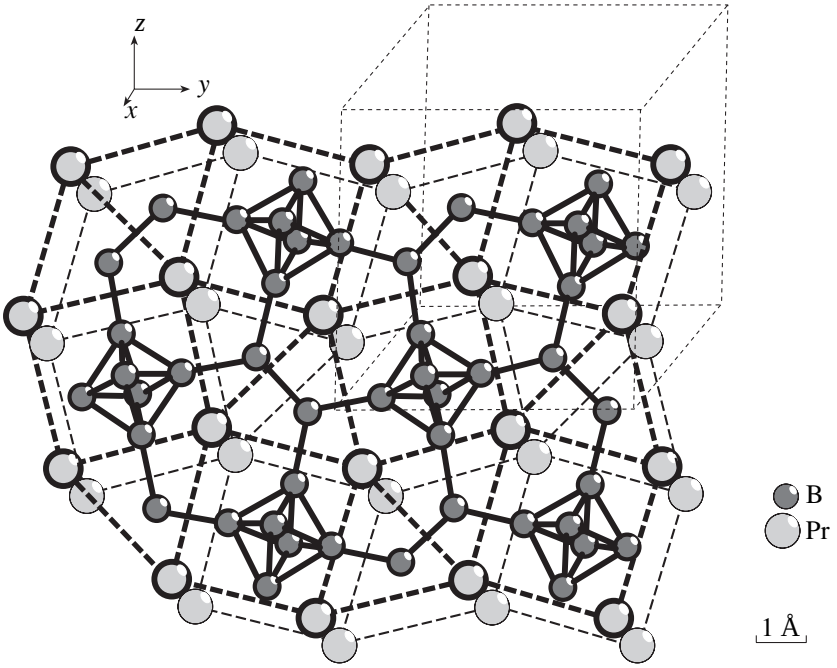

Fig. 2. Pr_2B_5 structure as a packing of the Pr_8 cubes centered with B_6 octahedra and Pr_6 trigonal prisms centered with boron atoms.

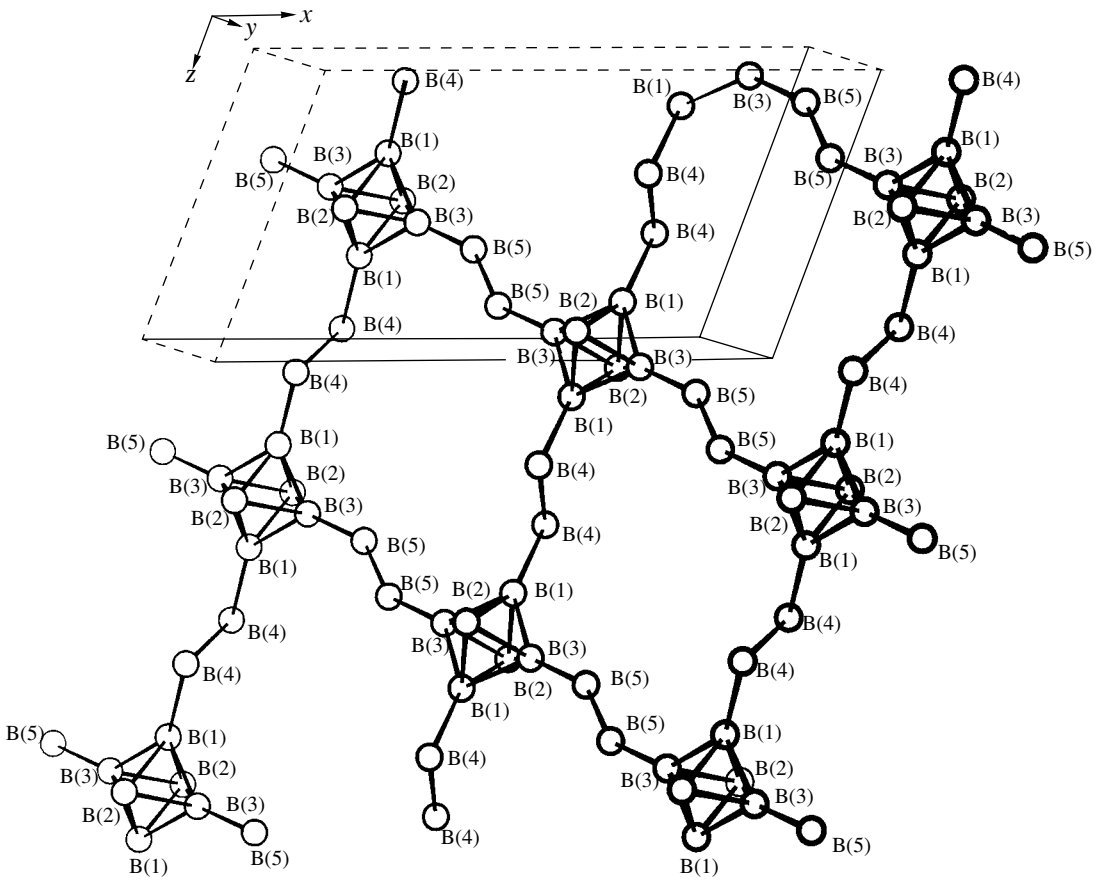

Fig. 3. Framework of boron atoms in the Pr_2B_5 structure.

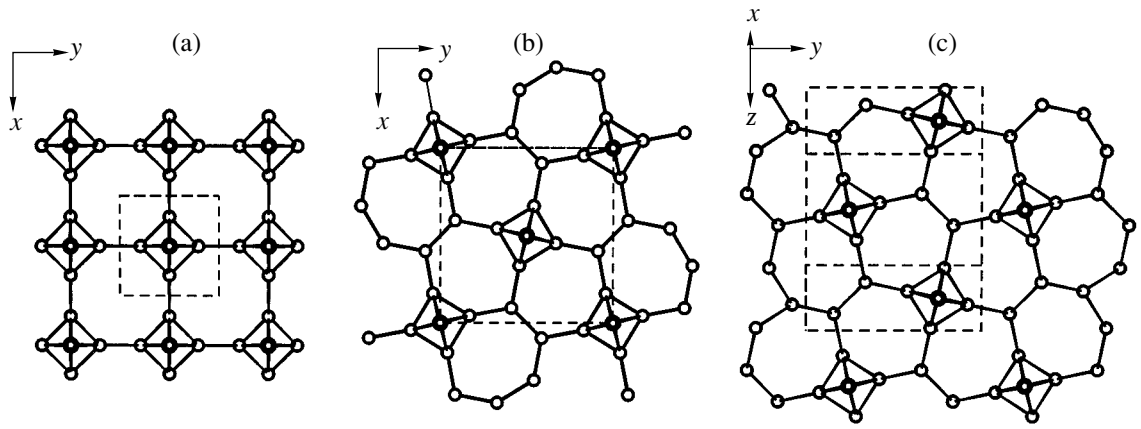

Fig. 4. Comparison of the frameworks built by boron atoms in the (a) CaB_6, (b) ThB_4, and (c) Pr_2B_5 structures.

slightly. The structure of the PrB_6 boride consists of regular octahedra (the *x* coordinate of the boron atom was not determined). In the SmB_4 boride isomorphous to ThB_4, the B(1)–4B(3) and B(3)–2B(3) distances are equal to 1.76 and 1.86 Å, respectively, i.e., an octahedron is slightly flattened in the *z* direction [7]. In the Pr_2B_5 structure, these distances are as follows: B(1)–2B(2), 1.81 Å; B(1)–2B(3), 1.78 and 1.84 Å; and B(2)–2B(3), 1.80 and 1.81 Å; i.e., the maximum difference is 0.06 Å. Hence, the difference in the B–B distances is much smaller than in the SmB_4 structure (0.10 Å) [7].

The unit-cell volume per formula unit of the Pr_2B_5 (95 $Å^3$), Sm_2B_5 (90.8 $Å^3$), and Gd_2B_5 (89.5 $Å^3$) borides linearly decreases with an increase in the proton number of REM, which may be indicative of the trivalent state of rare-earth atoms in Ln_2B_5 compounds.

REFERENCES

1. K. E. Spear, *Boron and Refractory Borides* (Springer, Berlin, 1977), p. 439.
2. B. Post, D. Moskowitz, and F. W. Glaser, J. Am. Chem. Soc. **78** (9), 1800 (1956).
3. Z. Fisk, A. S. Cooper, P. H. Schmidt, and R. N. Castellano, Mater. Res. Bull. **7**, 285 (1972).
4. C. Schwarz and A. Simon, Z. Naturforsch. B **42** (8), 935 (1987).
5. L. V. Zavaliĭ, Yu. B. Kuz'ma, and S. I. Mikhalenko, Poroshk. Metall. (Kiev), No. 6, 61 (1990).
6. Yu. B. Kuz'ma, *Crystal Chemistry of Borides* (L'vovsk. Gos. Univ., L'vov, 1983).
7. L. V. Zavaliĭ, V. A. Bruskov, and Yu. B. Kuz'ma, Izv. Akad. Nauk SSSR, Neorg. Mater. **24** (9), 1576 (1988).

Translated by T. Safonova

Crystallography Reports, Vol. 48, No. 4, 2003, pp. 573–575. Translated from Kristallografiya, Vol. 48, No. 4, 2003, pp. 624–626.

STRUCTURE OF INORGANIC COMPOUNDS

Crystal Structure and Specific Features of Formation of Vibrational Spectra of Pb_2GeS_4

D. I. Bletskan, Yu. V. Voroshilov, L. M. Durdinets, P. P. Migalko, V. A. Stefanovich, and V. N. Kabatsiĭ

Uzhgorod State University, ul. Podgornaya 46, Uzhgorod, Ukraine

Received May 31, 1999; in final form, September 3, 2002

Abstract—The structure of Pb_2GeS_4 single crystals is confirmed and the polarized Raman spectra of these crystals are recorded. The vibrational spectra was considered in terms of analysis of intramolecular vibrations of $[GeS_4]$ tetrahedral formations, the main structural elements of this compound. *© 2003 MAIK "Nauka/Interperiodica".*

According to the equilibrium PbS–GeS_2 phase diagram, two ternary compounds, $PbGeS_3$ and Pb_2GeS_4, are formed in this system [1]. The Pb_2GeS_4 compound melts the open maximum at 894 K with, which indicates its stability and the possibility of growing these crystals from melt. The Pb_2GeS_4 compound was synthesized either by melting lead sulfide and germanium disulfide in an equimolar ratio or by directly melting the elementary components in quartz ampules pumped out to 0.013 Pa under vibrational mixing. The maximum heating temperature was 1100 K. The melts were cooled in a switched-off furnace. The alloys were homogenized by 200-h-annealing at 830 K.

Pb_2GeS_4 single crystals were grown by the directional crystallization method from a Bridgman–Stockbarger melt in a vertical electric furnace. The velocity of the crystallization front (0.12–0.18 mm/h) and the temperature gradient in the crystallization zone (3–5 K/mm) were optimal for the growth of high-quality Pb_2GeS_4 crystals. Under these conditions, we obtained homogeneous single-crystal boules 16–20 mm in diameter and 60–70 mm in length.

The crystals grown were identified by X-ray phase analysis. Indexing of the X-ray diffraction pattern obtained on a DRON-05 diffractometer (CuK_α radiation) and subsequent calculation and the least-squares refinement of the unit-cell parameters were performed on a computer. The unit-cell parameters of the monoclinic (sp. gr. $P2_1/c$) unit cell of Pb_2GeS_4 (a = 8.01(3) Å, b = 8.86(4) Å, c = 10.91(3) Å, β = 114.4(4)°; Z = 4) proved to be close to the those reported in [2]. The main structural fragments are isolated coordination tetrahedra of germanium atoms $[GeS_4]$ (four germanium atoms per unit cell) located in infinite channels along the X axis. These channels are formed by ψ-octahedra of lead atoms $[PbS_5E]$, which share the edges (E is a lone electron pair of lead). Figure 1a shows isolated tetrahedra of the structure projected onto the XZ plane. Figures 1b and 1c show the projection of the structure onto the $bc\sin\beta$ plane. The $[GeS_4]$ "junctions" are shown in Fig. 1b; the $[PbS_5]$ junctions, in Fig. 1c. Two such germanium tetrahedra are located in the voids formed by eight $[PbS_5]$ junctions. The interatomic Ge–S distances range within 2.18–2.22 Å (which is consistent with the sum of the corresponding covalent radii (1.22 + 1.04 = 2.26 Å)), while the Pb–S distances, range within 2.28–3.25 Å (which is close to the sum of the ionic radii of S^{2-} and Pb^{2+} (1.82 + 1.26 = 3.08 Å)).

Raman spectra were measured in polarized light on a DFS-24 spectrometer at room temperature. The spectra were excited by the radiation of an He–Ne laser (wavelength λ = 6328 Å). The polarized Raman spectra of the Pb_2GeS_4 crystal are shown in Fig. 2 for all the components of the scattering tensor.

The frequencies of the Raman-active modes are summarized in the table. The factor-group analysis of the normal vibrations of the Pb_2GeS_4 lattice was performed by the positional symmetry method [3]. The primitive unit cell contains 84 branches, while the long-wave phonons are distributed over the irreversible representations as follows:

$$\Gamma = 21A_g + 21B_g + 21A_u + 21B_u.$$

Consider the formation of the Pb_2GeS_4 vibrational spectrum proceeding from analysis of the transformation of intramolecular vibrations under deformation of isolated $[GeS_4]$ tetrahedra (main structural element) in a crystal field. The intramolecular vibrations of the regular tetrahedral $[GeS_4]$ molecules not distorted by the crystal field are decomposed into irreducible representations of the factor-group T_d as follows:

$$\Gamma = A_1 + E + 2F_2.$$

The A_1 representation corresponds to the totally symmetric valence vibration ν_1. Since the direction of the displacement of a sulfur atom with respect to the central

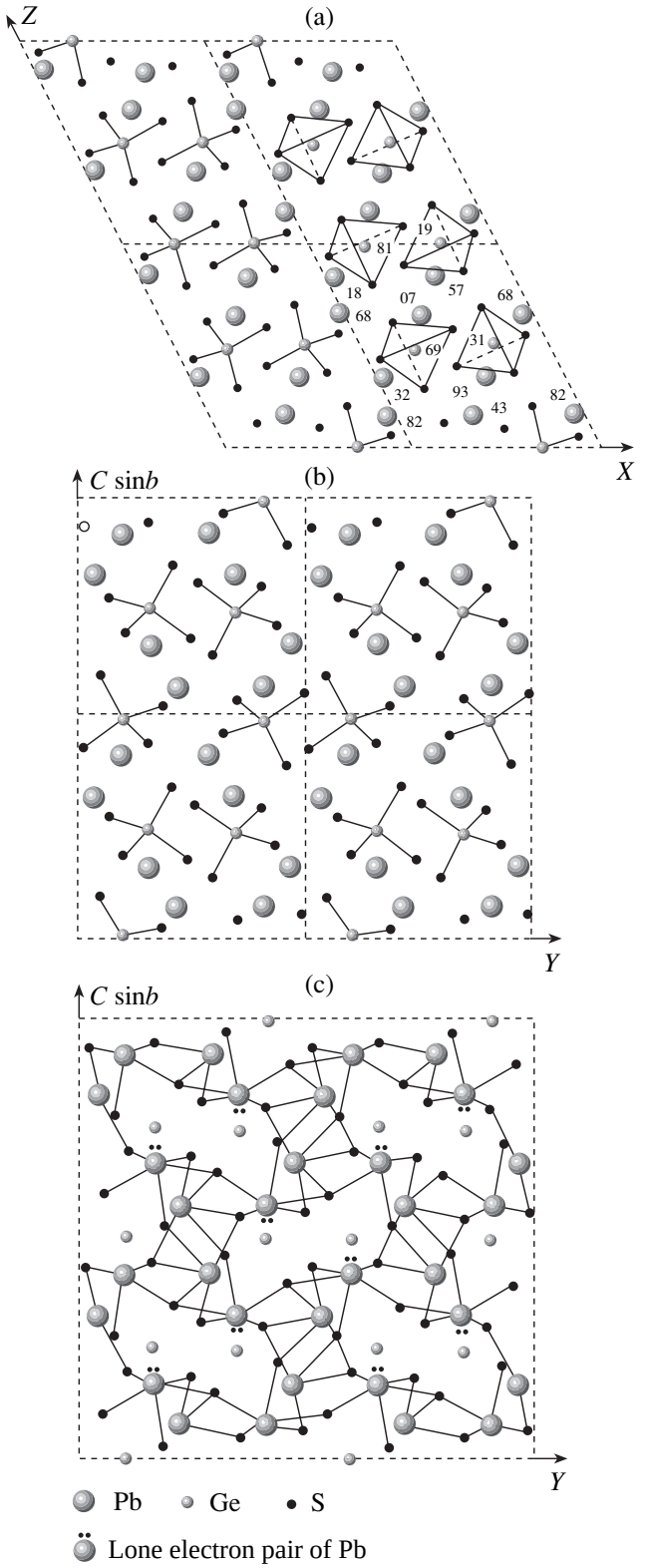

Fig. 1. Projections of the Pb_2GeS_4 structure onto the (a) *XZ* and (b, c) *bc*sinβ planes. Four unit cells are shown with (a, b) coordination $[GeS_4]$ tetrahedra. Infinite channels containing the $[GeS_4]$ tetrahedra are formed by (c) ψ-octahedra $[PbS_5E]$ sharing their edges.

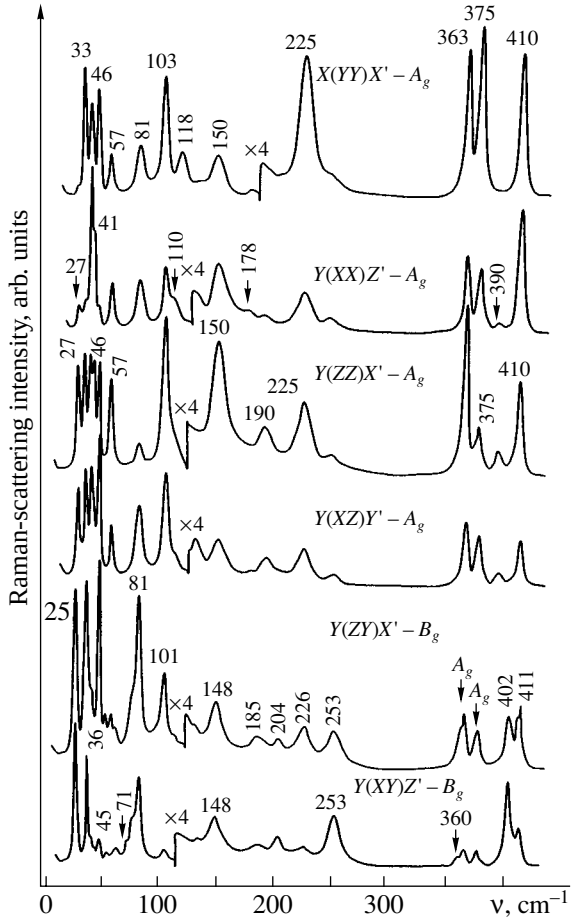

Fig. 2. Polarized Raman spectra of Pb_2GeS_4.

germanium atom at rest coincides with the direction of the Ge–S valence bonds, and, therefore, the ν_1 vibration is of a purely valent nature. Of two triply degenerate vibrations with the symmetry F_2, one, ν_3, is responsible for the variations in the Ge–S bond lengths and the other, ν_4, for the variation in the S–Ge–S angles. The doubly degenerate *E*-representation describes deformation vibrations of tetrahedra with the frequency ν_2. For a free $[GeS_4]$ molecule, $\nu_1 = 386$, $\nu_2 = 170$, $\nu_3 = 417$, and $\nu_1 = 205$ cm^{-1} [4].

Deformation of $[GeS_4]^{4-}$ anions in a static crystalline field results in the removal of the degeneracy of the ν_2, ν_3, and ν_4 vibrations, whereas their frequencies are split into two ($\nu_2 \longrightarrow \nu_2^1 + \nu_2^2$) and three ($\nu_3 \longrightarrow \nu_3^1 + \nu_3^2 + \nu_3^3$; $\nu_4 \longrightarrow \nu_4^1 + \nu_4^2 + \nu_4^3$) components. Since the Pb_2GeS_4 unit cell contains four translationally nonequivalent $[GeS_4]^{4-}$ anions, each of the modes considered above also forms a Davydov quartet with the components polarized in the A_g, B_g, A_u, and B_u geometries. An individual Davydov quartet is also formed by the valence vibration of a tetrahedron ν_1. Thus, four

Frequencies (cm^{-1}) of vibrational modes in a Pb_2GeS_4 crystal

Frequency		A_g				B_g		IR
vibration type		*XX*	*YY*	*ZZ*	*XZ*	*YZ*	*YX*	
Internal	ν_3^1	410	410	410	410	411		410
	ν_3^2	390		390	390	402	402	389
	ν_3^3	363	363	363	363	360	360	359
	ν_1	375	375	375	375	374	374	
	ν_4^1	248	248	248	248	253	253	240
	ν_4^3	225	25	225	225	226	226	215
	ν_4^2	190	190	190	190	204	204	
	ν_2^1	178	178		178	185	185	184
	ν_2^2	150	150	1150	150	148	148	
External	Translational–librational						133	
		130	130		130	113		
			118			101	101	120
		110		110	110	81	81	
		103	103	103	103	76	76	103
		81	81	81	81		71	70
	Translational, Pb^{2+}	57	55	57	57	61	61	
		46	46	46	46	58	58	57
		41		41	41	52	52	52
		39	39	39	39	45	45	
		33	33	33	33	6	36	
		27		27	27	25	25	

valence modes should be observed in the high-frequency range of the Raman spectrum, which is consistent with the experiment (see Fig. 2). Usually, the intensity of the ν_1 mode in the Raman spectra of the tetrahedral molecules is much higher than the intensity of the ν_3 modes. In the IR spectra, the intensity of this mode is low because of the almost spherical symmetry of the anion [4]. In the Pb_2GeS_4 crystal, considerable splitting of the vibration is associated with strong deformation of a $[GeS_4]^{4-}$ anion by the crystal field, whereas the intensities of the ν_1 and ν_3 modes are comparable, which hinders their identification.

It is assumed that the deformation vibrations in the $[GeSe_4]$ complex are in the frequency range 148–253 cm^{-1}, while the translational-librational vibrations are in the range 81–118 cm^{-1}. The range of the Raman spectrum of Pb_2GeS_4 characterized by the lowest frequency, 25–61 cm^{-1}, is formed by the translational vibrations of Pb^{2+} cations with respect to the anion sublattice.

REFERENCES

1. M. Elli and A. Mugnoli, Atti Accad. Naz. Lincei, Cl. Sci. Fis. Mat. Nat. Rend. **33** (5), 316 (1962).
2. K. Susa and H. Steinfink, J. Solid State Chem. **3** (1), 75 (1971).
3. W. B. Faterley, N. T. McDevit, and F. Beutley, Appl. Spectrosc. **25**, 155 (1972).
4. S. Pohl, W. Schiwy, N. Weinstok, and B. Krebs, Z. Naturforsch. B **28** (3), 556 (1973).

Translated by A. Zolot'ko

Crystallography Reports, Vol. 48, No. 4, 2003, pp. 576–582. Translated from Kristallografiya, Vol. 48, No. 4, 2003, pp. 627–633.

STRUCTURE OF ORGANIC COMPOUNDS

X-ray Mapping in Heterocyclic Design: XI. X-ray Diffraction Study of 1-Benzoyl-3-(Pyridin-2-yl)-Thiocarbamide and the Product of Its Reaction with Oxidants

V. B. Rybakov*, L. G. Boboshko, N. I. Burakov**, M. Yu. Zubritskiĭ**, V. I. Kovalenko**, V. A. Savelova**, A. F. Popov**, and V. A. Mikhaĭlov****

** Faculty of Chemistry, Moscow State University, Vorob'evy gory, Moscow, 119899 Russia*

e-mail: rybakov@biocryst.phys.msu.su

*** Institute of Physicoorganic and Coal Chemistry, National Academy of Sciences of Ukraine, Donetsk, Ukraine*

Received October 31, 2002

Abstract—The structures of 1-benzoyl-3-(pyridin-2-yl)-thiocarbamide $C_{13}H_{11}N_3O_1S_1$ (**I**) and 2-benzoylimino-1,2,4-thiadiazole[2,3-*a*]pyridine $C_{13}H_9N_3O_1S_1$ (**II**) are studied by X-ray diffraction. Structures **I** [*a* = 5.342(4) Å, *b* = 20.428(5) Å, *c* = 11.784(4) Å, β = 90.55(2)°, *Z* = 4, space group $P2_1/n$) and **II** [*a* = 6.258(6) Å, *b* = 18.068(14) Å, *c* = 10.185(10) Å, β = 95.45(8)°, *Z* = 4, space group $P2_1/n$) are determined by direct methods and refined to R_1 = 0.0673 and 0.0802, respectively. In structure **I**, both intramolecular (involving the O atom) and intermolecular (involving the N and S atoms) hydrogen bonds are observed. The latter bonds are responsible for the formation of centrosymmetric molecular dimers. In structure **II**, a short intramolecular contact (2.168 Å) is observed between the S and O atoms. © *2003 MAIK "Nauka/Interperiodica"*.

INTRODUCTION

This study continues our structural investigations of heterocyclic compounds that are able to enter readily into various rearrangements, in particular, cyclization reactions [1–11]. As in our previous studies, we step-by-step perform the X-ray diffraction analysis of all the intermediates and final products of multistage cyclization reactions and rearrangements. Specifically, acylated thiocarbamides are characterized by the multiside reactivity and serve as interesting objects for such investigations. This paper reports on the results of the structural study of 1-benzoyl-3-(pyridin-2-yl)-thiocarbamide ($C_{13}H_{11}N_3O_1S_1$, **I**) and the product of its reactions with oxidants (halogens, hydrogen peroxide, and hydroxylamine), namely, 2-benzoylimino-1,2,4-thiadiazole[2,3-*a*]pyridine ($C_{13}H_9N_3O_1S_1$, **II**). The data on the crystal structures of **I** and **II** are unavailable in the Cambridge Structural Database (version 04.02) [12].

Compounds **I** and **II** were synthesized by schemes 1 and 2, respectively.

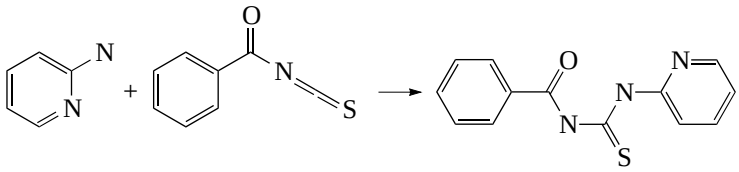

Scheme 1.

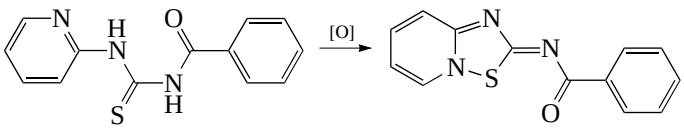

Scheme 2.

EXPERIMENTAL

The analysis of the reaction mass composition and the control of the purity of the products were carried out with a GPC liquid chromatograph [acetonitrile : water = 7 : 3, phosphoric acid to pH = 3, and sodium dodecylsulfate (0.1%) as a mobile phase; Separon C18 as a stationary phase; column, 150 × 3 mm; grain size, 5 μm; an LCD 2567 spectrophotometric detector; filter with a maximum transmission of 254 nm].

1063-7745/03/4804-0576$24.00 © 2003 MAIK "Nauka/Interperiodica"

The NMR spectra were recorded on a Gemini-200 spectrometer (field intensity, 1.4 Tl, working frequency, 200.14 MHz for protons). The IR spectra were recorded on a Perkin-Elmer Spectrum BS spectrophotometer (KBr pellets). The UV spectra were recorded on a Specord M40 spectrophotometer. The mass spectra were obtained on a Finnigan spectrometer using electron impact ionization (70 eV). The signals in the ^{1}H and ^{13}C spectra were assigned according to the data taken from [13–17] and the results of two-dimensional experiments.

1-Benzoyl-3-(pyridin-2-yl)-thiocarbamide was synthesized according to the procedure described in [18]. ^{1}H NMR (δ, ppm, DMSO-d_6, TMS as an internal standard): 7.2 tr (H6), 7.6 m (H13, H14, H15), 7.8 tr (H5), 8.4 d (H7), 8.8 d (H12, H16), 8.9 d (H4), 11.5 s (NH), 13.4 s (NH). ^{13}C NMR (δ, ppm, DMSO-d_6, TMS as an internal standard): 115.3(C4), 120.8 (C6), 128.0 (C13 and C15, or C12 and C16), 128.4 (C12 and C16, or C13 and C15), 131.9 (C11), 132.6 (C14), 137.2 (C4), 147.9 (C7), 151.1 (C3), 168.0 (C10), 177.5 (C1). IR (ν, cm^{-1}): 3281, 3006, 1678, 1552, 1525, 1438, 1341, 1252, 1158, 714. Mass spectrum (intensity expressed as a percentage of the strongest peak): 257 (45), 152 (10) 137 (10) 120 (25), 105 (100), 94 (40), 77 (95), 51 (40).

Reaction of **I** *with Bromine*

Bromine (0.15 ml, 2.9×10^{-3} mol) was poured in a solution of **I** (0.5 g, 1.9×10^{-3} mol) in 1.4-dioxane (2.5 ml). An orange oily precipitate was formed. The reaction mass was heated for 5 min, and after cooling, the precipitate was filtered off, washed with dioxane (1 ml) and ethanol (1 ml), and dried in air. The precipitate contained 2-benzoylimino-1,2,4-thiadiazole[2,3-*a*]pyridine (0.4 g, 77% yield) of the chromatographic grade (99.9%). ^{1}H NMR (δ, ppm, DMSO-d_6, TMS as an internal standard): 7.37 tr (H6), 7.5 m (H13, H14, H15), 7.82 d (H4), 8.08 tr (H5), 8.25 d (H12, H16), 9.04 d (H7). ^{13}C NMR (δ, ppm, DMSO-d_6, TMS as an internal standard): 117.0 (C4), 118.6 (C6), 128.4–128.7 (C12–C16), 132.5 (C14), 133.2 (C11), 134.4 (C5), 139.3 (C7), 155.5 (C10), 175.8 and 176.8 (C1 and C3). IR (ν, cm^{-1}): 3436 s, 1625 w, 1528 s, 1490 s, 1451 s, 1391 s, 1331 s, 765 s, 719 s. Mass spectrum: 255 (90), 178 (50), 152 (15), 136 (25), 105 (100), 77 (80), 51 (25).

Reaction of **I** *with Hydrogen Peroxide*

Hydrogen peroxide (5.3 ml, 4.6×10^{-2} mol) was poured in a solution of **I** (6 g, 2.3×10^{-2} mol) in 1.4-dioxane (30 ml). The reaction mass was boiled for 20 min, and after cooling, the precipitate was filtered off, washed with water, and dried in air. According to the data of highly efficient liquid chromatography, the precipitate contained 99.9% **II** (1.3 g, 21% yield).

Table 1. Crystal data, data collection, and refinement parameters for structures **I** and **II**

Compound	$C_{13}H_{11}N_3O_1S_1$ (**I**)	$C_{13}H_9N_3O_1S_1$ (**II**)
Molecular weight	257.31	255.29
Crystal system	Monoclinic	Monoclinic
Space group	$P2_1/n$	$P2_1/n$
a, Å	5.342(4)	6.258(6)
b, Å	20.428(5)	18.068(14)
c, Å	11.784(4)	10.185(14)
β, deg	90.55(2)	95.45(8)
V, Å^3	1285.9(11)	1146.4(18)
Z	4	4
ρ_{calcd}, g/cm^3	1.329	1.479
$\mu(MoK_\alpha)$, cm^{-1}	0.243	0.272
Crystal size, mm	$0.30 \times 0.30 \times 0.30$	$0.35 \times 0.35 \times 0.10$
θ_{max}, deg	25.98	23.96
Number of reflections with $I \geq 2\sigma(I)$/number of parameters	1261/208	1421/154
R_1/wR_2	0.0673/0.1466	0.0802/0.1453
$\Delta\rho_{max}/\Delta\rho_{min}$, e/Å^3	0.263/–0.222	0.247/–0.277

Reaction of **I** *with Hydroxylamine in Dimethylformamide*

Hydroxylamine hydrochloride (3.6 g, 4.6×10^{-2} mol) was added to a solution of **I** (12 g, 4.6×10^{-2} mol) in dimethylformamide (36 ml), and the mixture was heated for 10 min. During this period, the initial compound **I** underwent a complete conversion. The reaction mass was allowed to stand inside a freezing chamber for 1 h. The precipitate obtained was filtered off, washed with water, and dried in air. The precipitate contained 96% **II**. After the precipitate was treated with ethanol (2×5 ml) and dried to constant weight (2 g, 16% yield), it acquired the chromatographic grade (99%).

The experimental intensities of the diffraction reflections for **I** and **II** were collected on a CAD4 four-circle diffractometer [19] at room temperature (MoK_α radiation, graphite monochromator, ω scan mode). The unit cell parameters were determined and refined using 25 reflections in the θ range 14.5°–14.8° for **I** and 7.7°–9.9° for **II**. The main experimental parameters and the crystal data for **I** and **II** are summarized in Table 1.

Since the crystals of the compounds studied have small linear absorption coefficients and small size, the data were not corrected for absorption. The primary processing of the experimental data for **I** and **II** was performed with the WinGX98 program package [20]. All further calculations were carried out with the SHELX97 program package [21]. The crystal structures were solved by direct methods, and all the non-hydrogen atoms in both structures were refined in the

Table 2. Selected bond lengths *d* (Å) in structures **I** and **II**

Bond	*d* (**I**)	*d* (**II**)
S(1)–C(1)	1.651(4)	1.736(10)
S(1)–N(8)		1.795(9)
S(1)–O(1)		2.167(8)
O(1)–C(10)	1.233(4)	1.297(12)
C(1)–N(2)	1.342(5)	1.318(11)
C(1)–N(9)	1.377(5)	1.356(11)
N(2)–C(3)	1.409(5)	1.375(11)
C(3)–N(8)	1.322(5)	1.307(12)
C(3)–C(4)	1.368(6)	1.413(13)
C(4)–C(5)	1.384(7)	1.344(14)
C(5)–C(6)	1.335(7)	1.352(14)
C(6)–C(7)	1.345(8)	1.338(13)
C(7)–N(8)	1.337(6)	1.339(11)
N(9)–C(10)	1.373(5)	1.317(12)
C(10)–C(11)	1.468(6)	1.498(13)

anisotropic approximation of thermal parameters. In both compounds, the system of atomic numbering is the same. Selected interatomic distances, bond angles, and torsion angles in compounds **I** and **II** are listed in Tables 2, 3, and 4, respectively. The crystallographic data for both structures are deposited in the Cambridge Structural Database (deposit nos. 208 798 and 208 799). The molecular structures of compounds **I** and **II** and the atomic numberings are shown in Figs. 1 and 2, respectively, which were drawn with the PLUTON96 program [22]. The intramolecular and intermolecular contacts involving hydrogen atoms in structures **I** and **II** calculated using the PARST95 program [23] are listed in Tables 5 and 6, respectively.

RESULTS AND DISCUSSION

In molecule **I**, the *A* [C(3)⋯N(8)] and *B* [C(11)⋯C(16)] six-membered rings are planar within 0.006(4) and 0.003(3) Å, respectively, and form a dihedral angle of 32.5(2)°. In **I**, the S(1)⋯H(4), O(1)⋯H(2), and O(1)⋯H(12) intramolecular contacts are observed (Table 5). The first two of these contacts are responsible for the flattening of the O(1)C(10)N(9)C(1)S(1)N(2)[C(3) … N(8)] fragment, which is planar within 0.094(3) Å. The planarity is also indicated by the torsion angles about the bonds involved in this molecular fragment (Table 4). The torsion angle about the C(10)–C(11) bond [–23.6(6)° and –29.7(6)°] is determined by the O(1)⋯H(12) van der Waals interaction, and the O(1)⋯H(12) contact is comparable in length with the S(1)⋯H(4) contact (Table 5). The intermolecular N(9)–H(9)⋯S(1) contacts link molecules **I** into centrosymmetric dimers (Fig. 1, Table 5). Molecules of 1-benzoyl-3-*R*-2-yl-thiocarbamides, where *R* = 4,5-$(Me)_2Ph$ [24], *R* = *n-Pr* [25], *R* = *p-Ph*NO_2 [26], and *R* = *p-Ph*O*Me* [27], have similar dimeric structures.

In **I**, the positions of the sulfur atom and the pyridyl substituent with respect to the C(1)–N(2) bond correspond to the synperiplanar conformation [if C(1)–N(2) is considered an ordinary bond; if this bond is treated as a multiple bond, the configuration of the fragment is *Z*].

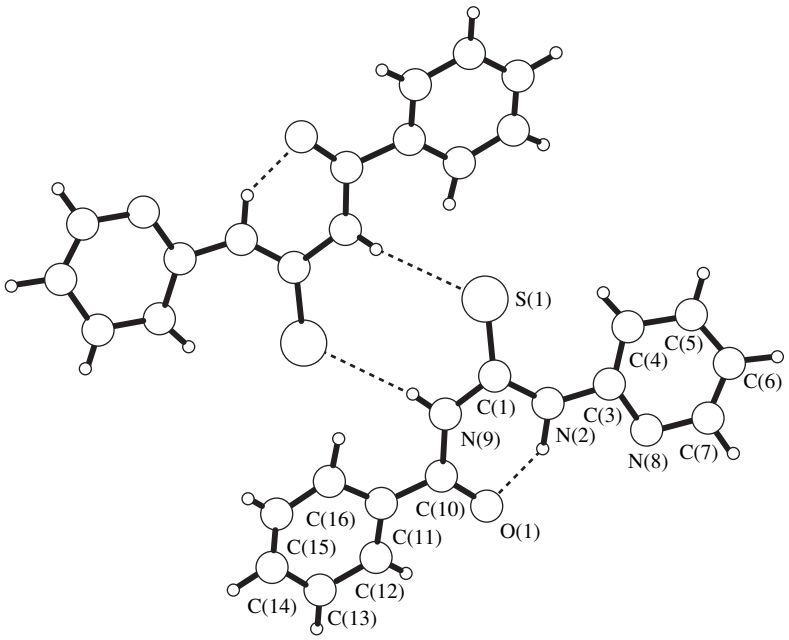

Fig. 1. Molecular structure, atomic numbering, and the formation of centrosymmetric dimeric fragments in compound **I**.

In all the *N*-aryl-*N*'-(2-pyridyl)thiocarbamides studied earlier, the positions of the sulfur atom and the pyridyl fragment correspond to the antiperiplanar conformation (or the *E* configuration) [28–31], which is due to the intramolecular N–H···N hydrogen bond involving the pyridine nitrogen. In **I**, the N–H···O hydrogen bond contains the carbonyl oxygen and the pyridine nitrogen is not involved in hydrogen bonding. The pyridine fragment is rotated in such a way that the nitrogen atom is removed from the sulfur atom, whereas the S(1) and H(4) atoms are brought close to each other. Judging from the large shift of the H(4) signal toward the low-field region, this configuration remains in the solution (see also [15]). The signals of the hydrogen atoms in the ^{1}H NMR spectrum (DMSO) remain unchanged in the temperature range 20–50°C. However, at room temperature, the signals of the carbon atoms, particularly of the pyridine carbons, in the ^{13}C NMR spectrum broaden, which is indirect evidence of rather rapid rotation about the N(2)–C(3) bond.

In contrast, the antiperiplanar arrangement of the substituents about the other amide bond, C(1)–N(9), is common for *N*-benzoyl-*N*'-arylthiocarbamides [24, 26, 27]. This can in part be attributed to the favorable conditions for the intramolecular N(2)–H(2)···O(1) hydrogen bond. In the case where the methyl group substitutes for the H atom at N(2) [32], the O(1)C(10)N(9)C(1)N(2)S(1) structural fragment becomes nonplanar.

Pyridine substituted thiocarbamides are of interest as complexing agents and biologically active compounds (for example, inhibitors of the reverse transcriptase of the human immunodeficiency virus [33]). A large number of various compounds of halogens with pyridines [34], thiocarbamides [35], and, to a lesser degree, amides [36] are known. However, all attempts to prepare halide compounds with benzoylthiocarbamide **I** resulted in the same product, namely, thiadiazole **II**. Even for the reaction of **I** with a very soft oxidant (iodine), the UV spectrum of the reaction mass, which was prepared by mixing diluted dichloroethane solutions, contains no bands of molecular iodine or its compound with benzoylthiocarbamide. The spectrum of thiadiazole **II** hydroiodide is recorded immediately after the mixing. Stronger oxidants (bromine or hydrogen peroxide) act in a similar manner. The reaction of **I** with a weaker oxidant (hydroxylamine) takes a more intricate path, and the structure of its products other than **II** will be reported elsewhere.

In molecule **II**, similar to **I**, the six-membered *A* [C(3)···N(8)] and *B* [C(11)···C(16)] rings are planar within 0.004(7) and 0.014(7) Å, respectively. The five-membered heteroring *C* [S(1)C(1)N(2)C(3)N(8)], which is formed by the reaction shown in scheme 2, is also planar within 0.006(5) Å. The *A*–*B* and *A*–*C* dihedral angles are 4.9(6)° and 0.8(6)°, respectively.

In the course of the reaction (scheme 2), molecule **I** undergoes the following transformations: the detachment of two hydrogen atoms [H(2) and H(9)] followed by bond-type redistribution results in the rotation of the pyridine ring *A* about the N(2)–C(3) bond by approximately 180°. This can lead to the formation of the S(1)–N(8) chemical bond and the closing of the five-membered heteroring *C* in compound **II**. The resultant nine-membered bicycle (*AC*) is planar within 0.010(7) Å. In addition to the pyridine rotation, the rotation of the benzoyl fragment [O(1)C(10)···C(16)] about the C(1)–N(9) bond occurs in the course of the reaction. As a result of this rotation, the S(1) and O(1) atoms closely approach each other (2.168 Å) and this short intramolecular contact is governed by the σ interaction between the nonbonding orbital of the O(1) atom and the *p* and *d* orbit-

Table 3. Selected bond angles ω (deg) in structures **I** and **II**

Angle	ω (**I**)	ω (**II**)
C(1)–S(1)–N(8)		86.5(5)
C(1)–S(1)–O(1)		79.2(4)
N(8)–S(1)–O(1)		165.7(4)
C(10)–O(1)–S(1)		104.0(7)
N(2)–C(1)–N(9)	113.8(4)	120.9(9)
N(2)–C(1)–S(1)	126.2(3)	116.2(7)
N(9)–C(1)–S(1)	119.9(3)	122.9(9)
C(1)–N(2)–C(3)	132.8(4)	109.8(8)
N(8)–C(3)–N(2)	110.0(4)	117.2(10)
N(8)–C(3)–C(4)	122.7(4)	117.6(10)
N(2)–C(3)–C(4)	127.3(4)	125.2(10)
C(5)–C(4)–C(3)	117.6(5)	118.0(10)
C(4)–C(5)–C(6)	120.4(6)	121.2(11)
C(7)–C(6)–C(5)	118.0(6)	120.7(11)
N(8)–C(7)–C(6)	124.3(6)	117.6(10)
C(3)–N(8)–C(7)	116.9(5)	124.9(10)
C(3)–N(8)–S(1)		110.4(7)
C(7)–N(8)–S(1)		124.7(8)
C(10)–N(9)–C(1)	129.9(4)	111.0(9)
O(1)–C(10)–N(9)	120.7(4)	122.6(10)
O(1)–C(10)–C(11)	121.3(4)	118.3(10)
N(9)–C(10)–C(11)	117.9(3)	118.9(10)

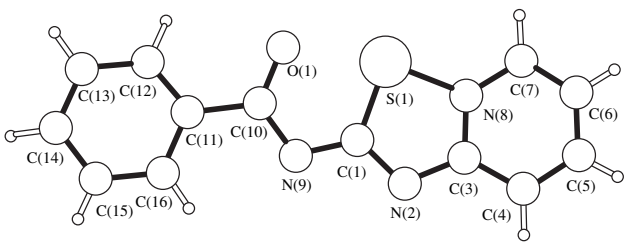

Fig. 2. Molecular structure and atomic numbering in compound **II**.

Table 4. Selected torsion angles φ (deg) in structures **I** and **II**

Angle	φ (**I**)	φ (**II**)
N(9)–C(1)–N(2)–C(3)	178.1(4)	179.0(8)
N(2)–C(3)–C(4)–C(5)	–179.3(5)	–179.8(9)
C(1)–N(9)–C(10)–C(11)	–176.4(4)	–178.3(8)
N(9)–C(10)–C(11)–C(12)	154.5(4)	178.3(1.0)
O(1)–C(10)–C(11)–C(16)	152.1(4)	179.1(9)
C(1)–N(2)–C(3)–N(8)	178.2(4)	–1.2(1.1)
C(1)–N(2)–C(3)–C(4)	–1.1(7)	178.7(9)
S(1)–C(1)–N(9)–C(10)	173.9(3)	–4.5(1.2)
N(2)–C(1)–N(9)–C(10)	–4.4(6)	177.9(9)
N(2)–C(3)–N(8)–C(7)	179.4(5)	–179.8(8)
C(10)–C(11)–C(12)–C(13)	176.4(4)	–177.5(1.0)
C(10)–C(11)–C(16)–C(15)	–175.8(4)	178.0(9)
S(1)–C(1)–N(2)–C(3)	0.0(7)	1.2(1.0)
N(8)–C(3)–C(4)–C(5)	1.5(7)	0.2(1.3)
C(3)–C(4)–C(5)–C(6)	–1.3(9)	–0.1(1.6)
C(4)–C(5)–C(6)–C(7)	0.9(0.9)	–0.3(1.8)
C(5)–C(6)–C(7)–N(8)	–0.8(1.1)	0.6(1.6)
C(4)–C(3)–N(8)–C(7)	–1.3(8)	0.2(1.4)
C(6)–C(7)–N(8)–C(3)	0.9(1.0)	–0.6(1.5)
C(1)–N(9)–C(10)–O(1)	1.8(7)	6.2(1.4)
O(1)–C(10)–C(11)–C(12)	–23.6(6)	–6.1(1.4)
N(9)–C(10)–C(11)–C(16)	–29.7(6)	3.6(1.4)

als of S(1). An analogous interaction and its association with spectral and chemical properties of the corresponding compounds were described in detail in [37]. A similar structure of the molecular fragment was reported in [38].

A remarkable feature of molecule **II** is that the formally double bonds N(2)–C(3) and C(1)–N(9) are longer than the formally ordinary adjacent bonds C(1)–N(2) and N(9)–C(10). Taking into account that the carbonyl O(1)–C(10) bond length is substantially larger than its normal value (1.22 Å), the structure of **II** is more correctly represented by the following combination of resonance structures:

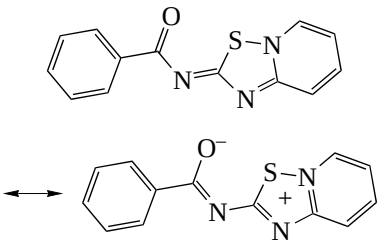

This structure of the molecules is apparently responsible for the high stability of compound **II** (high-melting crystalline compound able to sublimate under vacuum) as compared to other 2-amino-1,2,4-thiadiazole[2,3-*a*]pyridine derivatives, which are considered to be unstable under normal conditions [39, 40].

The cyclization leads to the following pronounced changes in the NMR spectra: the signal of the proton at C(4) shifts to the high-field region (by 1 ppm), and the signals of all other protons of the pyridine ring and *ortho* protons of the benzene ring shift to the low-field region (by 0.2–0.6 ppm); the signal of the C(10) carbon atom shifts to the high-field region (by ~14–15 ppm), and the signal of the C(3) carbon atom shifts to the low-field region (by 13 ppm). The positions of other carbon atoms change to a lesser degree. The IR spectra of **I** and **II** differ significantly. Indeed, in the spectrum of **II**, no bands of the NH vibrations appear in the range 3000–3300 cm^{-1}; the range of the carbonyl group vibrations (1600–1700 cm^{-1}) contains only a weak band at 1627 cm^{-1}, whereas in the spectrum of benzoylthiocarbamide **I**, a strong band is observed at 1678 cm^{-1}. Other changes in the IR spectra are less evident and require detailed analysis of the force field. In the mass spectra of both compounds, intense signals of molecular ions are observed. However, the routes of fragmentation under the electron impact are essentially different. For benzoylthiocarbamide **I**, the most probable (if not the only) route consists in the detachment of the benzoyl fragment from the molecular ion followed by the

Table 5. Parameters of interatomic contacts* in structure **I**

D–H	*d*(*D–H*)	*d*(*D*…*A*)	*d*(H…*A*)	ω*DHA*	*A*	(Symmetry operation)
N(2)–H(2)	0.95(4)	2.591(5)	1.77(4)	144(4)	O(1)	[*x*; *y*; *z*]
C(4)–H(4)	0.91(5)	3.214(5)	2.56(5)	129(4)	S(1)	[*x*; *y*; *z*]
C(12)–H(12)	0.92(5)	2.809(6)	2.55(5)	96(3)	O(1)	[*x*; *y*; *z*]
N(9)–H(9)	0.79(4)	3.581(4)	2.81(4)	168(4)	S(1)	[–*x*; –*y*; –*z*]
C(16)–H(16)	0.97(4)	3.394(5)	2.87(3)	115(2)	S(1)	[–*x*; –*y*; –*z*]
C(12)–H(12)	0.92(5)	3.428(6)	2.57(5)	154(4)	O(1)	[–*x*; –*y*; 1–*z*]
C(13)–H(13)	0.98(5)	3.677(7)	2.75(5)	157(4)	N(8)	[–*x*; –*y*; 1–*z*]
C(13)–H(13)	0.98(5)	3.367(6)	2.87(5)	112(3)	O(1)	[–*x*–1; –*y*; 1–*z*]

* *D* is a donor, *A* is an acceptor, and H is a hydrogen atom; the *d* distances and ω angles are given in Å and degrees, respectively.

Table 6. Parameters of interatomic contacts* in structure **II**

D–H	*d*(*D–H*)	*d*(*D*…*A*)	*d*(H…*A*)	ω*DHA*	*A*	(Symmetry operation)
C(12)–H(12)	0.93(1)	2.82(1)	2.492(7)	100.7(7)	O(1)	[*x*; *y*; *z*]
C(16)–H(16)	0.93(1)	2.80(1)	2.494(8)	99.5(7)	N(9)	[*x*; *y*; *z*]
C(4)–H(4)	0.93(1)	3.48(1)	2.633(8)	150.9(7)	N(2)	[1 – *x*; –*y*; –*z*]
C(7)–H(7)	0.93(1)	3.41(1)	2.521(8)	159.1(7)	O(1)	[–*x*; –*y*; 1 – *z*]
C(7)–H(7)	0.93(1)	3.36(1)	2.902(8)	111.9(7)	N(2)	[*x* – 1; *y*; *z*]
C(14)–H(14)	0.93(1)	3.37(1)	2.577(9)	143.1(7)	N(9)	[1/2 + *x*; 1/2 – *y*; 1/2 + *z*]
C(15)–H(15)	0.93(1)	3.32(1)	2.969(7)	103.7(6)	O(1)	[1 + *x*; *y*; *z*]

* *D* is a donor, *A* is an acceptor, and H is a hydrogen atom; the *d* distances and ω angles are given in Å and deg, respectively.

detachment of the sulfur atom and, finally, the formation of the aminopyridine ion. Although the peak of C_6H_5 is very strong (*m*/*e* = 77), the signal of the residual particle is not observed. Unlike this spectrum, the spectrum of thiadiazolepyridine **II** exhibits a strong peak (*m*/*e* = 178) corresponding to the residual particle, which is formed after the phenyl detachment, whereas the aminopyridine peak is absent. These differences in the NMR, IR, and mass spectra emphasize the existence of an extended strongly conjugated π system in the molecule of 2-benzoylimino-1,2,4-thiadiazole[2,3-*a*]pyridine (**II**).

ACKNOWLEDGMENTS

We acknowledge the support of the Russian Foundation for Basic Research in the payment of the license for using the Cambridge Structural Database, project no. 02-07-90322.

REFERENCES

1. V. B. Rybakov, S. G. Zhukov, E. V. Babaev, *et al.*, Kristallografiya **44** (6), 1067 (1999) [Crystallogr. Rep. **44**, 997 (1999)].
2. V. B. Rybakov, S. G. Zhukov, E. V. Babaev, *et al.*, Kristallografiya **45** (1), 108 (2000) [Crystallogr. Rep. **45**, 103 (2000)].
3. V. B. Rybakov, S. G. Zhukov, E. V. Babaev, *et al.*, Kristallografiya **45** (2), 292 (2000) [Crystallogr. Rep. **45**, 261 (2000)].
4. V. B. Rybakov, S. G. Zhukov, K. Yu. Pasichnichenko, and E. V. Babaev, Koord. Khim. **26** (9), 714 (2000).
5. V. B. Rybakov, S. G. Zhukov, E. V. Babaev, and E. J. Sonneveld, Kristallografiya **46** (3), 435 (2001) [Crystallogr. Rep. **46**, 385 (2001)].
6. V. B. Rybakov, S. I. Troyanov, E. V. Babaev, *et al.*, Kristallografiya **46** (5), 1069 (2001) [Crystallogr. Rep. **46**, 986 (2001)].
7. V. B. Rybakov, E. V. Babaev, K. Yu. Pasichnichenko, and E. J. Sonneveld, Kristallografiya **47** (1), 76 (2002) [Crystallogr. Rep. **47**, 69 (2002)].
8. V. B. Rybakov, E. V. Babaev, and V. V. Chernyshev, Kristallografiya **47** (3), 473 (2002) [Crystallogr. Rep. **47**, 428 (2002)].
9. V. B. Rybakov, E. V. Babaev, and K. Yu. Pasichnichenko, Kristallografiya **47** (4), 678 (2002) [Crystallogr. Rep. **47**, 622 (2002)].
10. V. B. Rybakov, E. V. Babaev, A. A. Tsisevich, *et al.*, Kristallografiya **47** (6), 1042 (2002) [Crystallogr. Rep. **47**, 973 (2002)].
11. D. V. Al'bov, V. B. Rybakov, E. V. Babaev, and L. A. Aslanov, Kristallografiya **48** (2), 315 (2003) [Crystallogr. Rep. **48** (2), 280 (2003)].
12. F. H. Allen and O. Kennard, Chem. Design Automat. News **8** (1), 31 (1993).
13. A. Preiss, W. Walek, and S. Dietzel, J. Prakt. Chem. **323**, 279 (1981).
14. G. L'abbe, J. Buelens, W. Dehaen, *et al.*, Tetrahedron **50**, 7019 (1994).
15. A. Kasheres and M. Ueno, J. Heterocycl. Chem. **28**, 2057 (1991).
16. L. V. Sudha, D. N. Sathyanarayana, and S. Manogaran, Spectrochim. Acta A **42**, 1373 (1986).
17. J. Jirman and A. Lycka, Collection **52**, 2474 (1987).
18. G. Y. Sarkis and E. D. Faisal, J. Heterocycl. Chem. **22**, 137 (1985).
19. *Enraf–Nonius CAD4 Software: Version 5.0* (Enraf–Nonius, Delft, The Netherlands, 1989).
20. L. J. Farrugia, *WinGX98: X-ray Crystallographic Programs for Windows* (Univ. of Glasgow, UK, 1998).
21. G. M. Sheldrick, *SHELX97: Program for the Solution and Refinement of Crystal Structures* (Univ. of Göttingen, Germany, 1997).
22. A. L. Spek, *PLUTON96: Molecular Graphics Program* (Univ. of Utrecht, The Netherlands, 1996).
23. M. Nardelli, J. Appl. Crystallogr. **28**, 659 (1995).
24. S. S. S. Raj, K. Puviarasan, D. Velmurugan, *et al.*, Acta Crystallogr., Sect. C: Cryst. Struct. Commun. **55**, 1318 (1999).
25. A. Dago, Yu. Shepelev, F. Fajardo, *et al.*, Acta Crystallogr., Sect. C: Cryst. Struct. Commun. **45**, 1192 (1989).
26. Zhang De-Chun, Zhang Yan-Qin, Cao Yang, and Zhao Bo, Acta Crystallogr., Sect. C: Cryst. Struct. Commun. **52**, 1716 (1996).
27. Cao Yang, Zhao Bo, Zhang Yan-Qin, and Zhang De-Chun, Acta Crystallogr., Sect. C: Cryst. Struct. Commun. **52**, 1772 (1996).
28. A. K. Hermetet, L. J. Ackerman, K. K. Eilts, *et al.*, J. Mol. Struct. **605**, 241 (2002).

29. L. F. Szczepura, K. K. Eilts, A. K. Hermetet, *et al.*, J. Mol. Struct. **607**, 101 (2002).
30. L. F. Szczepura, D. R. Kelman, A. K. Hermetet, *et al.*, J. Mol. Struct. **608**, 245 (2002).
31. J. M. Giesen, K. A. Claborn, K. I. Goldberg, *et al.*, J. Mol. Struct. **613**, 223 (2002).
32. S. S. S. Raj, K. Puviarasan, D. Velmuguran, *et al.*, Acta Crystallogr., Sect. C: Cryst. Struct. Commun. **55**, 1318 (1999).
33. F. M. Uckun and O. D'Cruz, US Patent No. 6376504 (April 23, 2002).
34. O. Hassel, C. Romming, and T. Tufte, Acta Chem. Scand. **15**, 967 (1961).
35. H. Hope and G. Hung-Yin Lin, J. Chem. Soc. Chem. Commun. **3**, 169 (1970).
36. N. I. Burakov, A. L. Kanibolotskiĭ, G. Yu. Osichenko, *et al.*, Zh. Org. Khim. **37**, 1276 (2001).
37. C. Cohen-Addad, M. S. Lehmann, P. Becker, *et al.*, J. Chem. Soc., Perkin Trans. 2, 191 (1984).
38. V. V. Chernyshev, K. A. Paseshnichenko, V. A. Makarov, *et al.*, Acta Crystallogr., Sect. C: Cryst. Struct. Commun. **57**, 72 (2001).
39. R. L. N. Harris, Aust. J. Chem. **25**, 993 (1972).
40. K. T. Potts and J. M. Kane, Synthesis, No. 12, 1027 (1986).

Translated by I. Polyakova

Crystallography Reports, Vol. 48, No. 4, 2003, pp. 583–590. Translated from Kristallografiya, Vol. 48, No. 4, 2003, pp. 634–641.

STRUCTURE OF ORGANIC COMPOUNDS

New Rubidium Pentaborate $Rb[B_5O_7(OH)_2] \cdot 0.5H_2O$ with a 5 : [4Δ + 1*T*] Anionic Block and Its Relation to Larderellite $(NH_4)[B_5O_7(OH)_2] \cdot H_2O$ on the Basis of the *OD* Theory

E. L. Belokoneva, T. A. Borisova, and O. V. Dimitrova

Faculty of Geology, Moscow State University, Vorob'evy gory, Moscow, 119992 Russia

e-mail: elbel@geol.msu.ru

Received August 20, 2002

Abstract—A new rubidium pentaborate is synthesized under hydrothermal conditions. Its crystal structure is studied by the heavy-atom method without any *a priori* knowledge of chemical formula. The chemical formula is $Rb[B_5O_6(OH)_4] \cdot 0.5H_2O$, sp. gr. $P\bar{1}$, lattice parameters a = 7.679(4) Å, b = 9.253(6) Å, c = 12.053(9) Å, α = 98.55(5)°, β = 106.80(5)°, γ = 91.71°, R = 0.0573, R_w = 0.0638, S = 1.07. The anionic part of the structure consists of a chain of fundamental building blocks 5:[4Δ + 1*T*] built by four B triangles bound to one B tetrahedron, which are common to Na, K, Rb, and Cs pentaborates. This new pentaborate is closely related to the mineral larderellite $(NH_4)[B_5O_6(OH)_4] \cdot H_2O$ but possesses an original structure, which manifests itself in the different morphology of the new pentaborate and the absence of perfect cleavage. The Dornberger-Schiff *OD* theory allows one to describe in detail the structural relationships, predict possible hypothetical structures, and write the *OD* groupoid. © *2003 MAIK "Nauka/Interperiodica".*

INTRODUCTION

Among all the natural and synthetic alkali metal pentaborates, more than ten phases have been studied structurally. The majority of the pentaborate structures are based on a pentaborate block consisting of four triangles and one tetrahedron, 5:[4Δ + 1*T*]. All the known structures containing such blocks were considered within the framework of the *OD* theory [1, 2]. It is remarkable that all the compounds with the largest alkali metal cations Rb^+ and Cs^+ and an NH_4^+ cation include this block. The nonlinear optical properties in the UV range are well studied for a $K[B_5O_6(OH)_4] \cdot 2H_2O$ crystal, which increases the interest in the search for new promising alkali metal pentaborates and the study of their structure and crystal chemistry.

EXPERIMENTAL

Single crystals of a new rubidium pentaborate were synthesized in 5–6-cm^3 standard autoclaves under hydrothermal conditions in order to study the phase formation in the Ga_2O_3–Rb_2O–P_2O_5–B_2O_3–H_2O system. We used Teflon protective coating. The synthesis parameters were $P \sim 70$ atm and t = 270–280°C. The lower temperature limit was set by the kinetics of the hydrothermal reactions; the upper one, by the possibilities provided by the growth apparatus. The duration of the experiments (18–20 days) was selected proceeding from the calculation of the complete proceeding of the reaction. The filling coefficient of the autoclave was selected so as to provide a constant pressure. At the weight ratio $Rb_2O : B_2O_3$ = 1 : 2, we synthesized 0.05-mm colorless, transparent, and mainly isometric crystals with a prismatic habit.

The test for the second-harmonic generation performed with the aid of a pulsed YAG : Nd laser according to the reflection scheme described elsewhere [3] showed that the crystal structure of the new borate had a center of inversion. The powder diffraction pattern (Co radiation, 40 kV, 30 mA) had no analogues in the PDF database, which confirmed that the compound synthesized was really new. In order to determine its composition, we performed a qualitative X-ray spectral analysis in a CAMSCAN 4DV scanning electron microscope with a LINK energy-dispersive attachment at the Department of Petrography of the Faculty of Geology at Moscow State University. The analysis showed the presence in the sample only of Rb atoms, which confirmed once again that we synthesized a new borate.

Using the Syntex $P\bar{1}$ diffractometer, we studied a 0.075 × 0.1 × 0.15-mm prismatic crystal and determined the parameters of its triclinic unit cell, which has no analogues among the known alkali metal borates. The unit-cell parameters were refined over 15 reflections, and the data set for the crystallographically independent region of the reciprocal space was obtained (3690 reflections altogether). Processing of

1063-7745/03/4804-0583$24.00 © 2003 MAIK "Nauka/Interperiodica"

Table 1. Crystallographic data and characteristics of the experiment for $Rb[B_5O_7(OH)_2] \cdot 0.5H_2O$

Sp. gr., Z	$P\bar{1}$, 4
a, Å	7.679(4)
b, Å	9.253(6)
c, Å	12.053(9)
α, deg	98.55(5)
β, deg	106.80(5)
γ, deg	91.71(5)
V, Å^3	808(2)
F(000)	564
ρ_{calcd}, g/cm^3	2.420(6)
μ_{Mo}, cm^{-1}	65.02
Radiation, λ	MoK_α 0.71069
Scanning mode	θ–2θ
Scanning rate, deg/min	4–12
Mode of refinement	F_{hkl}
Observed F_{hkl}	$F_{hkl} > 6.00\sigma(F_{hkl})$
Weighting scheme, w	$1/[\sigma(F)^2 + 0.003F^2]$
Number of atomic positions	37
Number of parameters to be refined	304
$2\omega_{max}$, deg; $\sin\theta/\lambda_{max}$, Å^{-1}	90.20, 0.997
Number of reflections used in refinement	2645
R, R_w	0.0573, 0.0638
S	1.070

the I_{hkl} intensities and their conversion to F^2_{hkl} was performed using the PROFIT program [4], with all the other computations being performed using the CSD complex of programs. At first, the structure was solved by the heavy-atom method in the sp. gr. $P1$. Analyzing the Patterson function, we determined the coordinates of four Rb atoms occupying the general positions, of which only two were confirmed in the course of further study. Using the electron-density syntheses, four peaks were first identified with water molecules. The LS refinement of their positional and thermal parameters confirmed that two of these positions are occupied by Rb atoms. Using the difference electron-density syntheses and the interatomic distances, we managed to localize the oxygen, alkali metal, and boron atoms, as well as the missing oxygen atoms. Then, centers of inversion were found, and the coordinates of half of the found atoms, i.e., independent basis atoms (2 Rb, 18 O, 10 B, and 1 H_2O) of the structure model described by the formula $Rb[B_5O_9] \cdot 0.5H_2O$, were recalculated with respect to a new origin of coordinates. It should be emphasized that all the atoms are located in general positions. In order to maintain the electrostatic balance of the formula, two O atoms should be attributed to OH groups. Analysis of the shared oxygen vertices of B polyhedra (which reflect the balance of valence strengths) allowed us to reveal OH groups [O(2), O(5), O(16), and O(17) atoms]. The structure was refined by the LS method with due regard for anomalous scattering of the Mo radiation in the anisotropic approximation of thermal vibrations of non-hydrogen atoms. Absorption was corrected using the DIFABS program for a crystal of an arbitrary shape [5].

The zeroth electron-density synthesis allowed us to identify four peaks located at distances ~0.76–1.06 Å from the O atoms of hydroxyl groups with hydrogen atoms H(1)–(4). In a similar way, two peaks located at distances of ~0.91–1.05 Å from the O*w* atom of the water molecule were identified with H*w*(1) and H*w*(2) atoms. The refinement of the positional parameters showed the displacement of H atoms toward O atoms; therefore, the coordinates obtained from the syntheses were fixed, so that we refined only the isotropic thermal parameters. The crystallographic data and characteristics of the experiment are indicated in Table 1; the coordinates and thermal parameters of atoms are given in Table 2. The geometry of hydrogen bonds is indicated in Table 3.

RESULTS AND DISCUSSION

In the crystal structure $Rb[B_5O_7(OH)_2] \cdot 0.5H_2O$ (**I**), the Rb(1) and Rb(2) atoms are characterized by high coordination numbers (c.n. = 9) typical of alkali metals with large ionic radii and large irregular polyhedra. The Rb(1)–O distances range from 2.756(10) to 3.482(8) Å, with the average distance being 3.085 Å; the Rb(2)–O distances range from 2.927(10) to 3.381(10) Å, with the average distance being 3.188 Å. The B(1) and B(2) atoms have tetrahedral coordination, and the B(3)–B(10) atoms, triangular coordination with typical interatomic distances (1.465–1.503 and 1.332–1.409 Å, respectively). The tetrahedra and triangles are combined to form a pentablock in which two mutually perpendicular edges of the central tetrahedron are connected with pairs of sharing-vertex triangles. The blocks form a corrugated chain similar to the chain in the mineral larderellite $(NH_4)[B_5O_7(OH)_2] \cdot H_2O$ (**II**) [6]. The new synthetic rubidium pentaborate and larderellite are described by almost identical formulas that differ by only 0.5 H_2O. The structures of these two compounds are also closely related. Comparing the unit-cell parameters of the new triclinic pentaborate and monoclinic larderellite (sp. gr. $P2_1/c$, a = 9.470(10) Å, b = 7.630(1) Å, c = 11.650(10) Å, β = 97.1(2)°), we assumed that their metrics are also very close if one changes a to b in the new pentaborate (Table 1). However, thorough analysis of the structures did not confirm this assumption. Both structures (**II** and **I**) have typical larderellite chains along the b axes. In other words, the axes selected in the structure determinations are crystallochemically identical, but the unit cells are mutually

distorted: the *a* axis is "compressed," whereas the *b* axis is elongated in structure **I** in comparison with these axes in structure **II**. The consideration of structure **II** [1] with the invocation of the symmetry approach used in the Dornberger-Schiff theory [7] showed that the chains are formed by pentablocks 5 : [4Δ + 1*T*] with the partial symmetry (pseudosymmetry) $\bar{4}2m$ by the "condensation" of the apical O atoms and their multiplication along *b* by the 2_1 axes of the space group of the mineral. The chains alternate along the *c* axis because of their multiplication by centers of inversion. The chains in triclinic compound **I** have the pseudosymmetry 2_1 (partial symmetry operation according to the Dornberger-Schiff terminology [7]) and the same law of symmetry multiplication.

The main difference between the two structures reduces to the chain alternation along the *c* axis common to both structures (Figs. 1, 2). The pairs of chains *L*(1), *L*(2) in both structures are the same, whereas the pairs of chains *L*(2), *L*(3) are different. The analysis of the pseudosymmetry of structure **II** showed that it has a pseudotranslation *C* violated only by water molecules. Thus, the anionic pairs of the structure and the positions of ammonium ions obey the symmetry of the pseudosupergroup $C2/c$ (C_{2h}^6) in the setting used (with respect to the true group $P2_1/c$ (C_{2h}^5)). The manifestation of pseudosymmetry is associated with the pseudosymmetry of the block corresponding to the group $\bar{4}2m$: in the *ac* projection (Fig. 2b), pseudoaxes 2 of the block alternate with the axes 2_1 along *a* in the *L*(1), *L*(2) layers as in the sp. gr. *C*2/*c*. The pseudosupergroup has two systems of centers of inversion. The existence of the pseudocenter of inversion 1/4 1/4 0 allows one to locate the second larderellite *L*(2) chain of the *L*(1), *L*(2) pair along the *c* axis in structure **II** by two different ways: by multiplying the first chain by the system of centers of inversion inherent in structure **II** or by multipliying the chain by the second system of pseudocenters of inversion displaced along the *a* and *b* axes by 1/4. Arrows in Figs. 3a and 3b indicate the displacements of the *L*(3) chain with respect to the *L*(2) chain in structure **II** (~1/4 along *a* and *b*); as a result, a new pair of chains *L*(2), *L*(3) from structure **II** exactly corresponds to the pair *L*(2), *L*(3) of structure **I**.

Thus, in structure **II**, all pairs of chains along the *c* axis are equivalent, whereas in structure **I**, there are pairs chains of two types. The *b* parameter along the chain in structure **I** is somewhat elongated, whereas the parameter *a* is somewhat compressed, which can be explained by structure deformation because of the necessary transformation of the pseudoelement into a true symmetry element. Figures 3a and 3b show the projections of the new triclinic unit cell corresponding to the projections of the triclinic unit cell of structure **I**. Now, angle α is not equal to 90° as in structure **II** but is rather close to angle α in structure **I**; the angle β is close to the angle β in structure **I** and exceeds the angle α. Thus, one can imagine a structure in which all the pairs of layers would correspond to the variant of the location of the *L*(2), *L*(3) pair in structure **I**. Such a structure (**III**) is shown in Fig. 3c. It is also triclinic, with the unit-cell parameters being close to those of compound **I**. In the

Table 2. Coordinates of basis atoms and the parameters of their thermal vibrations B_{eq}/B_{iso} in the $Rb[B_5O_7(OH)_2] \cdot 0.5H_2O$ structure. $B_{eq} = 1/3[B_{11}a^{*2}a^2 + \ldots + 2B_{23}b^*c^*bc\cos\alpha]$

Atom	*x*/*a*	*y*/*b*	*z*/*c*	B_{eq}/B_{iso}
Rb(1)	0.4893(1)	0.0488(1)	0.25701(7)	2.14(2)
Rb(2)	−0.0946(1)	0.7195(1)	0.20986(7)	2.63(3)
O(1)	−0.0930(1)	0.1522(6)	0.0198(4)	1.4(1)
O(2)	−0.3031(8)	0.9506(6)	−0.0244(4)	1.9(1)
O(3)	0.1145(7)	0.3522(6)	0.0515(4)	1.4(1)
O(4)	0.2958(7)	0.5395(6)	0.0227(4)	1.6(1)
O(5)	0.4785(7)	0.7299(6)	−0.0094(5)	1.6(1)
O(6)	−0.1544(7)	0.0505(6)	0.1759(4)	1.4(1)
O(7)	0.0934(7)	0.2418(6)	0.2164(4)	1.6(1)
O(8)	0.2567(7)	0.5454(6)	0.2127(4)	1.4(1)
O(9)	0.4789(7)	0.7168(6)	0.1833(4)	1.3(1)
O(10)	0.1249(7)	0.0419(6)	0.3259(4)	1.3(1)
O(11)	−0.0782(7)	0.2325(6)	0.3527(4)	1.4(1)
O(12)	−0.4522(7)	0.6059(6)	0.3566(4)	1.4(1)
O(13)	0.3234(7)	0.7887(6)	0.3250(4)	1.4(1)
O(14)	0.2951(7)	−0.0517(6)	0.4950(5)	1.4(1)
O(15)	0.1171(7)	0.1458(6)	0.5185(4)	1.3(1)
O(16)	−0.0528(7)	0.3430(6)	0.5511(5)	1.6(1)
O(17)	−0.2908(7)	0.5744(6)	0.5472(4)	1.5(1)
O(18)	−0.5070(7)	0.7587(6)	0.5210(4)	1.3(1)
O*w*	0.6428(13)	0.3685(10)	0.2334(6)	5.9(3)
B(1)	−0.0036(11)	0.1406(10)	0.2658(7)	1.4(2)
B(2)	0.4028(12)	0.6623(9)	0.2680(7)	1.4(2)
B(3)	−0.1841(11)	0.0518(9)	0.0600(7)	1.2(2)
B(4)	0.0415(11)	0.2492(9)	0.1004(7)	1.1(2)
B(5)	0.2252(11)	0.4797(9)	0.0999(7)	1.0(2)
B(6)	0.4188(11)	0.6635(9)	0.0656(7)	1.2(2)
B(7)	0.1773(11)	0.0440(9)	0.4418(7)	1.1(2)
B(8)	−0.0059(11)	0.2440(8)	0.4712(6)	0.9(2)
B(9)	−0.4190(11)	0.6449(10)	0.4732(7)	1.2(2)
B(10)	0.3648(11)	0.8277(9)	0.4411(7)	1.2(2)
H(1)	0.36880	0.10080	0.01010	2.5(1)
H(2)	0.56220	0.30410	0.10160	2.5(1)
H(3)	0.85550	0.38510	0.54520	2.5(1)
H(4)	0.26550	0.36190	0.39300	2.5(1)
H*w*(1)	0.73140	0.43360	0.22920	2.5(1)
H*w*(2)	0.71870	0.29800	0.28690	2.5(1)

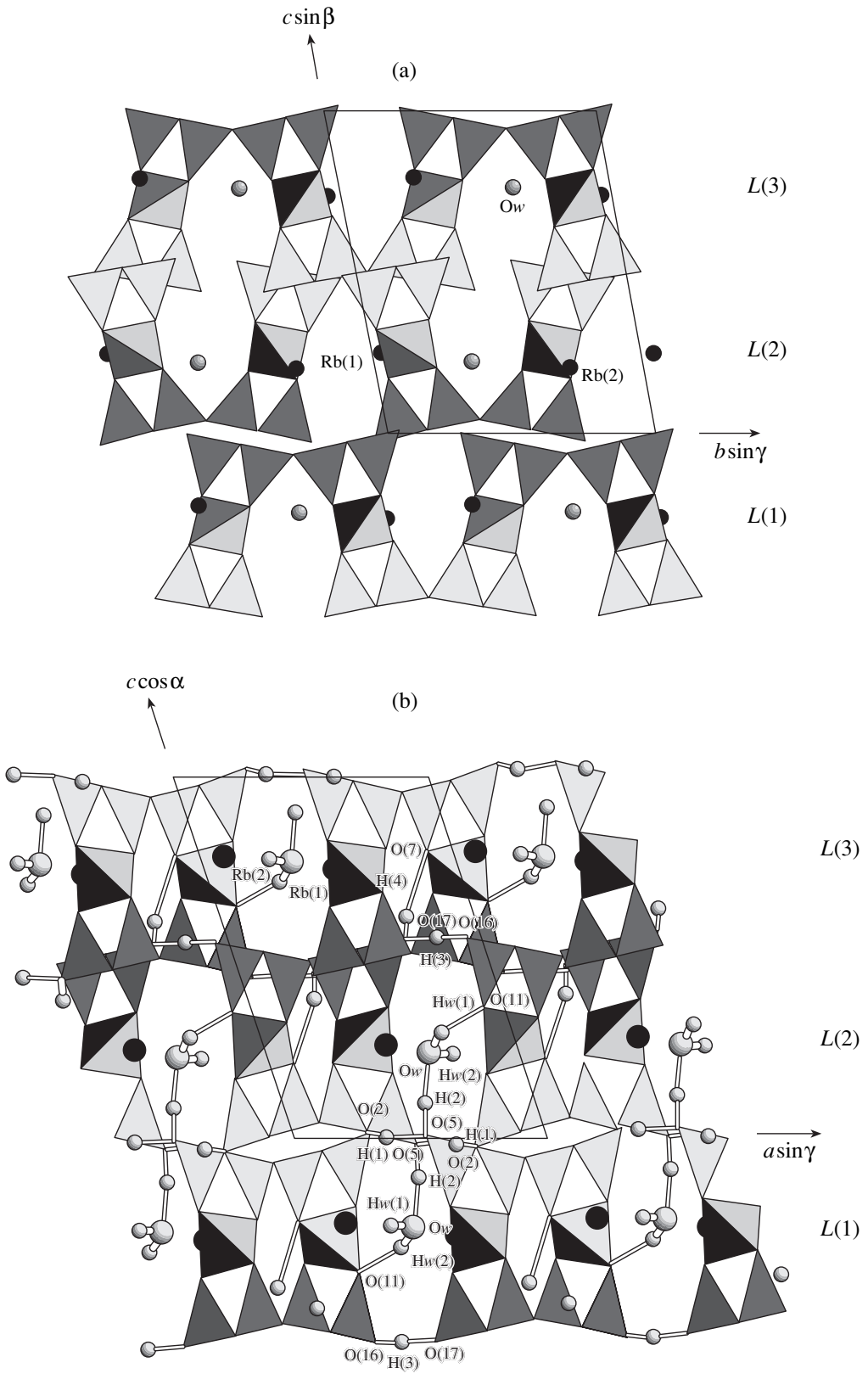

Fig. 1. Crystal structure **I**: (a) *bc* projection, (b) *ac* projection showing the system of hydrogen bonds. One can see B polyhedra; Rb atoms are depicted by filled circles, oxygen atoms of water molecules O*w* are shown by large open circles, and hydrogen atoms, by small open circles. For H atoms, bond lengths are indicated. Hereafter, the letters *L*(1), *L*(2), *L*(3) indicate the layers along the *c* axis.

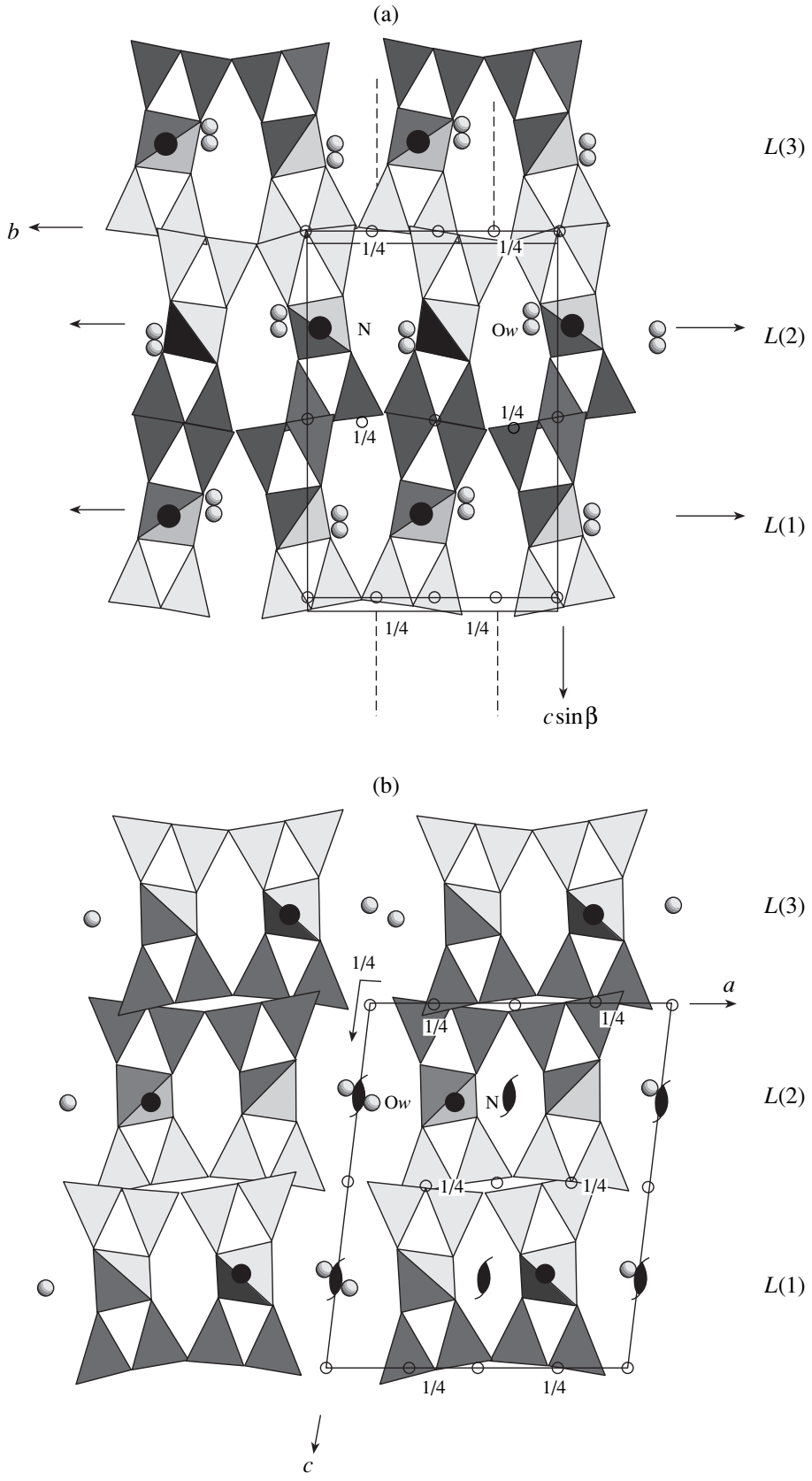

Fig. 2. Crystal structure **II** projected onto the (a) *bc* and (b) *ac* planes. One can see B polyhedra; N atoms are depicted by filled circles, and oxygen atoms of water molecules O*w* are indicated by light circles; one can also see the symmetry elements of the group and pseudocenters of inversion.

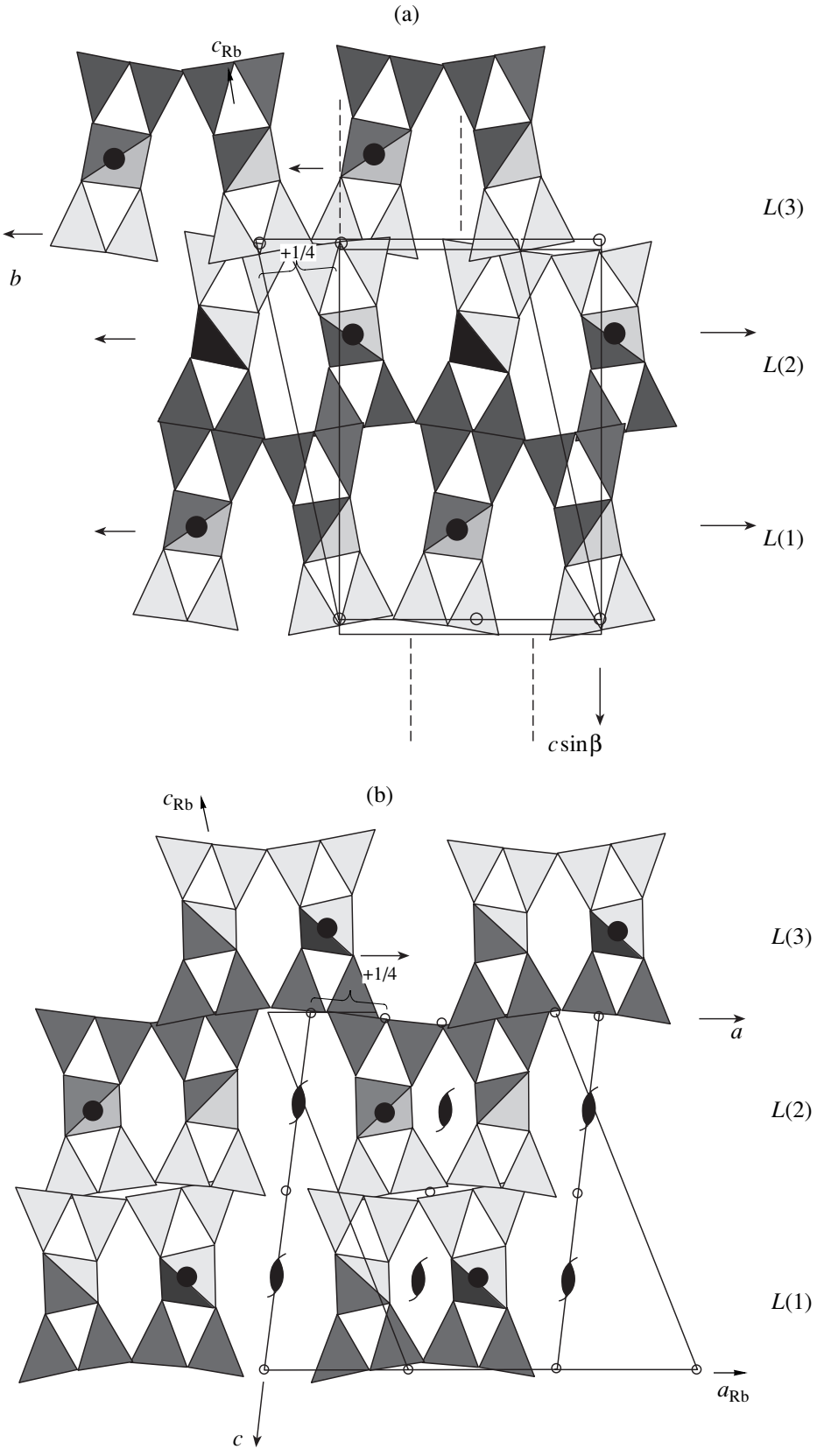

Fig. 3. Construction from structure **II** of the structure equivalent to **I**: (a) *bc* projection, (b) *ac* projection, (c) hypothetical structure **III** projected onto the *ac* plane.

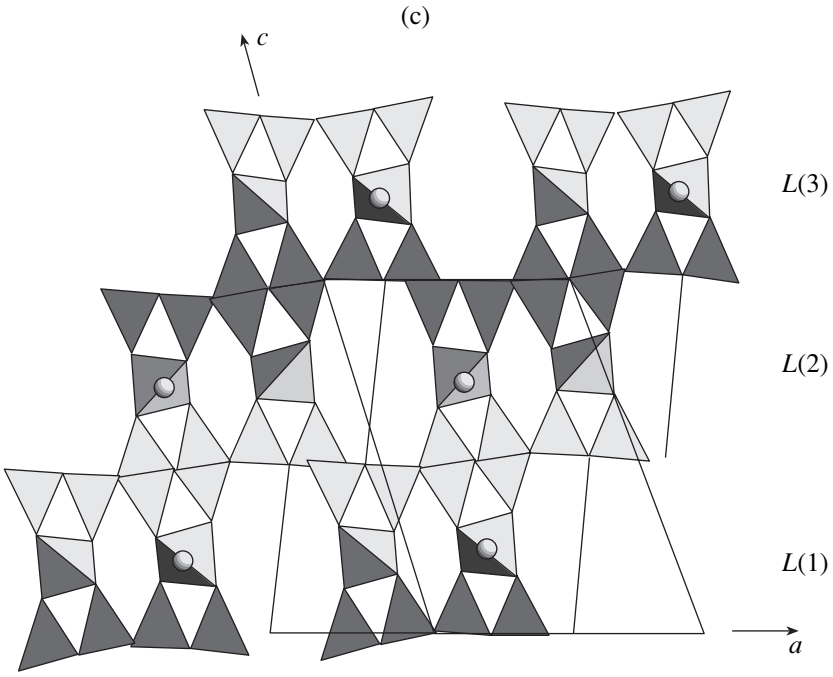

Fig. 3. (Contd.)

Dornberger-Schiff notation, structures **II** and **III** are MDO polytypes and are characterized by the maximum order; i.e., all the pairs, triads, and other combinations of building units (layers or chains) are equivalent. Structure **I** is the so-called periodic structure with two types of chain pairs. One can also imagine structures with a more diverse alternation of chains and a corresponding increase of the period along the *c* axis up to the formation of endless *c* parameter in the case of their random alternation. This structural *OD* family can be written in the symmetry groupoid, whose first line gives the partial (local) symmetry of variable units, and the second line indicates the variants of their multiplication

$$P1(2_1) \quad \lambda(\rho)\text{-}PO$$

$$\{1(\bar{1})(\pm 1/4)\} \quad \sigma(\rho)\text{-}PO.$$

According to [7], the symbol ρ indicates that, along the multiplication direction or the broken periodicity (*c* axis), the units (chains, in our case) are nonpolar. The multiplication of these chains by centers of inversion also proceeds in a nonpolar way, which allows one to relate this family of structures to the first category (Dornberger-Schiff notation [7]). In terms of the *OD* theory, multiplication of the chains (one-dimensionally periodic units) was first analyzed in wollastonite and parawollastonite [8].

Different topologies of the mutual arrangement of chains determine the main differences between structures **I** and **II**. The vast space between the chains filled with pairs of water molecules in structure **II** that determines the {100} platelike shape of these crystals (Fig. 2b) is not observed in structure **I**, because it is closed by a displaced chain (Fig. 1b); crystals **I** have no perfect cleavage along {001} either. Lowering the symmetry from monoclinic to triclinic and the corresponding loss of 2_1 axes result in the fact that the voids between the chains in structure **I** may contain only one water molecule, whereas in structure **II**, the voids contain two water molecules. A double decrease in the number of water molecules and distortion of structure **I** promotes the approach of the intersecting chains in the *L*(1), *L*(2) pairs, which is accompanied by a "shortening" of parameter *a* (Fig. 1a). It is this part of the structure that is reinforced by the system of hydrogen bonds.

As in structure **II** [6], the apical O atoms of the chains in structure **I** belong to OH groups. Hydrogen bonds with the participation of H(1) and H(3) atoms connect the apical vertices of the chains: O(16)–

Table 3. Geometrical characteristics of hydrogen bonds in the $Rb[B_5O_7(OH)_2] \cdot 0.5H_2O$ structure

D–H···*A*	Distance, Å			Angle *DHA*, deg
	D···*A*	*D*–H	H···*A*	
O(2)–H(1)···O(5)	2.66(1)	0.76	1.93	163
O(5)–H(2)···O*w*	2.60(1)	1.06	1.55	172
O(16)–H(3)···O(17)	2.85(1)	0.81	2.11	154
O(17)–H(4)···O(7)	3.04(1)	0.83	2.26	156
O*w*–H*w*(2)···O(11)	2.68(1)	1.05	1.71	151
O*w*–H*w*(1)		0.91		
H*w*(1)–O*w*–H*w*(2)				103

H(3)···O(17) and O(2)–H(1)···O(5) (Fig. 1b). The role of donors of H(2) and H(4) atoms is played by the apical O(5) and O(17) atoms (both atoms are acceptors of hydrogen bonds formed by H(2) and H(4)atoms). The hydrogen bonds formed by H(2) and H(4) are normal to the hydrogen bonds directed toward water molecules (as is also the case in structure **II**) and O(7) atoms, playing the role of acceptors. Water molecules are kept in the voids by two hydrogen bonds H*w*(2)–O*w*··O(11) and O(5)–H(2)··O*w*. The bond lengths (Table 3) show that hydrogen bonds formed by the atoms H(1), H(2), and H*w*(2) are rather strong. As in structure **II**, the shortest O(5)–H(2)··O*w* bond is close to symmetric. The angles formed by hydrogen bonds and water molecules have the usual values. The pronounced atomic thermal vibrations (Table 2) are explained by a rather loose structure in which the fragments are bound by hydrogen bonds.

The formation of various *OD* modifications is usually explained by the stability of some building-unit configurations such as pairs and triads of chains or layers. In nature, larderellite crystallizes in the fumaroles of geothermal regions (in open thermodynamic systems). Under hydrothermal conditions of synthesis in a closed autoclave (~70 atm, ~280°C), the above described new configuration of building units (chains) turned out to be quite stable. We cannot exclude the possibility of discovering and synthesizing compounds with the structure described above, its hypothetical variety, and other structures mentioned above.

ACKNOWLEDGMENTS

The authors are grateful to S.Yu. Stefanovich for conducting the test for nonlinear optical properties and to N.N. Korotaeva for determining the chemical composition of the crystals. This study was supported by the Russian Foundation for Basic Research, project no. 02-03-33316.

REFERENCES

1. E. L. Belokoneva, T. A. Korchemkina, and O. V. Dimitrova, Zh. Neorg. Khim. **45** (11), 1838 (2000).
2. T. A. Borisova, E. L. Belokoneva, and O. V. Dimitrova, Zh. Neorg. Khim. **47** (3), 378 (2002).
3. S. Yu. Stefanovich, in *Extended Abstracts of European Conference on Lasers and Electro-Optics, CLEO-Europe'94* (Amsterdam, 1994), p. 249.
4. V. A. Strel'tsov and V. E. Zavodnik, Kristallografiya **34** (6), 1369 (1989) [Sov. Phys. Crystallogr. **34**, 824 (1989)].
5. N. Walker and D. Stuart, Acta Crystallogr. Sect. A: Found. Crystallogr. **39**, 158 (1983).
6. S. Merlino and F. Sartori, Acta Crystallogr., Sect. B: Struct. Crystallogr. Cryst. Chem. **25**, 2264 (1969).
7. K. Dornberger-Schiff, Abh. Dtsch. Akad. Wiss. Berlin **3** (1), 1 (1964).
8. S. Merlino, Per. Mineral. **59**, 69 (1990).

Translated by L. Man

Crystallography Reports, Vol. 48, No. 4, 2003, pp. 591–593. Translated from Kristallografiya, Vol. 48, No. 4, 2003, pp. 642–644.

STRUCTURE OF ORGANIC COMPOUNDS

Parameters of Anisotropic Atomic Displacements in Chemical Compounds as Criteria for Chemical Bond Types

V. N. Khrustalev and M. Yu. Antipin

Nesmeyanov Institute of Organoelement Compounds, Russian Academy of Sciences, ul. Vavilova 28, Moscow, 119991 Russia

e-mail: vkh@xrlab.ineos.ac.ru

Received February 21, 2002; in final form, July 3, 2002

Abstract—Analysis of the parameters of anisotropic atomic displacements in various chemical compounds reveals a feature characteristic of a donor–acceptor bond: the ellipsoids of anisotropic displacements of the atoms involved in this bond are elongated in the direction of the bond. The explanation of the effect observed is proposed. © *2003 MAIK "Nauka/Interperiodica".*

The chemical bond is one of the key notions of chemistry. However, the variety of phenomena treated by modern chemistry does not fall into simple classical and quantum-chemical schemes used to describe molecules and chemical bonds. The notions of a chemical bond are continuously developing based on experimental data and the results of quantum-chemical calculations to give rise to new models and concepts of chemical bonding.

This paper is devoted to the description of a specific feature in the donor–acceptor chemical bond that was revealed in the analysis of the parameters of anisotropic atomic displacements obtained from the X-ray diffraction data.

As a rule, the donor–acceptor bond is associated with the formation of a localized molecular orbital occupied by an electron pair that, before the bond was formed, belonged to one of the atoms included in the bond. Formally, the electron density distribution of this bond does not differ from that of the polar covalent chemical bond. However, a comparison of the experimental parameters of these bonds and the chemical properties of compounds with polar covalent and donor–acceptor bonds reveals some differences in the nature of these bonds. For example, the lengths of the donor–acceptor bonds fall in wider ranges and depend to a larger degree on the environment of the atoms involved in the bond. Moreover, the donor–acceptor bonds, as a rule, are chemically weaker and, hence, can be more readily broken in chemical reactions.

In recent studies of the crystal structures of new organogermanium and organotin *ate* complexes $(Me_3Si)_3C–M–(\mu\text{-}SBu^n)_2–Li(THF)_2$ [1], we found that the ellipsoids of anisotropic displacements of the μ-bridging sulfur atoms are elongated in the direction of the S–Li bond. This observation was supported by the calculations of the differences Δ between the rms amplitudes of the longitudinal vibrations of the *M* and S atoms along the chemical bond between them (Hirshfeld test [2]; Figs. 1, 2; table). Since the S–Li bonds in the compounds studied are of the donor–acceptor type, we assume that the vibrations of the bound atoms predominantly along the bond between them correspond to the donor–acceptor type of chemical bond (as distinct from the polar covalent chemical bond, which is characterized by the vibrations of the bound atoms in a direction perpendicular to the line of chemical bonding [3]). It is evident that atomic vibrations in covalent (rigid) and donor-acceptor (nonrigid) chemical bonds are conveniently illustrated by vibrations of macrophysical objects, such as a mathematical pendulum and a spring, respectively.

The difference Δ ($Å^2 \times 10^4$) between the rms amplitudes of the longitudinal vibrations of atomic pairs in germanium and tin *ate* complexes

M	S
Ge, Li	$\Delta_1^{Li} = 22$
	$\Delta_2^{Li} = 12$
	$\Delta_1^{Ge} = 4$
	$\Delta_2^{Ge} = 2$
Sn, Li	$\Delta_1^{Li} = 43$
	$\Delta_2^{Li} = 15$
	$\Delta_1^{Sn} = 8$
	$\Delta_2^{Sn} = 6$

1063-7745/03/4804-0591$24.00

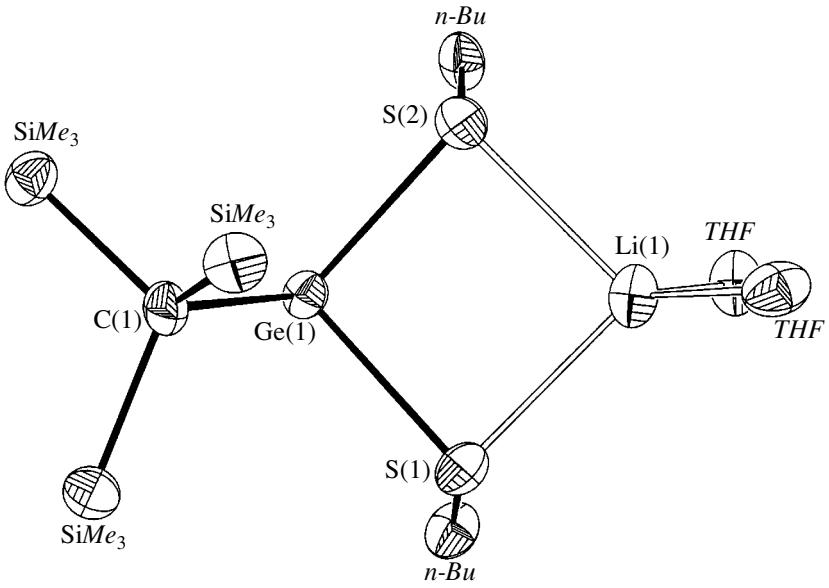

Fig. 1. Molecular structure of the germanium *ate* complex. The ellipsoids of anisotropic displacements are drawn at the 50% probability level.

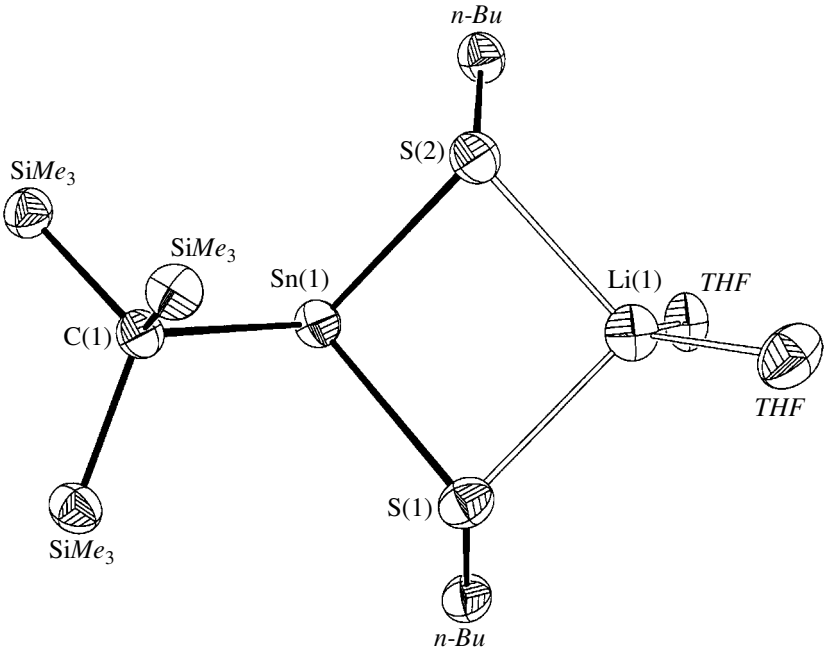

Fig. 2. Molecular structure of the tin *ate* complex. The ellipsoids of anisotropic displacements are drawn at the 50% probability level.

The validity of our hypothesis was confirmed by the analysis of the ellipsoids of anisotropic displacements in compounds with donor–acceptor chemical bonds with the use of the Cambridge Structural Database [3], specifically in the compounds reported in [4–9] and other transition-metal complexes with carbene, nitrene, and carbonyl ligands, as well as with molecular nitrogen.

Our hypothesis explains not only the observed specific features of the donor–acceptor chemical bonds but also some structural features of the coordination compounds. Based on our hypothesis, the difference revealed in the coordination of alkali metal atoms in [10] can be explained by the difference in the type of vanadium–nitrogen chemical bonds: in the $^{-}$[V]–N=N–[V]$^{-}$ dianion (scheme 1), the negative charge is delocal-

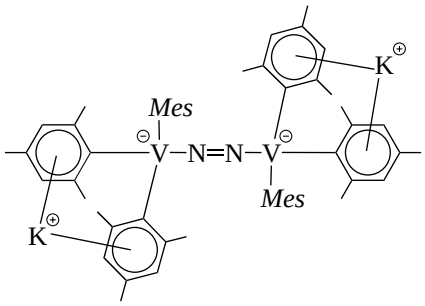

Scheme 1.

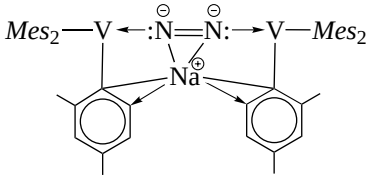

Scheme 2.

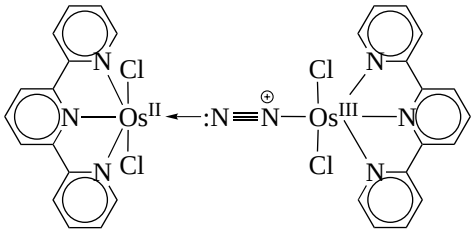

Scheme 3.

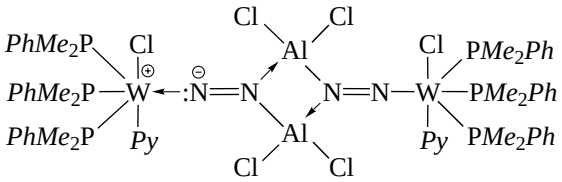

Scheme 4.

ized mainly over the aryl ligands, which coordinate the K^+ cation, and in the [V] ⟵ $^-$:N=N:$^-$ ⟶ [V] dianion (scheme 2), the Na^+ cation is coordinated by the negatively charged bridging nitrogen atoms. In [11] (scheme 3), the shortening of the Os^{II}–N(N) bond with respect to the Os^{III}–N(N) bond is attributed to the stronger effect of the back donation of the lone electron pair in the case of the Os^{II} atom. With our hypothesis, the explanation of this shortening can be complemented by the existence of the [Os^{II}] ⟵ :N≡N^+–[Os^{III}] resonance form. Finally, in [12] (scheme 4), the unusual ellipsoids of anisotropic displacements of the diazo nitrogen atoms, which are bound to tungsten, were explained by the poor quality of the experiment. Following the hypothesis, we suggest that the compound studied in that paper has the asymmetric zwitterionic structure $^+$[W] ⟵ $^-$:N=N–(μ–AlR_2)$_2$–N=N–[W]. In all the compounds mentioned above, the directions of the polar axes of the ellipsoids of anisotropic displacements of the bridging nitrogen atoms agree with the types of the corresponding chemical bonds.

Our hypothesis needs rigorous and objective proof. In order to analyze the observed effect, we are going to perform precision X-ray diffraction investigations of various chemical compounds with donor–acceptor bonds at different temperatures. In our opinion, organometallic compounds with μ-bridging halogen atoms are the most suitable objects for such studies.

ACKNOWLEDGMENTS

This study was supported by the Russian Foundation for Basic Research, project nos. 00-03-32807a and 00-15-97359. We also acknowledge the support of the Russian Foundation for Basic Research in the payment of the license for using the Cambridge Structural Database, project no. 99-07-90133.

REFERENCES

1. I. V. Borisova, N. N. Zemlyansky, V. N. Khrustalev, *et al.*, Organometallics **21** (19), 4005 (2002).
2. F. L. Hirshfeld, Acta Crystallogr., Sect. A: Cryst. Phys., Diffr., Theor. Gen. Crystallogr. **32** (2), 239 (1976).
3. *Cambridge Crystal Structure Database* (Cambridge, 2002).
4. W. A. Herrmann, P. W. Roesky, M. Wang, and W. Scherer, Organometallics **13**, 4531 (1994).
5. P. Legzdins, P. J. Lundmark, and S. J. Rettig, Organometallics **15**, 2988 (1996).
6. C. Newton, K. D. Edwards, J. W. Ziller, and N. M. Doherty, Inorg. Chem. **38**, 4032 (1999).
7. T. Yoshida, T. Okano, D. L. Thorn, *et al.*, J. Organomet. Chem. **181**, 183 (1979).
8. J. Gil-Rubio, M. Laubender, and H. Werner, Organometallics **17**, 1202 (1998).
9. M. Hidai, S. Aramaki, K. Yoshida, *et al.*, J. Am. Chem. Soc. **108**, 1562 (1986).
10. R. Ferguson, E. Solari, C. Floriani, *et al.*, J. Am. Chem. Soc. **119**, 10104 (1997).
11. K. D. Demadis, T. J. Meyer, and P. S. White, Inorg. Chem. **36**, 5678 (1997).
12. T. Takahashi, T. Kodama, A. Watakabe, *et al.*, J. Am. Chem. Soc. **105**, 1680 (1983).

Translated by I. Polyakova

Crystallography Reports, Vol. 48, No. 4, 2003, pp. 594–601. Translated from Kristallografiya, Vol. 48, No. 4, 2003, pp. 645–652.

STRUCTURE OF ORGANIC COMPOUNDS

Polymorphism and Design of Noncentrosymmetric Crystals of 4-Hydroxybenzaldehyde-4-Nitrophenylhydrazone and *N*'-(2-Phenyl-1*H*-Indole-3-Aldehyde)-4-Nitrophenylhydrazone

L. N. Kuleshova, M. Yu. Antipin, V. N. Khrustalev, D. V. Gusev, G. V. Grintselev-Knyazev, and E. S. Bobrikova

Nesmeyanov Institute of Organoelement Compounds, Russian Academy of Sciences, ul. Vavilova 28, Moscow, 119991 Russia

e-mail: lukul@xrlab.ineos.ac.ru

Received June 26, 2002

Abstract—The products of crystallization of 4-hydroxybenzaldehyde-4-nitrophenylhydrazone (**I**) and *N*'-(2-phenyl-1*H*-indole-3-aldehyde)-4-nitrophenylhydrazone (**II**) from different solvents are studied by X-ray diffraction with the aim of examining the polymorphism of hydrazone derivatives. The structural features of the crystals prepared are analyzed. It is shown that, in the case when molecules of organic compounds with a high molecular hyperpolarizability are capable of forming stable acentric supramolecular associates in the crystal, knowledge of their polymorphism offers strong possibilities for designing the noncentrosymmetric crystal structure necessary for a manifestation of the nonlinear optical activity. *© 2003 MAIK "Nauka/Interperiodica".*

INTRODUCTION

Donor–acceptor hydrazone derivatives belong to the class of crystalline materials that are promising for use in nonlinear optics, because these compounds possess high molecular hyperpolarizabilities, are prone to the formation of noncentrosymmetric crystals, and can be readily synthesized through the condensation of different donor derivatives of aromatic aldehydes (*D*) and nitrophenylhydrazine (*A*). By now, the nonlinear optical characteristics of molecules and crystals of 4-nitrophenylhydrazones have been investigated thoroughly [1–3]. In particular, Serbutoviez *et al.* [1] theoretically proved that the molecular hyperpolarizabilities β are characterized by large vector components, because hydrazone molecules involve a bichromophore conjugated fragment of the *D*–*A*'–*D*'–*A* type, where *A*' is the C=N azomethine double bond and *D*' is the central amino group. Among the great variety of 4-nitrophenylhydrazones with different groupings *D*, the maximum first-order hyperpolarizabilities β were obtained by introducing multidonor derivatives[1] of benzaldehyde [2] and thiophenealdehyde [3] into molecules. Experimental investigations into the nonlinear optical properties of crystals (powders) have revealed that more than 38% of the polycrystalline samples of hydrazones synthesized (more than 30 derivatives) are capable of generating the second harmonic of laser radiation; i.e., they should have a noncentrosymmetric crystal structure. At the same time, X-ray diffraction studies of single-crystal (including nonlinear optically active) hydrazones are few in number despite the fact that systematic investigations into the influence of molecular association on the formation of crystal structures would provide valuable information for the design of noncentrosymmetric crystalline materials. Moreover, hydrazone derivatives are convenient objects for crystal design, because their use makes it possible to control the formation of the crystal structure by varying crystallization conditions or introducing additional functional groupings (such as donors of hydrogen bonds) into molecules.

In this work, we synthesized two new hydrazones with additional donor groupings capable of forming hydrogen bonds, namely, 4-hydroxybenzaldehyde-4-nitrophenylhydrazone (**I**) and *N*'-(2-phenyl-1*H*-indole-3-aldehyde)-4-nitrophenylhydrazone (**II**). Crystals of these compounds were grown from several solvents and the products of crystallization were studied.

EXPERIMENTAL

Synthesis and Crystallization

Compounds **I** and **II** were synthesized through the condensation of 4-hydroxybenzaldehyde and 2-phenylindole-3-aldehyde with 4-nitrophenylhydrazine in acetic acid. Two crystalline forms of hydrazone **I** (**Ia** and **Ib**) and four crystalline modifications of hydrazone **II** (**IIa**, **IIb**, **IIc**, and **IId**) were prepared by the crystallization from different solvents. Dark red small-sized prismatic crystals **Ia** of satisfactory quality were grown through slow evaporation from a dioxane solution. Light-colored elongated prismatic crystals **Ib** precipi-

[1] Dihydroxy and trihydroxy (or methoxy) derivatives of benzaldehyde.

1063-7745/03/4804-0594$24.00 © 2003 MAIK "Nauka/Interperiodica"

tated upon evaporation from acetone and acetonitrile solutions. Dark red small-sized needle-shaped crystals **IIa** were grown by slow evaporation from a pyridine solution, whereas dark red prismatic crystals **IIb** were formed upon slow evaporation from a dioxane solution. Dark red (almost black) large-sized, well-faceted, needle-shaped crystals **IIc** were grown by slow evaporation from an acetonitrile solution. Moreover, very small-sized dark red needle-shaped crystals **IId** were prepared through rapid recrystallization from acetonitrile.

X-ray Diffraction Analysis

The unit cell parameters and the reflection intensities were measured on a Siemens P3/PC automated diffractometer (MoK_α radiation, $\theta/2\theta$ scan mode) for compound **Ia** and a Bruker SMART CCD 1000 automated diffractometer (MoK_α radiation, φ and ω scan modes) for compounds **Ib**, **IIa**, **IIb**, **IIc**, and **IId**.[2] The crystal data are presented in Table 1. The structures were solved by direct methods and refined using the full-matrix least-squares procedure on F^2 in the anisotropic approximation for the non-hydrogen atoms. In structures **IIb** and **IIc**, the phenyl substituents are disordered over two positions with equal occupancies due to the rotation about the C(15)–C(16) bond through ~70° and ~84°, respectively. The solvate dioxane molecule occupying a special position at the inversion center was revealed in crystal **Ia**. Two solvate dioxane molecules disordered over two positions with occupancies of 0.5 : 0.5 and 0.75 : 0.25 were found in crystal **IIb**. The dioxane molecule with equal occupancies is located in a special position at the inversion center. In structures **Ia** and **Ib**, all the hydrogen atoms were independently located from the difference Fourier syntheses and refined in the isotropic approximation. The positions of the hydrogen atoms in the solvate dioxane molecule in structure **Ia**, the disordered phenyl substituent in structure **IIb**, and all the hydrogen atoms in structure **IIa** were calculated geometrically and refined in the isotropic approximation with the following fixed positional (a riding model) and thermal parameters: $U_{iso}(H) = 1.5U_{eq}(C)$ for CH_3 groups and $U_{iso}(H) = 1.2U_{eq}(C)$ for all the other groups. The other hydrogen atoms in structures **Ia** and **IIb** were located independently and refined in the isotropic approximation. All the calculations were performed with the SHELXTL PLUS (Version 5.10) software package [4]. The tables of the atomic coordinates, bond lengths, bond and torsion angles, and anisotropic thermal parameters have been deposited with the Cambridge Structural Database.

[2] Since the sizes of crystals **IId** were very small and their scattering power was relatively low, it was possible to determine only their crystal system (monoclinic) and the unit cell parameters: a = 5.22 Å, b = 12.16 Å, c = 26.27 Å, and β = 85°.

Calculation of the Nonlinear Optical Characteristics of Molecules and Crystals

The molecular hyperpolarizability β was evaluated by the finite-field method [5–8] (included in the MOPAC program package [9]) within the framework of AM1 parametrization [10]. The data derived from the MOPAC program were processed with the HYPER program [11] in order to calculate all the components of the β tensor. Then, the vector component β_{vec} of the hyperpolarizability was estimated from the β tensor components. The molecular geometry determined experimentally was used in calculations. The components of the nonlinear optical susceptibility tensor d_{ijk} for the crystals were evaluated using the original NLOP program based on the oriented-gas model [12, 13]. The computational technique was described in more detail in [14].

The synthesized molecules of hydrazones possess high first-order molecular hyperpolarizabilities β ($\times 10^{-30}$): 56.1 ± 0.3 cm^3/V^2 for molecule **I** (with a geometry similar to that of crystal **Ia**) and 63.4 ± 0.3 cm^3/V^2 for this molecule with the geometry revealed in crystal **Ib**. An analysis of the molecular hyperpolarizabilities β calculated for molecule **II** with the geometries observed in different polymorphic modifications demonstrates that the inclusion of the observed differences in the geometries does not lead to a noticeable change in the calculated values of β: 67.2 ± 0.1 cm^3/V^2 for the molecule in crystal **IIa** and 65.7 ± 0.1 cm^3/V^2 for the molecule in crystal **IIc**. Note that the hyperpolarizability β calculated with the same parametrization is equal to 44.3 ± 0.7 cm^3/V^2 for molecule **I'**, which, according to [2], is characterized by the maximum experimentally determined molecular hyperpolarizability. Therefore, the compounds synthesized in this work are superior to the previously known compounds in the molecular hyperpolarizability.

For noncentrosymmetric crystals **IIc**, we also calculated the components of the susceptibility tensor d_{ijk}: d_{31} = –8.9 cm/V, d_{32} = –7.9 cm/V, and d_{33} = –23.2 cm/V. These results indicate that, most likely, the molecular packing is not optimum in the crystal.

RESULTS AND DISCUSSION

It was found that, for the most part, the crystals grown from different solvents involve solvate molecules. These crystal modifications are frequently referred to as pseudopolymorphs.[3] The solvent (dioxane or pyridine) molecules are incorporated into the crystal lattice of the pseudopolymorph due to the formation of hydrogen bonds with the proton of the hydroxyl group (as in molecule **I**) or the central amino group (as in molecule **II**). Note that the solvate molecules of dioxane in the crystals, as a rule, occupy posi-

[3] See, for example, G. R. Desiraju, A. Nangia, J. K. Howard, *et al.*, Chem. Commun., No. 17, 1676 (1999).

Table 1. Crystal data, data collection, and refinement parameters for the studied structures

Compound	**Ia** × $1/2C_4H_8O_2$	**Ib**	**IIa** × *Py*	**IIb** × $1.5C_4H_8O_2$	**IIc**
Empirical formula	$C_{13}H_{11}N_3O_3 \cdot 1/2C_4H_8O_2$	$C_{13}H_{11}N_3O_3$	$C_{21}H_{16}N_4O_2 \cdot C_6H_5N$	$C_{21}H_{16}N_4O_2 \cdot 1.5C_4H_8O_2$	$C_{21}H_{16}N_4O_2$
Molecular weight	301.30	257.25	435.48	488.53	356.38
T, K	293(2)	110(2)	295(2)	120(2)	140(2)
Crystal system	Monoclinic	Monoclinic	Triclinic	Monoclinic	Orthorhombic
Space group, *Z*	$P2_1/c$, 4	$P2_1/n$, 8	$P\bar{1}$, 2	$P2_1/c$, 4	$Pna2_1$, 4
a, Å	6.256(1)	18.193(3)	8.347(4)	12.407(3)	11.059(4)
b, Å	15.458(3)	6.8949(11)	9.152(4)	15.603(3)	30.644(14)
c, Å	14.979(3)	19.387(3)	14.628(7)	13.225(3)	5.129(2)
α, deg	90	90	101.729(11)	90	90
β, deg	91.91(3)	108.088(4)	93.525(12)	107.003(4)	90
γ, deg	90	90	94.375(13)	90	90
V, Å^3	1447.7(5)	2311.6(7)	1087.4(9)	2448.2(9)	1738.4(12)
d_{calcd}, g/cm^3	1.382	1.478	1.330	1.325	1.362
μ, mm^{-1}	0.102	0.108	0.087	0.093	0.091
θ_{max}, deg	25.06	25.04	30.03	25.01	27.06
R_{int}	0.0118	0.0526	0.0227	0.0811	0.0434
Number of reflections measured	2796	9345	13000	9730	7157
Number of unique reflection	2549	4059	6147	4147	3575
Number of reflections with ($I > 2\sigma(I)$)	1878	1487	2755	1704	1971
Number of parameters refined	243	431	382	442	328
R_1	0.0454	0.0532	0.0486	0.0551	0.0469
wR_2 (on F^2)	0.1210	0.1214	0.0967	0.0881	0.0821
S	1.024	0.842	1.211	0.927	0.934
$\Delta\rho_{max}$, $\Delta\rho_{min}$, e Å^{-3}	0.22, –0.30	0.25, –0.19	0.19, –0.16	0.21, –0.18	0.16, –0.16

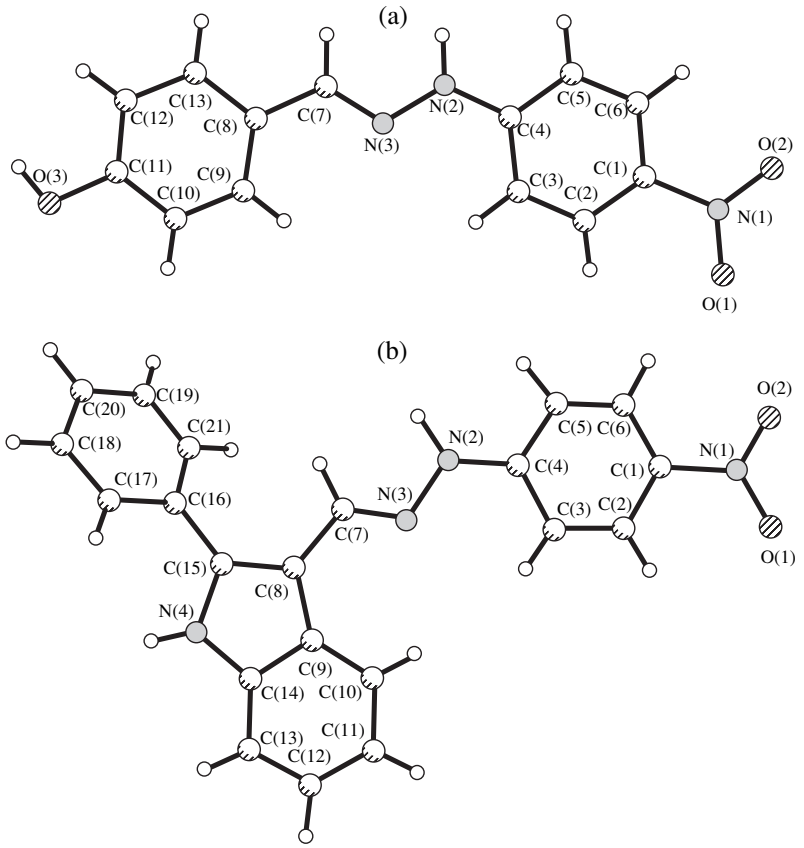

Fig. 1. A general view of molecules (a) **I** and (b) **II** and the atomic numbering.

tions at the centers of symmetry. Crystals **Ib** grown from the acetone and acetonitrile solutions contain two crystallographically independent molecules in the asymmetric part of the unit cell. Noncentrosymmetric crystals **IIc** are formed upon slow evaporation of the acetonitrile solution. Therefore, among the used solvents, acetonitrile is most suitable for preparing the nonlinear optically active hydrazone crystals (the same inference was drawn in [3]).

Molecular Geometry

A general view of the studied molecules and the atomic numbering are given in Fig. 1. The selected geometric characteristics of molecule **I** in pseudopolymorphs **Ia** and **Ib** are presented in Table 2. For comparison, the geometric parameters for the molecule of 3,4-dihydroxybenzaldehyde-4-nitrophenylhydrazone (**I'**) previously studied in [2] are also listed in Table 2. It should be noted that, although the hydrazones have conformationally nonrigid molecules, their geometric parameters only slightly change in different crystals and the independent molecules of crystal **Ib**. The bond lengths and bond angles in the molecules have typical values [15, 16]. The mean difference between the coordinates of the independent molecules (when their centers of gravity are brought into coincidence) in crystal **Ib** is equal to 0.59 Å. In all the polymorphic modifications, molecule **I** is planar: the torsion angles along the N(2)–N(3) and N(3)=C(7) bonds vary from 171.5° to 179.5° and the dihedral angles between the hydroxybenzene and nitrophenyl groupings do not exceed 6°–8°. The alternation of bond lengths is observed in the central bridge (triad group) connecting two aromatic rings in the molecule. This circumstance together with the planar structure indicate the formation of the conjugate molecular chain.

The selected geometric characteristics of molecule **II** are given in Table 2. As for molecule **I**, in molecule **II**, the chemically equivalent bond lengths and bond angles in different crystals differ insignificantly. At the same time, it should be noted that the N(3)–C(7) bond in molecule **II** (except for structure **IIc**) is somewhat longer than that in molecule **I**. The parameters characterizing the molecular planarity differ more considerably. For example, the angle between molecular planes **1** and **2** (see Table 2) varies from 8.8° in structure **IIb** to 18.1° in structure **IIa**. The observed change is substantially larger than the change in this angle in different pseudopolymorphs of compound **I**. Note that this angle in different polymorphic modifications of the known hydrazone with a heterocyclic donor ring (thiophene-

Table 2. Selected geometric parameters of molecules **I** and **II** in the studied crystals

Parameter	**Ia** ($P2_1/c$)	**Ib** ($P2_1/n$)		**I'** (Cc) [2]	**IIa** ($P\bar{1}$)	**IIb** ($P2_1/c$)	**IIc** ($Pna2_1$)
		A	*B*				
Bond lengths, Å							
C(4)–N(2)	1.356(2)	1.375(4)	1.364(4)	1.358	1.360(2)	1.355(3)	1.355(3)
N(2)–N(3)	1.376(2)	1.364(4)	1.372(4)	1.368	1.375(1)	1.375(3)	1.382(3)
N(3)–C(7)	1.279(2)	1.273(4)	1.287(4)	1.273	1.290(2)	1.305(3)	1.278(3)
C(7)–C(8)	1.451(3)	1.447(4)	1.433(4)	1.454	1.431(2)	1.448(4)	1.433(4)
Bond angles, deg							
C(4)–N(2)–N(3)	121.6(2)	122.1(3)	120.7(3)	121.6	120.3(1)	120.3(3)	120.0(3)
C(7)–N(3)–N(2)	114.8(2)	116.1(3)	116.1(3)	115.7	114.9(1)	115.6(3)	115.4(2)
C(8)–C(7)–N(3)	122.9(2)	122.7(4)	122.6(4)	118.7	122.8(1)	119.2(3)	120.5(3)
Torsion angles, deg							
C(7)–N(3)–N(2)–C(4)	171.5(2)	179.4(3)	178.9(3)	179.9	173.1	173.2	–179.8
C(8)–C(7)–N(3)–N(2)	–179.5(2)	179.2(3)	177.4(3)	179.3	174.2	179.8	177.5
Basal molecular planes							
N(1),C(1)–C(6),N(2) (plane **1**) δ, Å	0.006	0.003	0.024		0.012	0.014	0.010
C(7),C(8)–C(13), (plane **2**) δ, Å	0.005	0.006	0.013		0.025	0.018	0.024
C(16)–C(21); C(16')–C(21') (planes **3**, **3'**) δ, Å					0.003	0.004; 0.018	0.012; 0.022
Angles between the basal molecular planes, deg							
1–**2**	8.0	6.2	7.9	8.8	18.1	8.8	10.3
2–**3**					58.9	33.6	46.1
2–**3'**						38.5	35.4
3–**3'**						108.1	81.4

carboxaldehyde) [3] also varies over a wide range from 3° to 16°.

Crystal Structure

It was noted earlier in [1] that, in crystals, hydrazone molecules free of additional functional groupings form acentric Λ-shaped planar chains. These chains are formed by the NH···O hydrogen bonds of the central amino group with one of the oxygen atoms in the nitro group and the CH···O additional contacts between the CH azomethine group and the same oxygen atom, which most likely stabilizes the coplanar arrangement of molecules in the chain. Upon introduction of other groupings (such as donors of hydrogen bonds) into the molecule, the formation of a crystalline associate can occur in a different manner. Actually, crystals **Ia** (Fig. 2a) involve typical Λ contacts [N(2)···O(2), 3.008 Å; H(N2)···O(2), 2.12 Å; angle at the H atom, 161° and C(7)···O(2), 3.367 Å; H(7)···O(2), 2.53 Å; angle at the H atom, 141.5°]. In turn, these chains are linked into the crystal structure through the O(3)H(O3)···O(1^s) hydrogen bonds (O···O, 2.741 Å; H···O, 1.86 Å; angle at the H atom, 171°) between the hydroxy groups and the oxygen atoms of the solvate dioxane molecules. As was noted above, the dioxane molecules in the crystal occupy special positions. Therefore, it is this circumstance that is most likely responsible for the formation of the centrosymmetric structure (Fig. 2a).

As in the case of molecule **I**, molecule **II** (Fig. 1b) containing the NH indole fragment as an additional hydrogen-bond donor can also form intermolecular hydrogen bonds. Indeed, identical structural fragments are formed in crystal structures **I** and **II** grown in the same solvent. In crystal **IIb** grown in dioxane (Fig. 2b), as in crystal **Ia**, the molecules form Λ-shaped planar chains [N(2)···O(1), 2.877 Å; H(N2)···O(1), 2.01 Å; angle at the H atom, 166° and C(7)···O(1), 3.328 Å; H(7)···O(1), 2.54 Å; angle at the H atom, 140°]. As in structure **Ia**, these chains are joined into the centrosymmetric structure through the N(4)H··O^s hydrogen bonds [N(4)··O^s, 2.712 Å; H···O, 1.84 Å; angle at the H atom, 169°] between the NH indole groups and the oxygen atoms of the dioxane molecules, which occupy the special positions at the symmetry center. The presence

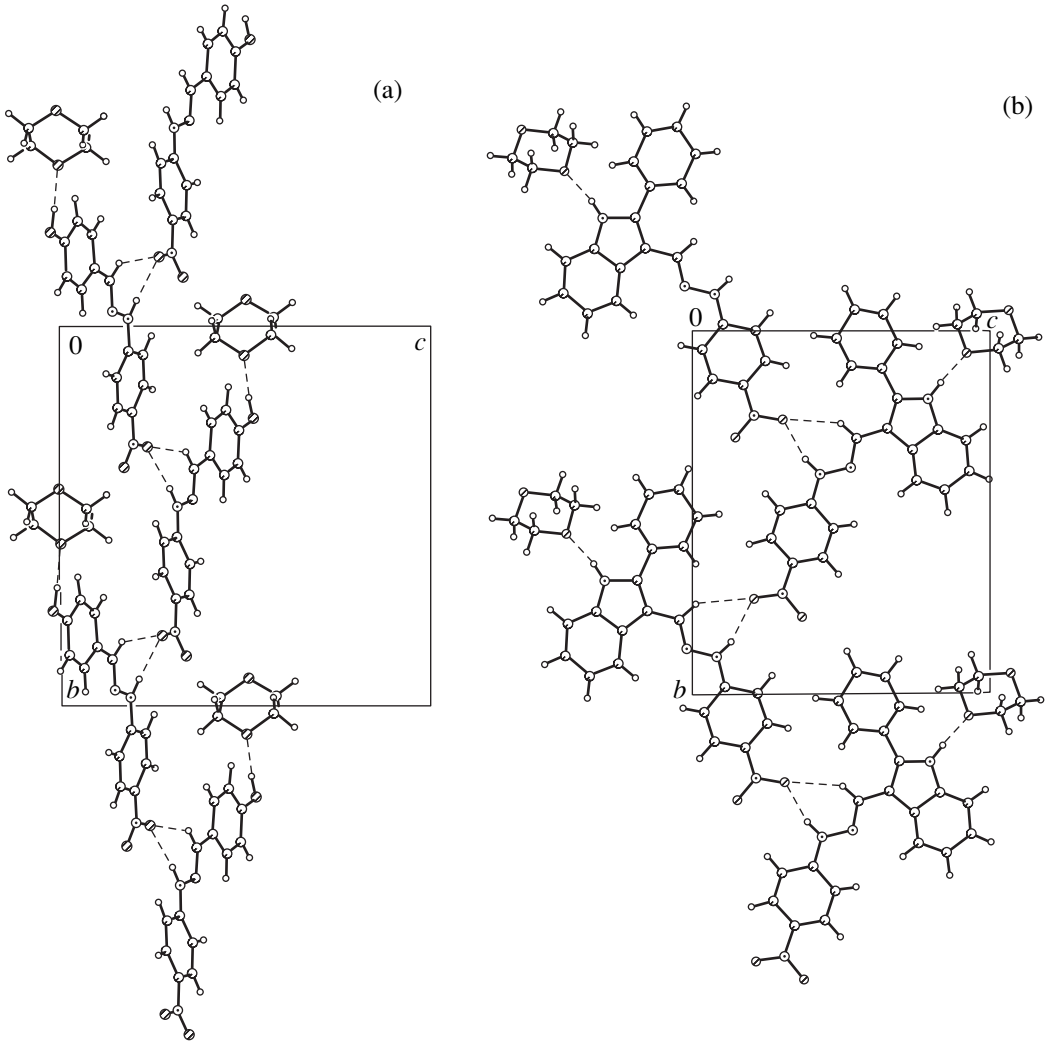

Fig. 2. Λ-shaped chains formed by molecules in crystals (a) **I** and (b) **II** grown from dioxane solutions.

of the additional (disordered) phenyl ring in the indole fragment of molecule **II** leads to the formation of a rather loose structure. As a result, one more dioxane molecule is incorporated into the holes due to the van der Waals interactions.

In crystals **IIa** grown in pyridine, acentric molecular chains of the head-to-tail type (Fig. 3a) are formed by the hydrogen bonds [N(4)···O(1), 2.974 Å; H(4)···O(1), 2.05 Å; angle at the H atom, 168°] between the NH indole fragments and the oxygen atoms of the nitro groups. Moreover, the solvate pyridine molecules are linked to the chains through the hydrogen bonds (N(2)··N^s, 3.091 Å; H(2N)··N^s, 2.11 Å; angle at the H atom, 173°] with the central amino groups of the hydrazone molecules. In the crystal, the chains are arranged in an antiparallel manner to form the centrosymmetric crystal structure. It is worth noting that molecules in the pseudopolymorphs under consideration are joined together into strong acentric supramolecular associates. This gives grounds to hope that noncentrosymmetric structures can be formed in other solvents.

As was mentioned above, crystal structure **Ib** containing no solvate molecules is formed in two solvents, namely, acetone and acetonitrile. The proton affinity of these solvents is less than that of dioxane and pyridine. In crystals **Ib**, as in crystals **IIb**, the head-to-tail chains are formed through the O(3)H(3)···O(1) and O(3)H(3)···O(2) hydrogen bonds of the hydroxyl groups with both oxygen atoms of the nitro groups in neighboring molecules (Fig. 3b). However, in the chains formed by molecules *A* and *B* due to these interactions, the parameters of the O(3)H(3)···O(1) and O(3)H(3)···O(2) hydrogen bonds differ noticeably: the H···O distances in chains *A* are equal to 1.90 and 2.38 Å and these distances in chains *B* are 2.23 and 2.21 Å. The alternating centrosymmetric layers composed of molecules of the same sort are formed through the stacking contacts between the chains arranged in an antiparallel fashion (with interplanar distances of 3.5 Å) in the crys-

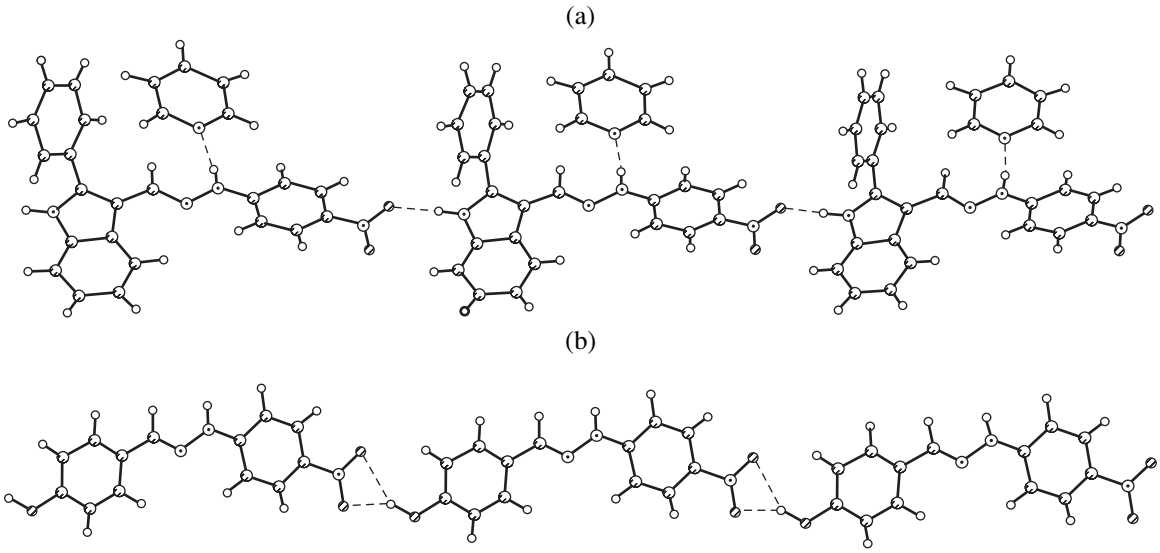

Fig. 3. Molecular chains of the head-to-tail type in crystals (a) **IIa** (grown from a pyridine solution) and (b) **Ib** (grown from acetone and acetonitrile solutions).

tal. These layers are shifted in pairs with respect to each other so that molecules of different layers are differently joined together. In this case, the molecules of layers *A* form a typical (even though slightly weakened) contact of the Λ type, in which the central amino group and the CH azomethine fragment are the donors of the hydrogen bonds, whereas the nitro groups of the molecules of adjacent layer *B* are the acceptors of the hydrogen bonds (N···O, 3.186 Å; H···O, 2.40 Å; angle at the H atom, 151° and C···O, 3.321 Å; H···O, 2.47 Å; angle at the H atom, 141°). On the other hand, the molecules of layer *B* cannot form such contacts due the aforementioned shift. These molecules are linked only to the oxygen atoms of the hydroxyl groups of molecules *A* via the N(2)H(2N)···O(1) hydrogen bond formed with the central amino group (N···O, 3.045 Å; H···O, 2.17 Å; angle at the H atom, 162°). As a result, the crystal involves only separate fragments of Λ-shaped chains. It should be noted that, among all the studied structures, crystal structure **Ib** is characterized by the closest molecular packing. The crystal structure of 3,4-dihydroxy derivative **I'** [2] (also grown in acetonitrile) is topologically very similar to structure **Ib**, with the only difference that crystal **I'** has a noncentrosymmetric structure (space group *Cc*). Crystal **I'** is built up of parallel layers that are composed of the same acentric molecular chains as in structure **Ib** (Fig. 3a). However, unlike crystals **Ib**, the layers in crystal **I'** are formed by the stacking contacts between parallel molecular chains. In this case, the chains are shifted with respect to each other so that the donor fragment of the molecule is located above the acceptor fragment and the distance between the molecular planes is equal to 3.3 Å.

A closer examination of the packing of crystal structure **Ib** (according to the procedure proposed in [1]) allows us to reveal a set of additional pseudosymmetric operations that approximately transform the independent molecules into each other. These are the pseudocenter (with the coordinates [0.766, 0.758, –0.010]); the *2* rotation axis, which is parallel to the *OY* axis and intersects the *XOZ* plane at the point [x = 0.512, z = 0.238]; and the *a* glide-reflection plane parallel to the *XOZ* plane. These operations indicate the potentialities for forming the structure of a higher symmetry. This structure is determined by the hypothetical shift ($|\Delta r|$ = 0.35 Å) of the pseudoinversion operation from the coordinates [0.766, 0.758, –0.010] to the nearest crystallographic point [0.75, 0.75, 0]: ($P2_1/n$, Z' = 2) + $\bar{1}$ (0.75, 0.75, 0) ⟶ ($B2/b$, Z' = 1). The impossibility of forming the structure in this space group is associated both with the above difference between the systems of the hydrogen bonds formed by molecules *A* and *B* and with the more energetically favorable packing of crystals **Ib**, which have the highest density among the crystals under consideration (see Table 1).

The noncentrosymmetric crystal structure is formed upon slow evaporation of the acetonitrile solution of compound **II**. In crystals **IIc**, as in crystals **IIb**, the protons of the central amino groups participate in the formation of a supramolecular associate (chain) (Fig. 4). The parameters of the N(2)H(2)···O(2) hydrogen bond are as follows: N(2)···O(2), 2.901 Å; H(N2)···O(2), 1.85 Å; angle at the H atom, 168°. However, it seems likely that, owing to the steric hindrances associated with the bulky molecule, the contact between the CH group of the azomethine fragment and the oxygen atom of the nitro group is not formed in the chain. (Note that this contact stabilizes the planar structure of the Λ chain in the crystals of compounds **Ia** and **IIb** and other known hydrazones [1–3].) Consequently, the molecules in the chain are rotated with respect to each other. The

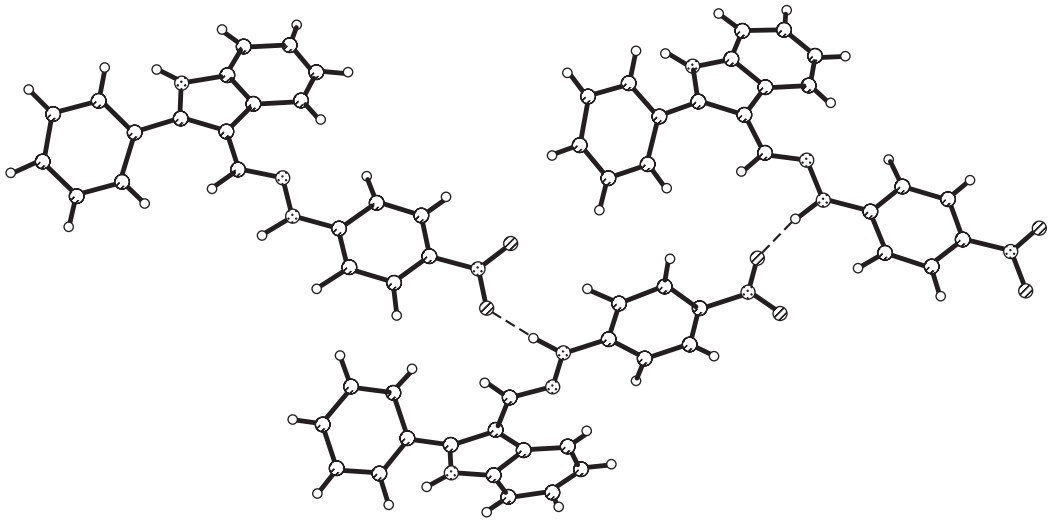

Fig. 4. Molecular chain in crystal structure **IIc**.

angle between the root-mean-square molecular planes is 70.2°.

CONCLUSION

Thus, the result obtained experimentally confirmed the following inference made in our earlier works [17, 18] from analyzing the data available in the Cambridge Structural Database: in the case when molecules in a crystal are capable of forming stable acentric supramolecular associates, the investigation into the possible polymorphism of organic compounds with a nonlinear optical activity offers strong possibilities for designing the noncentrosymmetric crystal structure.

ACKNOWLEDGMENTS

We would like to thank K.Yu. Suponitskiĭ for performing the calculations of the susceptibilities of the molecules and crystals studied in our work.

This work was supported by the Russian Foundation for Basic Research, project nos. 00-03-32840a and 00-15-97359.

REFERENCES

1. C. Serbutoviez, C. Bossard, G. Knopfle, *et al.*, Chem. Mater. **7**, 1198 (1995).
2. I. Liakatas, M. S. Wong, V. Gramlich, *et al.*, Adv. Mater. **10** (10), 777 (1998).
3. F. Pan, C. Bossard, M. S. Wong, *et al.*, Chem. Mater. **9**, 1328 (1997).
4. G. M. Sheldrick, *SHELXTL: Version 5.10* (Bruker AXS, Madison, WI, 1997).
5. M. J. S. Dewar and J. J. P. Stewart, Chem. Phys. Lett. **111**, 416 (1984).
6. H. A. Kurtz, J. J. P. Stewart, and K. M. Dieter, J. Comput. Chem. **11**, 82 (1990).
7. J. Zyss, J. Chem. Phys. **70**, 3333 (1979).
8. J. Zyss, J. Chem. Phys. **70**, 3341 (1979).
9. *QCPE; MOPAC: Quantum Chemistry Program Exchange. Version 6* (1990).
10. B. H. Cardelino, C. E. Moore, and R. E. Stickel, J. Phys. Chem. **95**, 8645 (1991).
11. M. J. S. Dewar, E. G. Zoebish, E. F. Healy, *et al.*, J. Am. Chem. Soc. **107**, 3902 (1985).
12. J. L. Oudar and J. Zyss, Phys. Rev. A **26**, 2016 (1982).
13. J. Zyss and J. L. Oudar, Phys. Rev. A **26**, 2028 (1982).
14. L. N. Kuleshova, V. N. Khrustalev, K. Yu. Suponitskiĭ, *et al.*, Kristallografiya **48** (1), 78 (2003) [Crystallogr. Rep. **48** (1), 73 (2003)].
15. F. H. Allen, O. Kennard, D. G. Watson, *et al.*, J. Chem. Soc., Perkin Trans. 2, S1 (1987).
16. A. G. Orpen, L. Brammer, F. H. Allen, *et al.*, J. Chem. Soc., Dalton Trans. 1, S1 (1989).
17. L. N. Kuleshova, V. N. Khrustalev, and M. Yu. Antipin, Kristallografiya **45** (6), 1034 (2000) [Crystallogr. Rep. **45**, 953 (2000)].
18. L. N. Kuleshova and M. Yu. Antipin, Kristallografiya **47** (2), 303 (2002) [Crystallogr. Rep. **47**, 268 (2002)].

Translated by O. Borovik-Romanova

Crystallography Reports, Vol. 48, No. 4, 2003, pp. 602–605. Translated from Kristallografiya, Vol. 48, No. 4, 2003, pp. 653–656.

STRUCTURE OF ORGANIC COMPOUNDS

Insertion of Ethyl Isothiocyanate into Tungsten Hexachloride: Crystal Structure of Ethyl-(4-Ethyl-5-Thioxo[1.2.4]dithiazolidin-3-ylidene)ammonium Oxopentachlorotungstate(VI)

N. A. Ovchinnikova, A. E. Sinyakov, V. S. Sergienko, and G. G. Aleksandrov

Kurnakov Institute of General and Inorganic Chemistry, Russian Academy of Sciences, Leninskiĭ pr. 31, Moscow, 119991 Russia

e-mail: talan@igic.ras.ru

Received May 28, 2002

Abstract—A product of the insertion of two isothiocyanate molecules into the same W–Cl bond, namely, W–Cl–WCl_5{N(*Et*)C(S)N(*Et*)C(S)Cl} (**I**), is synthesized by the reaction of WCl_6 with *Et*NCS in a dichloroethane solution. The hydrolysis of compound **I** results in the formation of single crystals of the complex {N(*Et*)C(S)–S–S–C=NH(*Et*)}$[WOCl_5]$ (**II**). The structure of crystals **II** is determined using X-ray diffraction. It is demonstrated that structural units of crystals **II** are the $[W^{VI}OCl_5]^-$ anionic complexes and the ethyl-(4-ethyl-5-thioxo[1.2.4]dithiazolidin-3-ylidene)ammonium cations. © *2003 MAIK "Nauka/Interperiodica".*

INTRODUCTION

It is known [1] that phenyl isothiocyanate and phenyl isocyanate enter into reactions with mixed molybdenum complexes $[Mo(NR)_2(O\text{-}tert\text{-}Bu)_2]$ (*R* = *tert-Bu* or 2,6-*iso*-$Pr_2C_6H_3$) and can be selectively inserted into the Mo=N and Mo–O bonds, respectively. It should be noted that the product of the insertion of isothiocyanate is relatively unstable, and, in excess phenyl isocyanate, isothiocyanate is displaced from the coordination sphere of the complex.

Our previous investigations revealed that some heterocumulenes can be inserted into higher chlorides of Group VI transition metals. In particular, it was found the reaction of WCl_6 with *Et*NCO in dichloroethane is attended by the insertion of three *Et*NCO molecules into the same W–Cl bond [2] and that ethyl isothiocyanate can be inserted into $MoCl_5$ to form the product of the insertion of two *Et*NCS molecules into the same Mo–Cl bond [3].

In the present work, we analyzed the ability of organic isothiocyanate to be inserted into the W–Cl bonds by using the interaction of tungsten hexachloride with ethyl isothiocyanate in a dichloroethane solution as an example.

EXPERIMENTAL

Synthesis. The reactions were carried out with tungsten hexachloride (purified from impurities through vacuum distillation) and ethyl isothiocyanate (Fluka). Dichloroethane was purified and dried using a standard method. All the procedures with reactants and products were performed in a dry argon atmosphere. Crystalline products of the reaction were isolated from the mother solution by decantation, washed several times with carbon tetrachloride, and dried under vacuum to constant weight.

IR absorption spectra were recorded on a Specord 75 IR spectrophotometer in the range 4000–400 cm^{-1} with the use of KBr pellets and on a Nicolet Nexus FTIR spectrometer in the range 4000–200 cm^{-1} with the use of KRS-5 pellets. Samples were prepared as suspensions in vaseline oil.

Elemental analysis for hydrogen, carbon, nitrogen, and sulfur was performed on a Carlo Erba EA 1108 N,C,H,S-analyzer. The chlorine content was determined according to the Volhard method.

Ethyl isothiocyanate (1.01 ml, 11.55 mmol) was added to a suspension of tungsten hexachloride (1.53 g, 3.85 mmol) in dichloroethane (20 ml) at room temperature (23°C). The solution changed its color from orange to brown. Within one week, the solution became dark brown and dark brown crystals of compound **I** precipitated.

For $C_6H_{10}Cl_6N_2S_2W$, anal. calcd. (%): N, 4.91; C, 12.62; H, 1.77; S, 11.23; Cl, 37.26.

Found (%): N, 4.25; C, 11.78; H, 3.00; S, 9.79; Cl, 36.68.

IR (cm^{-1}): 1596 s, 1531 w, 1410 m, 1339 m, 1310 m, 1264 m, 1224 s, 1120 s, 1033 m, 975 s, 962 w, 791 w, 722 w, 696 w, 651 m, 580 w, 544 w, 529 m, 484 m, 436 m, 398 w, 373 w, 333 vs, 254 s.

Prolonged storage of crystals **I** in excess of *Et*NCS in the presence of atmospheric moisture traces resulted in the precipitation of dark brown crystals **II**. These crystals were isolated from the mother solution, washed with carbon tetrachloride, and dried under vacuum.

For $C_6H_{11}Cl_5N_2OS_3W$, anal. calcd. (%): N, 5.44; C, 14.01; H, 2.35; S, 18.70.

Found (%): N, 5.09; C, 13.07; H, 2.74; S, 17.09.

IR (cm^{-1}): 3180–3150 w, 1700 w, 1600 vw, 1340 m, 1270 w, 1225 s, 1120 s, 1110 w, 1070 w, 980 s.

X-ray structure analysis. The crystal data and the data collection parameters for compound **II** are presented in Table 1.

The experimental data were collected using a faceted crystal on an Enraf–Nonius CAD4 four-circle automated diffractometer (λMoK_α, graphite monochromator, ω scan mode) at room temperature. The crystal unstable in air was placed in a capillary.

The structure was solved by direct methods [4] and refined using the least-squares procedure on F^2 in the full-matrix anisotropic approximation [5] for all the non-hydrogen atoms. The positions of the hydrogen atoms were calculated geometrically (C–H, 0.96 Å and N–H, 0.90 Å). The hydrogen atoms at fixed positions were included in the refinement. The low accuracy in the structure determination (large factors *R*) is most likely associated with the instability of the crystals in air.

The crystal data (CIF file) have been deposited with the Cambridge Crystallographic Data Center (CCDC, no. 196355).

The interatomic distances and the bond angles are listed in Table 2.

Table 1. Crystal data, data collection, and refinement parameters for the crystal structure of compound **II**

Empirical formula	$C_6H_{11}Cl_5N_2OS_3W$
Molecular weight	584.45
Crystal system	Monoclinic
Space group	$P2_1/n$
Unit cell parameters:	
a, Å	7.646(3)
b, Å	14.494(9)
c, Å	15.583(9)
β, deg	102.86(4)
Z	4
V, Å^3	1684(2)
ρ_{calcd}, g/cm^3	2.306
μ_{Mo}, cm^{-1}	80.15
F(000)	1104
$2\theta_{max}$, deg	53.8
Index ranges	$-8 \le h \le 8$; $0 \le k \le 18$; $0 \le l \le 19$
Number of reflections measured	4500
Number of reflections with $I \ge 2\sigma(I)$	1494
R_{int}	0.029
R_1, wR_2 ($I \ge 2\sigma(I)$)	0.077, 0.198
R_1, wR_2 (for all reflections)	0.100, 0.215
GOOF	1.079
Number of parameters refined	164
$\Delta\rho_{max}$, $\Delta\rho_{min}$, e/Å^3	3.472, −2.435

RESULTS AND DISCUSSION

The reaction of WCl_6 with *Et*NCS in dichloroethane results in the formation of complex **I**. The IR spectrum of this complex involves two intense ν(C=S) bands at 1596 and 1531 cm^{-1} and the ν(C–Cl) band at 775 cm^{-1}. At the same time, the characteristic absorption bands of coordinated isothiocyanate are not observed in the spectrum. This indicates that two *Et*NCS molecules are inserted into the same W–Cl bond, that is,

$$WCl_6 + 2Et\text{–}N{=}C{=}S \longrightarrow \underset{\mathbf{I}}{Cl_5W\text{–}\overset{Et}{\overset{|}{N}}\text{–}\overset{S}{\overset{\|}{C}}\text{–}\overset{Et}{\overset{|}{N}}\text{–}\overset{S}{\overset{\|}{C}}\text{–}Cl}. \quad (1)$$

The structure of complex **II** formed through the partial hydrolysis of the solution of complex **I** suggests that compound **II** results from the interaction of compound **I** with hydrogen sulfide. In turn, hydrogen sulfide evolved owing to the hydrolysis of excess isothiocyanate [6] upon prolonged storage of the reaction mixture

$$Et\text{–}N{=}C{=}S \xrightarrow{2H_2O} H_2S + EtNH_2 + CO_2. \quad (2)$$

The formation of ethylammonium according to the above scheme of hydrolysis is in good agreement with the data available in the literature. Actually, Beck and Walter [7] obtained ethylammonium chloride and ethyl-(4-ethyl-5-thioxo[1.2.4]dithiazolidin-3-ylidene)-ammonium chloride through the reaction of $WOCl_4$ with *Et*NCS. In our previous work [3], we showed that the hydrolysis of the product formed by the insertion of *Et*NCS into $MoCl_5$ leads to the formation of the complex containing the ethylammonium cation. On this basis, the scheme for the hydrolysis of complex **I** can be

represented in the following form:

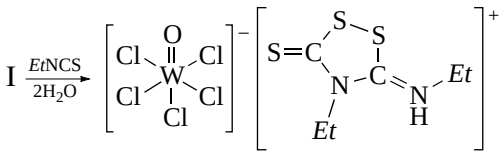

$$\mathbf{I} \xrightarrow[2H_2O]{Et\text{NCS}} \mathbf{II} + Et\text{NH}_3\text{Cl} + CO_2. \quad (3)$$

Table 2. Bond lengths *d* (Å) and angles ω (deg) for the crystal structure of compound **II**

Bond	*d*	Bond	*d*
W(1)–Cl(1)	2.29(1)	W(1)–Cl(2)	2.32(1)
W(1)–Cl(3)	2.29(1)	W(1)–Cl(4)	2.28(1)
W(1)–Cl(5)	2.542(8)	W(1)–Cl(1)	1.72(2)
S(1)–S(2)	2.05(1)	S(1)–C(1)	1.75(3)
S(2)–C(4)	1.73(4)	S(3)–C(1)	1.58(3)
N(1)–C(1)	1.37(4)	N(1)–C(4)	1.35(4)
N(2)–C(4)	1.33(4)	N(2)–C(5)	1.44(4)
C(2)–C(3)	1.51(4)	C(5)–C(6)	1.46(6)
Angle	ω	Angle	ω
Cl(1)–W(1)–Cl(2)	168.3(4)	Cl(1)–W(1)–Cl(3)	87.7(4)
Cl(1)–W(1)–Cl(4)	90.1(4)	Cl(1)–W(1)–Cl(5)	85.3(3)
Cl(1)–W(1)–O(1)	95.0(9)	Cl(2)–W(1)–Cl(3)	89.9(4)
Cl(2)–W(1)–Cl(4)	90.2(4)	Cl(2)–W(1)–Cl(5)	83.0(3)
Cl(2)–W(1)–O(1)	96.6(9)	Cl(3)–W(1)–Cl(4)	169.9(4)
Cl(3)–W(1)–Cl(5)	85.1(4)	Cl(3)–W(1)–O(1)	96.8(9)
Cl(4)–W(1)–Cl(5)	84.9(4)	Cl(4)–W(1)–O(1)	93.2(9)
Cl(5)–W(1)–O(1)	178.0(8)	S(2)–S(1)–C(1)	97(1)
S(1)–S(2)–C(4)	93(1)	C(1)–N(1)–C(4)	119(3)
C(4)–N(2)–C(5)	126(3)	S(1)–C(1)–S(3)	119(2)
S(1)–C(1)–N(1)	113(2)	S(3)–C(1)–N(1)	128(2)
S(2)–C(4)–N(1)	118(2)	S(2)–C(4)–N(2)	118(3)
N(1)–C(4)–N(2)	124(3)	N(2)–C(5)–C(6)	110(3)

The $[WOCl_5]^-$ anionic complexes and the $[C_6H_{11}N_2S_3]^+$ cations are the structural units of crystal **II** (see figure). The cation in compound **II** is a protonated organic heterocycle, namely, the dithiazolidine derivative formed by the condensation of two ethyl isothiocyanate molecules and one sulfur atom.

The coordination polyhedron of tungsten atoms is a distorted octahedron that contains four chlorine atoms [Cl(1), Cl(2), Cl(3), and Cl(4)] in the equatorial plane and the oxo oxygen atom at one of the axial positions. The second axial position in the coordination octahedron of the metal is occupied by the Cl(5) atom. The length of the $W{=}O_{oxo}$ double bond [1.72(1) Å] agrees with the relevant bond lengths in d^0-W(VI) oxo complexes according to the data available in the literature for 14 monomeric compounds [1.698(12) Å] [8] and 12 monomeric octahedral oxo complexes [1.71(4) Å] [9].

The lengths of the equatorial W–Cl bonds lie in the range 2.28(1)–2.32(1) Å. The mean length of $W–Cl_{eq}$ bonds [2.29(3) Å] falls in a wide range of $W–Cl_{eq}$ bond lengths (2.290–2.436 Å; mean bond length, 2.33 Å) found in 16 monomeric octahedral oxo complexes of tungsten(VI) [9]. The fifth W–Cl bond in the *trans* position with respect to the O(oxo) atom, as usual, is noticeably lengthened [to 2.542(8) Å] due to the *trans* effect of the doubly bonded oxo ligand. In the structure of the only previously studied compound (H_5O_2 × 21-crown-7)$[WOCl_5]$ (**III**) containing a similar anionic complex [10], the $W–Cl_{trans}$ bond length is equal to 2.666(5) Å [the mean length of the equatorial $W–Cl_{cis}$ bonds in compound **III** is 2.366(5) Å]. The parameter $\Delta_{trans–cis}$,

Table 3. Geometric parameters of short interionic contacts in the crystal structure of compound **II**

A–H···*B* contact	*d A*···*B*	*d* H···*B*	*AHB*, ω	Symmetry codes for the *B* atom
N(2)–H(N2)···Cl(5)	3.16(3)	2.33	152	1.5 –*x*, 0.5 + *y*, 0.5 – *z*
N(2)–H(N2)···O(1)	3.31(4)	2.99	111	0.5 –*x*, 0.5 + *y*, 0.5 – *z*
Cl(1)···S(3)	3.62(2)			1 –*x*, 1 – *y*, –*z*
Cl(1)···N(1)	3.50(3)			–1 +*x*, *y*, *z*
Cl(3)···S(3)	3.66(2)			–0.5 +*x*, 0.5 – *y*, 0.5 + *z*
Cl(5)···S(1)	3.19(1)			*x*, *y*, *z*
Cl(5)···S(2)	3.21(1)			*x*, *y*, *z*
S(1)···S(3)	3.67(1)			1 –*x*, 1 – *y*, –*z*

Note: *d* is the distance (Å), and ω is the angle (deg). The N(2)–H(N2) bond length is equal to 0.90 Å.

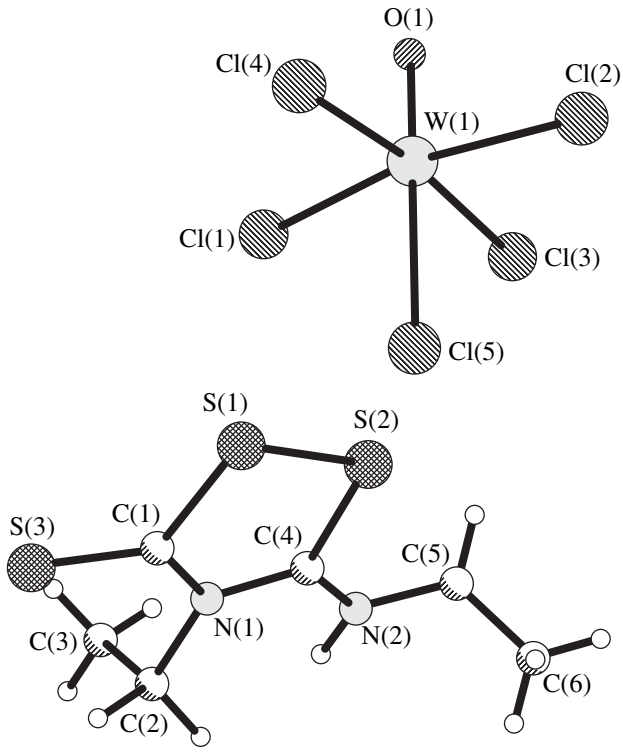

Structural units in complex **II**.

which is the difference between the corresponding bonds in the *trans* and *cis* positions with respect to the O(oxo) atom and quantitatively characterizes the structural manifestation of the *trans* effect of the doubly bonded oxo ligand, is equal to 0.248 Å in structure **II** and 0.300 Å in structure **III**.

The distortion of the tungsten coordination polyhedron manifests itself in the displacement of the W atom from the equatorial plane toward the doubly bonded O(oxo) ligand by 0.217 Å (the equatorial Cl ligands are coplanar to within ±0.02 Å).

In the organic dithiazole cation, the S(1)S(2)C(4)N(1)C(1) five-membered heterocycle adopts a planar conformation (to within ±0.01 Å). The C(2), N(2), S(3), and C(5) atoms deviate from the plane of this heterocycle by 0.02, 0.04, –0.12, and 0.11 Å, respectively. The S(1)–S(2) distance [2.05(1) Å] corresponds to the standard length of the ordinary bond (S–S, 2.048 Å) [11]. In the heterocycle, the mean S–C distance [1.74(3) Å] also agrees with the standard length of the C_{sp^2}–S ordinary bond (1.75 Å) [11], whereas the S(3)–C(1) distance [1.58(3) Å] is less than the standard length of the C_{sp^2}=S double bond (1.660 Å) [11]. The N(1)–C(1) and N(1)–C(4) bond lengths [mean length, 1.36(4) Å], within the limits of experimental error, are in agreement with the standard length (1.344 Å) of C_{sp^2}–S sesquibonds in heterocycles [11].

The geometric parameters of the interionic contacts comparable in length to the sums of the van der Waals radii or twice the van der Waals radii of the corresponding atoms (H, 1.16 Å; C, 1.71 Å; N, 1.50 Å; O, 1.29 Å; Cl, 1.90 Å [12]; and S, 1.84 Å [13]) are given in Table 3. The NH group is involved in the hydrogen bond with the Cl atom and also forms the N–H···O shortened interionic contact with the adjacent anionic complex. Each anionic complex is in contact with two adjacent anionic complexes and four dithiazole cations. It should be noted that the Cl(5) atom occupying the *trans* position with respect to the oxo ligand takes the most active part in the interionic contacts. In addition to the participation in the hydrogen bond N(2)–H(N2)···Cl(5) [N(2)···Cl(5), 3.16(3) Å], the Cl(5) atom is involved in contacts with the S(1) and S(2) atoms of the nearest cation: the Cl(5)···S(1) [3.19(1) Å] and Cl(5)···S(2) [3.21(1) Å] distances, on average, are 0.54 Å less than the sum of the van der Waals radii for chlorine and sulfur [12, 13]. Possibly, these short interionic contacts make an additional contribution to the weakening (elongation) of the W–Cl(5) bond due to the *trans* effect of the doubly bonded oxo ligand.

ACKNOWLEDGMENTS

This work was supported by the Russian Foundation for Basic Research, project no. 00-15-97432. We also acknowledge the support of the Russian Foundation for Basic Research in the payment of the license for using the Cambridge Structural Database, project no. 02-07-90322.

REFERENCES

1. V. C. Gibson, C. Redshaw, W. Clegg, *et al.*, J. Chem. Soc., Chem. Commun., No. 22, 2635 (1994).
2. N. A. Ovchinnikova, A. E. Sinyakov, A. M. Reznik, *et al.*, Koord. Khim. **29** (2003) (in press).
3. V. S. Sergienko, N. A. Ovchinnikova, G. G. Aleksandrov, *et al.*, Zh. Neorg. Khim. **46** (12), 1989 (2001).
4. G. M. Sheldrick, Acta Crystallogr., Sect. A: Found. Crystallogr. **46** (5), 467 (1990).
5. G. M. Sheldrick, *SHELXL93: Program for the Refinement of Crystal Structures* (Univ. of Göttingen, Göttingen, 1993).
6. J. Houben, *Die Methoden der organischen Chemie* (George Thieme, Leipzig, 1924), Vol. 4, p. 36.
7. J. Beck and J. Walter, Acta Crystallogr., Sect. C: Cryst. Struct. Commun. **55** (2), 260 (1999).
8. J. M. Mayer, Inorg. Chem. **27** (22), 3899 (1988).
9. V. S. Sergienko, Russ. J. Inorg. Chem. **45**, S37 (2000).
10. P. C. Junk and J. L. Atwood, J. Chem. Soc., Dalton Trans., No. 22, 4393 (1997).
11. F. H. Allen, O. Kennard, D. G. Watson, *et al.*, J. Chem. Soc., Dalton Trans., No. 1, S1 (1987).
12. Yu. V. Zefirov and P. M. Zorkiĭ, Zh. Strukt. Khim. **15** (1), 118 (1974).
13. Yu. V. Zefirov and P. M. Zorkiĭ, Zh. Strukt. Khim. **17** (4), 745 (1976).

Translated by O. Borovik-Romanova

Crystallography Reports, Vol. 48, No. 4, 2003, pp. 606–609. Translated from Kristallografiya, Vol. 48, No. 4, 2003, pp. 657–660.

STRUCTURE OF ORGANIC COMPOUNDS

X-ray Diffraction Studies of 6-Methyl-5-Acetyl-4-α-Furyl-2-Keto-1,2,3,6-Tetrahydropyrimidine and 6-Methyl-5-Acetyl-4-γ-Bromophenyl-2-Thio-1,2,3,6-Tetrahydropyrimidine

V. K. Belsky*, A. I. Stash*, O. V. Koval'chukova, S. B. Strashnova**, L. S. Shebaldina**, B. E. Zaĭtsev**, and V. G. Pleshakov****

** Karpov Research Institute of Physical Chemistry, State Scientific Center, ul. Vorontsovo pole 10, Moscow, 103064 Russia*

*** Russian University of People's Friendship, ul. Miklukho-Maklaya 6, Moscow, 117198 Russia*

e-mail: okovalchukova@sci.pfu.edu.ru

Received September 4, 2002

Abstract—6-Methyl-5-acetyl-4-α-furyl-2-keto-1,2,3,6-tetrahydropyrimidine (**I**) and 6-methyl-5-acetyl-4-γ-bromophenyl-2-thio-1,2,3,6-tetrahydropyrimidine (**II**) are prepared by the modified Biginelli reaction, and their crystal and molecular structures are studied. It is shown that, in crystals **I** and **II**, the pyrimidine ring has an amide tautomeric form and adopts a sofa conformation. The IR absorption spectra are analyzed, and the stability of the tautomers of the pyrimidine fragments is evaluated using quantum-chemical calculations. © *2003 MAIK "Nauka/Interperiodica".*

INTRODUCTION

It is known that pyrimidine derivatives are among the most effective agents for the chemotherapy of tumors [1]. In this respect, many research centers give considerable attention to the synthesis and chemicobiological investigations of new pyrimidine derivatives, specifically tetrahydropyrimidines.

Our purpose was to synthesize furyl and bromophenyl derivatives of 1,2,3,4-tetrahydropyrimidines and to elucidate their structures. 6-Methyl-5-acetyl-4-α-furyl-2-keto-1,2,3,6-tetrahydropyrimidine (**I**) and 6-methyl-5-acetyl-4-γ-bromophenyl-2-thio-1,2,3,6-tetrahydropyrimidine (**II**) were synthesized by the modified Biginelli reaction [2].

The presence of the pyrimidine fragment in molecules **I** and **II** suggests the existence of the following tautomeric forms:

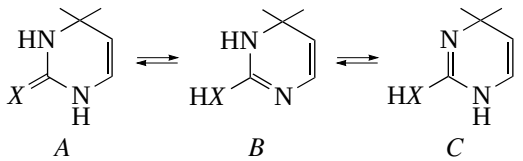

A *B* *C*

Formation of one or several tautomeric forms depends on the type of substituents, the aggregate state of the substance, and the acidity of the medium. This paper reports on the results of the synthesis and X-ray diffraction studies of compounds **I** and **II**, quantum-chemical calculations, and IR spectroscopy.

EXPERIMENTAL

The Biginelli reaction [2] involves the cyclocondensation of a β-dicarbonyl compound, aldehyde, and carbamide or thiocarbamide. Aromatic aldehydes are commonly used in this procedure. Reactions with heterocyclic aldehydes have not been adequately investigated.

With due regard to the target compounds, we chose *para*-bromobenzaldehyde and furfurol as aldehyde components and acetyl acetate as the β-dicarbonyl component. The compounds were introduced in a specified amount (~0.1 mol). The condensation proceeded for 3–4 h.

Single crystals **I** and **II** of X-ray quality were prepared by a recrystallization from acetone. Single crystals were white in color with a melting temperature of 199–201°C for **I** and 233–234°C for **II**. Main crystal data and experimental parameters are summarizied in Table 1. The experimental data processing and subsequent calculations were carried out with the SHELX97 program package [3]. Both structures were solved by direct methods, and the non-hydrogen atoms were refined by the least-squares procedure in the full-matrix anisotropic approximation. All the hydrogen atoms were included in the refinement in the fixed calculated positions with isotropic thermal parameters. The coordinates and isotropic equivalent thermal parameters of the non-hydrogen atoms are listed in Tables 2 and 3. The bond lengths and angles in the pyrimidine fragment of molecules **I** and **II** are given in Table 4. The

1063-7745/03/4804-0606$24.00 © 2003 MAIK "Nauka/Interperiodica"

Table 1. Crystal data, data collection, and refinement parameters for the crystal structure of compounds **I** and **II**

Parameter	**I**	**II**
Crystal system	Monoclinic	Triclinic
Space group	$P2_1/n$	$P\bar{1}$
a, Å	14.917(2)	7.2230(10)
b, Å	8.2170(10)	8.203(2)
c, Å	8.8690(10)	13.127(3)
α, deg	90	106.32(3)
β, deg	103.120(10)	89.04(8)
γ, deg	90	107.08(3)
V, Å^3	1058.7(2)	711.7(3)
Z	4	2
ρ_{calcd}, Mg/m^3	1.382	1.518
Diffractometer	Syntex $P\bar{1}$	CAD-4
Radiation type	CuK_α	MoK_α
Index ranges	$0 \le h \le 16$	$0 \le h \le 8$
	$0 \le k \le 8$	$-8 \le k \le 8$
	$-9 \le l \le 9$	$15 \le l \le 15$
Number of unique reflections	1380	979
$R1$	0.038	0.031
wR_2	0.098	0.077

parameters of the hydrogen bonds in structures **I** and **II** are presented in Table 5.

The IR spectra of the crystalline samples were recorded on a Specord 75IR spectrophotometer (KBr pellets and nujol mulls) in the range 400–4000 cm^{-1}.

RESULTS AND DISCUSSION

According to the X-ray diffraction data, the pyrimidine fragments of crystalline compounds **I** and **II** exist in an amide form (structure *A*) and adopt a sofa conformation with the C(4) carbon atom deviating from the plane of the remaining atoms by 0.470 Å in **I** and 0.380 Å in **II**.

The lengths of the C=O and C=S bonds (1.233 and 1.678 Å, respectively) are typical of double bonds [4]. In the N(3)–C(2)–N(1)–C(6)–C(5) ring (Fig. 1), the bond lengths are essentially smoothened, which indicates that the ρ_π electron density is delocalized. The bond angles in the heterocycles of **I** and **II** fall in the range 115°–124°. The exception is provided by the N(3)C(4)C(5) angle, whose value (108.69° and 109.2°) indicates the sp^3 hybrid state of the carbon atom in the 4-position.

The C(2)–N(3) and C(2)–N(1) bond lengths in the ring depends only slightly on the type of heteroatom in the 2-position: when going from –C=O to –C=S, these

Table 2. Coordinates ($\times 10^4$) and equivalent isotropic thermal parameters U_{eq} (Å$^2 \times 10^3$) of the non-hydrogen atoms in structure **I**

Atom	x	y	z	U_{eq}
O(1)	3776(1)	–141(2)	–274(2)	48(1)
O(2)	3658(1)	5752(2)	3993(2)	52(1)
O(3)	3904(1)	688(2)	4042(2)	49(1)
N(1)	4726(1)	1765(2)	1095(2)	40(1)
N(3)	3174(1)	1868(2)	954(2)	40(1)
C(2)	3874(1)	1079(2)	557(2)	37(1)
C(4)	3311(1)	2926(2)	2313(2)	36(1)
C(5)	4186(1)	3917(2)	2408(2)	35(1)
C(6)	4873(1)	3237(2)	1849(2)	36(1)
C(7)	5836(1)	3860(3)	1984(3)	47(1)
C(8)	4205(1)	5493(2)	3172(2)	38(1)
C(9)	4834(2)	6844(3)	2943(3)	57(1)
C(10)	3295(1)	1960(2)	3734(2)	36(1)
C(11)	2793(1)	2000(3)	4813(2)	46(1)
C(12)	3099(2)	700(3)	5855(2)	51(1)
C(13)	3758(2)	–52(3)	5347(3)	52(1)

Table 3. Coordinates ($\times 10^4$) and equivalent isotropic thermal parameters U_{eq} (Å$^2 \times 10^3$) of the non-hydrogen atoms in structure **II**

Atom	x	y	z	U_{eq}
Br	591(2)	1743(1)	4164(1)	121(1)
S	8048(2)	6191(2)	9665(1)	43(1)
O	1519(6)	9402(6)	8298(4)	54(1)
N(1)	7484(8)	8499(7)	8739(4)	36(1)
N(3)	4757(8)	6716(7)	9174(4)	37(1)
C(2)	6668(9)	7157(8)	9172(4)	31(1)
C(4)	3495(9)	7225(7)	8546(4)	29(1)
C(5)	4569(8)	9015(7)	8394(4)	31(1)
C(6)	6512(9)	9557(7)	8466(4)	32(2)
C(7)	7854(1)	11213(9)	8268(7)	46(2)
C(8)	3249(9)	9961(8)	8177(5)	35(1)
C(9)	3931(13)	11547(11)	7748(8)	55(2)
C(10)	2781(9)	5806(7)	7496(5)	36(2)
C(11)	821(11)	5080(10)	7210(6)	58(2)
C(12)	182(15)	3848(11)	6208(7)	81(3)
C(13)	1465(15)	3340(9)	5529(5)	66(2)
C(14)	3404(16)	3985(10)	5821(6)	69(2)
C(15)	4052(13)	5226(9)	6797(6)	56(2)

Table 4. Bond lengths *d* (Å) and angles ω (deg) in the pyrimidine fragment of molecules **I** and **II**

Bond	*d*		Angle	ω	
	I	**II**		**I**	**II**
*X**–C(2)	1.233(2)	1.678(6)	C(2)N(3)C(4)	122.1 (6)	125.3(5)
N(3)–C(2)	1.342(2)	1.320(7)	C(2)N(1)C(6)	124.6(2)	124.9(5)
N(3)–C(4)	1.463(2)	1.458(7)	N(3)C(4)C(5)	108.7(2)	109.2(5)
N(1)–C(2)	1.374(2)	1.357(7)	N(3)C(4)C(10)	110.7(2)	111.0(5)
N(1)–C(6)	1.375(2)	1.385(7)	C(5)C(4)C(10)	114.5(2)	112.0(4)
C(4)–C(5)	1.525(2)	1.513(8)	C(6)C(5)C(8)	126.8(2)	127.9(5)
C(4)–C(10)	1.494(3)	1.514(8)	C(6)C(5)C(4)	117.9(2)	119.5(5)
C(5)–C(6)	1.356(3)	1.339(7)	C(8)C(5)C(4)	115.2(2)	112.6(5)
C(5)–C(8)	1.459(3)	1.470(8)	C(5)C(6)N(1)	119.3(2)	118.6(5)
C(6)–C(7)	1.503(3)	1.506(8)	C(5)C(6)C(7)	128.1(2)	128.1(6)
			N(1)C(6)C(7)	112.5(2)	113.2(6)
			N(3)C(2)N(1)	115.1(2)	114.8(5)
			N(1)C(2)*X**	123.8(2)	124.4(5)
			N(3)C(2)*X**	121.1(2)	120.8(5)

* The oxygen atom in **I** and the sulfur atom in **II**.

Table 5. Parameters of hydrogen bonds in structures **I** and **II**

Structure	Hydrogen bond	Distance, Å			N–H···*X* angle, deg
		N···H	H···*X*	N···*X*	
I	N(1)–H(1)···O(1)*	0.84	2.12	2.893	153.0
	N(3)–H(3)···O(2)**	0.85	1.99	2.836	176.8
II	N(1)–H(1)···O***	0.83	2.08	2.880	161.4
	N(3)–H(3)···S****	0.71	2.64	3.348	169.7

Note: Codes for transformation of symmetrically equivalent atoms: * $1-x, -y, -z$; ** $1/2-x, y-1/2, 1/2-z$; *** $1+x, y, z$; **** $1-x, 1-y, 2-z$.

Table 6. Energy parameters for tautomers *A*, *B*, and *C* (eV)

Tautomer	Δ*H**	E_{π}^{**}	E_{σ}^{***}	M_{sol}^{****}
A	63.43	11.75	17.00	3.46
B	62.49	10.59	16.98	1.81
C	63.01	10.92	17.00	2.32

* Heat of atomization.
, * The energies of the π and σ bonds, respectively.
**** Solvation coefficient.

bond lengths decrease by ~0.01 Å. Note that the C(2)–N(3) and C(2)–N(1) bonds differ by ~0.03 Å; that is, they are inequivalent. This is, most probably, due to the effect of the substituents in the 4-position. Actually, the substituent at the C(4) atom and the pyrimidine fragment are conjugated. This follows from the N(3)–C(4) bond length of 1.463 Å, which is characteristic of conjugated bonds [4].

As follows from the C(5)–C(8) bond lengths (1.459 and 1.470 Å for **I** and **II**, respectively), conjugation occurs also between the acetyl group in the 5-position and the C(5)–C(6) bond. The C(4)–C(5) bond lengths (1.526 and 1.503 Å) correspond to the single C–C bond.

The bond lengths in the furyl ring in **I** and the bromophenyl ring in **II** agree with the data reported for alkyl substituted molecules [4].

The structural parameters of the acetyl groups in compounds **I** and **II** are close to those in unsaturated or aromatic ketones; that is, the C(8)–O(2) bond is slightly elongated because of the conjugation with the double bond of the ring. The substituent in the 4-position (benzene or furane ring) is planar; it is rotated with respect to the plane of the pyrimidine ring by 83.1° in **I** and 89.1° in **II**.

In structures **I** and **II**, molecules are linked through the intermolecular hydrogen bonds NH···*X* (*X* = O or S) (Table 5) into layers parallel to the (101) plane (structure **I**) and the (001) plane (structure **II**) (Fig. 2).

Molecule **I** includes two –C=O carbonyl groups, namely, cyclic and acetyl (noncyclic) carbonyls. In the IR spectrum of **I**, two intense bands appear in the range of ν(CO) stretching vibrations (1627 and 1667 cm^{-1}). These bands were assigned using the spectrum of **II**, which includes only the acetyl group. In the IR spectrum of crystal **II**, a very intense band is observed at 1627 cm^{-1}. Apparently, this band overlaps with the band of the C=C stretching vibrations. It is known that

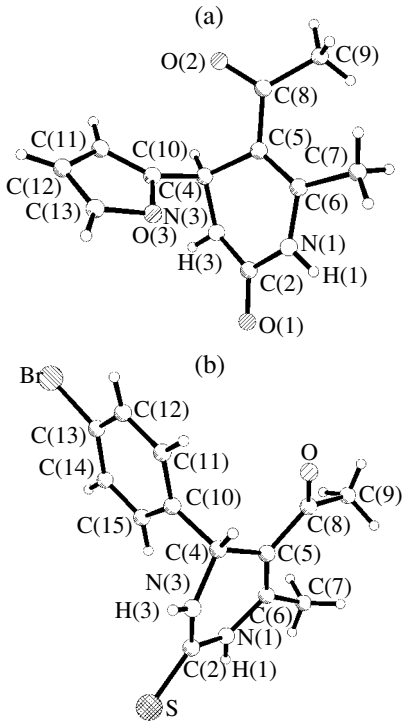

Fig. 1. Molecular structures of (a) **I** and (b) **II**.

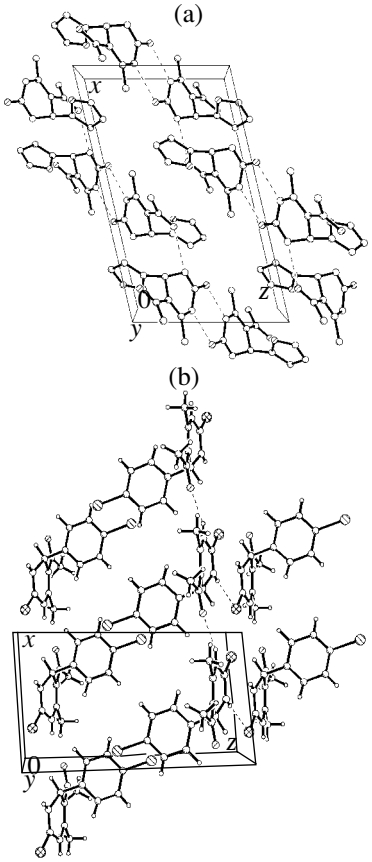

Fig. 2. Fragments of molecular packing in structures (a) **I** and (b) **II**.

ν(CO) of the acetyl group conjugated with multiple bonds [5] appears near ~1680 cm^{-1}. The shift observed in the spectrum is attributed to the strong hydrogen bond, which agrees with the X-ray diffraction data. Thus, the band at 1627 cm^{-1} is assigned to the stretching vibrations of the acetyl group, and the band at 1667 cm^{-1} is attributed to the stretching vibrations of the exocyclic C=O group of the six-membered pyrimidine ring.

This assignment agrees with the shift in the NH stretching frequencies by 220–320 cm^{-1} as compared to the frequency of free NH bonds [5]. A comparison between the spectra of compounds **I** and **II** shows that the band of the C=S stretching vibrations in **II** is located at 1015 cm^{-1}.

The relative stability of the tautomers of the pyrimidine ring was estimated from the results of quantum-chemical calculations (the Dewar variation of the Pariser–Parr–Pople method [6]). It follows from Table 6 that the heat of atomization for form *A* is 0.93 and 0.42 eV greater than those for forms *B* and *C*, respectively, which indicates that *A* is the most stable tautomer. The decisive contribution to the stability of the tautomers is made by the π-electron energy, whereas the energy of the σ bonds is actually the same for all the tautomeric forms. According to the solvation coefficients (M_{sol}), the *A* tautomer is solvated to a larger degree than the *B* and *C* tautomers.

Thus, the X-ray diffraction data demonstrated that, in the crystal state, compounds **I** and **II** exist in the amide form. The influence of the type of substituent in the 4-position of the pyrimidine ring on the molecular structure is insignificant. The results of the quantum-chemical calculations and the IR data agree with the data of the X-ray structure analysis.

REFERENCES

1. A. T. Soldatenkov, N. M. Kolyadina, and I. V. Shendrik, *Fundamentals of Organic Chemistry of Medicinals* (Khimiya, Moscow, 2001).
2. E. E. Stashenko, P. I. Zakharov, V. G. Pleshakov, and B. S. Subbotin, Khim. Geterotsikl. Soedin., No. 3, 360 (1989).
3. G. M. Sheldrick, *SHELX97: Programs for the Solution and Refinement of the Crystal Structures* (Univ. of Göttingen, Germany, 1997).
4. A. I. Kitaĭgorodskiĭ, P. M. Zor'kiĭ, and V. K. Bel'sky, *Structure of Organic Substances* (Nauka, Moscow, 1982).
5. L. V. Vilkov and Yu. A. Pentin, *Physical Methods in Chemical Studies* (Vysshaya Shkola, Moscow, 1987).
6. M. Dewar, *The Molecular Orbital Theory of Organic Chemistry* (McGraw-Hill, New York, 1969; Mir, Moscow, 1972).

Translated by I. Polyakova

Crystallography Reports, Vol. 48, No. 4, 2003, pp. 610–612. Translated from Kristallografiya, Vol. 48, No. 4, 2003, pp. 661–663.

STRUCTURE OF ORGANIC COMPOUNDS

Crystal Structure of an Yttrium Nitrate Complex with Tetramethylurea

A. S. Antsyshkina, G. G. Sadikov, M. N. Rodnikova, and S. E. Tikhonov

Kurnakov Institute of General and Inorganic Chemistry, Russian Academy of Sciences, Leninskiĭ pr. 31, Moscow, GSP-1, 119991 Russia

e-mail: sadgg@igic.ras.ru

Received May 17, 2002

Abstract—An X-ray diffraction study of $Y(NO_3)_3 \cdot 3TMU$ crystals is performed (heavy-atom method, difference electron-density maps, H atoms in calculated positions, full-matrix anisotropic–isotropic (H) least-squares refinement). The crystals are monoclinic, $a = 9.353(1)$ Å, $b = 15.966(3)$ Å, $c = 18.805(8)$ Å, $\beta = 95.41(2)°$, $Z = 4$, and space group $P2_1/c$. The structural units of the crystals are molecular complexes. The coordination number of the Y atom is nine due to three bidentate NO_3 groups and three monodentate tetramethylurea molecules. The mean Y–O bond lengths are 2.464 and 2.274 Å for NO_3 and tetramethylurea, respectively. © *2003 MAIK "Nauka/Interperiodica".*

INTRODUCTION

Tetramethylurea $C_5H_{12}N_2O$ (*TMU*) is commonly used as a ligand in the coordination chemistry of rare-earth elements. The tetramethylurea molecule exhibits a large dipole moment, 3.24 D at 25° [1], and a high electron-donating capacity, $DN_{SbC_{15}} \sim 28.1$ [2]. Molecular symmetry is characterized by the twofold axis, and the nitrogen atom slightly deviates from the plane of the three carbon atoms bound to it [3].

On complex formation, the number of rather bulky and noncompact tetramethylurea molecules in the coordination of a rare-earth ion depends on the size of both the central ion and the anion included in the coordination sphere. This number is 3.5 for lanthanum chloride and 3 for cerium and yttrium chlorides. For all the rare-earth perchlorates, the composition of the tetramethylurea complex is $Ln(ClO_4)_3 \cdot 6TMU$ [4]. For rare-earth nitrates, only the data for the $Eu(NO_3)_3 \cdot 3TMU$ structure are known [5]. Europium is a remarkable element of the rare-earth series due to the structure of its electron shell. Therefore, it was of interest to study the structure of a similar complex of a rare-earth ion situated at the end of the lanthanide series. For this purpose, we chose yttrium nitrate, which contains a central ion that is very similar to erbium in chemical and crystal chemical behavior.

EXPERIMENTAL

Synthesis

A crystal hydrate of yttrium nitrate $Y(NO_3)_3 \cdot 6H_2O$ and tetramethylurea (Merck) were used as starting substances for the preparation of $Y(NO_3)_3 \cdot 3TMU$ (**I**). The water amount in the crystal hydrate was determined by the Fischer method. The IR spectrum of tetramethylurea revealed no evidence of water in the range of the O–H stretching vibrations.

Heated tetramethylurea was added to the yttrium salt in the ratio 8 : 1, and the mixture was stirred until crystals of nitrate dissolved. On cooling, crystals **I** precipitated. The crystals were washed with absolute alcohol and dried over $CaCl_2$.

For $C_{15}H_{36}N_9O_{12}Y$ anal. calcd. (%): C, 39.18; H, 8.84; N, 11.19.

Found (%): C, 40.02; H, 9.20; N, 10.95.

X-ray Diffraction Study

Crystals **I** are monoclinic, $a = 9.353(1)$ Å, $b = 15.966(3)$ Å, $c = 18.805(8)$ Å, $\beta = 95.41(2)°$, $V = 2795.6(4)$ Å^3, $M = 623.4$, $F(000) = 1296$, $\rho_{calcd} = 1.481$ g/cm^3, $\mu_{Mo} = 2.16$ mm^{-1}, $Z = 4$, space group $P2_1/c$.

The experimental data were obtained on an Enraf–Nonius CAD4 diffractometer (λMoK_α, graphite monochromator, $\theta/2\theta$ scan mode, $2\theta_{max} = 56°$).

The intensities of 6687 unique reflections were measured. The structure was solved by direct methods. The positions of the hydrogen atoms were calculated. The structure was refined by the least-squares procedure using 6682 reflections. The non-hydrogen atoms were refined in the anisotropic approximation, and the hydrogen atoms were refined within a riding model with isotropic thermal parameters larger than the U_{eq} values of the corresponding carbon atoms by a factor of 1.5. Finally, $R_1 = 0.0587$, $wR_2 = 0.1340$, and $GOOF = 1.170$ for 1835 reflections with $F_0 \geq 4\sigma(F_0)$; $\Delta\rho_{max} = 0.473$ and $\Delta\rho_{min} = -1.14$ e/Å^3.

1063-7745/03/4804-0610$24.00 © 2003 MAIK "Nauka/Interperiodica"

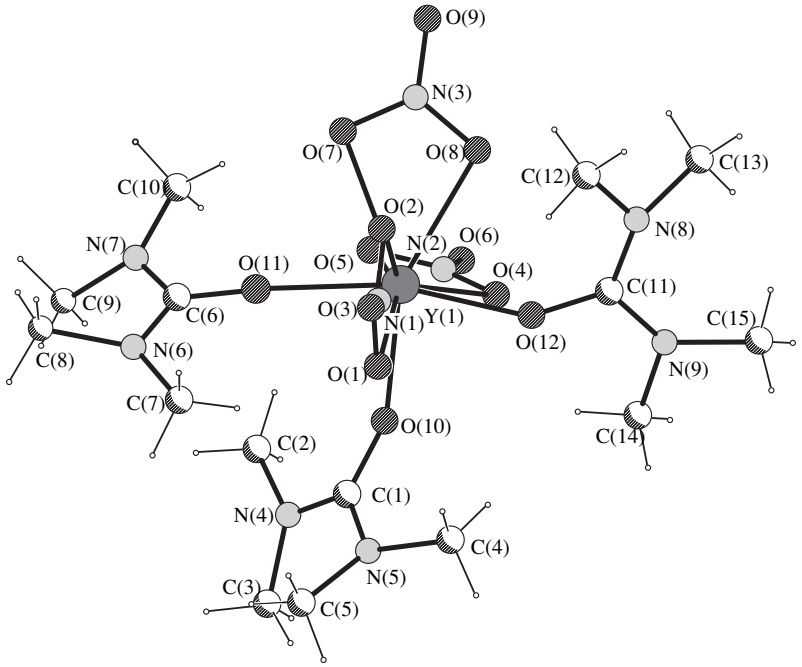

Fig. 1. Structure of the $Y(NO_3)_3(TMU)_3$ complex.

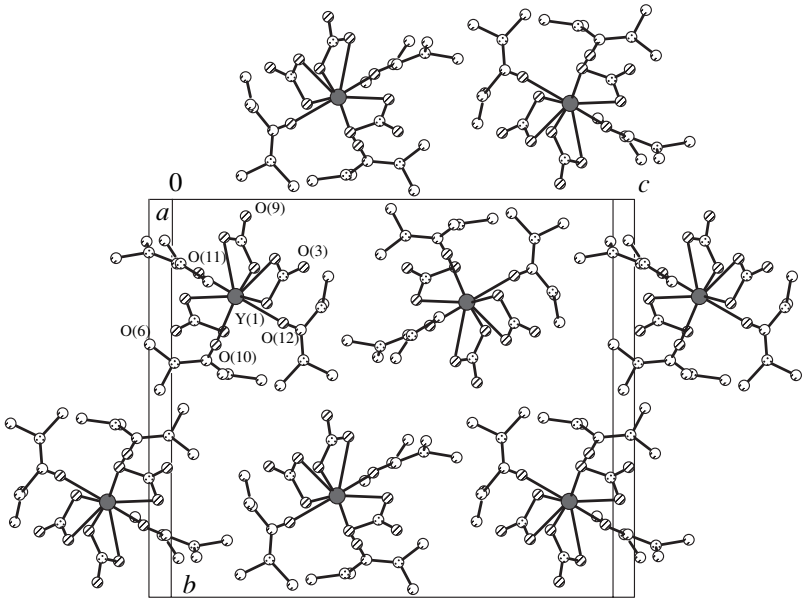

Fig. 2. Projection of a layer of structure **I** onto the (100) coordinate plane.

The calculations were performed with the SHELXS86 [6] and SHELXL93 [7] software packages.

The coordinates and thermal parameters of the nonhydrogen atoms in structure **I** are listed in the table.

RESULTS AND DISCUSSION

The structural units of crystals **I** are molecular complexes $Y(NO_3)_3(TMU)_3$ (Fig. 1). The NO_3 groups act as bidentate ligands. The coordination number of the Y atom is nine, and the coordination polyhedron is a tricapped trigonal prism. However, the coordination polyhedron is more conveniently described as an octahedron with three split *trans*-equatorial vertices, which are occupied by the NO_3 bidentate groups.

The most symmetric Y–O bonds are formed by the $N(1)O_3$ group (2.464 and 2.430 Å). The bonds formed by the $N(2)O_3$ group are less symmetric (2.493 and

Coordinates and thermal parameters U_{eq} of the non-hydrogen atoms in compound **I**

Atom	*x*	*y*	*z*	U_{eq}, Å^2
Y(1)	−0.7860(8)	0.24186(5)	0.13498(4)	0.0324(3)
O(1)	0.1451(6)	0.2578(4)	0.2142(3)	0.050(2)
O(2)	0.0256(7)	0.1447(4)	0.2250(4)	0.054(2)
O(3)	0.2188(8)	0.1679(5)	0.2966(4)	0.076(2)
O(4)	−0.2895(6)	0.3327(4)	0.0980(4)	0.049(2)
O(5)	−0.2220(6)	0.2475(4)	0.0195(3)	0.055(2)
O(6)	−0.4050(8)	0.3273(5)	−0.0075(4)	0.072(2)
O(7)	−0.1601(8)	0.0928(4)	0.1073(4)	0.066(2)
O(8)	−0.2939(6)	0.1718(4)	0.1645(4)	0.050(2)
O(9)	−0.3544(8)	0.0419(4)	0.1449(4)	0.080(2)
O(10)	0.0180(6)	0.3629(4)	0.0960(3)	0.044(2)
O(11)	0.0763(6)	0.1827(4)	0.0655(3)	0.048(2)
O(12)	−0.1386(6)	0.3085(3)	0.2359(3)	0.041(2)
N(1)	0.1317(9)	0.1902(5)	0.2470(5)	0.052(2)
N(2)	−0.3093(8)	0.3037(5)	0.0358(5)	0.048(2)
N(3)	−0.2717(9)	0.1011(5)	0.1388(4)	0.049(2)
N(4)	0.1547(8)	0.4103(5)	0.0132(5)	0.052(2)
N(5)	0.2183(8)	0.4378(5)	0.1326(4)	0.052(2)
N(6)	0.3005(8)	0.1602(5)	0.0347(4)	0.053(2)
N(7)	0.102(1)	0.1286(5)	−0.0440(4)	0.052(2)
N(8)	−0.3054(8)	0.2688(6)	0.3089(4)	0.058(2)
N(9)	−0.2932(9)	0.4037(6)	0.2706(5)	0.067(3)
C(1)	0.1295(9)	0.4013(5)	0.0812(5)	0.039(2)
C(2)	0.068(1)	0.3626(7)	−0.0424(6)	0.082(4)
C(3)	0.240(1)	0.4783(7)	−0.0136(7)	0.095(4)
C(4)	0.166(1)	0.4519(7)	0.2031(6)	0.093(4)
C(5)	0.375(1)	0.4376(7)	0.1295(8)	0.105(5)
C(6)	0.156(1)	0.1584(5)	0.0192(5)	0.043(2)
C(7)	0.361(1)	0.2040(6)	0.0975(7)	0.072(3)
C(8)	0.396(1)	0.0988(7)	0.0049(6)	0.088(4)
C(9)	0.171(1)	0.1442(7)	−0.1103(6)	0.090(4)
C(10)	−0.045(1)	0.1024(8)	−0.0555(6)	0.084(4)
C(11)	−0.243(1)	0.3255(6)	0.2698(5)	0.042(2)
C(12)	−0.228(1)	0.1915(7)	0.3289(6)	0.079(4)
C(13)	−0.465(1)	0.2591(9)	0.3075(7)	0.109(5)
C(14)	−0.242(1)	0.4659(6)	0.2240(8)	0.096(5)
C(15)	−0.368(1)	0.4391(8)	0.3310(8)	0.124(6)

2.444 Å), and the bonds formed by the $N(3)O_3$ group are the most asymmetric (2.539 and 2.414 Å). The tetramethylurea molecules are coordinated monodentately and form shorter Y–O bonds (2.282, 2.249, and 2.291 Å). A similar situation (bidentate coordination of the NO_3 groups, difference in the asymmetry of the Y–O bonds, and greater distances from the central atom to the nitrate groups as compared to other ligands) was observed also in the trinitrate complexes $M(NO_3)(DMSO)_3$ of ytterbium, erbium, and lutecium [8–10]. In all these compounds, the mean M–O(NO_3) and M–O(*Lig*) bond lengths agree rather closely [2.464 and 2.274 (**I**), 2.455 and 2.278 (M = Y), 2.465 and 2.270 (M = Er), and 2.461 and 2.260 Å (M = Lu)].

In the NO_3 groups of compound **I**, as usual, the N–O bond lengths with the terminal oxygen atoms are somewhat shorter than those with the coordinated oxygens (mean, 1.23 and 1.26 Å, respectively).

In the crystal, complexes are arranged according to simple hexagonal packing. The distances between the Y atoms in the pseudotrigonal network generated by the *c* glide plane, twofold screw axis, and centers of inversion are 9.13 × 2, 9.40 × 2, 9.43, and 9.86 Å (Fig. 2). The layers formed by these networks are spaced at the translation along the *x* axis (a = 9.353 Å).

Compound **I** is isostructural with the Eu complex studied earlier [5]. This suggests that compounds $Ln(NO_3)_3(TMU)_3$ are possibly isostructural throughout the rare-earth series.

REFERENCES

1. O. A. Osipov, V. I. Minkin, and A. D. Garnovskiĭ, *Handbook on Dipole Momenta* (Vysshaya Shkola, Moscow, 1971).
2. M. N. Rodnikova, L. P. Larina, N. A. Chumaevskiĭ, and S. E. Tikhonov, Zh. Neorg. Khim. **48** (2003) (in press).
3. C. S. Franpton and K. E. B. Parkes, Acta Crystallogr., Sect. C: Cryst. Struct. Commun. **52**, 3246 (1996).
4. G. Vicentini and R. Najjar, Inorg. Nucl. Chem. Lett. **6**, 571 (1970).
5. C. Chien, G. Toogood, D. Boyle, and C. M. Burgess, Acta Crystallogr., Sect. B: Struct. Crystallogr. Cryst. Chem. **32**, 1008 (1976).
6. G. M. Sheldrick, *SHELXS86: Program for the Solution of Crystal Structures* (Univ. of Göttingen, Germany, 1986).
7. G. M. Sheldrick, *SHELXL 93: Program for the Refinement of Crystal Structures* (Univ. of Göttingen, Germany, 1993).
8. A. S. Antsyshkina, G. G. Sadikov, M. N. Rodnikova, *et al.*, Zh. Neorg. Khim. **47** (3), 423 (2002).
9. L. A. Aslanov, L. I. Soleva, S. S. Goukhberg, and M. A. Poraĭ-Koshits, Zh. Strukt. Khim. **13** (6), 1101 (1972).
10. L. A. Aslanov, L. I. Soleva, and M. A. Poraĭ-Koshits, Zh. Strukt. Khim. **14** (6), 1064 (1973).

Translated by I. Polyakova

Crystallography Reports, Vol. 48, No. 4, 2003, pp. 613–622. Translated from Kristallografiya, Vol. 48, No. 4, 2003, pp. 664–673.

STRUCTURE OF ORGANIC COMPOUNDS

Supramolecular Architecture of Crown-Containing Styryl Dyes: Part I. Crystal and Molecular Structures of the Acetonitrile Solvate Monohydrate of the Potassium Iodide Complex with Benzo-15-Crown-5 Ether Dye Based on Methylquinoline Iodide

L. G. Kuz'mina*, A. V. Churakov*, J. A. K. Howard, O. A. Fedorova***, S. P. Gromov***, and M. V. Alfimov*****

** Kurnakov Institute of General and Inorganic Chemistry, Russian Academy of Sciences, Leninskiĭ pr. 31, Moscow, 119991 Russia*

e-mail: kuzmina@igic.ras.ru

*** Department of Chemistry, Durham University, Durham DH1 3LE, England*

**** Research Center for Photochemistry, Russian Academy of Sciences, ul. Novatorov 7a, Moscow, 117421 Russia*

Received October 17, 2002

Abstract—The structure of a single crystal of the acetonitrile solvate monohydrate of the potassium iodide complex with benzo-15-crown-5 ether dye based on methylquinoline iodide (**I**) is determined by X-ray diffraction. It is established that the single crystal contains positively charged molecules of benzocrown ether photodye (*D*), K^+ cations, I^- anions, and water and acetonitrile solvate molecules in the ratio 1 : 0.5 : 1.5 : 1 : 1, respectively. The K^+ cation and one of the I^- anions occupy special positions along the twofold axis. The K^+ cation is coordinated by ten oxygen atoms of the crown ether fragments of two *D* molecules to form the $[D_2K]^{3+}$ complex. Inside the complex, two aromatic quinoline fragments are involved in a stacking interaction. The crossed mutual arrangement of the ethylene fragments and the considerable distance between them exclude the occurrence of intramolecular photochemical [2 + 2]cycloaddition reactions. In the crystal, the $[D_2K]^{3+}$ cationic complexes form stacks along the *b* axis. The adjacent complexes in a stack are related through the center of symmetry and, therefore, are arranged in a head-to-tail manner. The double bonds of the neighboring molecular cations *D* in a stack are strictly parallel to each other and are separated by a distance of 3.754 Å. This geometry is favorable to the intermolecular cycloaddition reaction that should result in the formation of the *syn* head-to-tail isomer. © *2003 MAIK "Nauka/Interperiodica".*

INTRODUCTION

Crown ethers are good complex-forming compounds that are capable of selectively capturing cations into their cavities. This makes it possible to use crown ethers for the extraction of heavy metals from aqueous solutions, the separation of different-type cations, and the stabilization of metal cations in organic media. The ability of crown ether to bind metal cations depends on the cavity size and the nature of heteroatoms (O, N, or S) and substituents of the macrocycle and solvent. In this respect, it is clear that the prediction of the properties of crown ethers is an important theoretical problem. Similar investigations have been performed in a number of recent works [1–5] dealing with free crown ethers, protonated crown ether, and complexes of crown ethers with alkali and alkaline-earth metals.

Bagatur'yants *et al.* [6] carried out a theoretical study in terms of the density functional theory and *ab initio* calculations of the structure and the relative stability of 18-crown-6 complexes with heavy metals (such as silver and mercury) in different oxidation states. Moreover, these authors analyzed the influence of the counterion on the structure and the relative stability of the complexes under consideration. A number of inferences made in [6] are based on the comparison of the theoretical data with the results of the structural investigations performed earlier for 18-crown-6 complexes with mercury halides [7–9].

Humphy-Baker *et al.* [10] showed that a singly charged complex of monovalent silver with the diaza-18-crown-6 derivative can be reduced in a solution to the zero-valence state with a neutral silver atom in the cavity of the crown. This result suggests the possibility of creating an electron trap based on a highly polarized heavy metal enclosed in the crown cavity. This also means that the possibilities of using crown ethers are far from exhausted.

In recent years, crown ethers have found application as components of supramolecular systems [11]. The

1063-7745/03/4804-0613$24.00 © 2003 MAIK "Nauka/Interperiodica"

incorporation of a metal into the cavity of a crown ether or a change in the oxidation state of the metal in this cavity can affect the properties of a particular functional group bound to the crown ether in a supramolecular system. Supramolecular systems that contain a crown ether fragment and a photodye as a functional group can be used as molecular switches [12–14]. The influence of the metal coordination on the photosensory properties of crown ether complexes was investigated in [15–19].

Molecules of photosensitive systems involve a fragment that is capable of serving as an "antenna" for the absorption of photons and of using the photon energy to transform the molecular structure, as well as a fragment whose reactivity changes as a result of the structural transformation. It is this principle of operation that is embodied in natural photosensitive systems. Among artificial photosensitive systems, the most extensively studied are the compounds containing the N=N bond as a light-sensitive antenna, which, under exposure to light, undergoes a reversible *cis–trans* isomerization [20, 21]. The photosensitive compounds containing the C=C bond, which were discovered more recently, have the advantage that, apart from photoisomerization, they can undergo a reversible photochemical [2 + 2]cycloaddition reaction [12, 20]. This has opened up fresh opportunities for the multipurpose application of photosensitive systems based on olefins.

Gromov *et al.* [22, 23] suggested that crown-containing styryl dyes and their complexes with metal cations can be used as promising optical switches owing to their ability to be reversibly transformed with a high quantum yield from the *trans* isomer to the *cis* isomer and the substantial difference in the spectral and complex-forming properties of both dye isomers. Moreover, Gromov and Alfimov [12] demonstrated that these compounds can readily enter into the [2 + 2]photocycloaddition to form cyclobutane derivatives. This reaction is of great synthetic significance, because it opens up the way to the synthesis of a new class of complexones. It can easily be shown through the exhaustive selection that the above reaction of [2 + 2]photocycloaddition can produce 11 cycloadducts from crown-containing styryl dyes. However, under actual conditions, the formation of only one of these cycloadducts is usually observed. From both theoretical and practical standpoints, it is particularly important to predict and control the regioselectivity and stereoselectivity of the cycloaddition and to use properly the topochemical mechanism of this reaction in crystals.

The present work opens up a series of systematic studies concerned with the molecular and supramolecular structures of crown-containing styryl dyes and their complexes with different cations. In this paper, we discuss the crystal and molecular structures of acetonitrile solvate monohydrate of the potassium iodide complex with benzo-15-crown-5 ether dye based on methylquinoline iodide (**I**):

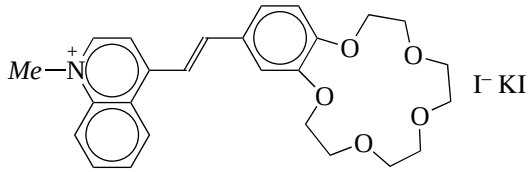

Details of the synthesis performed in this work and the properties of compound **I** will be described in a separate paper.

EXPERIMENTAL

The main crystal data, data collection, and refinement parameters for structure **I** are presented in Table 1. A set of experimental reflections was collected on a Bruker CCD SMART diffractometer [graphite monochromator; MoK_α radiation; exposure time per frame, 50 s; temperature, 100.0(2) K].

The structure was solved by direct methods and refined in the full-matrix anisotropic approximation (on F^2) for all the non-hydrogen atoms. The hydrogen atoms were located from the difference synthesis. Their positions were refined within a riding model. In this refinement, the isotropic thermal parameters were kept greater than the isotropic equivalent thermal parameters of the parent carbon and oxygen atoms by a factor of 1.2 (1.5 for the hydrogen atoms of the methyl groups).

The solution and the refinement of the structure were carried out with the SHELXS86 [24] and SHELXL97 [25] software packages.

The crystallographic data for the structures have been deposited with the Cambridge Crystallographic Data Center as supplementary publication no. CCDC 194520). Copy of the data can be obtained free of charge on application to CCDC, 12 Union Road, Cambridge CB21EZ, UK (fax: (+44) 1223-336-033; e-mail: deposit@ccdc.cam.ac.uk or http://www.ccdc.cam.ac.uk).

STRUCTURAL UNITS OF THE CRYSTAL

The structure of single crystal **I** is formed by positively charged molecules of benzocrown ether photodye (*D*), K^+ cations, I^{-1} anions, and water and acetonitrile solvate molecules in the ratio 1 : 0.5 : 1.5 : 1 : 1, respectively. Figure 1 shows all the structural units of the crystal and the atomic numbering. The coordinates and thermal parameters of the non-hydrogen atoms are listed in Table 2.

The K^+ cation occupies a special position on the twofold axis and is coordinated by all ten oxygen atoms of the crown ether fragments of two symmetry-related photodye molecules.

In the asymmetric part of the unit cell, the $I(2)^-$ anion also occupies a special position on the twofold axis, whereas the $I(1)^-$ anion is located in a general

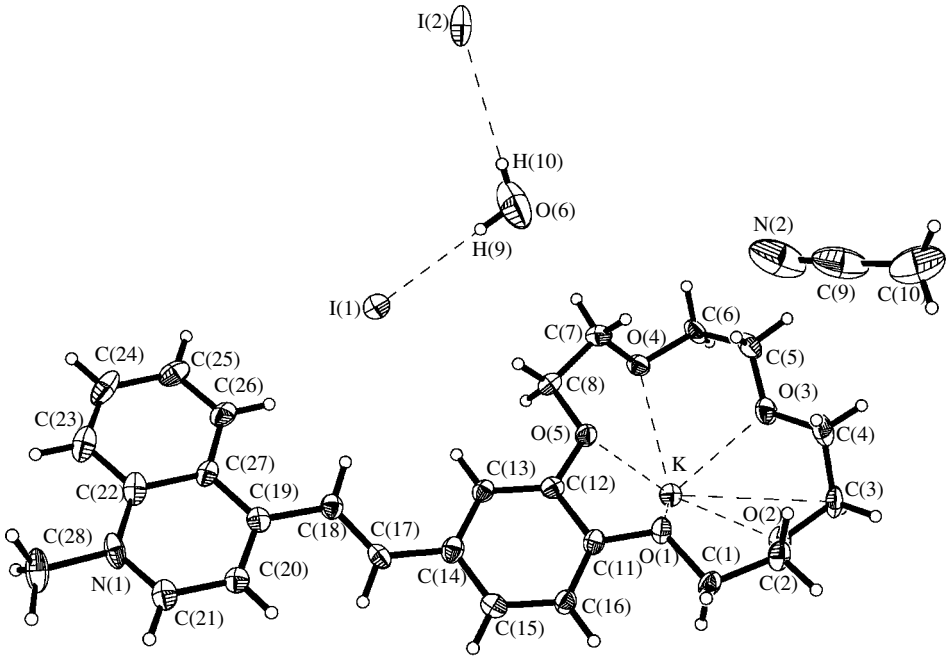

Fig. 1. Structural units of the crystal and the atomic numbering.

position. Both solvate (water and acetonitrile) molecules occupy general positions.

In the molecular cation *D*, it is possible to distinguish three planar fragments, namely, the *N*-methylquinoline (plane P^1) fragment, the C(14)C(17)C(18)C(19) ethylene (plane P^2) fragment, and the benzene (plane P^3) fragment. The dihedral angles P^1/P^2, P^2/P^3, and P^1/P^3 are equal to 18.5°, 14.2°, and 9.7°, respectively. Since the third angle is not an algebraic sum of the first two angles, the nonplanarity of the photodye molecule is caused not only by rotations about the formally single bonds but also by bending of the planar fragments. These features in the molecular geometry are apparently associated with the optimum compensation for different effects, such as steric stresses in the molecule with retention of an extended π-electron conjugation system, the favorable stacking arrangement of molecules, and the Coulomb repulsion of likely charged fragments in the crystal.

The bond lengths in the *N*-methylquinoline fragment actually coincide with those available in the Cambridge Structural Database [26]. In particular, the π-electron density is slightly delocalized at two peripheral bonds of the benzene ring [in our case, C(23)–C(24), 1.36(1) Å and C(25)–C(26), 1.373(9) Å] and one C–N bond [C(21)–N(1), 1.337(8) Å].

A comparison of the geometry of the styryl-15-crown-5 fragment in potassium complex **I** with the geometries of this fragment in iodide **II** (in which the crown ether fragment is uncoordinated) [27] and perchlorate **III** (in which the crown ether fragment coordinates the water molecule) [28],

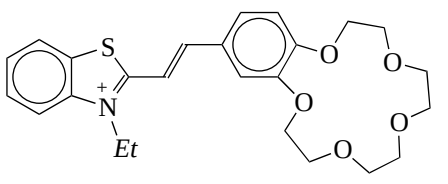

(**II**) I^-

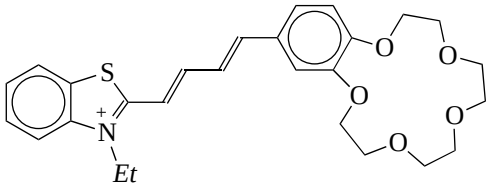

(**III**) $ClO_4^- \cdot H_2O$,

shows that, in these compounds, the electron density distributions over the fragment under consideration differ significantly.

In the molecular cation of compound **II**, which contains the uncoordinated benzocrown ether fragment, the *para* quinoid form makes a clearly defined, even though small, contribution to the structure of the benzene ring and the double bond in the ethylene fragment is well pronounced: the bond lengths in the C=C–C(*Ar*) fragment are equal to 1.333(7) and 1.463(8) Å, respectively. In a similar fragment of complex **III** with water, the bonds alternate in the lower part of the benzene ring

Table 1. Crystal data, data collection, and refinement parameters for the crystal structure studied

Empirical formula	$C_{28}H_{35}I_{1.50}K_{0.50}N_2O_6$
Molecular weight	705.48
Crystal system	Monoclinic
Space group	*C*2/*c*
a, Å	19.5150(3)
b, Å	22.3320(1)
c, Å	14.5117(1)
β, deg	111.948(1)
V, Å^3	5866.0(1)
Z	8
ρ_{calcd}, g/cm^3	1.598
F(000)	2832
$\mu(MoK_\alpha)$, mm^{-1}	1.732
Crystal size, mm	0.40 × 0.24 × 0.12
T, K	100.0(2)
Radiation wavelength, Å	MoK_α (0.71073)
Scan mode/θ range, deg	ω/1.45–27.54
Index ranges	$-25 \le h \le 25$
	$-28 \le k \le 27$
	$-18 \le l \le 18$
Number of reflections measured	21346
Number of unique reflections	6745 [R_{int} = 0.0644]
Number of reflections with $I > 2\sigma(I)$	5958
Absorption correction	Semiempirical (Siemens Analytical X-ray Instruments, 1995)
Transmission, min/max	0.493/0.613
Number of parameters refined	347
R factors for reflections with $I > 2\sigma(I)$	R_1 = 0.0652, wR_2 = 0.1259
R factors for all reflections	R_1 = 0.1072, wR_2 = 0.1807
Goodness-of-fit on F^2	1.170
Extinction coefficien	0.00012(4)
Residual electron density (min/max), e Å^{-3}	−1.441/1.441

C–C=C(O)–C(O) [1.414(4), 1.377(4), and 1.416(4) Å, respectively]. At the same time, the bond lengths in the upper part of the benzene ring are equal to each other; i.e., the *para* quinoid structure is retained by only half. In the C=C–C(*Ar*) fragment, the length of the double bond is equal to 1.349(4) Å and the length of the single bond is 1.457(4) Å. Therefore, the alternation of the bonds in complex **III** is less pronounced than in cation **II**.

In the styryl group of dye **I**, the bond lengths in the C(11)–C(12)–C(13)–C(14) fragment are equal to 1.415(8), 1.390(8), and 1.405(8) Å and the bond lengths in the C(11)–C(16)–C(15)–C(14) fragment are 1.378, 1.400, and 1.393 Å, respectively. Thus, the bonds alternate in the C(11)…C(16) benzene ring. The lengths of the C(17)=C(18) double bond [1.348(8) Å] and the C(17)–C(14) single bond [1.456(8) Å] in the C=C–C(*Ar*) fragment nearly coincide with those observed in complex **III**.

In the crown ether fragments of all the three compounds under consideration, the O(1) and O(5) oxygen atoms, which are directly attached to the benzene ring, differ from the other three oxygen atoms. The bond angles at the O(1) and O(5) atoms [118.0(5)° and 119.2(4)° in **I**, 118.3(4)° and 118.4(4)° in **II**, and 116.4(2)° and 117.5(2)° in **III**] are larger than those at the other oxygen atoms [113.6(5)°–114.9(6)° in **I**, 111.8(5)°–113.7(5)° in **II**, and 111.6(3)°–113.0(2)° in **III**]. Moreover, the C(*Ar*)–O–C(sp^3) fragments involving the O(1) and O(5) atoms are almost coplanar with the benzene ring plane (the dihedral angles in **I** are equal to –1.6° and –8.0°). These findings suggest that the hybridization of the O(1) and O(5) atoms is similar to the sp^2 state, whereas the hybridization of the other oxygen atoms is similar to the sp^3 state. Consequently, for the O(1) and O(5) atoms each, the lone electron pair at the *p* orbital can interact with the π*-orbital system of the benzene ring and, thus, affects its geometry. The difference between the geometries of the studied fragments in **I** and **II** is associated with the fact that the oxygen atoms in **I** interact with the K^+ cation, which is absent in **II**. The K^+ cation deviates from the mean plane of the oxygen atoms in the crown ether, whereas the bonds of the O(1) and O(5) atoms lie in this plane. As a result, for each of these atoms, the sp^2 orbital involving the second lone electron pair is directed toward the center of the macrocycle. Unlike the sp^2 orbital, the *p* orbital of the lone electron pair is perpendicular to the mean plane of the oxygen atoms; i.e., this orbital is oriented approximately toward the K^+ cation and interacts with it. The interaction of the *p* orbital with the K^+ cation leads to a considerable suppression of the contribution from this orbital to the conjugation with the benzene ring. This circumstance can be responsible for the disappearance of the contribution from the *para* quinoid form to the general distribution of bonds in the benzene ring, even though this contribution is observed in uncoordinated crown-containing styryl dye **II**. A similar (but less pronounced) situation occurs in complex **III** with water, in which the lone electron pairs of the oxygen atoms bound to the benzene ring are involved in the formation of hydrogen bonds with water molecules. The assumption regarding the competitive (partial) participation of the *p* orbitals of the lone electron pairs of the O(1) and O(5) atoms in two different interactions in **I** is confirmed by the fact that the $K^+\cdots O(1)$ and$K^+\cdots O(5)$ distances [2.941(4) and

Table 2. Coordinates ($\times 10^4$) and equivalent isotropic thermal parameters ($\times 10^3$) for non-hydrogen atoms in structure **I**

Atom	*x*	*y*	*z*	U_{eq}, Å^2	Atom	*x*	*y*	*z*	U_{eq}, Å^2
I(1)	7112(1)	393(1)	12736(1)	40(1)	C(10)	6934(6)	4752(6)	9303(9)	82(3)
I(2)	10000	1080(1)	12500	42(1)	C(11)	4306(3)	2191(3)	10516(4)	21(1)
K	5000	3228(1)	12500	23(1)	C(12)	4947(3)	1881(3)	11125(4)	20(1)
N(1)	4319(3)	–1984(2)	10602(4)	28(1)	C(13)	4933(3)	1263(3)	11227(4)	20(1)
N(2)	7150(5)	3676(6)	10149(6)	82(3)	C(14)	4273(3)	947(3)	10743(4)	23(1)
O(1)	4406(2)	2791(2)	10439(3)	23(1)	C(15)	3639(3)	1265(3)	10187(4)	25(1)
O(2)	4307(2)	3983(2)	10832(3)	26(1)	C(16)	3651(3)	1886(3)	10068(4)	22(1)
O(3)	5853(3)	4026(2)	11990(3)	30(1)	C(17)	4220(3)	296(3)	10725(4)	23(1)
O(4)	6524(2)	2946(2)	13040(3)	24(1)	C(18)	4769(3)	–111(3)	11008(4)	22(1)
O(5)	5552(2)	2238(2)	11564(3)	23(1)	C(19)	4631(3)	–755(3)	10864(4)	21(1)
O(6)	8101(4)	1587(3)	12243(5)	75(2)	C(20)	3961(3)	–968(3)	10189(4)	22(1)
C(1)	3780(3)	3142(3)	9819(5)	25(1)	C(21)	3821(4)	–1576(3)	10087(5)	27(1)
C(2)	4061(4)	3769(3)	9838(4)	25(1)	C(22)	5012(4)	–1809(3)	11264(4)	26(1)
C(3)	4735(4)	4516(3)	10992(5)	32(2)	C(23)	5040(4)	–2242(3)	11789(5)	31(2)
C(4)	5527(4)	4401(3)	11135(5)	36(2)	C(24)	6209(4)	–2058(3)	12435(5)	37(2)
C(5)	6588(4)	3859(3)	12126(5)	33(2)	C(25)	6386(4)	–1444(3)	12613(5)	30(1)
C(6)	6902(3)	3503(3)	13073(5)	28(1)	C(26)	5876(3)	–1020(3)	12102(5)	26(1)
C(7)	6775(3)	2475(3)	12576(5)	26(1)	C(27)	5177(3)	–1183(2)	11406(4)	20(1)
C(8)	6206(3)	1984(3)	12283(4)	24(1)	C(28)	4124(5)	–2629(3)	10446(5)	38(2)
C(9)	7038(5)	4165(7)	9774(7)	70(3)					

2.997(4) Å] are noticeably greater than the other three $K^+\cdots O$ distances [2.844(4), 2.723(4), and 2.847(4) Å].

Undeniably, the above inference is based on the assumption that the effect of the *Ar* substituent in the *Ar*–C=C and benzocrown fragments of compounds **I**–**III** (quinoline in **I** and benzothiazole or ethylbenzothiazole in **II** and **III**) on the distribution of bonds in the benzene ring of the benzocrown is weak compared to the effect of the coordination of the crown ether with the metal atom or the small-sized molecule. This assumption is consistent with all the available data on the chemical (complexation constants), spectral, and photochemical properties of both the dyes considered above and the related crown ether styryl and butadiene dyes [12, 22, 23, 28].

STRUCTURE OF THE $[D_2K]^{3+}$ COMPLEX

The K^+ cation is coordinated by two crown ether groups. The coordination polyhedron of the K^+ cation in the $[D_2K]^{3+}$ complex can be described as intermediate between a pentagonal prism and an antiprism. The aforementioned $K^+\cdots O$ distances in the polyhedron are somewhat shorter than those observed earlier in the 15-crown-5 complex with the K^+ cation (2.749–3.064 Å) [29].

In the complex, two *D* cations are related by the twofold axis, which passes through the metal cation in the plane parallel to the mean planes of the organic fragments arranged in a head-to-head manner. The side and front projections of the complex are depicted in Fig. 2. It can be seen that the quinoline fragments are projected onto each other. Their planes are aligned strictly parallel to each other at an interplanar distance of 3.40 Å. This value falls in the distance range 3.3–3.8 Å, which is characteristic of stacking interactions between two parallel π systems of nitrogen-containing heterocycles [30]. The shifted (or offset) mutual arrangement of aromatic heterocycles is rather typical and, according to the analysis performed by Janiak [30] for a large number of structures, is observed in the vast majority of cases.

Therefore, despite the positive charge localized at the aromatic heterocyclic system of quinoline, these systems in the complex are involved in the stacking interaction. It should be noted that, for the mutual projection observed for the aromatic systems in the studied structure, the positive charges localized in the vicinity of the quinoline nitrogen atoms appear to be widely spaced, which leads to a weakening of the Coulomb repulsion between the heterocycles. In the case when two parallel aromatic molecules are bound through the stacking interaction, the interatomic contacts, as a rule, correspond to the sums of the van der Waals radii. Table 3 presents the shortest interatomic contacts in the pair of parallel aromatic fragments under consideration. These contacts are close to the sums of the van

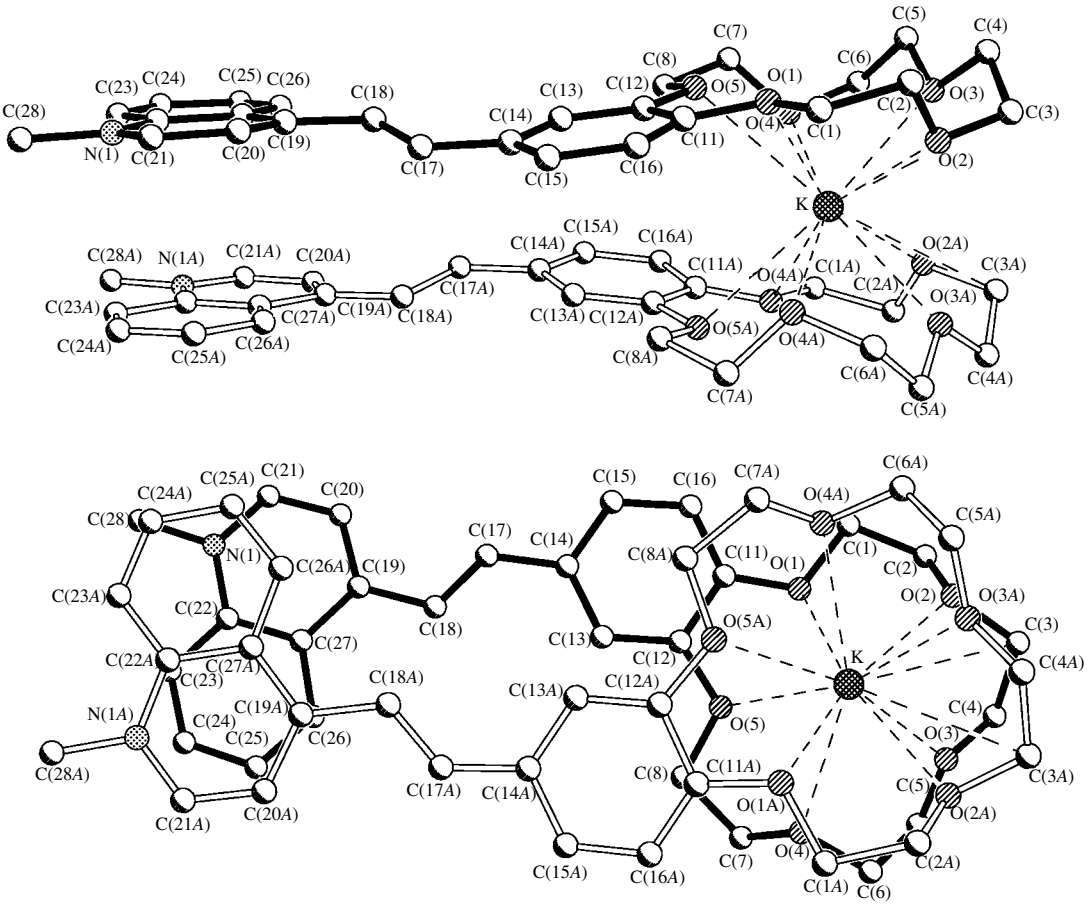

Fig. 2. Side and front projections of the K^+ complex.

der Waals radii of the relevant atoms; i.e., they are equal to those observed for the stacking interaction of neutral aromatic systems.

The ethylene bonds in the upper and lower parts of the complex are far apart (Fig. 2, front projection), which is unfavorable to the photochemical [2 + 2]cycloaddition reaction within the complex. It is highly improbable that the coordination of the K^+ ion in a solution can change so that the ethylene fragments of the two dye molecules in the complex will approach each other under conditions of favorable stacking interaction between likely charged aromatic systems. Note that, in the case when the ethylene fragments approach each other, the likely charged nitrogen atoms of the quinoline systems would also come close together, which must necessarily enhance the Coulomb repulsion between the nitrogen-containing heterocyclic systems. However, even though the two crown ether fragments were slightly rotated in the solution and then the ethylene fragments came close together, the latter fragments would have a crossed mutual orientation (the complex has C_2 symmetry). As was shown by Schmidt [31], in all cases, the photochemical [2 + 2]cycloaddition reaction in the solid phase was observed when the ethylene fragments had a parallel (or nearly parallel) mutual orientation and the distance between the centers of the ethylene bonds was equal to 3.5–4.2 Å. Only the parallel arrangement of the double bonds in the dimer was taken into consideration in the theoretical calculations performed by Baskin *et al.* [32] and Freĭdzon *et al.* [33] for the regioselectivity and stereoselectivity of the [2 + 2]photocycloaddition in complexes of crown-containing styryl dyes with M^{2+} metal cations. The results of these calculations are in good agreement with the experimental data. Theocharis *et al.* [34] analyzed the situation where the ethylene fragments of organic compounds in parallel planes in the crystal were characterized by a slightly nonparallel mutual orientation and the distance between the centers of the ethylene bonds was approximately equal to 3.7 Å, but the crystal was photochemically active with respect to the cycloaddition reaction. However, this situation can also be reduced to the general case of parallel double bonds.

It should be noted that, if the cycloaddition reaction in olefins proceeded at a crossed mutual orientation of the reacting ethylene bonds, no regioselectivity and stereoselectivity would be observed, because the addition of atoms to one another {1…3 and 2…4} or {1…4 and 2…3} must occur with an equal probability, which, in

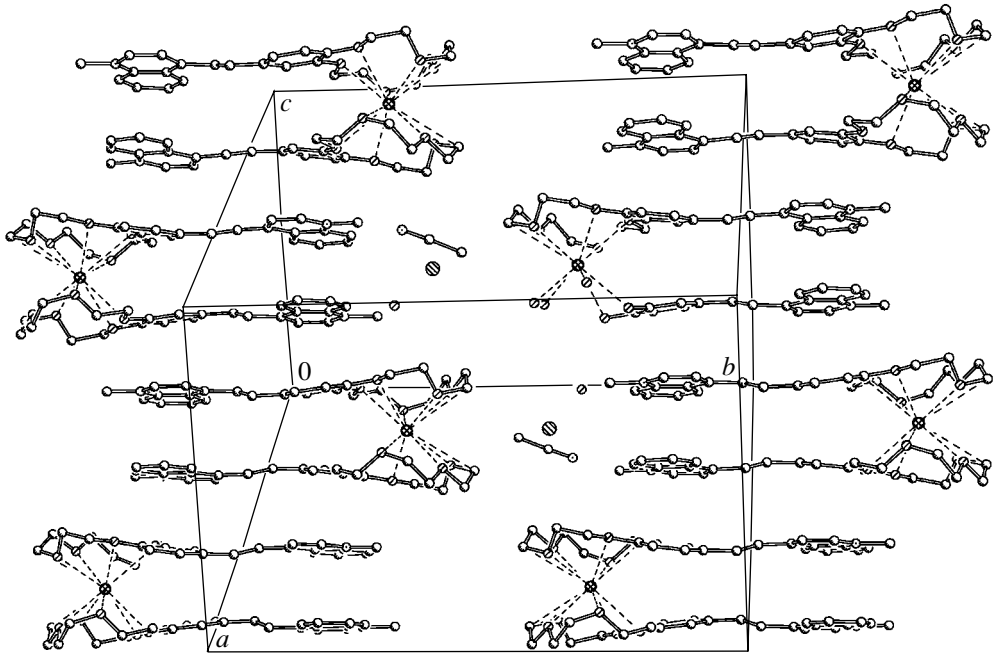

Fig. 3. A fragment of the crystal packing.

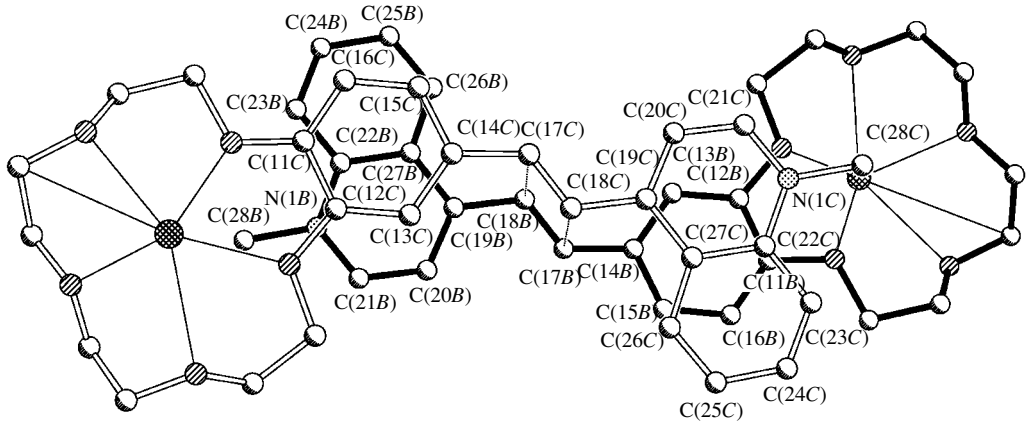

Fig. 4. Mutual arrangement of the two adjacent crown ether dyes in a stack.

turn, must necessarily result in the formation of an isomer mixture:

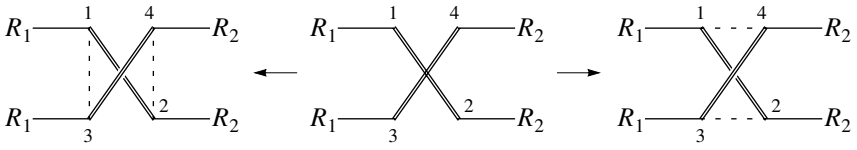

In the case of crown-containing styryl dyes, this situation is inconsistent with the experimental data, according to which only one out of the eleven cyclobutane isomers was formed in all the experimentally observed reactions in solutions [12, 35].

PACKING OF FORMULA UNITS IN THE CRYSTAL

In the crystal, the $[D_2K]^{3+}$ cationic complexes form stacks along the *b* axis. A fragment of the crystal packing free of solvate molecules and counterions is dis-

Table 3. Shortest interatomic contacts *d* (Å) between the quinoline fragments in the [D_2K] complex

Atoms	*d*	Atoms	*d*
C(19)···C(26A)	3.497	C(22)···C(24A)	3.594
C(20)···C(26A)	3.826	C(22)···C(23A)	3.515
C(20)···C(25A)	3.657	C(22)···C(22A)	3.605
C(21)···C(25A)	3.520	C(23)···C(23A)	3.459
N(1)···C(24A)	3.376	C(26)···C(27A)	3.517
N(1)···C(25A)	3.565	C(27)···C(27A)	3.491

Table 4. Shortest intermolecular contacts *d*(Å) in the stack

Atoms	*d*	Atoms	*d*
C(11*B*)···N(1*C*)	3.649	C(14*B*)···C(27*C*)	3.696
C(11*B*)···C(22*C*)	3.426	C(15*B*)···C(26*C*)	3.818
C(11*B*)···C(23*C*)	3.469	C(15*B*)···C(27*C*)	3.838
C(12*B*)···N(1*C*)	3.328	C(16*B*)···C(22*C*)	3.788
C(13*B*)···C(19*C*)	3.625	C(16*B*)···C(23*C*)	3.682
C(13*B*)···C(20*C*)	3.554	C(16*B*)···C(24*C*)	3.761
C(13*B*)···C(21*C*)	3.674	C(17*B*)···C(18*C*)	3.754
C(14*B*)···C(19*C*)	3.730		

played in Fig. 3. The adjacent complexes in a stack are related through the center of symmetry and, therefore, are arranged in a head-to-tail manner. Figure 4 shows the mutual arrangement of two adjacent molecular cations *D* belonging to different complexes in a stack. As can be seen, the quinoline fragments are located above the benzene rings, whereas the double bonds lie one above the other. The dihedral angle between the planes of the quinoline fragment and the benzene ring superposed one on the other in the stack is equal to 11.1°. The superposed ethylene fragments are strictly parallel to each other, and the distance between the centers of the ethylene bonds is 3.754 Å. This geometry is favorable to the [2 + 2]cycloaddition, which can result in the formation of the *syn* head-to-tail isomer when the heterocyclic residuals are located at opposite carbon atoms but on each side of the ring:

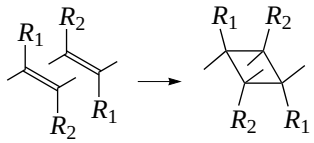

The results obtained give grounds to believe that the photochemical reaction under consideration can proceed in the crystal; however, this can be merely an intermolecular reaction between adjacent complexes. The shortest interatomic contacts in the stack are given in Table 4. These contacts correspond to the sums of the van der Waals radii, which is characteristic of the structures of photochemically active olefins [31, 34, 36–40].

Note that the cycloaddition reaction in solutions has never been observed in free crown-containing styryl dyes incapable of forming complexes with metal cations. It seems likely that, in solutions, only the coordination with a metal cation holds the dye molecules fairly close to each other and in the required orientation with respect to each other. A different situation arises in crystals. The crystal lattice itself is responsible for the close and proper location of two alkenes capable of entering into the cycloaddition reaction. The solid-phase topochemical cycloaddition reactions are well understood and described in [31, 34, 36–40].

In crystal **I**, the alkene has a more complex structure than that described in the case of topochemical cycloaddition. The alkene contains bulky fragments of crown ether and quinoline, and the crystal involves additional structural units, such as counterions and solvate molecules. In this respect, it is necessary to elucidate whether these structural units or neighbors in the crystal lattice can serve as obstacles to drawing the ethylene bonds together in stacks of the complexes either throughout the crystal bulk or, like crystal defects, in local regions.

An important feature of the crystal packing studied is that the crown ether molecular fragments are located close to each other and form extended regions. This is a common structural feature of all crown-containing styryl dyes [28, 41–43]. Another common feature is that the crown ether regions of the crystal have a very loose packing. A large number of intermolecular contacts with the participation of the crown ether atoms exceed the sums of the van der Waals radii. The looseness of this packing can also be judged either from the frequently observed disordering of the crown ether fragments or from the presence of two crystallographically independent molecules with different conformations of the crown ether fragment in the crystal structure. This stems from the high conformational flexibility of crown ethers. It can be assumed that the high conformational flexibility of the crown ether requires an additional free volume ΔV. As a consequence, the crystallization is accompanied by the formation of regions with a loose packing around the crown ether groups. In the systems containing crown ethers, the close packing inherent in crystals is attained in the case where the crown ether fragments are located close to each other in such a way that the additional volume ΔV of one molecule appears to be common to two and more molecules. The proposed model offers a satisfactory explanation of the formation of extended regions (channels) with a loose packing in the structure of crown ether compounds.

The adjacent stacks in crystal **I** are shifted with respect to each other along the *b* axis in such a way that zigzag loosely packed channels formed by the crown ether fragments arise in the crystal bulk. Inside these channels, all the intermolecular interatomic contacts

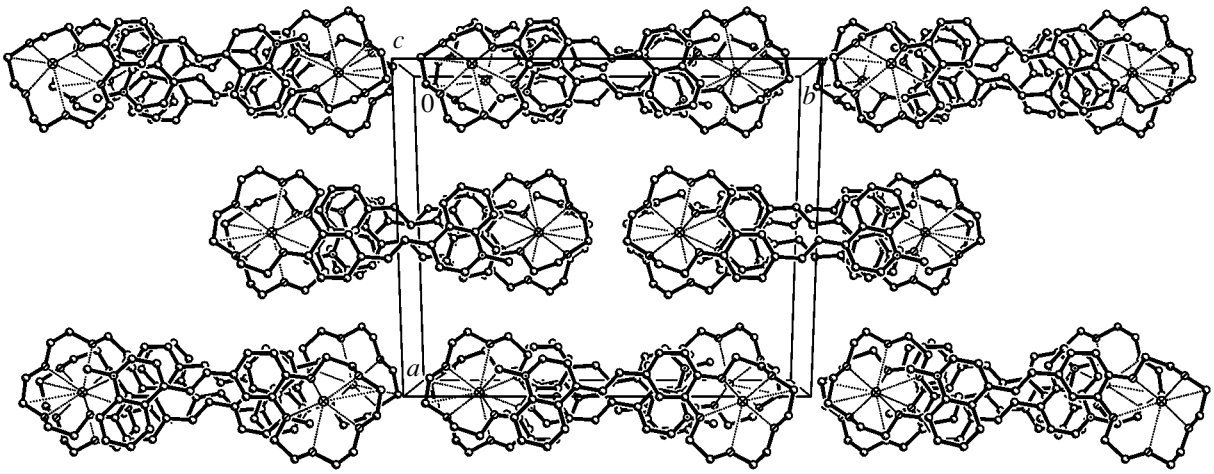

Fig. 5. Projection of the crystal structure along the *z* axis.

with the participation of oxygen atoms exceed the sums of the van der Waals radii of the corresponding atoms.

The stacks in the crystal are arranged so that regions of the ethylene fragments are surrounded by loosely packed crown ether regions (Fig. 5). Therefore, the crystal structure provides conditions under which the carbon atoms of the ethylene groups can be displaced toward each other in the course of the cycloaddition reaction without any obstacles produced by atoms of the surrounding crown ether groups. Moreover, since the cycloaddition reaction is attended not by an increase but by a decrease in the volume per interacting structural unit, the appearance of steric hindrances to the occurrence of this reaction is highly improbable. The cycloaddition reaction can also proceed in local regions of the crystal with the initial crystalline matrix rather than over the crystal bulk.

Certainly, in the case of crown ether complexes with metal cations, the flexibility of crown ether groups is substantially lower and the looseness of crown ether regions in the crystal is less pronounced than those in the case of uncoordinated crown-containing styryl dyes. Furthermore, the reaction in the crystal should result in a change in the coordination environment of the metal cation, because the styryl fragment changes its orientation, which, in turn, leads to the displacement of at least the nearest neighbor oxygen atoms. However, it is necessary to take into account that the interactions of the cation with the oxygen atoms are ionic (undirected) in character and that the system contains other atoms or groups capable of providing coordination saturation of the K^+ cation. On this basis, we believe that crown-containing styryl dyes and their complexes, generally, and the crystal studied, in particular, are candidates for use in analyzing the possibility of carrying out the solid-phase topochemical [2 + 2]photocycloaddition reaction in these systems.

In the crystal, the iodine counterions and the solvate molecules of water and acetonitrile are located in regions of loose channels and interstack holes. The acetonitrile molecules merely occupy holes and do not participate in specific interactions. The iodine anions are involved in the formation of hydrogen bonds with water molecules and form associates in which the central iodine anion is located along the twofold axis:

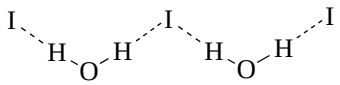

The distances from the central iodine anion to the hydrogen and oxygen atoms of the water molecule are equal to 2.90 and 3.758 Å, respectively. The distances from the terminal iodine anion to the hydrogen and oxygen atoms of the water molecule are 2.67 and 3.519 Å, respectively. These distances and angles at the hydrogen atoms (179.6° and 179.3°) correspond to a standard linear hydrogen bond.

ACKNOWLEDGMENTS

This work was supported by the Russian Foundation for Basic Research (project no. 01-03-32474), the Royal Society, and the Royal Society of Chemistry.

REFERENCES

1. E. D. Glendening, D. Feller, and M. A. Thompson, J. Am. Chem. Soc. **116**, 10657 (1994).
2. E. D. Glendening and D. Feller, J. Am. Chem. Soc. **118**, 6052 (1996).
3. D. Feller, A. Eldorado, J. A. Nichols, and D. E. Bernholdt, J. Chem. Phys. **105**, 1940 (1996).
4. S. E. Hill, D. Feller, and E. D. Glendening, J. Phys. Chem. A **102**, 3813 (1998).
5. H. Wasada, Y. Tsutsiu, and S. Yamabe, J. Phys. Chem. **100**, 7367 (1996).

6. A. A. Bagatur'yants, A. Ya. Freidzon, M. N. Alfimov, *et al.*, J. Mol. Struct.: THEOCHEM **588**, 55 (2002).
7. C. R. Paige and M. F. Richardson, Can. J. Chem. **62**, 332 (1984).
8. R. D. Rogers, A. H. Bond, and J. L. Wolf, J. Coord. Chem. **29**, 187 (1993).
9. M. El. Essawi, S. Abd El Khalik, and K.-F. Tebbe, Acta Crystallogr., Sect. C: Cryst. Struct. Commun. **52**, 818 (1996).
10. R. Humphy-Baker, M. Gratzel, P. Tundo, and E. Pelizzetti, Angew. Chem. **18**, 630 (1979).
11. V. Balzani, A. Credi, and M. Venturi, Coord. Chem. Rev. **171**, 3 (1998).
12. S. P. Gromov and M. V. Alfimov, Izv. Ross. Akad. Nauk, Ser. Khim. **46**, 611 (1997).
13. M. Takeshita, C. F. Soong, and M. Irei, Tetrahedron Lett. **39**, 7717 (1998).
14. S. H. Kawai, Tetrahedron Lett. **39**, 4445 (1998).
15. I. K. Lednev, R. E. Hester, and J. N. Moore, J. Phys. Chem. A **101**, 7371 (1997).
16. I. K. Lednev, T.-Q. Ye, R. E. Hester, and J. N. Moore, J. Phys. Chem. A **101**, 4966 (1997).
17. I. K. Lednev, R. E. Hester, and J. N. Moore, J. Am. Chem. Soc. **119**, 3456 (1997).
18. R. Bergonzi, L. Fabrizzi, M. Licchelli, and M. Mangano, Coord. Chem. Rev. **170**, 31 (1998).
19. L. F. Lindoy, Coord. Chem. Rev. **174**, 327 (1998).
20. *Photochromism: Molecules and Systems*, Ed. by H. Dürr and H. Bouds-Laurent (Elsevier, Amsterdam, 1990).
21. S. Shinkai, in *Comprehensive Supramolecular Chemistry*, Ed. by J. Lehn (Pergamon, New York, 1996), Vol. 1, p. 14.
22. S. P. Gromov, O. A. Fedorova, E. N. Ushakov, *et al.*, Dokl. Akad. Nauk SSSR **317**, 1134 (1991).
23. S. P. Gromov, O. A. Fedorova, E. N. Ushakov, *et al.*, Dokl. Akad. Nauk SSSR **321**, 104 (1991).
24. G. M. Sheldrick, Acta Crystallogr., Sect. A: Found. Crystallogr. **46**, 467 (1990).
25. G. M. Sheldrick, *SHELXL97: Program for the Refinement of Crystal Structures* (Univ. of Göttingen, Germany, 1997).
26. F. H. Allen and O. Kennard, Chem. Design Automat. News **8**, 1 (1993).
27. V. V. Tkachev, L. O. Atovmyan, S. P. Gromov, *et al.*, Zh. Strukt. Khim. **33** (4), 126 (1992).
28. S. P. Gromov, A. I. Vedernikov, E. N. Ushakov, *et al.*, Helv. Chim. Acta **85**, 60 (2002).
29. J. D. Owen, J. Chem. Soc., Perkin Trans. 2, 407 (1983).
30. C. Janiak, J. Chem. Soc. Dalton Trans., 3885 (2000).
31. G. M. Schmidt, J. Pure Appl. Chem. **27**, 647 (1971).
32. I. I. Baskin, A. A. Bagatur'yants, S. P. Gromov, and M. V. Alfimov, Dokl. Akad. Nauk **335**, 313 (1994).
33. A. Ya. Freĭdzon, I. I. Baskin, A. A. Bagatur'yants, *et al.*, Izv. Ross. Akad. Nauk, Ser. Khim., No. 11, 2185 (1998).
34. C. R. Theocharis, W. Jones, J. M. Thomas, *et al.*, J. Chem. Soc., Perkin Trans. 2, 71 (1984).
35. M. V. Alfimov, S. P. Gromov, O. B. Stanislavskiĭ, *et al.*, Izv. Ross. Akad. Nauk, No. 8, 1449 (1993).
36. W. Jones, H. Nakanichi, C. R. Theocharis, and J. M. Thomas, J. Chem. Soc. Chem. Commun., 610 (1980).
37. H. Nakanish, W. Jones, J. M. Thomas, *et al.*, J. Chem. Soc. Chem. Commun., 611 (1980).
38. G. W. Coates, A. R. Dunn, L. M. Henling, *et al.*, J. Am. Chem. Soc. **120**, 3641 (1998).
39. K. Tanaka, E. Mochizuki, N. Yasui, *et al.*, Tetrahedron **56**, 6853 (2000).
40. L. R. MacGillivray, Cryst. Eng. Commun. **7**, 1 (2002).
41. M. V. Alfimov, A. V. Churakov, Y. V. Fedorov, *et al.*, J. Chem. Soc., Perkin Trans. 2, 2249 (1997).
42. G. G. Aleksandrov, L. G. Kuz'mina, and A. V. Churakov, in *International Union of Crystallography: XVIII Congress and General Assembly, Abstract Book* (Glasgow, Scotland, 1999), P08.06.004.
43. O. A. Fedorova, Yu. V. Fedorov, A. I. Vedernikov, *et al.*, New J. Chem. **26**, 543 (2002).

Translated by O. Borovik-Romanova

Crystallography Reports, Vol. 48, No. 4, 2003, pp. 623–629. Translated from Kristallografiya, Vol. 48, No. 4, 2003, pp. 674–679.

STRUCTURE OF ORGANIC COMPOUNDS

Molecular and Crystal Structures of Mesomorphic Aromatic Esters: I. Structure of Two Isomers, *p*-Butoxyphenyl *p*'-Hexyloxybenzoate and *p*-Hexyloxyphenyl *p*'-Butoxybenzoate

O. V. Noskova*, A. V. Churakov, L. G. Kuz'mina**, J. A. K. Howard***, V. A. Molochko*, and S. M. Pestov***

** Moscow Academy of Fine Chemical Technology, pr. Vernadskogo 86, Moscow, 117924 Russia*
e-mail: ovnoskova@yandex.ru
*** Kurnakov Institute of General and Inorganic Chemistry, Russian Academy of Sciences, Leninskiĭ pr. 31, Moscow, 119991 Russia*
**** Department of Chemistry, Durham University, Durham DH1 3LE, England*
Received October 16, 2002

Abstract—Two isomers, *p*-butoxyphenyl *p*'-hexyloxybenzoate (**1**) and *p*-hexyloxyphenyl *p*'-butoxybenzoate (**2**), are studied by X-ray diffraction. Crystals **1** contain two crystallographically independent molecules, which differ in the conformation of one of their side chains. In both compounds, bond lengths and angles have standard values. The geometry of the central fragment *Ph–Est–Ph* is essentially the same in both isomers. One of the benzene rings is coplanar with the *Est* group, and the other ring, which is linked with this group through the oxygen atom, is almost perpendicular to the *Est* plane. In crystal **1**, molecules are packed in such a fashion that, in any pair of neighboring molecules, the most closely spaced benzene rings are nearly perpendicular to each other, which corresponds to a weak C–H$\cdots\pi$ interaction. In the crystal packing of **2**, neither perpendicular nor stacking motifs are observed. The supramolecular architecture of this compound is determined by directional specific interactions of the hydrogen bond type between the C–H benzene fragment and the ester oxygen atom of the neighboring molecule. © *2003 MAIK "Nauka/Interperiodica".*

INTRODUCTION

The majority of organic compounds consisting of complicated molecules crystallize in the lowest crystal systems. As a rule, such molecules are able to adopt a number of stable conformations. As a consequence, each compound has more than one polymorphic modification. In particular, most mesomorphic organic compounds (liquid crystals) exhibit polymorphism.

In early structural studies of liquid crystals, primary emphasis was placed on the structure of mesophases [1]. For a long time, the only important research into solid phases was Bryan's studies [2–4], which are concerned with the systematization of structural data for mesomorphic acids, and publications on azoxybenzenes [5] and cholesteryl esters [6, 7]. Structural studies of liquid-crystalline solid phases have been intensively performed only over the last 10–15 years. Among the 70000 mesogenic compounds known to date [8], only 310 compounds and their solid phases have been characterized crystallographically [9]. This stems from the difficulties associated with the preparation of individual solid phases of mesomorphic compounds, not to mention the growth of single crystals. It was shown in [10] that, because of the close values of the Gibbs energy of polymorphic modifications, crystallization of liquid-crystalline substances is often accompanied by the violation of the Ostwald rule of consecutive reactions and results in the formation of very stable mixtures of several solid modifications [11–15]. Crystalline aromatic esters are the least known mesogenes: the crystallographic data are available only for *p*-methoxyphenyl *p*'-hexyloxybenzoate [16].

Our study is aimed at determining the molecular and crystal structures of two isomeric aromatic esters, namely, *p*-butoxyphenyl *p*'-hexyloxybenzoate (**1**) and *p*-hexyloxyphenyl *p*'-butoxybenzoate (**2**).

EXPERIMENTAL

The initial substances were of the analytical grade. Checking for purity by the cryometric method [17] revealed that the total impurity content was 3.0 ± 0.3 mol %. Recrystallization from a hexane solution lowered the impurity content to 1.5 mol %. Studies of the systems containing **1** or **2** and nonmesogens [18] allowed us to choose the temperature and concentration for the growth of individual polymorphic modifications.

X-ray Diffraction Study

We managed to grow single crystals of both isomers and to perform complete X-ray diffraction analysis. The main crystal data and parameters of the X-ray dif-

1063-7745/03/4804-0623$24.00 © 2003 MAIK "Nauka/Interperiodica"

Table 1. Crystal data, data collection, and refinement parameters for the crystal structures of isomers **1** and **2**

$C_{23}H_{30}O_4$ isomers	**1**	**2**
Molecular weight (kg/kmol)	370.47	370.47
Crystal system	Triclinic	Monoclinic
Space group	$P\bar{1}$	$P2_1/n$
a, Å	9.384(3)	19.6307(8)
b, Å	9.864(3)	5.3304(2)
c, Å	22.249(6)	20.2575(9)
α, deg	83.712(7)	90.0
β, deg	89.777(7)	104.734(2)
γ, deg	89.645(6)	90.0
V, Å^3	2047(1)	2050.0(2)
Z	4	4
ρ_{calcd}, g/cm^3	1.202	1.200
F_{000}	800	800
$\mu(MoK_\alpha)$, mm^{-1}	0.081	0.081
Crystal size, mm	$0.20 \times 0.10 \times 0.10$	$0.45 \times 0.20 \times 0.05$
T, K	120.0(2)	120.0(2)
Radiation, Å	MoK_α(0.71073)	MoK_α(0.71073)
Scan mode/θ range, deg	ω/0.92–27.00	ω/1.29–27.50
Index ranges	$13 \le h \le 13, -8 \le k \le 13, -30 \le l \le 31$	$-25 \le h \le 25, -6 \le k \le 6, -21 \le l \le 26$
Number of reflections measured	13059	12935
Number of unique reflections	8883 [$R_{int} = 0.0614$]	4667 [$R_{int} = 0.0762$]
Number of reflections with $I > 2\sigma(I)$	7563	4667
Number of parameter refined	573	365
R factors for reflections with $I > 2\sigma(I)$	$R_1 = 0.0613$, $wR_2 = 0.1340$	$R_1 = 0.0537$, $wR_2 = 0.1289$
for all reflections	$R_1 = 0.1717$, $wR_2 = 0.1826$	$R_1 = 0.0981$, $wR_2 = 0.1505$
Goodness-of-fit on F^2	0.779	0.959
Extinction coefficient	0.0006(4)	0.0016(9)
Residual electron density, min/max, e/Å^3	0.282/–0.238	0.236/–0.310

fraction experiments are presented in Table 1. Colorless single crystals of both compounds were coated with a perfluorinated oil and placed in a Bruker SMART CCD diffractometer with an area detector (MoK_α radiation) at a temperature of 120.0(2) K. Experimental reflections were measured in the ω scan mode (exposure time per frame, 15 s).

The structures were solved by direct methods and refined by the least-squares procedure on F^2. In structure **1**, two crystallographically independent molecules were found. In one of them, the *n*-butoxy fragment is disordered over two positions with approximately equal occupancies (0.47 and 0.53). Difference Fourier syntheses revealed all the hydrogen atoms in structures **1** and **2**, except for hydrogen atoms of the disordered fragments in **1**. The final least-squares refinement of the structures was performed in the full-matrix anisotropic approximation for all the non-hydrogen atoms and in the isotropic approximation for hydrogen atoms other than those of the aliphatic substituents in structure **1**, which were refined within a riding model.

The coordinates of the non-hydrogen atoms are listed in Tables 2 and 3. All the calculations were carried out with the SHELXS86 [19] and SHELXL97 [20] software packages.

Table 2. Coordinates ($\times 10^4$) and isotropic equivalent thermal parameters U_{eq} (Å^2, $\times 10^3$) of the non-hydrogen atoms in structure **1**

Atom	*x*	*y*	*z*	U_{eq}	Atom	*x*	*y*	*z*	U_{eq}
O(11)	−3751(3)	610(2)	899(1)	81(1)	C(123)	13568(4)	−3564(4)	4673(2)	68(1)
O(12)	1131(2)	−1286(2)	2101(1)	53(1)	O(21)	−13829(2)	4934(2)	1066(1)	53(1)
O(13)	1614(2)	827(2)	2333(1)	52(1)	O(22)	−8411(2)	4264(2)	2021(1)	45(1)
O(14)	6917(2)	−2445(2)	3515(1)	49(1)	O(23)	−9256(2)	4320(2)	2969(1)	49(1)
C(101)	−7925(4)	2620(4)	196(2)	100(2)	O(24)	−2964(2)	2338(2)	3557(1)	43(1)
C(102)	−6658(11)	1437(8)	404(4)	66(2)	C(201)	−18393(4)	6848(4)	397(2)	68(1)
C(103)	−6151(10)	1861(9)	977(4)	63(2)	C(202)	−17037(4)	7121(4)	737(2)	64(1)
C(132)	−7152(9)	2097(8)	789(5)	62(3)	C(203)	−16035(4)	5945(3)	765(2)	59(1)
C(133)	−5770(11)	1626(11)	582(6)	73(3)	C(204)	−14638(3)	6159(3)	1082(2)	52(1)
C(104)	−5051(5)	814(4)	1226(2)	100(2)	C(205)	−12500(3)	4864(3)	1319(1)	41(1)
C(105)	−2605(4)	92(3)	1228(2)	55(1)	C(206)	−11828(4)	3603(3)	1329(2)	48(1)
C(106)	−1340(5)	85(4)	911(2)	65(1)	C(207)	−10494(4)	3398(3)	1573(2)	46(1)
C(107)	−80(5)	−369(4)	1198(2)	62(1)	C(208)	−9819(3)	4470(3)	1799(1)	40(1)
C(108)	−136(4)	−782(3)	1810(2)	43(1)	C(209)	−10462(4)	5714(3)	1794(2)	47(1)
C(109)	−1375(4)	−809(3)	2135(2)	42(1)	C(210)	−11817(4)	5930(3)	1553(2)	47(1)
C(110)	−2634(4)	−357(3)	1833(2)	47(1)	C(211)	−8271(4)	4149(3)	2635(2)	41(1)
C(111)	1955(3)	−354(3)	2352(2)	42(1)	C(212)	−6819(3)	3780(3)	2841(2)	35(1)
C(112)	3241(3)	−974(3)	2645(1)	39(1)	C(213)	−5680(4)	3613(3)	2447(2)	41(1)
C(113)	3703(4)	−2293(3)	2576(2)	43(1)	C(214)	−4363(4)	3169(3)	2676(2)	41(1)
C(114)	4939(3)	−2819(3)	2854(2)	44(1)	C(215)	−4179(3)	2869(3)	3295(2)	37(1)
C(115)	5714(3)	−2026(3)	3210(2)	39(1)	C(216)	−5285(3)	3092(3)	3691(2)	40(1)
C(116)	5264(3)	−699(3)	3284(2)	45(1)	C(217)	−6586(3)	3546(3)	3461(2)	39(1)
C(117)	4057(3)	−183(3)	2994(2)	42(1)	C(218)	−1822(3)	1979(3)	3170(2)	48(1)
C(118)	7367(3)	−3855(3)	3506(2)	53(1)	C(219)	−782(3)	1081(3)	3545(2)	51(1)
C(119)	8510(3)	−4155(3)	3969(2)	48(1)	C(220)	−102(3)	1709(3)	4069(2)	43(1)
C(120)	9879(3)	−3351(3)	3857(2)	46(1)	C(221)	1157(3)	890(3)	4334(2)	45(1)
C(121)	11008(3)	−3779(3)	4324(2)	46(1)	C(222)	1902(3)	1474(3)	4848(2)	48(1)
C(122)	12445(3)	−3098(3)	4200(2)	57(1)	C(223)	3214(3)	675(3)	5069(2)	59(1)

Table 3. Coordinates ($\times 10^4$) and isotropic equivalent thermal parameters U_{eq} (Å^2, $\times 10^3$) of the non-hydrogen atoms in structure **2**

Atom	*x*	*y*	*z*	U_{eq}	Atom	*x*	*y*	*z*	U_{eq}
O(1)	5479(1)	−1933(3)	3465(1)	31(1)	C(11)	8861(1)	2294(4)	8287(1)	22(1)
O(2)	6120(1)	1329(3)	3231(1)	22(1)	C(12)	8852(1)	3568(4)	8957(1)	28(1)
O(3)	7890(1)	1044(3)	5848(1)	22(1)	C(13)	9395(1)	2453(5)	9565(1)	34(1)
O(4)	4012(1)	−144(3)	319(1)	21(1)	C(14)	5191(1)	−191(4)	2341(1)	18(1)
C(1)	5593(1)	−417(4)	3068(1)	20(1)	C(15)	4676(1)	−2016(4)	2083(1)	19(1)
C(2)	6555(1)	1242(4)	3910(1)	21(1)	C(16)	4293(1)	−1950(4)	1407(1)	20(1)
C(3)	6488(1)	3135(4)	4353(1)	21(1)	C(17)	4417(1)	−38(4)	978(1)	18(1)
C(4)	6935(1)	3141(4)	5015(1)	20(1)	C(18)	4920(1)	1802(4)	1226(1)	19(1)
C(5)	7428(1)	1229(4)	5211(1)	19(1)	C(19)	5308(1)	1700(4)	1910(1)	18(1)
C(6)	7489(1)	−665(4)	4755(1)	20(1)	C(20)	4080(1)	1842(4)	−140(1)	19(1)
C(7)	7046(1)	−660(4)	4097(1)	21(1)	C(21)	3576(1)	1293(4)	−827(1)	19(1)
C(8)	7816(1)	2750(4)	6378(1)	20(1)	C(22)	3655(1)	3218(4)	−1360(1)	21(1)
C(9)	8347(1)	1894(4)	7019(1)	20(1)	C(23)	3152(1)	2742(5)	−2056(1)	28(1)
C(10)	8321(1)	3316(4)	7665(1)	21(1)					

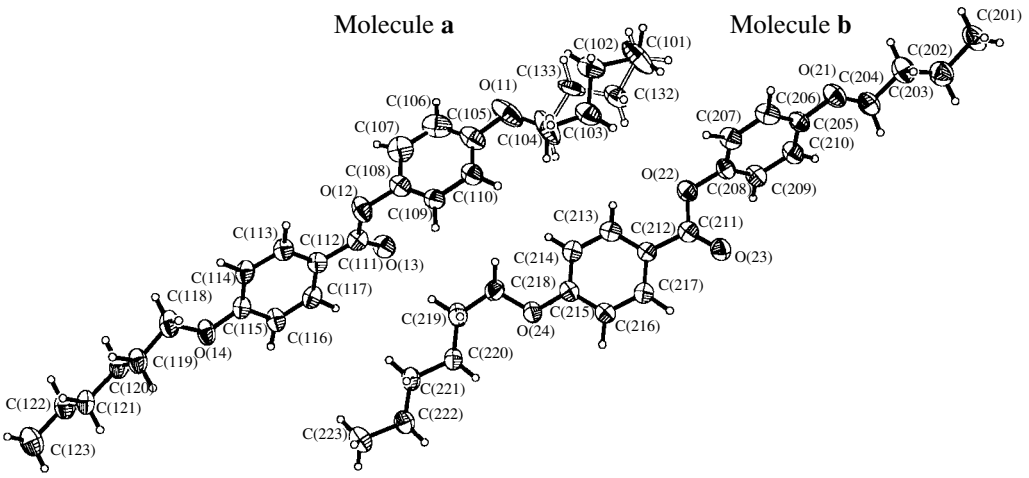

Fig. 1. Structure of two independent molecules (**a** and **b**) of isomer **1**. The atoms are represented as thermal ellipsoids at the 50% probability level. Two positions of the disordered *n*-butyl substituent in molecule **a** are shown.

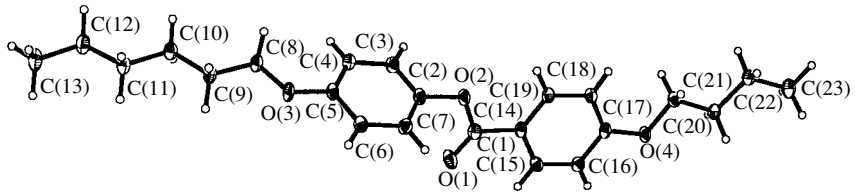

Fig. 2. Molecular structure of isomer **2**. The atoms are represented as thermal ellipsoids at the 50% probability level.

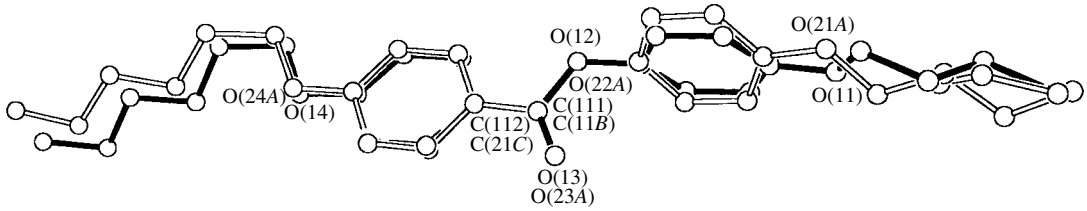

Fig. 3. Overlapping of two crystallographically independent molecules **1a** and **1b** by bringing the carboxyl groups into coincidence.

MOLECULAR STRUCTURES **1** AND **2**

The structure and the mutual arrangement of the two crystallographically independent molecules (**a** and **b**) of isomer **1** are shown in Fig. 1. The molecular structure of isomer **2** is displayed in Fig. 2.

The bond lengths in *n*-hexyl, *n*-butyl, ether, ester (*Est*), and benzene (*Ph*) groups of molecules **1a**, **1b**, and **2** actually coincide with standard values [21]. In particular, the C–O bond lengths in the O–C=O ester fragments are 1.372(3) and 1.202(3) Å for **1a**, 1.365(4) and 1.207(4) Å for **1b**, and 1.368(2) and 1.201(2) Å for **2**. The O–C_{sp^2} and O–C_{sp^3} bond lengths in the ethers have the following respective values: 1.368(4), 1.358(3) and 1.443(6), 1.453(3) Å for **1a**; 1.369(3), 1.358(3) and 1.428(4), 1.439(4) Å for **1b**; and 1.372(2), 1.378(2) and 1.438(2), 1.442(2) Å for **2**. No systematic distortions of the geometry of the benzene rings is observed.

The geometry of the central fragment *Ph–Est–Ph* is essentially the same in both isomers. One of the benzene rings is nearly coplanar with the *Est* group, whereas the other ring, which is linked with the *Est* group through the oxygen atom, is almost perpendicular to the *Est* plane. Actually, in molecules **1a**, **1b**, and **2**, the dihedral angles between the *Ph* planes are equal to 100.7°, 105.0°, and 112.2°, respectively. In molecule **1a**, the dihedral angle between the *Ph* [C(112)…C(117)] and *Est* [C(112), C(111), O(13), O(12)] planes is 10.2° and the angle between the *Ph* [C(105)…C(110)] and *Est* planes is 90.5°. In molecule **1b**, the corresponding angles [C(212)…C(217)/C(212), C(211), O(22), O(23) and C(205)…C(210)/C(212), C(211), O(22), O(23)] are equal to 7.7° and 109.2°,

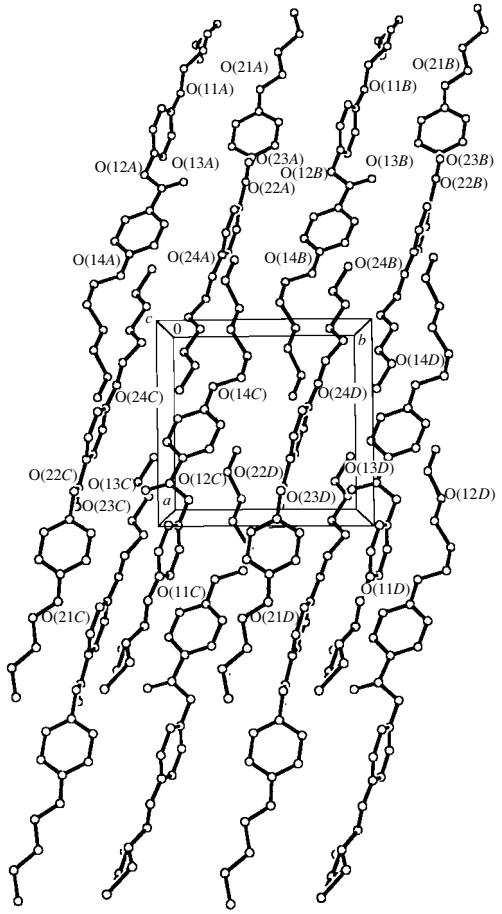

Fig. 4. A fragment of the crystal packing of molecules **1** projected along the *c* axis.

respectively. In molecule **2**, the corresponding angles [C(14)…C(19)/C(14), C(1), O(1), O(2) and C(2)…C(7)/C(14), C(1), O(1), O(2)] are 5.6° and 106.9°, respectively.

Although the molecular conformations as a whole are qualitatively similar, the differences in their quantitative parameters are essential. These differences are most pronounced in the conformations of the aliphatic substituents. In molecule **2**, both substituents are extended, and all the torsion angles in the C(6)–C(5)–O(3)–C(8)–C(9)–C(10)–C(11)–C(12)–C(13) [–173.2(2)°, 174.5(2)°, –175.3(2)°, 178.7(2)°, –178.2(2)°, 179.2(2)°] and C(16)–C(17)–O(4)–C(20)–C(21)–C(22)–C(23) [176.3(2)°, –179.6(2)°, –175.8(2)°, –179.5(2)°] correspond to the *anti* conformation. In molecules **1a** and **1b**, the torsion angles in the *n*-hexyl substituent [C(115)–O(14)–C(118)–C(119)–C(120)–C(121)–C(122)– C(123) and C(215)–O(24)–C(218)–C(219)–C(220)–C(221)–C(222)–C(223)] are –168.2(3)°, 63.9(3)°, –176.4(3)°, –179.1(3)°, and 175.0(3)° and 164.7(3)°, 59.9(3)°, –167.0(3)°, 178.7(3)°, and –175.9(3)°, respectively. One of these torsion angles in molecules **1a** and **1b**, namely, the angle about the C(118)–C(119) bond in **1a** and the angle about C(218)–C(219) bond in **1b**, corresponds to the *gauche* conformation.

In molecule **1b**, the *n*-butoxy fragment is extended and its conformation is described by the following values of the torsion angles along the C(206)–C(205)–O(21)–C(204)–C(203)–C(202)–C(201) chain: 175.0(3)°, 179.3(3)°, 179.8(3)°, and 178.3(3)°. At the same time, the analogous fragment in molecule **1a** is disordered over two positions with different conformations. The conformational difference between fragments of the two independent molecules is clearly seen in Fig. 3, which represents the overlapping of the molecules by bringing their ester groups into coincidence.

In addition to the noticeable difference in the orientation of aliphatic side chains, a slight difference is observed in the orientation of benzene rings, specifically, rings that bear the *n*-butoxy substituent. This indicates the conformational flexibility of not only the aliphatic chains but also of the central molecular fragment *Ph–Est–Ph*.

CRYSTAL PACKING OF **1** AND **2**

The molecular packings of **1** and **2** are of special interest, because these liquid-crystalline substances serve as objects of supramolecular chemistry; that is, they belong to systems whose main property is governed by the structure of their molecular packing.

A fragment of the crystal packing of compound **1** projected along the *c* axis is shown in Fig. 4. All the intermolecular interatomic contacts agree with the sums of van der Waals radii of the corresponding atoms. In the crystal, each benzene ring of the molecules is surrounded by aliphatic fragments and approaches the benzene rings of the neighboring molecules. In any pair of neighboring molecules, the most closely spaced benzene rings are nearly perpendicular to each other. The *ab initio* quantum-chemical calculations demonstrated that the mutually perpendicular orientation of the benzene rings, rather than their parallel arrangement, results in the most stable packing [22]. This geometry corresponds to a weak C–H$\cdots\pi$ interaction, which is considered a weak hydrogen bond between the CH group (a weak acid) and the π system (a weak base) [23]. A similar geometry is also favorable for attractive quadrupole–quadrupole interaction [24]. The specific interactions considered above are weak, and all the intermolecular contacts agree with the sums of the van der Waals radii.

Molecules **2** form a different crystal packing. A fragment of the crystal packing projected along the *b* axis is shown in Fig. 5. Neither perpendicular nor stacking motifs are observed. The supramolecular architecture of this compound is determined by directional specific interactions similar to hydrogen bonding between the benzene C–H fragment of one molecule and the ester oxygen atom of the neighboring molecule [O(3)$\cdots$H(16)–C(16)]. The O(3)$\cdots$H(16) distance

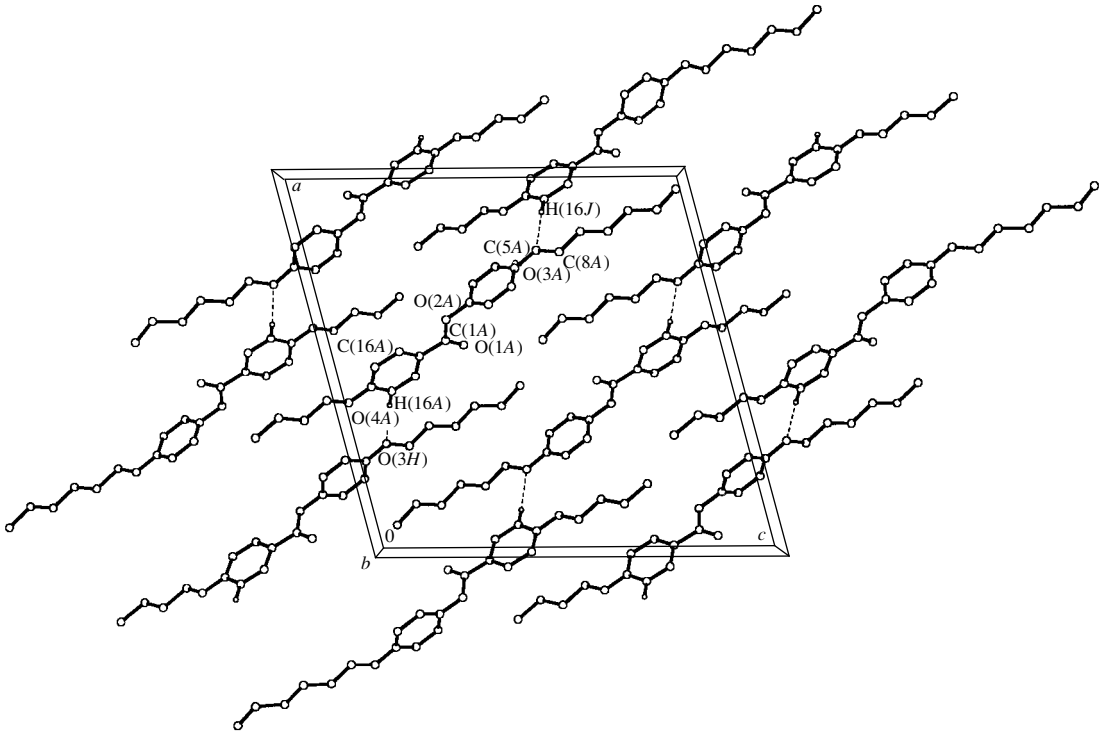

Fig. 5. A fragment of the crystal packing of molecules **2** projected along the *b* axis.

[2.52 Å] is shorter than the sum of van der Waals radii of the oxygen and hydrogen atoms (the minimum value is ~2.6 Å), and the angle (175.6°) at the hydrogen atom agrees with the typical linear arrangement of the interacting fragments.

ACKNOWLEDGMENTS

This study was supported by the Russian Foundation for Basic Research (project no. 01-03-32474) and the Royal Society of Chemistry (RSC Journal Grants for International Authors).

REFERENCES

1. J. M. Seddon, in *Handbook of Liquid Crystals*, Ed. by D. Demus *et al.* (Wiley–VCH, Weinheim, 1998), Vol. 1, p. 635.
2. R. F. Bryan, J. Chem. Soc., 2517 (1960).
3. R. F. Bryan and P. Hartley, Mol. Cryst. Liq. Cryst. **69**, 47 (1981).
4. R. F. Bryan and P. Hartley, Mol. Cryst. Liq. Cryst. **62**, 259 (1980).
5. J. D. Bernal and D. Crowfoot, Trans. Faraday Soc. **29**, 1032 (1933).
6. J. A. W. Barnard and J. E. Lydon, Mol. Cryst. Liq. Cryst. **26**, 285 (1974).
7. P. Sawzik and B. M. Craven, in *Liquid Crystals: Proceedings of International Conference, Bangalore*, Ed. by S. Chandrasekhar (Heyten, London, 1980), p. 171.
8. V. Vill, *Liqcryst 3.3—Database of Liquid Crystalline Compounds* (LCI, Hamburg, 1998).
9. S. Pestov, *Landolt–Boernstein. V. VIII/5A* (Springer, Berlin) (in press).
10. O. V. Noskova and V. A. Molochko, in *Abstracts of IV International Meeting on Lyotropic Liquid Crystals* (Ivanov. Gos. Univ., Ivanovo, 2000), p. 130.
11. V. A. Molochko, O. P. Chernova, G. M. Kurdyumov, and G. I. Karpushkina, Izv. Vyssh. Uchebn. Zaved., Khim. Khim. Tekhnol. **20** (7), 1088 (1977).
12. O. P. Chernova, V. A. Molochko, G. M. Kurdyumov, *et al.*, Zh. Prikl. Khim. (Leningrad) **55** (3), 517 (1982).
13. S. C. Jane, S. A. Agnihotry, S. Chandra, and V. G. Bhide, Mol. Cryst. Liq. Cryst. **104**, 161 (1984).
14. W. Haase and R. Pendzialek, Mol. Cryst. Liq. Cryst. **97**, 209 (1983).
15. S. C. Jane, S. A. Agnihotry, and V. G. Bhide, Mol. Cryst. Liq. Cryst. **87**, 281 (1982).
16. W. Haase, H. Paulus, G. Strobl, and W. Hotz, Acta Crystallogr., Sect. C: Cryst. Struct. Commun. **47**, 2005 (1991).
17. Z. A. Chernaya, V. A. Molochko, T. N. Orlova, and R. A. Lidin, *On Clearness of Liquid Crystals* (Mosk. Inst. Khim. Tekhnol., Moscow, 1985); Available from ONIITÉKhim, No. 224-khp-86.

18. O. V. Noskova, V. A. Molochko, L. G. Kuz'mina, *et al.*, in *Abstracts of XIV International Conference on Chemical Thermodynamics, St. Petersburg* (2002), p. 397.
19. G. M. Sheldrick, Acta Crystallogr. Sect. A: Found. Crystallogr. **46**, 467 (1990).
20. G. M. Sheldrick, *SHELXL93: Program for the Refinement of Crystal Structures* (Univ. of Göttingen, Germany, 1997).
21. F. H. Allen, O. Kennard, D. V. Watson, *et al.*, J. Chem. Soc., Perkin Trans. 2, S1 (1987).
22. K. Müller-Dethlefs and P. Hobza, Chem. Rev. **100**, 143 (2000).
23. H. Takahashi, S. Tsuboyama, Y. Umezawa, *et al.*, Tetrahedron **56**, 6185 (2000).
24. P. Hobza, H. L. Selzle, and E. W. Schlag, Chem. Rev. **94**, 1767 (1994).

Translated by I. Polyakova

Crystallography Reports, Vol. 48, No. 4, 2003, pp. 630–637. Translated from Kristallografiya, Vol. 48, No. 4, 2003, pp. 680–687.

STRUCTURE OF ORGANIC COMPOUNDS

Crystal Structure of Hydrazine 5-Amino-1-Benzyl-1,2,3-Triazole-4-Carboxylate Hexafluorosilicate Trihydrate

M. S. Fonar'*, Yu. A. Simonov*, J. Lipkowski, V. O. Gel'mbol'dt***, É. V. Ganin****, and A. A. Yavolovskiĭ*******

** Institute of Applied Physics, Academy of Sciences of Moldova, ul. Academiei 5, Chisinau, MD-2028 Moldova*
e-mail: fonari.xray@phys.asm.md
*** Institute of Physical Chemistry, Polish Academy of Sciences, Kasprzaka 44/52, Warsaw, 01-224 Poland*
**** Physicochemical Institute for Human and Environmental Protection, Education Department, National Academy of Sciences of Ukraine, Odessa State University, Odessa, Ukraine*
***** Odessa State Ecological University, Odessa, Ukraine*
****** Bogatskiĭ Physicochemical Institute, National Academy of Sciences of Ukraine, Chernomorskaya doroga 86, Odessa, Ukraine*

Received June 4, 2002

Abstract—Hydrazine 5-amino-1-benzyl-1,2,3-triazole-4-carboxylate hexafluorosilicate trihydrate (**I**) is synthesized. The crystal structure of the compound synthesized is determined. Crystals **I** are monoclinic, a = 13.353(1) Å, b = 21.094(2) Å, c = 20.233(2) Å, β = 94.05(3)°, space group $P2_1/c$, and R = 0.0584 for 16 601 reflections with $I > 2\sigma(I)$. In the asymmetric part of the unit cell, four organic cations protonated at the terminal hydrazine nitrogen atoms, two hexafluorosilicate anions, and six water molecules are linked into a three-dimensional framework through hydrogen bonds of the N–H···F, N–H···O, and O–H···F types

INTRODUCTION

Carboxylic acid hydrazides are widely used as N,O-ambidentate ligands in the synthesis of *p* and *d* metal complexes that exhibit a large variety of coordination modes [1, 2]. Hydrazide compounds possess base properties ($pK_a \approx 3$) [3] and readily undergo protonation in acid media. Since hydrazides are the simplest hard Lewis acids, they are of particular interest as model objects for investigation of directional interactions with protons. However, the data available in the literature on the structure of hydrazide compounds with mineral acids are very scarce. The interaction of fluorosilicic acid with N,O- and N,S-ambidentate organic bases and the structures and properties of the products of this interaction were studied in our earlier works [4–6]. The data on the crystal structure of the compound prepared by the reaction of fluorosilicic acid with isonicotinic acid hydrazide were published in [5, 6]. The compounds synthesized by the reaction of fluorosilicic acid with a number of hydrazides were investigated by IR spectroscopy and inferences regarding their possible structures were drawn in [6]. The present work is a continuation of our previous investigations [5, 6]. In this work, we studied the product of the interaction between fluorosilicic acid and 5-amino-1-benzyl-1,2,3-triazole-4-carboxylic acid hydrazide.

EXPERIMENTAL

5-Amino-1-benzyl-1,2,3-triazole-4-carboxylic acid hydrazide (*L*) was synthesized according to the procedure described in [7]. Hydrazide *L* (232 mg, 1 mmol) was dissolved in methanol (50 ml) at a temperature of 64°C. Then, 45% fluorosilicic acid (7.5 ml, 30 mmol) was added to the solution, and the resultant reaction mixture was allowed to stand for spontaneous evaporation of methanol and water until the onset of crystallization. Single crystals of the complex were prepared by recrystallization of the isolated product from a mixture of methanol (30 ml) and fluorosilicic acid (0.5 ml).

For $[HL]_2 \cdot [SiF_6] \cdot 3H_2O$ (complex **I**), anal. calcd. (%): Si, 4.24; F, 17.20.

Found (%): Si, 4.12; F, 18.31.

The mass spectrum of complex **I** (an MX-1321 spectrometer; a direct-inlet system for sample introduction into a source; energy of ionizing electrons, 70 eV) contains the peaks associated with the ions M^+L (m/z = 232, I = 32%), $[C_7H_7]^+$ (m/z = 91, I = 100%), $[C_5H_5]^+$ (m/z = 65, I = 11%), and $[SiF_3]^+$ (m/z = 85, I = 36%). X-ray diffraction analysis of compound **I** was performed on a Nonius CCD diffractometer (MoK_α radiation, graphite monochromator). The experimental data were processed using the DENZO program [8]. The measured reflections were transformed to the same

1063-7745/03/4804-0630$24.00

scale according to the SCALEPACK program [8]. The structure was solved by direct methods with the use of the SHELXS program [9] and refined with the SHELX97 software package [10]. In one hexafluorosilicate anion, the F(3), F(4), F(5), and F(6) equatorial fluorine atoms are disordered over two positions with occupancies of 62.3(1) and 37.7(1)%. The geometry will be discussed only for the position with the higher occupancy. The O(1*W*) water molecule is also disordered over two equiprobable positions (space group $P2_1/c$). In the structure refinement, the hydrogen atoms of the carbon-containing groups were placed at calculated ideal positions and refined as if they were rigidly bound to the parent carbon atoms. The functional hydrogen atoms (at the nitrogen atoms and in the water molecules) were located from the difference Fourier synthesis and refined in the isotropic approximation. The refinement was carried out by the full-matrix least-squares procedure on F^2. The crystal data, data collection, and refinement parameters for the studied compound are presented in Table 1. The final coordinates of the non-hydrogen atoms are listed in Table 2. The geometric parameters of the hydrogen bonds are given in Table 3.

Table 1. Crystal data, data collection, and refinement parameters for the crystal structure of complex **I**

Complex	**I**
Empirical formula	$C_{40}H_{64}F_{12}N_{24}O_{10}Si_2$
Molecular weight	1324.83
T, K	150
Crystal system	Monoclinic
Space group	$P2_1/c$
Unit cell parameters:	
a, Å	13.353(1)
b, Å	21.094(2)
c, Å	20.233(2)
β, deg	94.05(3)
V, Å^3	5684.8(1)
Z	4
d_{calcd}, g/cm^3	1.548
μ, mm^{-1}	0.178
F(000)	2750
Crystal size, mm	0.20 × 0.25 × 0.30
θ range, deg	2.12–30.04
Index ranges	$0 < h < 18$, $0 < k < 29$, $-28 < l < 28$
Diffractometer	Nonius CCD
Scan mode	ω/2θ
Number of reflections measured	17034
Number of unique reflections	16601
Refinement technique	Full-matrix, on F^2
Goodness-of-fit *S* on F^2	1.129
Final *R* factors for reflections with $I > 2\sigma(I)$	$R_1 = 0.0584$, $wR_2 = 0.1048$
Final *R* factors for all reflections	$R_1 = 0.0838$, $wR_2 = 0.1124$
	$w = 1/[\sigma^2(F_o^2) + (aP)^2 + bP]$
	$P = \max(F_o^2) + 2F_c^2/3$
	$a = 0.0366$, $b = 3.16$
Residual electron densities $\Delta\rho_{max}$, $\Delta\rho_{min}$, e Å^{-3}	0.425 and −0.416

RESULTS AND DISCUSSION

In the asymmetric part of the unit cell, four hydrazine 5-amino-1-benzyl-1,2,3-triazole-4-carboxylate cations (lettered as *A*, *B*, *C*, and *D*) protonated at the terminal amino groups of the hydrazine fragments, two hexafluorosilicate anions, and six water molecules occupy general positions. This structure corresponds to the stoichiometric composition $[HL]_2 \cdot [SiF_6] \cdot 3H_2O$ (Fig. 1). The relevant interatomic distances and bond angles in the organic cations are approximately equal to each other. The geometry of the cation framework is similar to that described for related compounds involving a benzotriazole fragment [11, 12] and for a 5-amino-1-benzyl-1,2,3-triazole-4-carboxylic acid hydrazide molecule in the complex with 18-crown-6 [13]. All the organic cations have a corner structure. The angles at the C(7*n*) bridging methylene carbon atoms (*n* = *A*, *B*, *C*, and *D*) are somewhat larger than the ideal tetrahedral angle and lie in the range 110.8(1)°–112.6(1)°. The dihedral angles between the planes of the triazole and phenyl rings fall in the range 70.86(5)°–79.26(6)°. The conformation of the cations is stabilized by the N–H···O intramolecular hydrogen bonds, in which the O(1*n*) carbonyl oxygen atom serves as a hydrogen acceptor, whereas the $N(6n)H_3^+$ terminal ammonium group and the $N(4n)H_2$ amino group of the triazole ring act as hydrogen donors. This leads to the formation of two rings closed by hydrogen bonds: the ··H–N(4*n*)–C(8*n*)–C(9*n*)–C(10*n*)–C(1*n*)··· six-membered ring with N(4*n*)··O(1*n*) distances varying from 2.916(2) Å (for cation *D*) to 3.090(2) Å (for cation *A*) and the ··H–N(6*n*)–N(5*n*)–C(10*n*)–O(1*n*)··· five-membered ring with N(6*n*)··O(1*n*) distances varying from 2.609(2) Å (for cation *D*) to 2.664(2) Å (for cation *A*) (Table 3). The dihedral angles between the six-membered hydrogen ring and the triazole ring fused along the C(8*n*)–C(9*n*) bond fall in the range from 1.60(5)° (for cation *A*) to 2.19(4)° (for cation *D*). The dihedral angles between the two hydrogen rings fused along the O(1*n*)–C(10*n*) bond vary from 3.66(7)° (for cation *A*) to 5.64(6)° (for cation *C*). Therefore, the triazole and two adjacent

Table 2. Coordinates of the non-hydrogen atoms ($\times 10^4$) and the equivalent isotropic thermal parameters U_{eq} ($Å^2 \times 10^3$) for complex **I**

Atom	*x*	*y*	*z*	U_{eq}	Atom	*x*	*y*	*z*	U_{eq}
Si(1)	1028(1)	3869(1)	4492(1)	19(1)	C(6*B*)	6526(2)	1722(1)	5395(1)	29(1)
F(1)	1065(1)	3188(1)	4921(1)	31(1)	C(7*B*)	7668(1)	2075(1)	6379(1)	22(1)
F(2)	1006(1)	4546(1)	4035(1)	34(1)	C(8*B*)	6367(1)	1739(1)	7169(1)	16(1)
F(3)	126(10)	3550(6)	3965(5)	34(2)	C(9*B*)	6418(1)	1286(1)	7690(1)	17(1)
F(4)	1801(8)	3561(7)	3942(5)	36(2)	C(10*B*)	5607(1)	1122(1)	8075(1)	15(1)
F(5)	2086(8)	4117(3)	4935(5)	50(2)	O(1*C*)	3645(1)	2618(1)	6751(1)	23(1)
F(6)	332(12)	4212(5)	5007(4)	48(2)	N(1*C*)	989(1)	1605(1)	7045(1)	17(1)
F(3*A*)	21(16)	3604(10)	4033(9)	37(3)	N(2*C*)	424(1)	1937(1)	6567(1)	19(1)
F(4*A*)	1918(12)	3604(11)	4057(11)	41(4)	N(3*C*)	1016(1)	2340(1)	6305(1)	19(1)
F(5*A*)	1761(14)	4205(7)	5047(5)	55(2)	N(4*C*)	2683(1)	1595(1)	7517(1)	28(1)
F(6*A*)	−25(9)	4118(4)	4911(5)	27(2)	N(5*C*)	2691(1)	3011(1)	5884(1)	23(1)
Si(1*B*)	3850(1)	6069(1)	4246(1)	13(1)	N(6*C*)	3503(1)	3411(1)	5746(1)	21(1)
F(1*B*)	3485(1)	5374(1)	4564(1)	24(1)	C(1*C*)	510(1)	471(1)	7058(1)	18(1)
F(2*B*)	4276(1)	6739(1)	3916(1)	23(1)	C(2*C*)	1347(1)	79(1)	7082(1)	28(1)
F(3*B*)	4199(1)	6332(1)	5015(1)	24(1)	C(3*C*)	1327(2)	−494(1)	6742(1)	34(1)
F(4*B*)	2712(1)	6383(1)	4309(1)	27(1)	C(4*C*)	467(2)	−676(1)	6372(1)	33(1)
F(5*B*)	3487(1)	5794(1)	3481(1)	30(1)	C(5*C*)	−374(2)	−295(1)	6345(1)	34(1)
F(6*B*)	5003(1)	5741(1)	4193(1)	28(1)	C(6*C*)	−353(1)	274(1)	6691(1)	26(1)
O(1*A*)	975(1)	6704(1)	3008(1)	28(1)	C(7*C*)	526(1)	1099(1)	7416(1)	19(1)
N(1*A*)	−1728(1)	6860(1)	1773(1)	24(1)	C(8*C*)	1950(1)	1808(1)	7087(1)	17(1)
N(2*A*)	−2213(1)	6412(1)	2125(1)	20(1)	C(9*C*)	1961(1)	2280(1)	6604(1)	16(1)
N(3*A*)	−1580(1)	6211(1)	2595(1)	21(1)	C(10*C*)	2825(1)	2642(1)	6433(1)	17(1)
N(4*A*)	−116(1)	7343(1)	1786(1)	30(1)	O(1*D*)	1963(1)	7584(1)	1568(1)	24(1)
N(5*A*)	66(1)	5923(1)	3443(1)	25(1)	N(1*D*)	4734(1)	6697(1)	1966(1)	18(1)
N(6*A*)	868(1)	5802(1)	3921(1)	23(1)	N(2*D*)	5213()	7025(1)	1490(1)	20(1)
C(1*A*)	−2166(1)	6665(1)	590(1)	25(1)	N(3*D*)	4560(1)	7404(1)	1194(1)	19(1)
C(2*A*)	−2978(2)	6283(1)	398(1)	40(1)	N(4*D*)	3096(1)	6646(1)	2372(1)	22(1)
C(3*A*)	−2914(2)	5843(1)	−108(1)	57(1)	N(5*D*)	2734(1)	8048(1)	741(1)	25(1)
C(4*A*)	−2041(2)	5790(1)	−427(1)	53(1)	N(6*D*)	1815(1)	8358(1)	559(1)	22(1)
C(5*A*)	−1235(2)	6166(1)	−244(1)	43(1)	C(1*D*)	5186(1)	5563(1)	2012(1)	18(1)
C(6*A*)	−1291(2)	6608(1)	261(1)	33(1)	C(2*D*)	5955(1)	5348(1)	1644(1)	30(1)
C(7*A*)	−2230(1)	7115(1)	1163(1)	24(1)	C(3*D*)	5868(2)	4779(1)	1303(1)	36(1)
C(8*A*)	−774(1)	6940(1)	2029(1)	18(1)	C(4*D*)	5015(2)	4415(1)	1332(1)	32(1)
C(9*A*)	−684(1)	6515(1)	2556(1)	18(1)	C(5*D*)	4250(2)	4618(1)	1708(1)	32(1)
C(10*A*)	189(1)	6397(1)	3003(1)	18(1)	C(6*D*)	4335(1)	5187(1)	2047(1)	26(1)
O(1*B*)	4784(1)	1381(1)	8016(1)	20(1)	C(7*D*)	5270(2)	6200(1)	2355(1)	20(1)
N(1*B*)	7301(1)	1739(1)	6950(1)	19(1)	C(8*D*)	3765(1)	6878(1)	1968(1)	16(1)
N(2*B*)	7902(1)	1305(1)	7290(1)	23(1)	C(9*D*)	3657(1)	7330(1)	1467(1)	17(1)
N(3*B*)	7368(1)	1036(1)	7725(1)	21(1)	C(10*D*)	2733(1)	7655(1)	1271(1)	18(1)
N(4*B*)	5611(1)	2102(1)	6918(1)	21(1)	O(1W)	1939(3)	5349(2)	5337(2)	35(1)
N(5*B*)	5811(1)	656(1)	8541(1)	19(1)	O(1WA)	2407(2)	5438(1)	5597(2)	27(1)
N(6*B*)	5027(1)	535(1)	8966(1)	19(1)	O(2W)	−2898(1)	5547(1)	3498(1)	52(1)
C(1*B*)	7458(1)	1698(1)	5751(1)	24(1)	O(3W)	−700(1)	2909(1)	5506(1)	37(1)
C(2*B*)	8185(2)	1289(1)	5542(1)	36(1)	O(4W)	3874(1)	3279(1)	4433(1)	30(1)
C(3*B*)	7987(2)	901(1)	5001(1)	50(1)	O(5W)	−996(1)	4770(1)	3406(1)	28(1)
C(4*B*)	7054(2)	915(1)	4657(1)	47(1)	O(6W)	3021(1)	4508(1)	3428(1)	25(1)
C(5*B*)	6326(2)	1326(1)	4853(1)	38(1)					

Table 3. Geometric parameters for the hydrogen bonds in complex **I**

D–H···*A*	*d*(*D*–H), Å	*d*(H···*A*), Å	*d*(*D*···*A*), Å	∠(*DHA*), deg
Intramolecular hydrogen bonds				
N(4*A*)–H(1N*A*)···O(1*A*)	0.86(3)	2.54(3)	3.090(2)	123(2)
N(6*A*)–H(5N*A*)···O(1*A*)	0.85(3)	2.21(2)	2.644(2)	113(2)
N(4*B*)–H(1N*B*)···O(1*B*)	0.88(2)	2.41(2)	2.9685(2)	122(2)
N(6*B*)–H(5N*B*)···O(1*B*)	0.89(2)	2.25(2)	2.6259(2)	105(2)
N(4*C*)–H(1N*C*)···O(1*C*)	0.87(3)	2.42(3)	2.998(2)	125(2)
N(6*C*)–H(5N*C*)···O(1*C*)	0.91(2)	2.14(2)	2.6290(2)	113(2)
N(4*D*)–H(2N*D*)···O(1*D*)	0.85(2)	2.34(2)	2.916(2)	125(2)
N(6*D*)–H(4N*D*)···O(1*D*)	0.91(2)	2.09(2)	2.6092(2)	115(2)
Intermolecular hydrogen bonds				
N(4*A*)–H(1N*A*)···O(1*D*)	0.86(3)	2.27(2)	2.886(2)	129(2)
N(4*A*)–H(2N*A*)···F(3)^{i}	0.85(3)	2.19(3)	2.964(1)	151(2)
N(5*A*)–H(3N*A*)···O(5*W*)	0.80(2)	2.04(2)	2.183(2)	162(2)
N(6*A*)–H(4N*A*)···F(2)	0.95(2)	1.73(2)	2.663(2)	166(2)
N(6*A*)–H(5N*A*)···F(4*B*)	0.85(3)	2.13(3)	2.8118(2)	136(2)
N(6*A*)–H(6N*A*)···F(6)^{i}	0.94(3)	1.93(3)	2.786(8)	151(3)
N(4*B*)–H(1N*B*)···O(1*C*)	0.88(2)	2.24(2)	2.840(2)	125(2)
N(4*B*)–H(2N*B*)···F(2*B*)^{iii}	0.86(2)	2.14(2)	2.981(2)	167(2)
N(5*B*)–H(3N*B*)···O(2*W*)^{v}	0.77(3)	2.43(3)	3.072(2)	141(3)
N(6*B*)–H(4N*B*)···F(3*B*)^{iv}	0.93(3)	1.92(3)	2.802(2)	157(2)
N(6*B*)–H(5N*B*)···O(6*W*)^{vi}	0.89(2)	1.98(2)	2.821(2)	157(2)
N(6*B*)–H(6N*B*)···F(6*B*)^{vi}	0.91(2)	1.82(3)	2.731(2)	171(2)
N(4*C*)–H(1N*C*)···O(1*B*)	0.87(3)	2.35(3)	2.949(2)	126(2)
N(4*C*)–H(2N*C*)···O(6*W*)^{vi}	0.84(2)	2.18(2)	2.983(2)	159(2)
N(5*C*)–H(3N*C*)···F(1)	0.86(2)	1.99(2)	2.837(2)	166(2)
N(6*C*)–H(4N*C*)···O(4*W*)	0.95(2)	1.80(2)	2.749(2)	173(2)
N(6*C*)–H(5N*C*)···F(2*B*)^{iii}	0.91(2)	2.24(2)	3.012(2)	143(2)
N(6*C*)–H(6N*C*)···O(2*W*)^{ii}	0.90(3)	1.98(3)	2.830(2)	156(2)
N(4*D*)–H(2N*D*)···O(1*A*)	0.85(2)	2.54(2)	3.195(2)	134(2)
N(4*D*)–H(1N*D*)···F(5*B*)	0.87(2)	2.03(2)	2.895(2)	171(2)
N(5*D*)–H(3N*D*)···F(3*W*)^{viii}	0.82(2)	2.06(2)	2.847(2)	158(2)
N(6*D*)–H(4N*D*)···F(3)^{i}	0.91(2)	2.18(3)	2.857(1)	130(2)
N(6*D*)–H(5N*D*)···O(1*W*)^{viii}	0.96(3)	1.82(3)	2.771(4)	169(2)
N(6*D*)–H(6N*D*)···O(3*W*)^{i}	0.95(3)	1.77(3)	2.703(2)	168(2)
O(1*W*)–H(1*W*1)···F(1*B*)	0.86(1)	1.88(3)	2.677(3)	152(5)
O(1*W*)–H(2*W*1)···F(5)	0.85(1)	2.30(5)	2.735(9)	111(4)
O(2*W*)–H(1*W*2)···N(3*A*)	0.86(1)	2.15(1)	2.975(2)	162(3)
O(2*W*)–H(2*W*2)···F(5)^{ii}	0.84(1)	2.53(2)	3.354(9)	165(3)
O(3*W*)–H(1*W*3)···F(1)	0.85(1)	2.01(2)	2.773(2)	150(3)
O(3*W*)–H(1*W*3)···N(3*C*)	0.85(1)	2.50(3)	2.964(2)	115(2)
O(4*W*)–H(1*W*4)···N(3*D*)^{viii}	0.85(1)	2.27(1)	3.125(2)	177(2)
O(4*W*)–H(2*W*4)···F(4)	0.85(1)	2.16(2)	2.935(12)	152(2)
O(5*W*)–H(1*W*5)···N(3*B*)^{ix}	0.86(1)	2.18(1)	3.023(2)	171(2)
O(5*W*)–H(2*W*5)···F(3)	0.85(1)	2.34(2)	3.148(1)	159(2)
O(5*W*)–H(2*W*5)···F(2)	0.85(1)	2.25(2)	2.916(2)	136(2)
O(6*W*)–H(1*W*6)···F(5*B*)	0.86(1)	1.95(1)	2.783(2)	163(2)
O(6*W*)–H(2*W*6)···F(4)	0.87(1)	2.10(2)	2.824(1)	140(2)
O(6*W*)–H(2*W*6)···F(2)	0.87(1)	2.32(2)	3.037(2)	139(2)

Note: Symmetry codes: *i*: $-x, y + 1/2, -z + 1/2$; *ii*: $-x, -y + 1, -z + 1$; *iii*: $-x + 1, -y + 1, -z + 1$; *iv*: $-x + 1, -y - 1/2, -z + 3/2$; *v*: $x + 1, -y + 1/2, z + 1/2$; *vi*: $x, -y + 1/2, z + 1/2$; *vii*: $x, -y + 3/2, z - 1/2$; *viii*: $-x + 1, y - 1/2, -z + 1/2$; *ix*: $x - 1, -y + 1/2, z - 1/2$.

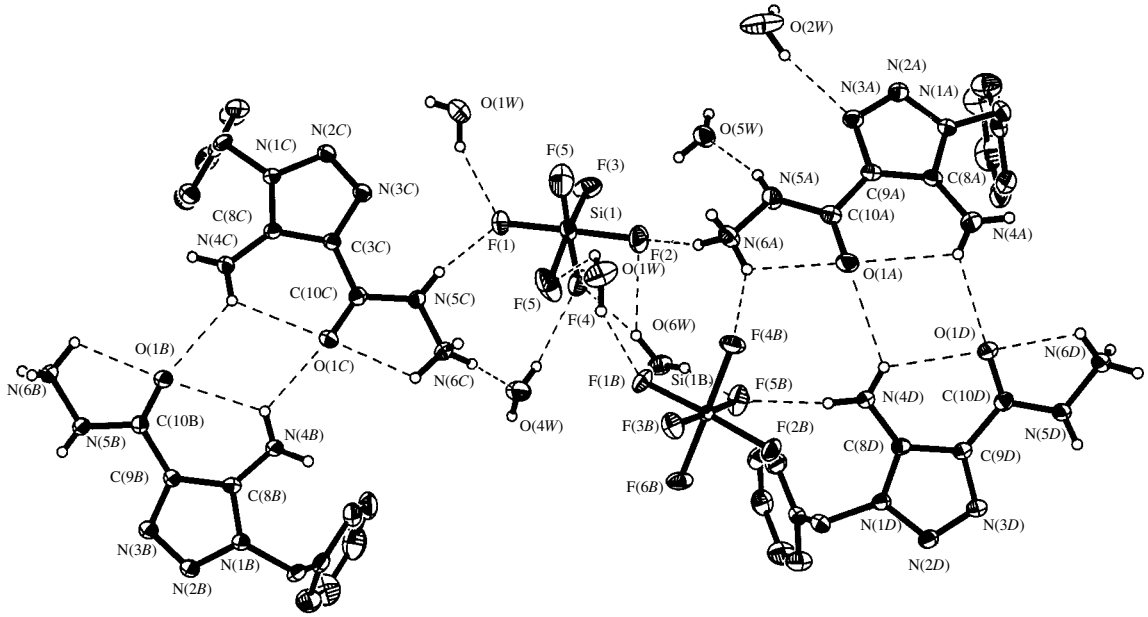

Fig. 1. An asymmetric part of the unit cell for compound **I** with the atomic numbering. One of the two disordered positions is shown for the hexafluorosilicate anion [associated with the Si(1) atom] and the O(1*W*) water molecule. Dashed lines indicate intramolecular and intermolecular hydrogen bonds.

hydrogen-bonded rings form a nearly planar tricyclic system. Organic cations *A* and *D* (*B* and *C*) are joined together into dimers through two intermolecular hydrogen bonds of the N(4*n*)···O(1*n*) type. The N···O distances are equal to 2.886(2) and 3.195(2) Å in the former dimer and 2.840(2) and 2.949(2) Å in the latter dimer. The dimerization results in the formation of two 12-membered pseudomacrocycles. The phenyl substituents are oriented toward the same direction with respect to the mean plane of these pseudomacrocycles.

The inorganic component of the crystal contains two hexafluorosilicate anions and six water molecules. Both anions have a structure of a distorted octahedron with the Si–F distances lying in the range 1.641(2)–1.704(2) Å. In anion *B*, the interatomic distances are closer to each other and fall in the range 1.671(1)–1.697(1) Å. The maximum deviations of the F–Si–F bond angle from right and straight angles do not exceed 4° and 3.2°, respectively. The geometry of both anions agrees with the data obtained in [14].

The O(1*W*) and O(6*W*) water molecules serve as bridges between two hexafluorosilicate anions. Both hydrogen atoms of these molecules are involved in the O–H···F hydrogen bonds: O(1*W*)···F(1*B*), 2.677(3) Å; O(1*W*)···F(5), 2.735(9) Å; O(2*W*)···F(5*B*), 2.783(2) Å; O(6*W*)···F(4), 2.824(1) Å; and O(6*W*)···F(2), 3.037(2) Å. The O(4*W*) water molecule fulfills the role of a bridge between the hexafluorosilicate anion and cation *C*. The parameters of the corresponding hydrogen bonds are as follows: O(4*W*)···F(4), 2.94(1) Å and N(6*C*)···O(4*W*), 2.749(2) Å. The associates composed of four hexafluorosilicate anions and six water molecules with the participation of the O(4*W*) water molecules and cations *C* are formed around inversion centers (Fig. 2).

In the *A*–*D* and *B*–*C* dimers, the same functional groups, namely, the $N(6n)H_3^+$ terminal ammonium group and the $N(4n)H_2$ amino group of the triazole ring, similarly participate in the system of hydrogen bonds. The F(3) fluorine atom is involved as a bridge between cations *A* and *D* in the system of the N–H···F hydrogen bonds: N(4*A*)···F(3) (–*x*, *y* + 1/2, –*z* + 1/2), 2.964(1) Å and N(6*D*)···F(3) (–*x*, *y* + 1/2, –*z* + 1/2), 2.857(1) Å. Another pair of similar functional groups, $N(6A)H_3^+$ and $N(4D)H_2$, participates in the N–H···F hydrogen bonds with the F(4*B*)–Si(1*B*)–F(5*B*) bridge: N(4*D*)···F(5*B*), 2.895(2) Å and N(6*A*)···F(4*B*), 2.812(2) Å. In the *B*–*C* dimer, the structural role of the F(2*B*) atom is similar to that of the F(3) atom. The hydrogen bonds with the participation of the F(2*B*) atom are characterized by the following parameters: N(4*B*)···F(2*B*) (–*x* + 1, –*y* + 1, –*z* + 1), 2.981(2) Å and N(6*C*)···F(2*B*) (–*x* + 1, –*y* + 1, –*z* + 1), 3.012(2) Å. The O(6*W*) water molecule as a hydrogen acceptor links the NH donor groups: N(6*B*)···O (6*W*) (*x*, –*y* + 1/2, *z* + 1/2), 2.821(2) Å and N(4*C*)···O (6*W*) (*x*, –*y* + 1/2, *z* + 1/2), 2.983(2) Å. The dimers in pairs form the double bridges between adjacent inorganic fragments (Fig. 2). Alternating inorganic fragments and organic bridges form orthorhombic cells that lie along the *bc* plane, are closed by hydrogen bonds, and have a side of 14.614 Å [between the centers of the $(SiF_6^{2-})_4$ associates] and diagonals equal to the unit cell parameters *b* and *c*. The phenyl substituents of

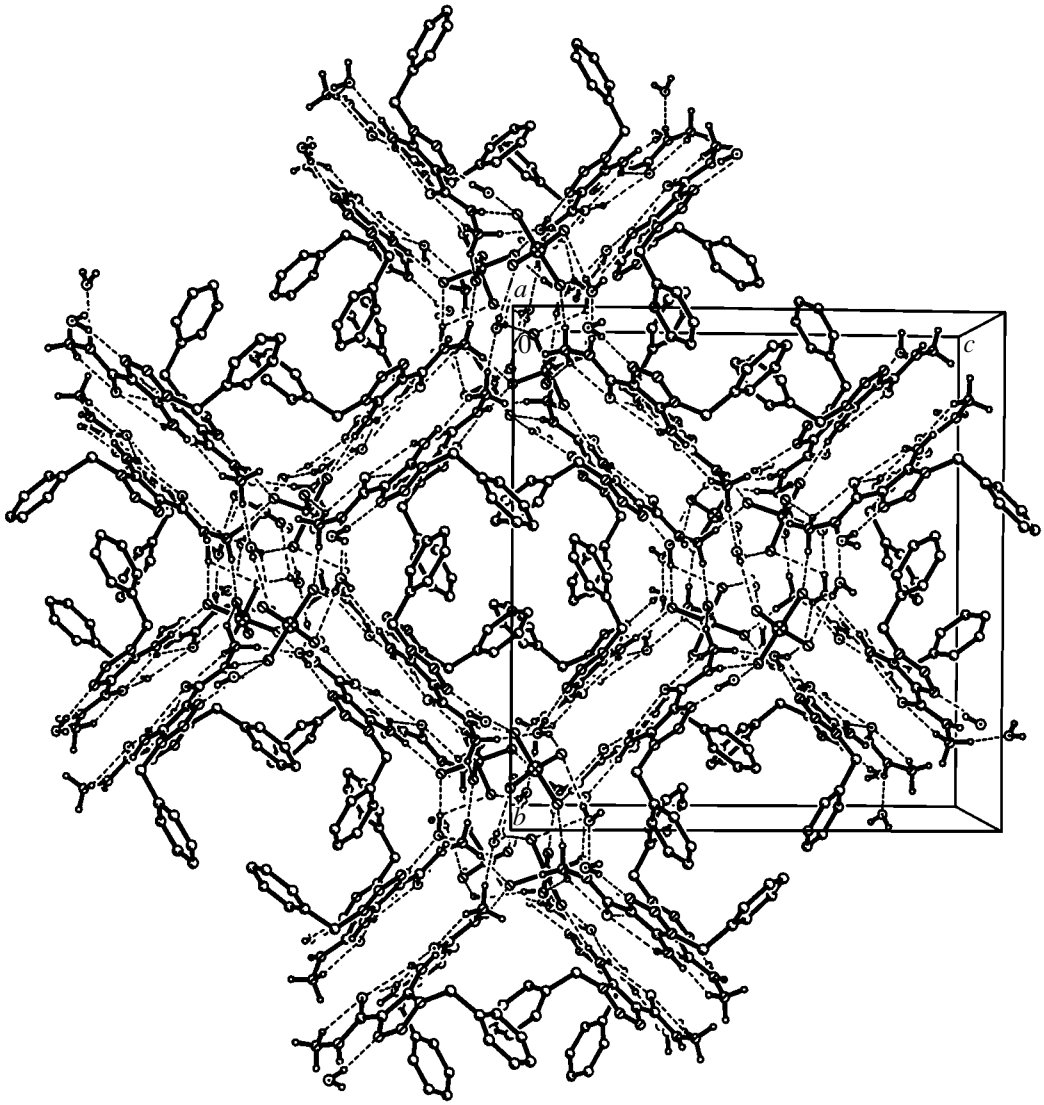

Fig. 2. A fragment of the packing of compound **I**.

the organic cations are directed toward the centers of these cells. Along the *a* axis, the inorganic (hexafluorosilicate anions) and organic components of the crystal are linked by the hydrogen bonds with the participation of the intermediate water molecules [O(2*W*), O(3*W*), O(4*W*), and O(5*W*)] and alternate in a three-dimensional framework (Fig. 3). The structural functions of two pairs of the water molecules O(2*W*), O(5*W*) and O(3*W*), O(4*W*) are similar to each other. The O(2*W*) and O(5*W*) water molecules join cations *A* and *B* of different dimers. The nitrogen atoms N(3*A*,*B*) and N(5*A*,*B*) are involved in the N···O interactions. The F(2) and F(5) fluorine atoms participate in the O(*W*)–H···F hydrogen bonds. The O(3*W*) and O(4*W*) molecules serve as bridges between cations *C* and *D* that also belong to different dimers. In this case, the N(3*C*,*D*) and N(6*C*,*D*) nitrogen atoms are involved in the N···O interactions and the F(1) and F(4) fluorine atoms participate in the O–H···F hydrogen bonds (Table 3). Therefore, the crystal structure represents a three-dimensional framework, which is built up of inorganic columns and organic walls in between. This motif manifests itself along the *a* axis of the unit cell.

Let us now consider the specific features of the interaction of the water molecules with the organic cations and the hexafluorosilicate anions. Despite a large number of water molecules in the structure (six molecules in the asymmetric part of the unit cell), all these molecules are individually involved in hydrogen bonds of different types; i.e., direct contacts of the water–water type are absent in the structure. Among the six molecules, only two molecules [O(2*W*) and O(6*W*)] each participate in four hydrogen bonds and realize all their donor–acceptor abilities (Table 3). About ten hydrate complexes of fluorosilicic acid with different

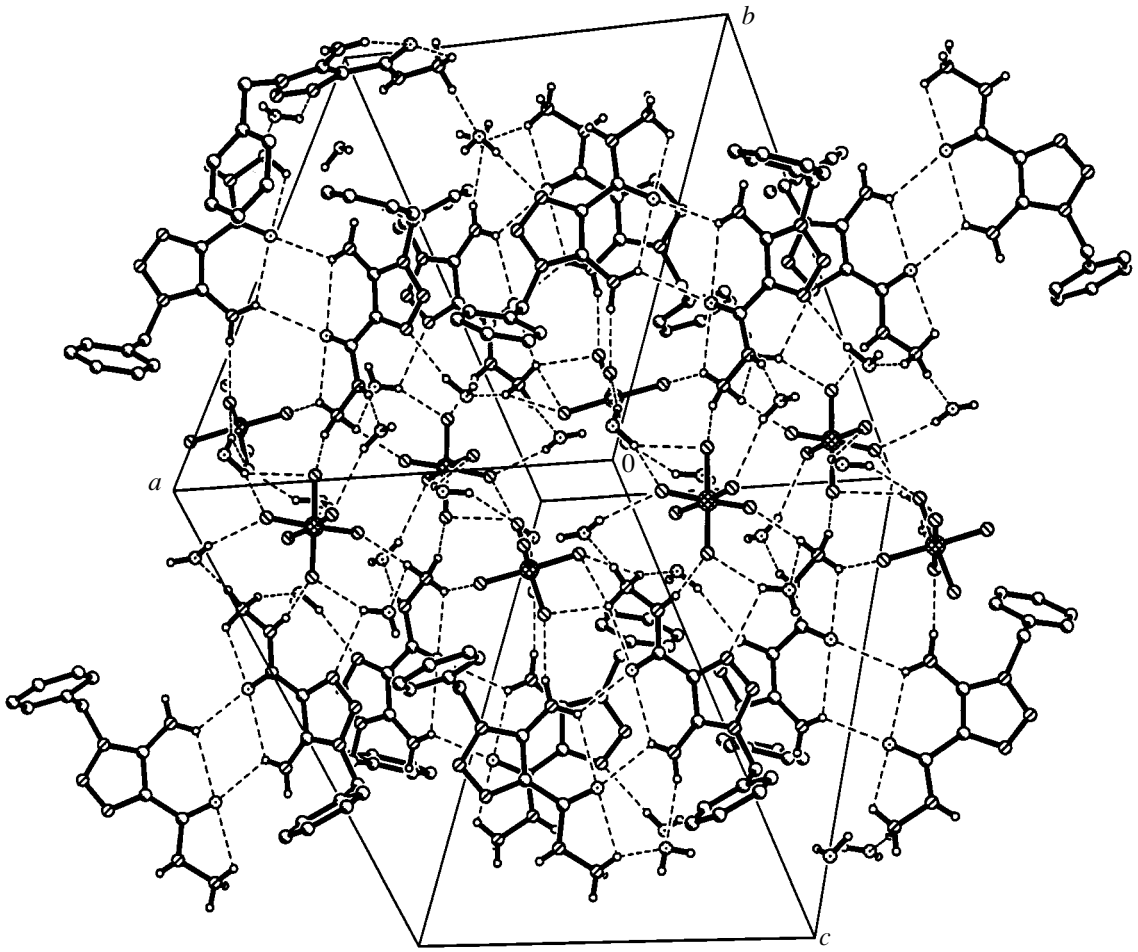

Fig. 3. A fragment of the packing of compound **I**. Columns of organic (hydrazine 5-amino-1-benzyl-1,2,3-triazole-4-carboxylate cations) and inorganic (hexafluorosilicate anions and water molecules) components joined through an extended system of hydrogen bonds in the crystal alternate along the *a* axis.

nitrogen-containing organic molecules are available in the Cambridge Structural Database [15]. A common feature of these complexes is that water molecules individually interact with fluorosilicic acid and nitrogen-containing ligands: a water molecule fulfills a bridging function; i.e., the hydrogen atoms of the water molecule are involved in O(*W*)–H···F hydrogen bonds and the lone electron pair participates in N–H···O interactions with the ligand [14, 16–19]. It was found that water molecules are differently involved in the three-dimensional framework in fluorosilicic acid complexes with nitrogen-containing macrocycles. For example, in the dihydrate complex of fluorosilicic acid with 1,4,7,10-tetraaza-pyridinophane, both water molecules serve as a bridge between two hexafluorosilicate anions [20]. In the dihydrate complex of fluorosilicic acid with *meso*-5,7,7,12,12,14-hexamethyl-1,4,8,11-tetraazacyclotetradecane, two water molecules are linked into a dimer with the O(1*W*)–O(2*W*) intermolecular distance equal to 2.743(9) Å [21]. In the heptahydrate complex of fluorosilicic acid with 1,4,7,10-tetraazacyclodecane, five water molecules form a linear cluster [22]. In our opinion, this is a rare example of such a large-sized water associate in hydrate complexes of fluorosilicic acid. In addition to the last compound, we may note the complex $\{[Pt_2(NH_3)_4(\mu\text{-}CH_3CO_2)_2][(SiF_6)(H_2O)_4]\}_n$, in which four water molecules form a hydrate bridge between two hexafluorosilicate anions [23].

REFERENCES

1. A. D. Garnovskiĭ, I. S. Vasil'chenko, and D. A. Garnovskiĭ, *Modern Aspects of Metallocomplex Synthesis: Main Ligands and Basic Methods* (LaPO, Rostov-on-Don, 2000).
2. R. I. Machkhoshvilli and R. N. Shchelokov, Koord. Khim. **26** (10), 723 (2000).
3. *Comprehensive Organic Chemistry: The Synthesis and Reactions of Organic Compounds*, Ed. by D. Barton and W. D. Oliss (Pergamon, Oxford, 1979; Khimiya, Moscow, 1983), Vol. 4.
4. V. O. Gel'mbol'dt, L. V. Koroeva, É. V. Ganin, and A. A. Énnan, Koord. Khim. **28** (2), 130 (2002).

5. V. O. Gel'mbol'dt, L. V. Koroeva, and V. N. Davydov, Koord. Khim. **27** (2), 159 (2001).
6. V. O. Gel'mbol'dt, V. N. Davydov, L. V. Koroeva, and É. V. Ganin, Zh. Neorg. Khim. **47** (7), 1094 (2002).
7. J. R. E. Hoover and A. R. Day, J. Am. Chem. Soc. **78** (22), 5832 (1956).
8. Z. Otwinowski and W. Minor, Methods Enzymol. **276**, 307 (1997).
9. G. M. Sheldrick, Acta Crystallogr., Sect. A: Found. Crystallogr. **46**, 467 (1990).
10. G. M. Sheldrick, *SHELX97: Program for the Solution and Refinement of Crystal Structures* (Univ. of Göttingen, Göttingen, 1997).
11. A. Dunand, Acta Crystallogr., Sect. B: Struct. Crystallogr. Cryst. Chem. **38**, 2299 (1982).
12. A. Albert and A. Dunand, Angew. Chem. Int. Ed. Engl. **19**, 310 (1980).
13. Yu. A. Simonov, M. S. Fonar', V. Kh. Kravtsov, *et al.*, Kristallografiya **47** (1), 79 (2002) [Crystallogr. Rep. **47**, 86 (2002)].
14. C. R. Ross, II, M. R. Bauer, R. Nielson, and S. C. Abrahams, Acta Crystallogr., Sect. B: Struct. Sci. **35**, 246 (1999).
15. F. N. Allen and O. Kennard, Chem. Des. Autom. News **8**, 31 (1993) (Version 5.20).
16. T. J. Kistenmacher, M. Rossi, C. C. Chiang, *et al.*, Adv. Mol. Relax. Interact. Processes **17**, 113 (1980).
17. W. A. Denne, A. McL. Mathieson, and M. F. Mackay, J. Cryst. Mol. Struct., No. 1, 55 (1971).
18. G. Rother, H. Worzala, and U. Bentrup, Z. Kristallogr. **212**, 310 (1997).
19. C. A. Mattia, O. Ortona, R. Puliti, *et al.*, J. Mol. Struct. **350**, 63 (1995).
20. Yu. A. Simonov, M. S. Fonar', V. Kh. Kravtsov, *et al.*, Zh. Neorg. Khim. **43** (12), 1982 (1998).
21. M. S. Fonar', V. Kh. Kravtsov, Yu. A. Simonov, *et al.*, Zh. Strukt. Khim. **40** (5), 1002 (1999).
22. M. S. Fonari, Yu. A. Simonov, V. Ch. Kravtsov, *et al.*, J. Inclusion Phenom. Mol. Recognit. Chem. **30**, 197 (1998).
23. K. Sakai, M. Takeshita, Yu. Tanaka, *et al.*, J. Am. Chem. Soc. **120**, 11353 (1998).

Translated by O. Borovik-Romanova

Crystallography Reports, Vol. 48, No. 4, 2003, pp. 638–640. Translated from Kristallografiya, Vol. 48, No. 4, 2003, pp. 688–690.

STRUCTURE OF ORGANIC COMPOUNDS

Crystal Structure of Hexakis(*N*,*N*-Dimethylacetamide)ytterbium(III) Dodecawolframophosphate $[Yb(DMAA)_6]PW_{12}O_{40}$

M. S. Grigor'ev*, I. B. Shirokova*, A. M. Fedoseev*, and C. Den Auwer**

** Institute of Physical Chemistry, Russian Academy of Sciences, Leninskiĭ pr. 31, Moscow, 119991 Russia*
e-mail: grigoriev@ipc.rssi.ru
*** CEA Marcoule, DEN/DRCP/SCPS/LCAM, 30207 Bagnols-sur-Céze, France*
Received May 15, 2002

Abstract—An X-ray diffraction study of the $[Yb(DMAA)_6]PW_{12}O_{40}$ complex (*DMAA* is *N*,*N*-dimethylacetamide) is performed. The structure contains isolated cationic complexes $[Yb(DMAA)_6]^{3+}$ and heteropolyanions $PW_{12}O_{40}^{3-}$. The cationic complexes and the heteropolyanions occupy centrosymmetric positions. The coordination polyhedron of the Yb atom is a slightly distorted octahedron. Unlike the Nd complex of the same composition, which was studied earlier, O atoms of the heteropolyanion are not included in the Yb coordination. All the O atoms of the heteropolyanion are disordered. Analysis of the disordering reveals that the heteropolyanion has a Keggin structure (α isomer), and its disordering results from the centrosymmetric position. © *2003 MAIK "Nauka/Interperiodica".*

In this paper, we continue the structural studies of the *f*-element complexes with molecular organic ligands and saturated heteropolyanions. Earlier [1], it was found that the oxygen atoms of the $PW_{12}O_{40}^{3-}$ heteropolyanion with a Keggin structure are included in the coordination polyhedron of the Nd atom in the $[Nd(DMAA)_6PW_{12}O_{40}]$ complex (**II**). It was of interest to elucidate the coordination mode of the heteropolyanion in complexes of this type with other metal atoms. The object of the study reported in this paper is an Yb(III) complex, namely, $[Yb(DMAA)_6]PW_{12}O_{40}$ (**I**).

The synthesis of the ytterbium complex was performed according to the procedure described in [1] for the related neodymium compound. The composition of **I** was determined in the X-ray diffraction study.

A fragment of a single crystal ~$0.15 \times 0.15 \times 0.10$ mm in size was used for the X-ray diffraction study. The experiment was carried out on an Enraf–Nonius KappaCCD area-detector diffractometer (MoK_α radiation, graphite monochromator). The unit cell parameters were determined based on ten images with $\Delta\varphi = 1°$ and refined using a complete data set. At 20°C, a = 11.9031(3) Å, b = 14.8380(4) Å, c = 18.7510(4) Å, and $\beta = 106.456(1)°$. Compound **I** crystallizes in the monoclinic space group $P2_1/c$ ($Z = 2$, $d_{calcd} = 3.569$ g/cm^3). The intensities of the reflections were measured in a hemisphere of the reciprocal space with $\theta = 25.34°$. A total of reflections measured was 20564, of which 5787, including 4686 reflections with $I > 2\sigma(I)$, were unique. The large number of equivalent reflections allowed us to introduce the absorption correction with the MULABS program included in the PLATON software package [2]. The structure was solved by direct methods (SHELXS86 [3]) and refined on F^2 with the full-matrix least-squares procedure (SHELXL93 [4]) using all the reflections. The heteropolyanion is located at the center of symmetry, and all its oxygen atoms are disordered over two equiprobable positions with an occupancy of 0.5. The H atoms in the *DMAA* molecules were positioned from geometric considerations and assigned to thermal parameters larger than the U_{eq} values of the C atoms to which they are attached by a factor of 1.5. The final anisotropic refinement of all the non-hydrogen atoms, except for the disordered O atoms, (390 parameters) led to $R_1 = 0.0524$ and $wR_2 = 0.1144$ for reflections with $I > 2\sigma(I)$. The atomic coordinates in structure **I** have been deposited with the Cambridge Structural Database (CCDC deposit no. 198 687).

Structure **I** consists of isolated cationic complexes $[Yb(DMAA)_6]^{3+}$ (Fig. 1) and heteropolyanions $PW_{12}O_{40}^{3-}$. Both the cationic complexes and the heteropolyanions are located at the centers of symmetry. The Yb–O distances are 2.163(10), 2.194(8), and 2.194(9) Å. The coordination polyhedron of the Yb atom is a slightly distorted octahedron in which the largest angular deviation from 90° is 2.1°. In complex **I**, unlike Nd-containing complex **II**, which has a similar composition, the O atoms of the heteropolyanion are not included in the first coordination sphere. Note that, in the Cambridge Structural Database, there are no data

for *f*-element complexes with the first coordination sphere completely occupied by the *DMAA* molecules.

The structure of the heteropolyanion in **I** deserves detailed consideration. It is known that the symmetry of the heteropolyanion with a Keggin structure (α isomer) is T_d [5]. This anion consists of twelve MO_6 octahedra, which are arranged in four M_3O_{13} triangular units and linked through common vertices. The heteroatom is situated at the center of the anion. In each triad, one O atom is shared by three octahedra. Four oxygen atoms of this type form the tetrahedral environment of the heteroatom. Each MO_6 octahedron contains one terminal O_{term} atom, which lies in the *trans* position relative to the central atom of the triad bound to the heteroatom. Each octahedron also contains four bridging O atoms, two of which link the *M* atoms within a triad and the other two link the *M* atoms of different triads. The former O atoms are involved in the edge sharing of octahedra in the triad, and the latter O atoms are the corners shared by the neighboring triads.

In some structures, the Keggin heteropolyanions occupy special positions whose symmetry violates the anion's own symmetry (T_d) [6–11]. Two variants of structural description were proposed for such cases, namely, the Keggin structure with a disorder corresponding to the site symmetry of the anion [6] and the pseudo-Keggin structure in which the symmetry of the anion is increased to O_h [7]. In the latter case, the O_{term}–*M* axes of the MO_5 pyramids are directed toward the center of the anion and the oxygen tetrahedron about the heteroatom is statistically disordered over two orientations so that the O atoms form a cube with half-occupied vertices. A more detailed discussion of these variants is given in [5]. In both cases, the *M* atoms form a regular cubooctahedron. Note that the splitting of the positions has been observed experimentally only for the O atoms of the tetrahedral environment of the heteroatom, whereas the possible splitting of the positions of the remaining O atoms revealed itself only in the shape and size of the thermal ellipsoids [12].

In structure **I**, the heteropolyanion is located at the center of symmetry and the positions of all the O atoms are split (Fig. 2). In order to clarify whether this splitting corresponds to the Keggin structure with disordering, we compare the distances in the heteropolyanions of structures **I** and **II** [1]. In the latter structure, the W···W distances between the neighboring atoms in the heteropolyanion fall into two groups with mean values of 3.420(2) and 3.698(2) Å. These groups consist of the distances in the triad and between the triads, respectively. In the disordered heteropolyanion, the split positions of the W atoms should be approximately 0.2 Å distant from each other, which cannot be distinguished in the Fourier electron-density map. In structure **I**, all the W···W distances have close values. Their average is 3.560(2) Å, which coincides with the average of the distances of two types in complex **II**. The splitting of the positions of the O atoms that bridge two W atoms is

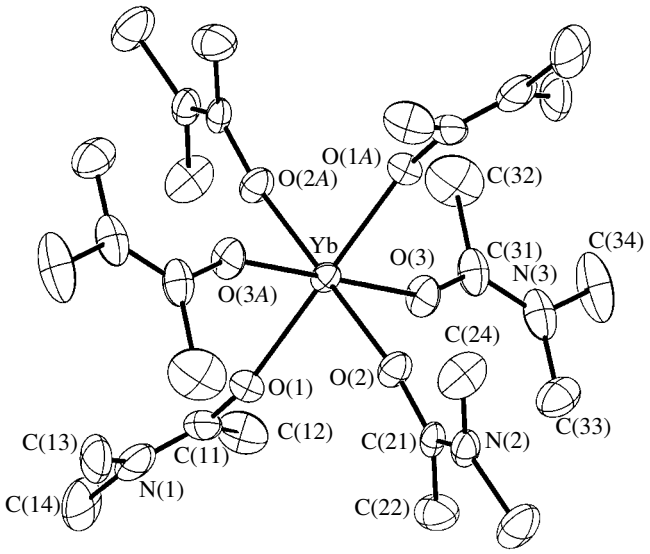

Fig. 1. Centrosymmetric cationic complex $[Yb(DMAA)_6]^{3+}$ in structure **I**. Thermal ellipsoids are shown at the 20% probability level. The hydrogen atoms are omitted.

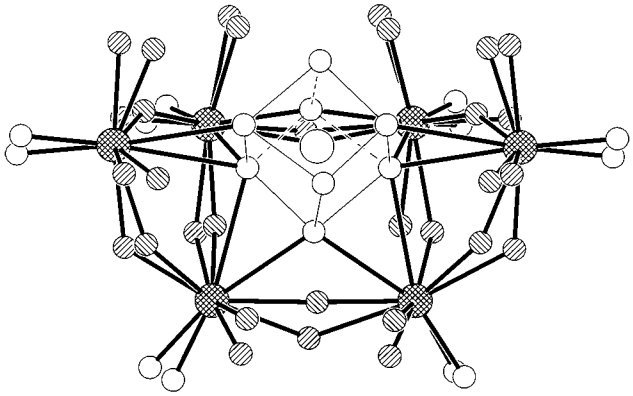

Fig. 2. A fragment of the $PW_{12}O_{40}^{3-}$ heteropolyanion in structure **I**. Two types of bridging O atoms (see text) are shown by different hatching.

of particular interest. This splitting can be most conveniently judged from the comparison of the P···O_{br} distances. In structure **II**, the mean P···O_{br} distances are 3.940(3) Å (in triads) and 3.378(3) Å (between triads). In complex **I**, the P···O_{br} distances fall into two groups with mean values of 3.93(2) and 3.40(2) Å, which coincide with the distances for two types of bridging atoms in the heteropolyanion. Thus, we conclude that the heteropolyanion in **I** has a Keggin structure and its disordering is a consequence of the centrosymmetric position.

REFERENCES

1. I. B. Shirokova, M. S. Grigor'ev, V. I. Makarenkov, *et al.*, Koord. Khim. **27**, 772 (2001).

2. A. L. Spek, *PLATON: Multipurpose Crystallographic Tool* (Univ. of Utrecht, Netherlands, 1998).
3. G. M. Sheldrick, Acta Crystallogr., Sect. A: Found. Crystallogr. **46**, 467 (1990).
4. G. M. Sheldrick, *SHELXL93: Program for the Refinement of Crystal Structures* (Univ. of Göttingen, Germany, 1993).
5. M. A. Poraĭ-Koshits and L. O. Atovmyan, Itogi Nauki Tekh., Ser.: Kristallokhim. **19**, 3 (1985).
6. V. S. Sergienko, M. A. Poraĭ-Koshits, M. A. Fedotov, *et al.*, Zh. Strukt. Khim. **18**, 976 (1977).
7. V. S. Sergienko, M. A. Poraĭ-Koshits, and É. N. Yurchenko, Zh. Strukt. Khim. **21**, 111 (1980).
8. A. Suten and L. Mizz, Rev. Roum Chim. **15**, 1563 (1970).
9. R. Björnberg and B. Hedman, Acta Crystallogr., Sect. B: Struct. Crystallogr. Cryst. Chem. **36**, 1018 (1980).
10. J. Fuchs, A. Thiele, and P. Palm, Z. Kristallogr. **376**, 1418 (1982).
11. K. Nishikava and Y. Sasaki, Bull. Chem. Soc. Jpn. **48**, 3152 (1975).
12. H. T. Evans and M. T. Pope, Inorg. Chem. **23**, 501 (1984).

Translated by I. Polyakova

Crystallography Reports, Vol. 48, No. 4, 2003, pp. 641–648. Translated from Kristallografiya, Vol. 48, No. 4, 2003, pp. 691–698.

STRUCTURE OF ORGANIC COMPOUNDS

Polymorphism of Dianilinegossypol

K. M. Beketov[1, 2], S. A. Talipov[1], B. T. Ibragimov[1], K. D. Praliev[2], and T. F. Aripov[1]

[1] *Institute of Bioorganic Chemistry, Tashkent, Uzbekistan*
e-mail: root@ibc.tashkent.su

[2] *Beturov Institute of Chemical Sciences, Academy of Sciences of Kazakhstan, ul. Krasina 106, Almaty, 480100 Kazakhstan*

Received April 18, 2002

Abstract—Polymorphs of dianilinegossypol are obtained by selecting the precipitation medium and the crystallization temperature. Four dianilinegossypol polymorphs are found. Two solvate forms and three polymorphic modifications of dianilinegossypol are prepared from an acetone solution by varying the crystallization temperature from room temperature to 60°C. The crystal structures of the **P1**, **P2**, and **P4** polymorphs are determined. The **P1** and **P2** polymorphs are characterized by the same hydrogen-bond system, but their crystal structures differ in the mode of packing of layers formed by dimers of dianilinegossypol molecules. In the **P4** polymorph, homochiral hydrogen-bonded dianilinegossypol molecules form trimers. This mode of H-agglomeraton of dianilinegossypol molecules is characteristic only of the **P4** polymorph. *© 2003 MAIK "Nauka/Interperiodica".*

INTRODUCTION

In recent years, interest expressed by researchers in studies of the tendency of organic compounds to polymorphism or pseudopolymorphism (solvate formation) has been increasing, because, in many cases, this research gives an insight into the origin of the inconstancy of physicochemical properties of biologically active compounds [1–3]. As a rule, routine systematic studies concerned with this problem take plenty of time [4–6]. For some substances, the results obtained in reexaminations of the polymorphic behavior were in conflict with the earlier data [7–9]. Such studies are mainly concerned with low-molecular organic compounds, which are of interest for the chemical and pharmaceutical industries. However, recent development of high technologies has initiated the investigation of protein polymorphism [10].

One of the representative examples of the aforesaid is a physiologically active natural compound, namely, gossypol. This compound has been the subject of investigation over the course of more than a century [11–16]. Many researchers noted the inconstancy of some physicochemical parameters of gossypol (melting point, solubility), but the nature of this phenomenon has long defied explanation [11, 12, 16–19]. A systematic study of the tendency of gossypol to polymorphism and solvate formation revealed that this compound can exist in seven crystalline nonsolvate modifications (polymorphs) and forms numerous molecular complexes with practically all the liquid low-molecular solvents (more than 120 examples) [20, 21]. We have performed analogous investigations of gossypol derivatives in order to find out if the specific features of gossypol are characteristic of its derivatives [22–26]. This paper concentrates on the study of polymorphism of a well-known and easily preparable gossypol derivative, namely, dianilinegossypol.

EXPERIMENTAL

The polymorphs of dianilinegossypol were obtained by the condensation reaction between gossypol and aniline. For this purpose, aniline (0.005 ml) was added to a gossypol solution (approximately 100 mg of gossypol in 4–6 ml of a solvent). The solutions were placed in thermostats. The temperature conditions for the formation of single crystals of the polymorphs suitable for X-ray diffraction studies were chosen empirically. Crystals of the **P1** and **P2** polymorphs were obtained from acetone solutions at 45 and 40°C, respectively, and crystals of the **P3** polymorph were obtained from a dichloroethane solution at 40°C. The **P4** polymorph was obtained at 60°C from an ethyl acetate solution. The time of forming single crystals varied from two to three hours. The choice of crystallization conditions was governed by the formation of high-quality single crystals for X-ray diffraction studies. The crystallization of this or that modification was checked by recording the diffraction patterns of the corresponding samples (DRON-2.0 diffractometer) or determining the crystallographic parameters (Syntex $P2_1$ diffractometer).

The crystallographic parameters of the polymorphs of dianilinegossypol were determined and refined on a Syntex $P2_1$ four-circle automated diffractometer with the use of 15 reflections (Table 1). The complete X-ray diffraction studies were performed only for the **P1**, **P2**, and **P4** polymorphs.

The integrated intensities of 3645, 8840, and 7042 reflections for **P1**, **P2**, and **P4**, respectively, were mea-

1063-7745/03/4804-0641$24.00 © 2003 MAIK "Nauka/Interperiodica"

Table 1. Crystallographic parameters of dianilinegossypol polymorphs

Parameter	Polymorph			
	P1	**P2**	**P3**	**P4**
a, Å	12.741(8)	11.458(2)	11.521(6)	50.972(27)
b, Å	30.191(9)	12.374(2)	30.21(1)	9.600(3)
c, Å	9.814(5)	26.003(7)	20.85(1)	23.066(6)
α, deg	90	82.99(2)	90	90
β, deg	110.60(5)	96.38(2)	104.16(4)	110.43(3)
γ, deg	90	74.33(1)	90	90
V, Å^3	3533	3483	7036	10527
Space group	$P2_1/c$	$P\bar{1}$	$P2_1/c$	$C2/c$
Z	4	4	8	12
D_x, g/cm^3	1.26	1.27	1.24	1.26

sured by the θ/2θ scan mode using CuK_α radiation monochromatized by reflecting from a graphite crystal. After correction for the Lorentz and polarization effects and rejection of weak $I < 2\sigma(I)$ reflections, the data sets contained 2078, 4528, and 4297 reflections for **P1**, **P2**, and **P4**, respectively. The structures were solved by direct methods with the SHELXS86 program package [27] adapted to an IBM-486 personal computer.

The structures were refined with the SHELXL93 software package [28]. The hydrogen atoms of the molecules were located from the difference Fourier syntheses. Finally, the refinement of the positional and anisotropic thermal parameters led to discrepancy factors of 0.127 for **P1**, 0.110 for **P2**, and 0.070 for **P4**. The atomic coordinates are listed in Table 2. The molecular graphics was performed with the XP program [29] included in the SHELXTL-Plus software package.

RESULTS AND DISCUSSION

Molecular Structures of the Polymorphs

The gossypol molecule can exist in three tautomeric forms, namely, the aldehyde, quinoid, and lactol forms [15]. In crystals, a dianilinegossypol molecule exists in a quinoid tautomeric form and consists of two identical fragments connected by a single C(2)–C(12) bond, which makes the molecule flexible (Fig. 1). The dihedral angles between the naphtyl nuclei in the polymorphs of dianilinegossypol vary between 75.3° and 94.8°. The aniline rings form different angles with the corresponding naphtyl nuclei (from 5.3° to 48.9°, Table 3). The orientation of the isopropyl groups in all the polymorphs is identical. The H(23) and H(28) hydrogen atoms of the isopropyl groups are directed toward the H(4) and H(14) atoms, respectively.

Crystal Structures of the Polymorphs

In the structure of the **P1** polymorph, the dianilinegossypol molecules form dimers through two centrosymmetric pairs of O(5)–H···O(3) and O(4)–H···O(5) hydrogen bonds. The geometric characteristics of the hydrogen bonds are listed in Table 4.

In the crystal of the **P1** polymorph, the O(1)–H···O(7) hydrogen bonds are formed between the centrosymmetric dimers related by the glide planes (Table 4). These hydrogen bonds (Fig. 2) are characteristic only of the **P1** and **P2** polymorphic modifications. The O(1)–H···O(7) hydrogen bonds link molecules into layers parallel to the *yz* plane. The layers are linked only through the van der Waals interactions. The crystal structure of the **P1** polymorph is shown in Fig. 3a.

The **P2** polymorph crystallizes in space group $P\bar{1}$ with two molecules of dianilinegossypol in the asymmetric unit (Table 1). In the structure of this polymorph, two independent dianilinegossypol molecules (*A* and *B*) are linked through centrosymmetric pairs of O(5)–H···O(3) and O(4)–H···O(5) hydrogen bonds (Table 4) into the *AA* and *BB* dimers. The O(1*A*)–H···O(7*B*) and O(1*B*)–H···O(7*A*) hydrogen bonds link the neighboring *AA* and *BB* dimers (Table 4) into layers parallel to the (011) plane. The packing of these layers results in the formation of the crystal structure of the **P2** polymorph (Fig. 3b).

Thus, the **P1** and **P2** polymorphs are characterized by the same hydrogen-bond system, but their crystal structures differ in the mode of packing of layers consisting of dimers of dianilinegossypol molecules. In the structure of the **P1** polymorph, the dimers of the neighboring layers are situated over one another, whereas the dimers in the **P2** polymorph are located between the regions of the adjacent layers, in which hydrogen bonds connect the dimers.

The **P4** polymorph crystallizes in space group *C*2/*c* with one and a half molecules in the asymmetric unit (molecules *A* and *B*). Molecules *A* occupy special positions, and molecules *B* occupy general positions. Molecule *A* lies in the twofold axis and forms the O(1*A*)–H···O(4*B*) and O(5*B*)–H···O(4*A*) hydrogen bonds with two *B* molecules. As a result, a hydrogen-bonded trimer is formed from the dianilinegossypol molecules of the same chirality (Fig. 4). This mode of H-agglomeration of dianilinegossypol molecules is a characteristic feature only of the **P4** polymorph (Table 4).

Molecules *B*, in turn, are linked through centrosymmetric pairs of the O(1*B*)–H···O(7*B*) and O(8*B*)–H···O(1*B*) hydrogen bonds (Table 4) with two neighboring trimers of opposite chirality into columns of dianilinegossypol molecules. The packing of these columns results in the formation of the crystal structure of the **P4** polymorph (Fig. 5).

Table 2. Atomic coordinates ($\times 10^4$) and equivalent isotropic thermal parameters ($Å^2 \times 10^3$) in structures of dianilinegossypol polymorphs

Atoms	*x*/*a*	*y*/*b*	*z*/*c*	U_{eq}	Atoms	*x*/*a*	*y*/*b*	*z*/*c*	U_{eq}
P1 polymorph					**P2** polymorph				
C(1)	3276(9)	5694(3)	150(12)	38(3)	C(1*A*)	272(2)	4793(5)	−1111(2)	40(2)
C(2)	2521(9)	5915(3)	−1008(13)	41(3)	C(2*A*)	−600(6)	4463(5)	−1551(2)	37(2)
C(3)	1879(10)	5676(3)	−2221(14)	52(3)	C(3*A*)	−1567(6)	3465(5)	−1586(2)	41(2)
C(4)	1997(9)	5214(3)	−2210(13)	50(3)	C(4*A*)	−1612(6)	2860(5)	−1174(2)	46(2)
C(5)	2852(10)	4498(3)	−1092(12)	41(3)	C(5*A*)	−830(6)	2503(5)	−293(2)	47(2)
C(6)	3622(10)	4303(3)	13(14)	44(3)	C(6*A*)	22(6)	2878(6)	136(2)	46(2)
C(7)	4441(10)	4528(4)	1221(13)	44(3)	C(7*A*)	1026(6)	3897(6)	206(2)	44(2)
C(8)	4343(9)	4996(3)	1373(11)	34(3)	C(8*A*)	1214(6)	4499(5)	−226(2)	39(2)
C(9)	3509(8)	5226(3)	218(12)	32(3)	C(9*A*)	283(6)	4166(5)	−687(2)	39(2)
C(10)	2775(8)	4992(3)	−1014(12)	37(3)	C(10*A*)	−726(6)	3175(5)	−725(2)	42(2)
C(11)	3017(9)	6691(3)	−1400(12)	41(3)	C(11*A*)	−1059(5)	6014(5)	−2012(2)	37(2)
C(12)	2349(9)	6402(3)	−976(12)	39(3)	C(12*A*)	−516(5)	5142(5)	−1995(2)	38(2)
C(13)	1463(9)	6585(3)	−617(11)	38(3)	C(13*A*)	108(5)	4893(5)	−2410(2)	39(2)
C(14)	1312(9)	7038(3)	−700(12)	42(3)	C(14*A*)	110(5)	5495(5)	−2822(2)	41(2)
C(15)	1732(8)	7809(3)	−1231(10)	29(3)	C(15*A*)	−502(5)	6892(5)	−3317(2)	38(2)
C(16)	2470(9)	8079(3)	−1577(12)	41(3)	C(16*A*)	−1199(6)	7603(6)	−3359(2)	56(2)
C(17)	3360(9)	7924(3)	−2027(12)	39(3)	C(17*A*)	−1887(6)	7895(6)	−2959(2)	56(2)
C(18)	3519(9)	7457(3)	−2087(12)	39(3)	C(18*A*)	−1817(5)	7434(5)	−2484(2)	39(2)
C(19)	2873(8)	7157(3)	−1542(11)	35(3)	C(19*A*)	−1127(5)	6616(5)	−2440(2)	38(2)
C(20)	1974(8)	7332(3)	−1124(11)	35(3)	C(20*A*)	−499(5)	6332(5)	−2855(2)	37(2)
C(21)	1013(11)	5887(4)	−3569(13)	82(5)	C(21*A*)	−2523(6)	3030(6)	−2069(2)	60(2)
C(22)	5056(9)	5197(4)	2641(13)	44(3)	C(22*A*)	2335(6)	5316(5)	−198(2)	44(2)
C(23)	1987(11)	4234(4)	−2326(15)	69(4)	C(23*A*)	−1873(6)	1393(6)	−337(3)	65(2)
C(24)	2449(14)	3891(5)	−3056(17)	118(6)	C(24*A*)	−1372(7)	376(6)	−321(3)	91(3)
C(25)	978(12)	4143(5)	−1995(18)	122(7)	C(25*A*)	−2702(7)	1464(7)	79(3)	89(2)
C(26)	682(10)	6292(3)	−144(14)	64(4)	C(26*A*)	737(6)	3967(5)	−2419(2)	62(2)
C(27)	4296(8)	7313(3)	−2712(11)	38(3)	C(27*A*)	−2454(6)	7797(5)	−2101(2)	44(2)
C(28)	658(9)	8008(3)	−1115(12)	39(3)	C(28*A*)	183(6)	6590(5)	−3756(2)	44(2)
C(29)	–375(9)	7860(4)	−2330(12)	58(4)	C(29*A*)	−617(6)	5510(6)	−4113(3)	72(2)
C(30)	532(10)	7982(4)	368(12)	64(4)	C(30*A*)	647(6)	7529(6)	−4081(2)	66(2)
C(31)	6555(10)	5120(4)	5027(12)	47(3)	C(31*A*)	4403(6)	6365(5)	253(2)	42(2)
C(32)	7387(12)	4843(5)	5802(16)	79(4)	C(32*A*)	4998(6)	6372(6)	−179(3)	56(2)
C(33)	8120(16)	4968(7)	7131(21)	118(7)	C(33*A*)	6212(7)	7013(7)	−130(3)	71(2)
C(34)	8090(15)	5381(8)	7649(19)	117(7)	C(34*A*)	6829(7)	7636(6)	338(4)	75(2)
C(35)	7261(14)	5672(6)	6886(16)	85(5)	C(35*A*)	6216(8)	7636(6)	766(3)	75(2)
C(36)	6476(11)	5538(4)	5527(14)	65(4)	C(36*A*)	5005(7)	7005(6)	724(3)	58(2)
C(37)	5685(9)	7464(3)	−3835(12)	39(3)	C(37*A*)	−3778(6)	8931(5)	−1804(2)	48(2)
C(38)	6219(10)	7795(4)	−4301(13)	55(3)	C(38*A*)	−4041(7)	8481(6)	−1357(3)	63(2)
C(39)	6998(11)	7696(5)	−4952(13)	69(4)	C(39*A*)	−4740(8)	8907(7)	−1042(3)	79(2)
C(40)	7264(11)	7265(5)	−5159(15)	69(4)	C(40*A*)	−5192(7)	9781(7)	−1164(3)	82(3)
C(41)	6770(12)	6940(5)	−4633(15)	78(4)	C(41*A*)	−4959(7)	10229(6)	−1611(3)	77(2)
C(42)	5992(11)	7028(4)	−3986(14)	64(4)	C(42*A*)	−4241(6)	9807(6)	−1931(3)	61(2)
N(1)	5811(8)	4974(3)	3658(10)	49(3)	N(1*A*)	3186(5)	5673(4)	226(2)	46(1)
N(2)	4909(7)	7580(3)	−3215(10)	46(3)	N(2*A*)	−3090(5)	8526(5)	−2160(2)	54(2)
O(1)	3919(6)	5930(2)	1351(8)	49(2)	O(1*A*)	1187(4)	5790(3)	−1062(1)	50(1)
O(3)	5169(7)	4285(2)	2135(9)	59(2)	O(3*A*)	1761(4)	4175(4)	641(1)	51(1)
O(4)	3711(6)	3848(2)	76(9)	65(3)	O(4*A*)	1(4)	2282(4)	549(2)	62(1)
O(5)	3845(6)	6512(2)	−1853(8)	52(2)	O(5*A*)	−1637(4)	6287(4)	−1599(1)	52(1)
O(7)	3892(6)	8230(2)	−2454(8)	54(2)	O(7*A*)	−2514(5)	8576(4)	−3060(2)	74(2)
O(8)	2343(6)	8530(2)	−1582(9)	65(3)	O(8*A*)	−1326(4)	8114(4)	−3788(2)	83(2)

Table 2. (Contd.)

Atoms	*x*/*a*	*y*/*b*	*z*/*c*	U_{eq}	Atoms	*x*/*a*	*y*/*b*	*z*/*c*	U_{eq}
		P2 polymorph					**P4** polymorph		
C(1*B*)	5367(6)	8196(5)	−4421(2)	38(2)	C(1*A*)	314(1)	−623(6)	7467(2)	56(1)
C(2*B*)	4497(6)	7310(5)	−4287(2)	39(2)	C(2*A*)	156(1)	−1555(6)	7662(3)	59(2)
C(3*B*)	3529(6)	6663(5)	−4674(2)	46(2)	C(3*A*)	288(1)	−2404(6)	8169(3)	60(2)
C(4*B*)	3433(6)	6962(5)	−5168(2)	50(2)	C(4*A*)	578(1)	−2314(6)	8459(3)	59(2)
C(5*B*)	4185(6)	8176(5)	−5827(2)	48(2)	C(5*A*)	1045(1)	−1261(5)	8660(2)	50(1)
C(6*B*)	5065(6)	9039(6)	−5948(2)	47(2)	C(6*A*)	1180(1)	−174(6)	8471(2)	50(1)
C(7*B*)	6100(6)	9729(5)	−5581(2)	42(2)	C(7*A*)	1060(1)	727(6)	7952(2)	54(1)
C(8*B*)	6283(6)	9405(5)	−5073(2)	40(2)	C(8*A*)	776(1)	532(6)	7557(2)	52(1)
C(9*B*)	5359(6)	8507(5)	−4922(2)	35(2)	C(9*A*)	610(1)	−475(5)	7747(2)	50(1)
C(10*B*)	4330(6)	7876(5)	−5303(2)	44(2)	C(10*A*)	739(1)	−1359(5)	8263(2)	51(1)
C(11*B*)	3969(5)	7431(5)	−3378(2)	39(2)	C(21*A*)	122(1)	−3417(7)	8398(3)	91(2)
C(12*B*)	4574(6)	6982(5)	−3748(2)	43(2)	C(22*A*)	679(1)	1291(6)	7007(3)	58(2)
C(13*B*)	5186(6)	6198(6)	−3626(2)	52(2)	C(23*A*)	1192(1)	−2334(6)	9083(2)	53(1)
C(14*B*)	5113(6)	5831(5)	−3150(2)	55(2)	C(24*A*)	1217(1)	−1892(8)	9728(3)	91(2)
C(15*B*)	4379(6)	5747(5)	−2290(2)	50(2)	C(25*A*)	1483(1)	−2756(6)	9071(3)	78(2)
C(16*B*)	3653(6)	6066(6)	−1972(2)	52(2)	C(31*A*)	745(1)	3008(6)	6283(3)	68(2)
C(17*B*)	3015(6)	6891(6)	−2058(2)	49(2)	C(32*A*)	944(2)	3529(9)	6069(4)	101(2)
C(18*B*)	3152(5)	7435(5)	−2510(2)	38(2)	C(33*A*)	865(2)	4356(10)	5553(4)	128(3)
C(19*B*)	3873(5)	7061(5)	−2889(2)	37(2)	C(34*A*)	595(3)	4677(10)	5257(4)	138(4)
C(20*B*)	4464(6)	6217(5)	−2779(2)	43(2)	C(35*A*)	391(2)	4161(10)	5465(4)	145(4)
C(21*B*)	2605(6)	5619(6)	−4563(2)	66(2)	C(36*A*)	463(1)	3335(8)	5997(4)	107(3)
C(22*B*)	7411(6)	9951(5)	−4759(2)	46(2)	O(1*A*)	186(1)	218(4)	6968(2)	86(1)
C(23*B*)	3095(8)	7488(7)	−6240(3)	83(3)	O(3*A*)	1224(1)	1620(4)	7850(2)	73(1)
C(24*B*)	3507(10)	6717(7)	−6635(3)	144(5)	O(4*A*)	1453(1)	147(4)	8814(2)	63(1)
C(25*B*)	2390(7)	8181(7)	−6517(3)	92(3)	N(1*A*)	832(1)	2195(5)	6833(2)	65(1)
C(26*B*)	5855(7)	5720(6)	−4026(3)	85(3)	C(1*B*)	3616(1)	2288(5)	156(2)	37(1)
C(27*B*)	2582(6)	8296(5)	−2551(2)	44(2)	C(2*B*)	3456(1)	2965(5)	−378(2)	43(1)
C(28*B*)	5009(6)	4838(6)	−2180(2)	56(2)	C(3*B*)	3586(1)	3812(6)	−685(2)	52(1)
C(29*B*)	4142(7)	3652(7)	−2375(3)	91(3)	C(4*B*)	3876(1)	3922(6)	−455(2)	51(1)
C(30*B*)	5553(7)	4972(7)	−1604(3)	79(3)	C(5*B*)	4345(1)	3479(6)	314(3)	55(1)
C(31*B*)	9439(6)	11282(6)	−4549(2)	48(2)	C(6*B*)	4495(1)	2899(6)	860(3)	59(2)
C(32*B*)	10029(7)	10590(6)	−4325(3)	65(2)	C(7*B*)	4381(1)	2067(6)	1226(3)	54(1)
C(34*B*)	11712(8)	12215(9)	−3941(3)	104(3)	C(8*B*)	4086(1)	1841(5)	1017(2)	42(1)
C(33*B*)	11159(8)	11068(8)	−4017(3)	83(3)	C(9*B*)	3915(1)	2445(5)	431(2)	39(1)
C(35*B*)	11097(9)	12875(8)	−4175(4)	108(4)	C(10*B*)	4043(1)	3270(5)	90(2)	44(1)
C(36*B*)	9973(7)	12438(7)	−4482(3)	78(3)	C(11*B*)	2976(1)	3537(5)	−390(2)	39(1)
C(37*B*)	1333(6)	9456(6)	−2186(3)	56(2)	C(12*B*)	3144(1)	2755(5)	−624(2)	41(1)
C(38*B*)	1169(9)	9991(7)	−2604(3)	102(3)	C(13*B*)	3022(1)	1816(6)	−1109(2)	52(1)
C(39*B*)	515(11)	10787(9)	−2562(5)	150(5)	C(14*B*)	2733(1)	1750(5)	−1359(2)	56(1)
C(40*B*)	60(11)	11017(9)	−2105(5)	147(5)	C(15*B*)	2253(1)	2446(5)	−1417(2)	43(1)
C(41*B*)	263(10)	10498(9)	−1692(4)	122(4)	C(16*B*)	2097(1)	2993(5)	−1114(2)	44(1)
C(42*B*)	872(8)	9698(7)	−1736(3)	86(3)	C(17*B*)	2206(1)	3865(5)	−572(2)	42(1)
N(1*B*)	8273(5)	10820(4)	−4860(2)	49(1)	C(18*B*)	2499(1)	4157(5)	−338(2)	37(1)
N(2*B*)	1951(5)	8604(4)	−2199(2)	48(1)	C(19*B*)	2677(1)	3428(5)	−611(2)	37(1)
O(1*B*)	6300(4)	8833(3)	−4030(2)	50(1)	C(20*B*)	2556(1)	2554(5)	−1127(2)	44(1)
O(3*B*)	6841(4)	10557(4)	−5732(2)	54(1)	C(21*B*)	3417(1)	4614(7)	−1256(3)	80(2)
O(4*B*)	5004(4)	9297(4)	−6443(2)	60(1)	C(22*B*)	3981(1)	1092(5)	1410(2)	48(1)
O(5*B*)	3393(4)	8222(3)	−3496(1)	48(1)	C(23*B*)	4487(1)	4314(8)	−46(3)	92(2)
O(7*B*)	2370(4)	7110(4)	−1710(2)	60(1)	C(24*B*)	4620(2)	5618(9)	266(5)	143(4)
O(8*B*)	3462(4)	5610(4)	−1523(2)	73(2)	C(25*B*)	4668(2)	3471(10)	−307(4)	139(4)

Table 2. (Contd.)

Atoms	*x*/*a*	*y*/*b*	*z*/*c*	U_{eq}	Atoms	*x*/*a*	*y*/*b*	*z*/*c*	U_{eq}
P4 polymorph					**P4** polymorph				
C(26*B*)	3195(1)	880(7)	−1344(3)	85(2)	C(39*B*)	2362(1)	8402(7)	1484(3)	80(2)
C(27*B*)	2592(1)	5169(5)	124(2)	40(1)	C(40*B*)	2629(1)	8928(7)	1719(3)	77(2)
C(28*B*)	2120(1)	1755(6)	−2045(2)	61(2)	C(41*B*)	2831(1)	8449(7)	1503(3)	71(2)
C(29*B*)	1995(2)	357(7)	−2006(3)	137(4)	C(42*B*)	2769(1)	7440(6)	1052(2)	55(1)
C(30*B*)	1901(1)	2675(7)	−2511(3)	87(2)	O(1*B*)	3491(1)	1398(4)	443(1)	49(1)
C(31*B*)	4037(1)	−249(6)	2335(2)	55(1)	O(3*B*)	4552(1)	1569(5)	1725(2)	76(1)
C(32*B*)	3768(1)	−95(7)	2336(3)	73(2)	O(4*B*)	4784(1)	3008(5)	1126(2)	90(2)
C(33*B*)	3676(2)	−907(9)	2714(3)	104(3)	O(5*B*)	3097(1)	4433(4)	91(1)	54(1)
C(34*B*)	3852(2)	−1847(10)	3110(4)	114(3)	O(7*B*)	2030(1)	4378(4)	−350(1)	49(1)
C(35*B*)	4124(2)	−1979(8)	3108(3)	102(2)	O(8*B*)	1810(1)	2860(4)	−1334(2)	60(1)
C(36*B*)	4217(1)	−1161(7)	2740(3)	76(2)	N(1*B*)	4135(1)	529(5)	1942(2)	54(1)
C(37*B*)	2505(1)	6890(5)	820(2)	43(1)	N(2*B*)	2430(1)	5817(4)	371(2)	45(1)
C(38*B*)	2302(1)	7370(6)	1031(3)	65(2)					

Table 3. Dihedral angles (deg) in molecules of dianilinegossypol polymorphs

Polymorph	Molecule	Angle		
		AB^CD	**AB^E**	**CD^E**
P1		81.7	14.2	9.3
P2	*A*	85.7	48.9	6.1
	B	87.6	46.2	5.7
P4	*A*	94.8	19.9	–
	B	75.3	24.4	12.3

Crystallization of Dianilinegossypol Polymorphs at Different Temperatures

Polymorphic modifications of dianilinegossypol were obtained by crystallization from solutions in the temperature range 40–220°C. The following solvents were used for the experiments: acetone, methyl acetate, ethyl acetate, butyl acetate, amyl acetate, ethanol, butanol, acetic and valeric acids, cyclopentanone, cyclohexanone, CCl_4, toluene, 1,2-dichloroethane, and

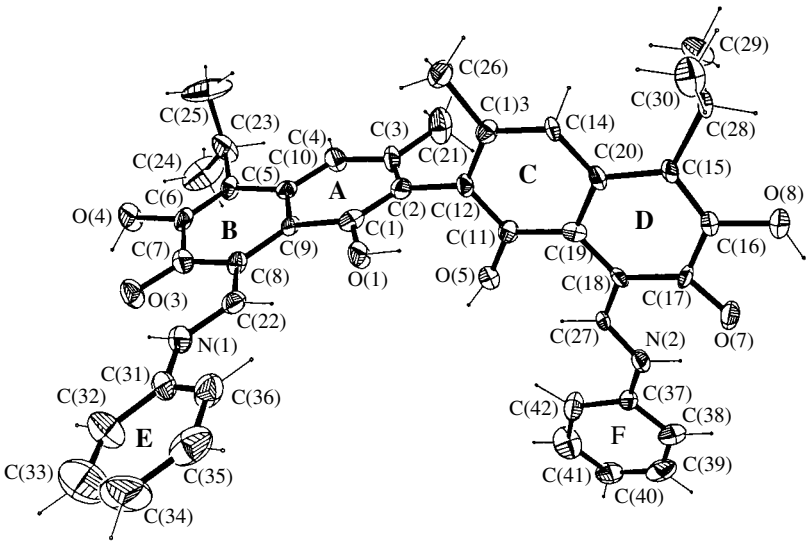

Fig. 1. Molecular structure of dianilinegossypol (the **P1** polymorph) and the atomic numbering.

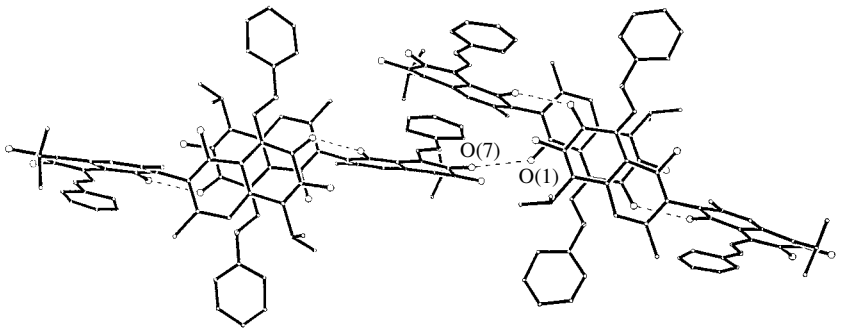

Fig. 2. H-association of dianilinegossypol molecules in the **P1** and **P2** polymorphs.

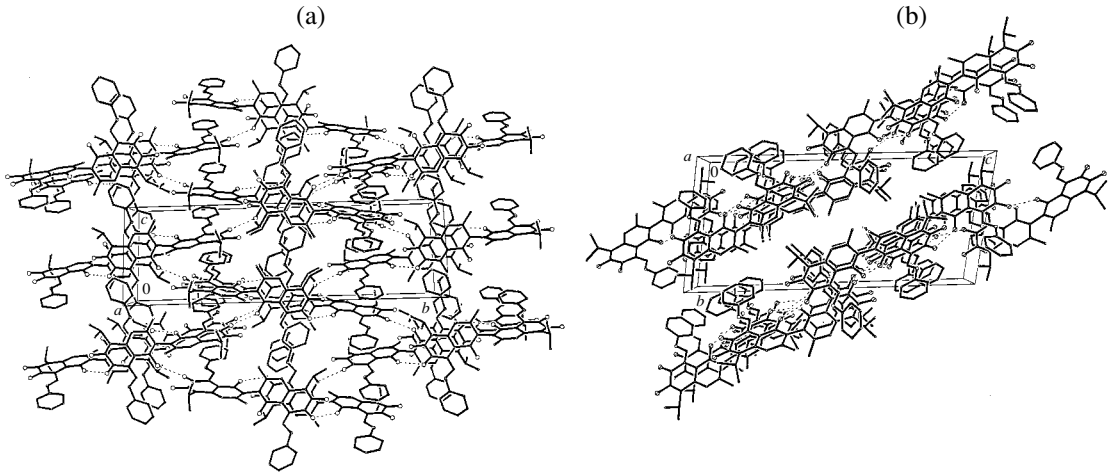

Fig. 3. Structures of (a) **P1** and (b) **P2** polymorphs.

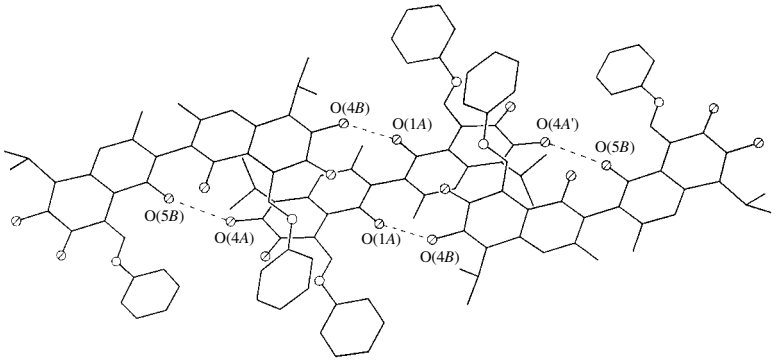

Fig. 4. H-association of dianilinegossypol molecules in the **P4** polymorph.

chloroform. Crystallization of dianilinegossypol at different temperatures revealed the existence of four polymorphic modifications. For all the polymorphs, single crystals were obtained and crystallographic parameters were determined (Table 1). The **P1** polymorph precipitates from ethanol, butanol, acetic and valeric acids, CCl_4, and amyl acetate at room temperature, whereas the **P4** polymorph is formed irrespective of the chemical nature of the solvent at temperatures from 60°C and higher (the temperature was raised to 220°C).

The crystallization of dianilinegossypol from acetone was studied in most detail. The precipitation temperature was raised at 5°C steps. Earlier [25], it was found that, at crystallization temperatures of 20 and

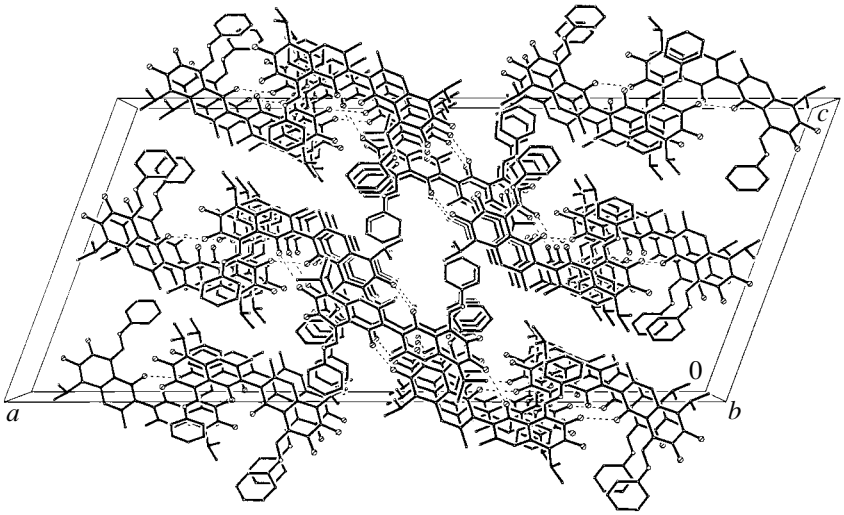

Fig. 5. Structure of the **P4** polymorph.

35°C, the α and β modifications of the host–guest complex between dianilinegossypol and acetone are formed. Further heating to 40 and 45°C resulted in the formation of two polymorphic modifications, **P2** and **P1**, respectively, and starting at 60°C, the **P4** polymorph precipitated. This means that polymorphic transitions between the host–guest complexes and the nonsolvate forms of dianilinegossypol (DAG) take place according to the following scheme: α-dimorph of DAG + acetone ⟶ β-dimorph of DAG + acetone ⟶ **P2** polymorph ⟶ **P1** polymorph ⟶ **P4** polymorph. Thus, by varying the crystallization temperature, one can obtain five crystalline modifications of dianilinegossypol (two solvate and three polymorphic modifications) from acetone solutions.

Very small crystals of the *P*3 polymorph precipitated from 1,2-dichloroethane at 45°C. We determined the unit cell parameters of the **P3** polymorph but failed to prepare single crystals suitable for a complete X-ray diffraction study. Crystallization at 60°C resulted in the formation of the **P4** polymorph. Taking into account that, at room temperature, dianilinegossypol crystallizes in the form of dichloroethane clathrate [26], the total number of crystalline forms obtained from dichloroethane solutions is three (one solvate and two nonsolvate polymorphic forms). Thus, the following transi-

Table 4. Geometric parameters of intermolecular hydrogen bonds in dianilinegossypol polymorphs

Bond	Symmetry	*D*··*A* (Å)	*D*–H (Å)	H··*A* (Å)	*D*–H··*A* (deg)
		P1			
O(1)–H···O(7)	$x, 1.5 - y, 0.5 + z$	2.815	0.92	2.09	142
O(5)–H···O(3)	$1 - x, 1 - y, -z$	2.710	1.05	2.33	135
O(4)–H···O(5)	$1 - x, 1 - y, -z$	3.120	0.92	2.57	133
		P2			
O(1*A*)–H···O(7*B*)		2.700	0.85	2.18	119
O(1*B*)–H···O(7*A*)	$1 + x, y, z$	2.810	0.83	2.03	155
O(5*A*)–H···O(3*A*)	$-x, 1 - y, -z$	2.639	0.96	2.27	102
O(4*A*)–H···O(5*A*)	$-x, 1 - y, -z$	3.110	0.97	2.40	129
O(5*B*)–H···O(3*B*)	$1 - x, 2 - y, -1 - z$	2.681	1.02	1.66	171
O(4*B*)–H···O(5*B*)	$1 - x, 2 - y, -1 - z$	3.105	1.10	2.04	145
		P4			
O(1*A*)–H···O(4*B*)	$x - 0.5, 0.5 - y, 0.5 + z$	2.843	0.85	2.46	108
O(5*B*)–H···O(4*A*)	$0.5 - x, 0.5 - y, 1 - z$	2.785	0.85	2.27	119
O(1*B*)–H···O(7*B*)	$0.5 - x, 0.5 - y, -z$	2.691	0.85	2.00	138
O(8*B*)–H···O(1*B*)	$0.5 - x, 0.5 - y, -z$	2.046	0.85	2.20	170

tions are observed: clathrate ⟶ **P3** polymorph ⟶ **P4** polymorph.

From alcohols and carboxylic acids, dianilinegossypol precipitates in two nonsolvate forms: **P1** at room temperature and **P4** at 60°C (*P*1 polymorph ⟶ **P4** polymorph). The crystallization of dianilinegossypol from solutions in methyl acetate, butyl acetate, chloroform, toluene, cyclopentanone, and cyclohexanone at different temperatures results in the formation of a solvate form of dianilinegossypol followed by the formation of the **P4** polymorph.

Thus, it is easy to obtain all the polymorphic forms of dianilinegossypol by varying the precipitation temperature. However, we failed to obtain all the polymorphs through crystallization from the same solution. It follows that preparation of the given dianilinegossypol polymorph requires the selection of the precipitation medium and temperature.

ACKNOWLEDGMENTS

This study was supported in part by the American Foundation for Civilian Research and Development for the promotion of cooperation with scientists from the New Independent States of the Former Soviet Union, project no. ZC1-2451-TA-02.

REFERENCES

1. T. Laird, in *Comprehensive Medicinal Chemistry*, Ed. by P. D. Kennewell (Pergamon Press, Oxford, 1990), Vol. 1, p. 321.
2. J. K. Haleblian, J. Pharm. Sci. **64**, 1269 (1975).
3. S. R. Byrn, *Solid-State Chemistry of Drugs* (Academic, New York, 1982).
4. K. Sato, J. Phys. D **26**, B77 (1993).
5. W. C. McCrone, in *Physics and Chemistry of the Organic Solid State*, Ed. by D. Fox, M. M. Labes, and A. Weissberger (Interscience, New York, 1965), p. 726.
6. D. Giron, Thermochim. Acta **248**, 1 (1995).
7. W. H. Ojala and M. C. Etter, J. Am. Chem. Soc. **114**, 10288 (1992).
8. R. J. Daley, S. J. Maginn, S. J. Andrews, *et al.*, J. Chem. Soc., Faraday Trans. **90**, 1003 (1994).
9. H. G. Gallagher and J. N. Sherwood, J. Chem. Soc., Faraday Trans. **92** (12), 2107 (1996).
10. M. Kitamura, S. Ueno, and K. Sato, in *Crystallization Processes*, Ed. by H. Othaki (Wiley, Chichester, 1998), Vol. 3, p. 99.
11. A. L. Markman and V. P. Rzhekhin, *Gossypol and Its Deriviatives* (Pishchevaya Promyshlennost', Moscow, 1965).
12. E. P. Clark, J. Biol. Chem. **75**, 725 (1927).
13. K. N. Campbell, R. C. Morris, and R. Adams, J. Am. Chem. Soc. **59**, 1723 (1937).
14. L. Marchlewski, J. Prakt. Chem. **60** (9), 84 (1899).
15. R. Adams, T. A. Geismann, and J. D. Edwards, Chem. Rev. **60**, 555 (1960).
16. J. D. Edwards, J. Am. Chem. Soc. **47**, 441 (1957).
17. Ch. H. Boathner, in *Cottonseed and Cottonseed Products. Their Chemistry and Chemical Technology*, Ed. by A. E. Bailey (Interscience, New York, 1948), p. 213.
18. K. Chander and T. R. Seshardi, J. Sci. Ind. Res., Sect. B **17**, 279 (1958).
19. L. E. Castillion, C. M. Hall, and Ch. H. Boathner, J. Am. Chem. Soc. **25**, 233 (1948).
20. M. Gdaniec, B. T. Ibragimov, and S. A. Talipov, in *Comprahensive Supramolecular Chemistry*, Vol. 6: *Solid State. Supramolecular Chemistry: Crystal Engineering*, Ed. by D. D. MacNicol, E. Toda, and R. Bishop (Pergamon, Oxford, 1996), p. 117.
21. B. T. Ibragimov and S. A. Talipov, J. Inclusion Phenom. Mol. Recognit. Chem. **17**, 325 (1994).
22. K. M. Beketov, B. T. Ibragimov, and S. A. Talipov, Khim. Farmats. **1**, 16 (1996).
23. B. T. Ibragimov, K. M. Beketov, S. A. Talipov, and T. F. Aripov, J. Inclusion Phenom. Mol. Recognit. Chem. **29**, 23 (1997).
24. K. M. Beketov, B. T. Ibragimov, and S. A. Talipov, Khim. Prir. Soedin. **30**, 58 (1994).
25. K. M. Beketov, B. T. Ibragimov, S. A. Talipov, and T. F. Aripov, J. Inclusion Phenom. Mol. Recognit. Chem. **28**, 141 (1997).
26. K. M. Beketov, B. T. Ibragimov, S. A. Talipov, *et al.*, J. Inclusion Phenom. Mol. Recognit. Chem. **27**, 105 (1997).
27. G. M. Sheldrick, Acta Crystallogr., Sect. A: Found. Crystallogr. **46**, 467 (1990).
28. G. M. Sheldrick, *SHELXL93: Program for the Refinement of Crystal Structures* (Univ. of Göttingen, Germany, 1993).
29. *Siemens XP: Molecular Graphics Program, Version 5.03* (Siemens Analytical X-ray Instruments Inst., Madison, Wisconsin, 1994).

Translated by I. Polyakova

Crystallography Reports, Vol. 48, No. 4, 2003, pp. 649–675. Translated from Kristallografiya, Vol. 48, No. 4, 2003, pp. 699–726.

STRUCTURE OF MACROMOLECULAR COMPOUNDS. REVIEW

Piezoelectricity in Crystallizing Ferroelectric Polymers: Poly(vinylidene fluoride) and Its Copolymers (A Review)

V. V. Kochervinskiĭ

Troitsk Institute for Innovation and Thermonuclear Research, Troitsk, Moscow oblast, 142092 Russia

e-mail: kochvae@mail.ru

Received January 28, 2002

Abstract—The piezoelectricity observed in poly(vinylidene fluoride) (PVDF) and its copolymers involves three components that are associated with the presence of at least two phases (crystalline and amorphous) in the polymer structure. The main contributions to the phenomenon observed are made by the size effect and electrostriction, which are related to each other. These contributions manifest themselves through the mechanism of strain-induced reversible transformations of a number of domains of the anisotropic amorphous phase into the crystalline state under the action of mechanical or electrical fields. With due regard for different packings of chains in the amorphous and crystalline phases, this mechanism accounts for the large Poisson ratios μ_{31} obtained for textured films of flexible-chain crystallizing polymers. The dependence of the piezoelectric coefficient d_{32} on the static stress in textured films is governed by the change in the fraction of the crystalline phase due to strong anisotropy of the elastic constants in the film plane. It is shown that the shear deformations of polymers are characterized by a strong piezoelectric response. The specific features revealed in the piezoelectric effect under bending deformations are described for films with an inhomogeneous distribution of polarization over the cross section. The general regularities of the electrostriction in the polymers and inorganic relaxor ferroelectrics studied are considered. © *2003 MAIK "Nauka/Interperiodica".*

CONTENTS

1. INTRODUCTION

Experimental investigations of poly(vinylidene fluoride) (PVDF) [1] have demonstrated that the deformation of textured films after their polarization (exposure to strong fields) induces charges on their surface. This implies that the crystallized polymers exhibit a high piezoelectric activity. Owing to the small *Q*-factor and low acoustic impedance, the above polymeric piezoelectrics have been used as materials for broadband energy converters and sensors of different types in medicine [2, 3].

The characteristic feature of the above materials (and other crystallizing polymers) is the presence of both the crystalline phase and disordered regions in the bulk. For poly(vinylidene fluoride), these regions at room temperature substantially differ from one another in elastic and electrical parameters. Such a structural–dynamic heterogeneity of the systems under consideration can be responsible for the complex mechanism of piezoelectric activity. In this respect, it is necessary to perform a critical analysis of the available experimental data with due regard for the specific features of the polymer structure of the condensed material. To the best of my knowledge, such an approach has never been used before. In the present review, an attempt was made to fill this gap.

2. GENERAL RELATIONSHIPS FOR THE PIEZOELECTRIC EFFECT

By definition, the piezoelectric effect can be described by four piezoelectric coefficients d_{ij}, e_{ij}, g_{ij},

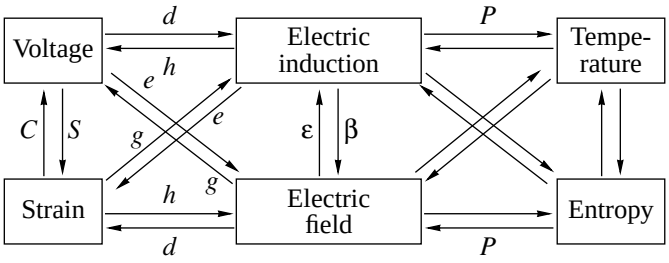

Fig. 1. Schematic diagram of the relation of the electromechanical coefficients for piezoelectric and pyroelectric materials [4].

and h_{ij} [4]:

$$d_{ij} = \left(\frac{\partial D_i}{\partial X_j}\right)^E = \left(\frac{\partial x_i}{\partial E_j}\right)^X,$$
$$e_{ij} = \left(\frac{\partial D_i}{\partial x_j}\right)^E = -\left(\frac{\partial X_i}{\partial E_j}\right)^x,$$
$$g_{ij} = -\left(\frac{\partial E_i}{\partial X_j}\right)^D = \left(\frac{\partial x_i}{\partial D_j}\right)^X, \quad (1)$$
$$h_{ij} = -\left(\frac{\partial E_i}{\partial x_j}\right)^D = -\left(\frac{\partial X_i}{\partial D_j}\right)^x,$$

which relate the electrical characteristics (the electric induction D and the electric field strength E) and the mechanical parameters (the mechanical stress X and the strain x) (Fig. 1).

In relationships (1)–(4), the first terms correspond to the direct piezoelectric effect, the second terms describe the inverse piezoelectric effect, and the subscripts are as follows: i = 1–3 and j = 1–6. The superscripts refer to the experimental conditions: E indicates zero electric field (a closed circuit), D corresponds to zero electric induction (an open circuit), X stands for zero mechanical stress (a free sample), and x denotes zero strain (a fixed sample).

The aforementioned piezoelectric coefficients are related to each other through the components of the compliance tensor S and the permittivity tensor ε, which can depend on the boundary conditions: $\varepsilon^X > \varepsilon^x$ and $S^D < S^E$. Their ratios are related to the electromechanical coupling coefficient K:

$$\varepsilon^x/\varepsilon^X = S^D/S^E = 1 - K^2. \quad (2)$$

The electromechanical coupling coefficient characterizes the efficiency of conversion of the mechanical energy to the electrical energy in the direct piezoelectric effect and the electrical energy to the mechanical energy in the inverse piezoelectric effect.

It is known that poly(vinylidene fluoride) crystallites can exist in at least four polymorphic modifications [5]. However, two modifications are observed in the majority of cases. Crystallization from a melt, as a rule, leads to the formation of the α phase with the point symmetry group C_{2h}. The unit cell parameters of the α phase are as follows: a = 0.496 nm, b = 0.964 nm, and c = 0.462 nm. Upon uniaxial drawing of a poly(vinylidene fluoride) film or chemical modification of a homopolymer chain [5], the crystallization results in the formation of the β phase in which the lattice is characterized by the point symmetry group C_{2v} and the parameters a = 0.858 nm, b = 0.491 nm, and c = 0.256 nm [6]. Consequently, the β phase whose lattice has no symmetry center can possess piezoelectric properties. In this phase, chains adopt a $(–TT–)_n$ planar zigzag conformation and the dipole moment (2.1 D per monomer unit) is perpendicular to the macromolecular axis and aligned along the b axis of the unit cell [5].

For poly(vinylidene fluoride), uniaxial drawing is used to transform nonpolar α crystallites into the noncentrosymmetric β phase [5]. In this case, the macromolecular axes (the c axis in the lattice of the β phase) are predominantly oriented along the acting mechanical stress [5]. As a result, anisotropy arises in the film plane. After exposure of this system to a strong field, the axial symmetry is broken (anisotropy appears over the film cross section), because the b polar axes of crystallites are predominantly oriented along the normal to the surface. The appearance of anisotropy in the film plane (owing to the texturing) is accompanied by an increase in the number of nonzero d_{ijk} components from three to five [6–8]. In the case when the axis *1* corresponds to the film drawing direction and the axis *3* indicates the normal to the film plane, the piezoelectric properties with due regard for the symmetry are characterized by the matrix of the piezoelectric coefficients [6]:

$$\begin{vmatrix} 0 & 0 & 0 & 0 & +d_{15} & 0 \\ 0 & 0 & 0 & +d_{24} & 0 & 0 \\ +d_{31} & +d_{32} & -d_{33} & 0 & 0 & 0 \end{vmatrix}. \quad (3)$$

3. COMPONENTS OF THE MEASURED PIEZOELECTRIC RESPONSE

When a polarized polymer electret with the permittivity ε' is characterized by the remanent (frozen) polarization P, the electric induction D (by omitting the indices) has the form [9]

$$D = \varepsilon'\varepsilon_0 E + P. \quad (4)$$

According to relationship (1), the piezoelectric constant d for the direct piezoelectric effect can be written in the following form:

$$d = \frac{\partial D}{\partial X} = \frac{\partial \varepsilon'}{\partial X}\varepsilon_0 E + \varepsilon'\varepsilon_0\frac{\partial E}{\partial X} + \frac{\partial P}{\partial X}. \quad (5)$$

This general relationship for any piezoelectric material, as applied to crystallizing polymers, has its own specific features. Actually, for inorganic materials, the first

two terms in formula (5) are ignored because of their smallness as compared to the third term [10]. In the case of crystallizing polymers, all three terms in the general case can be comparable in magnitude. The reason is that materials contain a liquidlike amorphous phase in addition to noncentrosymmetric crystallites. At temperatures above the glass transition point, intensive microscopic Brownian cooperative motions occur in the amorphous phase. Since the packing density of macromolecules in the amorphous phase is low, the compressibility of this phase is higher than that of crystallites. This means that the second term (associated with the size effect) in formula (5) can make a substantial contribution, because the term $\frac{\partial E}{\partial X} = \frac{\partial (VL^{-1})}{\partial X}$ even at a constant voltage V applied to a film of thickness L becomes nonzero due to a considerable change in the film thickness. The application of an electric field (or a mechanical stress) to this system, which is characterized by a large free volume and a pronounced rotational isomerism of segments in the amorphous phase, leads to a shift of equilibrium between the concentrations of groups in different conformations. Taking into account that the dipole moments of isomers are different, this shift should be attended by a change in the permittivity, which results in a change in the first term responsible for the electrostriction in formula (5).

The third term in formula (5) should allow for the contribution of crystallites to the piezoelectric effect, because the texturing of films should result in the appearance of a piezoelectric response (linear in the field) owing to the symmetry of the lattice of the polar β phase. In this respect, it is of interest to consider the results obtained by Tashiro *et al.* [11, 12], who calculated nonzero components of certain piezoelectric coefficients. The calculated volume compressibility is equal to 12.5×10^{-11} Pa^{-1}, which is in good agreement with an experimental value of 11.8×10^{-11} Pa^{-1}. However, a number of calculated piezoelectric coefficients disagree with experimental data. For example, the calculated piezoelectric coefficient d_{31} is equal to 0.25 pC/N, which is approximately two orders of magnitude less than the experimental coefficient (without regard for the opposite sign of this coefficient). The coefficient d_{31} calculated from the spectrum of normal vibrations (with allowance made for conformational analysis of a poly(vinylidene fluoride) single chain) appeared to be less than the experimental coefficient even by three orders of magnitude [13].

Since the contribution of noncentrosymmetric crystallites to the observed transverse piezoelectric effect turns out to be small, the first two terms in formula (5) should substantially contribute to the measured coefficients d. The size effect is taken to mean the contribution made by a decrease in the film thickness L to the change in the surface charge Q of an electrode with the area A under the action of the mechanical stress X. In order to separate this effect, the piezoelectric coefficient d_{3j} can be represented in the form [14]

$$d_{3j} = P[(\partial M/\partial X_j - S_{3j})], \quad (6)$$

where M is the dipole moment of a sample with the polarization P and $S_{3j} = \partial \ln L/\partial X_j$ are the components of the elastic compliance tensor. It is evident that the second term in relationship (6) describes the aforementioned size effect. The size contribution d^0_{3j} to the measured piezoelectric coefficient d can be estimated from the expression [14]

$$d^0_{3j} = \sum_{i=1}^{3} d_{3j} X_i / X_j. \quad (7)$$

By calculating the stresses X_i from the compliances S_{ij} [15], we obtain $d^0_{31} = 12.5$ pC/N for poly(vinylidene fluoride). This indicates that, for the typical experimental value $d_{31} = 21.4$ pC/N [16], the contribution of the size effect to the piezoelectric coefficient is equal to 58%.

For the piezoelectric voltage coefficients e_{ij}, the coefficient e_V for an open state is defined as [17]

$$e_V = e + V/A\partial C/\partial x, \quad (8)$$

where e is the piezoelectric coefficient for a short-circuited state and C is the capacitance of a sample with the permittivity ε_3, the thickness L, and the area A at the potential difference V. In the case of a plane capacitor, we have $C = \varepsilon_0 \varepsilon_3 A/L$ and

$$e_V = e + \frac{V}{A}\varepsilon_0 \frac{\partial}{\partial x}\left(\varepsilon_3 \frac{A}{L}\right). \quad (9)$$

Therefore, the second term in formula (9) in the general case includes the strain dependences of the permittivity ε_3 (the electrostriction) and the capacitor geometry (the size effect). By assuming that the Poisson ratios along and across the film surface are equal to each other, we obtain

$$e_V = e + \varepsilon_0(k + \varepsilon)V/L, \quad (10)$$

where the electrostrictive constant k is given by the expression

$$k = \partial\varepsilon/\partial x. \quad (11)$$

For uniaxially drawn films, the measured coefficient e^*_{31} can be written in the form [17]

$$e^*_{31} = e_{31} + \varepsilon_0[k_{31} + \varepsilon_3(1 + \mu_{31} - \mu_{21})]E. \quad (12)$$

Here, the Poisson ratios μ_{ij} under deformation of a uniaxially drawn film with the initial thickness L, length l, and width a can be expressed through the ratios of the corresponding compliance components S;

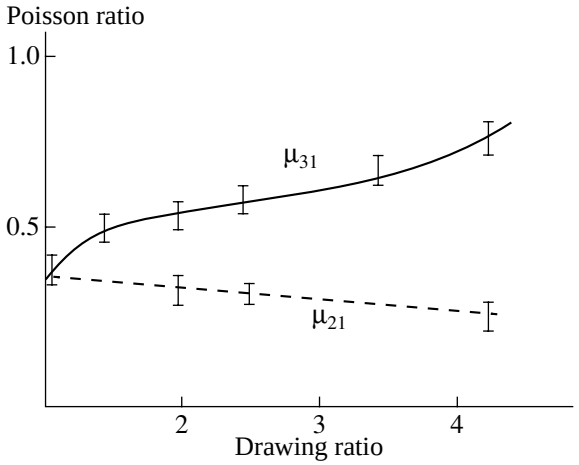

Fig. 2. Dependences of the Poisson ratios μ_{21} and μ_{31} on the drawing ratio for PVDF films [18].

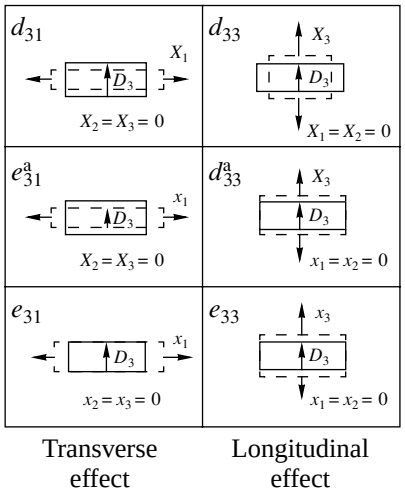

Fig. 3. Types of deformations of films for the piezoelectric coefficients *d* and *e* in the case of the transverse and longitudinal piezoelectric effects [4].

that is,

$$\mu_{21} = -\frac{S_{21}}{S_{11}} = -\frac{\Delta a/a}{\Delta l/l}, \quad \mu_{31} = -\frac{S_{31}}{S_{11}} = -\frac{\Delta L/L}{\Delta l/l}. \quad (13)$$

According to relationship (12), the contribution of the size effect to the measured piezoelectric coefficient e_{31}^* of a textured film is determined by the difference between the Poisson ratios μ_{31} and μ_{21}. The behavior of the Poisson ratios μ_{21} and μ_{31} with an increase in the drawing ratio of poly(vinylidene fluoride) films is illustrated in Fig. 2 [18]. In this case, an increase in the difference between μ_{31} and μ_{21} means that the coefficient e^* increases when changing over from an isotropic film ($\mu_{31} = \mu_{21}$) to a uniaxially drawn film, all other factors being the same. The thermal shrinkage upon free annealing of a textured poly(vinylidene fluoride) film is attended by a decrease in the Poisson ratio μ_{31} from 0.7 to 0.5 [18]. The sharp decrease in the coefficient e_{31}^* in the glass transition range of poly(vinylidene fluoride) (–40°C) [18] can also be explained by the contribution of the aforementioned effect, because the transformation of the polymer to the vitreous state leads to a drastic change in a number of physical characteristics [19, 20], including a decrease in the anisotropy of the Poisson ratio μ.

Specific features of film materials prepared from flexible-chain polymers, in particular, their elasticity, can result in the fact that it is difficult to provide certain boundary conditions when measuring the piezoelectric coefficients in practice. It can be seen from Fig. 3 that the piezoelectric coefficients e_{31} and d_{33} are different in the case of free (at the stress $X = 0$) and fixed (at the strain $x = 0$) samples.

In accord with formulas (5) and (12), the electrostriction can also contribute to the measured piezoelectric coefficients. Unlike the piezoelectricity, the electrostriction contribution is quadratic in field and can be observed in crystals of any symmetry. On the other hand, as follows from the phenomenological theory [21], the linearized electrostriction can contribute to the piezoelectricity of a ferroelectric material when its paraelectric phase has a lattice with a symmetry center. This situation is observed in the objects under consideration. Actually, the vinylidene fluoride–trifluoroethylene (VDF–TFE) copolymer (70 : 30) in the paraelectric phase has a hexagonal lattice with the parameters $a = 0.986$ nm and $c = 0.23$ nm [22]. Therefore, crystallites themselves can make the electrostriction contribution to the observed piezoelectric effect. One more problem is associated with the response of amorphous phase regions to an external field. When the structure of the amorphous phase is formed by mobile chains, it can be expected that the permittivity of this phase can change upon application of mechanical loads or electric fields.

More than 30 years ago, Nakamura and Wada [23] considered the problem of electrostriction in poly(vinylidene fluoride). More recently, Furukawa *et al.* [17] analyzed this problem in greater detail. According to relationship (10), the electrostrictive constant *k* (by omitting the indices) of a nonpolarized film (at the piezoelectric coefficient $e = 0$) was represented in the form [17]

$$k = \frac{1}{\varepsilon_0}\left(\frac{\partial e_V}{\partial V}\right)L - \varepsilon. \quad (14)$$

The temperature dependences of the real and imaginary parts of the electrostrictive constant *k* demonstrated that the electrostriction is virtually suppressed upon transformation of the polymer into the vitreous state [17]. In experiments on the inverse piezoelectric effect, the electrostrictive constant γ was determined from the

general expression relating the mechanical stress X generated in the sample and the field strength E [24], that is,

$$X = C^E x + eE + \gamma E^2, \quad (15)$$

where C^E is the elastic constant at $E = 0$. Since $X = \gamma E^2$ for the fixed ($x = 0$) and nonpolarized ($e = 0$) sample, the electrostrictive constant γ was determined as the proportionality coefficient between X and E^2. In the real experiment, the ac field E and the dc field E_0 (bias field) were applied to the film. For weak fields (when the sample remains nonpolarized), the mechanical stress generated in the sample is defined by the formula

$$X = \gamma(E_0 + E)^2 = \gamma E_0^2 + 2\gamma E_0 E + \gamma E^2. \quad (16)$$

Here, the first term describes the static stress and the second term characterizes the effective piezoelectricity induced by the electric field [24], which is characterized by the piezoelectric coefficient $e_0 = 2\gamma E_0$, because the stress varies linearly with the field. The electrostrictive constant was determined from the alternating component of the mechanical stress at the frequency ω (the second term) or 2ω (the third term) of the applied ac field. The stress generated by the electrostatic forces between capacitor plates in the sample with the permittivity ε and the Poisson ratio μ was estimated from the relationship

$$X_e = \varepsilon\varepsilon_0 E^2 \mu/8\pi. \quad (17)$$

Table 1. Effective piezoelectric coefficients e_0 and electrostrictive constants for poly(styrene), epoxy resin, poly(vinyl chloride), poly(methyl methacrylate), poly(γ-methyl-*L*-glutamate), and poly(vinylidene fluoride) in the field $E_0 = 10^5$ V/cm [24]

Polymer	e_0, 10^{-4} N (V m)$^{-1}$	γ_a, 10^{-12} N V^{-2}	γ_a, 10^{-12} N V^{-2}
	For $X(\omega)$	For $X(\omega)$	For $X(2\omega)$
Poly(styrene)	0.7	3.3	3.9
Epoxy resin	1.0	5.1	5.3
Poly(vinyl chloride)	1.1	5.3	6.2
Poly(methyl methacrylate)	1.6	8.2	5.7
Poly(γ-methyl-*L*-glutamate)	2.3	12.5	8.3
Poly(vinylidene fluoride)	9.4	48.0	39.0

A number of polymers in addition to poly(vinylidene fluoride) were investigated in order to separate experimentally the stresses under consideration from the stresses observed in piezoelectric materials. As can be seen from the data presented in Table 1, all the poly-

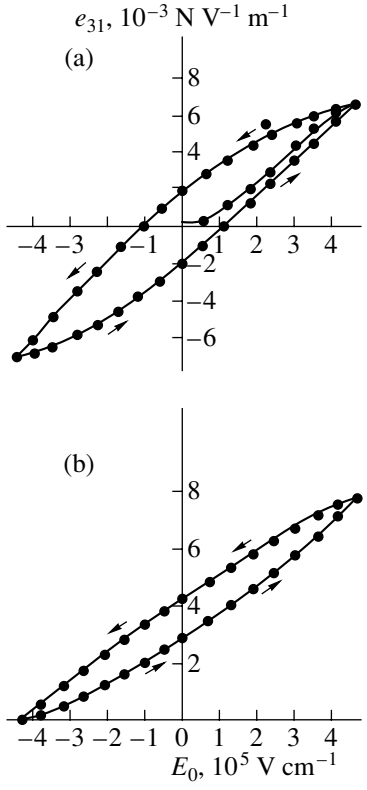

Fig. 4. Dependences of the piezoelectric coefficient e_{31} for (a) nonpolarized and (b) polarized PVDF films upon cycling change in the dc bias field [24].

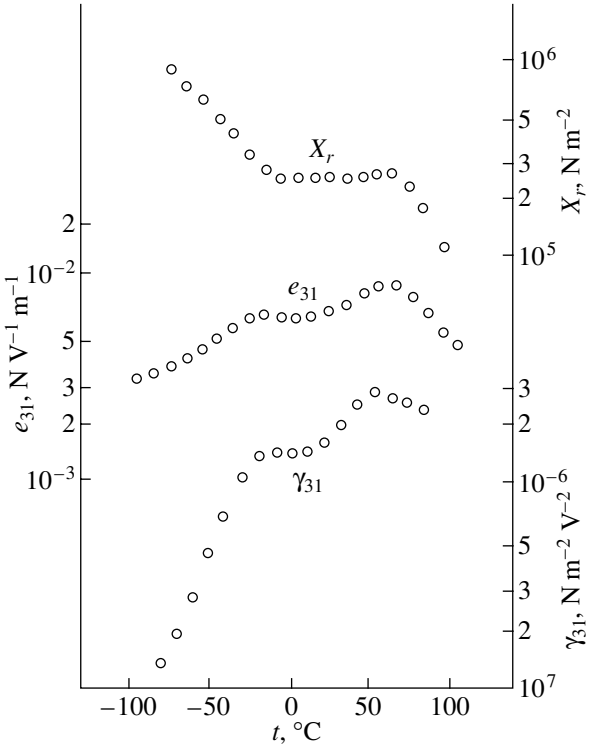

Fig. 5. Temperature dependences of the electrostrictive constant γ_{31}, the piezoelectric coefficient e_{31}, and the residual stress X_r for an oriented polarized PVDF film [24].

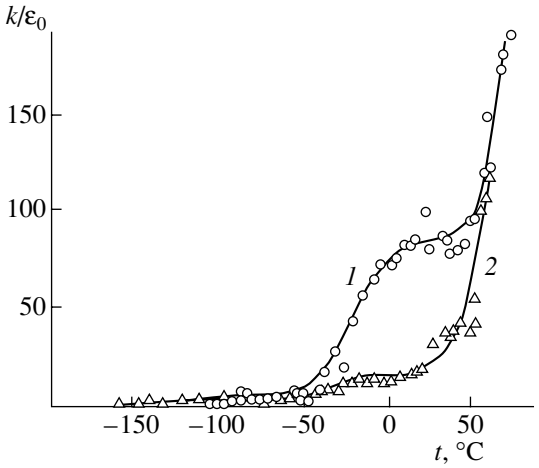

Fig. 6. Temperature dependences of the electrostrictive constant (*1*) prior to and (*2*) after polarization of the VDF–TFE copolymer (54 : 46) [26].

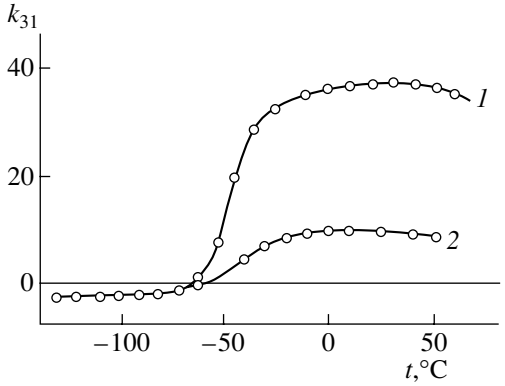

Fig. 7. Temperature dependences of the electrostrictive constant k_{31} for (*1*) uniaxially drawn and (*2*) annealed PVDF films [18, 27].

mers without exception [including nonpolar poly(styrene)] are characterized by nonzero effective piezoelectric coefficients; however, this coefficient for poly(vinylidene fluoride) is severalfold larger. Moreover, the electrostrictive constant γ for poly(vinylidene fluoride) also appears to be larger by one order of magnitude. The electrostrictive constants experimentally obtained for the other polymers are in reasonable agreement with the electrostrictive constant $\gamma = 6 \times 10^{-12}\,\mathrm{N\,V^{-2}}$ calculated from relationship (17). The larger values of e_0 and γ for poly(γ-methyl-*L*-glutamate) and poly(vinylidene fluoride) can be explained by the additional contributions to the observed piezoelectric effect. The manifestation of these contributions for poly(vinylidene fluoride) can be seen in Fig. 4. The piezoelectric coefficient for the nonpolarized sample (Fig. 4a) upon cyclic change in the bias field E_0 remains nonzero ($e_{31} \neq 0$) even with zero bias field. According to relationship (17), this behavior is associated with the contribution of the crystalline phase to the piezoelectric effect. The remanent field (450 kV/cm) induced by crystalline phase regions with a spontaneous polarization was determined after preliminary polarization of the film (Fig. 4b). Similar temperature dependences of the piezoelectric coefficient e_{31} and the electrostrictive constant γ_{31} for the preliminarily polarized film (Fig. 5) also confirm the above inference that the electrostriction in the studied polymers contributes to the macroscopically measured piezoelectric coefficient.

One more technique of investigating the electrostriction effects in the polymers under consideration was proposed in [25, 26]. In these works, the studied film was simultaneously exposed to an ac electric field

$$E_3 = E_0 \cos(\omega_1 t) \tag{18}$$

and an alternating mechanical stress (in the film plane), which produces the strain x varying as

$$x = x_0 \cos(\omega_2 t) + x_s, \tag{19}$$

where x_s is the static strain. The increment of the polarization component ΔP_3 (along the normal to the surface) can be written in the form [26]

$$\begin{aligned}\Delta P_3 = {} & \varepsilon_{33} E_3 + e_{31} x_1 + k_{331} E_3 x_1 \\ & + \zeta_{333} E_3^2 + \beta_{311} x_1^2 + \ldots,\end{aligned} \tag{20}$$

where ζ_{333} and β_{311} are constant coefficients of the nonlinear terms. The electrostrictive constant k_{331} can be determined from the increment of the polarization at the difference or total frequency with the use of the expression [26]

$$k = \frac{2|\Delta P(f_1 \pm f_2)|}{E_0 x_0}. \tag{21}$$

The temperature dependences of the electrostrictive constant thus calculated for the vinylidene fluoride–trifluoroethylene copolymer (54 : 46) are shown in Fig. 6. The data presented in this figure for the nonpolarized copolymer film leads to the inference identical to that drawn in [17] for the homopolymer: the freezing of the cooperative mobility in the amorphous phase (with a decrease in the temperature to the glass transition point) results in the suppression of the electrostriction effect. Interesting changes were found for the copolymer film after polarization (curve *2* in Fig. 6). The electrostrictive constant at temperatures above the glass transition point turns out to be substantially less than that for the film prior to the polarization. Note that the polarization is usually accompanied by the transformation of a number of chains from the amorphous state into the crystalline state [5]. Therefore, the above fact once again demonstrates that the electrostriction effects are associated with the disordered phase.

The influence of the microstructure of the disordered phase on the electrostriction effect was studied by Tasaka and Miyata [18, 27]. As can be seen from Fig. 7, the free annealing of a textured film leads to an appre-

ciable decrease in the electrostrictive constant k_{31} at temperatures above the glass transition range [18]. The data presented in Table 2 indicate that the permittivity ε_3 and the degree of crystallinity ϕ remain almost constant after free annealing. Since the fraction of the amorphous phase is unchanged, the decrease in the electrostrictive constant should be caused by other factors. It can be seen from Table 2 that the annealing results in a considerable decrease in the birefringence Δn. Reasoning from the two-phase model, to a first approximation, we can write

$$\Delta n = f_c \phi \Delta n_c^\circ + f_a(1-\phi)\Delta n_a^\circ, \quad (22)$$

where f_c and f_a are the second moments of the distribution function (orientation function) of chains in crystalline and amorphous regions, respectively. These regions are characterized by the birefringences Δn_c° and Δn_a°. When the degree of crystallinity ϕ is constant and the value of f_c varies insignificantly upon annealing, it follows from relationship (22) that the observed decrease in the birefringence Δn should be predominantly governed by a decrease in the second moment f_a. Furthermore, this parameter also determines the electrostrictive constant (Fig. 7). Indeed, in [18], it was shown that

$$k_{31} = \frac{\delta\varepsilon}{\delta x} \approx \frac{1}{2 - f_a}\left(\frac{\partial f_a}{\partial x}\right). \quad (23)$$

This relationship for the electrostrictive constant k_{31} accounts for the parameter f_a and the multiplier $(\partial f_a/\partial x)$, which reflects a strain-induced change in the chain orientation in the amorphous phase. The expression for the second moment f_a can be represented in the following form:

$$f_a = \frac{1}{2}(3\langle \cos^2\theta\rangle - 1). \quad (24)$$

Table 2. Characteristics of the uniaxially drawn PVDF film (at 20°C) in the initial state and after free annealing [18, 27]

Characteristic	ε_3	k_{31}	μ_{31}	c_{11}, GPa	ϕ	f_c	Δn, 10^{-3}
Initial state	14.4	28.0	0.7	2.2	0.4	0.97	37
After annealing	14.3	8	0.5	1.3	0.41	0.87	26

Judging from this expression, the last multiplier in relationship (23) describes the strain-induced change in the mean angle θ that is formed by a chain segment in the disordered phase with the drawing axis (strain direction). The dependence of the derivative $\partial f_a/\partial x$ on the drawing ratio λ for oriented poly(vinylidene fluoride) samples is plotted in Fig. 8a. It can be seen from this figure that the derivative $\partial f_a/\partial x$ for the films increases with an increase in the drawing ratio. According to formula (24), this implies that the angle θ more drastically decreases under deformation. The fact that the term $\partial f_a/\partial x$ makes the main contribution to the electrostrictive constant k_{31} is supported by the dependence of this constant on the drawing ratio (Fig. 8b). Actually, a comparison of Figs. 8a and 8b indicates that the dependences of $\partial f_a/\partial x$ and k_{31} exhibit a similar behavior. Moreover, it can be seen from Fig. 8b that the experimental electrostrictive constants k_{31} agree reasonably with those calculated using relationship (23).

Different relative contributions to the observed piezoelectric effect are schematically represented in Fig. 9. As can be seen from Fig. 9, a decrease in the temperature below the glass transition point is attended by a noticeable decrease in the electrostrictive constant and the Poisson ratio. As a result, the contribution of crystallites is as large as 45% [18]. This can be explained in terms of the two-phase model of the polymers under consideration in which crystallites with the noncentrosymmetric lattice and the amorphous matrix

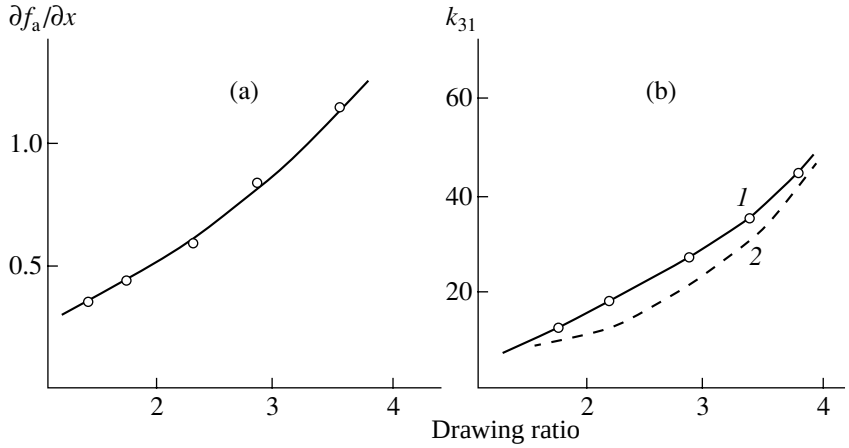

Fig. 8. Dependences of (a) the derivative $\partial f_a/\partial x$ and (b) the electrostrictive constant k_{31} on the drawing ratio for uniaxially oriented PVDF films: (*1*) the experimental data on k_{31} and (*2*) the results of calculations from relationship (23) [27].

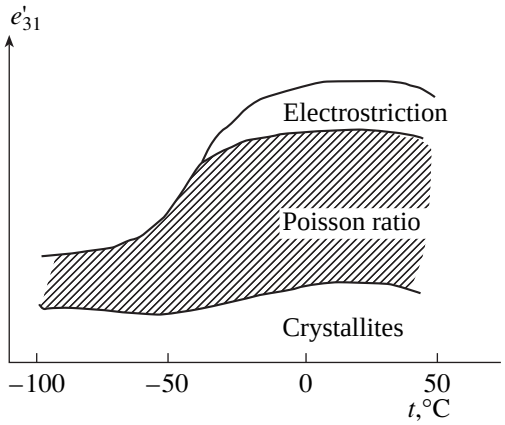

Fig. 9. Schematic representation of the relative contributions from different mechanisms of the transverse piezoelectric effect in uniaxially oriented PVDF films [18].

have different elastic and electrical parameters [17]. In this case, the contribution of polar crystals (with the volume fraction ϕ and the piezoelectric coefficient e_c) to the measured piezoelectric coefficient e_{ij} can be written in the form [17]

$$e = \phi L_E L_X e_c, \tag{25}$$

where L_E and L_X are the coefficients of the local electric field and the local mechanical stress in the vicinity of a crystallite, respectively. At temperatures above the glass transition point, the amorphous phase possesses a high permittivity and a small Young modulus due to an intensive microscopic Brownian motion. The external electric field (in the case of the inverse piezoelectric effect) in a crystallite region decreases owing to the depolarization influence of the amorphous polar matrix with the permittivity $\varepsilon_a > \varepsilon_c$. For the direct piezoelectric effect, the high compliance of the amorphous matrix favors relaxation of the external mechanical stress. Consequently, the mechanical stress decreases in the crystallite region. Both factors lead to a decrease in the contribution of crystallites to the observed piezoelectric effect. At temperatures below the glass transition point, the microscopic Brownian dynamics is frozen in the amorphous phase, which results in a decrease in the compliance and the permittivity of this phase [17]. As follows from the above, this circumstance should lead to an increase in the coefficients of the local electric field and the local mechanical stress in formula (25) and to an enhancement of the contribution of crystallites to the observed piezoelectric effect (Fig. 9).

However, there is no agreement among some authors as to the ratio between the different relative contributions represented in Fig. 9 [28]. In particular, it was proposed to revise the role played by the electrostriction in the piezoelectric effect. This is a constructive approach to solving the problem associated with the molecular mechanisms of electrostriction in polymers, because the elucidation of these mechanisms is of considerable fundamental [29] and practical [30–32] importance. In this respect, the justification of the mechanisms of electrostriction phenomena in the studied polymers will be considered below. In relationship (6) for the piezoelectric coefficient d_{ij}, the first term should correspond to the contribution of the crystalline phase and the electrostriction. When the remanent polarization is absent in the amorphous phase, the dipole moment M of the sample can be written as follows [14]:

$$M = N_c\zeta(\mu_0 + \alpha_c E_c) f(\varepsilon_s/\varepsilon_c)\langle\cos\theta\rangle + \alpha_L E_L. \tag{26}$$

Here, N_c is the number of crystals with the vacuum dipole moment μ_0, the polarizability α_c, and the permittivity ε_c; E_c and E_L are the local electric fields in the crystalline and amorphous phases, respectively; ζ is the ferroelectric order parameter; and α_L is the polarizability of the amorphous phase in the sample with the mean permittivity ε_s. The polar crystallites forming the angle θ with the normal to the film surface (axis 3) execute librations with respect to equilibrium positions. The contribution of these librations to the observed piezoelectric effect was examined by Broadhurst *et al.* [33]. If the dipole moment of the crystallite is equal to μ_c, the polarization under the assumption of the Onsager local field has the form [33]

$$P = \frac{\varepsilon_\infty + 2}{3}\frac{N}{V}\mu_c\langle\cos\theta\rangle. \tag{27}$$

With due regard for formula (27), the contribution of librations to the observed piezoelectric coefficient (for a short circuit) is given by the relationship

$$d_c = \frac{\partial P}{\partial X} = \frac{N}{\nu}\frac{(\varepsilon_\infty + 2)}{3}\mu_{c0}\frac{\partial\langle\cos\theta\rangle}{\partial X}. \tag{28}$$

Dvey-Aharon *et al.* [13] demonstrated that the contribution d_c to the observed piezoelectric coefficient d_{31} does exceed 1%. Consequently, other mechanisms should predominantly contribute to the transverse piezoelectric effect in the framework of the dipole theory.

In order to elucidate these mechanisms, let us consider the structural transformations of crystallizing polymers in response to external mechanical stresses. If these stresses are small (as is usually the case with the direct piezoelectric effect), isotropic and textured films should be analyzed separately. The structure of an isotropic sample is schematically depicted in Fig. 10a. As can be seen from this figure, folded (lamellar) crystals in the isotropic sample have equally probable orientations. Numerous experiments revealed that the loading of isotropic films leads to a loosening of the initial structure. This loosening can be observed directly using electron microscopy from the formation of microholes [35] or indirectly from an anomalous decrease in the sound velocity under small deformations of poly(vinylidene fluoride) and vinylidene fluoride–tet-

rafluoroethylene copolymer films [36–38]. The loosening should be accompanied by a decrease in N_c in formula (26) and should contribute to the observed piezoelectric response.

Upon uniaxial drawing, the *c* axes of lamellar crystals are predominantly oriented along the drawing axis (Fig. 10b). Folds in lamellar crystals are a special feature of flexible-chain crystallizing polymers (among these are poly(vinylidene fluoride) and its copolymers), and the fraction of folds decreases upon drawing. The lamellar crystals transform into fibrillar crystals through the mechanism of sliding and tilt of lamellas [39]. The formation of the fibrillar crystals can be revealed from the drastic increase in the intensity in the indicatrix of small-angle polarized light scattering in the direction of an incident beam [36, 40, 41], because this scattering is characteristic of a set of optically anisotropic cylinders that simulate the crystals under consideration.

In the initial (unstrained) uniaxially drawn film, the electron density regularly varies with a large period along the axis *1* (the *c* axis of the lattice). This is explained by the alternation of crystallites and disordered regions with a looser packing. The deformation of this film along the axis *1* results in a decrease in the fraction of segments with a more twisted **TG** conformation due to an increase in the fraction of segments with the *TT* planar zigzag conformation [42, 43]. Kober *et al.* [44] studied the Raman spectra of loaded poly(ethylene) and found that the deformation leads to a low-frequency shift in the band associated with the longitudinal acoustic mode, which indicates an increase in the length of segments with the *TT* conformation. In the amorphous phase, the packing of adjacent chains with the planar zigzag conformation is closer than that of chains with the twist conformation. This can be judged from the fact that the position of the amorphous halo at the equator is shifted to larger angles as compared to that at the meridian, for example, for textured poly(ethylene terephthalate) [45] and vinylidene fluoride–tetrafluoroethylene copolymer [46] films. Regions formed by chains with a preferential orientation with respect to the drawing axis are referred to as the anisotropic amorphous phase [45, 46]. The chain dynamics in these regions turns out to be more hindered than that in regions of the isotropic amorphous phase, and, hence, these two types of disordered regions can be distinguished by NMR spectroscopy [47]. In regions of the anisotropic amorphous phase, chains belonging to two adjacent crystallites can be in a strained state and, consequently, are termed taut tie chains. Under deformation of the oriented polymer along the drawing axis, fragments of taut tie chains bear loads. This can lead to the deformation of bonds and bond angles, because the shift in the characteristic absorption bands is observed in the IR [48] and Raman [49] spectra.

According to the IR spectroscopic data [5], segments of the studied polymers adopt *TG*, *TGTG*$^-$, and

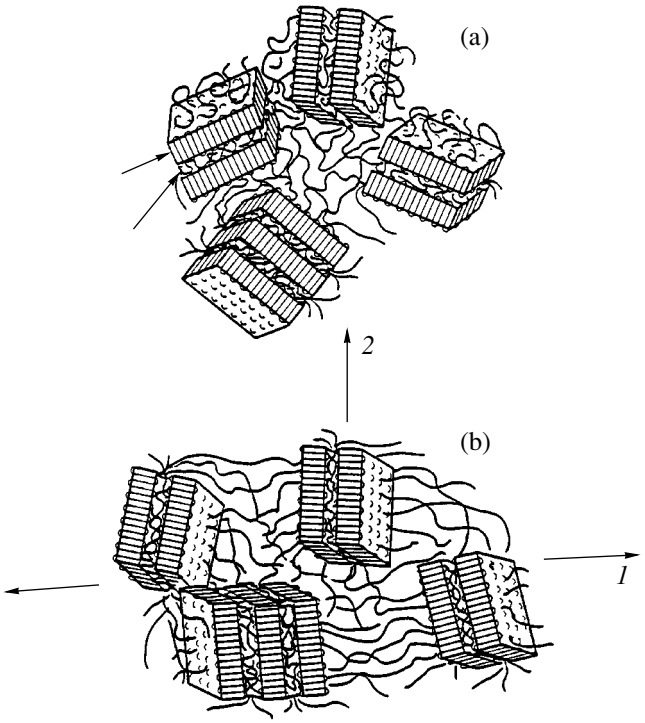

Fig. 10. Schematic representation of the structure of (a) isotropic and (b) uniaxially drawn samples of a flexible-chain polymer with lamellar crystallites: (*1*) the drawing direction and (*2*) the normal to the drawing axis [14].

$T_3GT_3G^-$ conformations in the amorphous phase. These conformations are identified from the characteristic absorption bands in the IR spectra. Upon loading of uniaxially oriented films along the drawing axis, disordered phase regions are characterized by the occurrence of different transitions, including transitions of the type [50]

$$TG \longrightarrow TT,$$
$$TGTG^- \longrightarrow (-TT-)_n;\ T_3GT_3G^- \longrightarrow (-TT-)_n. \quad (29)$$

As applied to the problem under consideration, it is expedient to examine the $TGTG^- \longrightarrow (-TT-)_n$ transition. It is known that, in the poly(vinylidene fluoride) polymer, the transverse component of the dipole moment is equal to 4.03×10^{-28} C m for a chain with a *TGTG*$^-$ conformation and 6.9×10^{-28} C m (2.1 D) for a chain with a planar zigzag conformation. Therefore, the above conformation transition is attended by a change in the transverse component of the permittivity of the film. According to expression (11), this results in the electrostriction effect. Furthermore, the normal component of the polarization also increases when the deformation of the film leads to a change in the angle between a domain of the amorphous phase and the direction of an external force. As follows from the above, the quantities $f(\varepsilon_s/\varepsilon_c)$ and $\langle\cos\theta\rangle$ in relationship (26) change upon mechanical loading of uniaxially drawn films.

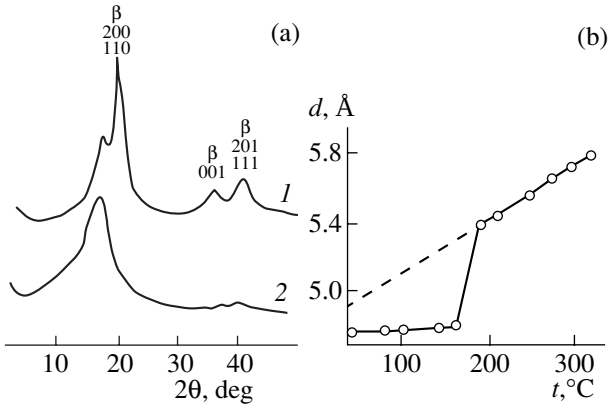

Fig. 11. (a) X-ray diffraction patterns of isotropic VDF–TFE copolymer (94 : 6) films at temperatures of (*1*) 160 and (*2*) 184°C and (b) the temperature dependence of the interplanar distance in the lattice of the paraelectric phase [56].

In the case when crystals are formed by chains with a planar zigzag conformation, the aforementioned conformational transitions proceeding in the amorphous phase upon loading can encourage the transformation of a number of chains into the crystalline state. The strain-induced crystallization in poly(ethylene) films was observed by Tsubakihara and Yasuniwa [51] in X-ray diffraction experiments. According to formula (26), a similar process upon loading of the polymers under consideration leads to an increase in the number N_c of polar crystals and, hence, to an increase in the polarization. In the case of poly(vinylidene fluoride) and its copolymers, an increase in the degree of crystallinity upon loading of textured films can also occur owing to an increase in the longitudinal size of crystals in microfibrils. In particular, for oriented vinylidene fluoride–trifluoroethylene copolymer (94 : 6) films, this was revealed from a narrowing of the 001 meridional reflection [50]. A similar increase in the degree of crystallinity was previously observed by Kaji [52] in oriented nylon 6 films. The strain-induced increase in the longitudinal size of crystals in the uniaxially drawn vinylidene fluoride–trifluoroethylene copolymer was indirectly confirmed by the acoustic method [38].

In poly(vinylidene fluoride), a number of amorphous regions in the form of interfacial layers are localized on the crystal boundaries [53]. The interfacial layers should have a closer packing of chains [54, 55]. This is consistent with the general concept according to which rigid (anisotropic) and isotropic amorphous phase regions exist in crystallizing polymers [56–58]. The diffraction pattern of the vinylidene fluoride–trifluoroethylene copolymer (94 : 6) at a temperature of 160°C (Fig. 11, curve *1*) indicates that the halo at $2\theta \sim 18°$, which is observed in addition to the reflections of the ferroelectric β phase, should be associated with the amorphous phase. Upon heating of the sample to 184°C, i.e., to the temperature above the melting point and, correspondingly, the Curie point (the temperatures of these transitions are close to each other [7]), the diffraction pattern should contain only the reflection of the paraelectric phase, which is actually observed in Fig. 11 (curve *2*). A comparison of curves *1* and *2* in Fig. 11 shows that the reflections in the range $2\theta \sim 18°$ have similar parameters. This implies that certain regions of the amorphous phase can be treated as paraelectric crystals. Therefore, at temperatures below the Curie point, the ferroelectric phase coexists with paraelectric crystals, which is frequently observed in the crystallizing polymers studied [7].

It can be seen from Fig. 11b that the lattices of the paraelectric phase (or the mean interchain distances in the amorphous phase) substantially differ at temperatures below and above the Curie temperature. The paraelectric phase below the Curie point is characterized by a considerably closer packing as compared to that above this point. Moreover, the thermal expansion coefficients appreciably differ in these temperature ranges. This is a very important circumstance from the viewpoint of the material response to external mechanical stress. Under deformation of the studied copolymer at temperatures below the Curie point, the paraelectric phase appears to be in a nonequilibrium state. The localization of this phase along the boundaries with ferroelectric crystals and the relatively close packing of chains in the considered regions of the paraelectric phase are energetically favorable for its transformation into the ferroelectric crystal upon loading.

The available data on the piezoelectric properties of the polymers under investigation also confirm the validity of the concept that part of the amorphous phase can be treated as crystals of the paraelectric phase. It was shown above that the electrostriction effects in the studied polymers are caused by the presence of the amorphous phase. If this phase is considered in the form of paraelectric crystals, the transformation of the ferroelectric crystal into the paraelectric state should be accompanied by a noticeable increase in the electrostrictive constant. The data presented in Fig. 12a corroborate this inference, because the heating above the Curie point leads to more than a twofold increase in the electrostrictive constant [59]. It can be seen from Fig. 12b that the electrostrictive constant of the polarized film decreases with an increase in the spontaneous and remanent polarization [59]. An increase in the remanent polarization, apart from an increase in the degree of orientation of the polar axes of crystals, can be associated with the partial transformation of the amorphous (or paraelectric) phase from the disordered state to the ferroelectric crystalline state [5, 7]. According to the concept developed, a decrease in the fraction of chains in the amorphous (paraelectric) phase should result in a decrease in the electrostrictive constant, which agrees with the data represented in Fig. 12b.

In the case when the strain-induced crystallization proceeds through the mechanism associated with an increase in the longitudinal size of crystals, a change in

the shape of the crystal embedded in an amorphous matrix can noticeably affect the piezoelectricity mechanism. The function $f(\varepsilon_s/\varepsilon_c)$ of the permittivities in relationship (26) for the dipole moment strongly depends on the crystal shape [14]. The crystal shape also has an effect on the field E_c. According to Broadhurst *et al.* [33], a change in the shape of a spherical polar crystal in a homogeneous medium under mechanical stress manifests itself as electrostriction. For ellipsoidal crystals, the electric moment of the sample can be written in the form [60]

$$M = \frac{N_c \mu_c \varepsilon_s \langle \cos\theta \rangle}{\varepsilon_s + D_c(\varepsilon_c - \varepsilon_s)}. \quad (30)$$

An increase in the longitudinal size of the sample in the course of strain-induced crystallization is equivalent to a change in the axial ratio of an ellipsoid. This leads to a change in the depolarization factor D_c and, as a consequence, in the electric moment of the sample.

As follows from relationship (26), the ferroelectric order parameter ζ also affects the electric moment M. Within a two-position model, the ferroelectric order parameter ζ and the Curie temperature T_C are related by the expression [61]

$$\zeta = \tanh T_C \zeta / T. \quad (31)$$

For the polymers under consideration, it has been experimentally found that the deformation of uniaxially drawn films along the axis *1* leads to a decrease in the Curie temperature [7, 62]. According to formula (31), this should result in a change in the ferroelectric order parameter ζ and, hence, in the electric moment of the sample.

Therefore, the above analysis demonstrates that, upon deformation of the polarized polymer, many factors can lead to a change in the dipole moment of the sample. Furukawa and Seo [28] argued that the size effect cannot be treated as responsible for the predominant contribution to the observed piezoelectricity, because this would require the use of a rigid dipole model. Since the deformation of the sample strongly affects its dipole moment, the electrostriction should predominantly contribute to the observed piezoelectric effect. This hypothesis was experimentally justified in [28]. The dependences of the strain x and the electric induction D on the electric field strength for two ferroelectric polymers and PZT ceramics are depicted in Fig. 13. For nonpolarized films (at $e = 0$), the induced X stress is given by the formula

$$X = Cx - \gamma D^2. \quad (32)$$

Since $X = 0$ for a free film, the strain is represented by the expression

$$x = S\gamma D^2 = kD^2, \quad (33)$$

where k is the dimensional electrostrictive constant. As can be seen from Fig. 14a, relationship (33) well describes the experimental data for the polymers under

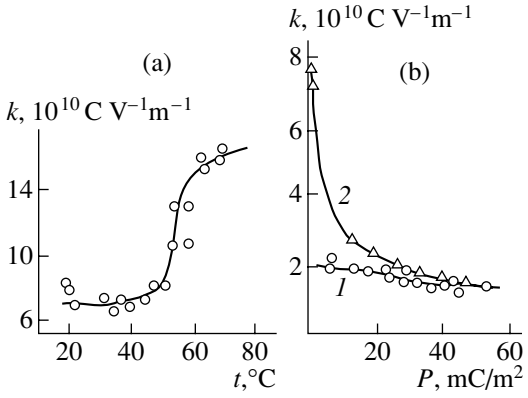

Fig. 12. Dependences of the electrostrictive constant on (a) the temperature and (b) (*1*) the remanent and (*2*) spontaneous polarization for the VDF–TFE copolymer (54 : 46) [59].

consideration. The data presented in Table 3 show that the electrostrictive constants k_{33} for all the organic ferroelectrics differ by no more than 10%. Four main piezoelectric coefficients d, e, g, and h, which are defined by relationships (1) under the assumption that $D = P_r$, $E = 0$, $x = x_r$, and $X = 0$, can be represented in the form

$$\begin{aligned} d &= 2\varepsilon k P_r, \\ e &= 2\varepsilon\gamma P_r, \\ g &= 2k P_r, \\ h &= 2\gamma P_r. \end{aligned} \quad (34)$$

As follows from these relationships, all the piezoelectric coefficients are proportional to the remanent polarization P_r. For two piezoelectric coefficients, this dependence is confirmed experimentally (see Fig. 15). Expression (33) is derived for the purely electrostrictive mechanism of the piezoelectric effect. Therefore, the piezoelectric coefficients d_{33} and g_{33} calculated from formulas (34) are compared in Table 3 with those measured experimentally (see Fig. 14b). It can be seen from the data presented in Table 3 that the experimental coefficients d_{33} and g_{33} coincide (in sign and magnitude) with the results of calculations from formulas (34). On this basis, in [28], the authors made the inference that the piezoelectricity is predominantly electrostrictive in nature.

The data presented in Table 3 and Fig. 13 demonstrate that the electrostrictive constant k_{33} is positive in the PZT ceramics and negative in the polymers. This means that the application of electric fields to the polymer samples results in a decrease in their thickness, which, most likely, reflects the behavior of the liquid-like amorphous phase in response to electric fields. Since the packing in the crystal is closer than that in the amorphous phase, a decrease in the thickness of the polymer film in the field should be attributed to the par-

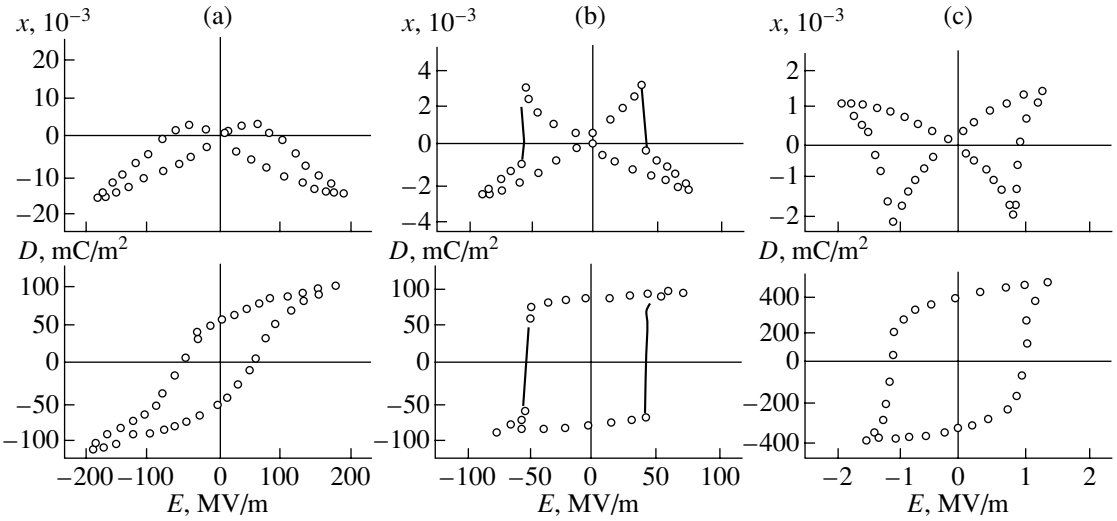

Fig. 13. Dependences of the strain x and the electric induction D on the electric field strength for (a) the uniaxially drawn PVDF film, (b) the VDF–TFE copolymer (65 : 35), and (c) the PZT piezoelectric ceramics [28].

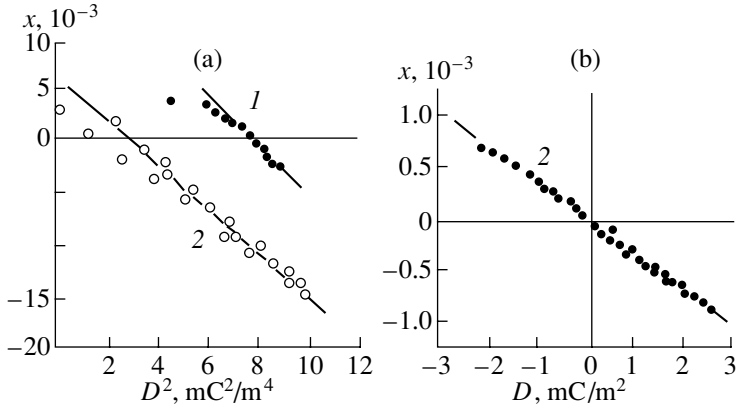

Fig. 14. Dependences of the strain on the electric induction for (*1*) PVDF and (*2*) VDF–TFE copolymer (65 : 35) films in the ranges of (a) strong and (b) weak fields [28].

tial transformation of chains from the anisotropic amorphous phase into the crystalline state [39]. A further argument in support of field-induced crystallization in the polymers can be found from a comparison of the dependences plotted in Figs. 13a and 13b. It can be seen from these figures that, at the maximum field strength, the strain of the poly(vinylidene fluoride) homopolymer is several times greater than that of the vinylidene fluoride–trifluoroethylene copolymer (65 : 35). For identical initial thicknesses of the films, a change in the volume of the poly(vinylidene fluoride) film appears to be larger than that of the copolymer film. As is known, the lattice in the copolymer along the *a* and *b* directions has a looser packing than that in the homopolymer [5, 7]. In the polarized uniaxially drawn film, the *b* axis of the unit cell is aligned along the axis *3* (normal to the surface). When the field is applied along this direction, a change in the film thickness due to the field-induced crystallization is determined by the packing of the initial crystal along the *b* direction. If the packing in the poly(vinylidene fluoride) is closer, the decrease in the thickness due to the partial transformation of chains from the amorphous state into the crystalline state should be larger, which is actually observed in the experiment (Figs. 13a, 13b).

Therefore, according to different estimates, the contributions of the electrostriction and the size effect to the observed piezoelectric effect in the polymers under consideration differ considerably. One may believe that this is an apparent contradiction, because these contributions cannot be separated. For example, when the polarized film of the uniaxially drawn polymer is subjected to mechanical stress along the axis *1*, the decrease in the film thickness along the direction *3* (the size effect) is caused by the conformational transformations (29) of molecular fragments in the amorphous phase. The chain fragments with a planar zigzag conformation have a closer packing, and, hence, the con-

Table 3. Electrical and elastic parameters and a comparison of the calculated and experimental piezoelectric coefficients and electrostrictive constants for poly(vinylidene fluoride), VDF–TFE copolymer, and PZT piezoelectric ceramics [28]

Material	k_{33}, $m^4 C^{-2}$	P_r, mC m^{-2}	$\varepsilon_3/\varepsilon_0$	g_{33}, m^2/C	$2k_{33}P_r$, m^2/C	d_{33}, pm V^{-1}	$2\varepsilon_3 k_{33}P_r$, pm/V	S_{33}, GPa^{-1}	$S_{33}P_r$, pm/V	S_{33}/ε_3, m^4/C^2
Oriented PVDF	−2.4	56	16.0	−0.17	−0.27	−26	−33	0.42	−24	−1.5
Oriented VDF– TFE copolymer (78 : 22)	−2.3	72	13.8	−0.36	−0.33	−39	−41	0.32	−23	−1.3
Oriented VDF–TFE copolymer (65 : 35)	−2.5	81	10.9	−0.43	−0.41	−35	−39	0.40	−34	−2.2
Isotropic VDF–TFE copolymer (65 : 35)	−2.1	86	10.4	−0.36	−0.36	−30	−33	0.32	−28	−1.7
Isotropic VDF–TFE copolymer (78 : 22)	−2.3	65	15.4	−0.34	−0.33	−44	−41	0.70	−46	−2.6
PZT	0.03	350	2940	0.02	0.02	560	550			

formational transformations should be accompanied by a decrease in the film thickness. This is a manifestation of the size effect. On the other hand, the conformational transformations are attended by a change in the dipole moment, i.e., in the permittivity of the sample, which is characteristic of the electrostriction. It is also difficult to separate these two effects when the case in point is the reversible partial crystallization of chains in the amorphous phase under the action of electric fields or mechanical stresses. As was noted above, this process should be accompanied by a decrease in the film thickness due to the closer packing in the crystalline phase as compared to that in the amorphous phase. When the film is characterized by remanent polarization, the size effect is responsible for the piezoelectricity. However, the reversible crystallization leads to a decrease in the permittivity because of the decrease in the fraction of the amorphous phase (with a higher permittivity), which, by definition, is a manifestation of the electrostriction effect [see relationship (14)].

4. MANIFESTATION OF ANISOTROPY OF THE MECHANICAL PROPERTIES OF TEXTURED FILMS IN THE PIEZOELECTRIC EFFECT

The above transformation of the microstructure in the studied polymers in response to mechanical stresses implies that their mechanical properties should exhibit a nonlinear behavior. Such a behavior was observed for a number of polymers [63]. Moreover, Reid and Steel [64] found that an increase in the electric voltage applied to a poly(vinylidene fluoride) film leads to a decrease in the resonance frequency. These phenomena were studied in detail in experiments on the direct piezoelectric effect in uniaxially oriented poly-

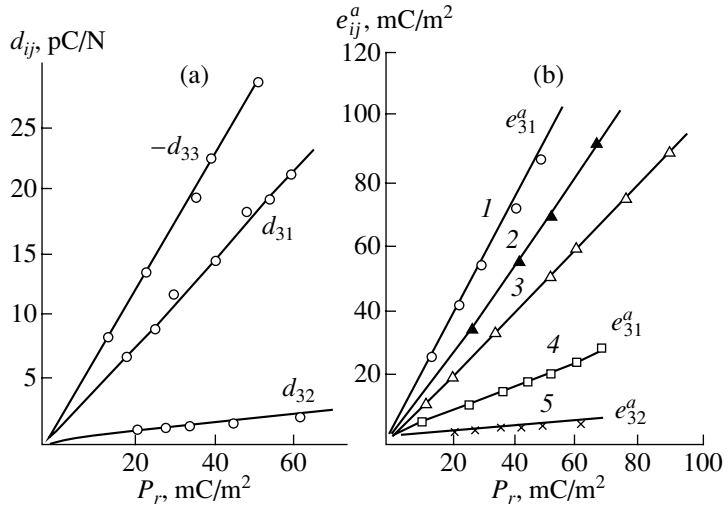

Fig. 15. Dependences of (a) the piezoelectric coefficients d_{ij} for oriented PVDF films and (b) the electrostrictive constants e_{ij} for oriented VDF–TFE copolymer films of compositions (*1*) 52 : 48, (*2*) 65 : 35, and (*3*) 73 : 27; (*4*) unoriented VDF–TFE copolymer films; and (*5*) oriented PVDF films [4].

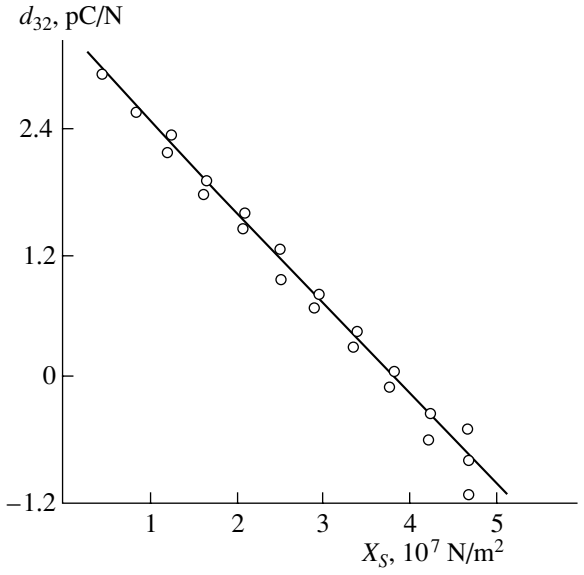

Fig. 16. Dependence of the piezoelectric coefficient d_{32} on the static mechanical stress X_S for uniaxially oriented PVDF [66].

(vinylidene fluoride) films [65, 66]. The experimental data are presented in Fig. 16. It can be seen from Fig. 16 that, with an increase in the constant mechanical stress (applied along the direction *2*), the piezoelectric coefficient d_{32} decreases and even changes sign [65, 66]. It should be emphasized that the piezoelectric coefficient d_{32} without loading turns out to be one order of magnitude less than the piezoelectric coefficient d_{31}. The piezoelectric coefficients d_{31} and d_{32} were measured by applying the mechanical stress along the direction *1* (microfibril axis) and in the perpendicular direction, respectively (see Fig. 14). Therefore, end surfaces of crystallites with covalent bonds in the former case and lateral surfaces with weak intermolecular interactions in the latter case were subjected to the stress. For this reason, the intermolecular bonds in the latter case can be broken under the action of the external stress, which explains the decrease in the piezoelectric coefficient d_{32}.

When considering the piezoelectricity as a linear effect, the polarization *P*, the field strength *E*, the strain *x*, and the mechanical stress *X* are related by two phenomenological expressions

$$P = dX + \chi^T E, \quad x = S^e X + dE, \tag{35}$$

where χ^T is the permittivity and S^e is the mechanical compliance. A decrease in the piezoelectric coefficient d_{32} with an increase in the stress X_2 can be taken into account by introducing the nonlinear terms of at least the second order. For an anisotropic film in the case of the short-circuited condition ($E = 0$), we have

$$x_2 = S^e_{22} X_2 + \alpha_{222} X_2^2, \quad P_3 = d_{32} X_2 + \beta_{322} X_2^2, \tag{36}$$

where the coefficients $\alpha_{222} = \frac{1}{2}\frac{\partial S^e_{22}}{\partial X_2}$ and $\beta_{322} = \frac{1}{2}\frac{\partial d_{32}}{\partial X_2} = \frac{1}{2}\frac{\partial S^e_{22}}{\partial E_3}$ characterize the nonlinear elasticity and the nonlinear piezoelectricity, respectively.

In experiments, the mechanical stress applied to the film involves the static and dynamic components and (omitting the indices) can be represented as

$$X = X_S + X_0 \sin(2\pi f t).$$

With due regard for formulas (36), we obtain

$$\begin{aligned} P_3 &= d[X_0 \sin(2\pi f t) + X_s] \\ &+ \beta[X_0 \sin(2\pi f t) + X_s]^2. \end{aligned} \tag{37}$$

Expression (37) can be rewritten in the form

$$P = P(0) + P(f) + P(2f),$$

where

$$\begin{aligned} P(0) &= \left(dX_s + \beta X_s^2 + \frac{1}{2}\beta X_0^2\right), \\ P(f) &= X_0(d + 2\beta X_s)\cos 2\pi f t, \\ P(2f) &= -(\beta/2)X_0^2 \cos[2\pi(2f)t]. \end{aligned} \tag{38}$$

It can be seen that the induced polarization has three components, namely, one static and two dynamic components. The dynamic components should be observed at the fundamental frequency and double frequency. The second harmonic is observed only for the nonlinear piezoelectric effect. At $\beta = 0$, the second harmonic disappears and expressions (38) transform into the usual linear relationships. The data represented in Fig. 17 confirm the validity of expressions (38). Indeed, the polarization component $P(f)$ at the fundamental frequency and the second harmonic $P(2f)$ are linear functions of x_0, and the coefficient β_{322} is estimated at -3.6×10^{-12} C/m^2 N^2. This value coincides accurate to within 20% with the coefficient β_{322} calculated using the data from Fig. 16.

The temperature dependences of the real and imaginary parts of the coefficients β_{322} and β_{311} (Fig. 18) characterize the nonlinearities of the piezoelectric coefficients d_{32} and d_{31}, respectively [67]. It can be seen that the piezoelectric coefficient d_{31} does not vary with the stress, because the coefficient β_{311} is equal to zero over the entire temperature range. A drastic increase in the coefficient β_{322} upon transition of the polymer from the vitreous states to the high-elasticity state was explained in [67] by the decrease in the dipole moment of crystals. This decrease can be associated with the "disintegration" of initial microfibrillar crystals [68] under the action of the stress X_s. The disintegration can be judged from the acoustic data (Fig. 19) obtained by measuring variations in the acoustic modulus upon reorientation of textured poly(vinylidene fluoride) films under their

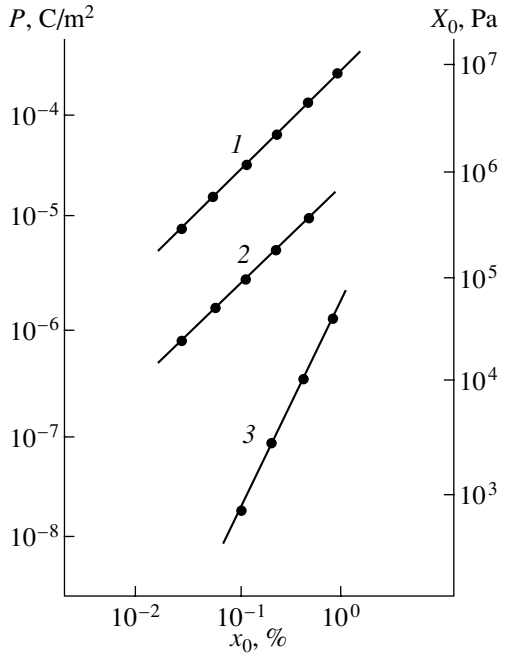

Fig. 17. Dependences of (*1*) the stress X_0 and the polarization P at (*2*) the fundamental and (*3*) double frequency on the amplitude of the alternating strain x_0 at a frequency of 0.8 Hz for uniaxially oriented polarized PVDF films at a static mechanical stress of 8.5 MPa [67].

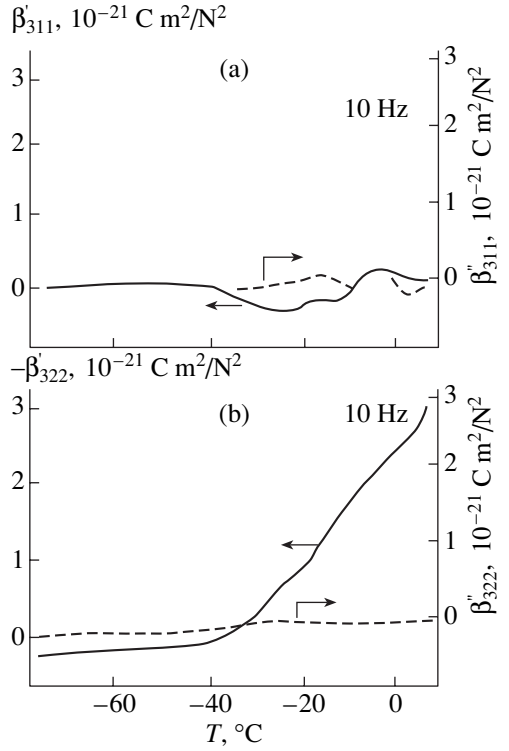

Fig. 18. Temperature dependences of the real and imaginary parts of the coefficients (a) β_{311} and (b) β_{322} for uniaxially oriented PVDF films [67].

deformation along different directions [5, 36]. As the strain increases, the acoustic velocity increases along the direction *1* ($\varphi = 0$) (Fig. 19, curve *2*') and decreases along the direction *2* ($\varphi = 90°$) (Fig. 19, curve *1*'). The acoustic velocity v_{s2} measured along the direction *2* can be written in the form

$$v_{s2} = (C_{S2}/\rho)^{0.5}. \quad (39)$$

According to the microfibrillar model of oriented polymers (Fig. 14), the change in the acoustic velocity is determined by the acoustic (dynamic) modulus C_{s2} in the direction perpendicular to the microfibril axis. In the case when interfibrillar amorphous regions of thickness l_a and modulus C_a alternate with crystallites of transverse size l_{ct} and modulus C_{22}, the elastic constant for this model has the form [39]

$$C_{s2} = \frac{C_a}{1 - (l_{ct}/l_a)(1 - C_a/C_{22})}. \quad (40)$$

As follows from relationship (40), a decrease in the transverse size l_{ct} of the crystal upon loading along the direction *2* should result in a decrease in the modulus C_{s2}, which is observed in experiments.

This interpretation is corroborated by the NMR data obtained by Clements *et al.* [69], who studied the deformation of uniaxially oriented poly(vinylidene fluoride) films. Two components of the absorption line (Fig. 20) correspond to mobile and immobile nuclei. The intensities of the components vary in an opposite way when the film is loaded along and across the drawing axis. The fraction of mobile nuclei decreases in the former case and increases in the latter case. A change in the dynamic degree of crystallinity [70] upon loading (Fig. 21) indicates that the crystallinity increases along the drawing axis ($\varphi = 0$) and decreases in the transverse direction ($\varphi = 90°$). This is in agreement with the strain-induced behavior of the acoustic velocity in the oriented poly(vinylidene fluoride) samples (Fig. 19) and supports the hypothesis that the decrease in piezoelectric coefficient d_{32} upon mechanical loading results from the disintegration of microfibrillar crystals.

5. PIEZOELECTRIC EFFECT UNDER SHEAR AND BENDING DEFORMATIONS

It can be seen from matrix (3) that, apart from nonzero piezoelectric coefficients corresponding to the compressive and tensile deformations, the piezoelectric coefficients with subscripts 15 and 24 are also nonzero. Taking into account interesting applications of transducers using the shear properties of poly(vinylidene fluoride) [71, 72], it is advisable to examine the mechanism of piezoelectric response under shear deformation. This mechanism was studied by the resonance method proposed in [19, 73–75]. The geometry of *X*-cut and *Y*-cut resonators is schematically depicted in

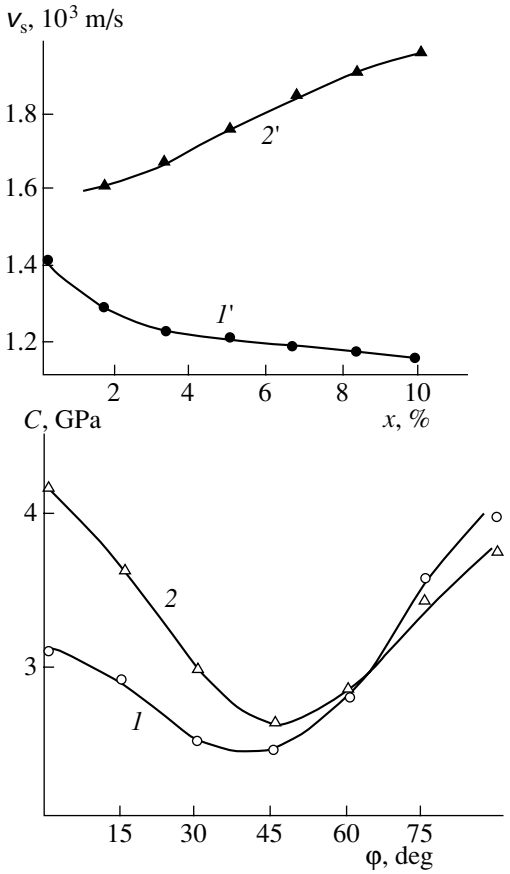

Fig. 19. (*1*, *2*) Anisotropy of the acoustic modulus C and (*1*', *2*') strain-induced changes in the ultrasonic velocity v_s in (*1*, *1*') extruded and (*2*, *2*') uniaxially oriented PVDF films [36] under deformation along (*1*, *1*') the axis *2* and (*2*, *2*') the axis *1*.

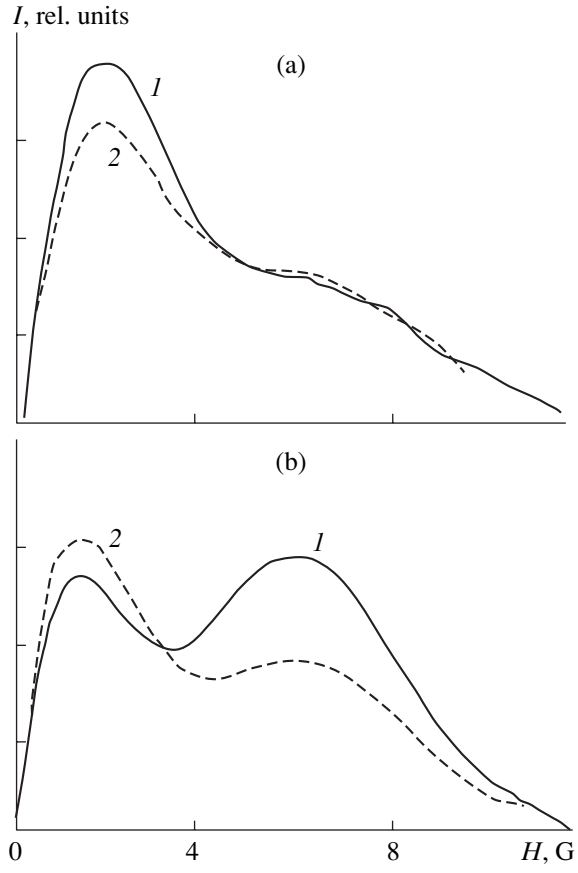

Fig. 20. Evolution of the line shape in the NMR spectra of PVDF samples prepared by uniaxially drawing at 80°C (drawing ratio $\lambda = 4$) under loading (a) along and (b) across the drawing axis at a stress of 85 MPa: (*1*) initial and (*2*) loaded samples [69].

Fig. 22. This figure shows that the motion modes associated with the displacement of atoms along the chain (e_{15} and d_{15}) and their rotation (e_{24} and d_{24}) can be excited when macromolecular axes are appropriately arranged with respect to an external field. A comparison between the piezoelectric coefficients determined by the resonance and quasi-static methods [76] demonstrates their good agreement. The calculated piezoelectric coefficients d_{15} and d_{24} are equal to 30.7 and 4.28 pC/N, respectively [77]. The calculated coefficient d_{15} agrees well with experimental data, whereas the difference between the measured and calculated coefficients d_{24} is as much as 500%.

Another aspect of the problem under consideration is the appearance of the piezoelectricity under bending deformations. As is known, when the arising polarization has a gradient across the film thickness, the film bending induces additional polarization. The increment of the electric induction component along the normal to the film plane (axis *3*) in the general has the form [78]

$$D_3 = \varepsilon_3 E_3 + \beta_{31}(1/R), \qquad (41)$$

where ε_3 is the permittivity, $1/R$ is the curvature or the strain gradient, R is the radius of curvature, and β_{31} is the measured bending piezoelectric stress coefficient taking into account that a strip of length l and width ω is cut along the drawing axis (direction *1*) and the deformation is performed by rotation about the axis *2*. Under the short-circuited condition ($E_3 = 0$), in the general case of inhomogeneous polarization ($D_3 = \text{const}$), the charge induced on electrodes is written in the form $Q_3 = D_3 l\omega = l\omega\beta_{31}/R$. Since $1/R = 2\Delta z/l^2$, we obtain

$$\beta_{31} = (1/2\omega)(Q_3/\Delta z), \qquad (42)$$

where Δz is the deviation of the free plate (strip) end from an equilibrium position.

Under bending, the upper part of the film (with respect to the midline) undergoes a tensile strain, whereas the lower part of the film undergoes a compressive strain. In this case, the general expression (41) describing the electric induction for the bending piezoelectric effect can be rewritten in the following

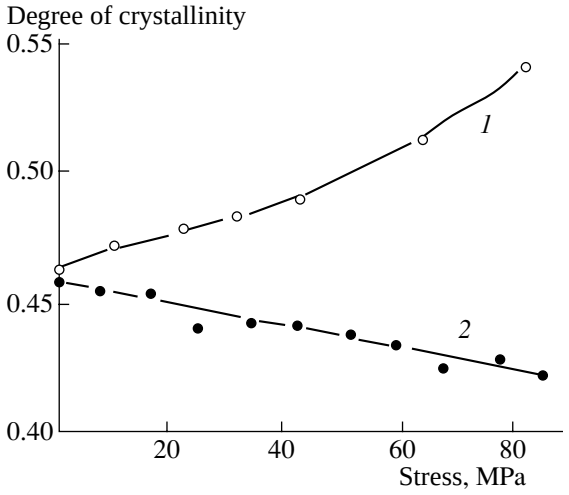

Fig. 21. Reversible changes in the dynamic degree of crystallinity in uniaxially oriented PVDF films under loading (*1*) along and (*2*) across the drawing axis [69].

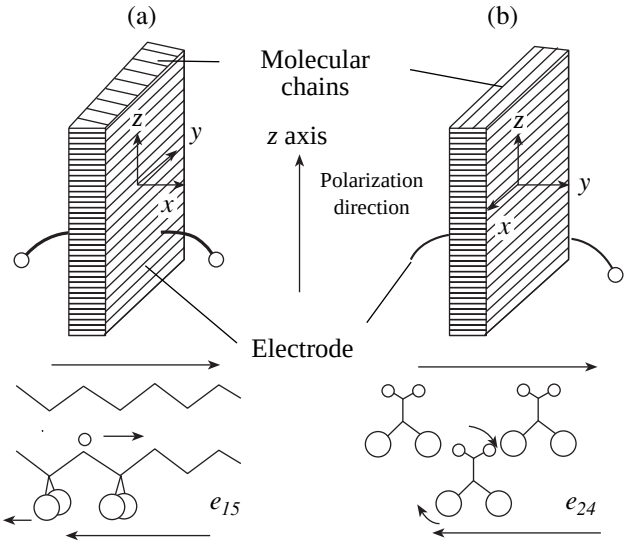

Fig. 22. Electrode configurations in *X*-cut and *Y*-cut resonators with VDF–TFE copolymer (75 : 25) films for examining piezoelectric characteristics upon shear [75].

from [78]:

$$D_3 = \varepsilon_3 E_3 + d_{31} X_1 + f_{31} dX_1/dz, \quad (43)$$

where X_1 is the mechanical stress along the direction *1*, d_{31} is the piezoelectric strain coefficient, and f_{31} is the bending piezoelectric strain coefficient characterizing the polarization under stress gradient conditions. Formulas (41) and (43) makes it possible to derive the expression relating two bending piezoelectric coefficients, that is,

$$1/R\beta_{31} = d_{31} X_1 + f_{31} dX_1/dz. \quad (44)$$

In the general case (for an inhomogeneous polarization), the quantities d_{31}, f_{31}, and X_1 are functions of the z coordinate (along the axis *3*) and the coefficient β_{31} describes the bending piezoelectric effect for a fixed plate. Therefore, the terms on the right-hand side of relationship (44) should be averaged, that is,

$$(1/R)\beta_{31} = \overline{d_{31} X_1} + \overline{f_{31}(dX_1/dz)}. \quad (45)$$

For an elastic plate with the thickness L and the Young modulus C, the mechanical stress along the x direction (axis *1*) is defined by the formula $X_1 = C(1/R)z$ and we obtain

$$\overline{d_{31} X_1} = (C/RL) \int_{-L/2}^{L/2} d_{31}(z) z dz,$$
$$\overline{f_{31}(dX_1/dz)} = (c/RL) \int_{-L/2}^{L/2} f_{31}(z) dz. \quad (46)$$

Substitution of expression (46) into relationship (45) gives

$$\beta_{31} = C/L \left(\int_{-L/2}^{L/2} d_{31}(z) z dz + \int_{-L/2}^{L/2} f_{31}(z) dz \right). \quad (47)$$

Relationship (47) allows us to estimate the coefficients β_{31} for a number of distributions $d_{31}(z)$ observed in practice. Four distributions are depicted in Fig. 23. For a symmetric bimorph (Fig. 23a), we have $d_{31}(z) = -d_0$ for z from $-L/2$ to 0 and $d_{31}(z) = d_0$ for z from 0 to $L/2$. In both cases, the bending piezoelectric coefficient is represented as $f_{31}(z) = f_0$. The piezoelectric coefficient d_{31} under tensile deformation in the general case has the form

$$d_{31} = 1/L \int_{-L/2}^{L/2} d_{31}(z) dz \quad (48)$$

and is determined to be $d_{31} = 0$. According to formula (47), the bending piezoelectric coefficient takes the form

$$\beta_{31} = C[(L/4)d_0 + f_0]. \quad (49)$$

Since $d_{31}(z) = d_0$ and $f_{31}(z) = f_0$ for a uniform polarization (Fig. 23b), we find

$$\beta_{31} = C f_0, \quad d_{31} = d_0. \quad (50)$$

For an asymmetric bimorph (Fig. 23c), we have $d_{31}(z) = -d_2$ and $f_{31}(z) = f_2$ in the range from $-L/2$ to $\xi/2$ and $d_{31}(z) = d_1$ and $f_{31}(z) = f_1$ in the range from $\xi/2$ to $L/2$. In

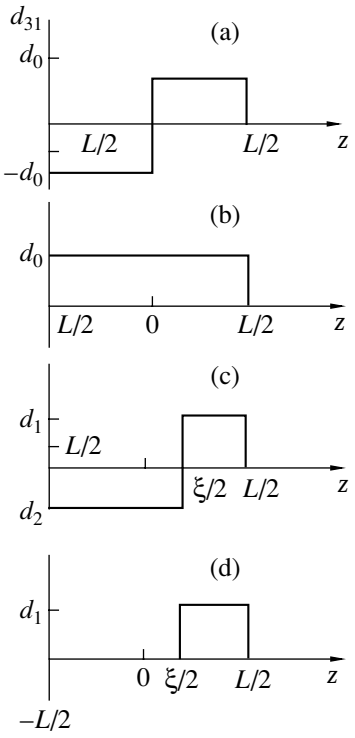

Fig. 23. Four types of the distribution $d_{31}(z)$: (a) antisymmetric bimorph, (b) uniform distribution, (c) asymmetric bimorph, and (d) monomorph [78].

this case, the sought piezoelectric coefficients are as follows:

$$\beta_{31} = C\left[\frac{L}{4}\frac{d_1 + d_2}{2}\left(1 - \frac{\xi^2}{L^2}\right) + \frac{f_1 + f_2}{2} + \frac{f_2 - f_1}{2}\frac{\xi}{L}\right],$$
$$d_{31} = \frac{d_1 - d_2}{2} - \frac{d_1 + d_2}{2}\frac{\xi}{L}. \quad (51)$$

In the case of a monomorph (Fig. 23d), the film of thickness L is separated into two parts: one part of thickness $L_1 = (L - \xi/2)$ is unpolarized and another part of thickness $\xi/2 = (L - L_1)$ is characterized by the constant piezoelectric coefficients d_1 and f_1. The piezoelectric coefficients for this distribution are represented by the expressions [79]

$$\beta_{31} = C\left[\frac{L}{8}d_1\left(1 - \frac{\zeta^2}{L^2}\right) + \frac{1}{2}f_1\left(1 - \frac{\zeta}{L}\right)\right],$$
$$d_{31} = \frac{d_1}{2}\left(1 - \frac{\zeta}{L}\right). \quad (52)$$

The validity of expressions (52) was verified with the use of poly(vinylidene fluoride) samples polarized in an electron beam. The sample polarized by this method has a monomorph structure, because the mean free path of accelerated electrons in a material is finite, and this region of the sample remains unpolarized. For a monochromatic beam, a layer of electrons captured in traps at the end of the path can be considered a virtual electrode, in the field of which the polarization of the remaining region of the film takes place. An increase in the energy of electrons leads to an increase in their mean free path and, hence, to a decrease in the thickness of the polarized layer in the monomorph structure (Fig. 23d). According to expression (52), this should result in a decrease in the measured piezoelectric coefficient d_{31} when the piezoelectric coefficient d_1 is constant in the polarized layer. It is this situation that was experimentally observed by Sessler and Berraissoul [79].

As follows from expressions (52), the piezoelectric coefficients β_{31} and d_{31} should vary in a correlated manner for films polarized under different conditions in an electron beam. Fukada *et al.* [78] checked this inference for biaxially oriented poly(vinylidene fluoride) films by varying the irradiation time at a constant beam current density and electronic energy. The data obtained are presented in Fig. 24. It can be seen that the experimental points fit a linear dependence. The slope of this dependence determines the contributions of the tensile piezoelectric coefficient d_{31} and the bending piezoelectric coefficient f_{31} to the observed coefficient β_{31}. The estimates made in [78] for the monomorph with a thin polarized layer demonstrate that the contributions of the tension and bending are equal to 1/3 and 2/3, respectively. A similar correlation between variations in the piezoelectric coefficients d_{31} and β_{31} was also observed in [79] for biaxially oriented poly(vinylidene fluoride) films polarized by an electron beam at energies of 10 and 15 keV. An increase in the energy of electrons leads to an increase in the thickness of the unpolarized region in the film. According to expressions (52), this should result in smaller values of the coefficients d_{31} and β_{31} (if the coefficients f_1 and d_1 are constant), which was observed experimentally (see Fig. 25). It can be see from Fig. 25 that the annealing of polarized films in a free state leads to a correlated decrease in both piezoelectric coefficients. This behavior is not a specific feature of the polarization technique used, because a similar decrease was observed for films polarized in a corona discharge [79] and by the contact method [80].

Upon annealing above a certain temperature, the slope of the curves depicted in Fig. 25 changes for both films. Specifically, the free annealing of the film at temperatures below 70°C is accompanied by a more drastic change in the tensile piezoelectric coefficient d_{31}. By contrast, the annealing at higher temperatures leads to a more drastic decrease in the piezoelectric coefficient β_{31}. According to Wintle and Diirsam [81], in order to explain this behavior, it is necessary to allow for the contribution of the space charge, in addition to the dipole contribution, to the piezoelectric effect [7, 82–86]. The space charge (formed by intrinsic carriers and carriers injected from electrodes), together with dipoles, should contribute to the piezoelectric coeffi-

cient β_{31}. A sharper decrease in the piezoelectric coefficient β_{31} at higher annealing temperatures was attributed to the release of carriers captured in traps. The annealing temperature corresponding to a drastic decrease in the piezoelectric coefficient β_{31} is equal to 70°C [79] (Fig. 25) or 80°C [80]. Analysis of the data on the relaxation phenomena in poly(vinylidene fluoride) demonstrates that the mobility in the crystalline phase is defrozen (α_c dispersion) approximately at these temperatures [5]. Free carriers are localized in the vicinity of polar planes in ferroelectric crystals [85, 86]. Therefore, the defreezing of mobility in these crystals favors the release of charges from traps. In [81], the authors stated that the change in the distribution of the space charge is responsible for the sharp decrease in the piezoelectric coefficient β_{31} at high annealing temperatures.

We do not deny such a role of the space charge but consider other possible reasons for the aforementioned fact. As was shown above, the mechanism of the transverse piezoelectric effect under tensile deformation of the studied polymers is predominantly governed by the electrostriction. The electrostrictive constant for textured films considerably depends on the orientation of chains in the amorphous phase. The free annealing at low temperatures results in the disturbance of local orientation of segments in the disordered phase, which should be attended by a decrease in the electrostrictive constant and, correspondingly, the piezoelectric coefficient d_{31}. The annealing at temperatures above the temperature of defreezing of mobility in the crystalline phase is accompanied by the disturbance of the orientation of crystallites in the polar β phase [87]; i.e., the *c* axes of the lattice become more disordered with respect to the drawing axis (the axis *1* in Fig. 14). This can lead to a decrease in the stress gradient dX_1/dz and, according to formula (45), in the bending piezoelectric coefficient β_{31}.

It is of interest to compare the characteristics of the bending piezoelectricity in poly(vinylidene fluoride) with those for other piezoelectric materials, such as $BaTiO_3$, PZT, etc. Such a comparison is conveniently performed for bimorph plates. When the bimorph plate is supported as a cantilever, the deviation ($\delta = 2\Delta z$) of the free end of the plate (*l* in length and *L* in thickness) from an equilibrium position upon application of the field *E* to the bimorph is given by the formula [88]

$$\delta_F = \frac{3}{2} d_{31} \frac{l^2}{L} E.$$

Note that this formula holds true up to the frequency *f* of the first resonance, which can be written in the form

$$f = 0.162 \sqrt{\frac{C_{11}^E}{\rho}} \frac{l}{L^2}.$$

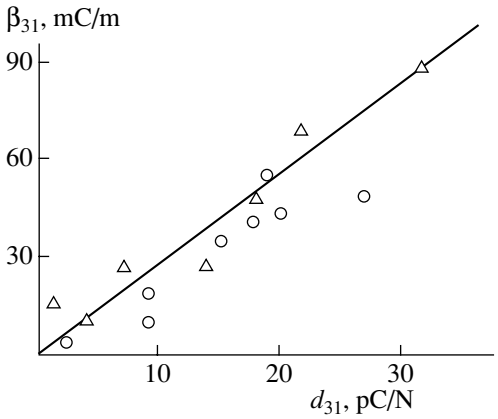

Fig. 24. Correlation between the piezoelectric coefficients β_{31} and d_{31} for two types of PVDF films with a monomorph distribution of polarization induced by electron beams with different energies [78]. Open circles and triangles indicate the experimental data for Kureha and Solvay films, respectively.

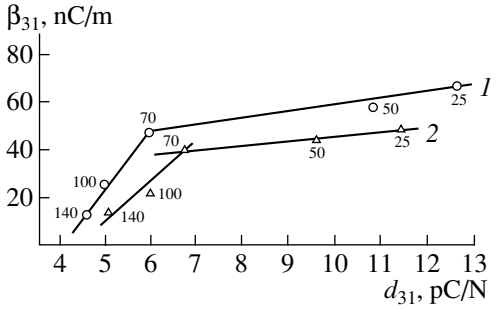

Fig. 25. Correlation between the piezoelectric coefficients β_{31} and d_{31} for biaxially oriented PVDF films polarized in an electron beam at energies of (*1*) 10 and (*2*) 15 keV for 15 min at a beam current of 0.13 μA. Numbers near experimental points indicate the annealing temperatures of the polarized films [79].

Important information is provided by the product

$$\delta_F f = 0.243 \sqrt{\frac{C_{11}^E}{\rho}} d_{31} E, \qquad (53)$$

which is determined only by material constants, including the maximum electric field strength (breakdown voltage). The values of this product for bimorph plates (supported as a cantilever) based on different materials are listed in Table 4. It can be seen from this table that the parameter $\delta_F f$, which characterizes the operating bandwidth (to the first resonance) and the maximum bending upon application of electric field to the bimorph, appears to be considerably larger for poly(vinylidene fluoride) as compared to those for other materials. For the most part, this is achieved owing to the higher operating voltage, which is approximately 30 times higher than those for inorganic piezoelectric materials.

Table 4. Parameters of bending piezoelectricity in bimorph elements (supported as a cantilever) fabricated from different piezoelectric materials [88]

Piezoelectric material	c_{11}, GPa	ρ, kg/m^3	d_{31}, pm/V	E_{max}, MV/m	$\delta_F f$, m Hz
PZT-4	139	7.5	–123	1.0	0.129
PZT-5B	121	7.75	–171	1.0	0.164
G-1278	60	7.4	–270	0.7	0.130
G-1408	90	7.5	–80	2.3	0.154
$BaTiO_3$ (EC-31)	116	5.55	–59	2.2	0.144
PVDF (Kureha)	3	1.78	+30	30.0	0.284

The parameters δ_F and f can be changed by inserting the third layer (from a nonpiezoelectric material with a low density and a small modulus) between poly(vinylidene fluoride) films [88]. These parameters can also be changed by fabricating an asymmetric bimorph in which the polarization in layers can differ not only in direction but also in magnitude. This is achieved by producing a temperature gradient across electrodes in the course of polarization. The polarization conditions at different temperatures at a cathode and an anode in not very strong fields (0.6 MV/cm) and the corresponding distributions of polarization [piezoelectric coefficient $d_{31}(z)$] [89] are given in Fig. 26. The

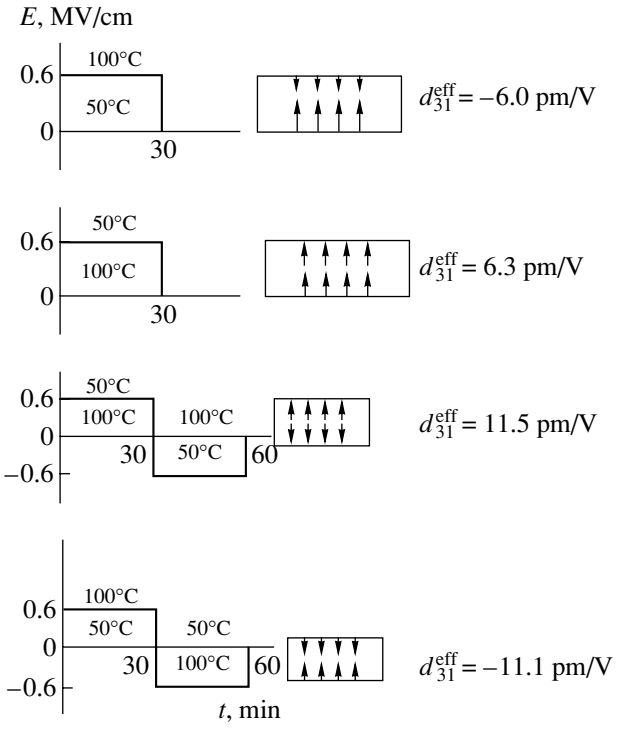

Fig. 26. Polarization conditions in the presence of a temperature gradient across the electrodes and the polarization distributions in the bimorphs based on PVDF [89].

effective piezoelectric coefficient $d_{31}^{eff} = 2\delta L^2/3Vl^2$ can be introduced for the film of thickness L and length l. These effective piezoelectric coefficients d_{31}^{eff} calculated from the measured parameters δ and the applied voltages V for different polarization types are also presented in Fig. 26. As can be seen from this figure, the unipolar polarization with the temperature gradient leads to the asymmetric distribution $d_{31}(z)$. The changeover from a cold cathode to a cold anode is accompanied by a change in the sign of the effective piezoelectric coefficient d_{31}^{eff}. The bipolar polarization results in the formation of a bimorph structure in which the sign of the effective piezoelectric coefficient d_{31}^{eff} can be changed using a colder cathode in the first polarization cycle. The parameters of the bending piezoelectric effect can be varied by increasing the number of layers in a bending piezoelectric element. In particular, Lee and Marcus [88] calculated the parameters δ for a trilayer element in which outer layers are piezoelectrically active and a middle layer is electrically neutral. In [89], it was demonstrated that, for a more complex variant (multimorph), the parameter $\delta_F f$ can be increased owing to an increase in the number of layers in an element.

6. STABILITY OF THE PIEZOELECTRIC PROPERTIES OF POLY(VINYLIDENE FLUORIDE) AND ITS COPOLYMERS

Different types of mobility and relaxation phenomena in crystallizing polymers, including poly(vinylidene fluoride) [5], create the prerequisites for the deterioration of the piezoelectric characteristics. The results obtained in a number of works devoted to the ageing of piezoelectric materials will be considered below. For films, poly(vinylidene fluoride) crystals in the polar β phase are usually prepared by choosing appropriate conditions of texturing. According to the phase diagram, polymorphic transitions of the type $\beta \longrightarrow \alpha$ can occur at elevated temperatures [5]. Since crystals of the α phase are nonpolar, the above transitions affect the piezoelectric response [39]. The problems of ageing were studied in [84, 90–93]. Let us analyze the results obtained by Kolbeck [91]. The kinetic curves of change in the piezoelectric coefficient d_{31} depending on the annealing temperature indicate that this coefficient at temperatures below 40°C remains constant over the course of more than a year. At temperatures above 100°C, the kinetics of decrease in the piezoelectric coefficient d_{31} involves two stages whose rates differ considerably. An increase in the temperature leads to an increase in the difference between the rates of these stages. Note that the fast stage results in a decrease in the piezoelectric response by 70–90%. This can be caused by several factors. One of the factors is associated with the possibility of changing the rema-

nent polarization P_r upon high-temperature annealing. As can be seen from relationship (34) and Fig. 15, the coefficient d is directly proportional to the remanent polarization P_r. In turn, the remanent polarization P_r for a uniaxially drawn film can be written in the form

$$P_r \approx NP_{sc}\langle \cos\theta \rangle, \quad (54)$$

where N is the number of polar crystals that have the spontaneous polarization P_{sc} and form the mean angle θ with the normal to the film surface. Since the oriented state of polymers is metastable in nature, the orientation can vary upon free annealing. The X-ray diffraction data at large angles after high-temperature free annealing (at 140°C) of uniaxially drawn vinylidene fluoride–trifluoroethylene copolymer films [87] suggest the misorientation of initial crystallites. This inference is confirmed by a substantial decrease in the dichroic ratio for the crystallinity band at 442 cm^{-1} [5, 87]. The misorientation should lead to a decrease in the quantity $\langle \cos\theta \rangle$ and, according to relationship (54), in the remanent polarization P_r. One more factor responsible for the decrease in the remanent polarization at high ageing temperatures is a change in the morphology. This follows from the small-angle X-ray scattering data obtained in [87]. The X-ray data indicate that a prime reflection transforms into a droplet reflection, which is explained by the transformation of fibrillar crystals into lamellar crystals. This transformation leads to a change in the distribution of the space charge stabilizing the remanent polarization [85, 86] and, hence, to a decrease in P_r. The lamellar crystals formed upon high-temperature annealing have a larger number of folded regions [94], which should result in a decrease in the spontaneous polarization P_{sc} [39]. The high-temperature annealing is also attended by a change in the microstructure of intercrystallite regions. In this case, a substantial decrease in the birefringence and the acoustic modulus is attributed to a decrease in the number of taut tie chains (or the fraction of the anisotropic amorphous phase) [87]. As was noted above, it is these taut tie chains that can be nuclei of the strain-induced crystallization and determine the piezoelectric coefficient.

The introduction of trifluoroethylene units (5–6 mol %) into the poly(vinylidene fluoride) homopolymer chain leads to a decrease in the degree of crystallinity. It seems likely that the last circumstance results in a change in the kinetics of variation in the piezoelectric coefficient d_{31} during the ageing of vinylidene fluoride–trifluoroethylene copolymer (94 : 6) films. This change consists in the fact that the temperature at which there appear two stages of ageing with a fast relaxation of the piezoelectric response is equal to 70–80°C for the above copolymer [92, 93] and 110°C for the homopolymer (Fig. 27). A comparison of the data obtained in [92, 93] shows that the characteristics of thermal ageing depend not only on the fraction of trifluoroethylene in the copolymer but also on the synthesis procedure. Indeed, in the copolymer synthesized by emulsion polymerization [93], the piezoelectric coefficient d_{31} decreases more slowly and the ageing rate at the first stage decreases by more than one order of magnitude.

The boundary conditions should play an important role in the high-temperature ageing. The structural transformations of poly(vinylidene fluoride) radically differ in the case of free ($X = 0$) and isometric ($x = 0$) annealings [87]. Recently, it was demonstrated that, in the latter case, the structural transformations lead to an increase in the remanent polarization [95]. Finally, it is possible to assess the prospects of operating sensors based on poly(vinylidene fluoride) films under usual room conditions. Long-term tests give optimistic assessments. For example, examination of the characteristics of pyrosensors show that their storage for ten years results in a decrease in the pyroelectric signal by only 7% [90].

7. THE INFLUENCE OF PRESSURE ON THE PIEZOELECTRIC EFFECT

Qualitatively similar results were obtained in a number works [96–98]. An increase in the pressure leads to a decrease in the coefficient d_h (Fig. 28a). It was found that the location of the characteristic maximum in the temperature dependence of the coefficient d_h and the glass transition point vary with pressure virtually in a symbate way [96]. Since the glass transition occurs in the amorphous phase, variations in d_h with an increase in the pressure should be attributed to changes in the disordered regions of poly(vinylidene fluoride). It was shown above that the piezoelectric coefficients are governed by the size effect and electrostriction, which are characteristic of the amorphous phase. The contribution of the size effect was examined from the dependence of the linear compressibility β_L on the pressure [97]. It was revealed that the dependence of the linear compressibility β_L exhibits a point of inflection at a pressure of 5 kbar (at 25°C), which was interpreted as the transition of the amorphous phase to the vitreous state. This change in the physical state of the polymer is accompanied by a considerable decrease in the Poisson ratio [20, 39]. On the other hand, it can be seen from Fig. 7 that the glass transition also results in a substantial decrease in the electrostrictive constant. According to relationship (38), the piezoelectric coefficient d depends also on the permittivity ε. The dependences of the permittivity ε on the pressure for poly(vinylidene fluoride) samples crystallized in the α (ε_α) and β (ε_β) phases are plotted in Figs. 28 and 29a. As can be seen from Figs. 29a and 29b, a decrease in the permittivity ε is predominantly caused by its decrease in the amorphous phase, whose compliance is one order of magnitude less than that of the crystalline phase. Therefore, a decrease in the piezoelectric coefficient d_h with an increase in the pressure should be associated with the decrease in the Poisson ratio, the electrostrictive con-

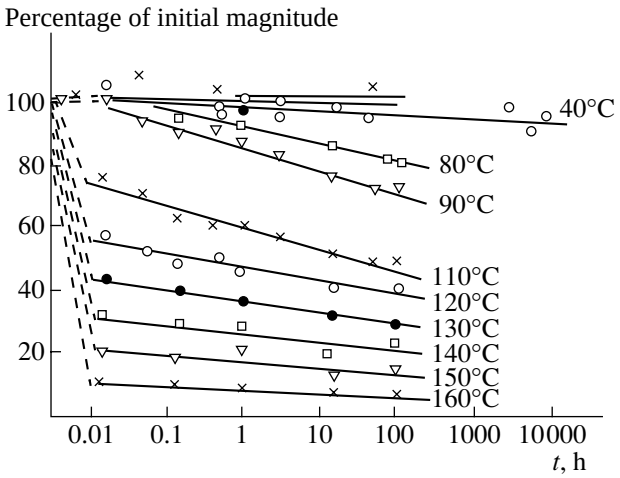

Fig. 27. Kinetics of variation in the piezoelectric parameters during the ageing of a uniaxially drawn PVDF film upon free annealing at different temperatures [91].

stant, and the permittivity. The same inference was drawn in the study of the influence of the pressure on the piezoelectric coefficient *e* [99]. A comparison of the experimental and calculated piezoelectric coefficients *e* [99, 100] demonstrates that the electrostriction and the size effect make the main contribution to the decrease in this coefficient with an increase in the pressure.

The polymers considered possess a low acoustic impedance and, hence, are promising materials for use in hydroacoustics [2]. In this respect, Weeks and Ting [98] analyzed the possibility of using poly(vinylidene fluoride) in hydrophones. These authors studied films prepared from a commercial poly(vinylidene fluoride) and a polymer synthesized according to a special procedure. One way to increase the sensitivity of hydrophones is to increase the piezoelectric coefficient g_h. This can be achieved by forming a microporous structure in the matrix, which provides a decrease in the permittivity ε_{33} [101] and an increase in the piezoelectric coefficient g_h. It can be seen from Fig. 28a that, as the pressure increases to 70 MPa, the quantities ε_{33}, d_h, and g_h for the poly(vinylidene fluoride) film containing no micropores decrease by 5, 17, and 11%, respectively. According to [98], this corresponds to a decrease in the sensitivity of a hydrophone by 1 dB. The behavior of the above characteristics for materials having a microporous structure with an increase in the pressure is illustrated in Fig. 28b. Unlike the films without micropores, the materials with micropores are characterized by a substantial irreversible decrease in both quantities with an increase in the pressure. It is believed that an increase in the pressure leads to the collapse of a microporous structure, which affects the quantities ε_{33}^T and g_h.

Upon cyclic loading of the usual films at a pressure of 70 MPa, the piezoelectric coefficient g_h remains constant after 25 cycles. For the poly(vinylidene fluoride) films with micropores, the piezoelectric coefficients d_h and g_h noticeably decrease after the first three or five cycles and then reach steady-state values. However, the steady-state value of g_h turns out to be larger than that for the films without micropores. Upon dynamic loading by pressure pulses (at amplitudes of up to 70 MPa and a duration of 1–3 ms), the linearity of the response as a function of the pressure amplitude was investigated in [98]. The results obtained for different poly(vinylidene fluoride) films (KF and EMI) are presented in Table 5. Moreover, the data for tourmaline, which is the classical material for underwater sound detectors [98], are also given in Table 5. As can be seen from this table, the parameters of the linearity of response for poly(vinylidene fluoride) films are somewhat worse than those of tourmaline. However, with due regard for larger piezoelectric coefficients d_h, these films seem to be promising materials for recording shock waves in liquid media [98]. The films with a microporous structure are characterized by a high degree of linearity of response at pressures of up to

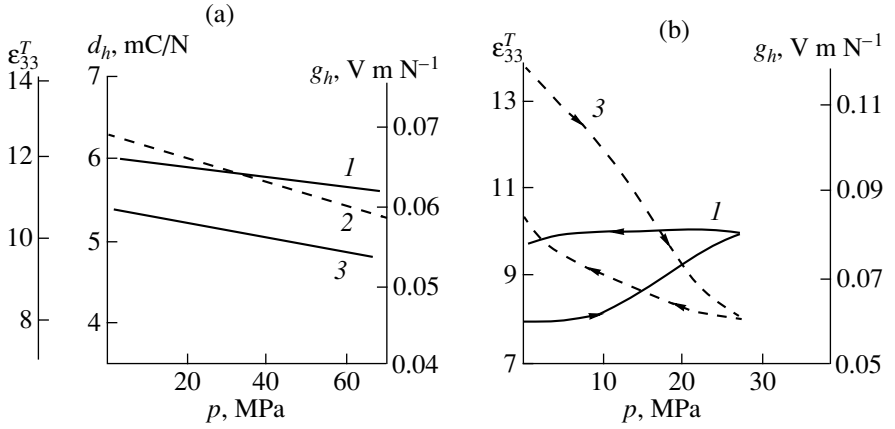

Fig. 28. Dependences of the parameters (*1*) ε_{33}^T, (*2*) d_h, and (*3*) g_h on the static pressure p for PVDF films (a) without micropores and (b) with micropores.

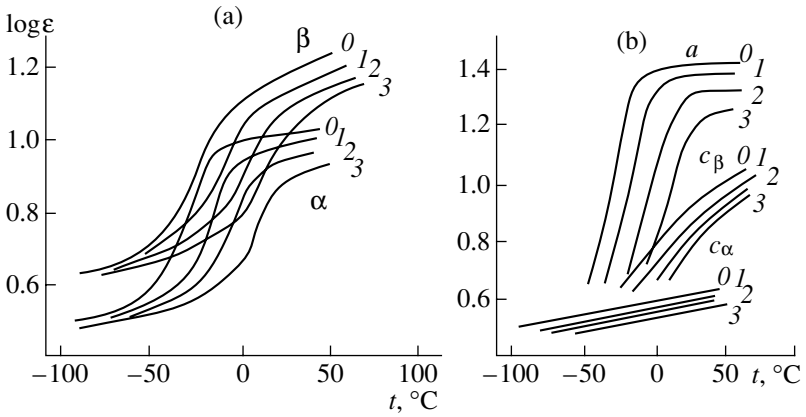

Fig. 29. Temperature dependences of (a) the permittivity at a frequency of 1 kHz for PVDF samples with crystals in the β and α phases and (b) the permittivity of the amorphous (*a*) and crystalline (c_α and c_β) phases [98] at different pressures (kbar): (*0*) 0, (*1*) 1, (*2*) 2, and (*3*) 3.

30 MPa. An increase in the pressure results in the collapse of the porous structure and, correspondingly, in the deterioration of the linearity of response.

8. GENERAL REGULARITIES OF PIEZOELECTRICITY IN INORGANIC FERROELECTRICS AND ORGANIC FERROELECTRIC POLYMERS

It is expedient to compare the large electrostrictive constants observed for the polymers under consideration (Table 3) with those of inorganic crystals. First and foremost, these are relaxor ferroelectrics [102–104], which also have large electrostrictive constants. Such a comparison is of interest because the polymers studied can also be assigned to the class of relaxor ferroelectrics. In the Curie transition range, the permittivity of relaxor ferroelectrics exhibits a broad diffuse maximum whose intensity decreases with an increase in the frequency of the electric field. A smeared maximum in the dependence of the permittivity ε' in the transition range with the above frequency dispersion was repeatedly observed for ferroelectric vinylidene fluoride copolymers [7, 105, 106]. For classical relaxor atomic crystals, one of the reasons for the smeared Curie transition is the formation of defects of a particular type when the arising heterogeneity has small scales and can be recorded neither by X-ray nor by optical methods [107].

The structural–dynamic heterogeneity of ferroelectric polymers was repeatedly noted above. This heterogeneity can be characterized by different scale levels. As applied to a ferroelectric crystal, the heterogeneity can be localized within several interatomic bonds. If all chains in an ideal crystal adopt a planar zigzag conformation, conformational defects (kink bonds) can be formed in real crystals [5]. In particular, these defects can be produced by introducing bulky substituents (for example, hexafluoropropylene comonomer [105]) into the poly(vinylidene fluoride) chain. Upon incorporation into the lattice of the ferroelectric crystal, these substituents can lead to a local change in the chain conformation due to steric reasons. This local heterogeneity can be revealed by spectroscopic techniques from the appearance of isomers with the $TGTG^-$ and $T_3GT_3G^-$ conformations in addition to chain fragments with the $(–TT–)_n$ planar zigzag conformation [105]. These defects result in a considerable decrease in the Curie point and a smearing of the maximum in the dependence of the permittivity ε' in the transition range [105]. Moreover, these defects in the polymers can be formed under the action of corrosive media [105] or upon irradiation [105, 108, 109].

The synthesis of polymer molecules can also be attended by the formation of addition defects of the head-to-head type. In poly(vinylidene fluoride), defects of the type $\cdots CH_2CF_2CH_2CF_2CH_2CF_2CH_2CF_2\cdots$ can arise apart from a regular addition of monomer units $\cdots CH_2CF_2CF_2CH_2CH_2CF_2CH_2CF_2\cdots$. The presence of these defects in poly(vinylidene fluoride) chains can be found by high-resolution NMR spectroscopy [110, 111]. It turned out that these defects can be incorpo-

Table 5. Linearity and dynamic piezoelectric coefficients d_h for different piezoelectric materials [98]

Material	Deviation from true linearity		Initial, d_h, pC/N	Δd_h, %
	%	dB		
Tourmaline	3.5	0.3	2.8	−3.6
KF piezoelectric film	6.5	0.5	8.0	−7.8
EMI film without micropores	6.7	0.6	6.9	−10.6
EMI film with micropores	8.3	0.7	7.3	−9.3
High-microporosity film	31.0	2.3	10.4	−33.7

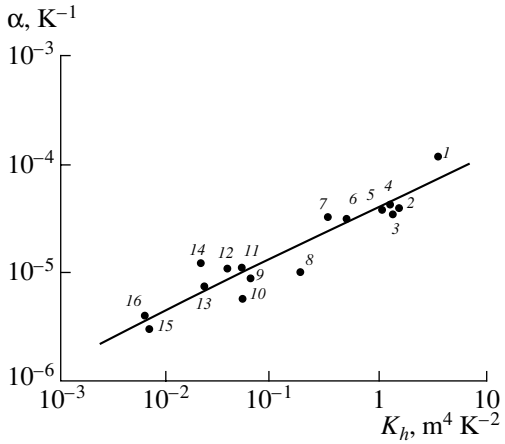

Fig. 30. Correlation between the hydrostatic electrostrictive constant K_h and the thermal expansion coefficient α for different materials: (*1*) PVDF, (*2*) KBr, (*3*) KCl, (*4*) NaBr, (*5*) NaCl, (*6*) NaF, (*7*) LiF, (*8*) MgO, (*9*) Pyrex, (*10*) $KTaO_3$, (*11*) $SrTiO_3$, (*12*) $KNbO_3$, (*13*) $PbTiO_3$, (*14*) $BaTiO_3$, (*15*) $Pb(Zn_{1/3}Nb_{2/3})O_3$, and (*16*) $Pb(Mg_{1/3}Nb_{2/3})O_3$ [112, 113].

rated into the lattice of the ferroelectric crystal with the formation of additional defects [5]. Analysis of the characteristics of the Curie transition in vinylidene fluoride–trifluoroethylene copolymers with different contents of head-to-head defects demonstrates that an increase in their concentration leads to an increase in the smearing of the transition from the ferroelectric phase to the paraelectric phase [106]. Consequently, the objects under consideration exhibit the properties of relaxor ferroelectrics of an inorganic nature and, hence, should satisfy dependences common to relaxor systems. In particular, two such dependences are depicted in Figs. 30 and 31. The linear dependence between the electrostrictive constant and the thermal expansion coefficient is plotted in Fig. 30. It can be seen that poly(vinylidene fluoride) possessing the largest thermal expansion coefficient fits well the observed dependence. The dependence shown in Fig. 31 indicates that an increase in the electrostrictive constant is accompanied by a decrease in the permittivity of ferroelectrics. In this case, too, the data for poly(vinylidene fluoride) are consistent with the dependence observed.

Therefore, ferroelectric polymers obey the empirical regularities characteristic of relaxor ferroelectrics. In this respect, it is advisable to compare the regularities in the piezoelectricity of the polymers and inorganic relaxor ferroelectrics. For comparison, we choose perovskite piezoelectric ceramics of the $Pb(Zr,Ti)O_3$ (PZT) type and electrostriction materials of the $Pb(Mg_{1/3}Nb_{2/3})O_3$ (PMN) type. It is known that PZT ceramics can exist in two ferroelectric modifications, namely, the tetragonal and rhombohedral ferroelectric phases. According to [115, 116], the piezoelectric and electrostrictive characteristics become more pronounced in the region of the morphotropic phase boundary in which both phases coexist in the materials under consideration. A qualitatively similar situation is observed for ferroelectric polymers. Ferroelectric crystals and the amorphous phase, which can be treated as the paraelectric or even antiferroelectric phase [117], always occur in the film bulk. This means that two phases with different symmetries coexist in the film. The amorphous halo at $2\theta \approx 18°$ (see Fig. 11) can serve as an indication that nanocrystals (2–3 nm in size) with a symmetry differing from that of ferroelectric regions exist in the bulk of polymer films. Similar small-sized crystals are also observed in inorganic relaxor ferroelectrics [103, 104]. Nanocrystals first respond to the application of an electric field. Actually, an increase in the electric field strength leads to a sharp weakening of diffuse scattering and an increase in the intensity of the Bragg reflection associated with PMN [118]. According to the phase diagram of the PMN system (Fig. 32), this increase in the field is attended by the transition from vitreous phase **II** or paraelectric phase **I** (depending on the temperature) to ferroelectric phase **III**. It can be believed that this phenomenon is common to all relaxor ferroelectrics, because qualitatively similar transitions from weakly ordered phases to the ferroelectric phase in response to electric fields were observed in a number of other systems, such as $Pb(Sc_{1/2}Ta_{1/2})O_3$, $Pb(Sc_{1/2}Nb_{1/2})O_3$ [119, 120], and $Pb(Mg_{1/3}Nb_{2/3})O_3$–$PbTiO_3$ [121].

The phase scheme shown in Fig. 32 can be applied to the polymers under investigation. According to the scheme, their preliminary polarization resulting in the appearance of the piezoelectric activity corresponds to an increase in the fraction of the ferroelectric phase owing to a partial transformation of amorphous regions (phase **I** or **II** in Fig. 32) into the ferroelectric phase. This process in poly(vinylidene fluoride) is identified using X-ray diffraction methods [5]. Moreover, this is indirectly confirmed by the data presented in Fig. 6. As can be seen from Fig. 6, the electrostrictive constant at room temperature substantially decreases after polarization. Since the electrostrictive constant is proportional to the fraction of the amorphous phase, the inference can be made that the polarization leads to a substantial decrease in the fraction of the amorphous phase. As follows from the scheme in Fig. 32, this can occur as a result of the transformation of phase **II** (or **I**) into phase **III**.

According to the scheme in Fig. 32, the application of the ac electric field should lead to the reversible transformation of phase **II** (**I**) into ferroelectric phase **III**. As applied to the ferroelectric polymers, this mechanism of the field-induced (reversible) transformation of a number of chains from the amorphous state into the ferroelectric crystalline state follows from analysis of numerous experimental data [5, 39].

The behavior of PMN crystals in mechanical fields is characterized by the following features. Xue *et al.* [122] synthesized PMN crystals by mechanical activa-

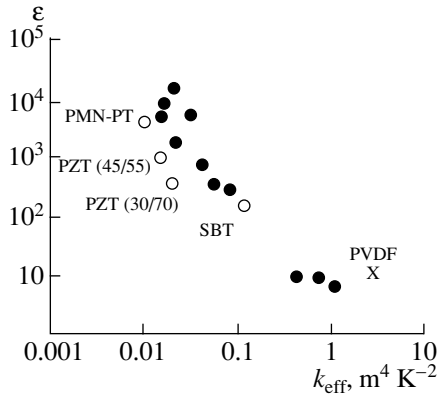

Fig. 31. Correlation between the effective electrostrictive constant k_{eff} and the permittivity ε for different thin ferroelectric films (open circles) and ferroelectric block materials (closed circles) [114, 115]. The cross indicates the data for PVDF in the block state.

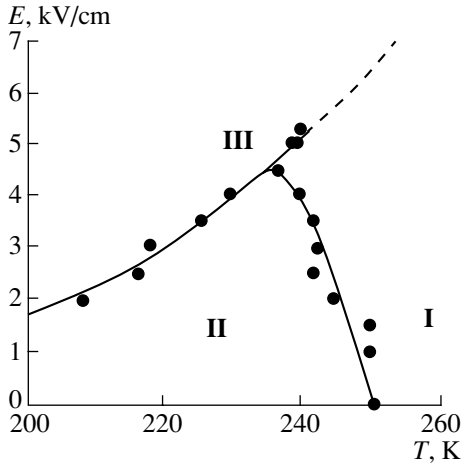

Fig. 32. *E–T* phase diagram for the PMN system along the ⟨111⟩ direction [118].

tion of initial oxides. Strongly defect perovskite crystallites arose at an intermediate stage of the activation. A further mechanical activation in this system led to the formation of more perfect crystals. Such structural transformations in PMN crystals at this activation stage qualitatively resemble the strain-induced structural transformations in textured films of the ferroelectric polymers. As was noted above, the loading of uniaxially drawn vinylidene fluoride–trifluoroethylene copolymer films along the direction *1* also resulted in an improvement in the perfection of ferroelectric crystals. As in the case of the aforementioned mechanical activation of PMN crystals, this was attended by a narrowing of the characteristic X-ray reflections [50].

The above mechanism of structural transformations in the ferroelectric polymers can be treated as the motion of domain walls in response to the mechanical stress (the direct piezoelectric effect) or the electric field (the inverse piezoelectric effect). This motion is a thermoactivated process [123]. Therefore, the character of thermal motion in the amorphous phase in the vicinity of domain walls plays an important role in the ferroelectric polymers. At room temperature, the microscopic Brownian dynamics in the amorphous phase is characterized by large amplitudes of vibrational and rotational motion with short relaxation times. This is a favorable factor for a change in the location of domain walls when the mechanical or electrical field is applied to the system. As a result, the electrostrictive constants and a number of piezoelectric coefficients for the polymers studied are very large at room temperature. The data presented in Figs. 5 and 7 indicate that the large values of the electrostrictive constant and the piezoelectric coefficient e_{31} are governed by intensive motions in the amorphous phase in the vicinity of domain walls. Actually, the freezing of the microscopic Brownian motion in the amorphous phase of poly(vinylidene fluoride) at a temperature of ~–40°C leads to a decrease in the electrostrictive constant to approximately zero and to a substantial reduction in the piezoelectric coefficient e_{31} [18, 24, 27].

9. CONCLUSIONS

Thus, it was demonstrated that the mechanism of the piezoelectric effect observed in the ferroelectric films based on poly(vinylidene fluoride) should account for the structural and dynamic heterogeneity of crystallizing polymers. The size effect and the electrostriction make the main contribution to the observed parameters of the transverse piezoelectric effect. In turn, the size effect and the electrostriction are governed by the processes occurring in regions of the disordered phase. These effects are related to each other, and their mechanism should include molecular rearrangements in the mobile phase of the polymer in response to mechanical or electrical fields.

Progress in the understanding of the mechanisms responsible for the macroscopic piezoelectric effect (and, as a consequence, the possibility of controlling the piezoactivity) is determined, to a great extent, by the current state of the art in the problem of the structure of flexible-chain crystallizing polymers in the isotropic and textured states. The knowledge of subtle details of the microstructure and dynamics of the amorphous phase can provide a way of developing a consistent theory of the phenomena under consideration.

REFERENCES

1. H. Kawai, Jpn. J. Appl. Phys. **8**, 975 (1969).
2. V. V. Kochervinskiĭ, Usp. Khim. **63**, 383 (1994).
3. *The Application of Ferroelectric Polymers*, Ed. by T. T. Wang, J. M. Herbert, and A. M. Glass (Blackie, Glasgow, 1988).
4. T. Furukawa, IEEE Trans. Electr. Insul. **24**, 375 (1989).

5. V. V. Kochervinskiĭ, Usp. Khim. **65**, 936 (1996).
6. E. Fukada and T. Furukawa, Ultrasonics, No. 1, 31 (1981).
7. V. V. Kochervinskiĭ, Usp. Khim. **68**, 904 (1999).
8. T. Yamada, J. Appl. Phys. **53**, 6335 (1982).
9. M. G. Broadhurst and G. T. Davies, in *Electrets*, Ed. by G. M. Sessler (Springer, Berlin, 1980; Mir, Moscow, 1983).
10. L. D. Landau and E. M. Lifshitz, *Course of Theoretical Physics*, Vol. 8: *Electrodynamics of Continuous Media*, 4th ed. (Pergamon, New York, 1984; Nauka, Moscow, 1992).
11. K. Tashiro, H. Tadokoro, and M. Kobayashi, Ferroelectrics **32**, 167 (1981).
12. K. Tashiro, H. Tadokoro, M. Kobayashi, and E. Fukada, Macromolecules **13**, 691 (1980).
13. H. Dvey-Aharon, T. J. Sluckin, and P. L. Taylor, Ferroelectrics **32**, 25 (1981).
14. M. G. Broadhurst and G. T. Davies, Ferroelectrics **60**, 3 (1984).
15. H. Scheve, in *IEEE 1982 Ultrasonics Symposium Proceedings* (1982), Vol. 1, p. 519.
16. R. G. Kepler and R. A. Anderson, J. Appl. Phys. **49**, 4918 (1978).
17. T. Furukawa, J. Aiba, and E. Fukada, J. Appl. Phys. **50**, 3615 (1979).
18. S. Tasaka and S. Miyata, Ferroelectrics **32**, 17 (1981).
19. H. Ohigashi, J. Appl. Phys. **47**, 949 (1976).
20. H. Sussner, Phys. Lett. A **58**, 426 (1976).
21. G. A. Smolenskiĭ, V. A. Bokov, V. A. Isupov, N. N. Kraĭnik, R. E. Pasynkov, and M. S. Shur, *Ferroelectrics and Antiferroelectrics* (Nauka, Leningrad, 1971).
22. E. Bellet-Amalric and J. F. Legrand, Eur. Phys. J. B **3**, 225 (1998).
23. K. Nakamura and Y. Wada, J. Polym. Sci. A2 **9**, 161 (1971).
24. M. Oshiki and E. Fukada, J. Mater. Sci. **10**, 1 (1975).
25. S. Ikeda, H. Suzuki, and I. Maruyoshi, Rep. Prog. Polym. Phys. Jpn. **31**, 387 (1988).
26. T. Watanabe, E. Uamaguchi, H. Suzuki, and S. Ikeda, Kobunshi Ronbunshu **49**, 585 (1992).
27. S. Tasaka and S. Miyata, Kobunshi Ronbunshu **36**, 689 (1979).
28. T. Furukawa and N. Seo, Jpn. J. Appl. Phys. **29**, 675 (1990).
29. G. Kloos, J. Polym. Sci., Part B: Polym. Phys. **34**, 683 (1996).
30. M. Zhenyi, J. I. Schenbeim, J. W. Lee, and B. A. Newman, J. Polym. Sci., Part B: Polym. Phys. **32**, 2721 (1994).
31. X.-Z. Zhao, V. Bharti, O. M. Zhang, *et al.*, Appl. Phys. Lett. **73** (14), 2054 (1998).
32. V. Bharti, Z.-Y. Cheng, T.-B. Xu, and O. M. Zhang, Appl. Phys. Lett. **75** (17), 2653 (1999).
33. M. G. Broadhurst, G. T. Davis, J. E. McKinney, and R. E. Collins, J. Appl. Phys. **49**, 4992 (1978).
34. G. H. Michler, J. Macromol. Sci., Phys. B **38**, 787 (1999).
35. H. Zhou and G. L. Wilkes, J. Mater. Sci. **33** (2), 287 (1998).
36. V. V. Kochervinskiĭ, V. A. Glukhov, V. G. Sokolov, *et al.*, Vysokomol. Soedin., Ser. A **31** (12), 2590 (1989).
37. V. V. Kochervinskiĭ, V. A. Glukhov, V. F. Romadin, *et al.*, Vysokomol. Soedin., Ser. A **30** (9), 1916 (1988).
38. V. V. Kochervinskiĭ, V. A. Glukhov, and S. Yu. Kuznetsova, Vysokomol. Soedin., Ser. A **29** (7), 1530 (1987).
39. V. V. Kochervinskiĭ, Vysokomol. Soedin. **45** (2003) (in press).
40. V. V. Kochervinskiĭ, T. E. Danilyuk, and L. Ya. Madorskaya, Vysokomol. Soedin., Ser. A **28** (3), 619 (1986).
41. K. Eichhom, C. Sinn, and M. Dettenmaier, Appl. Opt. **36** (18), 4259 (1997).
42. W. Glenz and A. Peterlin, J. Macromol. Sci., Phys. B **4** (3), 473 (1970).
43. P. Spiby, M. A. O'Neil, R. A. Duckett, and I. M. Ward, Polymer **33** (21), 4479 (1992).
44. K. Kober, I. A. Gorshkova, A. V. Savitsky, and A. E. Tshmel, J. Polym. Sci., Part B: Polym. Phys. **36**, 2829 (1998).
45. N. S. Murthy, C. Bednarczuk, P. B. Rim, and C. J. Nelson, J. Appl. Polym. Sci. **64** (7), 1363 (1997).
46. V. V. Kochervinskiĭ, Vysokomol. Soedin., Ser. A **44**, 1127 (2002).
47. R. Schreiber, W. S. Veeman, W. Gabriesle, and J. Arnauts, Macromolecules **32** (14), 4647 (1999).
48. V. I. Vettegren', Fiz. Tverd. Tela (Leningrad) **26**, 1699 (1984) [Sov. Phys. Solid State **26**, 1030 (1984)].
49. W.-Y. Yeh and R. J. Young, Polymer **40**, 857 (1999).
50. V. V. Kochervinskiĭ, V. A. Glukhov, V. G. Sokolov, *et al.*, Vysokomol. Soedin., Ser. A **31** (9), 1829 (1989).
51. S. Tsubakihara and M. Yasuniwa, Polym. J. (Tokyo) **28** (7), 563 (1996).
52. K. Kaji, Makromol. Chem. **175**, 311 (1974).
53. B. H. Hahn, O. Herrmann-Schonherr, and J. H. Wendorff, Polymer **28**, 201 (1987).
54. P. J. Flory, D. J. Yoon, and K. Dill, Macromolecules **17**, 862 (1984).
55. D. J. Yoon and P. J. Flory, Macromolecules **17**, 86 (1984).
56. V. V. Kochervinskiĭ, Vysokomol. Soedin. **42** (10), 1669 (2000).
57. A. Ionas and R. Legras, Macromolecules **26** (4), 813 (1993).
58. G. Teyssedre and C. Lacabanne, Ferroelectrics **171**, 125 (1995).
59. S. Ikeda and T. Watanabe, Rep. Prog. Polym. Phys. Jpn. **32**, 335 (1989).
60. F. Schaffner and B. J. Jungnikel, IEEE Trans. Dielectr. Electr. Insul. **1** (4), 553 (1994).
61. M. G. Broadhurst and G. T. Davies, Ferroelectrics **31**, 177 (1981).
62. K. Tashiro, S. Nishimura, and M. Kobayashi, Macromolecules **23**, 2802 (1990).
63. M.-C. Wu and W. P. Winfee, Ultrason. Symp. Proc., No. 2, 1242 (1989).
64. W. M. Reid and M. R. Steel, J. Appl. Phys. **51**, 1860 (1980).

65. B. R. Hahn, J. Appl. Phys. **57**, 1294 (1985).
66. E. Fukada, M. Date, H. E. Neumann, and J. H. Wendorff, J. Appl. Phys. **63**, 1701 (1988).
67. M. Date, E. Fukada, and J. H. Wendorff, IEEE Trans. Electr. Insul. **24**, 457 (1989).
68. V. I. Gerasimov and M. V. Ivanov, Vysokomol. Soedin. **38**, 1706 (1996).
69. J. Clements, G. R. Davies, and I. M. Ward, in *Proceedings of 2nd International Conference on Electrical, Optical and Acoustical Properties of Polymers, Cantenbury, 1990* (London, 1990).
70. J. Clements, G. R. Davies, and I. M. Ward, Polymer **26**, 208 (1985).
71. W. N. Chen, H. J. Shaw, D. L. Weinstein, and L. T. Zitelli, in *IEEE Ultrasonics Symposium Proceedings* (IEEE, New York, 1978), p. 780.
72. M. Toda, Ferroelectrics **32**, 127 (1981).
73. H. Ohigashi, K. Koga, H. Suzuki, *et al.*, Ferroelectrics **60**, 363 (1984).
74. B. A. Auld and J. J. Gagnepain, J. Appl. Phys. **50**, 5511 (1979).
75. K. Omate and H. Ohigashi, Appl. Phys. Lett. **66**, 2215 (1995).
76. E. L. Nix and I. M. Ward, Ferroelectrics **67**, 137 (1986).
77. K. Tashiro, M. Kobayashi, H. Tadokoro, and E. Fukada, Polym. Bull. **2**, 397 (1980).
78. E. Fukada, G. M. Sessler, J. E. West, and P. Gunther, J. Appl. Phys. **62**, 3643 (1987).
79. G. M. Sessler and A. Berraissoul, IEEE Trans. Electr. Insul. **24**, 249 (1989).
80. H. Kawai, Oyo Butsuri **39**, 869 (1970).
81. H. J. Wintle and R. Diirsam, Phys. Rev. B **39**, 3862 (1989).
82. N. Murayama, J. Polym. Sci., Polym. Phys. Ed. **13**, 929 (1975).
83. N. Murayama, K. Nakamura, H. Obara, and M. Segawa, Ultrasonics **14**, 15 (1976).
84. G. E. Johnson, L. L. Blyler, G. R. Crane, *et al.*, Ferroelectrics **32**, 43 (1981).
85. G. M. Sessler, D. K. Das-Gupta, A. S. DeReggi, *et al.*, IEEE Trans. Electr. Insul. **27** (4), 872 (1992).
86. W. Eisenmenger, H. Schmidt, and B. Dehlen, Braz. J. Phys. **29** (2), 295 (1999).
87. V. V. Kochervinskiĭ, V. A. Glukhov, V. G. Sokolov, *et al.*, Vysokomol. Soedin., Ser. A **31**, 282 (1989).
88. J. K. Lee and M. A. Marcus, Ferroelectrics **32**, 93 (1981).
89. M. A. Marcus, Ferroelectrics **57**, 203 (1984).
90. G. E. Johnson, L. L. Blyler, and N. M. Hulton, Ferroelectrics **28**, 303 (1980).
91. A. G. Kolbeck, J. Polym. Sci., Polym. Phys. Ed. **20**, 1987 (1982).
92. V. F. Romadin, V. G. Sokolov, V. V. Kochervinskiĭ, *et al.*, Plast. Massy, No. 6, 21 (1988).
93. M. Ya. Sherman, O. D. Lesnykh, N. B. Vlader, *et al.*, Plast. Massy, No. 10, 46 (1990).
94. B. Wunderlich, *Macromolecular Physics* (Academic, New York, 1980; Mir, Moscow, 1984), Vol. 3.
95. V. V. Kochervinskiĭ, Vysokomol. Soedin., Ser. A **43** (9), 1518 (2001).
96. K. T. Chang, B. A. Newman, J. I. Scheinbeim, and K. D. Pae, J. Appl. Phys. **52**, 6557 (1982).
97. K. D. Pae, K. Vijayan, R. W. Renfree, *et al.*, Ferroelectrics **57**, 249 (1984).
98. S. W. Weeks and R. Y. Ting, J. Acoust. Soc. Am. **74**, 1681 (1983).
99. T. Takemura, Ferroelectrics **57**, 243 (1984).
100. Y. Wada and R. Hayakawa, Ferroelectrics **32**, 115 (1981).
101. V. V. Kochervinskiĭ, Neorg. Mater. **31** (6), 851 (1995).
102. G. S. Smolenskiĭ and A. Agranovskaya, Fiz. Tverd. Tela (Leningrad) **1**, 1420 (1960) [Sov. Phys. Solid State **1**, 1302 (1960)].
103. L. E. Cross, Ferroelectrics **76**, 241 (1987).
104. L. E. Cross, Ferroelectrics **151**, 305 (1994).
105. V. V. Kochervinskiĭ, Vysokomol. Soedin., Ser. A **40**, 1636 (1998).
106. V. V. Kochervinskiĭ, in *Abstracts of XV All-Russian Conference on Physics of Ferroelectrics, Rostov-on-Don* (1999).
107. V. Bokov and I. Myl'nikova, Fiz. Tverd. Tela (Leningrad) **3**, 3 (1961) [Sov. Phys. Solid State **3**, 1 (1961)].
108. K. A. Verkhovskaya and V. V. Kochervinskiĭ, Vysokomol. Soedin., Ser. A **32**, 1669 (1990).
109. H. Smogor, B. Hilczer, and S. Warchol, Ferroelectrics **258**, 291 (2001).
110. V. V. Kochervinskiĭ, V. A. Glukhov, V. G. Sokolov, *et al.*, Vysokomol. Soedin., Ser. A **30**, 1969 (1988).
111. V. V. Kochervinskiĭ and E. M. Murasheva, Vysokomol. Soedin., Ser. A **33**, 2096 (1991).
112. K. Uchino and L. Cross, Jpn. J. Appl. Phys. **19**, L171 (1980).
113. S. Nomura and K. Uchino, Ferroelectrics **41**, 117 (1982).
114. R. E. Newnham, V. Sundar, R. Yimnirun, *et al.*, Ceram. Trans. **88**, 15 (1998).
115. A. Kholkin, Ferroelectrics **258**, 209 (2001).
116. V. A. Isupov and M. Boudys, Ferroelectrics **41**, 111 (1982).
117. V. V. Kochervinskiĭ, Vysokomol. Soedin., Ser. A **44**, 1925 (2002).
118. E. V. Colla, E. Yu. Koroleva, A. A. Nabereznov, *et al.*, Ferroelectrics **151**, 337 (1994).
119. F. Chu, I. M. Reaney, and N. Setter, Ferroelectrics **151**, 343 (1994).
120. L. S. Kamzina, Ferroelectrics **253**, 69 (2001).
121. G.-S. Xu, D.-L. Li, H.-S. Luo, *et al.*, Ferroelectrics **253**, 39 (2001).
122. J. M. Xue, J. Wang, D. M. Wan, *et al.*, Ferroelectrics **253**, 21 (2001).
123. Q. M. Zhang, W. Y. Pan, S. J. Jang, and L. E. Cross, J. Appl. Phys. **64**, 6445 (1988).

Translated by O. Borovik-Romanova

Crystallography Reports, Vol. 48, No. 4, 2003, pp. 676–681. Translated from Kristallografiya, Vol. 48, No. 4, 2003, pp. 727–733.

PHYSICAL PROPERTIES OF CRYSTALS

Charge Transport in $Li_2B_4O_7$ in Single Crystal and Glassy States

I. M. Rizak*, V. M. Rizak, N. D. Baisa***, V. S. Bilanich**, M. V. Boguslavskiĭ****, S. Yu. Stefanovich****, and V. M. Goloveĭ*******

** Dnepropetrovsk National University, Ukraine*

*** Uzhgorod National University, Ukraine*

**** Kiev Institute of Management and Information Technologies at the National Aviation University, Ukraine*

***** Moscow State University, Vorob'evy gory, Moscow, 119992 Russia*

e-mail: stefan@tech.chem.msu.ru

****** Institute of Electronic Physics, National Academy of Sciences of Ukraine, Uzhgorod, Ukraine*

Received August 22, 2002

Abstract—The electrophysical properties of $Li_2B_4O_7$ single crystals and glasses are studied in the temperature range 290–1100 K and the frequency range 1–1000 kHz. The strong frequency dispersion of ionic conductivity at temperatures close to room temperature is explained by the low-frequency hoppings of lithium ions from the basic to the interstitial positions. The dielectric relaxation accompanying the transport of lithium ions is analyzed within the framework of the Debye–Skanavi model. The minimum hopping length of Li^+ ions and the height of the potential barrier between their closest positions are determined. The parameters obtained are compared with the known structural data. © *2003 MAIK "Nauka/Interperiodica".*

INTRODUCTION

Because of a combination of physical properties (high coefficient of electromechanical coupling, low velocity of propagation of a surface acoustic wave, the existence of a direction with the zero thermal expansion coefficient, high mechanical strength and stability to radiation, and low electrical conductivity at room temperature), lithium tetraborate $Li_2B_4O_7$ (LTB) single crystals are widely used in various electroacoustic devices [1–3], pyroelectric sensors [3, 4], and laser-radiation converters [5].

The conductivity of lithium tetraborate single crystal and glasses at elevated temperatures have been studied rather poorly. In [6–8], the temperature dependence of conductivity, dielectric constant, and tangent of the angle of dielectric losses along the [100] and [001] directions were measured, and it was established that conductivity along the tetragonal axis of lithium tetraborate single crystals is higher by almost 5 orders of magnitude than along the perpendicular direction. Thus, the conductivity of LTB crystals is purely electronic along the [100] direction and purely ionic along the [001] direction (transport of lithium ions). High dielectric constant of lithium tetraborate at low frequencies was explained by thermal ionic polarization of the lithium ions [6, 7] and the LTB single crystal was related to one-dimensional superionics. One should note that the ionic conductivity of lithium tetraborate at 396 K, i.e., at the point of the order–disorder phase transition [6], does not exceed 10^{-7} Ω^{-1} cm^{-1}, which can hardly be associated with the transition to the superionic state. At the same time, the rapid increase in the conductivity with temperature allows one to consider LTB crystals as an efficient conductor with respect to lithium already at $T > 600$ K. Considerable ionic conductivity was also reported [9] in the glassy state of lithium tetraborate.

The structural mechanism of high ionic conductivity of LTB crystals is still somewhat mysterious. The point is that the atomic packing in this crystal is one of the most dense, with the volume per oxygen atom being $V_0 = 16.4$ Å^3. This value is much lower than in the related oxides (with respect to cation–anion stoichiometry) such as pseudoilmenite $LiNbO_3$ ($V_0 = 17.7$ Å^3) or Li-containing perovskites (about 20 Å^3). The high packing density and rigidity of triangular and tetrahedral boron–oxygen polyhedra forming the structure of LTB crystals prevent direct jumps of lithium cations between the main crystallographic positions, which are separated by distances exceeding 3 Å. It is necessary to note that the absence of an extended homogeneity region on the pseudobinary Li_2O–B_2O_3 phase diagram allows one to assume that the main lithium positions in $Li_2B_4O_7$ are fully occupied, which excludes the existence of the number of vacancies sufficient for the vacancy mechanism of ionic conductivity. Moreover, precision X-ray diffraction analysis at room temperature [10] also showed the absence of peaks of residual electron density that could be associated with interstitial positions of lithium ions.

A comparison of the structural characteristics and microscopic parameters of the cationic transport would

provide a better understanding of the nature of the ionic conductivity of lithium tetraborate. However, at present there exist no quantitative estimates of the parameters of the cationic motion that characterize the process of the charge transfer such as the length and duration of a hopping and the height of the energy barriers between the basic and interstitial positions of mobile cations. There is no detailed information on the physical properties of lithium tetraborate in the glassy state.

It is very important that the conductivity of lithium tetraborate was measured on samples obtained by different methods [6–9], which might explain the inconsistent results, because stoichiometric and impurity compositions of lithium tetraborate samples in the crystalline and glassy states were different. Below, the mechanism of ionic transport in the $Li_2B_4O_7$ compound is determined by comparing the temperature and frequency behavior of the conductivity and the real and imaginary components of the permittivity of single crystals and glasses of the same composition.

EXPERIMENTAL

Synthesis of $Li_2B_4O_7$ *Crystals and Glasses*

The phase diagram of the pseudobinary Li_2O–B_2O_3 cut [11–13] shows that the $Li_2B_4O_7$ compound, which melts congruently at 1190 K, can be obtained, depending on the cooling mode, both in the crystalline and the glassy states. The compound in the crystalline state has a tetragonal structure, sp. gr. $I4_1cd$; the unit-cell parameters $a = 0.9479$ nm and $c = 1.0290$ nm [10].

The initial LTB was obtained by melting boron oxide (high purity grade 12–3) and lithium carbonate (high purity grade 20–2) in the stoichiometric ratio in a platinum crucible in air. The temperature and time of the synthesis were optimized with due regard for lithium carbonate decomposition during heating, dehydration of the initial components, and the character of their interaction. For better use of the crucible volume and prevention of ejection of interacting components, we used the stepwise mode of synthesis and introduced the necessary doses of lithium carbonate into the boron oxide melt [14]. The product obtained was used as an initial charge for synthesis of single crystals without "overloading" the crucible.

LTB single crystals were grown by the Czochralski method in air in platinum crucibles 60 mm in diameter and 60 mm in height placed into a HX-620 device with automatic control of the crystal diameter. The growth modes were selected depending on high melt viscosity and its rapid increase with a lowering of the temperature [15] and also by the incongruent character of evaporation [16]. Taking into account the incongruent character of LTB evaporation, we added an excessive amount of boron oxide (0.5 mol %) into the initial charge to compensate its losses during growth. [001]- and [100]-oriented seeds were used. The pooling rate was 3 mm per day, the rotation velocity was 4.4 rpm, the axial temperature gradient was equal to 20–30 K/cm, the duration of postgrowth annealing was 24 h, and the cooling rate was 10–15 K/h. The single crystals thus synthesized were 35 mm in diameter and 40 mm in length; they contained no solid-phase or gas inclusions.

The X-ray phase analysis on a DRON-2 X-ray diffractometer (CuK_α-radiation) showed that single crystals synthesized had a stoichiometric $Li_2B_4O_7$ composition. With due regard for the fact that crystals were grown from the charge with an excess of boron oxide, we expected a certain excess of B_2O_3 also in the crystals grown, but it was within the homogeneity range of this compound and did not exceed 0.1 mol % [11] and, therefore, could not be detected by X-ray phase or microstructure analyses. We assume that under such growth conditions, the Li/B ratio along the length of quality single crystals is more or less stable and corresponds to the boundary of the homogeneity range of lithium tetraborate, whereas the structure has a certain deficit of lithium ions.

In order to attain complete consistency of the stoichiometric composition and the amount of noncontrollable impurities in the single crystal and glassy samples, single crystals were cut along their growth axes. Then one half of the crystal was used to prepare a single crystal sample, and the other half was used as the charge for preparing glassy lithium tetraborate. With this aim, the LTB melt was heated for 2–4 h at 1220–1250 K, was periodically stirred to remove gaseous inclusions, and then was cooled in a switched-off furnace. To remove thermal stresses, the glass taken away from the crucible was annealed for 2–4 h at 550–600 K. X-ray patterns from glassy LTB showed no peaks corresponding to the peaks of the pattern from crystalline LTB. However, noticeable intensification of scattering on the patterns from glassy LTB corresponded to the groups of the most intense X-ray reflections from single crystals. Qualitatively, this indicates that the network of boron–oxygen bonds is preserved in the short- and long-range orders of LTB glass.

Samples for further studies were cut out from the best regions of single crystals and glass; then they were polished to achieve the optical quality of the surface. Samples had the shape of rectangular parallelepipeds $5 \times 5 \times 2$ mm^3 in size. Single crystal samples were oriented within an accuracy of 0.5°.

Methods of Electrophysical Studies

Electrophysical characteristics were studied on an automated setup that allowed one to record the active and reactive components of conductivity in the frequency range 1–1000 kHz and the temperature range 293–1380 K. The rate of the temperature variation did not exceed 2 K/min both on heating and cooling. We used *c* cuts of LTB single crystals and glass plates with

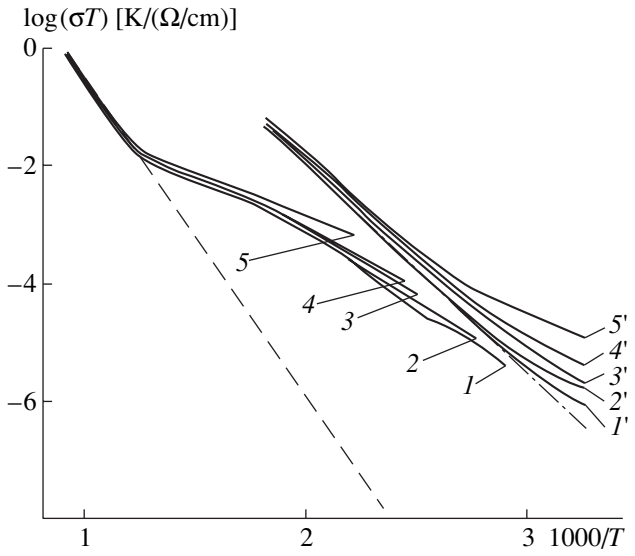

Fig. 1. Conductivity of a $Li_2B_4O_7$ single crystal (along the tetragonal axis) and a glassy sample at frequencies: (*1*, *1*') 2, (*2*, *2*') 5, (*3*, *3*') 10, (*4*, *4*') 20, and (*5*, *5*') 80 kHz.

platinum (on single crystal) or Aquadag (on glass) electrodes.

RESULTS

Ionic Conductivity

The temperature curves shown in Fig. 1 of conductivity for crystalline and glassy LTB in the $\ln(\sigma T) = F(1/T)$ coordinates obtained at various frequencies can be approximated by pieces of straight lines only in a very rough approximation. The high-temperature portion of the conductivity curve measured from the *c* cut of an LTB single crystal can be described by a straight line rather well. The linear dependence of the conductivity in the $\ln(\sigma T) = F(1/T)$ coordinates satisfies the Arrhenius equation in the form [17]

$$\sigma = (\sigma_0/T)\exp(-E_\sigma/kT), \qquad (1)$$

where E_σ is the energy of conductivity activation used to describe ionic conductivity in the solid phase. In the vicinity of 1000 K, conductivity has the value $\sigma \sim 10^{-3}\ \Omega^{-1}\ cm^{-1}$ and the activation energy has the value $E_\sigma = 1.22$ eV. Both these parameters only slightly depend on the electric-field frequency, which allows one to compare these values with DC conductivity. Assuming that DC conductivity also obeys the Arrhenius law, we obtain the conductivity of LTB single crystals at room temperature by extrapolation: $\sigma_{DC} \sim 10^{-14}\ \Omega^{-1}\ cm^{-1}$. It is much lower than the experimental values of AC measurements: $\sigma_{AC} \sim 10^{-6}\ \Omega^{-1}\ cm^{-1}$ (at the frequency 1 kHz, our data and data [6]).

The discrepancy between σ_{AC} and σ_{DC} can be explained by the contribution of dielectric polarization to conductivity at the frequency ω. Dielectric polarization arises as a result of charge-carrier motion from the main to interstitial positions under the action of the electric field. In the simplest form, this contribution is described by well-known West expression [18]:

$$\sigma_{AC}(\omega) = \sigma_{DC}\{1 + (\omega/\omega_j)^p\}, \qquad (2)$$

where ω_j is the frequency of ion jumps between the nearest positions along the conductivity channel, $p \sim 1$. At low temperatures, ω_j is low, the contribution of the second term results in the inequality $\sigma_{AC} \gg \sigma_{DC}$ at the characteristic pronounced increase in σ_{AC} with frequency. Such a behavior is observed at temperatures close to room temperature for both single crystals and glassy LTB (Fig. 1).

It should be noted that in the glassy state the frequency dispersion of conductivity in the vicinity of 500 K turns out to be less, and the σ_{AC} values are higher by almost an order of magnitude than in single crystals. It shows a pronounced increase in ionic conductivity in glass in comparison with single crystals. The semiquantitative estimation made using Eq. (2) yields a rather high value, $\sigma_{DC}(500\ K) \sim 10^{-3}\ \Omega^{-1}\ cm^{-1}$. The latter fact seems to be of importance because of the availability of the glass material. A higher value of lithium conductivity and the lower activation energy of conductivity (0.71 eV) in LTB glass can be explained by an increase in the free volume in glass and disordering typical of glassy materials. As a result, charge carriers overcome the potential barrier at lower energies.

Dielectric Relaxation

The hopping mechanism of motion of lithium ions from the main to interstitial positions used to explain the frequency dependence of ionic conductivity are similar to the general concepts of the Debye–Skanavi theory of dielectric relaxation [19, 20]. Low ionic conductivity of the LTB single crystal at room temperature allows one to observe obvious anomalies of permittivity and the dielectric-loss tangent with the temperature–frequency behavior characteristic of Debye-type relaxation (Figs. 2a, 2b). Figure 2 shows that $\varepsilon(T)$ and $\tan\delta(T)$ curves have maxima whose temperatures and amplitudes increase with an increase in the measuring-field frequency.

For the quantitative interpretation of dielectric properties of lithium tetraborate, we used the Debye model of dielectric relaxation formulated earlier for the interpretation of the dielectric response of polar molecules in a liquid [19]

$$\varepsilon^* = \left(\varepsilon_\infty + \frac{\varepsilon_s - \varepsilon_\infty}{1 + \omega^2\tau^2}\right) - i\left(\frac{\varepsilon_s - \varepsilon_\infty}{1 + \omega^2\tau^2}\omega\tau\right),$$

where $\tau = \exp(U/kT)/2\nu$, *k* is the Boltzmann constant, ε_s and ε_∞ are the permittivities of the medium at the infinitely low and infinitely high frequencies, ω is the frequency of the applied electric field, ν is the frequency

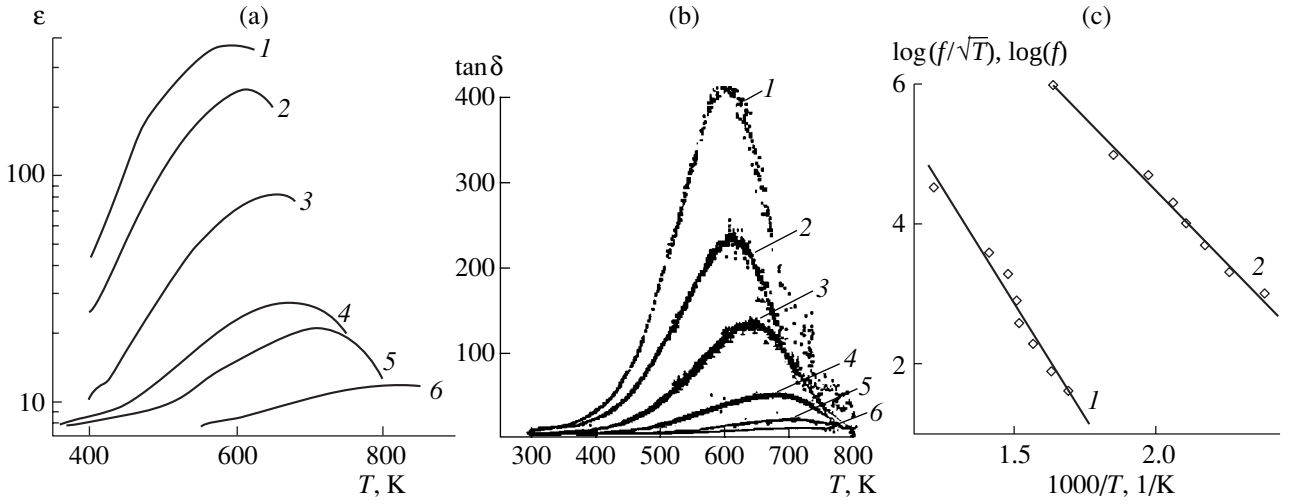

Fig. 2. (a) Permittivity and (b) tangent of dielectric-loss angle as functions of temperature along the tetragonal axis of a $Li_2B_4O_7$ crystal at frequencies of (*1*) 1, (*2*) 2, (*3*) 10, (*4*) 50, (*5*) 100, and (*6*) 1000 kHz; (c) the corresponding temperature–frequency positions of the relaxation maxima of (*1*) permittivity in the 1000/K– $\log(f/\sqrt{T})$ coordinates and (*2*) tangent of dielectric-loss angle in 1000/K– $\log(f)$ coordinates.

of the particle jumps over potential barriers, and τ is the relaxation time. According to Skanavi, the model parameters acquire a different meaning when applied to the behavior of the charge carriers in shallow potential wells in solids. In particular, ν is treated as a trial frequency of hopping of the charged particle over the potential barrier U between two ion positions along the conductivity channel, and ε_∞ is treated as high-frequency permittivity.

For static permittivity of the dielectrics with "rigid" dipoles, Skanavi suggested using the expression [20]

$$\varepsilon_s - \varepsilon_\infty \propto 4\pi n_0 \mu^2/kT,$$

where $\mu = ql$ is the magnitude of the dipole formed by the displacement of a unit charge q and n_0 is the volume density of mobile charges. In a dielectric possessing ionic conductivity, the dipole shoulder is equal to the length of one ion hopping along the conductivity channel, whereas the Skanavi hypothesis is based on the concept of permittivity of a paraelectric formed by the system of the dipoles interacting in their mean field. The Debye–Skanavi model allows one to describe the temperature–frequency behavior of the complex permittivity of ionic conductors at the initial portion of the temperature range of conductivity where the number of strongly excited mobile ions that weakly interact with the crystal lattice is rather small.

Under these conditions, the temperatures of the ε' and $\tan\delta$ maxima are determined on the condition that $d\varepsilon/dT = 0$, $d\tan\delta/dT = 0$.

As is shown in [21], at low temperatures ($kT \ll U$), the equation

$$-E_{(\varepsilon)}/kT_{\max}^{(\varepsilon)} = \text{const} + \ln(f_{\max}^{(\varepsilon)}/\sqrt{T_{\max}^{(\varepsilon)}})$$

allows one to determine the height of the energy barrier $U = E_\varepsilon$ between two equilibrium ion positions ($T_{\max}^{(\varepsilon)}$ and $f_{\max}^{(\varepsilon)}$ are the temperature and the frequency of the maxima in ε), as well as the length l of the ion hopping

$$l \approx (0.03\ \text{Å}/q)\sqrt{(E_{(\varepsilon)} - E_{(\tan\delta)})\varepsilon_\infty (V/N)}, \qquad (3)$$

where q and N are the charge and the number of mobile ions in the cation sublattice within the unit-cell volume V(Å^3) and $E_{\tan\delta}$ is determined from the relationship

$$-E_{(\tan\delta)}/kT_{\max}^{(\tan\delta)} = \text{const} + \ln(f_{\max}^{(\tan\delta)})$$

($T_{\max}^{(\tan\delta)}$ and $f_{\max}^{(\tan\delta)}$ are the temperature and frequency of the maxima in $\tan\delta$) [21].

Mathematical processing of the dependences $\varepsilon(T)$ and $\tan\delta(T)$ with the separation of the maxima or inflection points allowed us to determine the temperatures $T_{\max}^{(\varepsilon)}$ and $T_{\max}^{(\tan\delta)}$ for single crystals (Fig. 2) and glasses (Fig. 3). Using the temperatures thus determined, we constructed the dependences $\ln(f_{\max}^{(\tan\delta)}) = F\left(\frac{1000}{T_{\max}^{(\tan\delta)}}\right)$ and $\frac{f_{\max}^{(\varepsilon)}}{\sqrt{T_{\max}^{(\varepsilon)}}} = F\left(\frac{1000}{T_{\max}^{(\varepsilon)}}\right)$ shown in Figs. 2c and 3c.

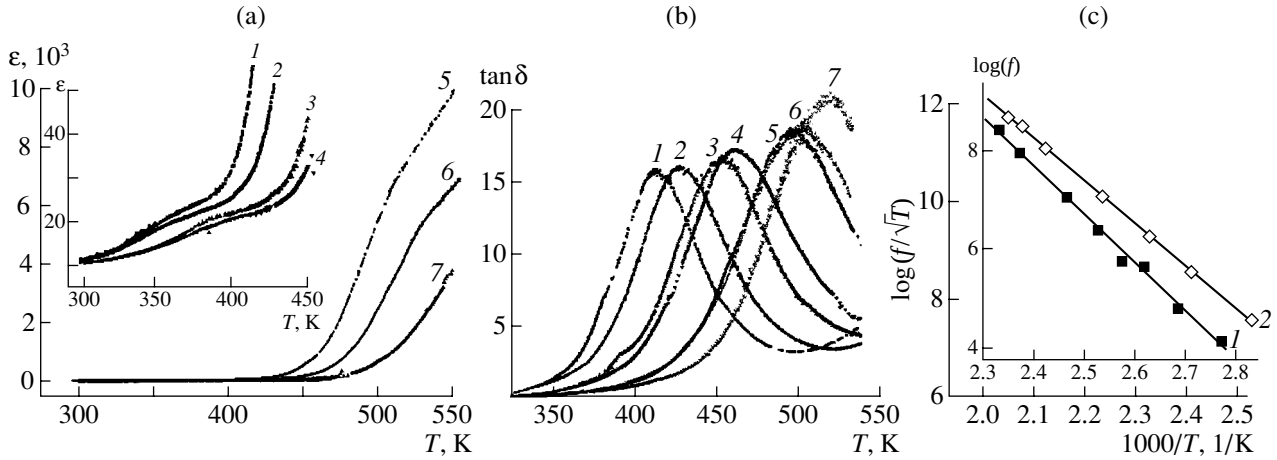

Fig. 3. (a) Permittivity and (b) tangent of dielectric-loss angle as functions of temperature in the $Li_2B_4O_7$ glass at frequencies of (*1*) 2, (*2*) 5, (*3*) 10, (*4*) 20, (*5*) 50, (*6*) 80, and (*7*) 100 kHz; (c) the corresponding temperature–frequency positions of the relaxation maxima of (*1*) permittivity in the 1000/K–$\log(f/\sqrt{T})$ coordinates and (*2*) tangent of dielectric-loss angle in the 1000/K–$\log(f)$ coordinates.

The temperature–frequency curves obtained are well extrapolated by straight lines. The slope of lines *1* and *2* in Figs. 2c and 3c allow one to calculate the height of the potential barrier between two positions of the relaxation oscillator, $U = E_\varepsilon$, and also the $E_{\tan\delta}$ value corresponding to the activation energy of a dipole. The parameters E_ε and $E_{\tan\delta}$ determined from the tangent of the slope angle of the straight lines in Figs. 2c and 3c are $E_\varepsilon = 1.28$ and $E_{\tan\delta} = 0.74$ eV for crystals and $E_\varepsilon = 0.71$ and $E_{\tan\delta} = 0.67$ eV for glasses.

Structural Substantiation of Ionic Conductivity in $Li_2B_4O_7$

Using the ε_∞ values of $Li_2B_4O_7$ measured at the frequency 1 MHz ($\varepsilon = 10$) and the *q*, *N*, $V/Z = 115$ Å^3 parameters for LTB crystals known from the literature, from formula (3) we can determine the lengths *l* of ion hopping equal to 0.61 and 0.16 Å in a crystal and in a glassy material, respectively. The lengths of ion jumps obtained are much less than the distances between the main lithium positions in an LTB crystal equal to 3.114 Å [10]. Comparing these data, one has to keep in mind that direct ion jumps for distances exceeding 3 Å are not allowed energetically. Moreover, the geometry of the conductivity channel in a lithium tetraborate crystal along the [001] direction excludes lithium transport along the straight line and requires the existence of at least one intermediate position that would correspond to the kink of the trajectory of a mobile cation.

The chain of (001)-oriented oxygen polyhedra around the general positions of lithium ions in Fig. 4 sets a zigzag trajectory for Li^+ transport through the large triangular faces of the two nearest oxygen five-vertex polyhedra facing each other. In these polyhedra, the distances between the lithium ions in their centers to surrounding oxygen ions range within 1.967–2.611 Å [10]. The hopping length 0.61 Å approximately corresponds to the distance from the main position of a lithium ion in the center of each the polyhedron to the centers of its largest faces (depicted as light and dark polyhedron faces below and above the fragment of the chain in Fig. 4). Thus, the centers of these faces of the five-vertex polyhedra are close to the interstitial positions (*M*) of lithium ions, and, simultaneously, are the kinks of the trajectory of their motion. Thus, the distance between the main Li^+ positions has three segments and can be written as Li(1)–*M*–*M*'–Li(1'). The lengths of the first and last segments are about 0.6 Å; the average distance between the polyhedra is about 2 Å.

The above scheme of the ion motion in a lithium tetraborate crystal agrees with the known structural data on the length of the maximum jumps of lithium cations, 2.2 Å, in the well-known ionic conductor $Li_3Sc_2(PO_4)_3$ [22] and 0.3–0.95 Å in a $LiNbGeO_5$ crystal [23]. At the same time, as in $LiNbGeO_5$, too small a distance between the main and interstitial positions of lithium ions in LTB does not allow the latter to play the role of a vacancy. This reduces ionic conductivity, especially at low temperatures (up to 10^{-14} Ω^{-1} cm^{-1}). High conductivity at 1000 K (~10^{-3} Ω^{-1} cm^{-1}) allows one to assume that a vacancy mechanism is in action because of the existence of one more interstitial position, *M**, which should be located in the middle between the main positions. Indeed, such a location of *M** is consistent with the existence of large space between LiO_5 polyhedra (Fig. 4). The center of this space lies far from the main position at a distance exceeding two ionic radii of lithium. This allows the lithium cation to enter this space even if the neighboring main positions are also filled with lithium.

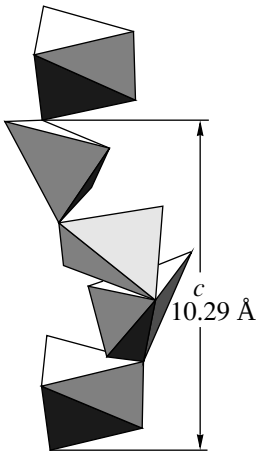

Fig. 4. Helical chain of five-vertex oxygen polyhedra of lithium along the tetragonal axis of a $Li_2B_4O_7$ crystal.

It is typical that the "bottleneck" of the conductivity channel (which corresponds to the maximum height of the potential barrier) is formed by triangular faces of the five-vertex oxygen polyhedra around the main lithium position. This is confirmed by the value of the activation energy of conductivity of an LTB crystal at high temperature, E_s = 1.22 eV (see the linear portion in Fig. 1), and the energy barrier near the main lithium position, U = 1.28 eV, determined from the dielectric relaxation data at lower temperatures.

Weak additional anomalies on the $\varepsilon(T)$ and $\tan\delta(T)$ curves of a lithium tetraborate crystal (Figs. 3a, 3b) seem to be associated with jumps of mobile cations along the conductivity channel for quite large distances ($l > 0.61$ Å). However, the quantitative processing of these data is hindered because of the insufficient accuracy of the measurements. The above anomalies can be made more pronounced and ionic transport can be made more intense if one manages to increase the number of vacancies in the sublattice of mobile cations via its partial or complete disordering. In the latter case, the glassy state of lithium tetraborate would be considerably more favorable for the action of the vacancy mechanism than the crystalline state. Higher ionic conductivity is attained here because of jumps of lithium ions for shorter distances (~0.2 Å against ~0.6 Å in a single crystal), with the potential barrier between the positions being almost twice as low. Apparently, the factor that is most important for ionic conductivity under the conditions of structural disorder is the three-dimensional ionic transport in glass, together with the looser packing of boron–oxygen structural units and the existence of a large number of additional cavities between these units for the location of lithium ions and their transport.

ACKNOWLEDGMENTS

The authors are grateful to I.A. Borodenko and A.M. Solomon for their help in conducting the experiments. The study was supported by the Interdisciplinary scientific and technical program "Scientific–Innovational Cooperation," project no. 2.08-23.

REFERENCES

1. M. Adachi, K. Nakazawa, and A. Kawabata, Ferroelectrics **195** (1–4), 123 (1997).
2. J. Filipiak, A. Majchrowski, and T. Lukasiewicz, Arch. Acoust. **19** (1), 131 (1994).
3. A. S. Bhalla, L. E. Cross, and R. W. Whatmore, Jpn. J. Appl. Phys., Part 2 **24**, 727 (1985).
4. Yu. L. Kopylov and V. B. Kravchenko, in *Extended Abstracts of 8th All-Union Conference on Crystal Growth* (Kharkov, 1992), Vol. 3, Part 1, p. 172.
5. R. Komatsu, T. Sugawara, and N. Watanabe, Rev. Laser Eng. **27** (8), 541 (1999).
6. A. É. Aliev, Ya. V. Burak, and I. T. Lyseĭko, Izv. Akad. Nauk SSSR, Neorg. Mater. **26** (9), 1991 (1990).
7. A. V. Burak, I. T. Lyseĭko, and I. V. Garapin, Ukr. Fiz. Zh. **34** (2), 226 (1989).
8. K. Byrappa, V. Rajeev, V. J. Hanumesh, *et al.*, J. Mater. Res. **11** (10), 2616 (1996).
9. J. H. Cho, G. W. Lee, and Y. S. Yang, Ferroelectrics **196** (1–4), 121 (1997).
10. S. F. Radaev, L. A. Muradyan, L. F. Malakhova, *et al.*, Kristallografiya **34** (6), 1440 (1989) [Sov. Phys. Crystallogr. **34**, 842 (1989)].
11. S. Uda, R. Komatsu, and K. Takayama, J. Cryst. Growth **171** (3–4), 458 (1997).
12. A. B. Kaplun and A. B. Meshalkin, J. Cryst. Growth **209** (4), 890 (2000).
13. A. B. Kaplun and A. B. Meshalkin, Neorg. Mater. **35** (11), 1349 (1999).
14. I. I. Turok, V. M. Goloveĭ, and P. P. Puga, Ukr. Patent No. 32242 (1986).
15. H. Liu, X. Wang, J. Wei, and D. Shen, Prog. Cryst. Growth Charact. Mater. **40** (1–4), 235 (2000).
16. D. S. Robertson and Y. M. Young, J. Mater. Sci. **17** (6), 172 (1982).
17. J. B. Goodenough, Proc. R. Soc. London, Ser. A **393** (1805), 215 (1984).
18. D. P. Almond, G. K. Duncan, and A. R. West, Solid State Ionics **8** (2), 159 (1983).
19. P. Debye, *Polar Molecules* (Chemical Catalog, New York, 1929; Gostekhizdat, Moscow, 1931).
20. G. I. Skanavi, *Physics of Dielectrics* (Tekhteorizdat, Moscow, 1949).
21. S. Yu. Stefanovich and A. V. Mosunov, Izv. Ross. Akad. Nauk, Ser. Fiz. **64** (6), 1163 (2000).
22. B. A. Maksimov, L. A. Muradyan, N. N. Bydanov, *et al.*, Kristallografiya **36** (6), 1431 (1991) [Sov. Phys. Crystallogr. **36**, 810 (1991)].
23. S. Yu. Stefanovich, B. V. Mill, and A. V. Mosunov, in *Proceedings of 7th International Seminar on Physics of Ferroelastics* (Kazan, 1997), p. L3.

Translated by E. Shtykova

Crystallography Reports, Vol. 48, No. 4, 2003, pp. 682–685. Translated from Kristallografiya, Vol. 48, No. 4, 2003, pp. 734–737.

PHYSICAL PROPERTIES OF CRYSTALS

Anisotropy of Microhardness of β-BaB_2O_4 Single Crystals

E. F. Dolzhenkova, M. B. Kosmyna, B. P. Nazarenko, and V. N. Baumer

Institute for Single Crystals, National Academy of Sciences of Ukraine, pr. Lenina 60, Kharkov, Ukraine

e-mail: dol@isc.kharkov.com

Received January 27, 2003

Abstract—The anisotropy of microhardness of β-barium borate single crystals β-BaB_2O_4 (BBO) is studied by the sclerometry method on the (0001) basal plane, the $(10\bar{1}0)$ plane of the hexagonal prism, and the $(11\bar{2}0)$ plane of the trigonal prism. It is shown that the anisotropy observed in the crystal is determined by the directions of covalent B–O bonds. It is established that the anisotropy of microhardness correlates with the system of cleavage planes. *© 2003 MAIK "Nauka/Interperiodica".*

INTRODUCTION

β-barium borate single crystals β-BaB_2O_4 (BBO) are a unique nonlinear optical material. These crystals are characterized by pronounced nonlinear optical properties, a wide spectral range (from ultraviolet to near infrared) of light transmission, a high radiation resistance, and a large width of phase synchronism. BBO crystals (low-temperature phase) have a trigonal structure, sp. gr. *R*3*c* with the unit-cell parameters in a hexagonal setting $a = 12.547$ Å, $c = 12.736$ Å [1]. The crystals are noncentrosymmetric, which determines the existence of nonlinear optical effects. Since BBO crystals are promising nonlinear materials, their optical properties have been studied rather well. However, the physical and mechanical properties of these crystals have been insufficiently studied. The problems arising during the mechanical treatment of BBO crystals in manufacturing nonlinear optical elements require a detailed study of their mechanical characteristics. Today, it is known that the hardness of BBO crystals equals 4 and the fracture toughness is rather high (1.5 MPa $m^{1/2}$) [1, 2]. It was determined by the indentation method that microhardness on the basal planes of these crystals differs from microhardness on the prism planes by almost a factor of 2. Below, we describe the study of anisotropy of microhardness of BBO crystals by the sclerometry method, which allows one to reveal anisotropy more clearly.

EXPERIMENTAL

BBO crystals were grown from flux [3]. Anisotropy of hardness was studied on the (0001) basal plane, the $(10\bar{1}0)$ plane of the hexagonal prism, and the $(11\bar{2}0)$ plane of the trigonal prism. The basal plane was obtained by cleavage, and the planes of prisms were prepared by grinding and polishing. The measurements were made on a PMT-3 device. Scratching was performed with an edge and a face of the trihedral diamond prism. The scratches were made after every 10°, the scratching rate was constant. The loads applied were 0.05 and 0.1 N. Microhardness was calculated by the formulae proposed in [4], the experimental error was 5–10%.

RESULTS AND DISCUSSION

The hardness rosettes obtained by scratching on the (0001) and $(10\bar{1}0)$ faces of a BBO single crystal are shown in Fig. 1. On the basal plane, hardness anisotropy is almost unseen. Two hardness peaks are revealed on the plane of the hexagonal prism, with the higher peak being parallel and the lower peak being normal to the optic *c* axis of a crystal. The polar dependence of microhardness obtained by scratching on the plane of the trigonal prism is similar to the dependence described above. The microhardness values obtained by scratching with the edge and face of the trihedral indenter are different, which indicates different fracture mechanisms.

Microhardness anisotropy observed can be explained by anisotropy of bonding in a crystal. The main structural elements in BBO single crystals are an anion group $(B_3O_6)^{3-}$ and a Ba eight-vertex polyhedron. The anion group has a shape of an almost planar ring consisting of three B-triangles, with each of them sharing two verities with another triangle. The boron–oxygen groups are normal to the optic axis and are parallel to one another; they are connected into two-dimensional layers by Ba^{2+} cations sharing the O^{2-} ions [1, 5].

The hardness rosettes on the basal plane correspond to a boron–oxygen ring—the microhardness determined by scratching in this plane is determined by the directions of covalent bonds (Fig. 2a). Hardness rosettes on the face of the hexagonal prism are also determined by the B–O bonds and clearly reflect the

1063-7745/03/4804-0682$24.00 © 2003 MAIK "Nauka/Interperiodica"

structural characteristics of a BBO crystal. Hardness in the directions parallel to the planar boron–oxygen groups is less than in the directions perpendicular to these structural units. It is evident that the hardness is higher if scratches are made normally to the rigid directal bonds, whose rupture resistance is very high, than for scratches made along covalent bonds (Fig. 2b).

To understand the origin of hardness anisotropy, it is not sufficient to consider the hardness rosette. It is also necessary to study the anisotropy of scratches. The scratches made along the directions of the higher and the lower maxima of hardness on the $(10\bar{1}0)$ plane of the hexagonal prism are essentially different. Scratching along the direction of the higher maximum of hardness (along the direction of the optical axis) resulted in no visible fracture, only some short cracks normal to the scratches appeared at the edges. This means that these scratches are caused by plastic deformation; the cracks propagated only along boron–oxygen groups. If the indenter moved along the lower maximum of hardness (parallel to the $[10\bar{1}0]$ direction), large hollows appeared; i.e., scratching along the boron–oxygen rings was accompanied by a brittle fracture of the crystal (Fig. 3a).

The scratches made by the pyramid face is similar to those made by the pyramid edge; however, in the first case, the brittle fracture of the crystal is more pronounced (Fig. 3b). Under these conditions, scratching is controlled by fracture processes.

The hardness on the scratched $(11\bar{2}0)$ face of the trigonal prism is higher than on the face of the hexagonal prism: 9.3 and 3.7 GPa in the directions of the higher [0001] and lower $[11\bar{2}0]$ maxima of hardness, respectively (scratcing by edge). If scratching is made by the face, these values are 18.4 and 9.6 GPa, respectively. These results can be explained by the fact that the reticular density of boron–oxygen groups on the plane of the trigonal prism exceeds this density on the plane of the hexagonal prism (Fig. 2a).

The scratches made along different directions on the basal plane differ only slightly. Scratching was accompanied by plastic deformation and also brittle fracture, with the predominance of the latter process. Scratching by edge gave rise to the heaping of plastically deformed material at scratch edges, whereas scratching by face resulted in brittle fracture around the scratches (Fig. 4).

Hardness anisotropy obviously correlates with the system of cleavage planes. It is well known that BBO single crystals are readily cleaved along the (0001) plane [6, 7]. It is indicated [3] that the $(10\bar{1}0)$ and $(11\bar{2}0)$ planes are also the planes of easy crack propagation. During scratching on the basal plane, the prism planes are under similar conditions with respect to the indenter and do not affect hardness, which explains the absence of microhardness anisotropy in this plane. If the indenter moves on the prism faces along the optic axis, it travels normally to cleavage lines, which explains the appearance of the higher maximum. The motion of the indenter along the direction normal to the optic axis coincides with the cleavage direction, which may be associated with the lower maximum.

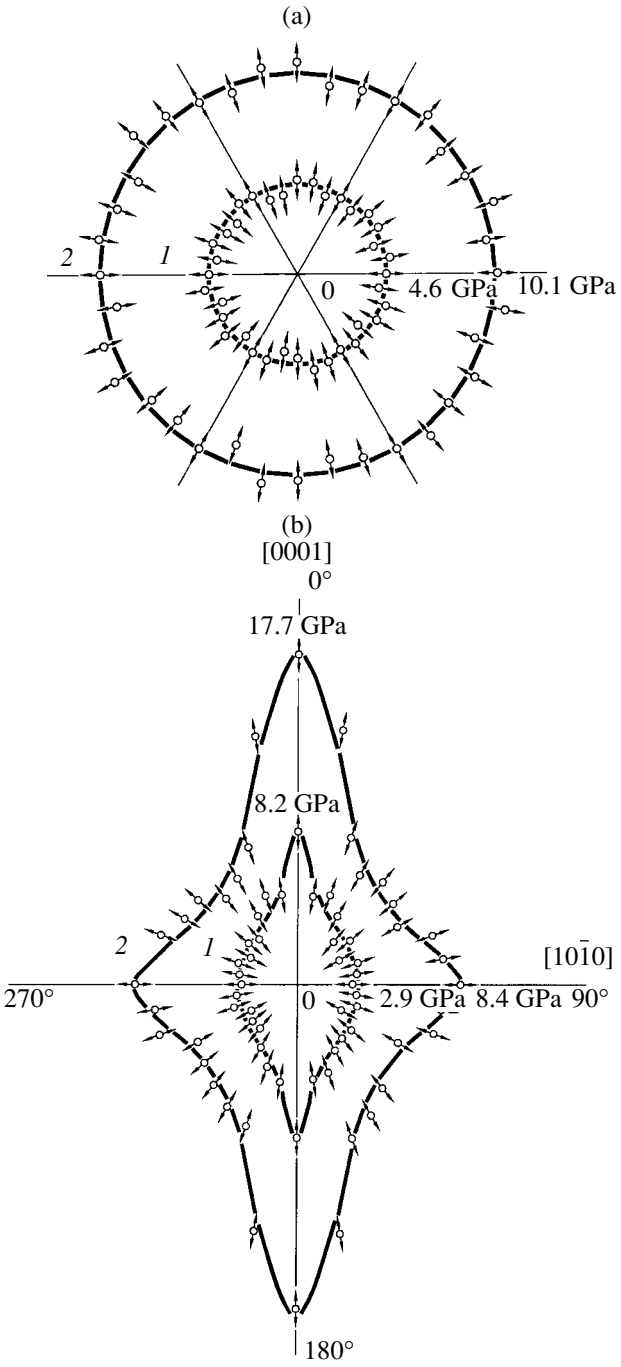

Fig. 1. The sclerometric hardness rosettes (a) on the (0001) (P = 0.05 N) and (b) $(10\bar{1}0)$ faces (P = 0.1 N). (*1*) Scratches were made by the indenter edge; (*2*) scratches were made by the indenter face.

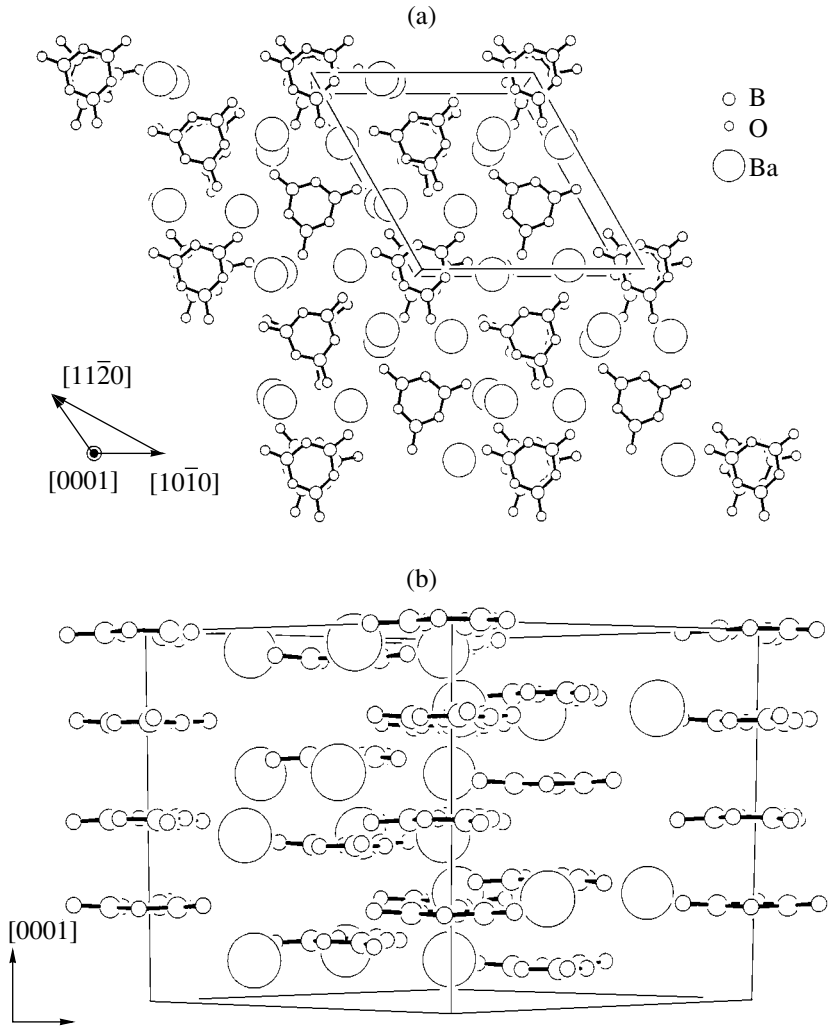

Fig. 2. The structure of a β-BaB_2O_4 single crystal projected (a) onto the basal plane and (b) along the optic axis.

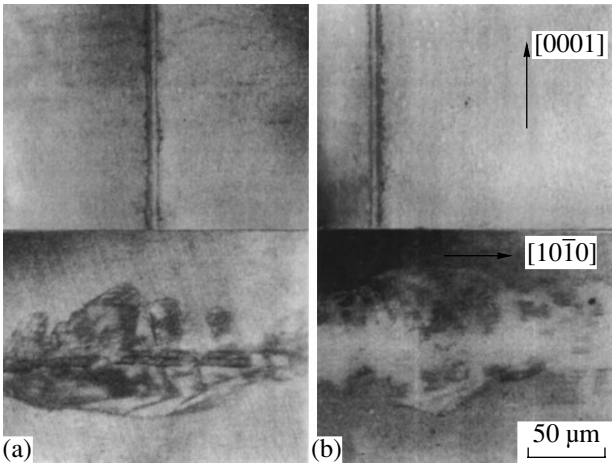

Fig. 3. Anisotropy of the scratches on the (10$\bar{1}$0) face (P = 0.1 N) made by (a) the indenter edge and (b) the indenter face.

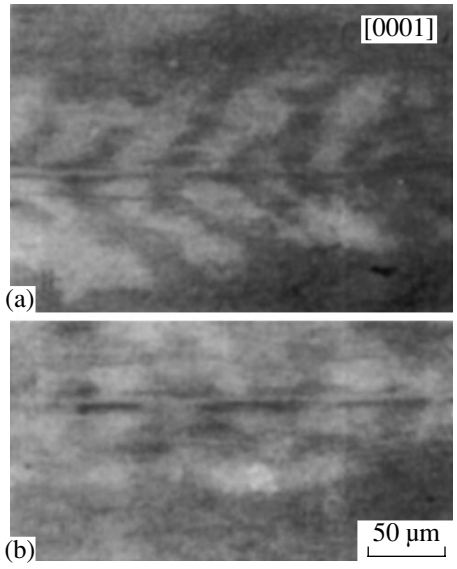

Fig. 4. Anisotropy of scratches on the (0001) face (P = 0.05 N) made by (a) the indenter edge and (b) the indenter face.

As is seen from the data obtained, anisotropy of microhardness in BBO single crystals is explained by their crystallographic characteristic—the existence of nearly planar boron–oxygen layers. The anisotropy observed is determined by the directed B–O covalent bonds despite the fact that the ionicity of these bonds in crystals is rather high: the boron–oxygen rings are discrete and are bound by ionic Ba^{2+}–O^{2-} bonds. Microhardness anisotropy correlates quite well with the crystallographic system of cleavage planes.

REFERENCES

1. D. Eimerl, L. Davis, S. Velsko, *et al.*, J. Appl. Phys. **62** (5), 1968 (1987).
2. D. Y. Tang, W. R. Zeng, X. Lin, *et al.*, in *Abstracts of 10th International Conference on Crystal Growth* (San Diego, California, 1992), p. 57.
3. I. P. Babiychuk, E. F. Dolzhenkova, B. P. Nazarenko, *et al.*, Funct. Mater. **6** (4), 721 (1999).
4. V. K. Grigorovich, *Hardness and Microhardness of Metals* (Nauka, Moscow, 1976).
5. S.-F. Lu, M.-Y. Ho, and J. L. Huang, Acta Phys. Sin. **31** (7), 948 (1982).
6. D. Y. Tang, R. K. Route, and R. S. Feigelson, J. Cryst. Growth **91** (1/2), 81 (1988).
7. D. Y. Tang, W. R. Zeng, and Q. L. Zhao, J. Cryst. Growth **123** (3/4), 445 (1992).

Translated by T. Dmitrieva

Crystallography Reports, Vol. 48, No. 4, 2003, pp. 686–692. Translated from Kristallografiya, Vol. 48, No. 4, 2003, pp. 738–744.

LIQUID CRYSTALS

Flexoelectric Effect and Statistical Properties in Polar Liquid Crystals

A. V. Zakharov and A. A. Vakulenko

Institute of Problems in Machine Science, Russian Academy of Sciences, Vasil'evskiĭ ostrov, Bol'shoĭ pr. 61, St. Petersburg, 199178 Russia

e-mail: avak@ipme.ru

Received September 19, 2002

Abstract—The structural properties and flexoelectric coefficients e_1 and e_3 of polar liquid crystals (LCs) such as 4-*n*-pentyl-4'-cyanobiphenyl (5CB) are studied in the nematic phase by the molecular-dynamics and statistical-mechanics methods. A number of order parameters, $\bar{P}_{2L}$ (L = 1, 2, 3) and $\bar{P}_2(r)$, and orientational correlations ξ_λ for the nearest and next-nearest neighbors were investigated. The calculations show the absence of spontaneous polarization ($\bar{P}_1 \simeq 0$) in the nondeformed polar 5CB liquid crystal over the entire range of temperatures corresponding to the nematic phase. The origination of spontaneous polarization (characterized by two independent flexoelectric coefficients e_1 and e_3) in response to an external deformation of a 5CB sample is studied. The calculated e_1 and e_3 coefficients agree well with the experimental data for 5CB obtained by the pyroelectric method. © *2003 MAIK "Nauka/Interperiodica".*

INTRODUCTION

Anisotropic systems, such as liquid crystals, possess a direction of the preferred orientation of molecules characterized by the director **n**, which is associated with the anisotropic nature of molecular interactions. Often, molecules of nematic LCs possess a pronounced dipole moment. Among such compounds are, e.g., cyanobiphenyls consisting of an elastic core with one or several flexible hydrocarbon chains attached. The dipole moment is directed from the polar core to the molecule tail and ranges from 4.5 to 5 D [1]. Another specific feature of these systems is spontaneous polarization **P** which arises in response to elastic deformation (flexoelectric effect) [2]. In nematic LCs, the transverse and longitudinal deformations give rise to two independent flexoelectric coefficients e_1 and e_3, and the spontaneous-polarization vector is represented in the form

$$\mathbf{P} = e_1\mathbf{n}\,\mathrm{div}\,\mathbf{n} + e_3[\mathbf{n}, \mathrm{rot}\,\mathbf{n}]. \quad (1)$$

The effect of the flexoelectric polarization on the electro-optical and structural properties of LCs and the low accuracy of the experimental measurements of the flexoelectric coefficients are rather important for the development of the theoretical models for calculating these coefficients over a wide range of thermodynamic parameters. At present, the methods of statistical mechanics and computational methods of molecular dynamics seem to be most effective for studying the relation between the measured macroscopic properties and the microscopic structure of LCs. The former allow one to calculate the macroscopic characteristics based on reasonable assumptions and the model potentials of molecular interactions; the latter, to calculate the averaged characteristics of the system on the basis of realistic interactions both between atoms located within the constituent molecules of the anisotropic systems and between atoms from different molecules [3, 4].

Below, we combine these methods to study the structural properties and the flexoelectric effect in the nematic phase of 4-*n*-pentyl-4'-cyanobiphenyl (5CB). We use the theory based on the conditional-distribution method [5], which allows one to take into account not only the translational and orientational correlations but also the mixed correlations [6, 7]. The model potential of the molecular interactions was the Gay–Berne dipolar potential [8]. We calculated the two-particle correlation function of the spatial distribution and the orientational distribution function for 5CB molecules in the temperature range of the nematic phase by methods of statistical mechanics. These two functions were also calculated by the molecular-dynamics methods using realistic potentials of interatomic interactions [3, 4]. Using this information, we calculated the direct correlation function of the distribution with the aid of the well-known Ornstein–Zernicke equation and then, using this function, the flexoelectric coefficients e_1 and e_3.

TWO-PARTICLE AND DIRECT CORRELATION FUNCTIONS OF THE DISTRIBUTION

Two-particle and direct correlation functions were calculated in the framework of the equilibrium statistical mechanics based on the conditional-distribution

1063-7745/03/4804-0686$24.00

method [5]. We considered a one-component system of ellipsoidal molecules with the length $\sigma_\parallel$ and the width $\sigma_\perp$ in the volume V_0 at the temperature T. The total volume occupied by the system was divided into N cells with the volumes $v = V_0/N$. As the first approximation, we considered only the states with one molecule in each cell [9]. The potential energy of this system was chosen in the form $U = \sum_{i<j}\Phi(\mathbf{i}, \mathbf{j})$, where $\Phi(\mathbf{i}, \mathbf{j})$ is the pair potential of the molecular interactions, $\mathbf{i} \equiv (\mathbf{r}_i, \mathbf{u}_i)$, and $\mathbf{r}_i$ and $\mathbf{u}_i$ are the vectors specifying the position and orientation of the ith molecule. Integrating the quantity $\exp[-U/k_BT]$ (where k_B is the Boltzmann constant), the probability density of finding the system at points 1, 2, 3, …, N at the temperature T [5, 9], we obtain the one-particle distribution function $F(\mathbf{i})$ (the probability density of finding a particle in a certain environment within the ith cell), the two-particle distribution function $F(\mathbf{i}, \mathbf{j})$ (the probability density of finding two particles in certain environment within two different cells i and j), and so on. Using this approach, we take into account only two-cell correlations.

The functions $F(\mathbf{i})$ and $F(\mathbf{i}, \mathbf{j})$ can be expressed in terms of the mean-force potentials [5, 9]

$$F(\mathbf{i}) = \frac{\Psi(\mathbf{i})}{\int\Psi_i(\mathbf{i})d(\mathbf{i})}, \quad (2)$$

$$F(\mathbf{i}, \mathbf{j}) = F(\mathbf{i})F(\mathbf{j})V(\mathbf{i}, \mathbf{j})\Psi^{-1}_{i,j}(\mathbf{i})\Psi^{-1}_{j,i}(\mathbf{j}), \quad (3)$$

where $\Psi_j(\mathbf{j}) = \prod_{i\neq j}\Psi_{j,i}(\mathbf{j})$, $\int d(\mathbf{i}) \equiv \int_v d\mathbf{r}_i\int_\alpha d\mathbf{u}_i$, $V(\mathbf{i}, \mathbf{j}) = \exp[-\Phi(\mathbf{i}, \mathbf{j})/k_BT]$, and α is the volume associated with the orientations of the ith molecule. The functions $F(\mathbf{i})$ automatically satisfy the normalization condition $\int F(\mathbf{i})d(\mathbf{i}) = 1$. The condition $F(\mathbf{i}) = \int F(\mathbf{i}, \mathbf{j})d(\mathbf{j})$ relating the one- and two-particle distribution functions allows one to obtain the closed integral equation with respect to the mean-force potentials $\Psi_{i,j}(\mathbf{i})$ [5, 9],

$$\Psi_{i,j}(\mathbf{i}) = \int V(\mathbf{i}, \mathbf{j})\Psi^{-1}_{j,i}(\mathbf{j})F(\mathbf{j})d(\mathbf{j}). \quad (4)$$

Equation (4) can be solved only by the numerical method described in detail in [6, 7]. Using the solution for $\Psi_{i,j}(\mathbf{i})$, we can calculate, with the aid of Eq. (3), the two-particle function $F(\mathbf{i}, \mathbf{j})$, the orientational distribution function $f_0(\cos\beta_i) = \int F(\mathbf{i})d\mathbf{r}_i d\varphi_i$ (where β_i and φ_i are the polar and azimuthal angles of the unit vector $\mathbf{u}_i$, respectively), and also the order parameters of the LC system

$$\bar{P}_L = \int F(\mathbf{i})P_L(\cos\beta_i)d(\mathbf{i}), \quad (5)$$

the correlations

$$\xi_\lambda = \langle\mathbf{u}_1\mathbf{u}_\lambda\rangle = \int d(\mathbf{1})\int d(\boldsymbol{\lambda})F(\mathbf{1}, \boldsymbol{\lambda})(\mathbf{u}_1\mathbf{u}_\lambda), \quad (6)$$

and the Helmholtz free energy

$$f = \frac{F}{N} = -k_BT\ln\int d(\mathbf{i})\Psi_i(\mathbf{i}). \quad (7)$$

Here, P_L are the Legendre polynomials (L = 1, 2, 4, 6). With due regard for the $F_{ij}(\mathbf{ij})$ function and the intermolecular potential $\Phi(\mathbf{ij})$, the expression for the direct correlation function in the framework of the classical Percus–Yevick approximation [10] takes the form

$$C(\mathbf{ij}) = F(\mathbf{ij})(1 - V^{-1}(\mathbf{ij})). \quad (8)$$

In the density-functional approximation, the expressions for the flexoelectric coefficients e_1 and e_3 can be written as [10]

$$e_1 = \rho^2\Delta\int r_x C(\mathbf{ij})f_0'(\cos\beta_j) \times f_0(\cos\beta_i)u_{i,z}drd\Omega\mathbf{u}_i d\mathbf{u}_j, \quad (9)$$

$$e_3 = \rho^2\Delta\int r_z C(\mathbf{ij})f_0'(\cos\beta_j) \times f_0(\cos\beta_i)u_{i,x}drd\Omega d\mathbf{u}_i d\mathbf{u}_j, \quad (10)$$

where Δ is the dipole moment of a 5CB molecule ($\Delta \sim 5D$ [11]); $\rho = 1/v$ is the density; $d\Omega = \sin\beta_{ij}d\beta_{ij}d\varphi_{ij}$; β_{ij} and φ_{ij} are the polar and azimuthal angles of the unit vector $\mathbf{u} = \mathbf{r}/|\mathbf{r}|$ parallel to the vector $\mathbf{r} = |\mathbf{r}_i - \mathbf{r}_j|$, respectively; $d\mathbf{u}_i = \sin\beta_i d\beta_i d\varphi_i$; and $u_{i,\alpha}$ and r_α are the projections of the $\mathbf{u}_i$ and $\mathbf{r}$ vectors onto the axis $\alpha = x, y$. And, finally, $f_0'(\cos\beta_i)$ is the derivative of $f_0(\cos\beta_i)$ with respect to $\cos\beta_i$. The kernel of integral equation (4) is determined in terms of the pair intermolecular potential $\Phi(\mathbf{i}, \mathbf{j}) = \Phi_{GB}(\mathbf{i}, \mathbf{j}) + \Phi_{DD}(\mathbf{i}, \mathbf{j})$ chosen as the sum of the Gay–Berne and dipole–dipole potentials. The first potential can be written as $\Phi_{GB}(\mathbf{i}, \mathbf{j}) = 4\varepsilon_0\varepsilon(R^{-12} - R^{-6})$, where $R = (r - \sigma + \sigma_\perp)/\sigma_\perp$ [8]. The quantities σ and ε are the width and depth of the potential well, respectively, which are dependent on the orientation of the unit vectors $\mathbf{u}_i$, $\mathbf{u}_j$, and $\mathbf{u} = \mathbf{r}/|\mathbf{r}|$; the geometric parameter of the molecule $\gamma = \sigma_\parallel/\sigma_\perp$; and two exponential parameters ν and μ, which enter the expression for $\omega = \varepsilon_1^\nu(\mathbf{u}_i, \mathbf{u}_j)\varepsilon_2^\mu(\mathbf{u}_i, \mathbf{u}_j, \mathbf{u})$ (expressions for ε_1 and ε_2 are given in [8]). The potential of the dipole-dipole interaction was chosen in the form $\Phi_{DD}(\mathbf{i}, \mathbf{j}) = \frac{\Delta^2}{r^3}[(\mathbf{u}_i\mathbf{u}_j) - 3(\mathbf{u}_i\mathbf{u})(\mathbf{u}_j\mathbf{u})]$. In our calculations, we used the following parameters of the molecular interactions: $\gamma = \sigma_\parallel/\sigma_\perp = 3$, ($\sigma_\parallel \sim 1.8$ nm, $\sigma_\perp \sim 0.6$ nm), $\nu = 2.0$, $\mu = 0.98$, and $\varepsilon_0 = 4.14\times10^{-21}$ J. We also used the following dimensionless quantities: the density $\rho = N\sigma_\perp^3/V_0 \approx 0.512$ corresponding to a 5CB density of 10^3 kg/m^3, the temperature $\theta = k_BT/\varepsilon_0$, and the dipole moment $\mu^* = \frac{\Delta}{(\varepsilon_0\sigma_\perp^3)^{1/2}} \approx 2.5$. It is worth noting that the calculations were performed only for a cubic structure with the six nearest neighbors and twelve next-nearest neighbors. In so

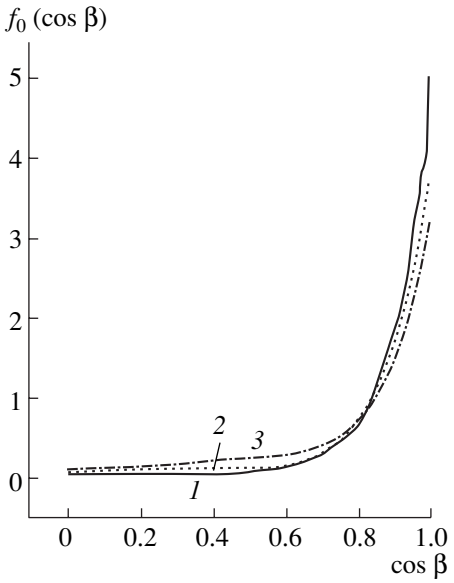

Fig. 1. Orientational distribution function for 5CB molecules calculated by the methods of (*1*) molecular dynamics and statistical mechanics (*2*) with and (*3*) without allowance for dipole–dipole interactions.

doing, we solved 18 nonlinear integral equations (4) in the five-dimensional space. In the molecular-dynamics calculations, we considered 120 5CB molecules in the cubic unit cell with an edge of 3.65 nm (the corresponding density is 10^3 kg/m^3). The temperature was kept constant, 300 K ($\theta = 1.0$) (*NVT* is a canonical ensemble). The equation of motion of 5CB molecules was solved using the Verlet algorithm [12] at a step of $2f_s$ [3, 4]. The initial configuration of the director **n** corresponded to the smectic phase of 5CB [4]. The orientation of the director **n** was determined with the aid of the matrix $Q_{zz}^{\nu\nu'}$ [13],

$$Q_{zz}^{\nu\nu'} = \frac{1}{N}\sum_{j=1}^{N}\frac{1}{2}(3\cos\beta_{z\nu}^{j}\cos\beta_{z\nu'}^{j} - \delta_{\nu\nu'}), \qquad (11)$$

where N is the number of 5CB molecules and $\beta_{z\nu}^{j}$ is the angle between the long axis of the jth molecule and the ν-axis related to the cubic cell. The molecular coordinates of the system were constructed using eigenvectors of the inertia tensor [3, 4]. The diagonalization of the $Q_{zz}^{\nu\nu'}$ matrix made it possible to determine all the eigenvectors, the largest of which corresponded to the direction specified by the director **n**. Figure 1 shows the results of the molecular-dynamics calculation of the $f_0(\cos\beta_i)$ function performed with due regard for the potential energy of the system (consisting of the intra- and extramolecular contributions [3, 4]) and the data for this function obtained using the integral equation for the polar ($\mu^* \sim 2.5$) and nonpolar ($\mu^* = 0$) systems at 300 K. Taking into account the fact that the calculations involved different intermolecular potentials, the results thus obtained agree well. It is of interest to study the correlations between the central particle and the nearest and next-nearest neighbors in the systems of polar liquid crystals. For a primitive cubic lattice, the **n** vector is parallel to the z axis, and we arrive at two types of $F_\lambda(\mathbf{ij})$ dependences. The first type corresponds to the case where the neighboring cell is located either above ($\lambda = 1$) or under ($\lambda = 2$) the central cell. The second type corresponds to the cells lying in one horizontal plane ($\lambda = 3, \ldots, 6$). Accordingly, we also distinguish two types of the correlations ξ_λ. Figure 2 shows the calculated moduli of the correlations $|\xi_\lambda|$ ($\lambda = 1, \ldots, 6$) as functions of the dimensionless temperature θ. The "vertical" correlations are characterized by positive values $\xi_\lambda > 0$ ($\lambda = 1, 2$), while the "horizontal" correlations, by negative values $\xi_\lambda < 0$ ($\lambda = 1, \ldots, 6$). This indicates the average parallel orientation of the dipoles for $\lambda = 1, 2$ and the antiparallel orientation for $\lambda = 3, \ldots, 6$. The averaged correlation for the nearest neighbors $\bar{\xi} = \frac{1}{3}\sum_{\lambda=1}^{6}\xi_\lambda$ is shown in Fig. 3. This correlation is negative over the entire range of the temperatures θ, thus indicating the antiparallel average orientation of the nearest dipoles. Using the analogy with the nearest neighbors, we also calculated the correlations for the next-nearest neighbors η_λ ($\lambda = 1, \ldots, 12$). The averaged correlation $\bar{\eta} = \frac{1}{12}\sum_{\lambda=1}^{12}\eta_\lambda$ is shown in Fig. 3 as a function of the temperature θ. The calculations showed that $\bar{\eta} < 0$ over the entire range of temperature variation. This indicates the antiparallel orientation of the dipoles that are the next-nearest neighbors with respect to the central dipole. In the temperature range of the nematic phase of 5CB, the calculation of the order parameter $\bar{P}_1$ yielded $\bar{P}_1 \sim 0.02$, which indicates the absence of the spontaneous polarization in a nondeformed polar 5CB liquid crystal.

The dimensionless Helmholtz free energy f/ε_0 was found to be –15.55 with allowance for only the nearest neighbors. If both the nearest and next-nearest neighbors were taken into account, the energy was –15.67. Such a minor change in this integral characteristic shows that the allowance for only the nearest and next-nearest neighbors is quite reasonable within the framework of the statistical theory that takes into account the translational, orientational, and mixed correlations.

In turn, the molecular-dynamics methods make it possible to calculate the two-particle distribution function $F_\lambda(\mathbf{ij}) = G(\mathbf{r}, \mathbf{u}_i, \mathbf{u}_j)$ and a number of order parameters $\bar{P}_{2L}(L = 1, 2, 3)$ and $\bar{P}_2(r) = \overline{P_2(\cos\beta_{ij})} = \int P_2(\cos\beta_{ij})G(\mathbf{r}, \mathbf{u}_i, \mathbf{u}_j)d\Omega d\mathbf{u}_i d\mathbf{u}_j$, where β_{ij} is the polar angle of the vector $\mathbf{r} = \mathbf{r}_i - \mathbf{r}_j$, i.e., the angle between the vectors **n** and **r**. Figure 4 shows the calculated order parameter $\bar{P}_2(r)$ for 5CB molecules at 300 K. Since the

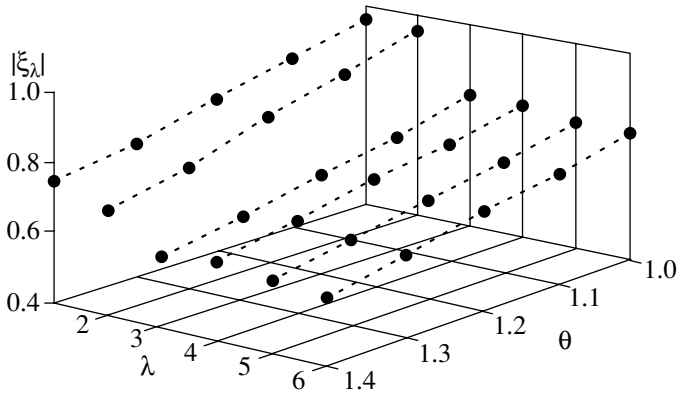

Fig. 2. Temperature dependences of the orientational correlations $|\xi_\lambda|$ ($\lambda = 1, \ldots, 6$) for the nearest neighbors; $\xi_\lambda > 0$ ($\lambda = 1, 2$) for the vertical neighbors and $\xi_\lambda < 0$ ($\lambda = 3, \ldots, 6$) for the horizontal neighbors.

initial configuration of the dipoles corresponded to the smectic phase (SmA), the averaging of $\bar{P}_2(r)$ within the first picosecond yielded $\bar{P}_2(r) = -0.5$. Since the orientation of the dipoles $\mathbf{u}_i$ and $\mathbf{u}_j$ does not correlate with the direction of the **r** vector and $\bar{P}_2 \simeq 0.8$, the vector **r** is normal to the vector $\mathbf{r} \perp \mathbf{n}$ for any pair of 5CB molecules, whereas the vectors $\mathbf{u}_i$ and $\mathbf{u}_j$ are parallel to **n**. Upon 600-ps averaging, the equilibrium configuration corresponded to the nematic phase of 5CB with $\bar{P}_2 = 0.51$, $\bar{P}_4 = 0.18$, and $\bar{P}_6 = 0.09$. The behavior of $\bar{P}_2(r)$ indicates that the distribution of the **r** vectors is nonspherical (at least, at short distances $r < 2$ nm). At distances $r \le r_{max1}$, the molecules "prefer" side-by-side packing, which results in the value $\bar{P}_2(r) \simeq -0.5$. This agrees with the behavior of the radial distribution function $G(r) = \int G(\mathbf{r}, \mathbf{u}_i, \mathbf{u}_j) d\Omega d\mathbf{u}_i d\mathbf{u}_j$, which exhibits the first maximum at $r \simeq 0.6$ nm (Fig. 5). The width of the 5CB molecule, $\sigma_\perp \simeq 0.6$ nm, confirms our assumption about the preferred side-by-side packing of molecules. The first maximum in Fig. 4 ($\bar{P}_2(r) > 0$ at $r \simeq 0.8$ nm) indicates the preferred head-to-head packing of the molecules; then, the situation is repeated once again up to $r \simeq 2$ nm. At distances $r \ge 2$ nm, we have $\bar{P}_2 \simeq 0$, which indicates the spherical distribution of the **r** vectors. The radial distribution function $G(r)$ allows us to calculate the radial part of the direct correlation function $C(r)$ [4] with the aid of the Ornstein–Zernicke equation,

$$C(r_{12}) = G(r_{12}) - 1 - \frac{\rho}{4\pi}\int dr_3 C(r_{13}) G(r_{23} - 1). \quad (12)$$

Equation (12) is a linear integral equation with respect to $C(r)$ and can be solved by numerical methods described elsewhere [4]. Figure 6 shows the calculated function $C(r)$ for the nematic phase of 5CB at 300 K. In

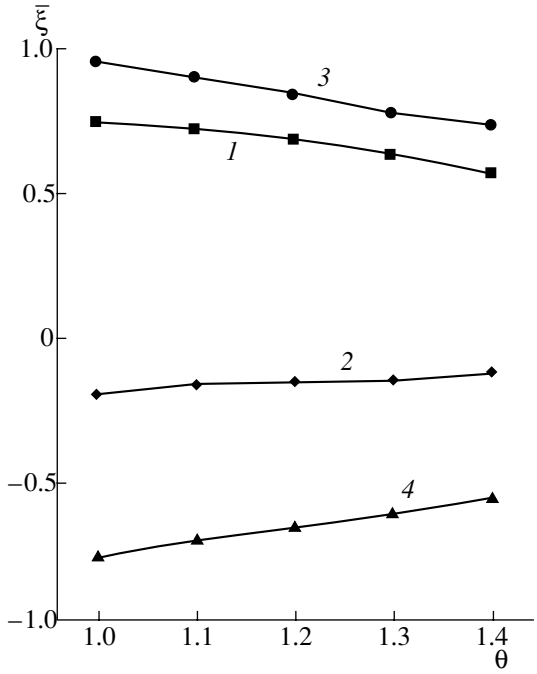

Fig. 3. Temperature dependence of the average orientational correlations $\bar{\xi}$ for the (*1*) nearest and (*2*) next-nearest neighbors. Temperature dependences for the averaged (*3*) vertical and (*4*) horizontal nearest neighbors are shown separately.

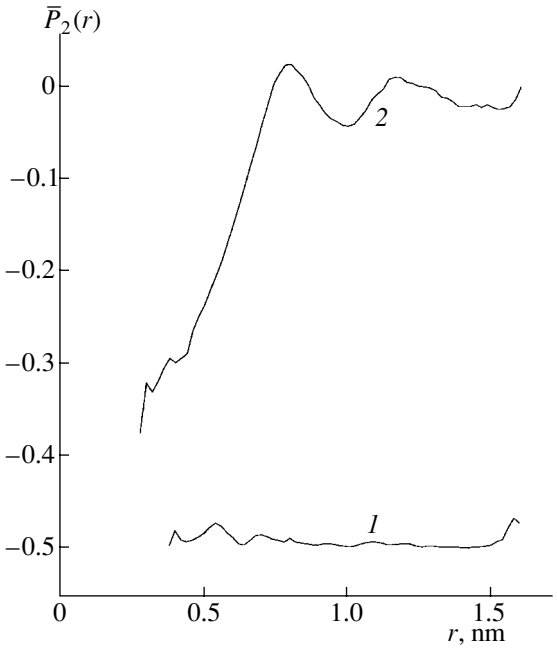

Fig. 4. Spatial dependences of the order parameter $\bar{P}_2(r)$ obtained by the molecular-dynamics method and averaged (*1*) within the first picosecond in the smectic *A* phase and (*2*) within the period of 600 ps in the nematic phase.

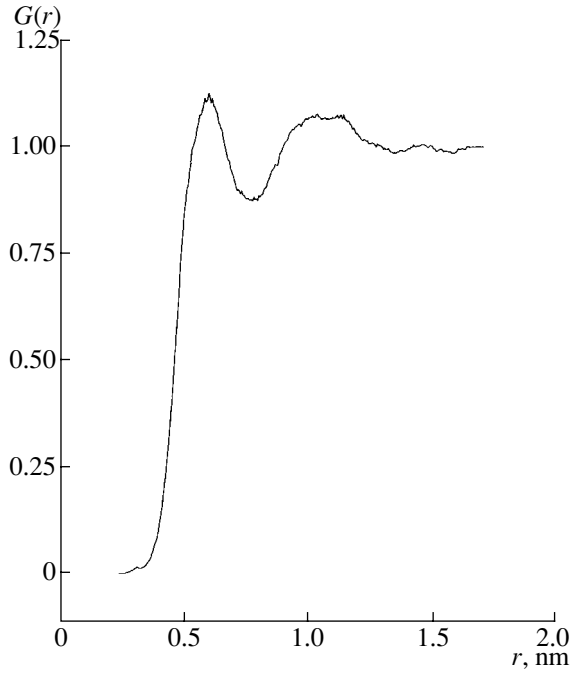

Fig. 5. The radial distribution function $G(r)$ for 5CB molecules calculated by the molecular-dynamics methods.

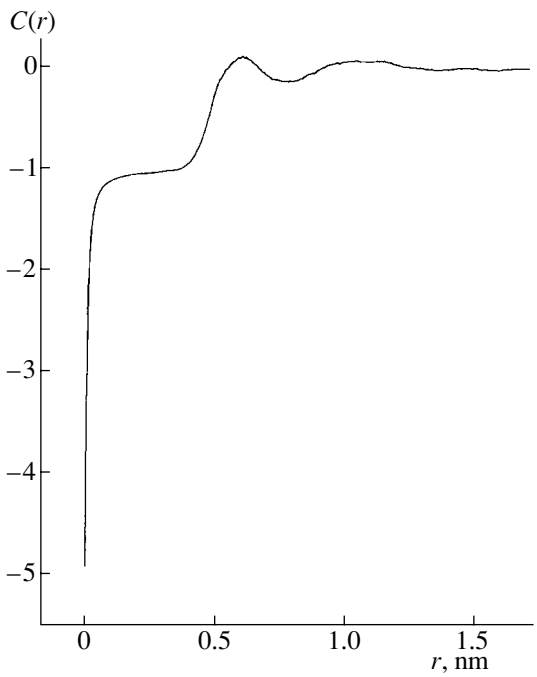

Fig. 6. Radial part of the direct correlation function $C(r)$ for 5CB molecules calculated by the molecular-dynamics methods.

fact, the function $C(r)$ is the first term of the spherical-harmonic expansion of the function $C(\mathbf{r}, \mathbf{u}_i, \mathbf{u}_j)$,

$$C(\mathbf{r}, \mathbf{u}_i, \mathbf{u}_j) = 4\pi \sum_{l_i, l_j, l} \sum_{m_i, m_j, m} C_{l_i, l_j, l}(r) \times C_{l_i, l_j, l; m_i m_j, m} Y_{l_i, m_i}(\mathbf{u}_i) Y_{l_j, m_j}(\mathbf{u}_j) Y^*_{l, m}(\mathbf{u}), \quad (13)$$

where $C_{l_i, l_j, l; m_i, m_j, m}$ are the Clebsch–Gordan coefficients and $Y_{l, m}$ are the spherical functions. In what follows, we shall restrict ourselves to the first five $C_{l_i, l_j, l}(r)$ coefficients, namely,

$$C_{000} = C(r),$$

$$C_{020}(r) = \frac{\sqrt{5}}{2} C(r) \langle 3\cos^2\beta_i - 1 \rangle,$$

$$C_{220}(r) = \frac{5}{4} C(r) \langle (3\cos^2\beta_i - 1)(3\cos^2\beta_j - 1) \rangle,$$

$$C_{221}(r) = \frac{15}{8} C(r) \langle \sin 2\beta_i \sin 2\beta_j \exp(i(\varphi_i - \varphi_j)) \rangle,$$

$$C_{222}(r) = \frac{15}{8} C(r) \langle \sin^2\beta_i \sin^2\beta_j \exp(i(\varphi_i - \varphi_j)) \rangle.$$

Thus, now we have at our disposal all the necessary information to calculate the flexoelectric coefficients in a deformed polar LC using Eqs. (9), (10).

CALCULATION OF FLEXOELECTRIC COEFFICIENTS

The temperature dependences of the flexoelectric e_1 and e_3 coefficients and their combinations e_+/K_i and e_-/K_i (i = 2, 3) were first measured for a number of cyanobiphenyls nCB (n = 5, …, 8) [14]. Here $e_+ = e_1 + e_3$; $e_- = e_1 - e_3$; and K_i (i = 2, 3) are the Frank elastic constants for twist and bend deformations, respectively [1]. It was found that the temperature dependences of e_-/K_2 for higher nCB homologues (n = 6, 7, 8) are the curves with the characteristic maximum. At the same time, this dependence for 5CB decreases with an increase in temperature, with both flexoelectric coefficients, e_1 and e_3, being positive [14]. The recent pyroelectric measurements of the flexoelectric coefficients of 5CB showed that $e_+ < 0$ over the entire range of temperatures corresponding to the nematic phase [15]. Since the dipole moments for all the molecules of cyanobiphenyls range within ~4.5–5 D and are directed from the polar core of the molecule to its tail, the character of the molecular interactions and correlations seems to play a key role in the determination of the e_1 and e_3 values. Here again the molecular-dynamics and statistical-mechanics methods are most efficient, because they allow one to calculate the measured macroscopic characteristics of the system based on reasonable approximations and model potentials of molecular interactions. Expressions for the flexoelectric coefficients e_1 and e_3 (see Eqs. (9), (10)) include integration over seven independent variables, which can only be performed by numerical methods.

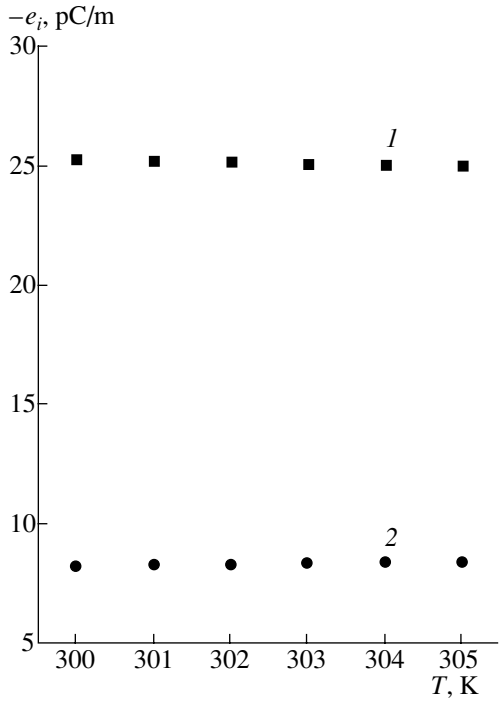

Fig. 7. Temperature dependences of flexoelectric coefficients (*1*) e_1 and (*2*) e_3 calculated by the statistical-mechanics methods.

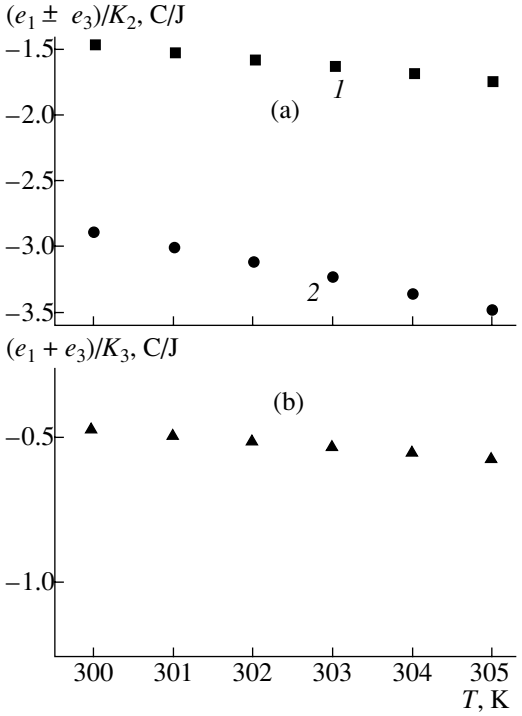

Fig. 8. Temperature dependences of $(e_1 \pm e_3)/K_2$ (a, curves *1* and *2*) and (b) $(e_1 + e_3)/K_3$ calculated by the statistical-mechanics methods.

For the $C(\mathbf{ij})$ and $f_0(\cos\beta_i)$ functions obtained from nonlinear integral equations (4), the integration can be performed numerically using the method of Haar functions [16] and for the $C(\mathbf{ij})$ and $f_0(\cos\beta_i)$ functions obtained within the framework of molecular dynamics, by the formulas of the Simpson numerical integration with a very small step [17]. The results of the statistical-mechanics calculation of the temperature dependences of $e_1(T)$ and $e_3(T)$ are shown in Fig. 7. The calculations also showed that both flexoelectric coefficients, e_1 and e_3, are negative in the temperature range corresponding to the nematic 5CB phase and the signs of the e_+ and e_- combinations are determined by the sign of the e_1 coefficient ($|e_1| \simeq 3|e_3|$). As flexoelectric coefficients $e_1(T)$ and $e_3(T)$ are often measured not separately but in combination with K_i, we present in Fig. 8 the calculated e_+/K_3, e_+/K_2, and e_-/K_2 ratios as functions of temperature. The Frank elastic constants K_i (i = 2, 3) of 5CB calculated by the statistical-mechanics methods using the same intermolecular potentials were reported in [18]. The table compares the values of e_1, e_3, e_+/K_3, and e_-/K_2 calculated by the statistical-mechanics and molecular-dynamics methods and the experimental data obtained by the pyroelectric technique.

Flexoelectric coefficients e_1, e_3, and e_+ and the ratios e_+/K_3 and e_-/K_2 calculated within the framework of statistical mechanics (SM) and molecular dynamics (MD), and the experimental data for e_+ obtained by the pyroelectric technique (PT) for 5CB molecules in the nematic phase at a temperature of 300 K

	$-e_1$, pC/m	$-e_3$, pC/m	$-e_+$, pC/m	$-\frac{e_+}{K_3}$, C/J	$-\frac{e_-}{K_2}$, C/J
SM	25.26	8.25	33.5	0.55	2.89
MD	11.6	4.3	15.9	1.14	1.43
PT			13		

CONCLUSIONS

We studied the structural properties of a nondeformed polar LC formed by molecules of 4-*n*-pentyl-4'-cyanobiphenyl by the methods of conditional distributions of molecular dynamics using realistic interatomic potentials. The calculated orientational ($f_0(\cos\beta_i)$) and two-particle ($F(\mathbf{ij})$) functions of the distribution of 5CB molecules, the order parameters $\bar{P}_{2L}$ (L = 1, 2, 3), and the orientational correlations ξ_λ showed the preferred orientations of molecules forming a polar 5CB crystal. We also determined the values and the signs of the flexoelectric coefficients e_1 and e_3 for the asymmetric system of 5CB. The analysis of the results obtained allowed us to conclude that a reliable calculation of e_1 and e_3 requires knowledge of the direct

correlation function of the distribution, which can be obtained independently by the statistical-mechanics and molecular-dynamics methods. In the statistical-mechanics calculations, the complex hierarchy of the correlations between rigid nonflexible molecules was taken into account. In the molecular-dynamics calculations, we took into account the flexibility of 5CB molecules, which, in the final analysis, resulted in values of e_1 and e_3 coefficients that yielded a e_+ value rather close to the value determined experimentally, whence it follows that allowing for molecule flexibility in the calculations of macroscopic parameters such as flexoelectric and elastic constants is even more important than rigorously allowing for intermolecular correlations.

Thus, we may conclude that the combined use of the molecular-dynamics and statistical-mechanics methods is a good tool for studying the macro- and microscopic properties of liquid-crystal compounds.

ACKNOWLEDGMENTS

This study was supported by the Russian Foundation for Basic Research (project no. 01-03-32084) and the Foundation for Natural Sciences (project no. E00-5.0-154).

REFERENCES

1. P. G. de Gennes and J. Prost, *The Physics of Liquid Crystals*, 2nd ed. (Oxford Univ. Press, Oxford, 1995; Mir, Moscow, 1982).
2. R. B. Meyer, Phys. Rev. Lett. **22**, 918 (1969).
3. A. V. Zakharov, A. V. Komolkin, and A. Maliniak, Phys. Rev. E **59**, 6802 (1999).
4. A. V. Zakharov and A. Maliniak, Eur. Phys. J. E **4**, 85 (2001).
5. L. A. Rott, *Statistical Theory of Molecular Systems* (Nauka, Moscow, 1978).
6. A. V. Zakharov, S. Romano, and A. Maliniak, Phys. Rev. E **60**, 1142 (1999).
7. A. V. Zakharov and R. Y. Dong, Eur. Phys. J. E **6**, 3 (2001).
8. J. G. Gay and B. J. Berne, J. Chem. Phys. **74**, 3316 (1981).
9. A. V. Zakharov, Physica A (Amsterdam) **166**, 540 (1990); Physica A (Amsterdam) **175**, 327 (1991).
10. R. Balescu, *Equilibrium and Nonequilibrium Statistical Mechanics* (Wiley, New York, 1975; Mir, Moscow, 1978).
11. A. M. Somoza and P. Tarazona, Mol. Phys. **72**, 911 (1991).
12. M. P. Allen and D. J. Tildesley, *Computer Simulation of Liquids* (Clarendon Press, Oxford, 1989).
13. R. Eppenga and D. Frenkel, Mol. Phys. **52**, 1303 (1984).
14. P. R. Murthy, V. A. Raghunathan, and N. V. Madhusudana, Liq. Cryst. **14**, 483 (1993).
15. L. M. Blinov, M. I. Barnik, M. Ozaki, *et al.*, Phys. Rev. E **62**, 8091 (2000).
16. I. M. Sobol', *Multidimensional Quadrature Formulae and Haar Functions* (Nauka, Moscow, 1969).
17. I. S. Berezin and N. P. Zhidkov, *Computing Methods*, 4th ed. (Fizmatgiz, Moscow, 1969; Pergamon Press, Oxford, 1965).
18. A. V. Zakharov and R. Y. Dong, Phys. Rev. E **64**, 031701 (2001).

Translated by A. Zolot'ko

Crystallography Reports, Vol. 48, No. 4, 2003, pp. 693–700. Translated from Kristallografiya, Vol. 48, No. 4, 2003, pp. 745–752.

LIQUID CRYSTALS

Effect of the Inhomogeneous Structure of Freely Suspended Smectic-*A* Films on the Dynamics of Fluctuations of Smectic-Layer Displacements

L. V. Mirantsev

Institute of Problems of Mechanical Engineering, Russian Academy of Sciences, Vasil'evskiĭ ostrov, Bol'shoĭ pr. 61, St. Petersburg, 199178 Russia

e-mail: miran@microm.ipme.ru

Received November 6, 2001

Abstract—The dynamics of fluctuations of smectic-layer displacements in freely suspended smectic-*A* films is studied theoretically with due regard for the dependence of the transverse-bending moduli *K* and extension (or compression) of smectic-*B* layers on the distance to the free surfaces of the films. The temperature dependences of the dynamic correlation functions are calculated for fluctuations of layer displacements in films of various thicknesses and then used to calculate the correlations between the X-ray intensities scattered by the film at different moments of time. The calculations were performed within a wide temperature range. It is shown that the influence of temperature on the X-ray dynamics of fluctuations of layer displacements in freely suspended smectic-*A* films can be detected in the experiments on the dynamical scattering by rather thick films (layer number $N \geq 100$) at considerably high values of the recoil-momentum component in the film plane ($\geq 10^6$ cm^{-1}). © *2003 MAIK "Nauka/Interperiodica".*

INTRODUCTION

Freely suspended smectic films are ideal objects for studying the physics of two-dimensional systems. The areas of such films can attain several square centimeters [1], whereas their thickness can be two or even only one smectic layer [2, 3]. The properties of freely suspended smectic films depend, on the one hand, on their finite dimensions along the layer-plane normal and, on the other, on the two limiting free surfaces. As a result, freely suspended smectic films show phenomena [4–16] that are not observed in the volume phase of liquid crystals (LCs). This has made freely suspended smectic films popular objects of experimental [1–22] and theoretical [23–37] study over the last 20 years.

The study of fluctuations of the layer displacements in freely suspended smectic films is of special interest. The point is that smectic LCs are a rare example of systems translationally ordered only along one direction. The possibility of varying the thicknesses of freely suspended smectic films over a wide range allows one to study the dependence of fluctuations of layer displacements and establish correlations between these fluctuations depending on the system's dimensions. Moreover, one can also study the effect of the limiting free surfaces on these fluctuations. At present, there are numerous experimental [12, 18–20] and theoretical [23–26, 31–33] publications on the static properties of such fluctuations. However, the dynamics of the fluctuations of layer displacements in freely suspended smectic films has attracted the attention of researchers only recently. Some special methods were developed for the experimental study of these fluctuations such as the method of dynamical scattering of coherent soft [21] and hard [22] X-ray radiation; the results obtained were interpreted theoretically in [35, 36]. The theoretical description of the experimental results is based on the linearized hydrodynamic equations of the smectic-*A* phase (*SmA*) and the discrete model of the energy of fluctuations of the layer displacements in freely suspended *SmA* films used earlier for the description of the static properties of these fluctuations [23, 24]. Later, the dynamics of fluctuation of smectic-layer displacements in freely suspended films was described within the continuum approach [37], which was equivalent to the description based on the discrete model [35, 36]. The models suggested in [35–37] allow one to determine the dynamic correlation functions for fluctuations of layer-displacements in the film and then, based on these functions, calculate the correlations between the intensities of X-ray scattering by the films at various moments of time. These models predict that neglecting the inertia terms in the hydrodynamic equations for a *SmA* phase allows one to describe the time dependences of the dynamic correlation function by a set of relaxation times $\tau^{(k)}$ ($k = 1, \ldots, N$), where N is the number of layers in the film, with the maximum relaxation time in the limit of the zero recoil-momentum component in the films being equal to

$$\tau^{(1)} = Nd\eta_3/2\gamma. \quad (1)$$

Here d is the interlayer spacing, η_3 is the viscosity coefficient of interlayer sliding, and γ is the surface tension

1063-7745/03/4804-0693$24.00

coefficient of the film. It also follows from these models that allowing for the inertia terms in the hydrodynamic equation for the *SmA* phase results in the appearance of oscillations of the time dependences of the dynamic correlation functions [36, 37]. The experiments [21, 22] on the dynamical scattering of a coherent X-ray radiation by freely suspended smectic films of various thicknesses confirmed the validity of Eq. (1) and the existence of oscillations of the dynamic correlation functions for fluctuations of smectic-layer displacements.

It is assumed in the models suggested in [35–37] that a freely suspended *SmA* film is a spatially homogeneous phase with the viscosity coefficient η_3 and that the transverse-bending elastic moduli, *K*, and extension (or compression), *B*, of smectic layers are the same for all the film layers irrespective of their positions and have the same viscoelastic characteristics in the bulk of the *SmA* phase. However, it was indicated [31–33] that these assumptions are physically justified only at temperatures considerably lower than the temperatures of the *SmA*–nematic (*SmA–N*) or *SmA*–isotropic (*SmA–I*) phase transitions in the bulk of a liquid crystal. In this case, the smectic structure is rather stable in the whole film bulk, whereas the orientational and translational order of the molecules and, therefore, the viscoelastic characteristics of the volume and surface layers of the film differ only slightly. However, freely suspended smectic films of some liquid crystals can exist at temperatures considerably higher than the temperature of disappearance of the smectic order in the bulk of mesogens [8–16]. The microscopic model of freely suspended *SmA* films that describes quite reliably their behavior on heating above the temperatures of the *SmA–N* and *SmA–I* phase transitions predicts that, in this case, both orientational and translational ordering in the internal layers of the film can be considerably less intense than in the vicinity of the limiting surfaces [27, 28, 30, 34]. This theoretical prediction was confirmed by the experimental studies of the transmission spectra of freely suspended *SmA* films in the optical wavelength range [14] and also by measurements of X-ray specular reflection from *SmA* films above the temperature of the *SmA–N* phase transition in the bulk of a liquid crystal [18]. It is well known that the transverse bending modulus *K* in the bulk of a LC is proportional to the squared orientational-order parameter *s*, whereas the extension (compression) modulus of smectic *B* layers is proportional to the squared translational-order parameter σ [38, 39]. Assuming that these relationships are also valid for freely suspended films, we obtain that in freely suspended *SmA* films, the transverse bending and extension (compression) moduli of smectic layers at temperatures exceeding the temperatures of the *SmA–N* and *SmA–I* phase transitions in the bulk of a LC should decrease with the distance to the free surface and attain minimum values in the center of the film. Since the existence of such an elastic-modulus profile is not taken into account either in the model considered in [35, 36] or in its continuum modification [37], these models should give erroneous time dependences of the dynamic correlation functions for fluctuations of the layer displacements in the film and, therefore, also erroneous correlations between the X-ray scattering intensities from the film at different moments of time. It should also be indicated that another serious disadvantage of the models considered in [35–37] is the complete neglect of the temperature dependence of viscoelastic characteristics of the layers in freely suspended *SmA* films.

Below, we consider a rather simple generalization of the discrete model [35, 36] with due regard for the dependence of the transverse bending *K* and extension (compression) *B* moduli of smectic layers depending on their distances to the limiting film surfaces. These dependences are determined based on the microscopic model for freely suspended smectic-*A* films suggested in [27, 28, 30, 34].

We also calculate the dynamic correlation functions for fluctuations of displacements of layers in freely suspended *SmA* films of various thicknesses, and we use the results obtained to calculate the correlations between the X-ray scattering intensities from the films at different moments of time. The calculations were performed both at temperatures that are considerably lower than the temperature of smectic-order disappearance in the bulk of a LC and at temperatures that are extremely high for the existence of freely suspended films of a given thickness. It is shown that the effect of temperature on the dynamics of fluctuations of layer displacement in freely suspended *SmA* films can be detected in the experiments on dynamical X-ray scattering from rather thick films ($N \geq 100$) at pronounced values of the recoil-momentum component in the film plane ($\geq 10^6$ cm^{-1}).

DESCRIPTION OF DYNAMICS OF FLUCTUATIONS OF LAYER DISPLACEMENTS IN A FREELY SUSPENDED SMECTIC-*A* FILM

Consider a freely suspended smectic-*A* film consisting of *N* discrete layers and denote the fluctuation in the displacement in the *n*th layer from its equilibrium position, $z_n = (n - 1)d$, along the *z* axis normal to the layer plane as $u_n(x, y)$. According to the model suggested in [35, 36], the variation of these fluctuation displacements in time is described by the following equations of motion:

$$\rho_0 \frac{\partial^2 u_n}{\partial t^2} = -\eta_3 \Delta_\perp \frac{\partial u_n}{\partial t} - \frac{1}{d}\delta F/\delta u_n. \qquad (2)$$

Here, ρ_0 is the average density of a LC forming the film, *t* is the time, $\Delta_\perp$ is the two-dimensional Laplacian in the (*x*, *y*) plane, and *F* is the excessive free energy of the freely suspended *SmA* film related to the fluctuation displacements of its layers. It was shown [31, 33] that,

with due regard for the dependence of the elastic moduli K and B of the smectic layers on their distances to the limiting surfaces of the film, this energy can be written as

$$F = \frac{1}{2}\int\left\{\sum_{n=1}^{N-1}\left(\frac{B_n + B_{n+1}}{2d}\right)[u_{n+1}(\mathbf{R}) - u_n(\mathbf{R})]^2 + \sum_{n=1}^{N} K_n d[\Delta_\perp u_n(\mathbf{R})]^2 + \gamma|\nabla_\perp u_1(\mathbf{R})|^2 + \gamma|\nabla_\perp u_N(\mathbf{R})|^2\right\}d\mathbf{R}, \quad (3)$$

where B_n is the extension (or compression) modulus of the nth layer of the freely suspended *SmA* film, K_n is the transverse-bending modulus in this layer of the film, $\mathbf{R}$ is the radius-vector in the plane of smectic layers ($R^2 = x^2 + y^2$), and $\nabla_\perp$ is the projection of the operator ∇ onto the (x, y) plane. It should be indicated that in a spatially homogeneous freely suspended smectic-*A* film for which the transverse-bending (K_n) and extension (compression) (B_n) moduli of all the film layers are the same and equal to K and B, respectively, Eq. (3) for the excessive free energy F of the film fully coincides with the analogous equation for the model suggested in [35, 36].

Equations (2) and (3) yield the following system of equations of motion:

$$\rho_0\frac{\partial^2 u_1}{\partial t^2} = -\eta_3\Delta_\perp\frac{\partial u_1}{\partial t} + \frac{(B_1 + B_2)}{2d^2}(u_2 - u_1) - K_1\Delta_\perp^2 u_1 - (\gamma/d)\Delta_\perp u_1, \quad (4)$$

$$\rho_0\frac{\partial^2 u_N}{\partial t^2} = -\eta_3\Delta_\perp\frac{\partial u_N}{\partial t} - \frac{(B_N + B_{N-1})}{2d^2}(u_N - u_{N-1}) - K_1\Delta_\perp^2 u_N - (\gamma/d)\Delta_\perp u_N, \quad (5)$$

$$\rho_0\frac{\partial^2 u_n}{\partial t^2} = -\eta_3\Delta_\perp\frac{\partial u_n}{\partial t} + \frac{(B_{n+1} + B_n)}{2d^2}(u_{n+1} - u_n) - \frac{(B_n + B_{n-1})}{2d^2}(u_n - u_{n-1}) - K_n\Delta_\perp^2 u_n, \quad n \neq 1, N. \quad (6)$$

The elastic moduli K_n and B_n for the layers of a freely suspended *SmA* film can be determined in the following way. As has already been indicated, the transverse bending modulus K in the bulk of a liquid crystal is proportional to the squared orientational-order parameter s, whereas the extension (or compression) modulus B of smectic layers is proportional to the squared translational-order parameter σ. Assuming that in freely suspended films the relationships between the elastic moduli and the translational- and orientational-order parameters are the same as in the bulk of the mesophases in the whole temperature range of the existence of these films, including temperatures exceeding those of the *SmA–N* or *SmA–I* phase transitions in the bulk of a liquid crystal, these relationships provide the determination of the elastic moduli K_n and B_n with the aid of the microscopic model described in [27, 28, 30, and 34]. The latter model allows one to determine the order parameters $s_n(T)$ and $\sigma_n(T)$ for each layer of a film irrespective of its thickness at any temperature T within the temperature range of the film's existence. Moreover, for extremely thick films ($N \longrightarrow \infty$), this model allows one to determine the values of the order parameters in the center of the film, which fully coincide with the results of the well-known McMillan theory for a bulk *A*-smectic phase [40]. Knowing the values of the elastic moduli K and B in the bulk of the *A*-smectic phase at a certain temperature T_0 ($K(T_0) \equiv K_0$, $B(T_0) \equiv B_0$) lower than the temperature of the *SmA–I* or *SmA–N* phase transition and using the model developed in [27, 28, 30, 34], one can also determine the order parameters $s(T_0) \equiv s_0$ and $\sigma(T_0) \equiv \sigma_0$ at this temperature. Then, using the equations

$$K_n(T) = K_0(s_n(T)/s_0)^2, \quad (7)$$

$$B_n(T) = B_0(\sigma_n(T)/\sigma_0)^2, \quad (8)$$

it is also possible to determine the elastic moduli K_n and B_n for all the layers of the film of a given thickness at any temperature T from the temperature range of the film's existence.

Now, applying the continuous Fourier transform

$$u_n(\mathbf{R}) = (2\pi)^{-2}\int u_n(\mathbf{q}_\perp)\exp(i\mathbf{q}_\perp\mathbf{R})d\mathbf{q}_\perp \quad (9)$$

and using the dimensionless variables $t' = [(K_0B_0)^{1/2}/(d\eta_3)]t$, $\mathbf{q}' = \mathbf{q}_\perp/q_0$, and $q_0^2 = [B_0/(K_0d^2)]^{1/2}$, one can rewrite system of equations (4)–(6) in compact matrix form as

$$(\rho_0K_0/\eta_3^2)\frac{\partial^2 u_n}{\partial t'^2} = -q'^2\frac{\partial u_n}{\partial t'} - M_{nm}u_m, \quad (10)$$

where M_{nm} are the elements of the symmetric "ribbon" matrix with only the diagonal elements having nonzero values and with all the neighboring elements being described by the following equations:

$$M_{11} = [(\sigma_1/\sigma_0)^2 + (\sigma_2/\sigma_0)^2]/2 + (s_1/s_0)^2q'^4 + \bar{\gamma}q'^2, \quad (11)$$

$$M_{NN} = [(\sigma_N/\sigma_0)^2 + (\sigma_{N-1}/\sigma_0)^2]/2 + (s_N/s_0)^2q'^4 + \bar{\gamma}q'^2, \quad (12)$$

$$M_{nn} = [(\sigma_{n-1}/\sigma_0)^2 + 2(\sigma_n/\sigma_0)^2 + (\sigma_{n+1}/\sigma_0)^2]/2 + (s_n/s_0)^2q'^4, \quad (13)$$

$$M_{n-1n} = -[(\sigma_n/\sigma_0)^2 + (\sigma_{n-1}/\sigma_0)^2]/2, \quad (14)$$

$$M_{n+1n} = -[(\sigma_n/\sigma_0)^2 + (\sigma_{n+1}/\sigma_0)^2]/2. \quad (15)$$

Here $\bar{\gamma} = \gamma(K_0B_0)^{-1/2}$ is the dimensionless surface tension coefficient of the film.

According to [35, 36], the solution of system of equations (10) can be represented in the form of an expansion in eigenvectors $v_n^{(k)}(q')$ of the matrix $M_{mn}(q')$ as

$$u_n(\mathbf{q}', t') = \sum_{k=1}^{N} u_n^{(k)}(\mathbf{q}', t')v_n^{(k)}(q'). \quad (16)$$

Then the time dependence of the kth normal mode $u_n^{(k)}(q', t')$ is described by the equations

$$u_n^{(k)}(\mathbf{q}', t') = u_{n+}^{(k)}(\mathbf{q}')\exp[\beta_+^{(k)}(q')t'] + u_{n-}^{(k)}(\mathbf{q}')\exp[\beta_-^{(k)}(q')t']. \quad (17)$$

In this case, the exponents $\beta_\pm^{(k)}(q')$ can be written in terms of the relaxation times $\tau_\pm^{(k)}(q')$ and frequencies $\omega^{(k)}(q')$ as

$$\beta_\pm^{(k)}(q') = -\frac{1}{\tau_\pm^{(k)}(q')} \pm i\omega^{(k)}(q'), \quad (18)$$

where

$$\omega^{(k)}(q') = 0, \quad (19a)$$

$$\tau_\pm^{(k)}(q') = \frac{(2\rho_0K_0/\eta_3^2)}{q'^2 \mp [q'^4 - 4\lambda^{(k)}(q')(\rho_0K_0/\eta_3^2)]^{1/2}} \quad (19b)$$

if $q'^4 \geq 4\lambda^{(k)}(q')(\rho_0K_0/\eta_3^2)$ and

$$\tau_\pm^{(k)}(q') = \frac{2\rho_0K_0}{\eta_3^2q'^2}, \quad (20a)$$

$$\omega^{(k)}(q') = (\eta_3^2/2\rho_0K_0)[|q'^4 - 4\lambda^{(k)}(q')(\rho_0K_0/\eta_3^2)|]^{1/2} \quad (20b)$$

if $q'^4 < 4\lambda^{(k)}(q')(\rho_0K_0/\eta_3^2)$.

The quantity $\lambda^{(k)}(q')$ in Eqs. (19b) and (20b) is the eigenvalue of the matrix $M_{mn}(q')$ corresponding to the eigenvector $v_n^{(k)}(q')$ of this matrix.

It follows from the condition of statistical independence of the normal modes $u_n^{(k)}(\mathbf{q}', 0)$ and their time derivatives $\partial_{t'}u_n^{(k)}(\mathbf{q}', 0)$ at the initial moment of time $t' = 0$ [36] that

$$u_{n+}^{(k)}(\mathbf{q}') = \frac{\beta_-^{(k)}(q')}{(\beta_-^{(k)}(q') - \beta_+^{(k)}(q'))}u_n^{(k)}(\mathbf{q}', 0), \quad (21a)$$

$$u_{n-}^{(k)}(\mathbf{q}') = \frac{-\beta_+^{(k)}(q')}{(\beta_-^{(k)}(q') - \beta_+^{(k)}(q'))}u_n^{(k)}(\mathbf{q}', 0). \quad (21b)$$

As was indicated above, our aim was to study the effect of the inhomogeneity of the structure of freely suspended *SmA* films on the dynamics of fluctuations in layer displacements with due regard for the fact that elastic moduli K_n and B_n of smectic layers depend on their distances to the free surface of the film, which, in turn, depends on film temperature. Obviously, this dependence can affect the dynamics of the displacement fluctuations in film layers determined by system of equation (10) if the volume part of the excessive free energy F of the film (proportional to the K_n and B_n moduli) is comparable with the surface contribution to F (either proportional to the surface tension coefficient γ or exceeding it). Otherwise the dynamics of the fluctuations of layer displacements in the film layers is independent of the internal structure of the film and is completely determined by the coefficient γ [see Eq. (1)], which, according to [17], is practically constant in the whole temperature range of the existence of freely suspended *SmA* films. Since the part of the volume contribution to the free energy F that depends on the momentum Q is proportional to $\sum_{n=1}^{N} K_n dq_\perp^4$, whereas the surface contribution to F is proportional to $\gamma q_\perp^2$, the condition of equality or prevalence of the volume part of F over the surface contribution to the free energy leads to the inequality

$$q_\perp^2 \geq \gamma\left(d\sum_{n=1}^{N} K_n\right)^{-1}, \quad (22)$$

which is valid at $\gamma \sim 30$ dyn/cm, $K_n \sim 10^{-6}$ dyn, and $d \sim 3 \times 10^{-7}$ cm if $q_\perp \geq 10^7N^{-1/2}$ cm^{-1}. For freely suspended *SmA* films consisting, e.g., of 100 layers, this inequality yields $q_\perp \geq 10^6$ cm^{-1}. The numerical calculations show that at such high values of momentum $q_\perp$, one has to use Eqs. (19a) and (19b). Moreover, it turns out that $\tau_-^{(k)}(q') \gg \tau_+^{(k)}(q')$, whence it follows that, first, $u_{n-}^{(k)}(\mathbf{q}') \gg u_{n+}^{(k)}(\mathbf{q}')$ and, second, the components of the normal modes $u_{n+}^{(k)}(\mathbf{q}')$ attenuate with time much faster than $u_{n-}^{(k)}(\mathbf{q}')$. Therefore, in what follows we assume that $u_{n-}^{(k)}(\mathbf{q}') \approx u_n^{(k)}(\mathbf{q}', 0)$, and we use the quantity $\tau_-^{(k)}(q')$ as the relaxation time $\tau^{(k)}(q')$.

Knowing the time dependences of normal modes $u_n^{(k)}(\mathbf{q}', t')$, one can calculate the dynamic correlation functions of layer displacements in freely suspended *SmA* films. In the Fourier representation, these functions are determined as (see [35, 36])

$$C_{m,n}(q', t') = \langle u_m(\mathbf{q}', t')u_n(-\mathbf{q}', 0)\rangle. \quad (23)$$

Here, the equilibrium averaging is performed over all possible layer displacements at $t' = 0$, with the probability of the given configuration being proportional to $\exp(-F/k_BT)$, where k_B is the Boltzmann constant. Using Eqs. (9) and (16), one can readily obtain the following expression for the free energy F:

$$F = \frac{B_0}{2d}\int d\mathbf{q}' \sum_{n=1}^{N}\sum_{k=1}^{N} \left|u_n^{(k)}(\mathbf{q}', 0)\right|^2 \lambda^{(k)}(q'). \quad (24)$$

Then, the dynamic correlation function is

$$C_{m,n}(q', t') = \frac{dk_BT}{B_0}\sum_{k=1}^{N}[\lambda^{(k)}(q')]^{-1} \times \exp[-t/\tau^{(k)}(q')]\nu_m^{(k)}(q')\nu_n^{(k)}(q'), \quad (25)$$

where the eigenvectors $\nu_m^{(k)}(q')$ are normalized to unity.

Knowledge of the dynamic correlation functions $C_{m,n}(q', t')$ allows one to calculate the correlation $\langle I(\mathbf{q}, t)I(\mathbf{q}, 0)\rangle$ between the X-ray intensities scattered by the film at the moments 0 and t. According to [37], the time-dependent part of the correlation function is proportional to $|S(\mathbf{q}, t)|^2$, where

$$S(\mathbf{q}, t) = \int d\mathbf{r}\langle\hat{\rho}(\mathbf{r}, t)\hat{\rho}(0, 0)\rangle\exp(i\mathbf{qr}). \quad (26)$$

Here, $\hat{\rho}(\mathbf{r}, t)$ is the electron-density operator of the system and $\mathbf{q}$ is the recoil momentum in the scattering of the X-ray radiation by these electrons. The expressions for $S(q_z, \mathbf{q}_\perp)$ (where q_z and $\mathbf{q}_\perp$ are the recoil-momentum components along the normal of the film and in its plane, respectively) for an N-layer freely suspended *SmA* film at $t = 0$ are considered in [32, 33] for both X-ray specular reflection ($\mathbf{q}_\perp = 0$) and diffuse scattering ($\mathbf{q}_\perp \neq 0$). As was indicated above, the influence of the internal structure of the film on the dynamics of fluctuations of the layer displacements established from the behavior of the correlation function $\langle I(\mathbf{q}, t)I(\mathbf{q}, 0)\rangle$ is essential at high values of the momentum $\mathbf{q}_\perp$. Thus, this effect can be studied by measuring the correlations $\langle I(\mathbf{q}, t)I(\mathbf{q}, 0)\rangle$ when there is pronounced X-ray diffuse scattering in the film. The simple calculations (analogous to the calculations of $S(q_z, \mathbf{q}_\perp)$ in [32, 33]) show that, in this case, the expression $\langle I(\mathbf{q}, t)I(\mathbf{q}, 0)\rangle/I^2(\mathbf{q}, 0)$ can be represented as

$$\langle I(\mathbf{q}, t)I(\mathbf{q}, 0)\rangle/I^2(\mathbf{q}, 0) = G^2(q_z, q', t)/G^2(q_z, q', 0), \quad (27)$$

where

$$G(q_z, q', t) \approx \sum_{k,n=1}^{N}\cos[(k-n)dq_z]p_k(q_z)p_n(q_z)F_{kn}(q_z)C_{k,n}(q', t'). \quad (28)$$

The value of $F_{kn}(q_z)$ is given by Eq. (13) from [32, 33], whereas the coefficients $p_k(q_z)$ coincide with the coefficients $\tau_k(q_z)$ considered in the same articles.

RESULTS OF NUMERICAL CALCULATIONS AND DISCUSSION

The numerical calculations of relaxation times $\tau^{(k)}(q_\perp)$, dynamic correlation functions $C_{m,n}(q_\perp, t)$, and correlations $\langle I(\mathbf{q}, t)I(\mathbf{q}, 0)\rangle$ between the intensities of the X-ray radiation scattered by a freely suspended *SmA* film at the moments 0 and $t\langle I(\mathbf{q}, t)I(\mathbf{q}, 0)\rangle$ were performed for freely suspended films of liquid crystals that undergo a weak first-order *SmA–N* phase transition. It is these films that were studied in the experiments on dynamical scattering of the coherent X-ray radiation by freely suspended *SmA* films of various thicknesses in [21, 22]. The values of the model parameters used in the calculations were the same as in the previous studies [31–33]. The viscosity coefficient of interlayer sliding, η_3, was taken to be $\eta_3 = 0.4$ g/(cm s), which is characteristic of smectic liquid crystals. The calculations were performed at temperatures considerably lower than the temperature of the *SmA–N* phase transition in the bulk of the liquid crystal and at the highest possible temperature from the existence range of a freely suspended smectic *A* film of a given thickness.

First of all, we calculated the temperature dependences of relaxation times $\tau^{(k)}(q_\perp)$ for different numbers N of the film layers and different values of the recoil-momentum components $q_\perp$ parallel to the film plane. Figures 1 and 2 show the results of these calculations for the maximum relaxation time $\tau^{(1)}(q_\perp)$ determining the behavior of the dynamic correlation functions $C_{m,n}(q_\perp, t)$ and correlations $\langle I(\mathbf{q}, t)I(\mathbf{q}, 0)\rangle$. Here, the dimensionless parameter T^* is the reduced temperature equal to $(k_BT)/V_0$, where V_0 is the intermolecular-interaction constant in the McMillan theory [40]. Figure 1 shows the temperature dependence $\tau^{(1)}(q_\perp)$ with three different values of the recoil-momentum component $q_\perp$ (10^4, 10^5, and 10^6 cm^{-1}) for a film consisting of N = 100 layers, while Fig. 2 shows an analogous dependence at $q_\perp = 10^6$ cm^{-1} for films consisting of N = 5, 25, and 100 layers. It is clearly seen that the effect of the internal structure of freely suspended *SmA* films on the dynamics of fluctuations of the layer displacement on heating can be recorded and studied in the experiments on the dynamical X-ray scattering from rather thick films ($N \geq 100$) at high values of the recoil-momentum

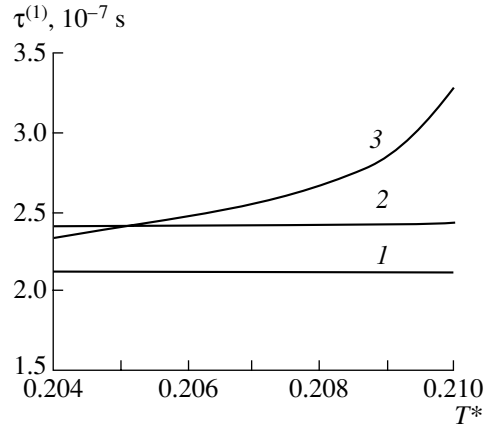

Fig. 1. Maximum relaxation times $\tau^{(1)}$ as functions of temperature for a freely suspended *SmA* film consisting of 100 layers at different values of the recoil-momentum component $q_\perp$: (*1*) 10^4, (*2*) 10^5, (*3*) 10^6 cm^{-1}.

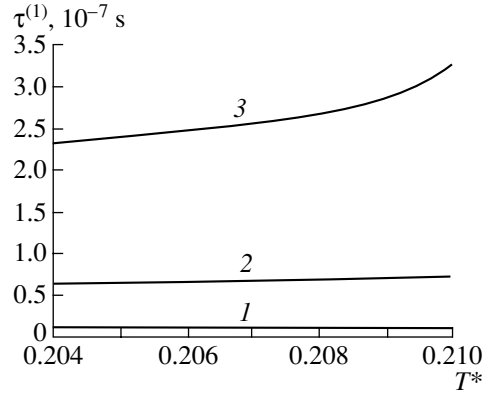

Fig. 2. Maximum relaxation times $\tau^{(1)}$ as functions of temperature for freely suspended *SmA* films consisting of 5, 25, and 100 layers; $q_\perp = 10^6$ cm^{-1}; N = (*1*) 5, (*2*) 25, (*3*) 100.

component in the film plane ($\geq 10^6$ cm^{-1}). Moreover, it is also seen that under these conditions film heating considerably increases the relaxation times, with the maximum being attained at the highest temperature of the film's existence. Obviously, such an increase in the relaxation time is caused by the reduced elastic moduli of the internal layers of freely suspended *SmA* films (see also Figs. 1 and 2 in [31, 33]). The independence of the maximum relaxation time $\tau^{(1)}(q_\perp)$ of film temperature at lower N and $q_\perp$ values (Figs. 1, 2, curves *1*, *2*) can be qualitatively explained by the prevalent surface contribution to the free energy of the film irrespective of its internal structure and is fully determined by the surface tension coefficient γ, which is practically constant in the whole temperature range of the existence of freely suspended *SmA* films.

After that, we also studied the influence of the temperature of a freely suspended smectic-*A* film on the behavior of its dynamic correlation functions $C_{m,n}(q_\perp, t)$. According to the results presented above, the film was considered to be rather thick ($N = 100$) and the value of the recoil-momentum component $q_\perp$, rather high ($q_\perp = 10^6$ cm^{-1}). The time dependences of the dynamic correlation functions $C_{1,1}$, $C_{1,50}$, and $C_{50,50}$ calculated at these N and $q_\perp$ values are shown in Figs. 3–5. The calculations were performed at temperatures much lower than the temperature of disappearance of smectic order in the liquid-crystal bulk (Figs. 3–5, curves *1*) and also at a temperature close to the highest temperature of the existence of freely suspended *SmA* films of the given thickness (Figs. 3–5, curves *2*). It follows from Fig. 3 that the time dependence of the dynamic correlation function $C_{1,1}$ for the fluctuations of the displacement of the first subsurface layer is practically temperature independent in the whole temperature range of the film's existence. At the same time, Figs. 4 and 5 clearly show that the temperature of freely suspended *SmA*

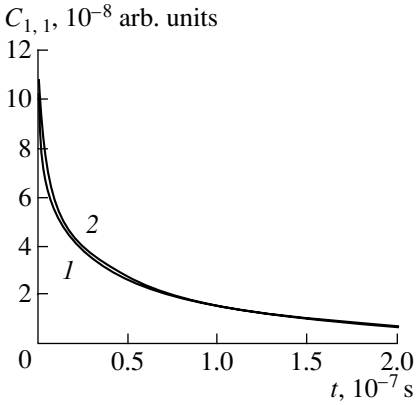

Fig. 3. Dynamic correlation function $C_{1,1}$ versus time; $N = 100$, $q_\perp = 10^6$ cm^{-1}, (*1*) $T^* = 0.204$, (*2*) $T^* = 0.210$.

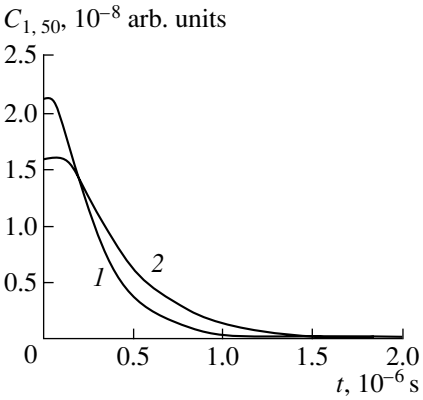

Fig. 4. Dynamic correlation function $C_{1,50}$ versus time; see Fig. 3 for the parameters.

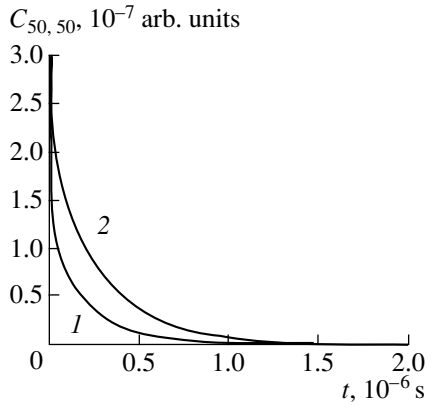

Fig. 5. Dynamic correlation function $C_{50,50}$ versus time; see Fig. 3 for the parameters.

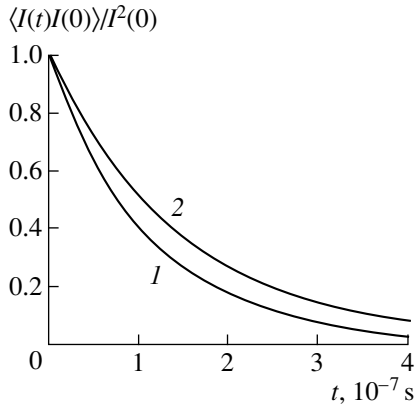

Fig. 6. Correlation function $\langle I(\mathbf{q}, t)I(\mathbf{q}, 0)\rangle$ versus time; N = 100, $q_\perp = 10^6$ cm^{-1}, (*1*) $T^* = 0.204$, (*2*) $T^* = 0.210$.

films noticeably affects the behavior of the dynamic correlation functions relating the fluctuations of the displacements of internal and external layers of the film ($C_{1,50}$) and also the behavior of the dynamic correlation functions ($C_{50,50}$) for the fluctuations of the displacements of the internal layers of the film. In both cases, the dynamic correlation functions at the highest temperature attenuate with time much slower than at lower temperatures. Such a considerable difference in the behavior of the dynamic correlation functions can be qualitatively interpreted in the following way. The time dependence of the dynamic correlation functions is determined by equations of motion (4)–(6) for fluctuations of layer displacements in the film. In this case, the equations of motion for fluctuation of the displacements of the first subsurface layers include the elastic moduli $K_{1,2}$ and $B_{1,2}$ of these layers, which slightly change as freely suspended *SmA* films are heated (Figs. 1 and 2 in [31, 33]), as well as the surface tension coefficient γ, which is almost temperature independent. At the same time, the equations of motion for fluctuations of displacement of the internal layers in the film depend on the elastic moduli of these layers, which considerably decrease with an increase in temperature (Figs. 1 and 2 in [31, 33]). This may explain the independence of the dynamic correlation function $C_{1,1}$ of the temperature of freely suspended *SmA* films and the noticeable changes of the time dependences of the dynamic correlation functions $C_{1,50}$ and $C_{50,50}$ on film heating.

Figure 6 demonstrates the results of the calculations of the correlation function $\langle I(\mathbf{q}, t)I(\mathbf{q}, 0)\rangle$ for a freely suspended smectic-*A* film consisting of 100 layers. The calculations were performed for the case of diffuse scattering of the coherent X-ray radiation in the vicinity of the main Bragg maximum ($q_z = 2\pi/d$) at a value of the recoil-momentum component $q_\perp$ in the film plane equal to 10^6 cm^{-1}. Curve *1* corresponds to a temperature lower than the temperature of the *SmA*–*N* phase transition in the bulk of a liquid crystal ($T^* = 0.204$), whereas curve *2* corresponds to the calculation at the temperature $T^* = 0.210$ close to the highest temperature of the film's existence. It is seen that on heating a freely suspended *SmA* film, the attenuation of the correlation function $\langle I(\mathbf{q}, t)I(\mathbf{q}, 0)\rangle$ with time dramatically decelerates. This deceleration is best seen at $t \sim 10^{-7}$ s.

ACKNOWLEDGMENTS

This study was supported by the Russian Foundation for Basic Research, project no. 01-03-32084.

REFERENCES

1. P. Pieranski, L. Beliard, J. P. Tournellec, *et al.*, Physica A (Amsterdam) **194**, 364 (1993).
2. C. Rosenblatt, R. Pindak, N. A. Clark, and R. B. Meyer, Phys. Rev. Lett. **42**, 1220 (1979).
3. M. Veum, C. C. Huang, C. F. Chou, and V. Surendranath, Phys. Rev. E **56**, 2298 (1997).
4. C. Rosenblatt and N. M. Amer, Appl. Phys. Lett. **36**, 432 (1980).
5. S. Heinekamp, R. A. Pelcovits, E. Fontes, *et al.*, Phys. Rev. Lett. **52**, 1017 (1984).
6. C. Bahr and D. Fliegner, Phys. Rev. A **46**, 7657 (1992).
7. I. Kraus, P. Pieranski, E. Demikhov, *et al.*, Phys. Rev. E **48**, 1916 (1993).
8. T. Stoebe, P. Mach, and C. C. Huang, Phys. Rev. Lett. **73**, 1384 (1994).
9. E. I. Demikhov, V. K. Dolganov, and K. P. Meletov, Phys. Rev. E **52**, 1285 (1995).
10. V. K. Dolganov, E. I. Demikhov, R. Fouret, and C. Gors, Phys. Lett. A **220**, 242 (1996).
11. P. Johnson, P. Mach, E. D. Wedell, *et al.*, Phys. Rev. E **55**, 4386 (1997).
12. E. A. L. Mol, G. C. L. Wong, J. M. Petit, *et al.*, Physica B (Amsterdam) **248**, 191 (1998).
13. S. Pankratz, P. M. Johnson, R. Holyst, and C. C. Huang, Phys. Rev. E **60**, 2456 (1999).

14. V. K. Dolganov, V. M. Zhilin, and K. P. Meletov, Zh. Éksp. Teor. Fiz. **115**, 1833 (1999) [JETP **88**, 1005 (1999)].
15. S. Pankratz, P. M. Johnson, A. Paulson, and C. C. Huang, Phys. Rev. E **61**, 6689 (2000).
16. P. Cluzeau, G. Joly, H. T. Nguyen, *et al.*, Phys. Rev. E **62**, 5899 (2000).
17. P. Mach, S. Grantz, D. A. Debe, *et al.*, J. Phys II **5**, 217 (1995).
18. J. D. Shindler, E. A. L. Mol, A. Shalaginov, and W. H. de Jeu, Phys. Rev. Lett. **74**, 722 (1995).
19. J. D. Shindler, E. A. L. Mol, A. Shalaginov, and W. H. de Jeu, Phys. Rev. E **54**, 536 (1996).
20. E. A. L. Mol, G. C. L. Wong, J. M. Petit, *et al.*, Phys. Rev. Lett. **78**, 3157 (1997).
21. A. C. Price, L. B. Sorensen, S. D. Kevan, *et al.*, Phys. Rev. Lett. **82**, 755 (1999).
22. A. Fera, I. P. Dolbnya, G. Grubel, *et al.*, Phys. Rev. Lett. **85**, 2316 (2000).
23. R. Holyst and D. J. Tweet, Phys. Rev. Lett. **65**, 2153 (1990).
24. R. Holyst, Phys. Rev. A **44**, 3692 (1991).
25. A. Poniewerski and R. Holyst, Phys. Rev. B **47**, 9840 (1993).
26. A. N. Shalaginov and V. P. Romanov, Phys. Rev. E **48**, 1073 (1993).
27. L. V. Mirantsev, Phys. Lett. A **205**, 412 (1995).
28. L. V. Mirantsev, Liq. Cryst. **20**, 417 (1996).
29. Y. Martinez-Raton, A. M. Somoza, L. Mederos, and D. E. Sullivan, Phys. Rev. E **55**, 2030 (1997).
30. L. V. Mirantsev, Phys. Rev. E **55**, 4816 (1997).
31. L. V. Mirantsev, Fiz. Tverd. Tela (St. Petersburg) **41**, 1882 (1999) [Phys. Solid State **41**, 1729 (1999)].
32. L. V. Mirantsev, Fiz. Tverd. Tela (St. Petersburg) **42**, 1511 (2000) [Phys. Solid State **42**, 1554 (2000)].
33. L. V. Mirantsev, Phys. Rev. E **62**, 647 (2000).
34. L. V. Mirantsev, Liq. Cryst. **27**, 491 (2000).
35. A. Poniewierski, R. Holyst, A. C. Price, *et al.*, Phys. Rev. E **58**, 2027 (1998).
36. A. Poniewierski, R. Holyst, A. C. Price, and L. B. Sorensen, Phys. Rev. E **59**, 3048 (1999).
37. A. N. Shalaginov and D. E. Sullivan, Phys. Rev. E **62**, 699 (2000).
38. P. G. de Gennes, *The Physics of Liquid Crystals* (Clarendon Press, Oxford, 1974; Mir, Moscow, 1977).
39. S. Chandrasekhar, *Liquid Crystals* (Cambridge Univ. Press, Cambridge, 1977; Mir, Moscow, 1980).
40. W. L. McMillan, Phys. Rev. A **4**, 1238 (1971).

Translated by L. Man

Crystallography Reports, Vol. 48, No. 4, 2003, pp. 701–704. Translated from Kristallografiya, Vol. 48, No. 4, 2003, pp. 753–757.

NANOMATERIALS

Generalized Size-Dependent Structural States of Materials with an Ultrafine Structure

V. A. Pozdnyakov

Institute of Physical Metallurgy, Bardin Central Research Institute for the Iron and Steel Industry, Vtoraya Baumanskaya ul. 9/23, Moscow, 107005 Russia

e-mail: glezer@imph.msk.ru

Received January 29, 2003

Abstract—The necessity of introduction of boundary and surface (crystalline, quasicrystalline, and amorphous) structural states at different scale levels is justified for micro- and nanocrystalline materials. The bulk and boundary size-dependent structural states of solids with an ultrafine structure are considered in a unified approach. The generalized structural states of nanostructured and nanomicrostructured materials are determined and systematized. © *2003 MAIK "Nauka/Interperiodica".*

Recently, a new class of so-called nanostructured materials was defined [1–3], some of which were thereafter obtained by various methods [1–8]. Nanostructured materials are solids consisting of nanoclusters (nanometer-sized structural components) separated by boundaries (two-dimensional clusters with another structure) [1–3]. The size of 100 nm is often considered as a conditional upper limit of the nanometer scale of structure.

Nanostructured materials include single- and multiphase nanocrystalline (nanophase) materials, i.e., polycrystalline solids with a grain size on the order of 10 nm (but not exceeding 100 nm). The specific features of the boundary states are as significant as the bulk effects, since the number of grain-boundary atoms in such systems is comparable with the number of bulk atoms [1, 8–10]. The volume fraction occupied by intergranular or interphase boundaries can reach up to 50% in nanocrystalline materials [1–3]. The concept of nanocrystalline materials can be defined using a physical criterion, i.e., as a material with the grain size (structural components) comparable with a characteristic correlation scale of a certain physical process, or a material with a grain size at which the mechanism of this process changes. An example of nanostructured materials are nanostructured pseudoalloys [2].

By analogy with nanocrystalline materials, the concept of nanostructured glass was introduced [2]. Nanoamorphous metallic materials (metallic nanoglasses) form one of the classes of nanostructured materials. Nanoamorphous solids are obtained by compaction of amorphous nanoparticles [2]. The structure and composition of the surface layers of nanoparticles differ from the corresponding bulk parameters of particles. As a result, a bulk amorphous material consisting of nanoclusters with one amorphous structure is formed; the boundaries between these clusters possess a different amorphous structure or atomic density. Nanoamorphous materials can also be formed as a result of a spinodal decomposition of an amorphous structure into two amorphous structural components of nanometric sizes.

The materials with the grain (phase) size D exceeding the nanometer range but considerably smaller than the grain size of usual coarse-grained (~100 μm) materials are also attributed to an individual group which contains microcrystalline (D ~ 1–10 μm) [11] and submicrocrystalline (superfine-grained) (100 nm < D < 1 μm) materials [12], which sometimes are also called nanostructured materials [6]. They form a mezoscopic (intermediate) scale level of structural states. This group of materials can be called micromaterials. Micromaterials have not only a different scale but also different physical characteristics. The parameters of metastable structural states of microcrystalline materials significantly depend on the method of their preparation and the history of the sample [11]. A decrease in the size of structural components of a material down to the level 1–10 μm leads to qualitative changes of several properties that are sensitive to the boundary state. These materials show the anomalies of the known dependences of their properties on the structural parameters, for example, the anomaly of the Hall–Petch relation [11]. Thus, a structural superplasticity is observed only at a grain size less than 10 μm. The grain boundaries of microstructured ceramic and quenched metallic materials (from the liquid state) and corresponding nanostructured materials can have an amorphous structure or include another phases [8, 13]. The analysis of the shape of Mössbauer spectra of a submicrocrystalline (D = 0.22 μm) iron allowed one to assume the existence of a "grain-boundary phase" [14]. The macroscopic scale level of structural states characterizes the materials with a grain size (structure fragments) considerably exceeding the micrometer range. Thus, three scale levels of the structural states of solids are distinguished.

1063-7745/03/4804-0701$24.00

Table 1. Atomic structures

Type of structure	Bulk	Boundary	Surface
Amorphous	Am(bl)	Am(bn)	Am(s)
Quasicrystalline	QuCr(bl)	QuCr(bn)	QuCr(s)
Crystalline	Cr(bl)	Cr(bn)	Cr(s)

Materials in which at least one dimension of a crystallite or a structural component is less than 100 nm are also attributed to nanostructured materials [1–3]. However, the separation of materials with essentially different sizes of structural component to an individual group of nanomicrostructured materials seems to be more reasonable. This group can contain low-dimensional structures such as nanofibers, "stressed superlattices," and so on. In recent years, much attention has been given to the preparation of amorphous and crystalline metallic nanofibers with a transverse size on the order of 10 nm and to the study of their properties [15]. The length of a nanofiber can be on the order of one micron or even more. Nanoamorphous materials—metal glasses with two characteristic scales of structural inhomogeneities (micrometric and nanometric) can be obtained by pressing nanofibers of amorphous alloys [16]. Thus, the materials with different scale levels of the structures can be attributed to independent groups—nanomicroscopic, nanomacroscopic, and micromacroscopic.

In 1984, quasicrystals, i.e., solids with a quasiperiodical translation and a long-range orientational order, were discovered [17]. In recent years, the structures and properties of quasicrystalline materials have been intensely studied [18–20]. Nanoquasicrystalline materials, i.e., polyquasicrystalline materials with a grain size on the order of 10 nm, were synthesized [21].

The quasicrystalline state is intermediate between the crystalline and amorphous states. Considering three main atomic structural states (amorphous, quasicrystalline, and crystalline), we mean the bulk structural states, but the state of the boundaries and free surfaces can also play an important role.

Recently, interest in grain boundaries with a quasicrystalline structure and the possible existence of such boundaries greatly increased. [22, 23]. The structure of quasiperiodical grain boundaries is characterized by the irrational ratios of the numbers of the different structural elements forming the boundary [22, 23]. It was proposed to separate nanocrystalline materials with quasicrystalline boundaries into an individual group of materials [24]. We cannot exclude the possible existence of boundaries with amorphous structures either.

As to materials with an ultrafine structure, in which the volume fractions of intragranular material and material associated with the boundaries (surface) are comparable, it is necessary to take into account both boundary and surface structures and consider the generalized size-dependent structural states.

In materials science, a material is characterized by its macro- (granular, phase, etc), micro- (amorphous, crystalline, grain-boundary, etc), and subgranular structure (defect, atomic-molecular, and so on) [25]. The macroscopic [26], crystalline [27], and grain-boundary [11] structures of conventional materials are independent of each other and can be characterized and studied separately. A similar differentiation of the structures of nanostructured materials makes no sense, since the structural state is characterized by the combination of the bulk, boundary, and surface structures. With a decrease in the grain size, the correlation between these structures becomes more pronounced and, apparently, may depend on the grain size. Thus, in order to determine the structural state of a nanostructured material, the establishment of the bulk structural states should be complemented by allowance for the structural state and the scale level of the boundaries and free surfaces.

Below, we assume that the grain and interphase boundaries and the free surface may be in crystalline, quasicrystalline, and amorphous states (Table 1). Therefore, in addition to the bulk structural states of material, we also consider the boundary (intergranular and interphase boundaries) and surface (free surfaces) structural states.

Furthermore, we also consider the following basic and mixed (heterophase) bulk structural states (without specifying boundary structures)—the amorphous–crystalline, amorphous–quasicrystalline, and crystalline–quasicrystalline states of different scale levels (Table 2).

Each structural state can be associated with one of the three main scale levels—nanoscopic, mezoscopic (micrometric), or macroscopic—and also with mixed scale levels depending on the characteristic sizes of structural components (Table 2). The generalized structural state is defined as a unified bulk–boundary–surface structure state of a specific scale level.

Different size-dependent structural states are also possible for boundaries and free surfaces (Table 1).[1] The nanostructured state of the grain boundary and free surface is of great importance. In addition to the boundaries between equal bulk structures (for example, the grain boundaries), we can also single out the following boundaries of mixed type: the boundaries of one structural state between different bulk structures (interfaces); the boundaries of mixed structural states (amorphous–crystalline, amorphous–quasicrystalline, and crystalline–quasicrystalline) between equal bulk structures; and the boundaries of mixed structural states between different bulk structures. We can consider as a natural minimum structural size for the grain boundaries with crystalline and quasicrystalline structures the size of boundary structural units. The nanofacets of the grain boundaries are two-dimensional analogues of the nanograins. The allowance for the surface structural

[1] A hypothesis of a new "gaslike" (without the short-range order) structural state of boundaries in nanocrystalline materials was proposed, but it received no experimental confirmation [9, 10].

Table 2. Bulk structures

Scale level	Main structures	Mixed (heterophase) structures with equal scale level
Macro	Am, QuCr, Cr	Am-QuCr, Am-Cr, Cr-QuCr
Micro	McAm, McQuCr, McCr	McAm-McCr, McAm-McQuCr, McCr-McQuCr
Nano	NAm, NCr, NQuCr	NAm-NCr, NAm-NquCr, NCr-NquCr
	Mixed size-dependent structural states	
Macro–micro, macro–nano, micro–nano	NAm-McCr, NAm-McQuCr, Am-NCr, Am-NQuCr……	

Table 3. Bulk–boundary structures

[McCr(bl)-NAm(bn)], [NCr(bl)-NQuCr(bn)], [(NCr- NQuCr)(bl)-Nam(bn)], [(NCr-McCr)(bl)-NQuCr(bn)]……

states is of importance for the low-dimensional systems, where the volume fraction of atoms adjacent to the free surface is comparable with the volume fraction of atoms inside the sample bulk, i.e., for nanoparticles, nanofibers, and nanofilms. Crystalline, quasicrystalline, and amorphous materials containing nanopores with an average distance between them on the order of 10 nm can also be classified as nanostructured materials [3]; the consideration of inner surface states of these materials is also of fundamental importance.

The next stage of differentiation of the structural types in the hierarchy of the generalized size-dependent structural states is the consideration of mixed bulk-boundary structures of different scale levels. Some of these structures are indicated in Table 3.

The approach to systematization of the size-dependent structural states suggested here is also applied to nanostructured materials (Table 4). The combination of bulk and boundary structural states allows one to assume the existence of nanocrystalline materials with amorphous, quasicrystalline, and crystalline boundaries; nanoquasicrystalline materials with quasicrystalline and amorphous boundaries; and, finally, nanoamorphous materials (Table 4).

The boundary structural states should have a less disordered atomic structure than the bulk material of bulk–boundary structures. For example, quasicrystalline grains can have boundaries with a quasicrystalline or amorphous structure. Otherwise, such a material should be considered composite. For example, if the surface crystallization of nanoparticles takes place during compaction of an amorphous powder, a composite nanoamorphous material with nanocrystalline boundaries (interlayers, NAm(bl)–NCr(bn)) (Table 4) will be obtained.

Table 4. Structural states of nanostructured materials

Name	Bulk structure	Boundary structure
NM	Nanocrystalline (NCr)	1. NCr
NM(bl)-NquCr(bn)		2. NQuCr
NM(bl)-Nam(bn)		3. NAm
NQuM	Nanoquasicrystalline (NQuCr)	1. NQuCr
NQuM(bl)-NAm(bn)		2. NAm
NAm	Nanoamorphous (NAm)	1. NAm
	Composite structures	
NQuCr(bl)-NCr(bn)	NQuXCr	1. NCr
NAm(bl)-NCr(bn)	NAm	1. NCr
NAm(bl)NQuCr(bn)	NAm	2. NQuCr
[(NAm-NQuCr)(bl)-NCr-QuCr(s);……	NAm-NQuCr……	1. NCr-NQuCr……
	Heterophase bulk structures	
NAmCr	NAm + NCr	NAm-NCr
NAmQuCr	NAm + NQuCr	NAm-NQuCr
NCrQuCr	NCr + NQuCr	NCr-NQuCr
NAmQuCrCr	NCr + NQuCr + NAm	NCr- NNAm; NQuCr-NAm
	Different scale levels	
Nanomicrocrystalline (NMcCr)	NCr + McCr	1. NCr
Nanoamorphous-microcrystalline……	NAm + McCr……	1. HAm-NCr; 2. NAm-NQuCr……

According to the definition of nanostructured materials [1–3], materials whose structural components have nanoscopic sizes but where the distance between these components exceeds 100 nm cannot be classified as nanostructured materials. Traditional dispersion-strengthened alloys containing nanocrystalline inclusions of other phases with a volume fraction not exceeding 10% are not nanostructured materials. If amorphous alloys contain nanocrystalline inclusions with a volume fraction much less than unity, these materials should be attributed to amorphous–nanocrystalline or amorphous materials with nanocrystalline inclusions [28]. However, if the volume fraction of nanoinclusions is high and the distance between these inclusions is on the order of 10 nm, then these materials should be called nanoamorphous–crystalline [28] and nanostructured materials (for example, alloys of the Finement type [8]).

The situation with nanocrystalline materials containing micrometric grains is analogous. If the volume fraction of grains exceeding 100 nm is low (not more than 10%), these materials should be called nanomicrocrystalline. If the volume fraction of micrograins is rather high, these materials are micronanocrystalline. This classification is rather conditional, and therefore one has to formulate a qualitative criterion for the transition from nanostructured to micronanostructured materials (with respect to the volume fraction, e.g., 50% of the structural component of one scale level), since in this case their properties should vary qualitatively.

The heterophase composition of the generalized structural state is defined by the existence of various bulk structural states, various boundary (surface) states, or the simultaneous existence of various bulk and boundary (surface) states in a material. Then, one has to take into account the possible heterophase composition of the main structural states—several phases of each (amorphous, crystalline, and quasicrystalline) state. The generalized heterophase bulk–boundary structural states, in which the bulk or boundary (surface) states are also heterophase, should be defined as "superheterophase" states. We also believe that nanostructured materials with different heterophase bulk or boundary structural states may exist (Table 4). Important representatives of heterophase nanostructured materials are zirconium- or aluminum-based nanoamorphous–crystalline and nanoamorphous–quasicrystalline alloys obtained by melt quenching [29].

The final stage of the classification is the consideration of different distributions and morphology of the structural or phase components [2], i.e., lamellar, columnar, and equiaxed forms of the elements of bulk multiphase structures with different types of boundary structures. A similar consideration of various morphologies and distributions is also possible for the structural components of boundary and surface heterophase structures.

ACKNOWLEDGMENTS

The author is grateful to V.I. Alshits for his interest in this study and for useful discussions. This study was supported by the Russian Foundation for Basic Research, project no. 03-02-17296.

REFERENCES

1. H. Gleiter, Prog. Mater. Sci. **33**, 223 (1989).
2. H. Gleiter, Nanostruct. Mater. **1**, 1 (1992).
3. H. Gleiter, Nanostruct. Mater. **6**, 3 (1995).
4. *Nanomaterials: Synthesis, Properties, and Applications*, Ed. by A. S. Edelstein and R. C. Kamarata (Inst. of Physics, Bristol, 1996).
5. A. I. Gusev, Usp. Fiz. Nauk **168** (1), 55 (1998).
6. R. Z. Valiev and I. V. Aleksandrov, *Nanostructured Materials Obtained as a Result of Intense Plastic Deformation* (Lotos, Moscow, 2000).
7. K. Lu, Mater. Sci. Eng. R **16**, 161 (1996).
8. R. A. Andrievskiĭ and A. M. Glezer, Fiz. Met. Metalloved. **88** (1), 50 (1999); Fiz. Met. Metalloved. **89** (1), 91 (2000).
9. R. W. Siegel, J. Phys. Chem. Solids **55**, 1097 (1994).
10. S. Wen and D. Yan, Ceram. Int. **21**, 109 (1995).
11. O. A. Kaibyshev and R. Z. Valiev, *Grain Boundaries and the Properties of Metals* (Metallurgiya, Moscow, 1987).
12. R. Z. Valiev and R. K. Islamgaliev, Fiz. Met. Metalloved. **85** (3), 161 (1998).
13. D. R. Clarke, J. Am. Ceram. Soc. **70**, 15 (1987).
14. V. A. Shabashov, V. V. Ovchinnikov, R. R. Mulyukov, *et al.*, Fiz. Met. Metalloved. **85** (3), 100 (1998).
15. B. Doudin and J. Ph. Ansermet, Nanostruct. Mater. **6**, 521 (1995).
16. V. A. Pozdnyakov, in *Abstracts of Conference on Structure Defects and Strength of Crystals* (Chernogolovka, 2002), p. 62.
17. D. Shechtman, I. Blech, D. Gratias, and J. W. Cahn, Phys. Rev. Lett. **53**, 999 (1984).
18. Ch. Janot and D. M. Dubois, J. Phys. F **18**, 2303 (1988).
19. *Introduction to Quasicrystals*, Ed. by M. V. Jaric (Academic, Boston, 1988).
20. V. E. Dmitrienko and N. Kleman, Kristallografiya **46** (4), 591 (2001) [Crystallogr. Rep. **46**, 527 (2001)].
21. A. Inoue, Nanostruct. Mater. **6**, 53 (1995).
22. A. P. Sutton, Acta Metall. **36**, 1291 (1988).
23. D. Gratias and A. Thalal, Philos. Mag. Lett. **57**, 63 (1988).
24. I. A. Ovid'ko, Fiz. Tverd. Tela (St. Petersburg) **39** (2), 306 (1997) [Phys. Solid State **39**, 268 (1997)].
25. S. M. Brekhovskikh, *Foundations of Materials Science* (Nauka, Moscow, 1981), p. 635.
26. *Physical Metallurgy*, Ed. by R. W. Cahn and P. Haasen (North-Holland, Amsterdam, 1983; Nauka, Moscow, 1987), Vol. 1.
27. N. V. Pashchenko and V. M. Talanov, Kristallografiya **40** (6), 973 (1995) [Crystallogr. Rep. **40**, 900 (1995)].
28. V. A. Pozdnyakov, Materialovedenie, No. 9, 39 (2002).
29. C. Fan, C. Li, A. Inoue, and V. Haas, Phys. Rev. B **61**, 3761 (2000).

Translated by T. Dmitrieva

Crystallography Reports, Vol. 48, No. 4, 2003, pp. 705–706. Translated from Kristallografiya, Vol. 48, No. 4, 2003, pp. 758–759.

CRYSTAL GROWTH

Regular Domain Structure in a Lithium Niobate Crystal—Period Stabilization

I. I. Naumova, N. F. Evlanova, S. A. Blokhin, T. O. Chaplina, and A. A. Novikov

Moscow State University, Vorob'evy gory, Moscow, 119992 Russia

e-mail: inna@crystal.acs465a.phys.msu.su

Received November 18, 2002

Abstract—High stability of the period and homogeneity of a regular domain structure was attained in Nd : Mg : $LiNbO_3$ crystals grown from melt with an excess of lithium oxide by the Czochralski method along the normal to the close-packed $\{01\bar{1}2\}$ face. © *2003 MAIK "Nauka/Interperiodica".*

Active periodically polarized niobate lithium crystals (PPLN) are promising material for designing compact lasers because of a combination of the advantageous quasiphase matched generation of harmonics, the possibility of frequency self-doubling, and more complex nonlinear optical processes, for example, frequency summation. This study aimed to increase the period stability of the domain structure (several microns in size) of a crystal.

The bulk periodically polarized domain structure was obtained in a Nd : Mg : $LiNbO_3$ crystal during its growth by the Czochralski method along the normal to the $\{01\bar{1}2\}$ face. Under conditions of an asymmetric thermal field at k_{eff} (Nd) < 1, the impurity incorporation is of a periodical character ("rotational" growth bands). The boundaries of ferroelectric domains are associated with the extreme values of the impurity modulation [1].

Practical application requires periodically polarized PPLN crystals with plane domain boundaries and a high periodicity. The face at the growth front provides the formation of plane boundaries of ferroelectric domains and increases their regular character. Nevertheless, as a rule, we observed the variations of the domain-structure period caused by changes in the conditions of heat removal in the growth chamber during the pulling of the crystal. Moreover, we also observed a gradual increase in the period with an increase in the crystal diameter because of the lowering of the melt level. As a result, the period stability within a length of 1–3 mm was 2%.

We grew Nd : Mg : $LiNbO_3$ crystals with a superstructure period of (4.2 ± 0.1) μm (Fig. 1). The ferroelectric domain structure of the polished *X*-cut was revealed by selective chemical etching [1]. Earlier, a stable period was reported within a length of 3 mm [2, 3].

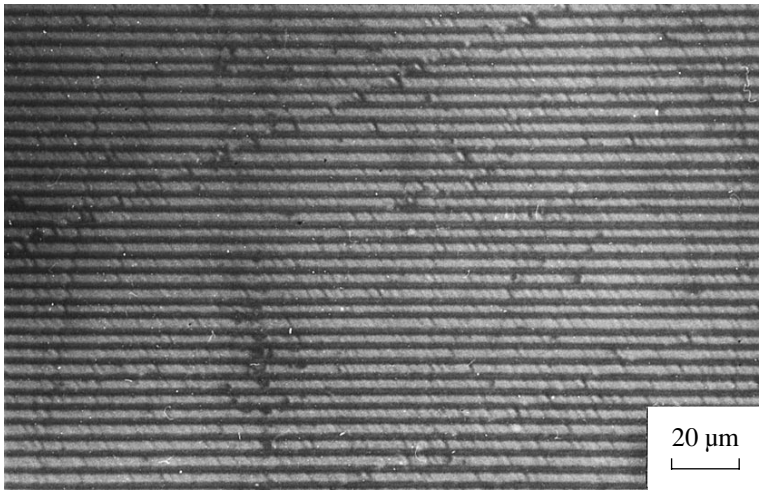

Fig. 1. Periodic domain structure of the *X*-cut of a Nd : Mg : $LiNbO_3$ crystal revealed by selective chemical etching.

1063-7745/03/4804-0705$24.00 © 2003 MAIK "Nauka/Interperiodica"

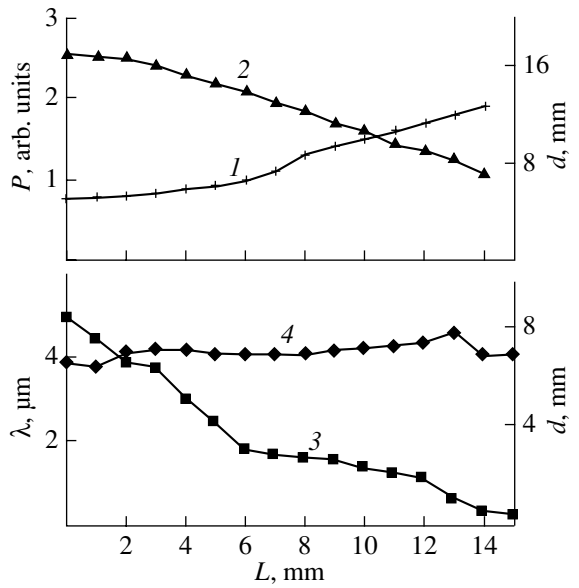

Fig. 2. Characteristics of the growth process of a Nd : Mg : $LiNbO_3$ crystal. (*1*) Heater power; (*2*) crystal diameter; (*3*) face size; (*4*) period of regular domain structure.

The initial melt contained an excess of lithium oxide with respect to the congruent composition (2 : 1, about 60 mol % Li_2O, see the phase diagram [4]); i.e., in fact, crystals were grown from flux. The rate of crystal pulling was 5 mm/h, and the rotation rate was 22 rpm (the calculated period was 3.8 μm, the diameter of the platinum crucible was 50 mm).

Earlier, an excess of Li_2O was used to grow faceted nominally pure $LiNbO_3$ crystals [5]. The addition of K_2O was used to grow homogeneous single-domain lithium niobate crystals [6]. We reduced the heater power during growth (Fig. 2, curve *1*), the crystal diameter and the face dimensions gradually increased as the crystal was pulled out from the melt (Fig. 2, curves *2*, *3*). In this case, the period of domain structure remained sufficiently constant (Fig. 2, curve *4*), the average relative error of the measurement of the period stability was 2% within a length of 13 mm (in the range 2–14.7 mm) and on the best portions, 1% within a length of 4 mm (in the range 4–8 mm). All the measurements were made beginning from the crystal bottom. We assume that the high stability of the regular domain structure is associated with the specific features of the mechanism of impurity (Nd^{3+}) incorporation during the crystal growth from flux (the excess of Li_2O) and also with the close-packed $\{01\bar{1}2\}$ face at the growth front.

It should be noted that the domain structure of the crystals obtained were free of such typical defects as single-domain clusters, which are usually several tens of microns in size. The impurity concentration in crystals determined by the X-ray microanalysis was 0.5 wt % for Nd_2O_3 and 0.8 wt % for MgO.

The element from a Nd : Mg : $LiNbO_3$ crystal with a domain-structure period of about 4 μm and 7 mm in length along the face normal was used in the experiment on summation of the frequencies of laser generation and semiconductor pumping

$$\omega_{laser} + \omega_{pump} = \omega_{sum}.$$

In this process, the radiation of a semiconductor laser with the wavelength $\lambda = 0.81$ μm is the pumping of an active media, whereas the nonabsorbed radiation takes part in the process of nonlinear interaction with the wave of laser generation $\lambda = 1.084$ μm. At the exit from the crystal, along with the wave of laser generation, we also recorded the radiation of a wave with the total frequency $\lambda = 0.464$ μm [7].

ACKNOWLEDGMENTS

This study was supported by the Russian Foundation for Basic Research, project nos. 00-02-16040 and 02-02-06470.

REFERENCES

1. I. I. Naumova, N. F. Evlanova, S. A. Blokhin, and S. V. Lavrishchev, J. Cryst. Growth **187**, 102 (1998).
2. I. I. Naumova and O. A. Gliko, Kristallografiya **41** (4), 749 (1996) [Crystallogr. Rep. **41**, 712 (1996)].
3. E. P. Kokanyan, V. G. Babajanyan, G. G. Demirkhanyan, *et al.*, J. Appl. Phys. **92** (3), 1544 (2002).
4. A. Reisman and F. Holizberg, J. Am. Chem. Soc. **80** (24), 6503 (1958).
5. V. A. D'yakov, N. F. Evlanova, and N. M. Rubinina, in *Abstracts of the Moscow Conference on Crystal Growth* (Moscow, 1980), Vol. 3, p. 93.
6. G. I. Malovichko, V. G. Grachev, L. P. Yurchenko, *et al.*, Phys. Status Solidi A **133**, K29 (1992).
7. G. D. Laptev, N. V. Kravtsov, A. A. Novikov, *et al.*, Kvantovaya Élektron. (Moscow) **32** (10), 923 (2002).

Translated by T. Dmitrieva

Crystallography Reports, Vol. 48, No. 4, 2003, pp. 707–713. Translated from Kristallografiya, Vol. 48, No. 4, 2003, pp. 760–766.

CRYSTAL GROWTH

Calculation of Volume Fraction of Phase Growing by a Diffusion-Type Law

N. V. Alekseechkin

National Research Center "Kharkov Physicotechnical Institute," Kharkov, 61108 Ukraine

e-mail: n.alex@kipt.kharkov.ua

Received May 23, 2002

Abstract—The problem of determining the volume fraction of a phase is considered for the case where the rate of nucleus growth is a decreasing function of its radius. The solution is obtained within the framework of the geometrical–probabilistic method suggested earlier. The procedure of successive approximations is described, which allows one to determine the volume fraction of a phase with the required accuracy. The errors arising in the calculation of the volume fraction of a phase from the Kolmogorov formula are estimated analytically. As an example of numerical estimates, the case of the diffusion growth mechanism is considered. It is shown that in the three-dimensional space, this error lies within 0.01 irrespective of the initial parameters of the problem.

INTRODUCTION

The classical Kolmogorov–Johnson–Mehl–Avrami theory [1–3] widely used in the calculations of crystallization kinetics has a number of obvious limitations [1, 4]. The present article is dedicated to the analysis of the restrictions imposed on growth rate.

As is well known, the growth rate of a new-phase nucleus, u, in the Kolmogorov or K-model is independent of its radius (otherwise the Kolmogorov expression for the volume fraction of the phase would not be accurate). At the same time, such a dependence is often observed in practice and is described by the following growth law:

$$\frac{dR}{dt} = F(R, t), \quad R(t') = R_0, \quad F(R, t) > 0 \qquad (1)$$

with $R_0 = 0$ in the K-model.

Solving the above equation, one obtains the radius $R(t', t)$ and the corresponding growth rate $u(t', t) = \partial R(t', t)/\partial t$ as functions of the current moment of time, t, and the moment of nucleus appearance, t'. Therefore, nuclei that appeared at different moments t', at the moment t grow with different rates and, thus, do not obey the initial assumption of the K-model about equal growth rates. In this case, the use of the Kolmogorov formula for calculating the volume fraction of the phase (hereafter called simply the volume fraction) is not justified and leads to a certain error. For the particular case of the diffusion growth mechanism, this error was estimated as [4, 5]

$$\frac{dR}{dt} = \frac{c}{2R}, \quad R(t') = 0, \quad c = \text{const}; \qquad (2)$$

$$R(t', t) = \sqrt{c(t - t')}, \quad u(t', t) = \frac{1}{2}\sqrt{\frac{c}{t - t'}}. \qquad (3)$$

However, it is shown below that the estimate of the upper bound of the volume fraction in [4, 5] is considerably overestimated and, moreover, fails to give the correct time dependence. In [6], the growth law described by Eq. (2) was studied by numerical simulation, and it was shown that the error did not exceed 0.01.

Below, we study the growth law described by Eq. (1) analytically using an arbitrary function of radius $F(R, t)$ decreasing at any moment t. The procedure for evaluating the accuracy of the Kolmogorov formula for an arbitrary growth law of this class is described. As an example of numerical estimates, we consider the growth law described by Eq. (2) and show the good agreement of the results obtained with the data in [6]. The consideration is performed within the framework of the mathematically rigorous geometrical–probabilistic method, whose efficiency was also demonstrated when solving other problems associated with the calculation of volume fractions [7–9].

Some remarks about nucleus shape and the related determination of nucleus radius. As is well known, the K-model admits an arbitrary convex shape of a nucleus, but requires that all the nuclei should be geometrically similar and be equivalently oriented in space [1, 4]. Therefore, the linear size of a nucleus can be characterized by its "radius" $R(t', t)$ measured from its center along a certain fixed direction. Then, the nucleus volume is $V(t', t) = gR^D(t', t)$, $D = 2, 3$, and g is the shape constant. The direction of measuring the radius can be chosen arbitrarily, but the constant g depends on this choice. Of course, the nucleus radius thus determined is

not associated with the curvature of its surface; e.g., the faces can be planar (zeroth curvature). Such a relation exists only for a spherical nucleus. The K-model admits an arbitrary shape of a nucleus, whereas the use of the growth laws described by Eqs. (1) and (2) suggests that the nucleus shape remains constant during its growth. In other words, the above laws, which describe the variation of the linear size of a nucleus, $R(t', t)$, do not change the curvature of the nucleus surface. Thus, in this case, it is more appropriate to consider the dependence of the growth rate of a nucleus on its "age" $(t - t')$ such that $u(t_1', t) > u(t_2', t)$ for $t_1' > t_2'$ (or $\partial u/\partial t' \equiv \partial^2 R(t', t)/\partial t'\partial t \geq 0$). The method considered below for a spherical nucleus can readily be modified also for this case. The only difference reduces to the fact that the shape and orientation of the critical region should be the same as for nuclei and, therefore, the expressions that describe intersection volumes $\Delta\Omega^{(D)}$ should be different.

Decreasing curves of growth rates as functions of radii are characteristic of the growth processes limited by diffusion. Thus, monograph [4] considers growth of a two-dimensional nucleus on a substrate during deposition from the gas phase. In this case, the growth laws are described by equations of type (2). An analogous equation is also obtained in the consideration of growth of a volume nucleus whose composition differs from the matrix composition.

The K-model, first formulated for considering various problems of crystal physics, was then also used in other fields (see [4] and references there). Thus, the dependence of the growth rate of a nucleus on its age can also take place in other processes. The methodological importance of the results described below is the possibility of extending the K model to such processes as well.

If the growth rate of a surface region depends on its curvature, the nucleus shape varies with time in different ways for different nuclei. Thus, the main assumption about nucleus shapes used in the K-model becomes invalid, and the question arises as to whether the Kolmogorov formula can be used for calculating the volume fraction. The study of the accuracy of this formula for nuclei of different shapes is a separate problem and is not considered here.

DESCRIPTION OF THE METHOD

The differential method of the critical region [7, 8] is based on the calculation of the probability $dX(t)$ of the fact that an arbitrary point O would be "absorbed" (transformed) by a growing phase within the time interval $[t, t + dt]$. Two conditions are necessary and sufficient for the occurrence of this process: (a) the point O should not be absorbed up to the moment t and (b) a nucleus of the new phase that can absorb the point O within the time interval $[t, t + dt]$ should appear at a certain moment t', $0 < t' < t$; hereafter, such a nucleus is called critical. Now, let $Q(t)$ and $dY(t)$ be the probabilities that the first and the second events occur, respectively. Then, we can write the following equation for $X(t)$:

$$dX(t) = Q(t)dY(t). \tag{4}$$

Since $X(t) = 1 - Q(t)$, the above equation is a differential equation for a volume fraction. Therefore, the problem reduces to the calculation of the probability $dY(t)$ of the appearance of a critical nucleus. Now, consider the space–time scheme of the process that meets both the above requirements.

Requirement (a) indicates that the appearance of nuclei of the new phase at earlier moments t' $(0 < t' < t)$ is forbidden in a certain neighborhood of the point O, i.e., in a certain critical region. The boundary of this region at the moment t' is determined from the condition that the nucleus appeared at this boundary at this moment would reach the point O at the moment t. Nuclei that appeared beyond the critical region would reach the point O after the moment t and, therefore, cannot absorb this point. Thus, the critical region is a sphere of radius $R(t', t)$ with the center at point O. With a change of t' from 0 to t, the radius of this region also changes from its maximum value $R_m(t) \equiv R(0, t)$ to $R(t, t) = 0$. At the moment t', the region boundary propagates with the velocity $u_t^{cr}(t') = \partial R(t', t)/\partial t'$. Obviously, this velocity can also be represented as a function of the critical-region radius.

Now, consider condition (b). The expressions for $dY(t)$ are different for different types of the dependence of R in Eq. (1). For the sake of simplicity, consider the particular case of $F(R, t)$, which corresponds to the separated variables, $F(R, t) = c(t)f(R)$. Then the solution of Eq. (1) has the form

$$w(R) \equiv \int_{R_0}^{R} \frac{dR'}{f(R')} = \int_{t'}^{t} c(\tau)d\tau, \tag{5}$$

whence

$$R(t', t) = w^{-1}\left(\int_{t'}^{t} c(\tau)d\tau\right), \tag{6}$$

where w^{-1} is the inverse function.

Then, the velocity of the critical-region boundary at the moment t' is

$$u_t^{cr}(t') = -f(R(t', t))c(t'), \tag{7}$$

whereas the growth rate of the nucleus that appeared at the moment t', at the moment t, is

$$u(t', t) = f(R(t', t))c(t). \tag{8}$$

Now, let τ be a certain later moment so that t': $t' < \tau < t$. Then, the absolute value of u_t^{cr} at the moment τ is

$$\left|u_t^{cr}(\tau)\right| = f(R(\tau, t))c(\tau), \quad (9)$$

whereas the growth rate of the nucleus that appeared at moment t' is

$$u(t', \tau) = f(R(t', \tau))c(\tau). \quad (10)$$

It is seen that, in the general case, $|u_t^{cr}(\tau)|$ and $u(t', \tau)$ are not equal. They can become equal only if the growth rate is independent of the radius, i.e., if $F(R, t) = c(t)$. Then $R(t', t) = R_0 + \int_{t'}^{t} c(\tau)d\tau$. The growth rate of a nucleus is independent of the moment of its appearance, t': $u(t) = \partial R(t', t)/\partial t = c(t)$. The velocity of the critical-region boundary is $|u_t^{cr}(t')| = c(t')$. At any moment τ, both velocities are equal: $u(\tau) = |u_t^{cr}(\tau)| = c(\tau)$. Thus, all the nuclei grow at the same rate, coinciding with the velocity of the critical-region boundary. This is the case with the K-model. The probability of the appearance of a critical nucleus at the moment t' is $dP(t', t) = I(t')dt'dV(t', t)$, where $dV(t', t) = \dot{V}(t', t)dt$ is the volume of the near-boundary layer with respect to the variation in t. Integration with respect to t' yields the probability $dY(t)$ of the appearance of a critical nucleus

$$dY(t) = \left(\int_0^t dt' I(t')\dot{V}(t', t)\right)dt. \quad (11)$$

Substituting Eq. (11) into Eq. (4), we arrive at the Kolmogorov formula

$$Q_0(t) = \exp\left\{-\int_0^t I(t')V(t', t)dt'\right\}. \quad (12)$$

THE CASE OF A DECREASING FUNCTION $f(R)$

In order to realize the consequences of the inequality $|u_t^{cr}(\tau)| \neq u(t', \tau)$, consider a monotonically decreasing dependence $f(R)$ (small nuclei grow at a higher rate than large ones) (Fig. 1). At the beginning, the growth rate of a critical nucleus is higher than the velocity of the critical-region boundary (the growth rate decreases, whereas the velocity of boundary propagation increases with time). As a result, this nucleus penetrates the critical region. Moreover, nuclei formed in the vicinity of the critical region also penetrate this region. Thus, at the time moment t', a part of the region volume is occupied by such nuclei. Denote the part of the critical-region volume free of nuclei at the moment t' by $\tilde{V}(t', t)$.

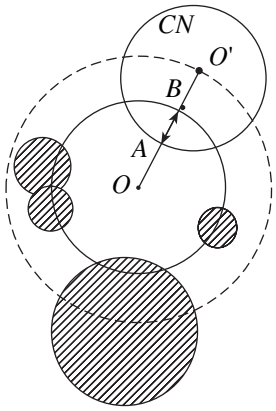

Fig. 1. Calculation of the penetration depth of a critical nucleus (*CN*). The positions of the critical-region boundary at the current moment τ and at the moment $t' < \tau$ are shown by solid and dashed lines, respectively (the corresponding radii of the region are $|OB| = R(\tau, t)$ and $|OO'| = R(t', t)$). The etched nuclei appear at different moments and penetrate the critical region at the moment τ. The depth of their penetration at the moment τ equals $|AB|$.

Then, one can readily calculate the maximum depth d_m of the nucleus penetration for the growth law described by Eq. (2). Obviously, of all the nuclei that appear at moment t', the critical nucleus penetrates to the maximum depth. As before, we assume that $t' < \tau < t$. The radius of the critical nucleus at the moment τ is $|AO'| = \sqrt{c(\tau - t')}$ (Fig. 1). In the time interval from t' to τ, the critical-region boundary is displaced for a distance of $|BO'| = \sqrt{c(t - t')} - \sqrt{c(t - \tau)}$. Thus, the penetration depth of the critical nucleus at the moment τ is

$$\begin{aligned} d(\tau) &= |AB| = |AO'| - |BO'| \\ &= \sqrt{c(\tau - t')} + \sqrt{c(t - \tau)} - \sqrt{c(t - t')}. \end{aligned} \quad (13)$$

The maximum of the function $d(\tau)$ at the fixed values of t and t' corresponds to $\tau_m = (t + t')/2$ and is equal to

$$d_m = (\sqrt{2} - 1)\sqrt{c(t - t')} \equiv (\sqrt{2} - 1)R(t', t). \quad (14)$$

The radius of the critical region at the moment τ_m is equal to $R(\tau_m, t) = (1/\sqrt{2})R(t', t)$.

One can readily see that nuclei that appear at the moment t' at distances $r \geq d_m$ from the critical region cannot penetrate this region.

Now, derive the expression for $dY(t)$ in this model. The probability of the appearance of a critical nucleus within the time interval $[t', t' + dt']$ equals $dP(t', t) = I(t')dt'\dot{V}(t', t)q(t', t)dt$, where $q(t', t)$ is the nontransformed part of the critical-region boundary at the

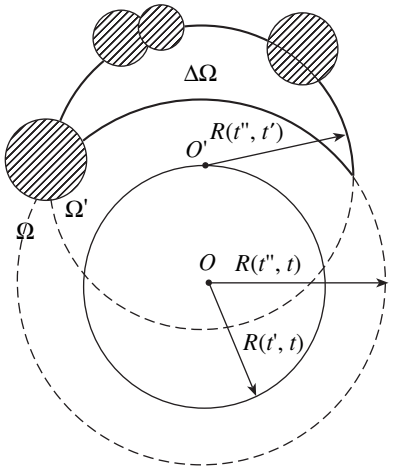

Fig. 2. Calculation of the function $q(t', t)$.

moment t'. As before, $dY(t)$ is the integral of $dP(t', t)$ with respect to t'. Thus, Eq. (4) acquires the form

$$\frac{dX(t)}{dt} = Q(t)\int_0^t dt' I(t')\dot{V}(t', t)q(t', t), \qquad (15)$$

whence the volume fraction sought is

$$Q(t) = \exp\left\{-\int_0^t d\tilde{t}\int_0^{\tilde{t}} dt' I(t')\dot{V}(t', \tilde{t})q(t', \tilde{t})\right\}. \qquad (16)$$

The expression for the volume fraction can also be obtained by the Kolmogorov method. In [1], the $Q(t)$ function was directly calculated based only on condition (a) (unlike the approach used in this article, the Kolmogorov method is "differential" with respect to the time variable, but "integral" with respect to the volume [7]). Applying the algorithm suggested in [1] to our case, one can readily obtain

$$Q(t) = \exp\left\{-\int_0^t dt' I(t')\tilde{V}(t', t)\right\}. \qquad (17)$$

Both Eqs. (16) and (17) can be reduced to one another. However, Eq. (16) is more convenient for obtaining estimates, because it has integrals only with respect to time variables, whereas Eq. (17) has the integral taken over the critical region; $\tilde{V}(t', t)$ is such an integral.

CALCULATION OF FUNCTION $q(t', t)$. APPROXIMATIONS FOR VOLUME FRACTION

The $q(t', t)$ function is calculated based on the geometrical construction shown in Fig. 2. We seek the probability that, at the moment t', an arbitrary point O' at the critical-region boundary would be located in the untransformed volume. This event should take place if the condition formulated earlier is met, i.e., the point O is located in the nontransformed volume up to the moment t. Thus, the function $q(t', t)$ is the conditional probability, so when calculating this function one has to take into account the correlation between the states at the points O and O'. The critical region of the point O' denoted by Ω' in Fig. 2 is a sphere of radius $R(t'', t')$ at $0 < t'' < t'$. If the above event really takes place, the appearance of nuclei of a new phase in the region Ω' at the time interval $0 < t'' < t'$ should be excluded. The similar condition for the point O excludes the appearance of nuclei inside the critical region of the point O, i.e., within a sphere of radius $R(t'', t)$ (indicated by Ω in Fig. 2). Thus, calculating $q(t', t)$, one has to consider only the part of the region Ω' lying outside the region Ω. This part is denoted as $\Delta\Omega$ in Fig. 2. The volume of this part is indicated as $\nu(t'', t', t)$. Considering two intersecting spheres of radii r_1 and r_2 with the distance between their center h in the spaces with $D = 3$ and $D = 2$, one can readily obtain the expressions for the part of the volume of the second sphere lying outside the first sphere,

$$\Delta\Omega^{(3)}(r_1, r_2, h) = \pi\left\{\frac{2}{3}(r_2^3 - r_1^3) - \frac{1}{12}h^3 + \frac{1}{2}h(r_1^2 + r_2^2) + \frac{1}{4}\frac{(r_1^2 - r_2^2)^2}{h}\right\}, \qquad (18)$$

$$\Delta\Omega^{(2)}(r_1, r_2, h) = r_2^2\left[\pi - \arccos\frac{h^2 - (r_1^2 - r_2^2)}{2hr_2}\right] - r_1^2\arccos\frac{h^2 + (r_1^2 - r_2^2)}{2hr_1} + \frac{1}{2}\sqrt{4h^2r_2^2 - [h^2 - (r_1^2 - r_2^2)]^2}. \qquad (19)$$

The volume $\nu(t'', t', t)$ is determined by substituting $r_1 = R(t'', t)$, $r_2 = R(t'', t')$, and $h = R(t', t)$ into the above expressions. If dependence (3) is valid, we arrive at the equality $h^2 = r_1^2 - r_2^2$, so that Eq. (19) is considerably simplified.

Like Ω, the region Ω' at the moment t'' contains the fragments of penetrated nuclei, which appeared at later moments $t''' < t''$ (Fig. 2). Denoting the free volume of the region $\Delta\Omega$ by $\tilde{\nu}(t'', t', t)$, we arrive at an expression for $q(t', t)$ similar to Eq. (17),

$$q_{ex}(t', t) = \exp\left\{-\int_0^{t'} dt'' I(t'')\tilde{\nu}(t'', t', t)\right\}. \qquad (20)$$

Ignoring the correlation between the states at the points O and O', i.e., using $\tilde{V}(t', t)$ instead of $\tilde{\nu}(t'', t', t)$ in Eq. (20), we obtain $q(t', t) = Q(t')$. However, now, instead of (16), we consider two other approximations

based on the direct calculation of

$$Q(t) = \exp\left\{-\int_0^t dt' I(t') V(t', t) Q(t')\right\}. \quad (21)$$

which yields one of possible approximations of $Q(t)$.

For definiteness, hereafter, we call them the first and second approximations and denote the corresponding volume fractions as $Q_1(t)$ and $Q_2(t)$.

Ignoring the correlation between the states at the points O and O' and the possible penetration of nuclei into the region Ω', we obtain the following Kolmogorov formula for $q(t', t)$:

$$q_1(t') = \exp\left\{-\int_0^{t'} dt'' I(t'') V(t'', t')\right\}. \quad (22)$$

Now, taking into account the correlation between the states at the points O and O', but ignoring the penetration of some nuclei into the region $\Delta\Omega$, i.e., using $\nu(t'', t', t)$ instead of the unknown function $\tilde{\nu}(t'', t', t)$ in Eq. (20), we obtain

$$q_2(t', t) = \exp\left\{-\int_0^{t'} dt'' I(t'') \nu(t'', t', t)\right\}. \quad (23)$$

Now, denote the exact value of the volume fraction obtained from Eqs. (16) and (20) by $Q_{ex}(t)$. It follows from the obvious inequalities $0 < \tilde{\nu}(t'', t', t) < \nu(t'', t', t) < V(t'', t')$ that

$$q_1(t') < q_2(t', t) < q_{ex}(t', t) < 1, \quad (24)$$

whence follow the inequalities for the volume fraction $Q_{ex}(t)$

$$Q_0(t) < Q_{ex}(t) < Q_2(t) < Q_1(t). \quad (25)$$

It should be noted that, if the point O' in Fig. 2 is taken not at the critical-region boundary but inside this region at a distance r from the point O, then the function $q(r, t', t)$ obtained in the same way yields the distribution of the nontranformed substance inside the critical region over r. The quantity $\tilde{V}(t', t)$ in Eq. (17) is calculated with the aid of this function. In a similar way, the quantity $\tilde{\nu}(t'', t', t)$ can be estimated with the aid of the analogous function $q(r, t'', t')$. Thus, it is possible to obtain more exact approximations of the volume fraction.

Determine also the functions $\Delta Q_i(t) \equiv Q_i(t) - Q_0(t)$, $i = 1, 2$, which are the estimates of the error in the volume fraction associated with the use of $Q_0(t)$ instead of $Q_{ex}(t)$.

Equation (16) can be represented as

$$Q(t) = \exp\left\{-\int_0^t dt' I(t') V(t', t) + \phi(t)\right\} \equiv Q_0(t)\exp(\phi(t)), \quad (26)$$

$$\phi(t) \equiv \int_0^t d\tilde{t} \int_0^{\tilde{t}} dt' I(t') \dot{V}(t', \tilde{t})[1 - q(t', \tilde{t})]. \quad (27)$$

Then $\Delta Q_i(t)$ can be represented as

$$\Delta Q_i(t) = Q_0(t)[\exp(\phi_i(t)) - 1]. \quad (28)$$

DISCUSSION

The main results of this study are the analytical estimates of the volume fraction for an arbitrary growth law with a decreasing function of the radius. As an example of the application of the theory, consider the growth rate given by Eq. (2) and the constant nucleation rate I. Introduce the parameter $\alpha = (8\pi/15)Ic^{3/2}$ in the three-dimensional space and pass from time t to the dimensionless variable $\xi = \alpha t^{5/2}$. The volume fraction calculated by Eq. (12) has the form $Q_0(\xi) = \exp(-\xi)$.

After the transition from t to ξ, we obtain from Eqs. (22) and (27)

$$\phi_1(\xi) = \frac{5}{2}\xi \int_0^1 dx (1 - x)^{3/2} [1 - \exp(-\xi x^{-5/2})]. \quad (29)$$

In order to determine the function $\phi_2(\xi)$ in the more accurate second approximation, substitute $\nu(t'', t', t) = \Delta\Omega^{(3)}(R(t'', t), R(t'', t'), \text{and } R(t', t))$ into Eq. (23), where R is given by Eq. (3). Taking the integrals and passing to ξ, we obtain

$$\phi_2(\xi) = \frac{3}{2}\xi \int_0^1 dx \sqrt{1 - x}\left\{1 - \frac{1 - \exp[-\xi p(x)]}{\xi p(x)}\right\},$$
$$p(x) \equiv \frac{1}{2}\left\{x^{5/2} + \sqrt{1 - x}\left[\frac{3}{8}x^2 + \frac{1}{2}x + 1\right] - 1\right\}. \quad (30)$$

It follows from Eqs. (29) and (30) that the expansion of the function $\phi(\xi)$ into a series has the form

$$\phi(\xi) = a\xi^2 - b\xi^3 \pm \ldots. \quad (31)$$

For the function $\phi_1(\xi)$, we have $a \sim 9.2 \times 10^{-2}$ and $b \sim 1.4 \times 10^{-2}$, whereas for $\phi_2(\xi)$, we obtain somewhat lower values,

$$a = \frac{3}{4}\int_0^1 dx \sqrt{1 - x} p(x) \approx 2.6 \times 10^{-2},$$

$$b = \frac{1}{4}\int_0^1 dx \sqrt{1 - x} p^2(x) \approx 9.46 \times 10^{-4}$$

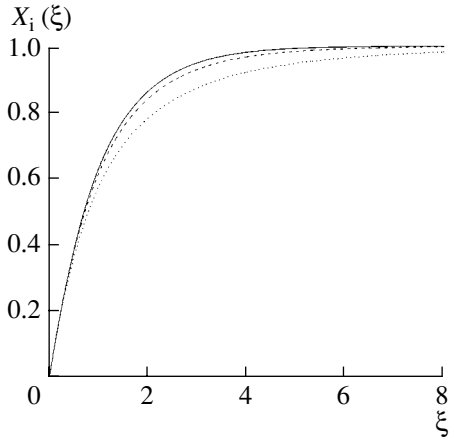

Fig. 3. Volume fraction of the transformed substance in the two-dimensional case for the growth law described by Eq. (2). The dependences shown were obtained using the Kolmogorov expression (solid line $X_0(\xi)$) and the first (dashed line, $X_1(\xi)$) and second (dashed line, $X_2(\xi)$) approximations.

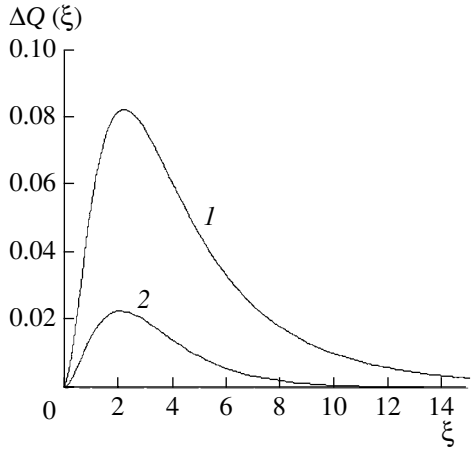

Fig. 4. Estimates of the error in the determination of the volume fraction. Lines *1* ($\Delta_1(\xi) = X_0(\xi) - X_1(\xi)$) and *2* ($\Delta_2(\xi) = X_0(\xi) - X_2(\xi)$) correspond to the first and second approximations; the $X_i(\xi)$ curves are shown in Fig. 3.

in full accordance with a more accurate approximation.

The functions $\Delta Q_i(\xi)$ are dome-shaped. The maximum values are $\max(\Delta Q_1(\xi)) \sim 4.4 \times 10^{-2}$ and $\max(\Delta Q_2(\xi)) \sim 1.4 \times 10^{-2}$.

Below, we give analogous estimates in the two-dimensional space. In this case, $V(t', t) = \pi R^2(t', t) = \pi c(t - t')$, $\nu(t'', t', t) = \Delta\Omega^{(2)}(R(t'', t), R(t'', t'), R(t', t))$, $\xi = \beta t^2$, and $\beta \equiv (\pi/2)Ic$. Performing the necessary calculations, we arrive at the following expressions:

$$\phi_1(\xi) = 2\xi\int_0^1 dx(1-x)[1-\exp(-\xi x^2)], \qquad (32)$$

$$\phi_2(\xi) = \xi\int_0^1 dx\left\{1-\frac{1-\exp[-\xi p(x)]}{\xi p(x)}\right\}, \qquad (33)$$

where

$$p(x) \equiv \frac{x^2}{2} - \frac{1}{\pi}\arccos\sqrt{1-x}$$
$$+ \frac{5}{3\pi}(1-x)^{1/2}x^{3/2} + \frac{1}{\pi}(1-x)^{3/2}x^{1/2}.$$

The maximum values of $\Delta Q(\xi)$ are $\max(\Delta Q_1(\xi)) \sim 8.2 \times 10^{-2}$ and $\max(\Delta Q_2(\xi)) \sim 2.2 \times 10^{-2}$.

The estimate made for the two-dimensional case in [4, 5], in our notation, has the form $\exp(-\xi) < Q_{ex}(\xi) < \exp(-\xi/3)$, which corresponds to $\phi(\xi) = (2/3)\xi$ and $\max(\Delta Q(\xi)) \sim 0.39$. Obviously, the first approximation is the crudest of all the possible approximations. Nevertheless, the estimate in [4, 5] is several times larger than $\max(\Delta Q_1(\xi))$.

Figures 3 and 4 show the dependences $X_i(\xi) = 1 - Q_i(\xi)$, $i = 0, 1, 2$ and $\Delta X_i(\xi) = \Delta Q_i(\xi)$, $i = 1, 2$ in the two-dimensional case.

Consider the results obtained in terms of the well-known Johnson–Mehl approach [2]. This approach to the calculation of a volume fraction is the most clear because it deals with nuclei. The key assumption is the admission of fictitious nucleation and growth mechanisms—nuclei of the new phase appear over the whole volume of the system (including the already transformed region) with equal probabilities (imaginary nuclei or phantoms). When colliding, nuclei grow into one another without changing their shapes. It is essential that, within the Kolmogorov model, the fictitious mechanism does not change the picture of the real process, so that Eq. (12) is quite accurate. If growth proceeds according to the diffusion-type mechanism, the situation is quite different. The growth rate of a phantom is much higher than the growth rate of a real nucleus containing this phantom. Therefore, with time the phantom can enter the nontransformed region and make its contribution to the increment in the real volume. Thus, taking into account the fictitious mechanism, one has to remove the contribution made by phantoms into the volume fraction. This can readily be made using the function $q(t', t)$. Ignoring the correlation between the states at the points O and O' described above (Fig. 2), one can readily transform Eq. (16) into Eq. (21), which can be represented in the form

$$Q(t) = \exp\{-[Y(t) - \phi(t)]\}, \qquad (34)$$

where

$$\phi(t) = t\int_0^t dt' I(t')V(t', t)X(t'), \quad X(t') = 1 - Q(t'),$$

$Y(t) = \int_0^t dt' I(t')V(t', t)$ is the extended volume of all the nuclei in the Johnson–Mehl approach without allowance for their possible overlap. The probability that a phantom will appear in the unit volume within time dt' is $I(t')X(t')dt'$. Therefore, the function $\phi(t)$ is the extended volume of all the phantoms without allowance for their possible overlap. In Eq. (34), this volume is subtracted from the total volume of all the nuclei. With due regard for the above correlation, the function $\phi(t)$ is the extended volume of only those phantoms that make a contribution to the increment in the real volume at the moment t.

It should be emphasized that the effect produced by phantoms also takes place in the presence of several competing phases growing at different rates [7]. The expression for the volume fractions of these phases in the above two problems are somewhat similar. The analysis shows that, if growth law (2) is valid or if there are several competing phases, the effect of phantoms is negligible. This is explained by the fact that the effect of phantoms develops with time rather slowly. This is reflected in the characteristic form of the function $\phi(\xi)$. Its expansion into series (31) begins with ξ^2 (for short times, the function ϕ is proportional to the squared volume fraction X), whereas coefficient a is small. Moreover, the series is sign-alternating and converges rather fast. Therefore, at the earlier stages of the process, $\xi < 1$, phantoms do not manifest themselves ($\phi(\xi) \ll 1$). At the late stages, the effect of phantoms is suppressed because no nontransformed volume exists any more, and the function $Q(t)$ tends to zero. At sufficiently low a values, the maximum value of the function $\Delta Q(\xi)$ is determined by this coefficient ($\max(\Delta Q(\xi) \sim 4a\exp(-2))$ and, therefore, also has a low value (it should be remembered that the a value is also determined by the growth law).

REFERENCES

1. A. N. Kolmogorov, Izv. Akad. Nauk SSSR, Ser. Mat., No. 3, 355 (1937).
2. W. A. Johnson and R. F. Mehl, Trans. AIME **135**, 416 (1939).
3. M. Avrami, J. Chem. Phys. **7**, 1103 (1939); J. Chem. Phys. **8**, 212 (1940); J. Chem. Phys. **9**, 177 (1941).
4. V. Z. Belen'kiĭ, *Geometric–Probabilistic Models of Crystallization: Phenomenological Approach* (Nauka, Moscow, 1980).
5. V. Z. Belen'kiĭ, Dokl. Akad. Nauk SSSR **228** (6), 1325 (1976) [Sov. Phys. Dokl. **21**, 307 (1976)].
6. M. P. Shepilov and V. B. Bochkarev, Kristallografiya **32** (1), 25 (1987) [Sov. Phys. Crystallogr. **32**, 11 (1987)].
7. N. V. Alekseechkin, Fiz. Tverd. Tela (St. Petersburg) **42** (7), 1316 (2000) [Phys. Solid State **42**, 1354 (2000)].
8. N. V. Alekseechkin, Fiz. Tverd. Tela (St. Petersburg) **42** (12), 2205 (2000) [Phys. Solid State **42**, 2273 (2000)].
9. N. V. Alekseechkin, J. Phys.: Condens. Matter **13**, 3083 (2001).

Translated by L. Man

Crystallography Reports, Vol. 48, No. 4, 2003, pp. 714–715. Translated from Kristallografiya, Vol. 48, No. 4, 2003, pp. 767–768.

INFORMATION

Review:
O. V. Frank-Kamenetskaya and I. V. Rozhdestvenskaya, *Atomic Defects and the Crystal Structure of Minerals*

Kosmosinform, Moscow, 2001; Advances in Science and Technique, Ser.: Crystal Chemistry, 2002, vol. 33

Success in the investigation of the real structure of crystalline materials achieved in the latter half of the last century gave us an insight into many of its properties and was useful for specialists in various fields of knowledge (physics, chemistry, materials science, geology, etc.). This high-priority problem is the subject of the monograph under review, which is the result of many year's work by the authors, who are well-known structure researchers and representatives of the St. Petersburg school of crystallography. The founder of this school was Viktor Al'bertovich Frank-Kamenetskiĭ, who was one of the first to look into the problem of the crystal imperfection of minerals.

O.V. Frank-Kamenetskaya and I.V. Rozhdestvenskaya investigated crystal structures of various natural and synthetic inorganic compounds (mainly minerals). Each structural group studied is widely represented by compounds of different composition, which allows one to understand the general laws that determine its real structure. Invoking the results of Russian and foreign crystallographers (the list of references contains 363 works), the authors distinguish three main symmetry-based types of crystal structures of solid solutions. Their nomenclature, ways of description, and the possibilities for diagnostics from diffraction patterns are considered, and the conclusion is drawn that the tendency to polymorphism is characteristic of real crystal structures.

In the first chapter of the book, a brief but thorough account of the current view of the defects of different dimensions in inorganic crystals and their diagnostics based on diffraction patterns is presented. The chemical inhomogeneity (impurity atoms, vacancies, and nonstoichiometry) and accompanying phenomena (short-range and long-range order, distortion of average structure, symmetry of disturbance, and symmetry of disturbed structure) are considered. The possibility and unambiguity of identification of the type of atomic defects from the specific features of diffraction patterns are analyzed. Special attention is given to the symmetry or quasi-symmetry of the defect structures, which often allows them to be solved by classical methods of structural analysis. It is shown that these methods are unsuitable for some defect types, for example, modulated incommensurate composite structures. In this case, special programs for crystal space dimensions larger than three are used. In addition, a large group of crystal structures in which the defect distribution is described only by statistical methods is considered.

A separate chapter is concerned with the procedure applied to the studies of chemically inhomogeneous crystals. The authors made a substantial contribution to the solution of this complex problem of the X-ray structure analysis of real single crystals with their studies of both the mixed occupancy of crystallographic positions and quasi-homogeneous irregular mixed-layer structures using probabilistic–statistical methods.

The requirements for the accuracy of measurement of the intensities of diffraction reflections in defect crystals are more stringent compared to those in the studies of ordered objects. It should be emphasized that the results of structural investigations should correlate with the data of chemical analysis. The most rational sequence of stages for the least-squares refinement of the mixed occupancy of atomic positions, which allows the highest accuracy of results, is proposed. For example, different angular ranges of scattering curves are used at different stages of refinement. The possibilities of the Fourier method are also discussed. Application of this method to precise diffraction data allows us to reveal not only deviations from specified positions but also new positions of impurity atoms and to correct the occupancies specified earlier.

The book contains a detailed description of the principles of application of the probabilistic–statistical model of irregular mixed-layer structures, which allow one to calculate intensities by the trial-and-error method with special programs based on Markov statistics and to achieve the best fit of the calculated values to the experiment. This procedure was successfully used in powder diffraction analysis of mixed-layer clay minerals. The prospects for using this method for single-crystal studies is shown. Unfortunately, this methodology has practically not been used in Russian and foreign studies of crystal structures with two-dimensional defects.

1063-7745/03/4804-0714$24.00

In the subsequent five chapters, the specific results of the structural investigations performed by the authors for different groups of natural and synthetic inorganic crystalline compounds (oxides, silicates, fluorides, and sulfides) are summarized. Using these compounds as an example, the characteristic features (chemical deformations, dissymmetrization, cluster formation, the occurrence of superperiods, and the formation of irregular mixed layers) of each of the three types of real structures are considered. A new module-based structural classification is proposed for sulfides that are built of two types of tetrahedra that differ in orientation.

In conclusion, it should be noted that O.V. Frank-Kamenetskaya and I.V. Rozhdestvenskaya's book summarizes the latest achievements in the rapidly developing science of the real structure of crystalline materials and methods of researching them. The book is of interest both to specialists in the field of crystal structure and properties and to students and postgraduates specializing in this subject.

N.I. Organova

Translated by I. Polyakova